Huaguang Zhang
Amir Hussain
Derong Liu
Zhanshan Wang (Eds.)

LNAI 7366

Advances in Brain Inspired Cognitive Systems

5th International Conference, BICS 2012
Shenyang, China, July 2012
Proceedings

Springer

Lecture Notes in Artificial Intelligence 7366

Subseries of Lecture Notes in Computer Science

LNAI Series Editors

LNAI Founding Series Editor

Huaguang Zhang   Amir Hussain   Derong Liu
Zhanshan Wang (Eds.)

Advances in Brain Inspired Cognitive Systems

5th International Conference, BICS 2012
Shenyang, China, July 11-14, 2012
Proceedings

Springer

Volume Editors

Huaguang Zhang
Zhanshan Wang
Northeastern University
College of Information Science and Engineering
Shenyang 110004, P.R. China
E-mail: zhanghuaguang@mail.neu.edu.cn; zhanshan_wang@163.com

Amir Hussain
University of Stirling
Dept. of Computing Science and Mathematics
Stirling FK9 4LA, Scotland, UK
E-mail: ahu@cs.stir.ac.uk

Derong Liu
Institute of Automation, Chinese Academy of Sciences
State Key Laboratory of Managment and Control for Complex Systems
Beijing 100190, P.R. China
E-mail: derong.liu@ia.ac.cn

ISSN 0302-9743 e-ISSN 1611-3349
ISBN 978-3-642-31560-2 e-ISBN 978-3-642-31561-9
DOI 10.1007/978-3-642-31561-9
Springer Heidelberg Dordrecht London New York

Library of Congress Control Number: 2012940661

CR Subject Classification (1998): I.2.11, I.2, H.3, I.4, H.4, F.1, F.2.2, I.5

LNCS Sublibrary: SL 7 – Artificial Intelligence

Typesetting: Camera-ready by author, data conversion by Scientific Publishing Services, Chennai, India

Printed on acid-free paper

Springer is part of Springer Science+Business Media (www.springer.com)

Preface

BICS 2012—the 5th International Conference on Brain-Inspired Cognitive Systems—was held in Shenyang, China, as a sequel of BICS 2004 (Stirling, Scotland, UK), BICS 2006 (Lesvos, Greece), BICS 2008 (Sao Luis, Brazil), and BICS 2010 (Madrid, Spain). BICS has now become a well-established conference series on brain-inspired cognitive systems around the world, with growing popularity and increasing quality. As the biggest city in northeastern China, Shenyang is now an important political, industrial, and cultural center, and serves as the transportation and commercial hub of northeastern China. All participants of BICS 2012 had a technically rewarding experience as well as memorable experiences in this great city.

This book constitutes the proceedings of BICS 2012. The conference aimsed to provide a high-level international forum for scientists, engineers, and educators to present the state of the art of brain-inspired cognitive systems research and applications in diverse fields. The conference featured plenary lectures given by world-renowned scholars, regular sessions with broad coverage, and some special sessions focusing on popular and timely topics.

The conference received a total of 116 submissions from more than 200 authors in 19 countries and regions across four continents. Based on rigorous reviews by the Program Committee members and reviewers, 46 high-quality papers were selected for publication in the conference proceedings. We would like to express our sincere gratitude to all reviewers of BICS 2012 for the time and effort they generously gave to the conference. We are very grateful to the Institute of Automation of the Chinese Academy of Sciences, the University of Stirling, the Chinese University of Hong Kong, the University of Illinois at Chicago, and the National Natural Science Foundation of China for their financial support. We would also like to thank the publisher, Springer, for cooperation in publishing the proceedings in the prestigious series of *Lecture Notes in Artificial Intelligence*.

Huaguang Zhang
Amir Hussain
Derong Liu
Zhanshan Wang

BICS 2012 Organization

General Chair

Derong Liu, China

Advisory Committee Chairs

Ruwei Dai, China
Aike Guo, China

Steering Committee Chair

Huaguang Zhang, China

Organizing Committee Chairs

Bhaskar DasGupta, USA
Jun Wang, Hong Kong

Program Chairs

Amir Hussain, UK
Robert Kozma, USA
Leslie Smith, UK
Liang Zhao, Brazil

Plenary Sessions Chair

Marios Polycarpou, Cyprus

Special Sessions Chairs

Sanqing Hu, China
Stefano Squartini, Italy

Finance Chair

Dongbin Zhao, China

Publicity Chairs

Song Ci, USA
Qinglai Wei, China
Erik Cambria, Singapore

European Liaisons

John Taylor, UK
Anna Esposito, Italy
Mohamed Chetouani, France
Giacomo Indiveri, Switzerland
Stefan Wermter, Germany

Publications Chairs

Jinhu Lu, China
El-Sayed El-Alfy, Saudi Arabia
David Gamez, UK

Registrations Chair

Zeng-Guang Hou, China

Local Arrangements Chair

Zhanshan Wang, China

Electronic Review Chair

Tao Xiang, China

Conference Secretariat

Ding Wang, China

Program Committee

Yousef A. Alotaibi, Saudi Arabia
Shun-ichi Amari, Japan
Peter Andras, UK
Hughues Bersini, Belgium
John Bishop, UK
Roman Borisyuk, UK
Steven Bressler, USA
Fabricio Breve, Brazil
Erik Cambria, Singapore
Jordi Soléi Casals, Spain
Goutam Chakraborty, Japan
Zengqiang Chen, China
Mohamed Chetouani, France
Damien Coyle, UK

Table of Contents

Biologically Inspired Systems

Cognitive Neuroscience

Models of Consciousness

Neural Computation

COGPARSE: Brain-Inspired Knowledge-Driven Full Semantics Parsing

Radical Construction Grammar, Categories, Knowledge-Based Parsing & Representation

Daniel J. Olsher

Cognitive Science Program, Temasek Laboratories, National University of Singapore
dan@intmind.com

Abstract. Humans use semantics during parsing; so should computers. In contrast to phrase structure-based parsers, COGPARSE seeks to determine which meaning-bearing components are present in a text, using world knowledge and lexical semantics for construction grammar form selection, syntactic overlap processing, disambiguation, and confidence calculation. In a brain-inspired way, COGPARSE aligns parsing with the structure of the lexicon, providing a linguistic representation, parsing algorithm, associated linguistic theory, and preliminary metrics for evaluating parse quality. Given sufficient information on nuanced word and construction semantics, COGPARSE can also assemble detailed full-semantics meaning representations of input texts. Beyond the ability to determine which parses are most likely to be intended and to use knowledge in disambiguation, full-semantics parsing enables nuanced meaning representation, learning, summarization, natural language user interfaces, and the taking of action based on natural language input.

1 Towards a Next Generation of Brain-Inspired Parsers

COGPARSE is a natural language parsing framework combining semantics and world knowledge with syntax, demonstrating brain-inspired natural language processing (NLP) along the way. Its ultimate goal is to enable *full-semantics processing*, defined here as both 1) the generation of highly nuanced semantic representations from input texts and 2) the use of semantics to directly inform parsing.

COGPARSE offers a unique way of thinking about what parsing is and how it should be done. Instead of attempting to determine 'correct parses' grounded in phrase structures, COGPARSE discovers the meaning-bearing components present in a text, using lexical semantics and world knowledge for linguistic form selection, overlap detection, and disambiguation.

Viewing texts in terms of meaning-bearing components enables NLP systems to much more closely and easily align text spans with the meaning they contribute to the overall whole. It allows parsers to process text more like humans do (as modeled by cognitive linguistics), and to create systems that process inputs at the same level of syntactic and semantic granularity at which they were

H. Zhang et al. (Eds.): BICS 2012, LNAI 7366, pp. 1–11, 2012.

originally generated. Systems that better 'understand' what they are parsing can use this knowledge to improve outcomes; as an example, knowledge about what words mean allows COGPARSE to realize that certain words fit better into particular forms than others, aiding greatly in disambiguation.

When creating texts, language users select specific linguistic forms best conveying the meanings they wish to express. COGPARSE computes the semantic specificity of potential form matches during processing, enabling it to discover which candidate forms precisely match the semantics of the words within them (as these are most likely to be what the language user intended). This semantic disambiguation process is brain-inspired both in terms of how the process is implemented as well as through the observation that humans must undertake a similar process during comprehension. Despite ambiguities and multiple potential parses, humans typically only become aware of possibilities that are semantically sensible.

In COGPARSE, 'meaning-bearing components' are defined as *constructions*, or form-meaning pairings, (Goldberg 1995, 2003) and *lexical items* (words). Word and construction semantics can be encoded in a network-based representation formalism entitled INTELNET (Olsher 2011), intended to allow the representation of highly nuanced semantics and the construction of detailed meaning representations.

Generally speaking, the form, length and content of COGPARSE constructions are intended to be substantially the same as what is stored in the human lexicon and learned by language users, enabling the system to quickly move from form to meaning. Under such a design, syntax is structured such that meaning can be easily extracted, with required syntactic processing minimized as far as possible.

Syntactically, COGPARSE is based in a computational adaptation of Radical Construction Grammar (RCG) (Croft 2001) designed to rely strictly on *empirically-observable form-meaning pairings* and *cognitively-plausible categories*.

'Empirically-observable' means that no structural components (such as X-bar syntax, features, or noun phrases, etc.) are posited that cannot be explicitly induced from natural text data. Constructions are only posited when: 1) a specific group of semantic categories reoccurs frequently within natural texts, and 2) instances of these groupings possess reliable semantics conveying essentially the same overall meanings, each drawing on the same categories in similar ways.

'Cognitively-plausible categories' are those structured so as not to violate typical category constraints and attributes found in the psychological and cognitive linguistics literatures (Rosch (1976) being the prototypical example).

Instead of using parts of speech or phrase structure, COGPARSE syntactic restrictions are purely semantic and may be satisfied by any linguistic structure providing the proper semantics, from 'a car' to 'incredibly interesting moon vehicles covered in silvery paint', both of which have the semantics of {vehicle} and are parsed as such by the COGPARSE algorithm. The parser does not know whether a given lexical item is a noun phrase or an adjective, etc. - and, arguably, this is as it should be; in full-semantics systems, questions of structure should always be pre-empted by questions of meaning.

In this vein, COGPARSE explicitly supports RCG's rejection of part-of-speech (POS) tags. Beyond the difficulties so ably laid out in the cognitive linguistics literature, POS tags are often found to be identical across multiple linguistic forms, meaning that questions of which syntactic structures should be identified and how those structures should combine during the generation of meaning representations *can only be answered via reference to the meaning of the words used within those structures.* When choosing among structures, making the correct choice is essential as each possesses its own unique, highly idiosyncratic semantics. This phenomenon is pervasive in natural language, and it can be stated generally that in nuanced full-semantics applications, *accurate parsing always requires access to semantics.*

A unique COGPARSE capability is the ability to produce nuanced sentence meaning representations, combining both syntactic and word semantics, by 'piecing together' the semantics attached to both words and constructions. In order to enable this, each construction must be provided with an INTELNET network specifying its overall semantics and the ways in which each of its slots contributes to those semantics. Similarly, each word must be provided with an INTELNET network representing its own unique semantics across its various senses. Word sense disambiguation can be facilitated through use of the semantic information available in lexical items and slot prototypes.

Shifting from phrase structure to construction grammar as adapted here brings a multitude of benefits. Many natural-language processing tasks can be accomplished by looking at the types of constructions that are present in a text, the polarity and nature of actions and requests, people and objects that are mentioned, and so on. High-priority communications can be identified through the presence of certain construction classes or human participants, allowing for automatic sorting and dispatch of time- or otherwise-sensitive material.

The highly semantically-specific constructions found in COGPARSE allow for quick retrieval of the 'gist' of a text and can often recover significant meaning even if phrase structure is garbled or incomplete. Constructions only require minimal regions of correct grammar in order to extract meaning, allowing for successful inference upon texts that other parsers may simply be unable to process at all.

As COGPARSE immediately obtains a meaning representation after text analysis, it can act as a base for natural language interfaces. Because semantic information is used during construction selection and disambiguation, and output only results when successful semantic matches are made, COGPARSE output can be reasonably expected *a priori* to paint a usefully accurate picture of user intentions.

COGPARSE also enables learning; thanks to high semantic specificity, if a specific construction is identified in text the system can confidently assume that the information located within that construction will be of a specific form and type and can therefore be entered directly into a knowledge base.

2 Underlying Linguistic Theory

Every natural language parser must draw upon linguistic theory, especially with respect to the structure and nature of syntax (and of semantics in the case of parsers dealing with this aspect). COGPARSE's combined semantic and syntactic model is adapted from Radical Construction Grammar, chosen for its cognitive and linguistic plausibility, parsimony, and compatibility with brain sciences and cognitive linguistics.

RCG as adapted in COGPARSE views human language structure as composed of *constructions*, defined as ordered tuples of slots. Each slot can contain only a) an exact (fixed) *lexical item* or b) a *category*. While slot categories may have some semantic similarity to those typically found in knowledge bases (especially at the Roschian 'basic level') the specific semantic categories used in construction slots ultimately are construction-specific. These categories expressly do not correspond to parts of speech or phrase structure constructs: *they are semantic, not syntactic*. Generally speaking, the identification and learning of such categories constitutes a significant part of the language learning task, providing a meaningful source of cross-language incommensurability (and untranslatability).

Slot categories are defined through *prototypes* such as {things that are hard to obtain} or {sentient} - concepts whose semantics form the center of a semantic field. Categories and prototypes can be stored in any knowledge base capable of calculating degree of membership of a particular item given a category prototype. COGPARSE defines an algorithm for performing this calculation within the Scone (Fahlman 2010) knowledge base system.

Each COGPARSE construction has an *overall semantic type*, intended to summarize the unique semantics expressed by that construction. As an example, the construction *[<action> <object>]* (which could be instantiated as 'push the door', for example) has an overall type of {action}, as this best reflects the gist of the construction taken as a whole. In this construction, amongst all semantic elements (individual slots plus the unique meaning conveyed by the construction itself), the action-related semantics dominate. See sections 2.1 and 2.2 below for more information on how overall semantic types are used and generated.

2.1 Construction Overlaps / Semantic Overlap Disambiguation

COGPARSE offers full, efficient support for unlimited overlaps of constructions within one another. This is critical because constructions are nested by their very nature (cf. Croft); even short texts can be best understood as sets of nested constructions. COGPARSE mandates that each construction have an overall semantic type so that the parser can *intelligently handle overlaps by only positing overlap in cases where semantic specifications match sufficiently* (i.e. where the potential overlap 'makes sense').

An example of this would be the text "open the refrigerator door", within which there are three constructions:

1. *[<action> <concrete-object>]*
   (where <concrete-object> refers to something tangible)
2. *[the <object>]*
3. *[<complex-object> <part-of-complex-object>]*
   (where <complex-object> refers to an object having multiple salient parts)

The overall semantic type of each construction above would be set as follows in the parser lexicon: 1. {action}, 2. Semantic Passthrough (through the <object> slot - see section 2.2 below), and 3. {concrete-object}.

During matching, when construction 3 is identified as matching the text "refrigerator door", the overall type of this construction, {concrete-object}, fits the <object> slot in construction 2, so composing construction 2 and construction 3 allows a larger match to be made across the text span "the refrigerator door".

Via the passthrough mechanism (section 2.2 below) the overall semantic type of construction 2 becomes the same as whatever happens to be filling its <object> slot (here "refrigerator door"-a {concrete-object}). This then matches the <concrete-object> slot in construction 1, which also matches 'open' and thus, via overlaps, is able to match the entire text "open the refrigerator door".

A key feature of COGPARSE is the use of semantics to constrain overlap processing; without this, the parser would confront an immense number of possible permutations in which one construction could potentially fill another construction's slots. Such semantic disambiguation is highly cognitively realistic, paralleling that which must ultimately be performed by human language processors who must also seek to limit the search space of possible form-meaning pairings.

Overlap functionality allows the construction corpus to contain shorter but more powerful constructions, easing corpus development, reducing overall complexity, and increasing the range of coverage of the parser. Shorter constructions are also generally easier to furnish with accurate semantic descriptions.

When multiple short constructions are combined with one another, accurate semantic representations reflecting nuances intended by the speaker can be created by joining the INTELNET graphs of each construction and the lexical items that fill them. During this process, individual lexical items contribute semantics not only to the constructions they are most proximally located within, but also to each construction they participate in via the overlap mechanism.

2.2 Passthrough Slots: Runtime Determination of Semantic Type

In some cases, the overall semantics of a construction may depend more on the lexical items that actually fill a construction's slots when it is instantiated than on the construction itself. In these instances, COGPARSE supports runtime determination of construction overall semantics through *passthrough slots.*

An excellent example is the construction *[the <object>]*, where the overall semantics of the filled-in construction are best determined by reference to whatever happens to fill the construction's <object> slot. For example, the text "the dog" should have the overall semantics of "dog", and "the problem" the overall semantics of "problem".

The passthrough mechanism allows for a lexicon under which long stretches of text can be composed of smaller constructions, each of which is able to properly compute its own semantics (and thus which slots it may fill) at runtime.

Passthrough constructions as initially implemented here are 'strict' in the sense that if a construction has a passthrough slot it may not concurrently possess specific overall semantics of its own (i.e. its semantics are completely 'replaced' with those of the item in the passthrough slot).

2.3 Semantic Construction Disambiguation

Often, there are multiple possible constructions that could cover a certain portion of text, but the words found in the text being processed will only be semantically compatible with some of them, and to different degrees. Choosing the right constructions under such circumstances is vital, however, because each option may have significantly different semantics attached. Given that language users select constructions to convey as closely as possible the semantics they wish to communicate, an accurate full-semantics parser must be able to disambiguate as wisely as possible.

Among other examples, semantic disambiguation is required when processing sets of related constructions otherwise indistinguishable from one another via part of speech tags. A good example is the *[holy <object>]* set, wherein objects like "book", "water", "man", "woman" (things reasonably associated with religion) are part of one (straightforward) construction, and almost anything else is part of a completely different construction used to add emphasis in informal English. In this case, COGPARSE must consider the semantics of the filler of the <object> slot to determine which of these two constructions is the best fit. In some cases, parsing algorithms may also need to consider the semantic context within which a given usage occurs.

Another excellent example is *[<action> <object> off <surface>]* (i.e. "sneeze the napkin off the table") (Goldberg 1995), wherein active actions like "push" and "pull" point to a literal construction involving a 'pusher' and 'pushee', and actions like "sneeze" or "kick" suggest a different, indirect, action sequence. In both of the above cases, semantics are required to disambiguate between multiple constructions otherwise capable of matching the input text.

During processing, the COGPARSE algorithm performs disambiguation at the syntactic level by only matching constructions where potential slot fillers meet the semantic requirements of slot category prototypes. In cases where this level of combined semantic and syntactic disambiguation may be insufficient, the use of pre-existing semantics and world knowledge allows for the development of further disambiguation strategies.

3 Technical Realization: Parser Structure and Operation

COGPARSE requires: 1) a corpus of constructions, 2) sufficient world knowledge for calculating degree of category membership of lexical items, and (optionally) 3) INTELNET network fragments describing the idiosyncratic semantics of constructions and lexical items. When provided, INTELNET fragments allow nuanced per-sentence semantic representations to be produced.

In place of a parse tree, the parser returns a series of *paths*, each of which indicates one construction match over one span of text. In the case of overlaps, paths act as slot fillers within other paths. Only those construction matches meeting all semantic restrictions will be identified by the parser, thus avoiding spurious matches and providing semantic sensitivity. Generally, one large construction will tend to span each sentence, with all other components overlapped within that construction.

COGPARSE semantic representations are currently produced on a sentence-by-sentence basis; the parser benefits from the fact that the various elements of a particular sentence tend to demonstrate high semantic coherence. This coherence makes it easier to connect word and construction semantics together under the assumption that the various components of a sentence have been intended by the speaker to 'work together' to generate a unified meaning.

In terms of input formats, the present implementation only requires that: 1) something called a 'word' be identifiable in a text, and 2) that 'words' be separated from one another. While more or less trivial in English, these requirements may be more difficult to meet in the case of highly inflected or agglutinative languages. The current COGPARSE implementation is ideal for processing English, Mandarin Chinese, and other analytic/isolating languages, and can be readily adapted to handle many new scenarios. Agglutinative morphology, for example, can be implemented through specialized within-word constructions. Use of fixed-length-representation Unicode is fully acceptable in COGPARSE, requiring no special adaptations.

3.1 Parser Technical Definitions

Construction

Form-meaning pairing with two mandatory elements:

1. Slot List: Ordered tuple. Each element must be a *Construction Slot* drawn from the set of *Valid Slot Types.*
2. *Construction Semantic Category Prototype Spec* (defined next).

Construction Semantic Category Prototype Spec

A *Semantic Category Prototype* representing the overall semantic type of the construction itself, or a *Passthrough Slot Indicator* marking construction semantics as being determined by slot contents at runtime.

Semantic Category Prototype

Knowledge base element defining the center of a semantic field (grouping of related items). Used to determine whether or not item semantics fall within a particular category.

Construction Slot

An 'opening' or 'space' in a construction capable of accepting a word or overlapped construction; filled by a *Construction Slot Filler.*

Construction Slot Filler

A lexical item or overlapped construction.

Valid Slot Types
One of: a) Fixed lexical item (must match exactly), b) *Semantic Category Prototype* indicating potential slot fillers, c) Function, evaluated at parsing time, determining whether a word matches a slot (used for implementing complex functions on knowledge), or d) Passthrough slot indicator with slot *Semantic Category Prototype*.

Idiosyncratic Construction Meaning INTELNET Fragment
Graph segment in the INTELNET formalism, representing semantics unique to a construction (idiosyncratic semantics) and containing pointers to where information about slot filler contents may be inserted at runtime.

3.2 COGPARSE Parsing Algorithm

1. Matrix Creation
Create a match matrix as follows:

Columns: Slots of each construction in the order they are present within constructions (i.e. CONST**1**-SLOT**1**, CONST**1**-SLOT**2**, CONST**2**-SLOT**1**, and so on.) Construction order is unimportant, as long as slots are in the proper order within each construction.

Rows: Words from the input text (in order).

2. Marking of Semantically Compatible Slot Fillers
Examine each construction slot to determine which input words are semantically capable of filling them. If word X can fill slot Y semantically, mark True in matrix cell [X,Y].

3. Locating Matches in Match Matrix (Finding Diagonals)
Locate construction matches by identifying uninterrupted diagonals spanning any particular construction's first to last slots.

4. Overlap Detection and Processing
Overlay constructions found in the previous step on top of all slots they can fill within the matrix (taking overall semantic prototypes into account). Run Step 3 again. Repeat until all overlaps are found.

5. Best Path Identification
Return all construction matches found, choosing one particular parse ('path') as the 'best'. Metrics (described in section 3.3 below) are used to determine which parse is best; this parse will be reported in results and used in the semantic compositing process below.

6. Final Semantic Composition (Optional)
If necessary *Idiosyncratic Construction Meaning INTELNET Fragments* have been provided, generate a combined meaning representation (covering both words and constructions) via composition of the INTELNET networks for each construction and lexical item.

3.3 Construction 'Best Path' Metrics and Confidence/Quality Scoring

Even after categorical semantic restrictions are applied, multiple sets of constructions may remain capable of matching certain spans of text. In addition to further contextualized semantic analysis, the following metrics can be employed to help choose among various match possibilities and determine parse confidence and quality; higher values are better.

The first metric, *match length proportion*, is calculated as follows:

$$\frac{Words\ covered\ by\ current\ construction}{Words\ covered\ by\ construction\ with\ maximum\ coverage} \tag{1}$$

In general, constructions that start earlier on in a text and cover more words should be privileged over those that start later and/or cover less.

The following three metrics implement the intuition that increased semantic specificity in matched slot fillers and construction prototypes suggests better alignment of 1) the corpus and 2) a construction match with the overt and speaker-intended semantics of the input text:

$$\frac{\sum Specificity\ of\ Each\ \ Construction\ Overall\ Semantics\ Prototype}{Number\ of\ Overall\ Semantic\ Prototypes\ In\ Construction} \tag{2}$$

$$\frac{\sum Specificity\ of\ Each\ Construction\ Slot\ Prototype}{Number\ of\ Slots\ In\ Construction} \tag{3}$$

Metric (3) suggests that constructions with more specific slot prototypes should be preferred over those with more general prototypes.

$$\frac{\sum Specificity\ of\ Each\ Construction\ Slot\ Filler}{Number\ of\ Slots\ In\ Construction} \tag{4}$$

Metric (4) considers the words present in the text of filled constructions.

In the above metrics, slot fillers must be mapped to knowledge base elements (concepts), the semantic specificity of which is calculated as follows:

$$Specificity = \begin{cases} 0 & \text{if element not in knowledge base (KB)} \\ 0 & \text{if English article or function word} \\ 1 & \text{if no children below this node in KB} \\ 1 - \frac{|element\ children|}{|total\ elements|} & \text{otherwise.} \end{cases} \tag{5}$$

Only relative specificity differences between constructions are important.

A rough parser confidence measure can be obtained by looking at how much better the 'best' parse is than the other parses that were found; higher deltas suggest parses with semantics especially well-tailored to the input.

$$Confidence = \frac{highest\ metric\ sum - next\ highest\ metric\ sum}{highest\ metric\ sum} \tag{6}$$

The following rough quality measure draws on the intuition that very low word coverage and/or confidence measures are cause for concern, but, as they grow, become exponentially more indicative of good parser performance.

$$Quality = Moderate(\frac{\#\ of\ words\ covered}{total\ input\ words}, 12^{\dagger})Moderate(Confidence, 16^{\dagger}) \tag{7}$$

where the Moderate function is defined as follows:

$$Moderate(Ratio, Rate) = 1 - exp(-Rate \cdot Ratio) + (Ratio \cdot exp(-Rate)) \tag{8}$$

Ratio: [0-1], signifying the proportion by which a certain metric has been met.
Rate: Most usefully [0-20], determining rate by which Ratios become exponentially more valuable as they increase.

Both Rate constants (marked with † above) should be considered as rough indicators only, suggesting that low confidence is somewhat more impactful when determining quality than is low word coverage.

4 Conclusion

The confluence between world knowledge and construction grammars represents the 'royal road' to the next level in brain-inspired full-semantics language processing. COGPARSE represents a platform for research in cognitively-realistic language processing, nuanced AI knowledge representation, gisting, learning, and natural language computer interfaces.

Other future directions include research into the proper role of semantics within language processing and models of emotional (Cambria and Hussein 2012) and psychological content embedded within natural language texts.

Acknowledgments. The author wishes to thank Scott Fahlman for his detailed comments and support in funding and allowing for the creation of this work. Warmest thanks go also to Joshua Tan for his unwavering support.

This work was performed while at Carnegie Mellon University; from 2003 through 2008 this work was supported in part by the United States Defense Advanced Research Projects Agency (DARPA) under contract numbers NBCHD030010 and FA8750-07-D-0185. Any opinions, findings and conclusions or recommendations expressed in this material are those of the author and do not necessarily reflect the views of DARPA or other sponsors.

References

Cambria, E., Hussain, A.: Sentic Computing: Techniques, Tools, and Applications. Springer, Heidelberg (2012)

Croft, W.: Radical Construction Grammar: Syntactic Theory in Typological Perspective. Oxford University Press, Oxford (2001)

Fahlman, S.: The Scone Knowledge Base, http://www.cs.cmu.edu/~sef/scone/

Goldberg, A.: Constructions: A New Theoretical Approach to Language. TRENDS in Cognitive Sciences 7(5), 219–224 (2003)

Goldberg, A.: Constructions: A Construction Grammar Approach to Argument Structure. University of Chicago Press, Chicago (1995)

Olsher, D.: The INTELNET Knowledge Representation Formalism. Unpublished working paper (2011)

Rosch, E., Mervis, C., Gray, W., Johnson, D., Boyes-Braem, P.: Basic Objects In Natural Categories. Cognitive Psychology 8, 382–439 (1976)

Sentic Neural Networks: A Novel Cognitive Model for Affective Common Sense Reasoning

Thomas Mazzocco[1], Erik Cambria[2], Amir Hussain[1], and Qiu-Feng Wang[3]

[1] Dept. of Computing Science and Mathematics, University of Stirling, FK9 4LA, UK
{tma,ahu}cs.stir.ac.uk
[2] Temasek Laboratories, National University of Singapore, 117411, Singapore
cambria@nus.edu.sg
[3] National Laboratory of Pattern Recognition, Chinese Academy of Sciences, 100190, P.R. China
wangqf@nlpr.ia.ac.cn
http://sentic.net

Abstract. In human cognition, the capacity to reason and make decisions is strictly dependent on our common sense knowledge about the world and our inner emotional states: we call this ability affective common sense reasoning. In previous works, graph mining and multi-dimensionality reduction techniques have been employed in attempt to emulate such a process and, hence, to semantically and affectively analyze natural language text. In this work, we exploit a novel cognitive model based on the combined use of principal component analysis and artificial neural networks to perform reasoning on a knowledge base obtained by merging a graph representation of common sense with a linguistic resource for the lexical representation of affect. Results show a noticeable improvement in emotion recognition from natural language text and pave the way for more bio-inspired approaches to the emulation of affective common sense reasoning.

Keywords: AI, NLP, Neural Networks, Cognitive Modeling, Sentic Computing.

1 Introduction

Emotions are intrinsically part of our mental activity and play a key role in decision-making and cognitive communication processes. They are special states, shaped by natural selection, to adjust various aspects of our organism in order to make it better face particular situations, e.g., anger evolved for reaction, fear evolved for protection, and affection evolved for reproduction. Therefore, we cannot prescind from emotions in the development of intelligent systems: if we want computers to be really intelligent, we need to give them the ability to recognize, understand, and express emotions.

In the past, graph mining techniques and multi-dimensionality reduction techniques [1] have been employed on a knowledge base obtained by blending ConceptNet, a directed graph representation of common sense knowledge [2], with WordNet-Affect (WNA), a linguistic resource for the lexical representation of affect [3]. In this work, we exploit a novel cognitive model based on the combined use of principal component analysis (PCA) and artificial neural networks (ANNs) on the same knowledge

H. Zhang et al. (Eds.): BICS 2012, LNAI 7366, pp. 12–21, 2012.

base. Results demonstrate noticeable enhancements in emotion recognition from natural language text with respect to previously adopted strategies and pave the way for future development of more biologically inspired approaches to the emulation of affective common sense reasoning. The rest of this paper is organized as follows: section 2 describes the research background; section 3 illustrates the proposed model in detail; section 4 presents a description of the results; finally section 5 offers some concluding remarks and future work recommendations.

2 Background

Existing approaches to affect recognition from natural language text can be grouped into three main categories: keyword spotting, in which text is classified into categories based on the presence of fairly unambiguous affect words [4,5,6], lexical affinity, which assigns arbitrary words a probabilistic affinity for a particular emotion [7,8], and statistical methods, which calculate the valence of affective keywords, punctuation and word co-occurrence frequencies on the base of a large training corpus [9,10].

Our proposed alternative approach aims to focus on emulating the human reasoning process. The motivation is to enable machines to represent knowledge and perform reasoning in many different ways so that, whenever they reach a dead end, they can switch among different points of view and find one that may work. To bridge the cognitive and affective gap between 'word-level' natural language data and the 'concept-level' opinions and sentiments conveyed by them, we need more intelligent cognitive systems able to learn new affective common sense knowledge and perform reasoning on it [11].

2.1 The Hourglass of Emotions

Affect has been classified into six universal 'basic' categories or emotions, i.e., happiness, sadness, fear, anger, disgust and surprise [12]. Few tentative efforts to detect non-basic affective states, such as fatigue, anxiety, confusion or frustration, have been also made [13,14]. However, these categorical approaches classify emotions using a list of labels, failing to describe the complex range of emotions which can occur in daily communication. Unlike categorical approaches, the Hourglass model [15] is an affective categorization model which describes a number of affective states and intensities.

In this model, sentiments are organized around four independent but concomitant dimensions whose different levels of activation make up the total emotional state of the mind: each affective dimension is characterized by six levels of activation (measuring the strength of an emotion), termed 'sentic levels', which determine the intensity of the expressed/perceived emotion as an integer (ranging between -3 and 3 inclusive). These levels are also labelled as a set of 24 basic emotions [16], six for each of the affective dimensions. Mapping this space of possible emotions leads to an hourglass shape, as shown in Figure 1.

3 Methods

In this work, we investigate if an emulation of the biological neural system, represented by two ANNs, could outperform the state-of-the-art k-nearest neighbour (k-NN) clustering approach [17]. PCA is used to organize the space where concepts lie, and then an ANN is trained to recognize emotions based on the presented Hourglass model.

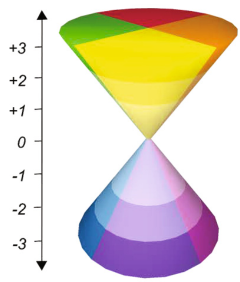

	Pleasantness	Attention	Sensitivity	Aptitude
+3	ecstasy	vigilance	rage	admiration
+2	joy	anticipation	anger	trust
+1	serenity	interest	annoyance	acceptance
0	—	—	—	—
-1	pensiveness	distraction	apprehension	boredom
-2	sadness	surprise	fear	disgust
-3	grief	amazement	terror	loathing

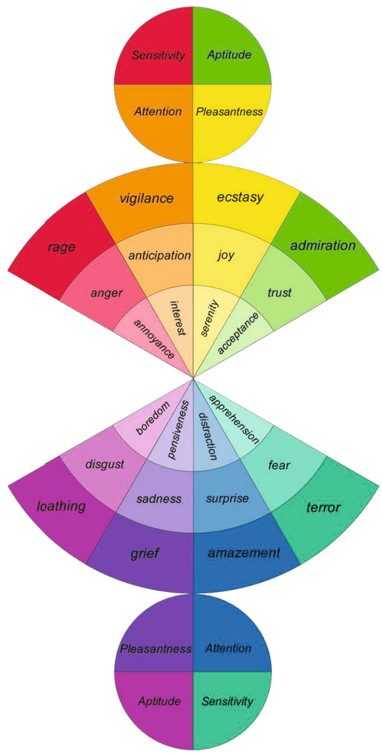

Fig. 1. Net of the Hourglass of Emotions

Contrary to any clustering algorithm, the emotion recognition task is independent from both concepts' absolute and relative positions in the vector space.

3.1 AffectiveSpace

AffectiveSpace [18] is a multi-dimensional vector space built by 'blending' [19] ConceptNet with WNA. Blending is a technique that allows simultaneous inference over multiple sources of data, taking advantage of the overlap between them: it combines linearly two matrices into a single one where the information between the two initial ones is shared. The result is a new matrix, A, in which common sense and affective knowledge coexist, where rows are concepts and columns are either common sense or affective features; the values in the matrix indicate truth values of assertions: to each concept is associated a vector of possible features whose values are positive for features that produce an assertion of positive valence, negative for features that produce an assertion of negative valence and zero when nothing is known about the assertion. The degree of similarity between two concepts is measured by the scalar product between their rows in A.

The value of the dot product is high when two concepts are described by the same features, and low when they are described by features that are negations of each other. For this reason, similarity between concepts depends primarily on the angle they make with the origin rather than on their absolute positions in the space. When we perform singular value decomposition (SVD) on a blended matrix, the result is that new connections are made in each source matrix taking into account information and connections present in the other matrix, originating from the information that overlaps. We then use truncated singular value decomposition (TSVD) [20] in order to obtain a new matrix containing both common sense and affective knowledge.

The resulting matrix has the form $\tilde{A} = U_k * \Sigma_k * V_k^T$ and is a low-rank approximation of A, the original data. This approximation is based on minimizing the Frobenius norm of the difference between A and $\tilde{A}$ under the constraint $rank(\tilde{A}) = k$. For the Eckart–Young theorem [21] it represents the best approximation of A in the least-square sense, that is:

$$\min_{\tilde{A}|rank(\tilde{A})=k} |A - \tilde{A}| = \min_{\tilde{A}|rank(\tilde{A})=k} |\Sigma - U^* \tilde{A} V| = \min_{\tilde{A}|rank(\tilde{A})=k} |\Sigma - S|$$

assuming that $\tilde{A}$ has the form $\tilde{A} = USV^*$, where S is diagonal. From the rank constraint, i.e., S has k non-zero diagonal entries, the minimum of the above statement is obtained as follows:

$$\min_{\tilde{A}|rank(\tilde{A})=k} |\Sigma - S| = \min_{s_i} \sqrt{\sum_{i=1}^{n} (\sigma_i - s_i)^2} =$$
$$= \min_{s_i} \sqrt{\sum_{i=1}^{k} (\sigma_i - s_i)^2 + \sum_{i=k+1}^{n} \sigma_i^2} = \sqrt{\sum_{i=k+1}^{n} \sigma_i^2}$$

Therefore, $\tilde{A}$ of rank k is the best approximation of A in the Frobenius norm sense when $\sigma_i = s_i$ $(i = 1, ..., k)$ and the corresponding singular vectors are the same as those of A. If we choose to discard all but the first 100 principal components, common sense concepts and emotions are represented by vectors of 100 coordinates: these coordinates can be seen as describing concepts in terms of 'eigenmoods' that form the axes of AffectiveSpace, i.e., the basis $e_1, ..., e_{100}$ of the vector space. Thus, by exploiting the information sharing property of TSVD, concepts with the same affective valence are likely to have similar features – that is, concepts conveying the same emotion tend to fall near each other in AffectiveSpace.

3.2 Experimental Data Description

We built a benchmark for affective common sense knowledge (BACK) by exploiting a corpus of 5,000 mood-tagged blogs from LiveJournal (LJ) [1], a virtual community that allow users to keep a blog, journal or diary and to label their posts with a mood label, by choosing from more than 130 predefined moods or by creating custom mood themes. In particular, we applied CF-IOF (concept frequency - inverse opinion frequency) [22] on the LJ corpus. CF-IOF is a technique that identifies common domain-dependent semantics in order to evaluate how important a concept is to a set of opinions concerning the same topic. Firstly, the frequency of a concept c for a given domain d is calculated by counting the occurrences of the concept c in the set of available d-tagged opinions and dividing the result by the sum of number of occurrences of all concepts in the set of opinions concerning d. This frequency is then multiplied by the logarithm of the inverse frequency of the concept in the whole collection of opinions, that is:

$$CF\text{-}IOF_{c,d} = \frac{n_{c,d}}{\sum_k n_{k,d}} \log \sum_k \frac{n_k}{n_c}$$

where $n_{c,d}$ is the number of occurrences of concept c in the set of opinions tagged as d, n_k is the total number of concept occurrences and n_c is the number of occurrences of c in the whole set of opinions. A high weight in CF-IOF is reached by a high concept frequency in a given domain and a low frequency of the concept in the whole collection of opinions. We exploited CF-IOF weighting to filter out common concepts in the LJ corpus and detect relevant mood-dependent semantics for each of the Hourglass sentic levels. The result was a benchmark of 689 affective concepts, which were screened by a number of English-speaking students who were asked to evaluate the level b associated to each concept $b \in \Theta = \{\theta \in \mathbb{Z} \mid -3 \leq \theta \leq 3\}$ (each integer corresponding to a level of the Hourglass model) for each of the four affective dimensions (i.e., Pleasantness, Attention, Sensitivity and Aptitude); the results obtained were averaged.

The idea behind sentic computing is to associate each concept (represented by an input vector on AffectiveSpace) an affective valence represented by an output vector $\mathbf{b} \in \Theta^4$ where each component is associated with one dimension of the Hourglass model. For proof of concept, in the next sections we will focus only on the dimension of Pleasantness, so that the task of the model being developed is to find the category b^* which best approximates the real category $b = f(\mathbf{a})$, $\mathbf{a}$ being a concept in AffectiveSpace. The distribution of affective classes in the used dataset is reported on Table 1.

3.3 Proposed Sentic Neural Networks: Design

The eventual aim of the proposed sentic neural networks (SNNs) developed in this study is to predict which class each concept belongs to (i.e., its level of affective valence in a specific dimension of the Hourglass model). Two different approaches may be adopted in order to set up an ANN: a 'discrete' approach (termed *SNN-D*) and a 'continuous' one (*SNN-C*). *SNN-D*, in particular, is expected to return seven different real-valued outputs $y_k \in [0, 1]$ for $k = 1, 2, ..., 7$, each showing the degree of belonging to a specified

[1] `http://livejournal.com`

Table 1. Distribution of concepts through Pleasantness dimension

Level	*Label*	*Freq.*
-3	Grief	99
-2	Sadness	71
-1	Pensiveness	79
0	Neutral	137
+1	Serenity	142
+2	Joy	126
+3	Ecstasy	35
	Total	**689**

affective level, while *SNN-C* provides a single real-valued output $y \in [-3, 3]$, corresponding to the best guess of the level of affective valence (assuming that categories are equispaced within the considered dimension).

In both cases, a further step is required in order to obtain a final classification output: for *SNN-D* the best selection strategy seems to be the choice of the class with the highest degree of belonging, while for *SNN-C* the easiest approach is to round off the output to get an integer corresponding to the class. Since the task of choosing from these two approaches is not easily solvable a priori, both approaches are adopted and compared in this study. Therefore, we have chosen to set up two multi-layer perceptron neural networks with three layers (one input layer, one hidden layer and one output layer). The input vector $\mathbf{x}_{(k)}$ is built so that $x_{(k)0} = 1$ (the 'bias node') and $\left[x_{(k)1}, x_{(k)2}, ..., x_{(k)100}\right] = \mathbf{a}_{(k)}$ for the k-th concept of our dataset. The target output is, for *SNN-D*, a vector $\mathbf{y}_{(k)}$ having $y_{(k)i} = 1$ if $b_{(k)} = i - 4$ and $y_{(k)i} = 0$ otherwise, for each $i = 1, 2, ..., 7$. On the other hand, for *SNN-C* the target output is a single value $y_{(k)} = b_{(k)}$. Let us assume that the hidden layer has H neurons; the input and the hidden layers are then linked by equation (1) where $w_{mn} \in \mathbf{W}$, that is the matrix of weights (of dimensions $H \times 101$) defined during the network training:

$$h_j = tanh\left(\sum_{i=0}^{100} w_{ji} x_i\right) \quad j = 1, 2, ..., H \tag{1}$$

The relationships between the hidden and the output layers are expressed in equations (2) and (3) for *SNN-D* and *SNN-C* respectively, where $v_{mn} \in \mathbf{V}$, which is a matrix of weights (of dimensions $7 \times H$) and $\mathbf{v}$ a vector of weights (of dimension H) built during the network training. The output is computed as follows:

$$y_j = tanh\left(\sum_{i=1}^{H} v_{ji} h_i\right) \quad j = 1, 2, ..., 7 \tag{2}$$

$$y = 3tanh\left(\mathbf{v}^{\mathbf{T}} \cdot \mathbf{h}\right) \tag{3}$$

It is worth noting that different choices of the activation functions, as well as other design choices, are possible; however, a definition of the best structure of the used neural networks besides being quite difficult to state (due to, for example, the dataset dependency) is beyond the scope of this study. Finally, further transformations of $\mathbf{y} \in \mathbb{R}^7 \mapsto b^* \in \Theta$ and $y \in \mathbb{R} \mapsto b^* \in \Theta$ are required. They are proposed in equations (4) and (5):

$$b^* = \mathbf{d^T} \cdot [-3, -2, -1, 0, +1, +2, +3] \tag{4}$$

$$b^* = round(y) \tag{5}$$

where $d_i = \delta_{i,m}$ for $i = 1, 2, ..., 7$, δ being the Kronecker's delta, $m = i \mid y_i = \max_j y_j$ and $round(x)$ a function $\mathbb{R} \mapsto \mathbb{Z}$ rounding x up to the closest integer.

The final structure of the two networks is depicted in Figure 2 and Figure 3.

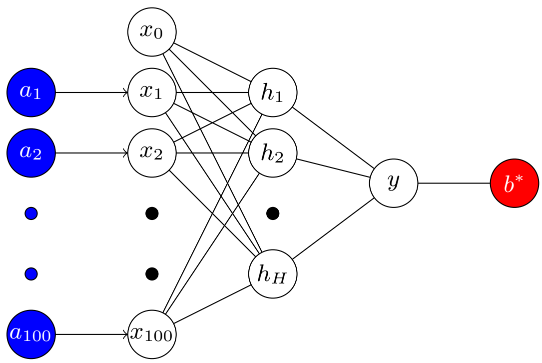

Fig. 2. *SNN-C* structure

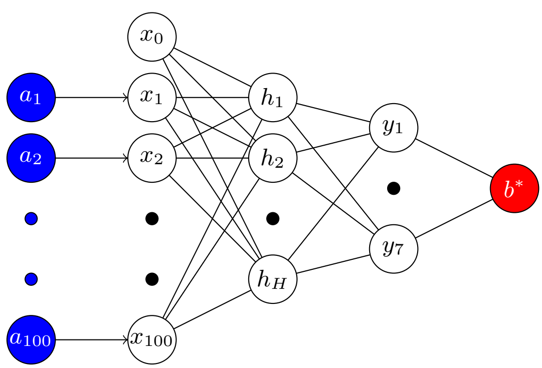

Fig. 3. *SNN-D* structure

The neural networks training is conducted using the gradient descent optimization algorithm with the inclusion of a momentum term, which has been proven to improve the algorithm speed of convergence [23]. The matrices (or vectors) of weights ($\mathbf{U}$) are then updated at each iteration τ according to equation (6), where $\mathbf{E}$ is calculated with

$e_j = b_j - b_j^*$ for the second layer of weights (where $j = 1, 2, ..., 7$ for *SNN-D* and $j = 1$ for *SNN-C*), and $e_j = \sum_k \frac{b^*_{j(\tau)}}{b^*_{j(\tau-1)}} u_{jk}$ for the first layer of weights respectively.

$$\Delta\mathbf{U}_{(\tau)} = -\nu\nabla\mathbf{E}(\mathbf{U}_{(\tau)}) + \mu\Delta\mathbf{U}_{(\tau-1)} \quad (6)$$

3.4 Experimental Setup

In order to evaluate the designed system on real-world data, we embedded the SNNs into a sentics extraction process, whose aim is to infer sentics (i.e., affective common sense information) from natural language text. In particular, we used a natural language processing (NLP) module to interpret all the affective valence indicators usually contained in text such as special punctuation, complete upper-case words, onomatopoeic repetitions, exclamation words, negations, degree adverbs and emoticons, and eventually lemmatize text. The Semantic Parser then deconstructs text into concepts using a lexicon based on 'sentic n-grams', i.e., sequences of lexemes which represent multiple-word common sense and affective concepts extracted from ConceptNet, WNA and other linguistic resources. This module also provides, for each retrieved concept, the relative frequency, valence and status, that is the concept's occurrence in the text, its positive or negative connotation and the degree of intensity with which the concept is expressed.

To avoid the risk of overfitting we adopted a cross-validation approach. The networks were trained 10 times (10-fold cross-validation), each of which excluded 10% of dataset entries that are used for evaluating the performance of the system; the excluded 10% is then cycled so that, at the end of all simulations, each dataset entry has been used exactly once to test the system. In order to evaluate the accuracy of the model, we considered the percentage of entries where $b^* = b$ ('strict accuracy'). However, since the used dataset can include noise and entries may incorporate a certain degree of subjectiveness, we relaxed this criterion by considering the accuracy of entries which have $|b^* - b| \leq 1$ ('relaxed accuracy').

4 Results

The results of the proposed SNNs are tabulated in Table 2 where they are compared with the state-of-the-art k-NN approach and a random classifier. A trial-and-error approach was adopted for the network parameters tuning: for *SNN-C* the best performance was obtained after 3 iterations (when the error stopped decreasing significantly) with $H = 10$, learning rate $\nu = 0.1$, momentum factor $\mu = 0.2$; for *SNN-D* the best set of parameters obtained were $H = 15$, $\nu = 0.05$, $\mu = 0.05$ with best performance reached after an average of 10 iterations.

As it can be seen from Table 2, the proposed sentic neural network approaches outperform the state of the art k-NN model, as well as the random classifier.

Both proposed models improved the 'relaxed accuracy' (with the *SNN-C* producing a considerable 10% performance improvement) while the *SNN-D* was able to outperform the benchmark for the 'strict accuracy' case.

Table 2. Performance comparison

	Strict acc.	Relaxed acc.
Random	14.3%	40.1%
k-NN	41.9%	72.3%
SNN-D	**43.8%**	76.2%
SNN-C	38.3%	**82.7%**

5 Conclusions and Future Work

With the advent of Web 2.0, the extraction of knowledge from the huge amount of available unstructured information – such as opinions and sentiments – derived from blog, wikis and social networks is a very arduous task. While existing approaches mainly work at a syntactic level, we employ computational techniques and tools to analyze text natural language at a semantic level: in particular, opinions and sentiments extracted from the Web are organized using AffectiveSpace, a multi-dimensional vector space for affective common sense reasoning.

The proposed SNNs, termed *SNN-C* and *SNN-D*, representing continuous and discrete valued outputs respectively, have embedded, for the first time in the AffectiveSpace, a bio-inspired way of reasoning to carry out cognitive tasks such as emotion recognition, demonstrating a significant performance improvement on real data – compared to both a standard random classifier as well as a state-of-the-art K-NN approach.

Since this study has shown promising results, further research is now planned to understand how artificial intelligence techniques can affectively analyze natural language text: structured data collection is planned to extend the BACK database, which will be made publicly available to enable comparison with other affective common sense reasoning models. This extended dataset will be exploited to assess how other state-of-the-art machine learning approaches could further improve the performance of the model, in order to select the best method for exploiting affective common sense knowledge databases and ultimately to improve affective common sense reasoning.

Acknowledgments. The work reported in this paper has also been supported by The Royal Society of Edinburgh (RSE) and The National Natural Science Foundation of China (NNSFC) joint-project (2010-12).

References

1. Cambria, E., Olsher, D., Kwok, K.: Sentic activation: A two-level affective common sense reasoning framework. In: AAAI, Toronto (2012)
2. Havasi, C., Speer, R., Alonso, J.: ConceptNet 3: A flexible, multilingual semantic network for common sense knowledge. In: RANLP, Borovets (2007)
3. Strapparava, C., Valitutti, A.: WordNet-Affect: An affective extension of WordNet. In: LREC, Lisbon (2004)
4. Nagano, S., Inaba, M., Kawamura, T.: Extracting semantic relations for mining of social data. In: SDoW 2010, Shanghai (2010)

5. Wiebe, J., Wilson, T., Cardie, C.: Annotating expressions of opinions and emotions in language. Language Resources and Evaluation 39(2), 165–210 (2005)
6. Elliott, C.D.: The Affective Reasoner: A Process Model of Emotions in a Multi-Agent System. PhD thesis, Northwestern University, Evanston (1992)
7. Somasundaran, S., Wiebe, J., Ruppenhofer, J.: Discourse level opinion interpretation. In: COLING, Manchester (2008)
8. Wilson, T., Wiebe, J., Hoffmann, P.: Recognizing contextual polarity in phrase-level sentiment analysis. In: HLT/EMNLP, Vancouver (2005)
9. Hu, M., Liu, B.: Mining opinion features in customer reviews. In: AAAI, San Jose (2004)
10. Goertzel, B., Silverman, K., Hartley, C., Bugaj, S., Ross, M.: The Baby Webmind project. In: AISB, Birmingham (2000)
11. Cambria, E., Hussain, A.: Sentic Computing: Techniques, Tools, and Applications. Springer, Heidelberg (2012)
12. Ekman, P., Dalgleish, T., Power, M.: Handbook of Cognition and Emotion. Wiley, Chichester (1999)
13. Kapoor, A., Burleson, W., Picard, R.: Automatic prediction of frustration. International Journal of Human-Computer Studies 65, 724–736 (2007)
14. Castellano, G., Kessous, L., Caridakis, G.: Multimodal emotion recognition from expressive faces, body gestures and speech. In: Doctoral Consortium of ACII, Lisbon (2007)
15. Cambria, E., Livingstone, A., Hussain, A.: The hourglass of emotions. In: Esposito, A., Vinciarelli, A., Hoffmann, R., Muller, V. (eds.) Cognitive Behavioral Systems. LNCS, Springer, Heidelberg (2012)
16. Plutchik, R.: The nature of emotions. American Scientist 89(4), 344–350 (2001)
17. Cambria, E., Benson, T., Eckl, C., Hussain, A.: Sentic PROMs: Application of sentic computing to the development of a novel unified framework for measuring health-care quality. Expert Systems with Applications 39(12), 10533–10543 (2012)
18. Cambria, E., Hussain, A., Havasi, C., Eckl, C.: AffectiveSpace: Blending common sense and affective knowledge to perform emotive reasoning. In: CAEPIA, Seville, pp. 32–41 (2009)
19. Havasi, C., Speer, R., Pustejovsky, J., Lieberman, H.: Digital intuition: Applying common sense using dimensionality reduction. IEEE Intelligent Systems 24(4), 24–35 (2009)
20. Wall, M., Rechtsteiner, A., Rocha, L.: Singular value decomposition and principal component analysis. In: Berrar, D., Dubitzky, W., Granzow, M. (eds.) A Practical Approach to Microarray Data Analysis, pp. 91–109. Springer (2003)
21. Eckart, C., Young, G.: The approximation of one matrix by another of lower rank. Psychometrika 1(3), 211–218 (1936)
22. Cambria, E., Hussain, A., Durrani, T., Havasi, C., Eckl, C., Munro, J.: Sentic computing for patient centered application. In: IEEE ICSP, Beijing, pp. 1279–1282 (2010)
23. Qian, N.: On the momentum term in gradient descent learning algorithms. Neural Networks 12, 145–151 (1999)

Individual Differences in Working Memory Capacity and Presence in Virtual Environments

Terry G. Rawlinson[1], Shulan Lu[2], and Patrick Coleman[3]

[1] Walters State Community College
[2] Texas A&M University-Commerce
[3] University of Toronto

Abstract. A major thrust in building intelligent systems is to encourage users to capitalize their existing real world non-digital skills and seamlessly integrate the representations users have built in real world activities with their ongoing interactions with computing systems. In virtual environments, studies have demonstrated that users treat virtual environments as if they were real even when the environments were a crude approximation to real environments. These results revealed that the feeling of presence is a fluid dynamic psychological state that could vary depending on individual users' characteristics. The current study aimed to investigate whether individual differences in working memory capacity impact the feelings of presence in virtual environments. Participants performed a vegetable cutting task on behalf of an avatar in a desktop virtual environment. Experiment 1 revealed that high working memory (HWM) individuals cut closer to the fingertip of the avatar than low working memory (LWM) individuals. Experiment 2 used eye-tracking measures and revealed that HWM participants mitigated the demonstrated risk by planning. Taken together, Experiments 1 and 2 provide evidence how individual differences in working memory capacity can impact the feelings of presence in virtual environments and demonstrated that our conscious experiences of what is real is malleable.

Keywords: presence, plausibility illusion, working memory capacity, eye-tracking, risk.

1 Introduction

In recent years, researchers have been very interested in building human computer interaction systems that could tap into users existing real world non-digital skills instead of requiring a totally different set of new interaction rules. For instance, many of the iPhone capabilities are successful examples of this context aware, reality-based computing movement [1]. However, different communities couch this idea in different terms. In virtual environments, the most important question has been how developers could leverage factors that enhance users physically transporting themselves to the computer-simulated environments and interact with the environments as if they were real.

H. Zhang et al. (Eds.): BICS 2012, LNAI 7366, pp. 22–30, 2012.

The concept of presence is central to the investigation of this question. The feelings of presence refer to a psychological state of being in the virtual environment, whereby behavior occurs similarly to everyday reality given similar circumstances [2]. For example, do users inflict potential injury upon an avatar knowing that the avatar cannot be truly injured? If users experience the feelings of presence, then users will not arbitrarily cut very close to the hand, which has greater chance of inflicting injuries in the corresponding real world. While many studies have focused on invoking presence by manipulating the fidelity of the virtual environment [3], few have considered human factors (endogenous) in interacting with such systems [4]. If presence is indeed a fluid psychological state, revealing individual differences in human capacity to demonstrate presence in virtual environments would appear to be an important area of investigation.

1.1 A Conceptual Framework for Presence

In further refining the terminology associated with the conceptualization of presence, Slater [5] has introduced the terms plausibility (Psi) and place illusion (PI) in a response-as-if-real (RAIR) framework for understanding of presence in virtual environments. Plausibility is the illusion that what is happening is real, whereas place illusion is the feeling of being in a place of virtual environment while knowing that it is not real. Researchers investigating presence have argued that experiments should include virtual environments where events and actions carried out by the system can be recorded by the system and participants are tracked to give a good idea of what they were looking at during the trial [6]. A majority of the studies have investigated the factors that promote place illusion. It is only until recently that attention has been given to plausibility. The realistic representations of events and actions that get updated upon user's bodily movements are hard to build. Place illusion can be more readily investigated using self-reported measures in conjunction with physiological measures, whereas plausibility calls for more real time behavioral measures.

1.2 Presence in the Current Experimental Task

In the current study, we sought to investigate presence by asking participants to control an avatar in performing a cutting vegetable task in a desktop virtual reality. More specifically, this study is concerned with plausibility, or the illusion that what is happening in the virtual environment is real (even though participants metacognitively know that it is not) [5]. For example, plausibility was measured in terms of how close to the avatar's finger (degree of risk) a cut is made in the current experimental task. If a participant demonstrated caution and planning when making cuts, a higher degree of plausibility was assumed. Alternatively, if the participant were to make cuts with greater risk taken and a lack of planning; a lower degree of plausibility was assumed. In the real world, many argue that there are no direct tangible consequences of taking on risks in virtual environments, and thus people are more willing to take risks. However, it is also equally hard to imagine that people will be conscious of such thoughts when performing tasks, as it could become very intrusive.

1.3 Working Memory Capacity as an Endogenous Factor

Working memory is a holding area in which humans manipulate information while thinking [7]. Working memory is a crucial construct of cognition and is related to moment-by-moment dispositions of body features such as eye movements [8]. Researchers have developed traditional, dual component (storage and processing components) span tasks aimed at measuring the capacity of one's working memory [9][10]. For example, one task used to measure individual differences in working memory capacity is the automated operations span (AOSPAN). The AOSPAN involves a 3-section practice component, followed by a problem screen displaying the math problem, next an answer screen with a true or false button, and finally a screen with a letter to be remembered.

Investigating individual differences in working memory capacity and presence in virtual environments requires a view that goes beyond conceiving the function of working memory strictly as storage. The executive attention theoretical perspective of working memory defines working memory capacity as attentional processes that allow for goal-directed behavior by maintaining relevant information in an active, easily accessible state outside of conscious focus, or to retrieve that information from inactive memory, under conditions of interference, distraction, or conflict [11].

In early studies of presence in virtual environments, two types of factors were proposed to impact presence: exogenous (technology based) and endogenous (participant dependent) [12]. While exogenous factors have received considerable focus in investigating presence, few studies have sought to investigate endogenous factors. In this paper, we argue that working memory capacity is indeed an important endogenous factor to consider in the extent to which humans can construct their own internal representations, or mental models of reality while in virtual environments.

The importance of working memory as an attentional, limited pool of cognitive resources needed to process the virtual environment, has been discussed in presence literature, but using a paradigm by which memory load is manipulated through integration of a virtual environment [13]. For example, participants remember a list of irrelevant items just before performing an experimental task, and then later recall the list of items. This manipulation comes at a cost when investigating presence. For example, in the present study participants were asked to perform the natural task of cutting a stalk of celery into multiple, equal pieces in a desktop virtual environment. If researchers had asked participants to hold an irrelevant list of items (e.g., shoe, desk, steel, cup, frame) while performing the natural task of cutting celery, it could have reminded the participant that they were indeed participating in an experiment, not the natural task of cutting a stalk of celery. Therefore, the current study aimed to immerse users as much as possible and see how much variability gets played in experiencing plausibility due to the cognitive abilities brought along by users.

1.4 Overview of the Current Study

Rather than manipulating working memory load through task integration in the virtual environment, the current investigation sought to reveal how individual differences in working memory capacity might impact presence. The task was designed such that as users internally thought about performing cuts onto the celery and controlled the avatar's hand performing the cutting via mouse movements, the external world played out this correspondingly. Creating such a synchrony is likely to foster a degree of immersion by participants [5]. A number of real time behavioral measures can be recorded in this task environment, which give us some access to what is going on in the conscious mind while the plausibility illusion is being created.

Our initial prediction concerning presence is that those experiencing the plausibility illusion would treat the task as if it were real by not cutting too close to the finger (demonstrating great risk to the avatar). Furthermore, HWM participants should be the most likely to demonstrate presence given their superior ability to maintain goal-directed behavior under conditions of distraction or conflict. In the case of presence and virtual environments, the conflict is between the illusion that what is happening is real and knowing that it is not. In the present study, two experiments were conducted to investigate individual differences in working memory capacity and presence in virtual environments. Experiment 1 sought to reveal if differences in presence would emerge between participants with high verses low working memory capacity by measuring the degree of risk / potential for injury demonstrated in the virtual environment. Experiment 2 conceptually replicated Experiment 1, but integrated eye-tracking measures to further ascertain the observed differences in presence between those with high verses low working memory capacity.

2 Experiment 1

2.1 Methods

Participants and Apparatus. Twenty-eight college students participated in the study. All trials involved participants utilizing a Dell™ Inspiron 6400 computer with a 15.4-inch XGA display. The virtual environment was displayed at 800X600 pixels.

Materials. The automated operation span (AOSPAN) material is a computer-based automated measurement task of working memory capacity that uses math operations as processing components [14].

A virtual environment, developed using the Autodesk® Maya® Version 8, simulated the task of a male avatar cutting pieces of celery. The objects presented in the virtual environment included a male actor, table, piece of celery, and knife (see Figure 1). Participants used the mouse, scrolling laterally, to determine the optimal cutting position of the knife over the celery. To begin the action, the participant clicked and held the left mouse button over the right hand of the male avatar. As the participant moved the mouse to the left, the hand and knife position of the avatar correspondingly moved to the left. Once the participant decided to cut the celery, the participant released the left-mouse button.

Procedure. Upon consenting to take part in the study, participants were introduced to the interface of the virtual environments and completed practice trials until they reached an adequate level of comfort in interacting with the environment. Participants were informed that the remaining task (experimental) was simply more practice. All participants completed the task of cutting 3 equal pieces. Participants next completed the AOSPAN working memory capacity task and a median-split method was utilized to assign participants into a low or high working memory capacity group.

Data Analysis. Analyses were carried out on three dependent measures. (1) Risk was determined by measuring how close each participant cut to the avatar's fingertip. (2) Accuracy was determined by measuring the variance of the width values (in creating equal pieces). (3) Time on task was determined by measuring the total elapsed time in a given trial.

2.2 Experiment 1 Results and Discussion

Results. Data were analyzed by ANOVAs, with working memory capacity (HWM vs. LWM) as the between-subject factor, and performed separately for accuracy, risk, and time on task. HWM participants were more accurate, $F(1, 26) = 5.28$, $p < .05$, demonstrated greater risk, $F(1, 26) = 13.62$, $p < .01$ and spent more time on task $F(1, 26) = 7.25$, $p < .05$ than LWM participants.

Discussion. Our initial prediction was that those experiencing greater plausibility illusion would treat the task as if it were real by not cutting close to the finger. Furthermore, HWM participants were predicted to be most likely to demonstrate greater presence given their superior ability to maintain goal-directed behavior under conditions of distraction or conflict (what is happening is real vs. knowing it is not). While HWM participants were more accurate, they also demonstrated greater risk by cutting very close to the finger. Were HWM participants demonstrating less presence in the virtual environment? Perhaps greater demonstrated risk combined with greater accuracy meant that HWM participants were just being efficient and indeed treating the virtual environment as if it were real. Further supporting this idea, HWM spent more time on task (M = 16.19s) than LWM participants (M =12.97s). If HWM participants were demonstrating less presence (making risky, haphazard cuts close to the finger), why would HWM participants spent more time on task and what might HWM participants have been doing for the significantly longer duration of elapsed time? One possibility is that HWM participants were demonstrating greater presence by planning the actions and therefore mitigating the risk. To reveal such a possibility, Experiment 2 integrated eye-tracking measures in a conceptual replication of Experiment 1.

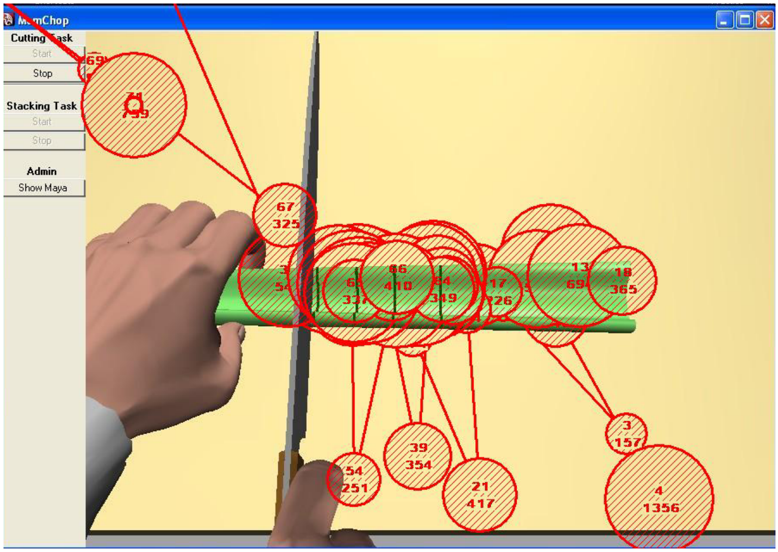

Fig. 1. Screenshot of experimental task / virtual environment / scan path map

3 Experiment 2

3.1 Methods

Participants and Apparatus. A total of thirty college students participated in Experiment 2. Trials involved participants utilizing a Dell™ Optiplex desktop computer with a 24-inch display. The virtual environment was displayed at 800X600 pixels. An iView X™ Hi-Speed eye tracker, with a sampling rate of 350 Hz, was fixed to the desk. The eye tracker camera was mounted in a standalone column and participants were affixed to the eye tracker ergonomically by a chin and headrest.

Materials. All materials from Experiment 1 were utilized for replication in Experiment 2. The virtual environment and the eye tracker software were synchronized in communication during the experiment, requiring little experimenter involvement.

Procedure. Training, AOSPAN completion, working memory capacity grouping, and demographic data collection procedures were all replicated from Experiment 1. In addition, participants completed a 13-point calibration process. Eye movement data were collected at 350Hz in separate trials (one low demand and one high demand trial for each participant) and included fixations, saccades, and blinks. Participants were asked to cut 3 equal pieces in the low demand task and 9 equal pieces in the high demand task.

Data Analysis. Analyses were carried out on two dependent measures. The measure of risk was determined by identifying how close each participant cut to the fingertip. Fixation duration by segment was the sum of fixation durations cast in each segment of the task (*planning* – start of the task until first cut, *executing* – after first cut until last cut, *ending* – after last cut until stopping the task). Before analyzing the data, outliers were removed from each of the dependent measures using a criterion of 3 standard deviations.

3.2 Experiment 2 Results and Discussion

Results. Data was were analyzed by mixed ANOVAs, with working memory capacity (HWM vs. LWM) as the between-subject factor and task demand (low vs. high) as the within-subject factor, and performed separately for accuracy, risk, and fixation duration by segment. The results on accuracy and risk replicated the findings of Experiment 1. HWM participants spent significantly more time in the planning task segment $F(1,28) = 5.98$, $p < .05$, which suggests HWM participants were experiencing a greater degree of plausibility illusion by planning the cuts. HWM and LWM participants appeared to spend similar amounts of time casting fixations in the execution segment of the task, however.

Discussion. The results indicated that while HWM participants were more accurate and demonstrate greater risk in the virtual environment. The longer looking time prior to beginning the cutting indicated that there is a deliberate planning ongoing on the part of HWM individuals. It is not the case that HWM individuals could simply launch into the task and rely on their superior cognitive reservoir to gain advantage in performance. These results did not support the possibility that HWM participants were able to perform the task efficiently and yet simultaneously entertain the thought that the environment is not real and thereby it is fine to chance on cutting very close to the fingertip.

4 General Discussion

This study aimed to investigate how fluid the feelings of presence can be by examining whether individual differences in working memory capacity impact presence in virtual environments. Plausibility, or the illusion that what is happening in the virtual environment is real was measured in terms of how close to the finger (degree of risk) a cut was made. Experiment 1 revealed that HWM participants were more accurate, but demonstrated greater risk by cutting very close to the finger. Experiment 2 integrated eye-tracking measures to further explain the observed differences between HWM and LWM participants. Results were similar to Experiment 1 in that HWM demonstrated greater risk, but eye-tracking measures revealed that HWM participants mitigated the risk by planning. Taken together, Experiments 1 and 2 provide evidence that individual differences in working memory capacity do impact the feelings of presence in virtual environments. Specifically, participants with HWM experienced greater plausibility illusion (treating the virtual environment as though it were real) by mitigating risk through planning (revealed via eye movements).

The current study uniquely investigated real time behavioral measures by using time on task, task performance measured in pixels, and eye-tracking. Those with HWM were predicted to be the most likely to demonstrate presence given their superior ability to maintain goal-directed behavior, while contemplating the conflicting thoughts of on one hand, 'what is happening is real' and on the other 'knowing it is not.' In the current investigation, WMC was found to be an important cognitive ability in participants experiencing greater plausibility illusion. The quality of conscious experience varies due to the ability of managing available information suppressing task irrelevant thoughts and immersing oneself in the now. However, the mechanism underlying this plausibility illusion is not clear. Are high ability individuals more capable of suppressing task irrelevant thoughts? Alternatively, are they so immersed in performing the task well and thus do not have enough resources to entertain the task irrelevant thoughts?

The current environment is desktop delivered, and thus lacks the place illusion that fully immersive environments can provide. This raises the question as to the relationship between plausibility and place illusion. Slater [4] maintains that plausibility can be independently invoked and is not dependent on experiencing place illusion. The current work suggested that plausibility may be more psychologically driven and rely less on technology based factors such as realistic representations and updating of the scene based on user’s bodily movements. In the midst of the efforts in developing context aware, reality-based computing systems, the current work demonstrated how properties of human minds impact the reality that gets construed. The good news for the intelligent system community is that psychological reality is fluid and can be triggered with less perfect and not so real technological artifacts.

Acknowledgment. This work is supported by grants from US National Science Foundation (#0742109, 0916749).

References

1. Jacob, R., Girouard, A., Hirshfield, L., Horn, M., Shaer, O., Solovey, E., Zigelbaum, J.: Reality-Based Interaction: A Framework for Post-WIMP Interfaces. In: CHI 2008: Proceedings of the Twenty-Sixth Annual SIGCHI Conference on Human Factors in Computing Systems, pp. 201–210. ACM Press, New York (2008)
2. Slater, M., Linakis, V., Usoh, M., Kooper, R.: Immersion, Presence, and Performance in Virtual Environments: An Experiment with Tri-Dimensional Chess. In: ACM Virtual Reality Software and Technology (VRST), pp. 163–172. ACM Press, New York (1996)
3. Khanna, P., Yu, I., Mortensen, J., Slater, M.: Presence in Response to Dynamic Visual Realism: A Preliminary Report of an Experiment Study. In: ACM Virtual Reality Software and Technology (VRST), pp. 364–367. ACM Press, New York (2006)
4. Lee, K.M.: Why Presence Occurs: Evolutionary Psychology, Media Equations, and Presence. Presence 13, 494–505 (2004)
5. Slater, M.: Place illusion and plausibility can lead to realistic behavior in immersive virtual environments. Philos. Trans. R Soc. Lond. B Biol. Sci. 364, 3549–3557 (2009)
6. Friedman, D., Brogni, A., Guger, C., Antley, A., Steed, A., Slater, M.: Sharing and analyzing data from presence experiments. Presence 15, 599–610 (2006)

7. Baddeley, A.D.: Human memory. Theory and practice. Allyn & Bacon, Needham Heights (1997)
8. Ballard, D., Hayhoe, M., Pook, P., Rao, R.: Deictic codes for the embodiment of cognition. Behavioral and Brain Sciences 20, 723–767 (1997)
9. Daneman, M., Carpenter, P.A.: Individual differences in working memory and reading. J. of Ver. Lea. and Ver. Beh. 19, 450–466 (1980)
10. Turner, M.L., Engle, R.W.: Is working memory capacity task dependent? J. of Mem. and Lan. 28, 127–154 (1989)
11. Kane, M.J., Conway, A.R., Hambrick, D.Z., Engle, R.W.: Variation in working memory capacity as variation in executive attention and control. In: Conway, A.R., Jarrold, C., Kane, M.J., Miyake, A., Towse, J.N. (eds.) Variation in Working Memory, pp. 21–48. Oxford University Press, New York (2007)
12. Slater, M., Usoh, M.: Representations systems, perceptual position, and presence in immersive virtual environments. Presence 2, 221–233 (1993)
13. Nunez, D.: Working Memory and Presence: Reconsidering the Role of Attention in Presence. In: Proceedings of PRESENCE 2004, the 7th Annual International Workshop on Presence, pp. 44–47. ASTC Press, Washington DC (2004)
14. Unsworth, N., Heitz, R.P., Schrock, J.C., Engle, R.W.: An automated version of the operation span task. Behavior Research Methods 37, 498–505 (2005)

An Ontology Driven and Bayesian Network Based Cardiovascular Decision Support Framework

Kamran Farooq[1], Amir Hussain[1], Stephen Leslie[2], Chris Eckl[3], Calum MacRae[4], and Warner Slack[5]

[1] Department of Computing Science and Mathematics, University of Stirling, FK9 4LA, UK
[2] Cardiac Unit, Raigmore Hospital, Inverness, IV2 3UJ, UK
[3] Sitekit Labs, Isle of Skye, Inverness, IV51 9HL, UK
[4] Brigham and Women's Hospital, Cardiovascular Division, Boston MA 02115, US
[5] Beth Israel Deaconess Medical Center, Harvard Medical School, Boston MA 02446, US
{kfa,ahu}@cs.stir.ac.uk, stephen.leslie@nhs.net, chris.eckl@sitekit.net, cmacrae@partners.org, wslack@bidmc.harvard.edu

Abstract. Clinical risk assessment of chronic illnesses in the cardiovascular domain is quite a challenging and complex task which entails the utilization of standardized clinical practice guidelines and documentation procedures to ensure clinical governance, efficient and consistent care for patients. In this paper, we present a cardiovascular decision support framework based on key ontology engineering principles and a Bayesian Network. The primary objective of this demarcation is to separate domain knowledge (clinical expert's knowledge and clinical practice guidelines) from probabilistic information. Using ontologies is a cost effective and pragmatic solution to implementing a shift from simple patient interviewing systems to more intelligent systems in primary and secondary care. The key components of the proposed cardiovascular decision support framework have been developed using an ontology driven approach. We have also utilized a Bayesian Network (BN) approach for modelling clinical uncertainty in the Electronic Healthcare Records (EHRs). The cardiovascular decision support framework has been validated using a sample of real patients' data acquired from the Raigmore Hospital's RACPC (Rapid Access Chest Pain Clinic). A variable elimination algorithm has been used to implement the BN Inference and clinical validation of the "Coronary Angiography" treatment has been carried out using Electronic Healthcare Records.

Keywords: cardiovascular decision support system, ontology driven decision support with uncertainty modeling, clinical decision support and Bayesian Network.

1 Introduction

Coronary heart disease (CHD) is the most common cause of death in the UK, and the death rate in the UK is still higher than many European countries. Approximately 2

H. Zhang et al. (Eds.): BICS 2012, LNAI 7366, pp. 31–41, 2012.

million people are currently living with angina in the UK. [http://www.heartstats.org]. This condition is associated with an annual mortality between 2.8% to 6.6% per annum [1]. The incidence of angina and acute coronary syndromes has been shown to vary according to risk factors such as age, gender and ethnicity. Patients who present with chest pain continue to present a major diagnostic challenge for both primary and secondary care physicians. This is due, in part, to the low specificity of chest pain as a symptom of significant coronary artery disease and the danger of misdiagnosis in patients at risk of major cardiac events. Furthermore, chest pain is a very common symptom, between 20% and 40% of the general population will experience chest pain in their lives [2] with up to 1% of visits to a general practitioner due to chest pain [3]. Chest pain is also common presenting complaint in patients attending A and E accounting for approximately 5% of visits to the emergency department. Furthermore, up to 40% of emergency hospital admissions are due to chest pain [4].

1.1 Rapid Access Chest Pain Clinic

In 2001, the National Service Framework for Coronary Heart Disease made a commitment to have 50 rapid access chest pain clinics (RACPC) in England by April 2001 [DOH 2000]. These clinics were designed to allow direct access to cardiology expertise without the need for accident and emergency assessment or admission to a medical ward. RACPCs would appear to be reliable and safe in the assessment of patients with suspected cardiac chest pain [5].

1.2 Bayesian Networks

Bayesian Networks hold an important position in modern clinical decision support systems. Bayesian networks are being exploited in the modern clinical decision support systems because of their ability to model causal (or diagnostic) relationships using a degree of clinical expert's belief, allowing reasoning under uncertainty [6]. In the Machine Learning world, there are several sophisticated probabilistic models which are used to model clinical uncertainty, such as fuzzy-logic, BNs, etc. Generally, a BN of n variables consists of a DAG (Direct Acyclic Graph) of *n* nodes and a number of arcs. Nodes *Xi* in a DAG corresponds to random variables, and directed arcs between two nodes represent direct causal or significant relationships among different variables. The uncertainty of the causal relationship is represented locally by the CPT (Conditional Probability Table) [6]. The $P(X_i/pa(X_i))$ is associated with each node *Xi*, where *pa*(*Xi*) is the parent set of *Xi*. The conditional independence assumption and the joint probability distribution of X = (*X*1*; X2;:::; Xn*) can be worked out to define CPTs in the Bayesian network, namely, the chain rule of BN: *P* (X) $= \prod_i P(X_i | X_i / pa(X_i))$. Using the joint probability distribution, BNs support probabilistic inference in the joint space. Besides the influence of probabilistic reasoning provided by BNs themselves, they are being utilized for the structural similarity between the DAG of a BN and activity graphs of the CPGs (RACPC guidelines for the chest pain risk assessment): both of them are directed graphs, and direct correspondence exists between many nodes and arcs in the two graphs [6]. Moreover, BNs can be used to represent the clinical uncertainty in the clinical practice guidelines and they also facilitate inference capabilities for the ease of understanding.

The rest of the paper is organized as follows:

Section 2 reviews the state of the art in the healthcare patients' information management systems. Section 3 explains our methodology for the development of Electronic Healthcare Records (in the form of a patient semantic profile). Section 4 presents preliminary results which includes ontology testing and validation results using real patients' data acquired from the Raigmore Hospital, this section also focuses on the clinical uncertainty modeling in the Electronic Healthcare Records using a novel Bayesian Belief Network and finally some concluding remarks are given in section 5.

2 Background

This research focuses on the comparative study of traditional patients' information management systems based on conventional hard-wired branching logic. These systems have significant limitations, including: lack of flexibility and adaptability to complex clinical requirements and processes and a general lack of astuteness [7]. These clinical interviewing systems do not go far beyond core functionalities and due to their rigid architectures, these conventional systems are hard to maintain and update [8]. We are developing an ontology driven decision support framework as shown in Fig 1 to solve such knowledge representation and clinical decision making issues in the cardiovascular domain.

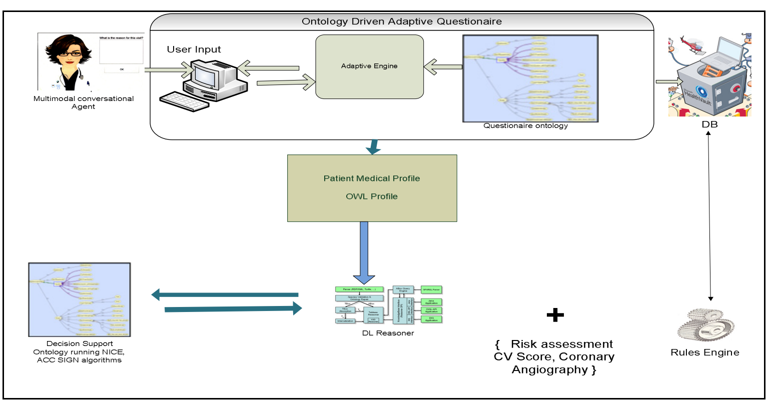

Fig. 1. Cardiovascular Decision Support Framework for Primary and Secondary Care

2.1 Ontology Driven Approach

Ontology engineering is a popular branch of artificial intelligence which is used in the simulation of complex computing systems, clinical decision support systems, emotions sensing, sentic computing, opinion mining using language corpuses and semantic web applications [9, 10]. The study conducted in [11], [12] showed exceptional results in the risk assessment and disease management of breast cancer patients which was deployed as a commercial clinical system. They utilized the semantic web approach to model the clinical practice guidelines which were encoded in the clinical decision support system for generating patient specific recommendations. The adoption of Ontologies inspired approach yields good results in terms of standardizing health care guidelines. The construction of knowledge base through an ontology inspired approach will have the benefit of problem independence. This knowledge base can be extended and reuse in a variety of different problems and therefore will have multiple mapping among knowledge base and decision models. The knowledge base will update the decision models without any costly software engineering work and maintenance will be cost effective across decision models and within the knowledge base.

3 Methodology

3.1 Electronic Healthcare Records

SNOMEDCT has become a de facto gold standard for the modern healthcare systems because of its easy to use interface with powerful search capabilities in clinical terms. We have utilized ontology driven approach to model patient's medical history in OWL from heterogeneous data sources in legacy clinical systems. We have used a reverse engineering approach to generate a patient semantic profile ontology using the patient's data provided by RACPC (Rapid access chest pain clinic) nurses at Raigmore Hospital in Inverness. The Patient Semantic Profile is one of the key components of the proposed decision support framework. The Clinical decision support framework relies on the data encapsulated in the form of electronic healthcare records to perform the decision support (using domain specific ontologies) and dynamic logic operations.

3.2 Ontology Development

The high level design of the classes was carried out with a view to incorporate the actors/participants which take part during the course of GP referral to RACPC clinics followed by the cardiologist consultation should they need to be consulted regarding abnormal ECG or failure to do an exercise tolerance test. They are also referred as agents in the ontology performing specific actions within the ontology domain. The ontology design incorporated different stages during the referral process through relationships among parent-subclasses. The information about patient's chest pain type, their past family history, previous cardiovascular history and personal demographics information is also modelled through domain-specific classes within the ontology design.

3.3 Object Properties and Data Properties

The object properties are defined in order to establish relationship between individual classes. The properties are also referred as Roles or relations in UML terms. The purpose of the data properties is to be able to define the relationship between individual class and the XML schema data type.

Object properties establish a relationship between specific classes in order to encapsulate and model the desired behaviour which is set as a clinical use case.

The modelling of chest pain patients who suffered from suspected angina has been achieved via the object property “has_chest_pain_type which binds the specific pain type with the patient using “Patient" and “Chest_Pain_Type” Classes. The XML schema data type comes from the data properties which describes pain _type as an enumerated type showing the values as “typical, atypical or nontypical”.

“Has_diagnosis_done” object type describes the relationship between “Patient” and “General Medical Practitioner”, “Cardiologist” and “RACPC” classes. This relationship encapsulates and models the behaviour of diagnosis done at each stage by the clinicians involved in the referral process.

3.4 Ontology Evaluation and Testing

In order to test the developed ontology, several test patients were introduced as part of the training. The patient semantic profile ontology was used to generate their electronic healthcare records. The information shown in Fig 2 is a formal representation of the information initially collected through the test data. After performing the consistency checking, Pellet dynamic logic reasoner was used to check the classification results.

3.5 Ontology Testing Results

The patient semantic profile component generated the clinical histories using legacy patients’ data. Many items of information which are clinically useful to the clinicians (GPs, Nurses, and Cardiologists) are being held using Boolean-type clauses.

The critical medical conditions are modelled using “ Has Presence and “ Has Absence” clauses , this sort of clinical information is very useful for clinicians involved in primary and secondary care and without spending too much time they can get a bigger picture of the patient’s medical history and diseases/conditions which need urgent attention from referral perspective. The purpose of this clinical history is to lend a helping hand to clinicians during clinical decision making and to flag potential clinical issues which need urgent attention or further examination by clinical experts.

3.6 Important Historical Information

In cardiology clinic the key information which is critical to make effective clinical decision making is the episodic information pertinent to a heart attack or a heart abnormality of any kind in the past. This critical information is of huge importance in pre-operative risk assessment before any surgical operation is scheduled for the patient. This information is modeled through an ontology using " has absence" and has Presence" data types.

Qualitative Information. The Qualitative information is presented in the Figure 2 by example 4. It shows that the patient is suffering from chest pain which is "Typical" chest pain. What clinically defines typical pain can be asserted in the chest pain risk assessment ontology developed as part of the chest pain risk assessment ontology.

Cardinal Information. In web ontology language, one of its best features to specify cardinal information using cardinal restrictions by expressing it in number and ranges. There are two types of cardinal restrictions you can apply in OWL; they are referred as Temporal and Quantity units.

Patient's age is modelled as 75 years in item 4 which personify temporal unit. One of the best selling features of OWL is the functionality it providers to define unit classes and storage information in a single unit which can be updated in a cost effective way when new clinical guidelines are provided by the healthcare authorities.

Range Information. The range information is modelled in 5 which can make clinicians aware that the patient in question was diagnosed with coronary angiography treatment 7 months ago.

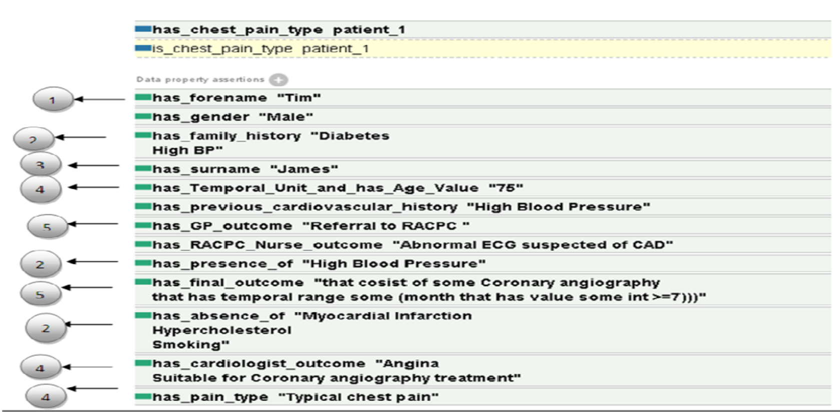

Fig. 2. Electronic Healthcare Records in the form of Patient Semantic Profile

4 Preliminary Results

4.1 Ontology Testing Using Real Patients

Web ontology language (OWL) allows ontology engineers to define individuals and then used them to assert specific properties to test the hierarchical relationship and domain logic implemented through various classes. These Individuals (Instances of the classes) can also be used in class descriptions, namely in "hasValue" restrictions and enumerated classes. Electronic Healthcare Records have been generated for the test patients represented in Fig 3. These test patients were inserted as individuals in the ontology for the training and testing purposes and also to assert specific clinical conditions which describes their clinical symptoms.

Patient's medical history encapsulates their demographics along with their past and present cardiac and non cardiac related clinical symptoms, location of the current chest pain (left side of the chest) association of the chest pain with breathing, its severity and whether or not their chest pain is spreading. After analyzing the patient's medical history generated through the Patient Semantic Profile ontology the semantics are extracted to generate electronic healthcare records. These EHRs are of utmost importance for the clinicians for the effective risk assessment operations and efficient clinical decision making.

ExampleSet (11 examples, 2 special attributes, 8 regular attributes)

Row No.	Diagnosis	Result	Age	Gender	Pain Type	Known CAD	HyperChol	High BP	Smoking	Family Hist...
1	prob	angio	71	m	typ	y	n	n	n	y
2	prob	angio	77	m	typ	y	y	n	y	y
3	prob	angio	67	m	typ	n	y	y	n	y
4	prob	angio	74	f	typ	n	n	n	n	n
5	prob	angio	52	m	atyp	n	n	n	y	y
6	prob	angio	74	f	typ	n	y	y	y	n
7	pos	ett	66	m	atyp	n	y	n	n	n
8	pos	angio	61	f	typ	n	n	y	y	n
9	prob	angio	64	f	typ	n	n	y	y	n
10	prob	medical	85	f	typ	n	n	n	n	n
11	def	admitted	66	f	typ	n	n	n	n	n

Fig. 3. Chest pain patients' data acquired from the RACPC at the Raigmore Hospital

4.2 Bayesian Network for Uncertainty Modelling in the Electronic Healthcare Records

We have developed a Bayesian network a model as presented in Fig 4, using the Electronic Healthcare Records generated in [13] for the clinical risk assessment of Coronary Angiography treatment, called AngioNet. This model has been created using patient's demographics and clinical exam findings data provided by the consultant cardiologist from the Raigmore Hospital. We have exploited the probabilistic risk assessment (BN) technique for the validation of clinical scenarios which are being followed in the RACPC (Nurse-Led Rapid Access Chest Pain Clinics). The main purpose of implementing this intelligent risk assessment mechanism is to assess the patient's suitability for the "Coronary Angiography" treatment. This treatment is overly prescribed because of misleading/wrong diagnosis and we aim to help NHS hospitals reduce excessive cost which is being spent on this overly exhaustive and expensive angiography treatment.

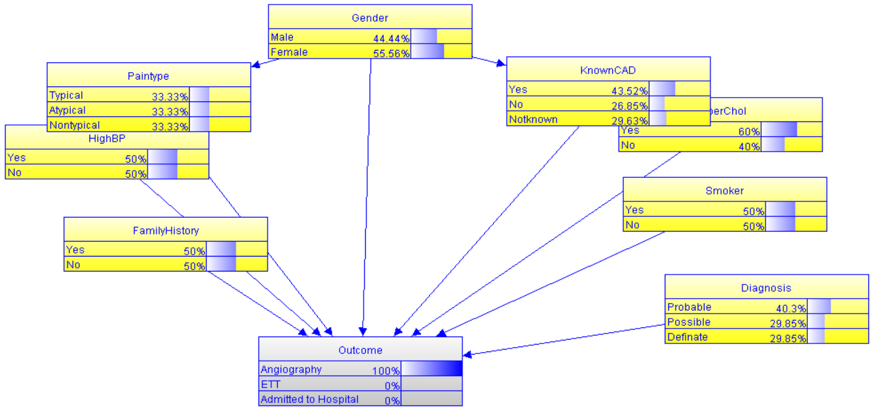

Fig. 4. A Bayesian Belief Network for the Coronary angiography risk assessment

4.3 Clinical Validation

A RACPC nurse is trying to perform a risk assessment of a chest patient (Tim James) who has been referred to this specialized chest pain clinic through a GP referral. Tim is 75 years of age, suffering from atypical chest pain. He also has a history of CAD, high blood pressure, diabetes and absence of myocardial infarction. Tim is also a passive smoker.

After loading the semantic profile ontology, the BN inference engine performs inference using patient's data encapsulated in the electronic healthcare records as shown in Fig 5. The patient's clinical history (risk factors, previous cardiac conditions) has been presented as observed evidence, such as observations of hypertensive disorder, smoking, previous CAD and myocardial infarction in this scenario. If the Nurse selects the target activities, the BN inference engine calculates the probability of each of these risk factors using the variable elimination algorithm. RACPC nurse gets a snapshot of the patient's clinical history and the observed evidence of historic CAD and previous cardiac treatments. RACPC nurses would like to know the probability of current activity high BP, Hyper cholesterol, age >75, with positive ETT", previous GP, cardiologist and nurse findings to help them ascertain patient's suitability for the coronary angiography treatment. In the BN inference engine, since *the* activity " has presence of problem high blood pressure " is found, its property *is Observed* is set *true* and the property *hasState* is set *false*. Similarly, the activities instances of historical myocardial infarction is set to *false*, occurrence of smoking is also set to true and observed in the same manner.

The developed AngioNet classifier calculates argmaxy p(y/x) using the distribution P(U), represented by the Bayesian Network as follows:

$$\begin{aligned} p(y/x) &= P(U)/P(x) \\ &\alpha\, p(U) \\ &= \prod_{\mu \in U} p(\mu \setminus pa(\mu)) \end{aligned} \tag{1}$$

Since all variables (risk factors) in x are learned through the patients‟ data, we applied Bayesian Inference algorithm for all available class values.

Bayesian Inference results have been presented in Figure 5 which shows the propagated probability distribution for all the variables. BN calculates the probability of activity instance "absence of myocardial infarction" which is used for the recommendation of coronary angiography treatment.

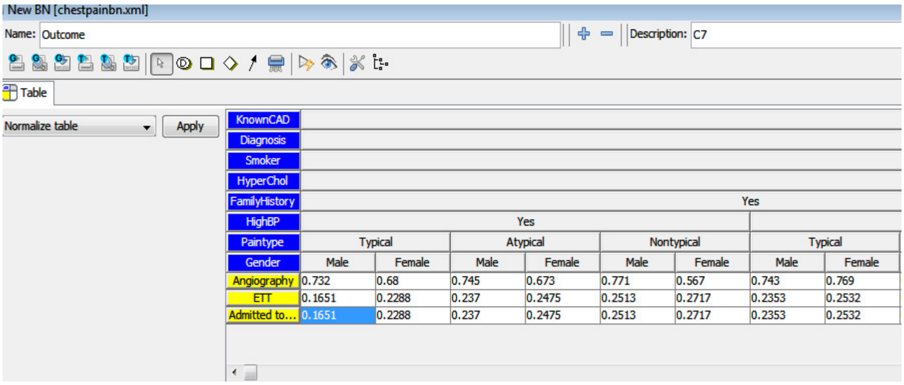

KnownCAD								
Diagnosis								
Smoker								
HyperChol								
FamilyHistory	Yes							
HighBP	Yes							
Paintype	Typical		Atypical		Nontypical		Typical	
Gender	Male	Female	Male	Female	Male	Female	Male	Female
Angiography	0.732	0.68	0.745	0.673	0.771	0.567	0.743	0.769
ETT	0.1651	0.2288	0.237	0.2475	0.2513	0.2717	0.2353	0.2532
Admitted to...	0.1651	0.2288	0.237	0.2475	0.2513	0.2717	0.2353	0.2532

Fig. 5. Bayesian Belief Network Inference Results

$$P(X_q|E) = \frac{P(X_q, E)}{P(E)} = \frac{\sum X \setminus \{X_q, X_E\} P(X)}{\sum X \setminus X_E P(X)} = 0.745 \quad (2)$$

Where X_q = {presence of CAD; recommend "angiography}, and E= {presence of high blood pressure, problem "myocardial infarction" = *false*, presence of "smoking" user finding = true, presence of risk factor "diabetes"= true}. BN provides a degree of uncertainty keeping in view the presence and absence of key clinical risk factors, a nurse can choose this target activity instance based on the observed evidence *E*. Through BN inference, we can obtain:

$$P(X_q / E = \frac{P(X_q, E)}{P(E)}) = 0.657 \quad (3)$$

The results in the two cases have demonstrated high probabilities for the target activities (risk factors), which can help RACPC nurses in clinical decision making on the basis of observed evidence presented by the Bayesian Network. The results of this clinical validation coincide with a clinical expert's outcome which was initially carried out using RACPC‘s clinical practice guidelines produced by the National Institute of Clinical Excellence in the UK. This approach also shows the feasibility of our approach which ensures effective and accurate clinical decision making by utilizing Bayesian Network and key ontology driven components, specifically electronic healthcare records.

5 Conclusions

We have presented an ontology driven and Bayesian Network based cardiovascular decision support framework. We have discussed the development of the key components which are Adaptive Information collection system using chest pain risk assessment questionnaire ontology and Patient Semantic Profile for the generation of Electronic Healthcare Records. We also presented a Bayesian Network for uncertainty modelling using Electronic Healthcare Records which have been developed as part of the cardiovascular decision support framework to facilitate accurate and effective clinical decision making. This approach has paved the way for the automation of RACPC service which is very much paper based and led by the cardiology nurses in most of the hospitals in the UK. The proposed system will be able to replace existing RACPC service in major cardiology clinics in the UK. The main advantages of the ontology driven approach are as follows: This allows cost effective maintenance of the chest pain decision support system because of a clear demarcation among knowledge base and decision support functions. Ontology layer enables the system to perform decision support operations which are hard to implement using distributed system technologies and centralized databases. This approach also facilitates the adoption of a generic component based approach for the ease of reuse and extension of this decision support framework to include other diseases in the cardiovascular domain and automate conventional nurse-led paper based clinics.

References

[1] Jones, M., et al.: Systematic review: prognosis of angina in primary care. Family Practice 23, 520 (2006)

[2] Stern, S., et al.: Presenting symptoms, admission electrocardiogram, management, and prognosis in acute coronary syndromes: differences by age. The American Journal of Geriatric Cardiology 13, 188–196 (2004)

[3] Ruigómez, A., et al.: Chest pain in general practice: incidence, comorbidity and mortality. Family Practice 23, 167 (2006)

[4] Nandalur, K.R., et al.: Diagnostic Performance of Stress Cardiac Magnetic Resonance Imaging in the Detection of Coronary Artery Disease: A Meta-Analysis. Journal of the American College of Cardiology 50, 1343–1353 (2007)

[5] Jain, A., et al.: Impact of a Clinical Decision Support System in an Electronic Health Record to Enhance Detection of 1-Antitrypsin Deficiency. Chest 140, 198 (2011)

[6] Zheng, H.-T., Kang, B.-Y., Kim, H.-G.: An Ontology-Based Bayesian Network Approach for Representing Uncertainty in Clinical Practice Guidelines. In: da Costa, P.C.G., d'Amato, C., Fanizzi, N., Laskey, K.B., Laskey, K.J., Lukasiewicz, T., Nickles, M., Pool, M. (eds.) URSW 2005 - 2007. LNCS (LNAI), vol. 5327, pp. 161–173. Springer, Heidelberg (2008)

[7] Bouamrane, M.-M., et al.: Experience of Using OWL Ontologies for Automated Inference of Routine Pre-Operative Screening Tests. Life Sciences

[8] Bouamrane, M.-M., Rector, A.L., Hurrell, M.: Ontology-Driven Adaptive Medical Information Collection System. In: An, A., Matwin, S., Raś, Z.W., Ślęzak, D. (eds.) ISMIS 2008. LNCS (LNAI), vol. 4994, pp. 574–584. Springer, Heidelberg (2008)

[9] Cambria, E., et al.: Sentic PROMs: Application of sentic computing to the development of a novel unified framework for measuring health-care quality. Expert Systems with Applications

[10] Cambria, E., Hussain, A.: Sentic Computing: Techniques, Tools, and Applications. In: SpringerBriefs in Cognitive Computation. Springer, Heidelberg (2012)

[11] Abidi, S.R., et al.: Ontology-based Modeling of Clinical Practice Guidelines: A Clinical Decision Support System for Breast Cancer Follow-up Interventions at Primary Care Settings Computerization of BC Follow-up CPG Development of Breast Cancer Ontology The BC ontology model. Computer

[12] Hurley, K.F., et al.: Ontology Engineering to Model Clinical Pathways: Towards the Computerization and Execution of Clinical Pathways 2. Developing a Clinical Pathway Ontology: Our Approach. Symposium A Quarterly Journal In Modern Foreign Literatures, 0–5 (2007)

[13] Farooq, K., et al.: Ontology-driven cardiovascular decision support system. In: 2011 5th International Conference on Pervasive Computing Technologies for Healthcare (PervasiveHealth), pp. 283–286 (2011)

Semantically Inspired Electronic Healthcare Records

Kamran Farooq[1], Amir Hussain[1], Stephen Leslie[2], Chris Eckl[3], Calum MacRae[4], and Warner Slack[5]

[1] Department of Computing Science and Mathematics, University of Stirling, FK9 4LA, UK
[2] Cardiac Unit, Raigmore Hospital, Inverness, IV2 3UJ ,UK
[3] Sitekit Labs, Isle of Skye, Inverness, IV51 9HL, UK
[4] Brigham and Women's Hospital, Cardiovascular Division, Boston MA 02115, US
[5] Beth Israel Deaconess Medical Center, Harvard Medical School, Boston MA 02446, US
{kfa,ahu}@cs.stir.ac.uk, stephen.leslie@nhs.net, chris.eckl@sitekit.net, cmacrae@partners.org, wslack@bidmc.harvard.edu

Abstract. The adoption of Electronic Healthcare Records (EHRs) holds the key for the success of next generation intelligent healthcare systems to improve the quality of healthcare and patient safety by facilitating the exchange of critical patient's episodic information among different stakeholders. The primary and secondary care healthcare systems store the episodic information for future reuse and for auditing purposes. The conventional healthcare information management systems for primary and secondary care are expected to be able to communicate and exchange complex medical knowledge (often expressed in numerous languages in different parts of the world) in an efficient and unequivocal way. For the purpose of this research, we present a novel technique to transform conventional patients' data into OWL-based Electronic Healthcare Records (EHRs) which addresses the issues of interoperability, flexibility, and scalability through the utilization of ontology inspired framework. Using ontologies is a cost effective and pragmatic solution to implementing a shift from simple patient interviewing systems to more intelligent systems in the primary and secondary care. The Patient Semantic Profile specifically developed for generating EHRs has been validated using a sample of real patients' data acquired from the Raigmore Hospital's RACPC (Rapid Access Chest Pain Clinic).

Keywords: Electronic Healthcare Records, OWL-based EHRs, Ontology driven cardiovascular decision support framework.

1 Introduction

Electronic Healthcare Records are widely renowned for providing good clinical indicators to the clinicians [1] for effective clinical decision making for disease management and in order for these systems to be fully effective, the healthcare provider must only see the relevant information needed to make a specific recommendation or diagnosis. As an example, a heart risk score may be sufficient for

H. Zhang et al. (Eds.): BICS 2012, LNAI 7366, pp. 42–51, 2012.

the clinician to come to a conclusion about prescribing a specific drug for a patient without the need for him to know the exact values/parameters used by the cardiac risk calculators to calculate patient's risk scores, etc.

Electronic Healthcare Records have not been rolled out at National Level despite heavy spending by the UK healthcare authorities, the core underlying issue which these healthcare information management systems are facing today is their failure to adapt to complex clinical requirements and processes and lack of general astuteness [2] which is expected of these systems. The underlying mechanics are hard-wired and based on rigid architectures which make maintenance and upgrade operations quite difficult.

In the presence of a powerful ontology based systems, it is a shame that we have not yet fully exploited the offerings of clinical Ontologies like SNOMEDCT and GALEN capable of providing appealing standardization solutions to the healthcare providers. SNOMEDCT has become a new gold clinical documentation standard for the modern healthcare systems because of extensive in depth clinical repositories with powerful search capabilities developed using ontology based techniques. Ontologies offer flexible, scalable, adaptive solutions for clinical systems. Using this approach we hope to transform the conventional health care into the next generation by using a pragmatic approach to develop next generation healthcare systems. In light of literature review and after evaluating the success case studies of SNOMED CT [3], we have started the development of an ontology driven decision support framework in the cardiovascular domain [4].

Using legacy patients' data acquired from the consultant cardiologist at the Raigmore Hospital in the UK, electronic healthcare records have been created in a semantically inspired OWL format which is the documentation standard for the proposed ontology driven cardiovascular decision support framework [4]. This helped us transform textual data held in distributed databases into semantic partitions using web ontology language. This transformed data has been used as an input by the DL Reasonser engine (Pellet) to perform risk assessment and classification of patients using their medical histories and domain specific decision support Ontologies.

The rest of the paper is organized as follows:

Section 2 reviews the state of the art in healthcare information management systems specifically from Electronic Healthcare Records perspective and section 3 explains our methodology for the development of novel ontology driven technique for the development of Electronic Healthcare Records. Section 4 presents preliminary results which include ontology testing and validation results using real patients' data acquired from the specialized chest pain clinic (RACPC) at the Raigmore Hospital and finally some concluding remarks are given in section 5.

2 Background

The fundamental goals of the modern healthcare information management systems are to promote interoperability by providing mechanisms for seamless information exchange between different healthcare organizations, healthcare trusts etc. The second most essential objective of these systems is to provide the ability to ascertain the uniformity of data from disparate sources/repositories. The third most important deliverable expected of these systems is to provide good quality clinical data (patient's data, lab tests etc) to ensure the measurement of completeness, accurateness and correctness [5].

2.1 Diversity in Healthcare Information Management Systems

Healthcare information management systems are quite diverse and their underlined communication and documentation standards are somewhat varied, utilizing different communication and documentation standards as. In conventional healthcare systems interoperability is a major issue which makes it difficult for the communication of data between heterogeneous systems. The Systematized Nomenclature of Medicine – Clinical Terms (SNOMED CT) is an ontological resource specifically developed some thirty years ago with a view to standardize healthcare systems [49]. SNOMED CT and UMLS are clinical thesauruses, aiming to resolve documentation standardization issues in clinical systems. These are large scale medical taxonomies which have been adopted in modern clinical systems showing significant good results in the targeted clinical systems. In [6] it shows that the clinicians using healthcare systems equipped with SNOMED outperformed clinicians using conventional systems without SNOMED CT capabilities.

The focus of this discussion is on the documentation standardization which is of vital importance for this case study. As a result of a literature review and analysis of healthcare management systems [7], [8] and inspired by the success stories of SNOMED CT (taxonomy driven approach), we have utilized ontology driven approach to model patient's medical history in OWL from heterogeneous data sources in legacy clinical systems. We used a reverse engineering approach to generate the patient semantic profile ontology using the patient's data provided by RACPC (Rapid access chest pain clinic) nurses at the Raigmore Hospital in Inverness. The Patient Semantic Profile is one of the key components of the proposed decision support framework [8]. The Clinical decision support framework relies on Electronic Healthcare Records to carry out the dynamic logic procedures and key decision support operations using domain specific ontologies.

2.2 Benefits of Ontologies Driven Systems

Ontology driven decision support systems have been used extensively in the clinical assessment of chronic diseases. They are well-known for their flexible architectures, easy to reuse knowledge modelling structures and inexpensive maintenance operations. Ontology engineering is a popular branch of artificial intelligence which is used in the simulation of complex computing systems, clinical decision support systems, emotions sensing, sentic computing, opinion mining using language corpuses and semantic web applications [9-11]. The study conducted in [8,12], showed exceptional results in the risk assessment and disease management of breast cancer patients which was deployed as a commercial clinical system. They utilized the semantic web approach to model the clinical practice guidelines which were encoded in the clinical decision support system for generating patient specific recommendations. The construction of knowledge base through an ontology inspired approach provides the key benefit of problem independence. This knowledge base can be extended and reused in a variety of different problems and therefore will have multiple mapping among knowledge base and decision models. The knowledge base updates the decision models without any costly software engineering work and maintenance operations are cost effective across decision models and within the knowledge base. Ontology inspired approach helps in knowledge structuring which also facilitates system developers and domain experts to acquire knowledge, reuse and ensuring knowledge consistency within the knowledge base.

3 Methodology

3.1 Electronic Healthcare Records

We have utilized ontology driven approach to model patient's medical history in OWL from heterogeneous data sources in legacy clinical systems. We have implemented a novel reverse engineering approach to generate a patient semantic profile ontology using the patient's data provided by RACPC (Rapid access chest pain clinic) nurses at Raigmore Hospital in Inverness. The Patient Medical Profile is one of the key components of the proposed decision support framework [4]. The clinical decision support framework relies on the data encapsulated in the form of Electronic Healthcare Records to perform the decision support operations using domain specific ontologies and dynamic logic procedures facilitated by the Protégé ontology development editor.

3.2 Reverse Engineering Methodology

Reverse engineering is a popular method in software engineering discipline which is the process of analyzing the system components and their relationships and replicate same data representation in the targeted domain in another structure or at a higher level of abstraction. The other concept used in this case study is forward engineering which allowed us to make a transition from high level abstractions to the physical implementation of the system.

The Re-engineering patterns describe the techniques/patterns which are applied to the data in order to achieve transformation from non ontological resources to the ontological definitions. These patterns contain the conditions and requirements which are requirements/ guidelines of the targeted system. The patient's data used for this case study came from a relational database hosted in the Raigmore Hospital. We used the ontology reverse engineering approach to transform legacy data to the patient semantic profile. We mapped the clinical processes and created clinical workflows through the development of a domain specific ontology encapsulating hierarchical classes-subclasses relationships.

We modelled clinical data of RACPC patients using Patient Semantic profile ontology. This allowed us to create patient medical histories in OWL which is the agreed data exchange format selected for the ontology driven clinical decision support system framework as represented in Fig 1. The CDSS can use this semantic profile along with decision support ontologies for risk assessment; lab tests recommendation and prescribing activities. These EHRs have been used for the generation of electronic doctor notes. EHRs will also be hosted on Microsoft Health vault for exchanging patients' critical information among different healthcare providers in the US.

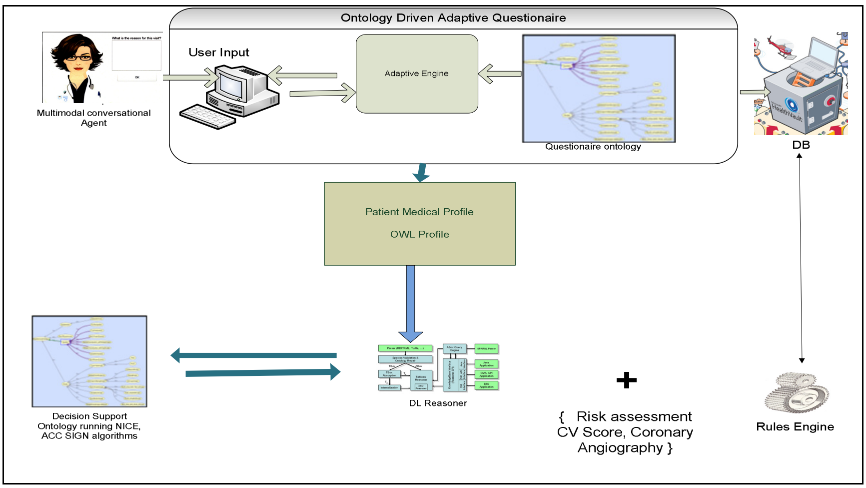

Fig. 1. High level view of the ontology driven cardiovascular decision support framework

3.3 Ontology Development

The high level design of the classes was carried out with a view to incorporate the stakeholders/participants which take part during the course of GP referral to RACPC clinics followed by Cardiologist consultation should they need to be consulted regarding abnormal ECG or failure to do an exercise tolerance test. The clinical workflow which has used for the development is as follows:

The patient goes into GP practice with chest pain symptoms; they get referred to specialized chest Pain clinics. The nurses in these clinics take patients through a series of assessment sessions to mitigate the risk of heart attack by assessing the seriousness of the chest pain. If the presentation suggests during the course of action that the chest pain patient has suffered from is not cardiac related then the patient gets discharged from these clinics after been given advice by these specialized nurses. Patients with suspected angina who are not able to carry out an exercise tolerance test or suffered pain during ETT are most likely to get coronary angiography as part of preventative measure. The ontology design incorporated different stages during the referral process through relationships among parent-subclasses. The information about patient's chest pain type, their past family history, previous cardiovascular history and personal demographic information is also modelled through domain-specific classes within the ontology design.

3.4 Object Properties and Data Properties

The object properties are defined in order to establish relationship between individual classes as represented in Fig 2. The properties are also referred as Roles or relations in UML terms. The purpose of the data properties is to be able to define the relationship between individual class and the XML schema data type.

Object properties establish a relationship between specific classes in order to encapsulate and model the desired behaviour which is set as a clinical use case.

The modelling of chest pain patients who suffered from suspected angina has been achieved via the object property “has_chest_pain_type which binds the specific pain type with the patient using “Patient" and “Chest_Pain_Type” Classes. The XML schema data type comes from the data properties which describes pain _type as an enumerated type showing the values as “typical, atypical or nontypical”.

“Has_diagnosis_done” object type describes the relationship between “Patient” and “General Medical Practitioner”, “Cardiologist” and “RACPC” classes. This relationship encapsulates and models the behaviour of diagnosis done at each stage by the clinicians involved in the referral process.

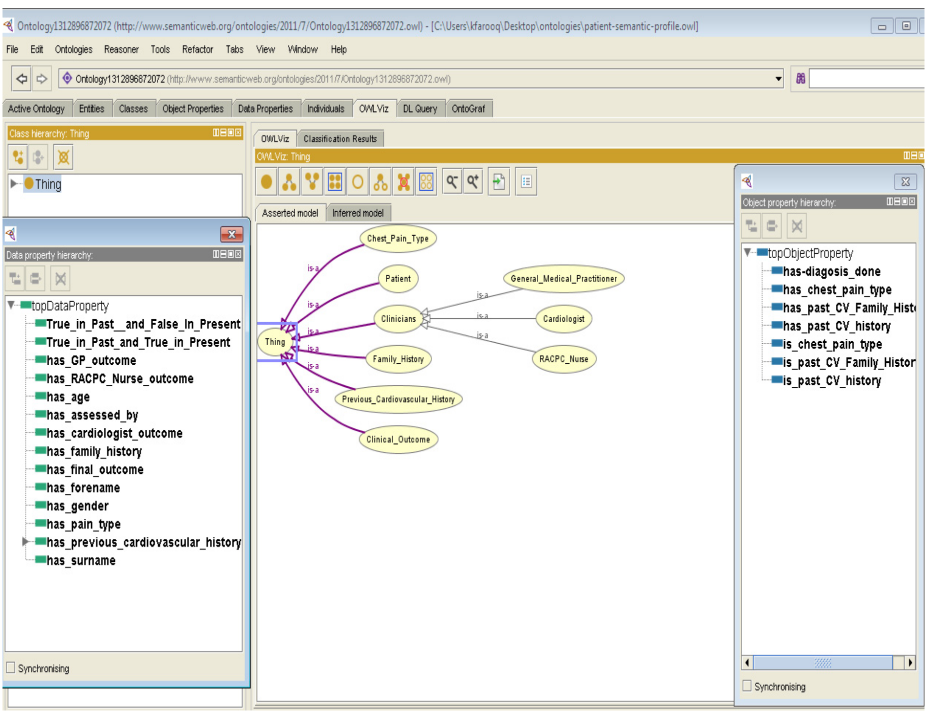

Fig. 2. Data Properties , Object properties and ontology consistency checking

3.5 Ontology Evaluation and Testing

In order to test the developed ontology, several test patients were introduced as part of the training. The patient semantic profile ontology was used to generate their electronic healthcare records. The information shown in Fig 3 is a formal representation of the information initially collected through the test data. After performing the consistency checking, Pellet dynamic logic reasoner was used to check the classification results.

3.6 Ontology Testing Results

The patient semantic profile component generated the clinical histories using legacy patients' data. Many items of information which are clinically useful to the clinicians (GPs, Nurses, and Cardiologists) are being held using Boolean-type clauses.

The critical medical conditions are modelled using " Has Presence and " Has Absence" clauses, this sort of clinical information is very useful for clinicians in the primary and secondary care and without spending too much time they can get a snapshot of the patient's medical history and diseases/conditions which require urgent attention from referral perspective. The purpose of this clinical history is to lend a helping hand to clinicians during clinical decision making and to flag potential clinical issues which need urgent attention or further examination by the clinical experts.

3.7 Important Historical information

In cardiology clinic the key information which is critical to the clinical decision making is the episodic information pertinent to a heart attack or a heart abnormality of any kind in the past. This critical information is of huge importance in pre-operative risk assessment before any surgical operation is scheduled for the patient. This information is modeled through an ontology using "Has absence" and Has Presence" data types.

3.7.1. Qualitative Information

The Qualitative information is presented in the Figure 3 by example 4. It shows that the patient is suffering from chest pain which is "Typical" chest pain. What clinically defines typical pain can be asserted in the chest pain risk assessment ontology developed as part of the chest pain risk assessment ontology.

3.7.2. Cardinal Information

In web ontology language, one of its best features to specify cardinal information using cardinal restrictions by expressing it in number and ranges. There are two types of cardinal restrictions you can apply in OWL; they are referred as Temporal and Quantity units.

Patient's age is modelled as 75 years in item 4 which personify temporal unit. One of the best selling features of OWL is the functionality it providers to define unit classes and storage information in a single unit which can be updated in a cost effective way when new clinical guidelines are provided by the healthcare authorities.

3.7.3 Range Information

The range information modelled in item 5 make clinicians aware that the patient in question was diagnosed with coronary angiography treatment 7 months ago.

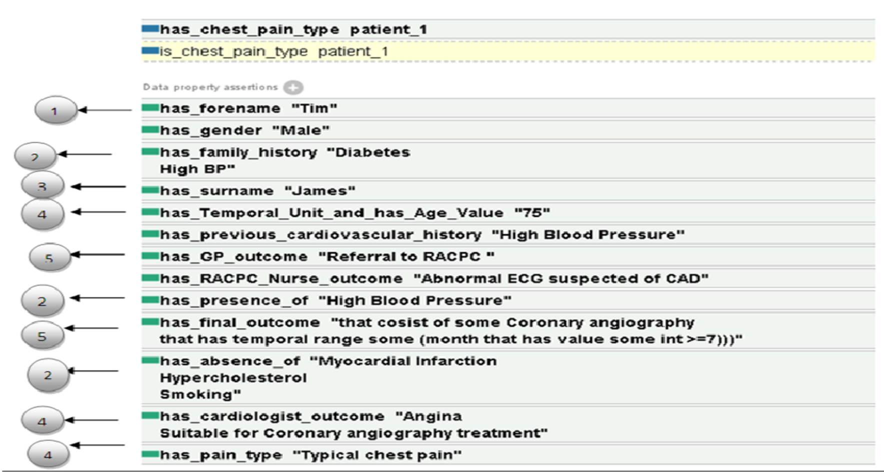

Fig. 3. Electronic Healthcare Records in the form of Patient Semantic Profile

4 Preliminary Results

4.1 Maintenance and Evaluation

The implemented ontology was tested and validated to verify whether it was fit for purpose and exhibits the clinical behaviour envisaged through the high level design by the domain experts. The implemented ontology was then evaluated on the basis of its clarity, possibilities of reuse, consistency, readiness to present held logic/information in a clear and unequivocal way. One of the important traits and key benefits of ontology driven solutions is its capability to provide knowledge designers and non expert users ease of reuse and cost effective maintenance.

4.2 Consistency Checking Using Pellet (OWL- DL) Reasoner

Protege-OWL supplies semantic web developers an intelligent validation facility which determines the sub-language of the ontology being edited. One of the important features offered through the Pellet Reasonser is its ability to be able to check class-subclass associations to ensure consistency. This additional capability will allow ontology designers to perform validation check on all of the classes included in the ontology and also to work out the inferred ontology class hierarchy [13].

4.3 Ontology Consistency Checking

The dynamic logic Reasoner (Pellet) was used for the consistency checking on all of the classes of Patient Semantic Profile ontology. During consistency checking, it shows the inferred class "chest pain type" is currently being inferred for consistency checking and Pellet performs a hierarchy check on the parent classes associated with this class under test. The purpose of the consistency checking is to ensure that the envisaged design has been implemented without any syntactical or programming errors during the course of the development of this ontology. This consistency check enabled us to do further validation testing using individuals in the Protégé development editor in order to insert real patients' data containing real clinical findings along with demographics information for the training and testing of the knowledgebase in its entirety using the defined data values and object properties.

4.4 Ontology Testing Using Real Patients

Web ontology language (OWL) allows ontology engineers to define individuals and then used them to assert specific properties to test the hierarchical relationship between different classes. These Individuals (Instances of the classes) can also be used in class descriptions, namely in "hasValue" restrictions and enumerated classes. In the Patient Semantic Profile ontology, we have defined specific test cases by defining these as individuals representing various patients and their demographics. Electronic Healthcare Records have been generated for the test patients. These test patients were inserted for the testing purposes and also to assert specific clinical conditions which describe their clinical symptoms.

Patient's medical history encapsulates their demographics information along with their past and present cardiac and non cardiac related clinical symptoms, location of the current chest pain (left side of the chest) association of the chest pain with breathing, its severity and whether or not their chest pain is spreading. After analyzing the patient's generated medical history generated through the Patient Semantic Profile ontology the semantics are extracted to generate electronic healthcare records. This information is of utmost importance for the clinicians to carry out efficient and accurate risk assessment operations.

5 Conclusions

In this paper we discussed the development of a novel technique to generate Electronic Healthcare Records using Patient Semantic Profile component which is one of the key components of the proposed cardiovascular decision support framework. We have also presented an intelligent reverse engineering technique for the transformation of legacy patients' data into Patient Semantic Profile using ontology driven knowledge modelling approach. This intelligent mechanism provides intrinsic meaning to the patient's data and facilitates this information to be utilised by the decision support components included in the proposed ontology driven cardiovascular decision support framework. We also exploited these EHRs for the development of doctor notes and used them for the clinical risk assessment to classify patients into different risk categories using ontology driven cardiovascular decision support framework. We will build on the work we have done so far as a proof of concept and aim towards building this model using ontology auto generation techniques.

References

1. Turley, M., et al.: Use Of Electronic Health Records Can Improve The Health Care Industry's Environmental Footprint. Health Affairs 30, 938 (2011)
2. Bouamrane, M.-M., Rector, A., Hurrell, M.: Using Ontologies for an Intelligent Patient Modelling, Adaptation and Management System. In: Meersman, R., Tari, Z. (eds.) OTM 2008. LNCS, vol. 5332, pp. 1458–1470. Springer, Heidelberg (2008)
3. Spackman, K.A., Reynoso, G.: Examining SNOMED from the perspective of formal ontological principles: Some preliminary analysis and observations. In: Proc. KR-MED 2004, Whistler, Canada, pp. 81–87 (2004)
4. Farooq, K., et al.: Ontology-driven cardiovascular decision support system. In: 2011 5th International Conference on Pervasive Computing Technologies for Healthcare (PervasiveHealth), pp. 283–286 (2011)
5. J.T. Case, et al.: Use of SNOMED in HL7 Messaging, pp. 1–22 (2008)
6. Cornet, R., De Keizer, N.: Forty years of SNOMED: a literature review. BMC Medical Informatics and Decision Making 8, S2 (2008)
7. Bouamrane, M.-M., Rector, A.L., Hurrell, M.: Ontology-Driven Adaptive Medical Information Collection System. In: An, A., Matwin, S., Raś, Z.W., Ślęzak, D. (eds.) ISMIS 2008. LNCS (LNAI), vol. 4994, pp. 574–584. Springer, Heidelberg (2008)
8. Abidi, S.R., et al.: Ontology-based Modeling of Clinical Practice Guidelines: A Clinical Decision Support System for Breast Cancer Follow-up Interventions at Primary Care Settings Computerization of BC Follow-up CPG Development of Breast Cancer Ontology The BC ontology model. Computer
9. Cambria, E., et al.: Bridging the Gap between Structured and Unstructured Health-Care Data through Semantics and Sentics. Science, 1–14 (2010)
10. Cambria, E., Hussain, A.: Sentic Computing: Techniques, Tools, and Applications. In: SpringerBriefs in Cognitive Computation. Springer, Heidelberg (2012)
11. Cambria, E., et al.: Sentic PROMs: Application of sentic computing to the development of a novel unified framework for measuring health-care quality. Expert Systems with Applications
12. Abidi, S.: Ontology-based knowledge modeling to provide decision support for comorbid diseases. Knowledge Representation for Health-Care, 27–39 (2011)
13. Horridge, M., et al.: A Practical Guide To Building OWL Ontologies Using The Protégé-OWL Plugin and CO-ODE Tools Edition 1.0, The University Of Manchester, vol. 27 (August 2004)

A CSP-Based Orientation Detection Model

Hui Wei and Zheng Dong

Department of Computer Science, Laboratory of Cognitive Model and Algorithm,
Fudan University, Shanghai 200433, China
{weihui,10210240013}@fudan.edu.cn

Abstract. Hubel and Wiesel's hypothesis on the emergence of orientation selectivity of simple cells meets some difficulties. It requires the receptive fields of GC and LGN to be highly similar in size and substructure while arranged in perfect order. The strict regularities make the model uneconomical in both evolution and neural computation. Varying from the classical model, we propose a new model based on an algebraic method, which estimates orientation by solving constraint satisfaction problems (CSP). The algebraic model needs not to obey the constraints of Hubel and Wiesel's hypothesis and it is easily implemented as neural network. We also prove that both precision and efficiency of the model are practicable in mathematics. This study is significant in the aspect of explaining the neural mechanism of orientation detection, as well as of finding the circuit structure and computational route in neural network.

Keywords: Receptive field, Orientation detection, Simple cell, Cell assembly, Satisfiability problem, Representation.

1 Introduction

From semantic point of view, orientation is a kind of geometrical feature in an intermediate level between the lower pixel level and the higher shape level. Almost every image, either natural or man-made image, contains a rich amount of information about orientation. Besides its universality, orientation always provides essential and structural information. Therefore orientation detection is task-independent and indispensable to image understanding.

1.1 Orientation Detection in Traditional Digital Image Processing

Many studies about orientation detection have been done in traditional digital image processing. Generally speaking, the process can be realized in two steps. The first step is edge detection. Pixels of large gradient are marked as edge points. The second step is line detection. Collinear edge points are aggregated and fitted into linear equations to stand for oriented edges. However, such methods based on combination, search and optimization techniques have several significant drawbacks. The algorithms are usually complicated and sensitive to parameter selection. It is difficult to integrate the algorithms with high-level

H. Zhang et al. (Eds.): BICS 2012, LNAI 7366, pp. 52–61, 2012.

knowledge. Furthermore, these methods provide few clues for successive operations such as synthesizing the result of orientation detection into high level structure description of image content. Due to these inadequacies, traditional orientation detection methods are hardly applied to high-level feature extraction in image processing.

1.2 Hubel and Wiesel's Hypothesis and Its Difficulties

According to neurobiological studies of mammalian vision, orientation detection is achieved by a multi-layer neural network, in which GC (ganglion cell) and LGN (lateral geniculate nucleus) play important roles. They serve as an indispensable link between stimuli and internal representations. Their concentric receptive fields achieve a preliminary integration of physical stimuli, from which subsequent processing tasks stem. Hubel and Wiesel, the Nobel Prize winners, proposed a famous hierarchical hypothesis [1] to explain the organization of simple receptive field.

This hierarchical model of simple receptive field (abbr. RF) assumes that every simple cell in V1 receives output of several LGN cells, of which the RFs are lined up in a regular band. From a computational perspective the model with geometric regularity pays little cost in calculation. However, the model is uneconomical in evolution: (1) RFs of LGN and GC are required to be arranged in strictly collinear order. (2) The size of the RF is required to be uniform. (3) In order to precisely detect and represent all orientations in different positions, the distribution of neurons and their RFs is required to be highly dense and ubiquitously ordered. These constraints are luxurious for biological system and hard to evolve [2].

Meanwhile, this classical hypothesis was doubted [3–5] recently. It is not sufficient [6] as in its original form. Some other models describing the mechanism of simple cells have being proposed. Some of them have studied the new structure of RFs [7–10]. Some improved the theory about the invariance of orientation contrast response [11]. Some re-studied the formation of orientation selection of simple cells [3, 12, 13]. The issues, such as how the function of simple cells emerges in primary visual cortex and how to design a dynamic model, have been studied in [14, 15]. But all these researches made little systematic conclusion on the computational essence. Speculation is remained: is there any other type of computational strategy possible under the same local neural connection?

1.3 Innovations in Our Model

The classic model emphasizes a highly ordered distribution of GC and LGN cells. We give up the strict arrangement and choose an economical fashion in which randomly distributed GC and LGN cells are employed.

Our idea is that simple cells make use of multiple GC or LGN cells' nonlinear response and reconstruct an inner representation of edges by solving a constraint satisfaction problem (CSP) in a group decision manner. In other words, the difference between the new model and the classical one is that it is an algebraic model rather than a geometric model.

The innovations of our work are: (1) LGN cells are no longer required to be orderly arranged as a line. (2) The system makes use of the response curve of a GC or LGN cell. (3) A large-scale simple-cell layer is established to represent every possible orientation. Balance between functional requirement and hardware complexity is also considered. (4) Mathematical test and error estimation are done to show how precisely the optimization method can achieve.

In Figure 1, two mechanisms ((a) Hubel-Wiesel's and (b) ours) are demonstrated.

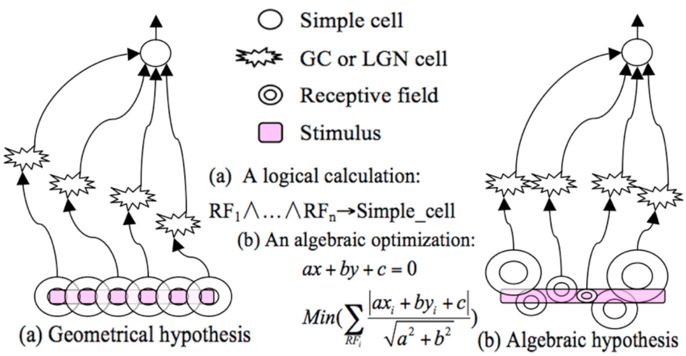

Fig. 1. The difference of two mechanisms

2 Model of a Single Ganglion-Cell

2.1 Traditional DOG Model

The model of difference of Gaussians (DOG) was proposed by Rodieck [16] for mathematically describing the receptive field of ganglion cells (Figure 2(a)(b) demonstrates such a DOG model).

$$\begin{aligned} R(x,y) &= R_c(x,y) - R_s(x,y) \\ &= k_c e^{-\frac{x^2+y^2}{r_c^2}} - k_s e^{-\frac{x^2+y^2}{r_s^2}} \end{aligned} \quad (1)$$

where k_c is a peak sensitivity of the central Gaussian and r_c is the radius. Correspondingly, k_s and r_s are the sensitivity and radius of the surrounding Gaussian. This model has been proved to be successful in simulating GC responses to several stimuli (spot and bar stimuli, grating drifting etc.).

2.2 Using DOG Model in a New Way

We apply the classical DOG model in a new manner as demonstrated below in details.

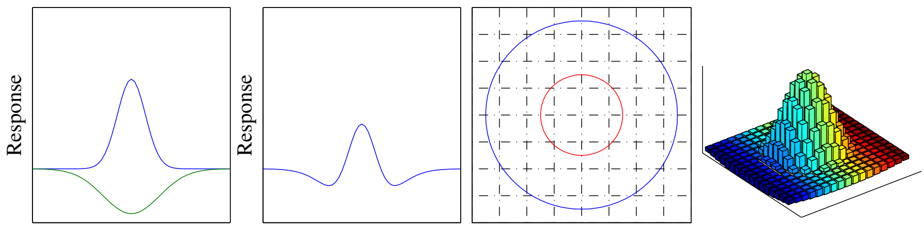

(a) Central and surrounding Gaussians
(b) Difference of Gaussians
(c) Squared grid
(d) Weight matrix

Fig. 2. Gaussian functions and DOG model

Step 1: Obtaining Weight Matrix. Let W_c , W_s and W be the weight matrix of positive central Gaussian, negative surrounding Gaussian and DOG respectively. An $x - y$ plane is divided into a squared grid (see Figure 2(c)). For each square in the grid, an integral of DOG function is calculated by:

$$W(x, y) = W_c(x, y) - W_s(x, y) = \iint_{Square} R(x, y)dxdy. \tag{2}$$

Figure 2(d) shows a weight matrix of DOG model.

Step 2: Obtaining Response Curve. Suppose that there is a sufficiently large shadow of which the boundary goes through a receptive field. The luminance of dark side is g_1 and the luminance of bright side is g_2. The GC response R can be calculated as

$$R = \sum_{A} W(x, y) \cdot g_1 + \sum_{S-A} W(x, y) \cdot g_2 \tag{3}$$

where S is the receptive field and A is the shadow. Given d as the boundary position relative to the center of the RF, R is a function of the ratio d/r_s. The function is a response curve (Figure 3(a)). It is very similar to the result of biological experiments (Figure 3(b), reprinted from [17]).

Step 3: Estimating Boundary Position. Using the response curve, a cell can judge the approximate position of an edge crossing its RF. When a shadow is projected to the RF, a response R_0 is calculated by the method mentioned above. Cutting the response curve by a horizontal line $R = R_0$, normally two intersections are obtained (Figure 4(a)). They correspond to possible boundary positions (Figure 4(b) and (c)). Thus the perpendicular distance r between the center of RF and the boundary is obtained.

Considering that the orientation of boundary may be arbitrary, any boundary with the same r forms a valid candidate (Figure 4(d)). Therefore the boundary prediction forms a circle of which the radius is r and the center is identical to the RF. The circle is tangent to all candidate boundaries (see Figure 4(e)).

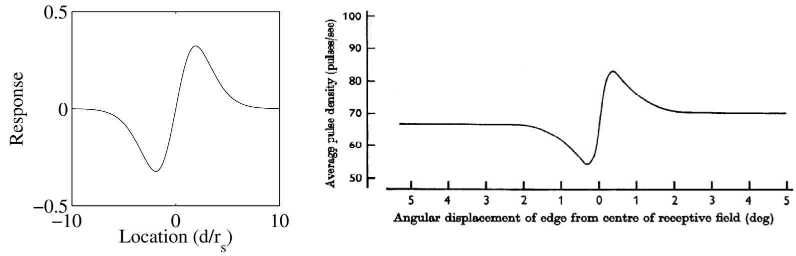

(a) Response curve in our model (b) Result of biological experiments

Fig. 3. Response curves

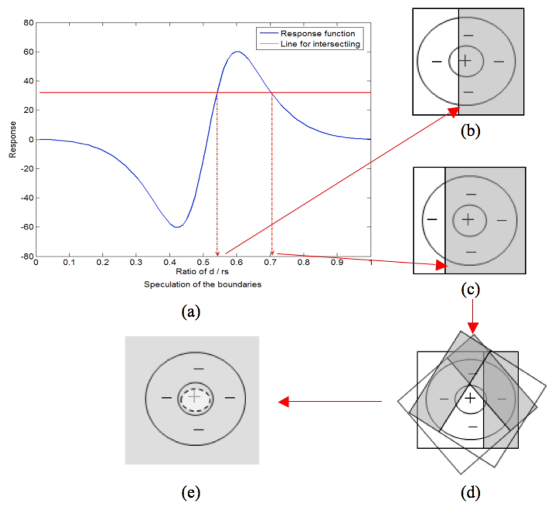

Fig. 4. Estimating boundary position. (a) Given a response line, normally two intersections exist. (b)(c) Two intersections correspond to two boundary positions. (d) Multiple candidates produce the same response. (e) Tangent lines of the dashed circle share the same response.

3 Simple Cells Drawing on Collective Junior Cells

Superimposed upon the RF of a simple cell are many RFs of LGN neurons. With RFs localized in a very limited area, these neurons generally respond to the same local feature. Therefore it is possible for a superior cell, i.e. the simple cell, to draw on conclusions according to their response with collective decision making policy applied on a neural computing basis.

Recent neurobiological experiments provided credible evidence for such a model. According to Reid & Alonso [18], they recorded 104 LGN neurons, among which RFs of 74 neurons were superimposed upon a simple RF and 23 of 74 neurons showed positive correlation with the superimposed simple cell. The

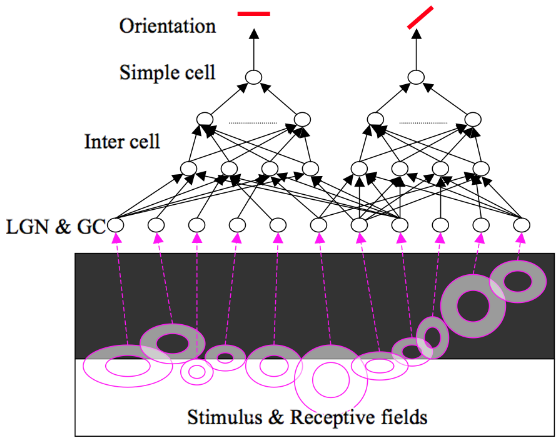

Fig. 5. Neural network model for collective decision-making

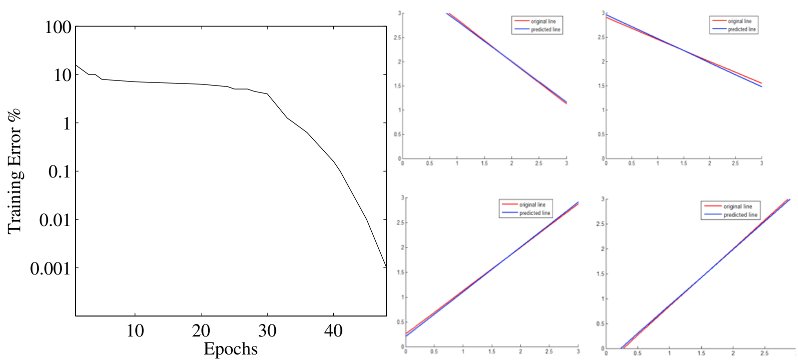

(a) Error rate reduced to 0.001 after 48 epochs.

(b) Original lines and reconstructed ones.

Fig. 6. Performance of the network

correlation analysis implied possible synaptic connections between these LGN neurons and the simple cell. However, biological experiments are not able to reveal the underlying neural computation process. Our model supplies a possible implementation of the process as follows.

Figure 5 shows a hierarchical neural network used to calculate boundary orientation. The network consists of several strictly localized BP (back propagation) subnets. Every subnet simulates a single simple cell and its corresponding junior cells. BP network has its solid foundation in neurobiology, which guarantees that the model is feasible in the visual cortex and well resembles the layered structure of primary visual cortex.

An experiment is designed to train and test the network in Figure 5. In the experimental network, the RFs of 8 GC neurons are distributed randomly within an elongated small region where a series of boundary stimuli is presented. Boundaries are formulated in line equations such as $y = ax + b$, where a, b are line parameters. The response of 8 GCs forms an input vector to the network. The network is trained so that the output vector approximates to line parameters. The performance of the network is shown in Figure 6. Significant convergence emerges after 40 epochs (Figure 6(a)). We reconstruct the boundary lines from the network output. A comparison between reconstructed lines and original ones indicates that the network is precise for boundary detection (Figure 6(b)).

4 Mathematical Essence and Limitations of Collective Estimation

Following the previously defined model of GC in section 2, we compute the response of a single GC as the convolution of the input stimulus and the weight matrix of the receptive field. The response can thus be expressed into the following integral.

$$\eta = \int_{-\infty}^{\infty}\int_{\infty}^{d} R(x,y)dxdy = \frac{k_c r_c^2 \pi}{2}\text{erf}\left(\frac{d}{r_c}\right) - \frac{k_s r_s^2 \pi}{2}\text{erf}\left(\frac{d}{r_s}\right) \qquad (4)$$

where d is the perpendicular distance between the center of RF and the boundary line, and $R(x, y)$ is the receptive field. Expanding the integral with the Gaussian error function (erf), it is apparent that the function resembles the response curve in Figure 3(a).

We then formulate boundary stimuli as line equations. With line parameters carefully chosen, lines are mapped to parameter pairs (a, b) in a one-to-one manner. Given a line and points P_1 and P_2 picked from the line, the perpendicular distance from the line to the center point C of the RF is calculated as:

$$d = (P_2 - P_1)\begin{bmatrix} 0, & -1 \\ 1, & 0 \end{bmatrix}(C - P_1)^T \cdot ||P_2 - P_1||^{-1}. \qquad (5)$$

Given a constant d, the equation above defines a curve in the real plane of (a, b). Every point in the curve corresponds to a possible boundary line. The intersection of several such curves determines a unique boundary line, which forms the final output of a simple cell.

The balance between performance and cost of physiological structures is achieved via evolution. The structure of our algebraic model meets the same problem of efficiency. The problem is often finally reduced to optimizing the quantity or RF size of GCs. To give a feasible interval for the RF size, two criteria are formed. The first one is discrimination, defined in the form of average variance of response (AVR). It ensures that a GC responds differently to different boundaries. The second criterion is robustness, defined in the form of signal noise ratio (SNR). The efficiency problem is thus reduced to maximizing both of these simultaneously:

$$\text{AVR} = \frac{1}{2r_s}\int_{RF} |d\eta|, \qquad (6)$$

$$\mathrm{SNR} = \frac{\max|\eta|}{|\int n \cdot R(x)dx|} \tag{7}$$

where n is the noise. For simplicity, one-dimensional model is used and n is assumed to be a sine wave with small amplitude and frequency approximate to the sample rate. Assuming digital images as input to our model and a sample rate of 1 pixel per sample, the two criteria are plotted as functions of the radius of RF (Figure 7). The figure implies that a RF radius of 2 to 3 pixels achieves the best efficiency.

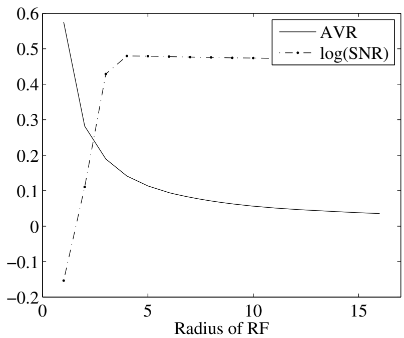

Fig. 7. AVR and SNR as functions of RF radius

5 Discussion

The criterion of biological evolution is "no better than barely enough" or "knowing when to stop". The neural system is a product of evolution and thus it obeys this discipline. Its structure meets its functional demand without over-evolution. It is extravagant in biological evolution to assume a model in which GC receptive fields of equal area line up coaxially in every direction. On the contrary, a random arrangement is employed in our model instead of the highly ordered one. Given a simple scheme working well, it is not necessary to evolve a complex one. The neurobiological experiments using biological staining techniques reveal possible synaptic connections and yet fail to explain the underlying neural computation [2, 19, 20]. Neither can electrophysiological recordings of single electrode explain the meaning of data or control flow carried by the signals [9, 19]. Owing to the complexity in decomposition and temporal coding of neural signals, even multi-channel electrophysiological recordings are not sufficient to explain the process of neural computing. In the neurobiological aspect, there is not enough evidence to prove which model, geometrical one or algebraic one, is absolutely impossible. Hubel and Wiesel's hypothesis, in its initial condition, is much too rigorous in the organization of RFs and neural computing. By loosing the constraints, we present in this paper a model, which is mathematically feasible and easily implemented as neural networks with lower computing complexity.

Neural systems generate an internal representation for the external world. With the representation it is able to accomplish many tasks such as scene understanding, object recognition and visual tracking. Meanwhile, neural systems have to balance two competing goals, the performance and the cost. The grid cells found in mammalian brains [21] precisely indicate that neural systems are able to carry out inference from a population of neurons of which each neuron generates only limited and rough information. Visual cortex proves to be such an example. Given coarse and localized output of GC and LGN neurons, visual cortex synthesizes the information successfully into vision. Our model serves as a possible implementation of such neural computation. Our future research is to integrate related evidence in anatomy, electrophysiology and animal behavior into the computational model and to achieve computer vision synthesized in a higher level.

Acknowledgments. This work was supported by the 973 Program (Project No. 2010CB327900), the NSFC major project (Project No. 30990263), and the NSFC project (No. 6115042). We thank the anonymous referees for their helpful comments.

References

1. Hubel, D.H., Wiesel, T.N.: Receptive fields, binocular interaction and functional architecture in the cat's visual cortex. The Journal of Physiology 160, 106–154 (1962)
2. Alonso, J.M., Usrey, M., Reid, C.: Rules of connectivity between geniculate cells and simple cells in cat primary visual cortex. J. Neurosci. 21(11), 4002–4015 (2001)
3. Wielaard, D., Shelley, M., McLaughlin, D., Shapley, R.: How simple cells are made in a nonlinear network model of the visual cortex. J. Neurosci. 21(14), 5203–5211 (2001)
4. Sompolinsky, H., Shapley, R.: New perspectives on the mechanisms for orientation selectivity. Current Opinion in Neurobiology 7(4), 514–522 (1997)
5. Ferster, D., Miller, K.D.: Neural mechanisms of orientation selectivity in the visual cortex. Annu. Rev. Neurosci. 23, 441–471 (2000)
6. Lauritzen, T., Miller, K.: Different roles for simple-cell and complex-cell inhibition in v1. J. Neurosci. 23(32), 10201–10213 (2003)
7. Kara, P., Pezaris, J., Yurgenson, S., Reid, C.: The spatial receptive field of thalamic inputs to single cortical simple cells revealed by the interaction of visual and electrical stimulation. PNAS 99(25), 16261–16266 (2002)
8. Lee, A.B., Blais, B., Shouval, H.Z., Cooper, L.N.: Statistics of lateral geniculate nucleus (lgn) activity determine the segregation of on/off subfields for simple cells in visual cortex. PNAS 97(23), 12875–12879 (2000)
9. Liu, B.H., Li, P., Sun, Y., Li, Y.T., Zhang, L., Tao, H.: Intervening inhibition underlies simple-cell receptive field structure in visual cortex. Nature Neuroscience 13(1), 89–96 (2010)
10. Hansen, T., Neumann, H.: A simple cell model with dominating opponent inhibition for robust image processing. Neural Netw. 17, 647–662 (2004)
11. Troyer, T.W., Krukowski, A.E., Miller, K.D.: Lgn input to simple cells and contrast-invariant orientation tuning: An analysis. Journal of Neurophysiology 87(6), 2741–2752 (2002)

12. Bhaumik, B., Mathur, M.: A cooperation and competition based simple cell receptive field model and study of feed-forward linear and nonlinear contributions to orientation selectivity. Journal of Computational Neuroscience 14(2), 211–227 (2003)
13. Gardner, J., Anzai, A., Ohzawa, I., Freeman, R.: Linear and nonlinear contributions to orientation tuning of simple cells in the cat's striate cortex. Visual Neuroscience 16(6), 1115–1121 (1999)
14. Cai, D., Tao, L., Shelley, M., McLaughlin, D.W.: An effective kinetic representation of fluctuation-driven neuronal networks with application to simple and complex cells in visual cortex. PNAS 101(20), 7757–7762 (2004)
15. Tao, L., Shelley, M., McLaughlin, D., Shapley, R.: An egalitarian network model for the emergence of simple and complex cells in visual cortex. PNAS 101(1), 366–371 (2004)
16. Rodieck, R.W.: Quantitative analysis of cat retinal ganglion cell response to visual stimuli. Vision Res. 5(11), 583–601 (1965)
17. Enroth-Cugell, C., Robson, J.G.: The contrast sensitivity of retinal ganglion cells of the cat. The Journal of Physiology 187(3), 517–552 (1966)
18. Reid, R.C., Alonso, J.M.: Specificity of monosynaptic connections from thalamus to visual cortex. Nature 378(6554), 281–284 (1995)
19. Miikkulainen, R., Bednar, J.A., Choe, Y., Sirosh, J.: Computational Maps in the Visual Cortex. Springer (2005)
20. Niu, W.Q., Yuan, J.Q.: Letters: Recurrent network simulations of two types of non-concentric retinal ganglion cells. Neurocomput. 70, 2576–2580 (2007)
21. Doeller, C.F., Barry, C., Burgess, N.: Evidence for grid cells in a human memory network. Nature 463(7281), 657–661 (2010)

Evaluation of UAS Camera Operator Interfaces in a Simulated Task Environment: An Optical Brain Imaging Approach

Murat Perit Çakır[1,2], Abdullah Murat Şenyiğit[3], Daryal Murat Akay[1], Hasan Ayaz[2], and Veysi İşler[3]

[1] Department of Cognitive Science, Informatics Institute, Middle East Technical University, Universiteler Mah., 06800, Ankara, Turkey
[2] CONQUER Collaborative, School of Biomedical Engineering, Science & Health Systems, Drexel University, 3508 Market St., 19104 Philadelphia, PA
[3] TAF Modelling and Simulation R&D Center, Middle East Technical University Universiteler Mah., 06800, Ankara, Turkey
perit@ii.metu.edu.tr, {senyigit,daryal.akay}@metu.edu.tr, hasan.ayaz@drexel.edu, isler@ceng.metu.edu.tr

Abstract. In this paper we focus on the effect of different interface designs on the performance and cognitive workload of sensor operators (SO) during a target detection task in a simulated environment. Functional near-infrared (fNIR) spectroscopy is used to investigate whether there is a relationship between target detection performance across three SO interfaces and brain activation data obtained from the subjects' prefrontal cortices that are associated with relevant higher-order cognitive functions such as attention, response selection and decision making. The preliminary findings of the study suggest that brain regions in the vicinity of medial frontal gyrus of the right hemisphere respond differentially to the cognitive workload induced by different interfaces.

Keywords: Optical brain imaging, functional near-infrared spectroscopy, target detection, interface evaluation, UAS camera operators.

1 Introduction

The use of Unmanned Aerial Systems (UAS) in military and civilian settings has dramatically increased in the past few years. Despite the recent advances in autonomous controls, operator interfaces and avionics, human operators continue to play an important role in the safety and efficiency of UAS operations. In particular, human operators are involved with various mission-critical tasks such as meaningful information extraction from a complex scene, intelligence gathering, target categorization and adaptive problem solving in response to mission contingencies [1]. Moreover, research on collaborating UASs suggests that operators will be expected to control multiple uninhabited aerial vehicles in the near future [2]. Consequently, the

H. Zhang et al. (Eds.): BICS 2012, LNAI 7366, pp. 62–71, 2012.

rapid expansion of the scope and complexity of UAS missions require operators to carry out cognitively-demanding tasks in an informationally-dense environment [3]. Therefore, the way the interfaces through which human operators control, monitor and coordinate UAS operations are designed will continue to play a critical role in the safety and success of UAS missions.

Despite the increased role of automation in UASs, various mission critical tasks are still carried out by human operators in most operational platforms. For instance, the MQ1 Predator platform used by the US Army is operated by a pilot and a sensor operator. Most human factors studies especially focus on interface design issues that influence the pilot's performance [4]. Nevertheless, the interfaces through which sensor operators monitor and control the payload of a UAS also play a key role during mission-critical tasks such as target detection and intelligence gathering. Carrying out such visual tasks on a moving platform is a cognitively demanding task for sensor operators, since they need to stay vigilant and attend to relevant features of the moving scene during long periods of time. Therefore, methods that can reliably evaluate design decisions in terms of the cognitive workload they induce on human operators are particularly important for improving sensor operator interfaces.

Most human factor studies on UAS operations rely on self-reporting surveys and behavioral performance measures to assess the cognitive workload induced by a particular interface. Despite their popularity, self-reporting instruments such as NASA TLX are criticized for being subjective measures of cognitive workload [1].Another issue with such methods is that they are administered after a trial is complete, and hence are not sensitive to changes in workload during the course of a task. Therefore, there is a need for devising more reliable indices for monitoring changes in cognitive workload due to temporal variations across tasks and interface conditions. In this paper we aim to respond to this need by exploring the use of optical brain imaging techniques to identify neuro-physiological correlates of cognitive workload induced by different sensor operator interface designs.

The potential use of optical brain imaging technology for this purpose has been initially explored in the context of UAS operations and air traffic control [5]. This paper builds on this line of work by focusing on the effect of different interface designs on the performance and cognitive workload of sensor operators during a target detection task in a simulated environment. In particular, functional near-infrared (fNIR) spectroscopy has been implemented to investigate whether there is a correlation between target detection performance across 3 sensor operator interfaces during simulated missions and brain activation data obtained from the subjects' prefrontal cortices that are known to be associated with higher-order cognitive functions such as attention, working memory, response selection and decision making [6]. The specific aim of the study is to identify neuro-marker(s) that can be used for assessing the cognitive workload induced by different interface designs.

The rest of the paper is organized as follows. Section 2 introduces the optical brain imaging technique employed in this study. The following section describes the experimental setup and the methodology. The next section summarizes the findings of the study. Finally, the paper concludes with a discussion of the findings and directions for future research.

2 Functional Near-Infrared Spectroscopy

fNIR is a neuroimaging modality that enables continuous, noninvasive, and portable monitoring of changes in blood oxygenation and blood volume related to human brain function. Neuronal activity is determined with respect to the changes in oxygenation since variation in cerebral hemodynamics are related to functional brain activity through a mechanism which is known as neurovascular coupling [7]. Over the last decade, studies in the laboratory have established that fNIR spectroscopy provides a veridical measure of oxygenation and blood flow in the brain [7, 8]. fNIR is not only non-invasive, safe, affordable and portable, it also provides a balance between temporal and spatial resolution which makes fNIR a viable option for *in-the field* neuroimaging.

fNIR technology uses specific wavelengths of light, introduced at the scalp, to enable the non-invasive measurement of changes in the relative ratios of deoxygenated hemoglobin (deoxy-Hb) and oxygenated hemoglobin (oxy-Hb) in the capillary beds during brain activity. Typically, an optical apparatus for fNIR Spectroscopy consists of at least one light source and a light detector that receives light after it has interacted with the tissue. Photons that enter tissue undergo two different types of interaction: absorption and scattering [9]. Whereas most biological tissues (including water) are relatively transparent to light in the near infrared range between 700 to 900 nm, hemoglobin is a strong absorber of light waves in this range of the spectrum.

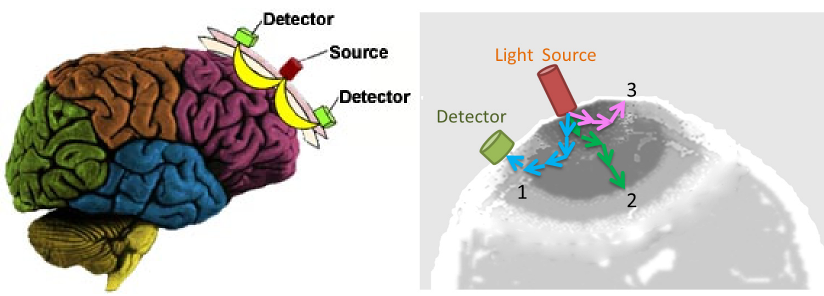

Fig. 1. The banana shaped path which includes the photons scattered back to the photodetector (left). Representative paths (right), enumerated as 2 and 3 correspond to photons absorbed by the tissue and scattered out of the scalp without reaching the detector, respectively.

Two chromophores, oxy- and deoxy-Hb, are strongly linked to tissue oxygenation and metabolism [7]. Fortuitously, the absorption spectra of oxy- and deoxy-Hb remain significantly different from each other allowing spectroscopic separation of these compounds to be possible by using only a few sample wavelengths. Once photons are introduced into the human head, they are either scattered by extra- and intracellular boundaries of different layers of the head (skin, skull, cerebrospinal fluid, brain, etc.) or absorbed mainly by oxy- and deoxy-Hb. If a photodetector is placed on the skin surface at a certain distance from the light source, it can collect the photons that are scattered and thus have travelled along a “banana shaped path” (Figure 1) from the source to the detector [7, 8].

Recent studies with fNIR indicate that this neuroimaging modality can effectively monitor cognitive tasks such as attention, working memory, target categorization, and problem solving [5, 10]. These experimental outcomes compare favorably with fMRI studies, and in particular, with the blood oxygenation level dependent (BOLD) signal. Since fNIR can be implemented in the form of a wearable and minimally intrusive device, it has the capacity to monitor brain activity under real life conditions and in everyday environments.

3 Materials and Methods

3.1 Continuous-Wave fNIR System

During our experiment the prefrontal cortex of the participants were monitored with a continuous wave fNIR system manufactured by fNIR Devices LLC (Potomac, MD; www.fnirdevices.com), which was developed at the Optical Brain Imaging Laboratory at Drexel University. The system is composed of a flexible headpiece that holds the light sources and the detectors, a control box for hardware management and a computer that runs the data acquisition software.

The flexible sensor pad contains 4 light-emitting diodes (LED) with built in peak wavelengths at 730, 805, 850 nm and 10 detectors designed to sample cortical areas underlying the forehead. The sensor has a temporal resolution of 500 miliseconds. . During data acquisition LED sources are activated one at a time and the four photodetectors that surround the active source are sampled. The positioning of the light sources and the photodetectors on the sensor pad provide a total of 16 measurement locations to monitor dorsal and inferior frontal cortical areas underlying the forehead.

3.2 Experimental Setup and Protocol

The experimental setup is composed of a Protocol-Computer, a Data-Acquisition computer and the fNIR system. The fNIR sensor is positioned on the forehead of the subject who is sitting in front of the Protocol Computer. COBI Studio Software [11] was used for fNIR data acquisition, monitoring and visualization. Statistical analysis was performed with IBM Inc.’s SPSS software, version 19.

The protocol computer runs the simulation platform, which is based on Microsoft’s Flight Simulator X with the MQ-1 Predator UAV add-on by Firstclass Simulations. The protocol and the fNIR data acquisition computers were linked via a serial cable to transfer time synchronization markers for marking the onset of target detection actions.

Before the experiment, each participant was first informed about the experimental process and then shown a demo flight which was pre-recorded in Microsoft Flight Simulator. They were also informed about the type of targets they were going to spot. During the experiment, subjects were asked to watch pre-recorded flight videos by using different interface setups. Participants pressed a button when they detected the specific land target. While subjects were performing the task, relative changes in cerebral oxy-hemoglobin and deoxy-hemoglobin concentrations in their prefrontal cortex, as well as their success rates for detecting visual targets were recorded. Moreover, at the end of the experiment, subjects were asked to rate their physical and mental activity within each task configuration based on an instrument derived from the NASA TLX.

Subjects performed 8 different target detection tasks by using 3 different interfaces. The trials were counterbalanced to minimize the effects of task order and fatigue. The overall duration of all experiments was approximately 2 hours, including breaks. The task scenarios differed in terms of duration, number of targets, number of distractors and the distribution of targets on the flight path (see Figure 2 and Table 1).

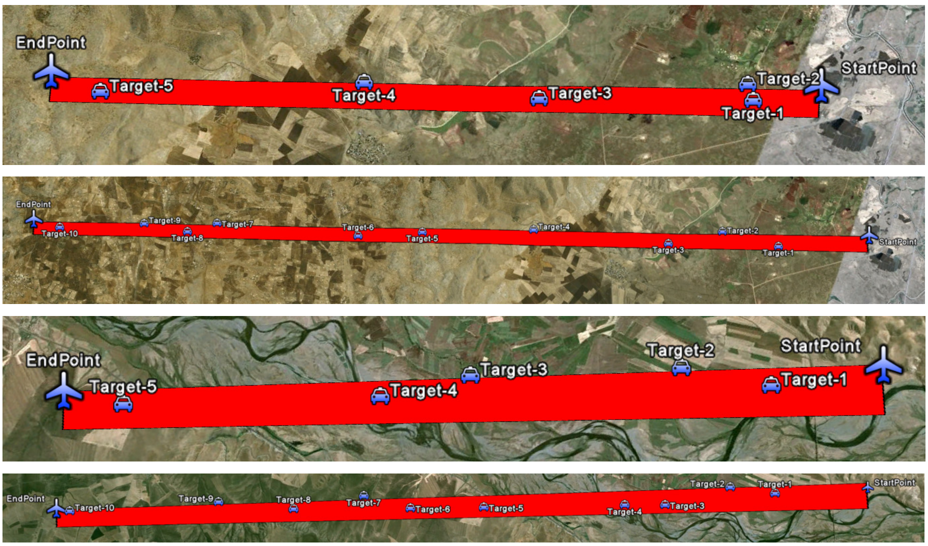

Fig. 2. The flight paths corresponding to 4 different task scenarios. The first two scenarios were used to compare single and dual camera interfaces, whereas the last two scenarios were used to compare monitor and projector conditions.

In the first interface condition, the flight video was displayed on a single 24 inch monitor at full screen mode at a resolution of 1280x800 pixels. In the second interface condition two separate displays were provided simultaneously on the same monitor. The first display covered most of the screen and provided the same video feed as the first interface. The smaller display was positioned on the right bottom of the screen, which aimed to model a camera mounted on the bottom of the plane. This second view was controllable by a joystick, which provided users the ability to rotate the camera to the desired position while the view of the main window remaining the same. Participants could zoom in and out via this window, and when they release the joystick the camera is reset to a default view angle. Such features were implemented in an effort to make the new display easier to control. In the last interface condition, the flight video was displayed on a projector screen at the same resolution. The size of the projection system was 158x99 cm. The projected image was displayed at a throw distance of 80 cm and at an aspect ratio of 16:10 (see Fig. 3).

Table 1. Task scenario definitions

Scenario	Duration (min.)	# of Targets	# of Distractors	Distribution of Targets
1	2.5	5	10	Close to center
2	5	10	15	Distributed
3	2.5	5	40	Close to center
4	5	10	60	Distributed

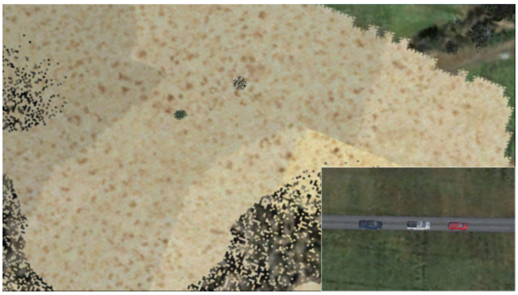


Fig. 3. Dual camera and projector conditions used in the experiment. Single camera condition used the same video feed as the projector condition.

First two scenarios were used to compare the single and dual camera interfaces. The remaining scenarios were used to compare the single camera and the projector interfaces. Hence, the single camera interface condition was treated as a baseline condition. 4 different task scenarios at two different durations were used in order to avoid participants remembering the positions of targets from one trial to the other.

Eight college students between the ages 18 to 25 volunteered to participate in this study. The participants were right-handed and reported no history of neurological disorders. Subjects did not have prior experience with UAS operations. All subjects completed the experiment at the TAF MODSIMMER Laboratory located at Middle East Technical University.

3.3 Data Analysis

For the preliminary processing, block analysis was used to identify fNIR data that corresponds to initial rest period and target detection tasks. First, linear phase, finite impulse (FIR) low pass filter with cut-off frequency of 0.14Hz was applied to the 16 voxel raw fNIR data to eliminate high frequency noise due to physiologically irrelevant data (such as respiration and heart pulsation effects) and equipment noise. Then, Sliding Windows Motion Artifact filter [12] was employed to minimize the effect of motion artifact on the measurements. Finally, modified Beer Lambert Law [10] was applied to the filtered fNIR data to calculate the changes in oxy- and deoxy-hemoglobin concentration. 3 of the subjects' data had to be eliminated due to the presence of excessive noise in the raw fNIR data. The statistical analysis presented in the next section is based on the data obtained from the remaining 5 subjects.

4 Results

Analysis of Behavioral Data. A 4x2 repeated measures ANOVA on mean response time for target detection at each task scenario found a significant interaction effect of task scenario condition and task duration ($F_{3,12}$=4.508, p<0.05, η^2=.530 with Mauchly's W=.464, p>.05). Response time values did not significantly differ in the first two scenario conditions. This seems to be due to the differential influence task duration had on tasks 1 and 2 versus 3 and 4. A Bonferroni corrected 2x2 repeated measures ANOVA on response times for the last two scenario conditions found a significant main effect of duration ($F_{1,4}$=14.994, p<0.025, η^2=.789). Same analysis did not find a significant difference between the first two scenarios.

Mean accuracy of target detection did not reveal a significant difference across task types. Accuracy was slightly decreased in the projector condition when the task duration was increased. Participants obtained close accuracy scores for the remaining task scenarios and durations.

A frequency analysis of missed targets showed that subjects tended to miss targets the most when the target object was presented alone. In 18 cases subjects could not detect the target when it was the only object in the scene. Remaining 13 instances involved cases where one or more distractors were visible together with the target object. Most misses occurred in the projector condition, but the conditions did not significantly differ in terms of number of misses.

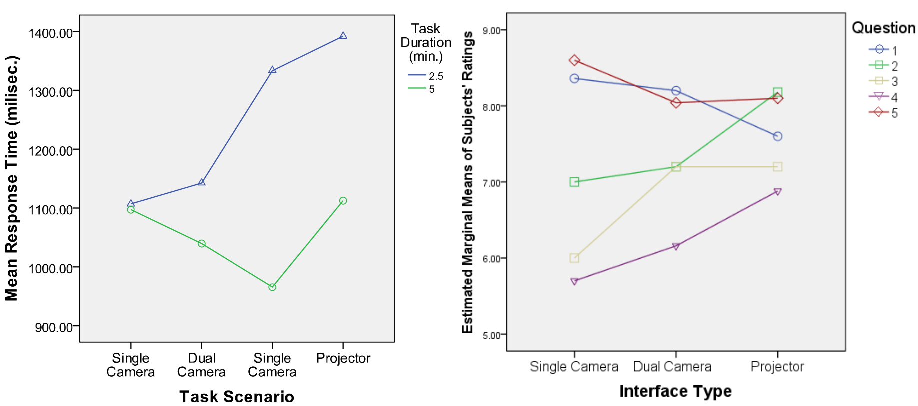

Fig. 4. Mean response time values observed at each condition for successfully detected targets (left), and subjects' ratings of each interface condition after the experiment (right)

After the experiment subjetcts were asked to rate each interface according to the difficulty of target detection (question 1), cognitive and physical load they experienced (questions 2 and 3) and the level of time pressure they perceived due to the pace of the missions (question 4). Finally, they were asked to make a self-assessment of their overall success at each condition (question 5). All assessments were made at a scale of 0 to 10. Figure 4 (right) shows the average ratings of each interface along these five dimensions. Subjects rated the projector case as the most difficult in terms of target detection. Projector case induced the most cognitive load as well. Dual camera and projector cases were reported to induce more physical load as compared to the baseline (single camera) conditions. Projector case induced the most time pressure according to the subjects, even though the pace of the flight videos were the same across all conditions. Self-assessed level of success was slightly higher in the baseline condition. Nevertheless, repeated measures ANOVA tests did not find any of these differences statistically significant at the p=0.05 level.

Analysis of fNIR Data. Statistical analysis on fNIR data was conducted on mean oxygenation values computed for each subject across 16 channels. Oxygenation refers to the difference between the concentrations of oxygenated and deoxygenated hemoglobin molecules. An increase in oxygenation suggests that there is an increasing level of neural activation under the cerebral region monitored by the corresponding optode.

A 2-way repeated measures ANOVA was conducted on the fNIR data with task and duration as the within-subjects factors. Mauchly's test indicated that the sphericity assumption was tenable. The analysis revealed main effects of task scenario at optode 12 ($F_{3,9}$=19.638, $p<0.01$, η^2=.867; Mauchly's W=.074, $p>0.05$), which is close to medial frontal gyrus of the right hemisphere. No main effect of duration or interaction effects were observed at voxel 12. LSD pair-wise comparisons indicated a significant difference between scenarios 1 and 3 ($p<0.01$), as well as between 2 and the rest of the scenarios ($p<0.01$, $p<0.05$, $p<0.05$). Figure 5 below displays the mean oxygenation values obtained across 4 task scenarios and 2 duration levels. 2-way repeated measures ANOVAs conducted at different optodes did not reveal any significant differences between task and duration conditions.

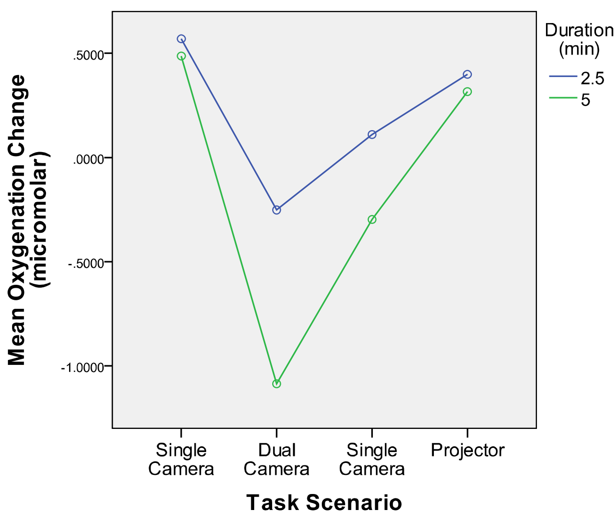

Fig. 5. Mean oxygenation change measured at optode 12

5 Discussion

In this study we aimed to evaluate three SO interface conditions in terms of their influence on the subjects' target detection performance and cognitive workload. A single camera interface that represents conventional SO interfaces was compared against projector and dual camera interfaces. The statistical analysis of behavioral and fNIR data suggests that the addition of a joystick-controlled camera in the dual camera condition neither induced excessive cognitive load nor impaired task performance. Participants using the dual camera interface experienced less activity at optode 12, which monitors the right medial frontal gyrus that is known to be responsive to cases where subjects need to choose between responding or not responding to an infrequent event (e.g. presence of a target stimulus) [13]. The decreased activity at this location during this interface condition may be due to the affordances of the additional camera, which enable users to zoom in/out over the field and make the response selection decision relatively easier as compared to other static interface conditions.

Although the difference was not statistically significant, the increase in missed cases and response time as well as the results of the post-experiment survey indicated that subjects experienced the most difficulty in the projector case. This observation is corroborated with fNIR findings at optode 12, which suggests that the projector case recruits significantly more activation in this region, particularly as compared to the dual camera condition. Thus, the preliminary findings of this study suggest that the dual camera condition can be a viable interface design choice, given the slight improvement in performance and a significant difference in terms of workload as measured by fNIR. The larger camera view provided by the projector condition did not bring any improvement in target detection accuracy as compared to other interface conditions.

We plan to expand this study further by increasing our sample size and incorporating eye tracking technology in an effort to better capture how subjects allocate their attention to objects in the scene at different interface conditions. We also plan to incorporate well-known paradigms such as odd-ball detection in our protocol in an effort to better isolate neural activity due to cognitive processes underlying visual target detection performance in a realistic setting like UAS operations.

Acknowledgments. This study was supported by the Turkish Armed Forces (TAF) & Middle East Technical University (METU) Modeling and Simulation R&D Center.

References

1. Cooke, N.J., Pringle, H., Pederson, H., Connor, O., Salas, E.: Human Factors of Remotely Operated Vehicles. Elsevier, The Netherlands (2006)
2. Bethke, B., Valenti, M., How, J.: Cooperative Vision Based Estimation and Tracking Using Multiple UAVs. In: Hirsch, M.J., et al. (eds.) Adv. In Cooper. Ctrl & Optimization. LNCIS, vol. 369, pp. 179–189 (2007)

3. Leduc, P.A., Rash, C.E., Manning, M.S.: Human factors in UAV accidents. Special Operations Technology 3(8) (2005)
4. Tvaryanas, A.P., Thompson, W.T.: Recurrent error pathways in HFACS data: analysis of 95 mishaps with remotely piloted aircraft. Aviation, Space, and Environmental Medicine 79(5), 525–532 (2008)
5. Ayaz, H., Shewokis, P.A., Bunce, S., Izzetoglu, K., Willems, B., Onaral, B.: Optical brain monitoring for operator training and mental workload assessment. Neuroimage 59(1), 36–47 (2012)
6. Curtis, C., D'Esposito: Persistent activity in the prefrontal cortex during working memory. Trends in Cognitive Sciences 7(9), 415–423 (2003)
7. Villringer, A., Chance, B.: Non-invasive optical spectroscopy and imaging of human brain function. Trends in Neurosciences 20(10), 435–442 (1997)
8. Chance, B., Anday, E., Nioka, S., Zhou, S., Hong, L., Worden, K., Li, C., Murray, T., Ovetsky, Y., Pidikiti, D., Thomas, R.: A novel method for fast imaging of brain function, non-invasively, with light. Optics Express 2(10), 411–423 (1998)
9. Strangman, G., Boas, D.A., Sutton, J.P.: Non-invasive neuroimaging using near-infrared light. Biol. Psychiatry 52(7), 679–693 (2002)
10. Izzetoglu, M., et al.: Functional near-infrared neuroimaging. IEEE Trans. Neural Syst. Rehabil. Eng. 13(2), 153–159 (2005)
11. Ayaz, H., Shewokis, P.A., Curtin, A., Izzetoglu, M., Izzetoglu, K., Onaral, B.: Using MazeSuite and Functional Near Infrared Spectroscopy to Study Learning in Spatial Navigation. J. Vis. Exp. e3443 (2011)
12. Ayaz, H., Izzetoglu, M., Shewokis, P.A., Onaral, B.: Sliding-window motion artifact rejection for functional near-infrared spectroscopy. In: EMBC 2010 (2010)
13. Huettel, S., McCarthy, G.: What is odd in the oddball task? Prefrontal cortex is activated by dynamic changes in response strategy. Neuropsychologia 42(2004), 379–386 (2004)

Cerebral Activation Patterns in the Preparation and Movement Periods of Spontaneous and Evoked Movements

Chunguang Li and Lining Sun

Robotics and Microsystems Center, Soochow University, 215021 Suzhou, China
lichunguang@suda.edu.cn

Abstract. Many BMI (brain machine interface) researches on the control of a prosthetic upper-limb/hand have been conducted. However, the BMI researches on the control of a walking-assistive device were few. Otherwise, brain activation was usually measured in a synchronous control mode. This reduced the naturality of brain activation. To realize asynchronous BMI control of a walking-assistive device, this paper studied cerebral activation pattern in both the spontaneous (asynchronous) and evoked (synchronous) movement states. Stepping and squatting stances movements were performed. Cerebral activation was simultaneously measured using NIRS (near-infrared spectroscopy) technology. Analysis of variation revealed that cerebral activation patterns in the two motion modes had a significant difference in both the imaginary/ preparation periods and movement periods. Particularly, the spontaneous movement achieved a more distinct difference than the evoked movement. It is confirmed that cerebral activation in the preparation periods of spontaneous movement is preferable for identifying motion intention of lower limbs.

Keywords: Cerebral activation, movement imaginary, actual movement, spontaneous state, evoked state.

1 Introduction

Recently, the number of disabled patients who have motor impairments has been increasing in worldwide. In order to support patients to control devices through thought processes, many researches on BMI (brain machine interface) were conducted. Meel Velliste *et al* have demonstrated that a monkey can control a prosthetic arm for self-feeding by using neural activity signals, which were detected with the mini-electrode-chip being implanted in the monkey's brain [1]. By using rtfMRI (real-time functional magnetic resonance imaging) technology, it was confirmed that BOLD (blood oxygenation level dependent) signals in brain can be used to control a robotic arm in horizontal or vertical movements [2]. By using EEG (electroencephalogram) technology, Tsinghua University realized the movement control of an artificial limb based on SSVEP (steady-state visual evoked potential). The movement patterns concluded 'hold a cup', 'turn over a cup', 'place a cup to the

H. Zhang et al. (Eds.): BICS 2012, LNAI 7366, pp. 72–81, 2012.

original position', and 'reset the position of the artificial limb' [3]. Meanwhile, Harbin Institute of Technology applied spontaneous EEG signals to distinguish three psychological assignments of virtual counting, conception of writing a letter, and complex multiplication [4]. Then, they controlled the movements of the thumb, forefinger, and medius of a prosthetic hand using the three psychological signals correspondingly. Also, LI *et al* could control the four movement patterns (free, moving, grabbing, and opening) of a neural prosthesis hand by distinguishing spontaneous EEG signals [5]. The online identification accuracy achieved 55%-65%. By analyzing the variations of cerebral blood and brain wave, which were measured using NIRS (near-infrared spectroscopy) and EEG respectively, the thought of a person who performed motor imaginary could be identified [6]. The identified thought could control Asimo, a robot of Honda, to raise hand or raise foot. The identification accuracy achieved 90%. Many other researches [7–9] on BMI control using NIRS technology were also performed recently.

However, the recent BMI researches mainly focused on the control of a prosthetic hand or an artificial upper limb. The researches on a walking assistive device or an artificial lower limb were very few. Patients will be in a motion state in walking assistive applications. Thus, brain activation measurements that are performed during static states [1–7, 9] are not practicable. In addition, the above BMI systems were in a synchronous control mode (there is a menu or a voice to evoke the beginning and ending of a task). A testing subject was not a real controller. This control method tends to cause false positive. Moreover, there are some other shortages in current BMI studies: ① The generation of SSVEP [2] requires an additional device to provide stimulus, which increases system cost. Besides, longtime operation may cause visual fatigue easily and reduce the prominence of evoked potential. This restricts operating time severely. ② As for BMI researches based on spontaneous EEG signals [4, 5], extensive prior training should be carried out to produce pattern-sensitive brain wave. And the patterns of this kind of brain wave are easily affected by subjective factors. ③ Even though the application of implanted electrode can enhance signal intensity and SNR (signal-to-noise) [1], implantation technology is difficult. And it is easy to cause immunologic reaction and callosity. Therefore, there exist psychological and ethical problems, which make this method not preferable in clinical application.

In order to make preparation for realizing asynchronous BMI control of a walking assistive device, this manuscript analyzed brain activation patterns of lower limbs in both the evoked and spontaneous movement states. Both the motor imaginary/preparation and the actual movement were performed. It is hypothesized that ① cerebral activation during motor imaginary/preparation can be used to identify motion intention. If the motor intention in the imaginary period is provided for walking assistive device before actual movement, the device may deliver a timely assistive force for patients to start movement. ② spontaneous movement state without a menu or a voice evocation is preferable for identifying motion intention than evoked movement state. In this study, cerebral activation was detected by applying NIRS technology. It supports non-invasive and dynamic measurement continuously. Using this technology, an additional stimulating device, such as a visual evoked device, or extensive prior training is not required. As well, NIRS has a higher temporal resolution than fMRI and PET (positron-emission tomography) and has a higher spatial resolution than EEG [10]. All these characteristics make NIRS technology favorable for dynamic BMI researches in rehabilitation fields.

2 Methods

2.1 Tasks

Both the stepping tasks and squatting stances tasks were performed by a subject. All the tasks were carried out in the following two states: ① evoked state: there was a beep to remind the start and end of a movement task; ② spontaneous state: the subject controlled the start and end of a movement task by himself. Therefore, there were four movement phases: stepping tasks in the evoked state, stepping tasks in the spontaneous state, crouching- standing tasks in the evoked state, and crouching-standing tasks in the spontaneous state. In each motion mode, there was a movement imaginary/preparation task before each actual movement task. In the evoked state, the imaginary task had a fixed period of three seconds. In the spontaneous state, the subject was requested to control the movement imaginary within a period of approximately three to five seconds. In the evoked state, there was a 30-s rest before a movement imaginary task. And the execution time of an actual movement task was 15 s. In the spontaneous state, the rest time and movement time were determined by the subject himself and were not fixed. The subject was instructed to rest the brain enough during the rest period. The start and end of each movement task was marked manually by another person. In all the four phases, the corresponding imaginary and movement tasks were repeated three times. The time sequences in one phase are shown in Fig. 1. During the movement period, the action of squatting stances was repeated several times rather than one time. In our experiment, the subject selected his favorable repetition frequency, which was around 1 Hz.

2.2 Cerebral Activation Measurement

As shown in Fig. 2, a FORIE-3000 brain imaging system (Shimadzu Corporation, Kyoto, Japan) was used to measure concentration changes of oxygenated hemoglobin (Oxy-Hb), deoxygenated hemoglobin (Deoxy-Hb), and total hemoglobin (Total-Hb), and further to analyze brain activation pattern in the preparation and execution periods of spontaneous and evoked movements. The emitter and detector probes were arranged in a 30 mm square grid. Three wavelengths of the near-infrared light were 780 mm, 805 mm, and 830 mm. Based on the Modified Beer Lambert law (MBLL) [11], the intensity changes at the three wavelengths were converted to relative changes in Oxy-Hb, Deoxy-Hb, and Total-Hb. The sampling period of hemoglobin signals was 0.22 s.

One set of 5×7 parietal flash holder was applied to fix emitters and detectors. Based on the international 10-20 system [12], the probe holder was placed on the top of the head with the midpoint in the posterolateral line (emitter 8) being placed in Cz portion. And the central vertical column of the probe holder was aligned to the median line that connects the nasion and inion. In this experiment, there were 28 probes in a 7 x 4 array. Therefore, the number of measurement channels was 45. The locations of each measurement channels are shown by the white rectangles with digital numbers in Fig .2. The measurement channels covered premotor cortices (PMC: channels 22, 28, 29, and 35 in the left hemisphere (PMC_L), and channels 24, 30, 31, and 37 in the right hemisphere (PMC_R)), supplementary motor areas (SMA: channels 10, 16, 17, and 23), medical prefrontal cortex (m-PFC: channels 2, 3, and 9 in the left hemisphere (m-PFC_L), and channels 4, 5, and 11 in the right hemisphere (m-PFC_R)), and dorsolateral prefrontal cortex (dl-PFC: channels 8, 14, 15, and 21 in the left hemisphere (dl-PFC_L), and channels 12, 18, 19, and 25 in the right hemisphere (dl-PFC_R)). The detected 7 regions were the regions of interest (ROI).

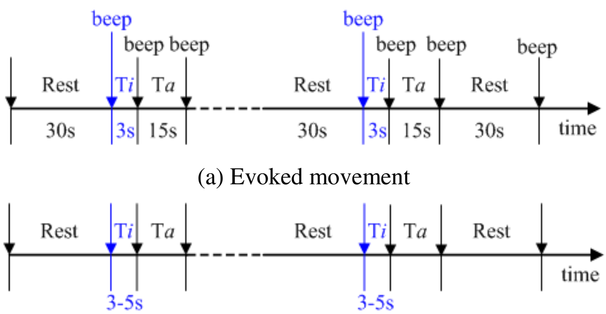

Fig. 1. Time sequence in one phase. T*i*: imaginary task; T*a*: actual movement task. The blue lines denote the start of movement imaginary. In the evoked state, another person gave a voice to remind the start of an imaginary task, and the NIRS system provided a beep to remind the start and end of a movement task; in the spontaneous state, the subject himself decided the time durations of rest, imaginary and actual movement.

2.3 Analysis Methods

The research [13] has demonstrated that the combination of Oxy-Hb and Deoxy-Hb is favorable for enhancing recognition accuracy and reducing delay. In addition, Lisa Holper [14] has confirmed that the mean and variance of the Oxy-Hb and Deoxy-Hb signals play a prominent role for mode identification. Therefore, both the mean and variance of the Oxy-Hb and Deoxy-Hb concentrations were analyzed to reflect brain activation pattern. Firstly, a smoothing operation with a 5-s moving average was performed to filter low-frequency noise that mixed in the channel signals. The obtained relative values of Oxy-Hb and Deoxy-Hb were recorded with ΔOxy-Hb and ΔDeoxy-Hb. Secondly, the means of ΔOxy-Hb and ΔDeoxy-Hb in the three imaginary and movement tasks were calculated for each channel. In the evoked state, the calculation was performed using the data in the whole periods of imaginary and movement tasks; in the spontaneous state, the moment of changing task form imaginary to actual movement was defined as a boundary, the calculation was performed using the data in the former 3.52 s and the latter 8.8 s. Thirdly, the durational mean and variance were calculated for the former 4 durations (the duration was defined as four sampling periods, 0.88s) and the latter 10 durations in each channel. The corresponding diagram is given in Fig. 3. The durational variance was calculated with the difference between the last and the first values dividing by 0.66. Fourthly, the mean concentration and average variance of ΔOxy-Hb and ΔDeoxy-Hb in ROI were calculated for the above 14 durations.

(a) FORIE-3000

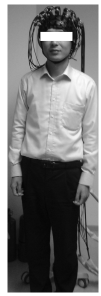

(b) Experimental setting

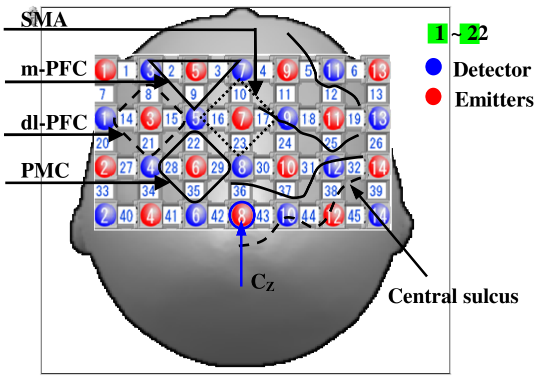

(c) Arrangement of the NIRS channels in the brain

Fig. 2. Cerebral activation measurement. PMC: premotor cortices; SMA: supplementary motor areas; m-PFC: medical prefrontal cortex; dl-PFC: dorsolateral prefrontal cortex.

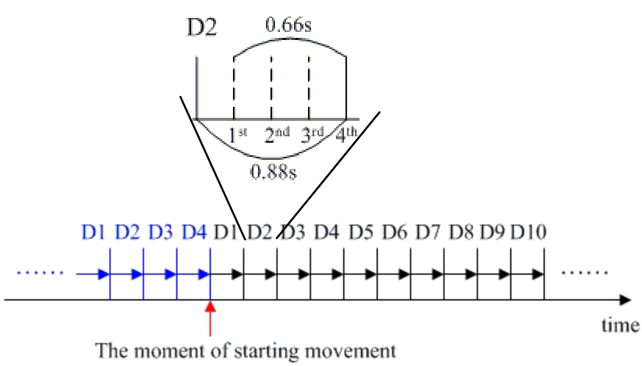

Fig. 3. Durations used for calculating the mean and variance of ΔOxy-Hb or ΔDeoxy-Hb in one imaginary task and one movement task

As for mean and variance of the Δ Oxy-Hb and Δ Deoxy-Hb in the preparation and execution tasks, three-way analysis of variation (ANOVA3) on ‘Mode’ (stepping and squatting stances) × ‘Region’ (SMA, as well as PMC, m-PFC and dl-PFC in the both hemispheres, 7 regions altogether) × ‘Duration’ (D1 to D4 in the preparation task and D1 to D10 in the execution task) was performed. The analysis model concluded the main effects of each factor and the interactions between ‘Mode’ and ‘Region’ and between ‘Mode’ and ‘Duration’. In this experiment, the two interactions were mainly analyzed. If an interaction between two factors were significant, simple main effect for the interaction would be further analyzed. Then the interaction between ‘Mode’ and ‘Region’ would be used to reflect the difference of the means and variations in the ROI between the two motion modes; The interaction between ‘Mode’ and ‘Duration’ would be used to reflect the difference of temporal changes in the means and variations between the two motion modes. All the above calculations and analysis were performed for the preparation task and execution task in both the spontaneous and evoked states. The analyses were performed with SPSS Statistics 17 software. The analyses used Tukey’s least significant difference (LSD) criterion. Statistical significance was set at $p < 0.01$.

3 Experimental Results

3.1 Spontaneous Movement

Preparation task: ANOVA3 revealed that the interaction between ‘Mode’ and ‘Region’ was significant for Δ Oxy-Hb_Mean (p = 0.00) and Δ Deoxy-Hb_Mean (p = 0.00), and the interaction between ‘Mode’ and ‘Duration’ was significant for Δ Oxy-Hb_Variation (p = 0.01) and Δ Deoxy-Hb_Variation (p = 0.00). As for Δ Oxy-Hb_Mean and Δ Deoxy-Hb_Mean, the simple main effect of the interaction between ‘Mode’ and ‘Region’ showed that the regional values had a significant difference in the both motion modes (p = 0.00 for both Δ Oxy-Hb_Mean and Δ Deoxy-Hb_Mean in each motion mode). The estimated marginal means of Δ Oxy-Hb and Δ Deoxy-Hb in different regions are displayed in Fig. 4. The regional orders of the Δ Oxy-Hb_Mean and Δ Deoxy-Hb_Mean are listed in the caption. Δ Oxy-Hb_Mean in PMC_R, m-PFC_L, and PMC_L had a distinctly different order in the two motion modes, and Δ Deoxy-Hb_Mean in PMC_R and m-PFC_R had a distinctly different order in the two motion modes. As for Δ Oxy-Hb_Variation and Δ Deoxy-Hb_Variation, the simple main effect of the interaction between ‘Mode’ and ‘Duration’ showed that ① Δ Oxy-Hb_Variation in D4 increased significantly than that in the former three durations in the squatting stances mode (p = 0.00); ② Δ Deoxy-Hb_Variation in D4 increased significantly than that in D1 and D2 in the stepping mode (p = 0.00). But Δ Oxy-Hb_Variation had no obvious difference among the four durations in the stepping mode, and Δ Deoxy-Hb_Variation had no obvious difference among the four durations in the squatting stances mode.

Movement task: As the results of the corresponding preparation task, the interaction between ‘Mode’ and ‘Region’ was significant for Δ Oxy-Hb_Mean (p = 0.00) and Δ Deoxy-Hb_Mean (p = 0.00). But the interaction between ‘Mode’ and ‘Duration’ was significant for ΔOxy-Hb_Mean (p = 0.00) and ΔOxy-Hb_Variation (p = 0.00). The simple main effect of the interaction between 'Mode' and 'Region' showed that the regional values had a significant difference in the both motion modes (p = 0.00 for both ΔOxy-Hb_Mean and ΔDeoxy-Hb_Mean in each motion mode). The estimated marginal means of regional ΔOxy-Hb and ΔDeoxy-Hb had the similar orders as that in the preparation task. The descending order of regional ΔOxy-Hb_Mean in the saquatting stances mode was m-PFC_L, m-PFC_R, dl-PFC_L, PMC_L, SMA, dl-PFC_R, and PMC_R. The descending order of regional ΔOxy-Hb_Mean in the stepping mode was PMC_R, m-PFC_L, SMA, dl-PFC_R, m-PFC_R, dl-PFC_L, and PMC_L. And the descending order of regional ΔDeoxy-Hb_Mean in the saquatting stances mode was PMC_R, dl-PFC_R, SMA, PMC_L, dl-PFC_L, m-PFC_R, and m-PFC_L. The descending order of regional ΔDeoxy-Hb_Mean in the stepping mode was dl-PFC_R, m-PFC_R, dl-PFC_L, SMA, PMC_L, PMC_R, and m-PFC_L. Also, ΔOxy-Hb_Mean in PMC_R, m-PFC_L, and PMC_L had a distinctly different order in the two motion modes, and ΔDeoxy-Hb_Mean in PMC_R and m-PFC_R had a distinctly different order in the two motion modes. The simple main effect of the interaction between 'Mode' and 'Duration' showed that both ΔOxy-Hb_Mean and ΔOxy-Hb_Variation had a significant difference among the 10 durations in the both motion modes (p = 0.00 for both the ΔOxy-Hb_Mean and ΔOxy-Hb_Variation in each motion mode). And the change of ΔOxy-Hb_Mean and ΔOxy-Hb_Variation in the saquatting stances mode had a higher speed than in the stepping mode.

3.2 Eovked Movement

Preparation task: The interaction between 'Mode' and 'Region' was significant for Δ Oxy-Hb_Mean (p = 0.00) and Δ Deoxy-Hb_Mean (p = 0.00), and the interaction between 'Mode' and 'Duration' was significant for ΔOxy-Hb_Mean (p = 0.00). As for the simple main effect of the interaction between 'Mode' and 'Region', the regional ΔOxy-Hb_Mean and ΔDeoxy-Hb_Mean were significantly different in the two motion modes (p = 0.00 for both ΔOxy-Hb_Mean and ΔDeoxy-Hb_Mean in each motion mode). The estimated marginal means are displayed in Fig. 5. ΔOxy-Hb_Mean in the two motion modes had the same regional order. Even though ΔDeoxy-Hb_Mean had different regional order in the two motion modes, only the adjacent SMA and dl-PFC_R, and the adjacent PMC_R and dl-PFC_L were reversed in the order. And the order difference was not so distinct as in the spontaneous state. As for the simple main effect of the interaction between 'Mode' and 'Duration', ΔOxy-Hb_Mean in D4 increased significantly than that in the former three durations in the both motion modes (p = 0.00).

Movement task: As the results of the corresponding preparation task, the interaction between 'Mode' and 'Region' was significant for ΔOxy-Hb_Mean (p = 0.00) and ΔDeoxy-Hb_Mean (p = 0.00). But the interaction between 'Mode' and 'Duration' was significant for ΔOxy-Hb_Mean (p = 0.00) and ΔOxy-Hb_Variation (p = 0.00). The simple main effect of the interaction between 'Mode' and 'Region' showed that the regional values had a significant difference in the both motion modes (p = 0.00 for both ΔOxy-Hb_Mean and ΔDeoxy-Hb_Mean in each motion mode).

As for the estimated marginal means of regional ΔOxy-Hb and ΔDeoxy-Hb, except that the order of ΔOxy-Hb_Mean in dl-PFC_L and m-PFC_L was reversed in the saquatting stances mode, all the other regional means had the same orders as that in the corresponding preparation task. As well, the difference in the orders of regional means between the two motion modes was not obvious. The simple main effect of the interaction between ‘Mode’ and ‘Duration’ reflected the similar results as in the movement task in the spontaneous state: ΔOxy-Hb_Mean and ΔOxy-Hb_ Variation in the 10 durations was significantly different ($p = 0.00$) in the both motion modes. And the change of ΔOxy-Hb_Mean and ΔOxy-Hb_Variation in the saquatting stances mode had a higher speed than in the stepping mode.

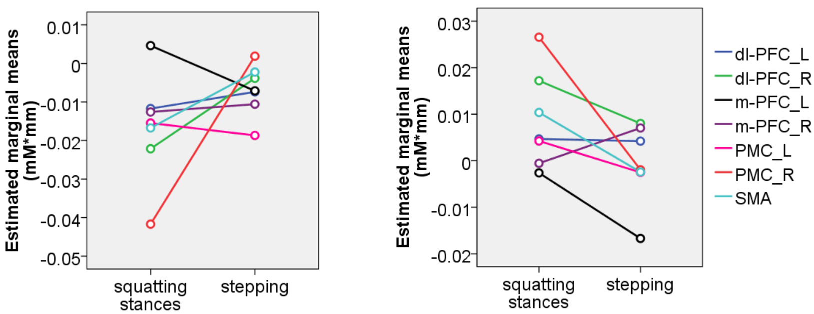

(a) ΔOxy-Hb (b) ΔDeoxy-Hb

Fig. 4. Estimated marginal means of regional ΔOxy-Hb and ΔDeoxy-Hb in spontaneous state. ΔOxy-Hb: m-PFC_L>dl-PFC_L>m-PFC_R>PMC_L>SMA>dl-PFC_R>PMC_R in the squatting stances mode; PMC_R> SMA>dl-PFC_R> m-PFC_L> dl-PFC_L> m-PFC_R>PMC_L in the stepping mode. Δ Deoxy-Hb: PMC_R>dl-PFC_R>SMA>dl-PFC_L>PMC_L>m-PFC_R>m-PFC_L in the squatting stances mode; dl-PFC_R>m-PFC_R>dl-PFC_L>PMC_R>PMC_L>SMA> m-PFC_L in the stepping mode.

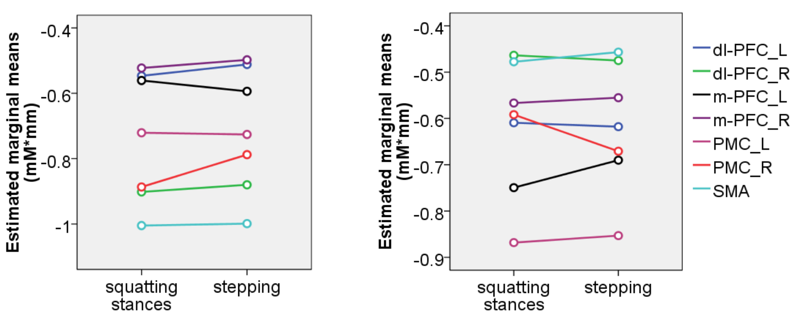

(a) ΔOxy-Hb (b) ΔDeoxy-Hb

Fig. 5. Estimated marginal means of regional ΔOxy-Hb and ΔDeoxy-Hb in evoked state. ΔOxy-Hb: m-PFC_R>dl-PFC_L>m-PFC_L>PMC_L>PMC_R>dl-PFC_R>SMA in both the squatting stances and stepping modes. ΔDeoxy-Hb: dl-PFC_R>SMA>m-PFC_R>PMC_R>dl-PFC_L>m-PFC_L>PMC_L in the squatting stances mode; SMA>dl-PFC_R>m-PFC_R>dl-PFC_L>PMC_R>m-PFC_L>PMC_L in the stepping mode.

4 Discussion

Regional difference: In the both motion modes of spontaneous and evoked movements, the preparation task and movement task had the similar regional order for both ΔOxy-Hb_Mean and ΔDeoxy-Hb_ Mean. Thus, the cerebral activation in the preparation task can be used to identify motion mode. This was consistant with our first hypothesis. In the spontaneous state, the regional orders were significantly different in the two motion modes. Especially were the regions of PMC_R, m-PFC_L, and PMC_L. However, in the evoked state, only ΔDeoxy-Hb_Mean had a different regional order in the two motion modes. And the difference was not so distinct as in spontanouse state. Therefore, spontaneous mvoement was more perferable for mode identification than evoked movement. This was consistant with our second hypothesis. In addition, Δ Oxy-Hb_Mean and Δ Deoxy-Hb_Mean in the spontaneous state had almost the reversed regional order. That is, as for the spontaneous moevment, the combination of Δ Oxy-Hb_Mean and Δ Deoxy-Hb_Mean may be preferable for enhancing the accuracy of mode identification.

Durational difference: As for the preparation task, ① in the spontaneous state, even though the interaction between 'Mode' and 'Duration' was not significant for ΔOxy-Hb_Mean, the simple main effect showed a significant increase of ΔOxy-Hb_Mean in D4 (p = 0.00). Besides, ΔOxy-Hb_Variation in D4 increased distinctly in the squatting stances mode and ΔDeoxy-Hb_Variation in D4 increased distinctly in the stepping mode; ② ΔOxy-Hb_Mean in D4 increased distinctly in the squatting stances mode and ΔDeoxy-Hb_Mean in D4 increased distinctly in the stepping mode. In addition, even though the interaction between 'Mode' and 'Duration' was not significant for ΔOxy-Hb_Variation, the simple main effect showed a significant increase of ΔOxy-Hb_Variation in D4 (p = 0.00). Actually, ΔOxy-Hb_Variation and ΔDeoxy-Hb_Variation in the spontaneous state and ΔOxy-Hb_Variation in the evoked mode increased obviously in D3, even though the differences between D3 and D2were not significant. Overall, the durational difference in the means and variations indicated that the obvious increase of signals was occurred around 2 to 3 s after the beginning of movement imaginary. If the increase of ΔOxy-Hb_Variation was considered as the start of movement intention, then to identify motion mode using the data in the corresponding durations, the mode identification time and applied data would be reduced. In fact, ANOVA3 on 'Mode' × 'Region' × 'Duration' was further performed for the durations of D2 and D3. And the results were same as the above analyses. Therefore, identifying the start of movement intention using ΔOxy-Hb_ Variation makes it possible to provide a timely movement control signal for a walking assistive device. Furthermore, in the spontaneous state, the difference of the increasing speed of ΔOxy-Hb_Variation and ΔDeoxy-Hb_Variation in the two motion modes may be used to enhance the accuracy of mode identification. For both the spontaneous and evoked movements, in the movement task, the change of ΔOxy-Hb_Mean and ΔOxy-Hb_Variation in the saquatting stances mode was faster than in the stepping mode. But in the preparation task, this trend can be found only for ΔOxy-Hb_Variation. Therefore, the increasing speed of ΔOxy-Hb_Variation in the preparation task may be useful for mode identification.

However, the experiment was performed only on one subject, experiments on many subjects and in many more motion modes should be further performed to confirm the statistical validity. And mode identification algorithm should be accomplished by using the mean and variation of both ΔOxy-Hb and ΔDeoxy-Hb, further to verify the preliminary conclusions of this study.

References

1. Meel, V., Perel Sagi, M., Chance Spalding, M., Whitford, A.S., Schwartz, A.B.: Cortical control of a prosthetic arm for self-feeding. Nature 453(7198), 1098–1101 (2008)
2. Lee, J.H., Ryu, J., Jolesz, F.A., Cho, Z.H., Yoo, S.S.: Brain-machine interface via real-time fMRI: Preliminary study on thought-controlled robotic arm. Neuroscience Letters 450(1), 1–6 (2009)
3. Cheng, M., Ren, Y., Gao, X., Wang, G., Ji, L., Gao, S.: A rehabilitation robot control technique based on EEG. Robot Technique and Application (4), 45–48 (2003)
4. Yang, D., Jiang, L., Zhao, J., Liu, H.: Control of prosthetic hand based on electrocephalogram. Journal of Jilin University 38(5), 1225–1230 (2008)
5. Li, Y., Zhanf, X., Wang, Y.: Development of A Control System of Neural Prosthesis Hand Driven by BCI. Features 26(4), 5–8 (2011)
6. Blain, L.: Honda's Brain-Machine Interface: controlling robots by thoughts alone (2009), http://www.gizmag.com/honda-asimo-brain-machine-interface-mind-control/11379/
7. Matsuyama, H., Asama, H., Otake, M.: Design of differential Near-Infrared Spectroscopy based Brain Machine Interface. In: 18th IEEE International Symposium on Robot and Human Interactive Communication, Toyama, Japan, pp. 775–780 (2009)
8. Tsubone, T., Tsutsui, K., Muroga, T., Wada, Y.: Estimation of Force Motor Command to Control Robot by NIRS-Based BCI. In: Ishikawa, M., Doya, K., Miyamoto, H., Yamakawa, T. (eds.) ICONIP 2007, Part II. LNCS, vol. 4985, pp. 969–978. Springer, Heidelberg (2008)
9. Sagara, K., Kido, K., Ozawa, K.: Portable single-channel NIRS-based BMI System for Motor Disabilities' Communication Tools. In: 31st Annual International Conference of the IEEE EMBS, Minneapolis, Minnesota, USA, pp. 602–605 (2009)
10. Lloyd-Fox, S., Blasi, A., Elwell, C.E.: Illuminating the developing brain: the past, present and future of functional near infrared spectroscopy. Neurosci. Biobehav. Rev. 34(3), 269–284 (2010)
11. Cope, M., Delpy, D.T., Reynolds, E.O., Wray, S., Wyatt, J., van der Zee, P.: Methods of quantitating cerebral near infrared spectroscopy data. Adv. Exp. Med. Biol. 222, 183–189 (1988)
12. Okamoto, M., Dan, H., Sakamoto, K., et al.: Three- dimensional probabilistic anatomical cranio-cerebral correlation via the international 10-20 system oriented for transcranial functional brain mapping. NeuroImage 21(1), 99–111 (2004)
13. Cui, X., Bray, S., Reiss, A.L.: Speeded Near Infrared Spectroscopy (NIRS) Response Detection. Journal of Nervous and Mental Disease 5(11), e15474 (2010)
14. Holper, L., Wolf, M.: Single-trial classification of motor imagery differing in task complexity: a functional near-infrared spectroscopy study. J. Neuroeng. Rehabil. 8(1), 34 (2011)

Neurobiologically-Inspired Soft Switching Control of Autonomous Vehicles

Erfu Yang[1], Amir Hussain[1], and Kevin Gurney[2]

[1] Division of Computing Science and Mathematics, University of Stirling
Stirling FK9 4LA, UK
{eya,ahu}@cs.stir.ac.uk
[2] Department of Psychology, University of Sheffield, Sheffield S10 2TP, UK
k.gurney@shef.ac.uk

Abstract. A novel soft switching control approach is presented in this paper for autonomous vehicles by using a new functional model for Basal Ganglia (BG). In the proposed approach, a family of fundamental controllers is treated as each of a set of basic controllers are thought of as an 'action' which may be selected by the BG in a soft switching regime for real-time control of autonomous vehicle systems. Three controllers, i.e., conventional Proportional-Integral-Derivative (PID) controller, a PID structure-based pole-zero placement controller, and a pole only placement controller are used in this paper to support the proposed soft switching control strategy. To demonstrate the effectiveness of the proposed soft switching approach for nonlinear autonomous vehicle control (AVC), the throttle, brake and steering subsystems are focused on in this paper because they are three key subsystems in the whole AVC system. Simulation results are provided to illustrate the performance and effectiveness of the proposed soft switching control approach by applying it to the abovementioned subsystems.

Keywords: Autonomous vehicles, switching control, basal ganglia, neurobiologically-inspired systems, multiple controller systems, action selection.

1 Introduction

Autonomous vehicle systems (AVS) have potential ability to perform dangerous, repetitive and automated tasks in remote or hazardous environments. The potential for AVS to accomplish challenging tasks such as autonomous and mobile surveillance in many important applications such as security and environment monitoring etc. is starting to draw together interdisciplinary researchers from several fields, including control systems, image processing, machine vision, robotics and computer science, etc. An important task in developing ground AVS such as autonomous cars is to design control systems for automatically controlling throttle, brake pedal and steering wheel so that the vehicle can follow a desired path and target speed, which could be a response to a leading vehicle, and at the same time keep a safe inter-vehicle

H. Zhang et al. (Eds.): BICS 2012, LNAI 7366, pp. 82–91, 2012.

separation under the constraints of driving safety, comfort and environmental requirements as well [1-3].

Conventional controller development methods may exhibit higher design and computational costs since the application object, an autonomous vehicle, is essentially a nonlinear plant and a complete mathematical representation (first principles model) is very difficult or nearly impossible. Therefore, alternative ways to reach human-like vehicle control have been extensively explored, for example, through the application of artificial intelligence techniques and system identification methods, etc. [1-3]. To address the important and challenging yaw motion problem in ACC (Adaptive Cruise Control), an alternative approach was developed in the Stirling AVC framework [1,3] in which the three drivetrain subsystems (i.e., throttle, brake and steering subsystems) were treated as one Multi-Input Multi-Output (MIMO) plant. Therefore, the interactions between the vehicle longitudinal and lateral dynamics, disturbances and nonlinearities can be treated together in multivariable MIMO control laws and also are able to be represented by using an MIMO neural network employed in the Generalized Learning Model (GLM) given in [1].

Preliminary collaborative work between the Stirling and Sheffield Groups [10-11] has revealed some intriguing similarities between the modular control architecture developed by the Stirling Group and the neurobiological ideas that are being independently explored by the Sheffield Group. Further to these previous research collaborations, this paper presents a novel neurobiologically-inspired soft switching control approach, which employs a BG-based soft switching and gating supervisor in order to automatically select and switch among a PID controller, a PID-structure based pole (only) placement controller, and a simultaneous pole-zero placement controller. Most importantly, the supervisor is able to gate online the outputs of multiple controllers, to form a soft switching solution to bumpless (nearly) real-time control of autonomous vehicles. This novel soft switching strategy is built on the new BG functional model that was successfully developed and validated by Gurney et al [7-9].The central role played in action selection by basal ganglia and related circuits including loops between thalamus and cortex and between BG and the thalamo-cortical loop were addressed in these pioneering papers.

All the controllers (actions or channels in the BG model) in the candidate bank are designed to operate using the same adaptive procedure and a selection among the various controller options is made on the basis of action request signals, i.e., salience [7-11]. The BG-based supervisor can use the relevant information such as reference input, overshoot, input variance, steady-state error, etc.) from the control system to evaluate the system behavior and choose the best controller ('hard' switching) or gate all the controllers to form a synthesized one ('soft' switching), for achieving the desired control specification.

In this paper, under the developed Stirling AVC framework [1,3] the proposed soft switching approach is applied to the benchmarking systems, i.e., the throttle, brake and steering subsystems for tracking the given reference signals (desired outputs) by using a new functional BG model as a soft action selector or switch.

Another aim of this work is also to develop a reference-based soft switching control solution which can be used as an alternative to the traditional gain scheduling strategy. In the classical gain scheduling, slow varying scheduling variables are used to capture nonlinearities and parameter dependencies. The control law is obtained by interpolating a number of locally valid linear controllers. In the proposed BG-based soft switching approach, the need for interpolating a number of controllers can be explicitly avoided. This would provide another advantage for the real-time control applications such as AVC.

2 Basal Ganglia and Action Selection in Animal Brains

Many converging lines of evidence point to the idea that the brain solves the problem of action selection by using a central 'switching' element implemented in a group of sub-cortical brain structures called the basal ganglia (BG)[12]. Command units within brain subsystems requesting behavioural expression send excitatory signals to BG whose strength is determined by the *salience* or 'urgency' of the requests. Within BG, each putative action is represented by discrete neural resources comprising an action *channel*. Output from the BG is inhibitory and normally active, and each channel forms a closed-loop with its command system. Actions are selected when competitive processes between channels within BG result in withdrawal of inhibition from the requesting command system.

At the input to BG, command signals in channel i may contain elements of motor planning, motor efference copy and sensory context. We refer collectively to the vector of such signals $\mathbf{s}_i$ as an action request. In order for this 'request' to result in selection it must be able to be 'listened to' by neurons at the input stage to BG - namely the striatum. In order for a striatal neuron in channel i to be receptive to $\mathbf{s}_i$, its vector of synaptic contacts or 'weights' $\mathbf{w}_i$ must make a good pattern match with $\mathbf{s}_i$; that is, if weights are normalised, we require $\mathbf{w}_i \cdot \mathbf{s}_i \approx \|\mathbf{x}_i\|$. This also serves to formalise what we mean by 'salience' of a request; it is the norm of the associated signal pattern vector.

In general, an action request may induce a response in several channels if there is a partial overlap between the action request and several neural weight vectors. BG will, in general, eliminate weak responses obtained in this way and we aim for a request to 'trigger' an action for behavioural enactment. However, where there is sufficient overlap between input and weights on multiple channel inputs, we may obtain suppression of BG output (removal of inhibition on target structures) on more than one channel, resulting in simultaneous channel selection. This situation may be most likely to occur as action requests transition from one to another. The result will be a process of soft switching between action channels at these transitions. This promises to make these transitions smoother than they might be otherwise - a feature we will seek to take advantage of in the new controller. We now describe how these ideas are deployed in the AVC model.

3 BG-Based Soft Switching in AVC

The proposed BG-based soft switching architecture is shown in Fig.1. The collection of controllers/'actions' is shown in the bottom left receiving the error signal e in the normal way. The figure shows the scheme generically for one of the three sub-systems: brake, throttle, steering, and is therefore repeated three times in all (see section 4). The reference signal r is used to form the salience signals for action request. The action request vector **s** = (s_1, s_2, s_3) is then supplied to the BG selection mechanism which is based on that in [11]. Here, responses $w_i \cdot s_i$ are formed which are used as inputs to the subsequent stages in BG for selection. The output of BG is a set of signals z_1, z_2, z_3, one for each channel. These are used, in turn to generate gating signals g_i which mimic inhibition (of the divisive or 'shunting' variety) on their targets (the controllers themselves). The g_i are formed according to

$$g_i = \begin{cases} 1 - z_i / z_0 & if\ 1 - z_i / z_0 > 0 \\ 0 & otherwise \end{cases} \tag{1}$$

The total controller output u is then formed from a mixture (soft selection) of the three component controllers. Thus, if $g = \sum_i g_i$ then

$$u = \frac{1}{g} \sum_i g_i v_i \tag{2}$$

This gives a mix of controllers in a natural, bio-inspired way. The dynamics in the BG will also make that this mixing is smoothly done (less `bumping' at switch over).

In the proposed BG-based soft switching architecture, the PID, pole-placement and pole-zero placement controllers are used as the family of candidate actions. Therefore, in the following, we will briefly describe these controllers to suit the convenience of the readers. For more details on these established controllers, one is referred to [1-3, 6] and the references therein.

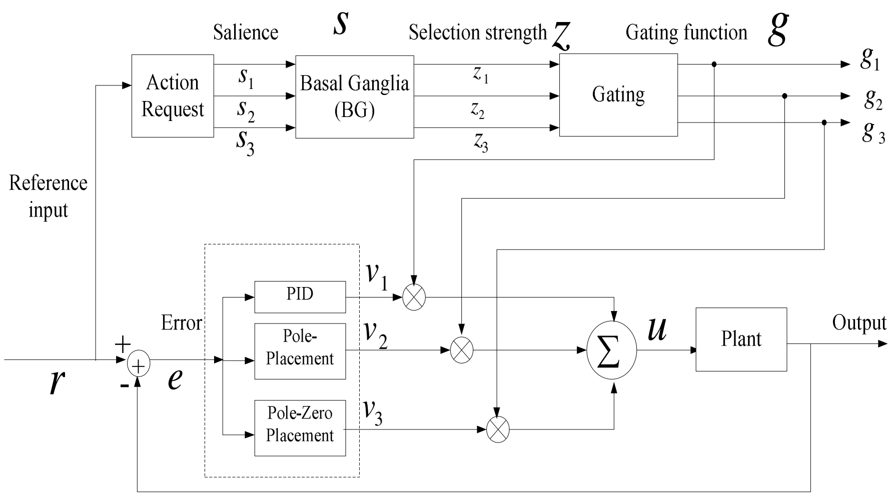

Fig. 1. The structure of BG-based soft switching control approach

3.1 Controller Description

Consider the following discrete-time dynamic control system [1-3,6]:

$$\mathbf{A}(z^{-1})\mathbf{y}(t+k) = \mathbf{B}(z^{-1})\mathbf{u}(t) + \mathbf{f}_{0,t}(Y,U) + \xi(t+k) \tag{3}$$

where $\mathbf{y}(t)$ $(n\text{x}1)$ is the measured output vector, $\mathbf{u}(t)$ $(n\text{x}1)$ is the control input vector, $\xi(t)$ is an uncorrelated sequence of random variables with zero mean at the sampling instant t=1,2,…, and k is the time delay of the process in the integer-sample interval. $\mathbf{f}_{0,t}(\mathbf{Y},\mathbf{U})$ is a nonlinear term. Furthermore, let $\mathbf{y}(t) \in \mathbf{Y}$, and $\mathbf{u}(t) \in \mathbf{U}$ $\{\mathbf{Y} \in R^{n_a}; \mathbf{U} \in R^{n_b}\}$ and $\mathbf{A}(z^{-1})$ and $\mathbf{B}(z^{-1})$ as follows:

$$\mathbf{A}(z^{-1}) = \mathbf{I} + \mathbf{A}_1 z^{-1} + \mathbf{A}_2 z^{-1} + \ldots + \mathbf{A}_{n_A} z^{-n_A} \tag{4a}$$

$$\mathbf{B}(z^{-1}) = \mathbf{B}_0 + \mathbf{B}_1 z^{-1} + \ldots + \mathbf{B}_{n_B} z^{-n_B} \;, \mathbf{B}(0) \neq 0 \tag{4b}$$

where z^{-1} is the backwards shift operator, n_A and n_B are the degrees of the polynomials $\mathbf{A}(z^{-1})$ and $\mathbf{B}(z^{-1})$, respectively.

The derived adaptive control law for the above nonlinear plant is given by [6]:

$$\mathbf{u}(t) = \frac{\mathbf{v}\tilde{\mathbf{H}}[\mathbf{H}(1)]^{-1}\mathbf{F}(1)\mathbf{w}(t) - \mathbf{v}\mathbf{F}\mathbf{y}(t) + \Delta\mathbf{v}\mathbf{H}'_{\mathbf{N}}\mathbf{f}_{0,t}(.,.)}{\Delta\mathbf{q}'} \tag{5}$$

where $\mathbf{w}(t)$ $(n\,\text{x}\,1)$ is the bounded set-point vector, $\mathbf{v}$ is a user-defined gain matrix, Δ is the integral action required for PID design, $\tilde{\mathbf{H}}$ is a user-defined polynomial which can be used to introduce arbitrary closed-loop zeros for an explicit pole-zero placement controller, $\mathbf{H}(1)$ is the value of $\tilde{\mathbf{H}}$ at the system steady state, $\mathbf{F}$ is a polynomial derived from the linear parameters of the controlled plant and includes the desired closed-loop poles, $\mathbf{F}(1)$ is the value of $\mathbf{F}$ at the steady state, $\mathbf{H}'_{\mathbf{N}}$ is a user-defined polynomial. The parameter $\mathbf{q}'$ is a transfer function used to bring the closed-loop system parameters in the stability unit disc, and is a polynomial in z^{-1} having the following form:

$$\mathbf{q}'(z^{-1}) = \mathbf{I} + \mathbf{q}'_1 z^{-1} + \mathbf{q}'_2 z^{-2} + \ldots + \mathbf{q}'_{n_{\mathbf{q}'}} z^{-n_{\mathbf{q}'}}$$

where $n_{q'}$ is the degree of the polynomial $\mathbf{q}'$.

1. PID Controller

The conventional self-tuning PID controller is expressed in the most commonly used velocity form [6], i.e.:

$$\Delta\mathbf{u}(t) = \mathbf{K_I}\mathbf{w}(t) - [\mathbf{K_P} + \mathbf{K_I} + \mathbf{K_D}]\mathbf{y}(t) - [-\mathbf{K_P} - 2\mathbf{K_D}]\mathbf{y}(t-1) - \mathbf{K_D}\mathbf{y}(t-2)$$

Let the degree of $\mathbf{F}(z^{-1})$ be 2, then the following self-tuning PID controller can be derived [6],

$$\Delta\mathbf{u}(t) = [\mathbf{vF}(1)\mathbf{w}(t) - \mathbf{v}(\mathbf{f}_0 + \mathbf{f}_1 z^{-1} + \mathbf{f}_2 z^{-2})\mathbf{y}(t) + \Delta\mathbf{vH}'_{\mathbf{N}}\mathbf{f}_{0,t}(.,.)]$$

in which $\mathbf{H}'_{\mathbf{N}} = -[\mathbf{B}(1)\mathbf{v}]^{-1}\mathbf{q}'(1)$ and both q' and $\tilde{H}$ are switched off:

2. Pole-Placement Controller

Substituting for $\mathbf{u}(t)$ given in (5) into the system model described by (3), the closed-loop system is obtained as [3,6]:

$$(\tilde{\mathbf{A}}\mathbf{q}' + z^{-1}\tilde{\mathbf{B}}\mathbf{F})\mathbf{y}(t) = z^{-1}\mathbf{Bv}\tilde{\mathbf{H}}[\mathbf{H}(1)]^{-1}\mathbf{F}(1)\mathbf{w}(t) + \Delta(Z^{-1}\mathbf{BvH}'_{\mathbf{N}} + \mathbf{q}')\mathbf{f}_{0,t} + \Delta\mathbf{q}'\xi(t) \qquad (6)$$

where $\tilde{\mathbf{A}} = \Delta\mathbf{A}$ and $\tilde{\mathbf{B}} = \mathbf{vB}$. The following identity is introduced [3,6]:

$$(\mathbf{q}'\tilde{\mathbf{A}} + z^{-1}\mathbf{F}\tilde{\mathbf{B}}) = \mathbf{T} \qquad (7)$$

where $\mathbf{T}$ represents the desired closed-loop poles polynomial with the order n_t and $\mathbf{q}'$ is the controller polynomial. The conditions for (7) to have a unique solution can be found in [3,6]. Combining (6) and (7) yields:

$$\mathbf{Ty}(t) = z^{-1}\mathbf{Bv}\tilde{\mathbf{H}}[\tilde{\mathbf{H}}(1)]^{-1}\mathbf{F}(1)\mathbf{w}(t) + \Delta(z^{-1}\mathbf{Bv}H'_N + \mathbf{q}')\mathbf{f}_{0,t} + \Delta\mathbf{q}'\xi(t) \qquad (8)$$

The pole-placement controller is obtained by switching off the explicit zero placement polynomial, namely $\tilde{\mathbf{H}} = 1$. Let $H'_N = -[B(1)v]^{-1}q'(1)$, we have

$$\mathbf{Ty}(t) = z^{-1}\mathbf{BvF}(1)\mathbf{w}(t) + \Delta(z^{-1}\mathbf{Bvq}'(1)\times[-(B(1)v)^{-1}] + \mathbf{q}')\mathbf{f}_{0,t} + \Delta\mathbf{q}'\xi(t) \qquad (9)$$

where $\mathbf{T}(z^{-1}) = (1 + t_1 z^{-1} + ... + t_{n_t} z^{-n_t})$.

3. Simultaneous Pole-Zero Placement Controller

The simultaneous pole-zero placement controller is derived by switching on the explicit zero placement polynomial, namely $\tilde{\mathbf{H}}(z^{-1}) = 1 + \tilde{h}_1 z^{-1} + ... + \tilde{h}_{n_{\tilde{h}}} z^{-n_{\tilde{h}}})$ in which $n_{\tilde{h}}$ is its order. The closed-loop poles and zeros are placed at their desired positions which are pre-specified by using the polynomials $\mathbf{T}(z^{-1})$ and $\tilde{\mathbf{H}}(z^{-1})$.The desired zeros polynomial can be used to reduce the excessive control action, which can be resulted from the set-point changes in the case the pole placement is used[6]. The closed-loop function for the simultaneous zero and pole-placement controller then has the following form:

$$\mathbf{Ty}(t) = z^{-1}\mathbf{Bv}[\tilde{\mathbf{H}}(1)]^{-1}\tilde{\mathbf{H}}\mathbf{F}(1)\mathbf{w}(t) + \Delta(z^{-1}\mathbf{Bvq}'(1)[-(\mathbf{B}(1)\mathbf{v})^{-1}] + \mathbf{q}')\mathbf{f}_{0,t} + \Delta\mathbf{q}'\xi(t) \quad (10)$$

4 Benchmarking Subsystems for Autonomous Vehicle l Control

In the developed Stirling AVC framework [1], shown in Fig 2, the overall problem is to deliver a target path *p(t)* and speed *v(t)*. Toward this end, the control process has two stages. In the first stage, the desired path and vehicle speed are determined on the basis of the driving environment. In the second stage, the vehicle is operated with the aim of realising the anticipated path and speeds. Basically, the AVC system is composed of three modules: a driver decision module, coordinates' transfer module and driver-following module. The driver decision model provides the desired path and speed described in the space domain. The coordinates' transfer module changes the target path and speed into the time domain in order to form the input for the driver-following module. On the other hand, the driver-following module outputs the desired control elements which are the steering wheel angle, throttle angle, and brake torque.

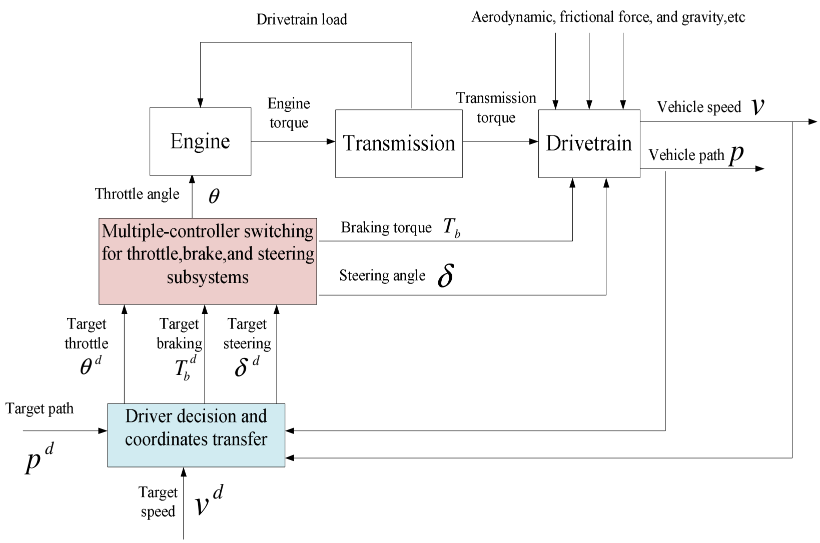

Fig. 2. Stirling's modular AVC framework

From the Stirling AVC framework described above, one of key control tasks is how to accurately track the desired internal control requests from the driver-following module for achieving the external control target, for example, the desired vehicle speed or trajectory, etc. Therefore, to illustrate the effectiveness and demonstrate the performance of the proposed BG-based soft switching approach to AVC internal control loops, the throttle, brake and steering subsystems are selected in which throttle angle θ, braking torque T_b, and steering angle δ are output variables. The controller in each subsystem is one of three candidate controllers. The selection of which is under control of the 'switching supervisor' by using the control system information such as system error, input variance, and output overshoot, etc. In this paper, only reference signals are used to trigger habitual control of the selected subsystems.

5 Simulation Results

The proposed BG-based soft switching approach was applied to the abovementioned subsystems in AVC in order to demonstrate the effectiveness of the proposed approach with respect to tracking the desired inputs (reference signals) to the throttle, brake, and steering subsystems with the changing set-points over the simulation period. The simulation was performed over 200 samples to track the reference signals representing the desired throttle angle, brake forces, and steering angle.

Figure 3 illustrates the salience signals formed by manually mapping the reference inputs (see Fig 3(a)-(c)) to trigger the habits in the BG model for the throttle, brake and steering wheel subsystems. The simulation results presented in Fig.4 (a)-(c) demonstrate that the proposed approach is able to (nearly) bump-less track the reference signals (desired outputs) for each subsystem, even the set-point is changing over the simulation period.

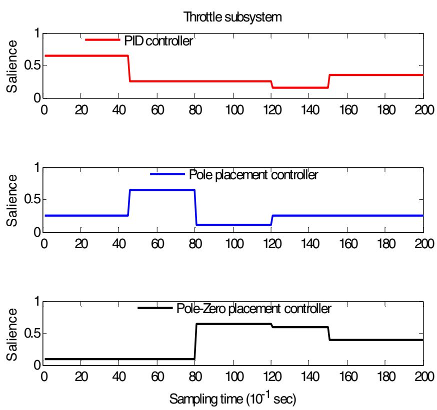

(a) Throttle subsystem

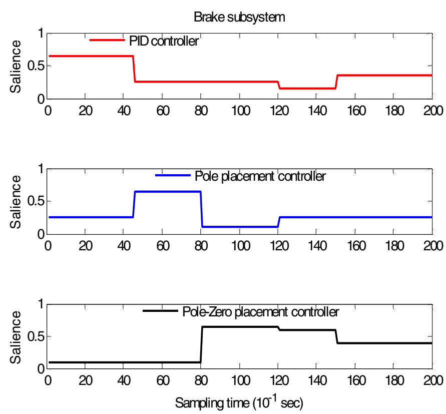

(b) Brake subsystem

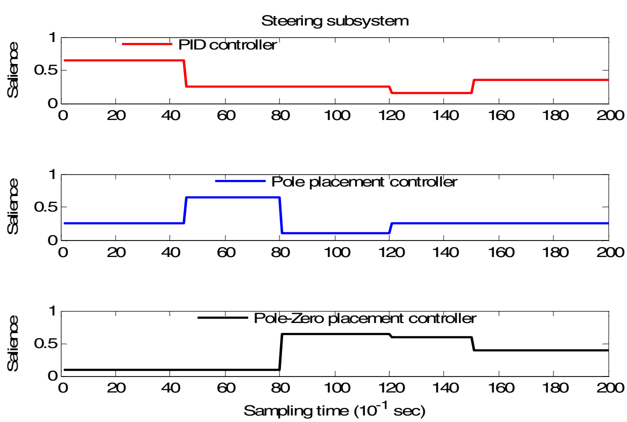

(c) Steering subsystem

Fig. 3. Salience signals used for throttle, brake, and steering subsystems

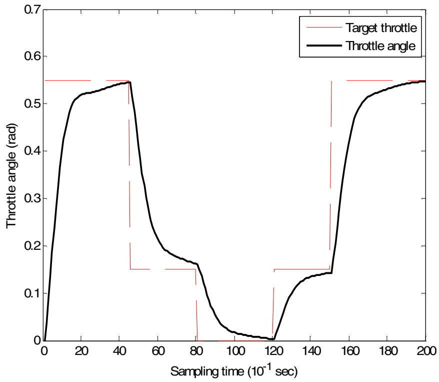

(a) Throttle subsystem

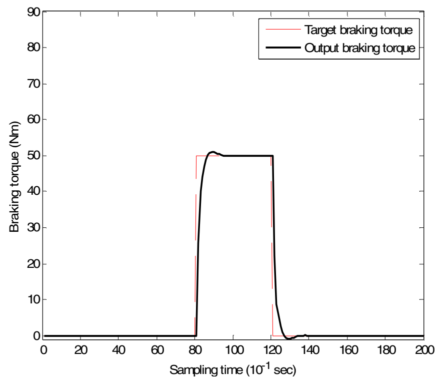

(b) Brake subsystem

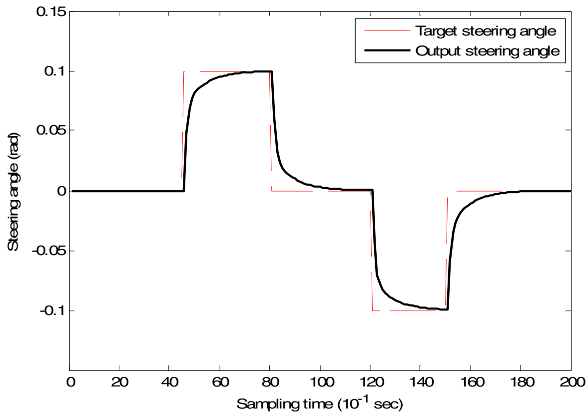

(c) Steering subsystem

Fig. 4. Output responses for throttle, brake, and steering subsystems to reach the required time-varying set-points

6 Discussion

Main Results. We have presented a novel, neurobiologically-inspired soft switching scheme for the real-time control of autonomous vehicle systems. It makes use of principles derived from the study of action selection in animals; principally the idea that basal ganglia (BG) may be used as a soft selection mechanism to gate the outputs of a family of controllers, before they are combined into a single plant controller. The throttle, brake and steering subsystems were chosen to benchmark the new architecture and simulation shows that it makes effective use of the soft selection to ensure bumpless control.

Future Work. The current model uses simple ‘sensory-like’ signals to trigger controller selection. This is akin to the evoking of habits in animals which are based on stimulus-response pairings. However, in animals, goal-directed or controlled behaviour can override this simple repertoire if it results in erroneous behaviour (see [11], for a review). We aim to build on the current work to incorporate this notion of dual control so that more sophisticated control strategies may be invoked if the simple stimulus-response pairings we use here break down. This promises the full flexibility of the biological solution to action selection in an AVC setting.

Acknowledgments. This work is supported by the UK Engineering and Physical Sciences Research Council (EPSRC) [grant number EP/I009310/1]. Both Erfu Yang and Amir Hussain are also supported by The Royal Society of Edinburgh (RSE) and The National Natural Science Foundation of China (NNSFC) under the RSE-NNSFC joint projects (2012-2014) with Prof Jun Wang, Beihang University, and Prof Bin Luo, Anhui University, China. The support from our industrial partners SciSys UK Ltd., and Industrial Systems Control (ISC) Ltd. is greatly appreciated.

References

1. Abdullah, R., Hussain, A., Polycarpou, M.: Fuzzy Logic based Switching and Tuning Supervisor for a Multi-variable Multiple Controller. In: Int. Conference on Fuzzy Systems, pp. 1644–1649. IEEE Press, London (2007)
2. Abdullah, R., Hussain, A., Warwick, K., Zayed, A.: Autonomous Intelligent Cruise Control Using a Novel Multiple-Controller Framework Incorporating Fuzzy-Logic Based Switching and Tuning. Neurocomputing 71, 2727–2741 (2008)
3. Abdullah, R.: Intelligent Methods for Complex Systems Control Engineering. PhD Thesis, University of Stirling, Stirling, UK (2007)
4. Güvenç, B., Bünte, T., Odenthal, D., Güvenç, L.: Robust Two Degree-of-Freedom Vehicle Steering Controller Design. IEEE Trans. Control Systems Tech. 12, 627–636 (2004)
5. Lennon, W., Passino, K.: Intelligent Control of Brake Systems. IEEE Trans. on Control System Tech. 7, 188–202 (1999)
6. Zayed, A., Hussain, A., Abdullah, R.: A Novel Multiple-Controller Incorporating a Radial Basis Function Neural Network based Generalized Learning Model. Neurocomputing 69, 1868–1881 (2006)
7. Gurney, K., Prescott, T., et al.: A Computational Model of Action Selection in the Basal Ganglia. I. A New Functional Anatomy. Bio. Cybernetics 84, 401–410 (2001)
8. Gurney, K., Prescott, T., Redgrave, P.: A Computational Model of Action Selection in the Basal Ganglia. II. Analysis and Simulation of Behaviour. Bio. Cybern. 84, 411–423 (2001)
9. Humphries, M.D., Gurney, K.: The Role of Intra-thalamic and Thalamocortical Circuits in Action Selection. Network: Computation in Neural Systems 13, 131–156 (2002)
10. Hussain, A., Gurney, K., Abdullah, R., Chambers, J.: Emergent Common Functional Principles in Control Theory and the Vertebrate Brain: A Case Study with Autonomous Vehicle Control. In: Kůrková, V., Neruda, R., Koutník, J. (eds.) ICANN 2008,, Part II. LNCS, vol. 5164, pp. 949–958. Springer, Heidelberg (2008)
11. Gurney, K., Hussain, A., Chambers, J., Abdullah, R.: Controlled and Automatic Processing in animals and machines with application to autonomous vehicle control. In: Alippi, C., Polycarpou, M., Panayiotou, C., Ellinas, G. (eds.) ICANN 2009, Part I. LNCS, vol. 5768, pp. 198–207. Springer, Heidelberg (2009)
12. Redgrave, P., Prescott, T.J., Gurney, K.: The Basal Ganglia: A Vertebrate Solution to the Selection Problem? Neuroscience 89, 1009–1023 (1999)
13. Redgrave, P., Rodriguez, M., Smith, Y., et al.: Goal-directed and Habitual Control in the Basal Ganglia: Implications for Parkinson's Disease. Nat. Rev. Neurosci. 11, 760–772 (2010)
14. Yin, H.H., Knowlton, B.J.: The Role of the Basal Ganglia in Habit Formation. Nature Reviews. Neuroscience 7, 464–476 (2006)

An Intelligent Multiple-Controller Framework for the Integrated Control of Autonomous Vehicles

Amir Hussain[1], Rudwan Abdullah[2], Erfu Yang[1], and Kevin Gurney[3]

[1] Division of Computing Science and Mathematics, University of Stirling
Stirling FK9 4LA, UK
{ahu,eya}@cs.stir.ac.uk
[2] Biruni Remote Sensing Centre, Tripoli, Libya
ra@lcrss.org
[3] Department of Psychology, University of Sheffield, Sheffield S10 2TP, UK
k.gurney@shef.ac.uk

Abstract. This paper presents an intelligent multiple-controller framework for the integrated control of throttle, brake and steering subsystems of realistic validated nonlinear autonomous vehicles. In the developed multiple-controller framework, a fuzzy logic-based switching and tuning supervisor operates at the highest level of the system and makes a switching decision on the basis of the required performance measure, between an arbitrary number of adaptive controllers: in the current case, between a conventional Proportional-Integral-Derivative (PID) controller and a PID structure-based pole-zero placement controller. The fuzzy supervisor is also able to adaptively tune the parameters of the multiple controllers. Sample simulation results using a realistic autonomous vehicle model demonstrate the ability of the intelligent controller to both simultaneously track the desired throttle, braking force, and steering changes, whilst penalising excessive control actions - with significant potential implications for both fuel and emission economy. We conclude by demonstrating how this work has laid the foundation for ongoing neuro-biologically motivated algorithmic development of a more cognitively inspired multiple-controller framework.

Keywords: Autonomous vehicle control, PID controller, pole-zero placement controller, fuzzy logic switching and tuning.

1 Introduction

A common approach to control complex dynamic systems is to design a set of controllers, each of which is optimized for a particular operating region or performance objective, and then to switch between them to achieve the overall control objective. This so called *multiple model* or *modular* approach has been used extensively and in various guises - e.g. gain-scheduling controllers, Tagaki-Sugeno fuzzy models, and logic-based switching controllers (for an overview, see [1][2]). Modular controllers have been the subject of increasing interest over the past decade or so. In spite of this, it remains to discover a principled approach to partitioning the

H. Zhang et al. (Eds.): BICS 2012, LNAI 7366, pp. 92–101, 2012.

system across controllers. In addition it is not clear how switching between the resulting sub-controllers could be 'learnt' if they are to act in an integrated fashion. Recent and ongoing work by the authors is emerging at the forefront of the drive to remedy this, focusing on modular learning controllers for challenging nonlinear, non-stationary and uncertain multi-variable real-world problems [1][2][13][16][17].

The field of autonomous vehicles is a rapidly growing one, which promises improved performance, fuel economy, emission levels, and safety [1-3]. Recently, a modular controller framework [1] for autonomous vehicle control (AVC) has been shown to exhibit improved longitudinal control performance, robustness and stability in realistic driving scenarios. An important component of generic AVC should aim to *simultaneously* control the throttle, wheel brake and steering systems so that the vehicle can follow a desired path *and* target speed (possibly governed by a `lead vehicle') and at the same time keep a safe inter-vehicle spacing under constraints of comfortable driving; this is the problem considered here. Conventional methods based on analytical control solutions can also generate good AVC results, but can exhibit high design and computational costs since the application object, a vehicle is a complex nonlinear plant and a complete mathematical representation is nearly impossible. Therefore, alternative ways to reach human-like vehicle control are being explored through the application of artificial intelligence techniques [1,9,10,16,17].

One important and challenging problem in AVC is related to the dangerous yaw motions of an automobile. The yaw motions may be resulted from unexpected yaw-disturbances caused by unsymmetrical vehicle-dynamics perturbations like side-wind forces, unilateral loss of tire pressure or braking on unilateral icy road. One approach for yaw dynamics improvement is to use individual wheel braking, thereby creating the moment that is necessary to counteract the undesired yaw motion. The second approach is to command additional steering angles to create the counteracting moment [6]. Another alternative approach, which is adopted in this work, is to treat the three drivetrain subsystems (i.e., throttle, brake and steering subsystems) as one Multi-Input Multi-Output (MIMO) plant. Therefore, the interactions between the vehicle longitudinal and lateral properties, disturbances and nonlinearities are considered in the multivariable MIMO control law and modeled by using the MIMO neural network employed in the Generalized Learning Model (GLM) presented in [1].

In this paper, the intelligent multiple controller framework is described building on previous work results reported in [1][16][17], which employs a fuzzy-logic based switching and tuning supervisor in order to automatically select and switch between a PID controller and a PID-structure based (simultaneous) pole-zero placement controller. Moreover, the supervisor possesses the ability to tune the parameters of the multiple controllers online, including the poles and zeros of the (simultaneous) pole-zero placement controller in addition to the PID gains. This novel tuning strategy builds on the conventional fuzzy gain scheduling strategies that have been conventionally employed for only PID controllers [11], [14]. All controllers are designed to operate using the same adaptive procedure and a selection between the various controller options is made on the basis of the required performance measure [13]. The fuzzy-logic supervisor can use any available data from the control system to characterise the system's current behaviour so that it knows which controller to choose, which parameters to tune, and the tuning value for each parameter that is ultimately required to achieve the desired specification. In this paper, the developed multiple-controller framework is employed for tracking a desired throttle, braking force, and steering changes by simultaneously controlling the throttle, brake and steering systems of a realistic autonomous vehicle model. The results reported here will also serve as benchmarks to support our related ongoing research in which the action selection using a new brain-inspired functional basal ganglia model is being explored for the real-time control of AVC [18].

The paper is organized as follows: Section 2 presents an overview of the intelligent multiple controller framework. Section 3 describes the autonomous vehicle model employed for switching control. Section 4 presents simulation results followed by some concluding remarks and future work proposals in Section 5.

2 Intelligent Multiple Controller Framework

In the developed framework shown in Fig.1, the plant (autonomous vehicle) can be modeled by using a neural network based Generalised Learning Model (GLM) as part of the multiple-controller scheme. A neural network based system model can be used in the design of a controller or can become a part of a model-based control scheme.

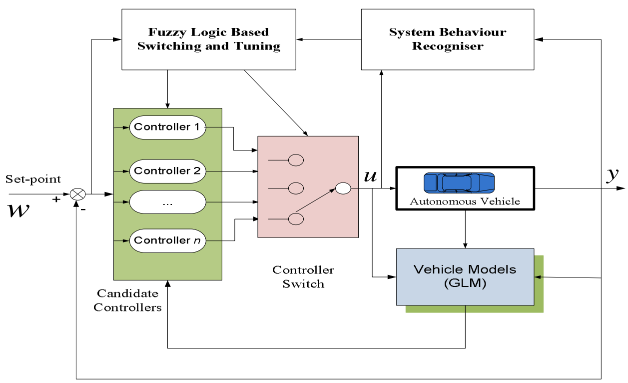

Fig. 1. Intelligent multivariable adaptive controller framework

2.1 Multiple Controller Description

Consider the following Controlled Auto-Regressive Moving Average (CARMA) representation for n-input n-output nonlinear plant model [13], [15]:

$$\mathbf{A}(z^{-1})\mathbf{y}(t+k) = \mathbf{B}(z^{-1})\mathbf{u}(t) + \mathbf{f}_{0,t}(Y,U) + \xi(t+k) \quad (1)$$

where $\mathbf{y}(t)$ is the measured output vector with dimension $(n\times 1)$, $\mathbf{u}(t)$ is the control input vector $(n\times 1)$, $\xi(t)$ is an uncorrelated sequence of random variables with zero mean at the sampling instant t=1,2,…, and k is the time delay of the process in the integer-sample interval. The term $\mathbf{f}_{0,t}(\mathbf{Y},\mathbf{U})$ in (1) is potentially a nonlinear function which accounts for any unknown time delays, uncertainty and nonlinearity in the complex MIMO plant model. Also, for (1) we define $\mathbf{y}(t) \in \mathbf{Y}$, and $\mathbf{u}(t) \in \mathbf{U}$; $\{\mathbf{Y} \in R^{n_a}; \mathbf{U} \in R^{n_b}\}$ and $\mathbf{A}(z^{-1})$ and $\mathbf{B}(z^{-1})$ as ($n \times n$) diagonal polynomial matrices with orders n_a and n_b, respectively.

2.2 Controller Mode1: PID Controller

In Mode 1, the controller operates as a conventional self-tuning PID controller, which can be expressed in the most commonly used velocity form [13], i.e.:

$$\Delta \mathbf{u}(t) = \mathbf{K}_{\mathbf{I}} \mathbf{w}(t) - [\mathbf{K}_{\mathbf{P}} + \mathbf{K}_{\mathbf{I}} + \mathbf{K}_{\mathbf{D}}]\mathbf{y}(t) - [-\mathbf{K}_{\mathbf{P}} - 2\mathbf{K}_{\mathbf{D}}]\mathbf{y}(t-1) - \mathbf{K}_{\mathbf{D}}\mathbf{y}(t-2) \quad (2)$$

The main disadvantage of PID self-tuning based minimum variance control designs is that the tuning parameters must be selected using a trial-and-error procedure [1]. In other words, the use of general heuristics could provide reasonable closed-loop performance. Alternatively, the tuning parameters could also be automatically and implicitly set online by specifying the desired closed-loop poles [2,4].

2.3 Controller Mode 2: Simultaneous Pole-Zero Placement Controller

The simultaneous pole-zero placement controller used in the developed intelligent framework was derived by using the CARMA model (1) and specifying the polynomials with the desired poles and zeros. The closed-loop poles and zeros are placed at their desired positions which are pre-specified by using the polynomials [1]. An arbitrary desired zeros polynomial can be used to reduce the excessive control action, which can be resulted from the set-point changes when pole placement is used.

The derivation of the simultaneous pole-zero placement controllers is long winded and is omitted due to lack of space. One is referred to [1] and the references therein.

2.4 Generalized Learning Model (GLM)

Zhu et al. [15] proposed a neural network based control structure such that the unknown complex plant is represented by an equivalent model consisting of a simple linear sub-model plus a nonlinear sub-model. It was termed the Generalized Learning Model (GLM) in [1]. The GLM model can be used in the proposed intelligent multiple controller framework given in Fig.1, where a recursive least squares algorithm is initially used to estimate the linear parameters **A** and **B** in (1), of the linear sub-model, and a Radial Basis Function (or another) neural network based learning model is subsequently used to approximate $\mathbf{f}_{0,t}(\mathbf{y},\mathbf{u})$ as in [15].

2.5 System Behaviour Recogniser

The desired behavior of control systems needs to be expressed in terms of a number of performance metrics. It is often preferable to formulate the behaviour in terms of time domain characteristics such as; steady-state error, overshoot, rise and fall time, variance of the control signals, etc.

In the developed intelligent framework for AVC, the behaviour recogniser seeks to characterise the current behaviour of the whole system in a way that will be useful for switching and tuning logic subsystem [1]. The behaviour of the system is characterized through the online estimation of four performance metrics, i.e., the *overshoot* of the output signal of the closed-loop control system, the *variance* of the control input signal, rise and fall times of the output signal (used for tuning purposes), and the PID controller steady-state error.

The rise and fall times of the output signal represent the amount of time for a signal to change state. To measure rise and fall times, the behavior recognizer uses 10% to 90% point of the output signal, or vice versa. The PID controller steady-state error is used to tune the controller's gain.

2.6 Fuzzy Logic-Based Switching and Tuning Supervisor

The idea of using fuzzy logic, originally proposed in [1], is to develop an adaptive supervisor for switching and tuning the multiple controllers, as shown in Fig.1. The advantage of fuzzy logic is that it provides a natural way to incorporate the heuristic knowledge and expert rules into the controller switching and tuning. Moreover, the supervisor can be used to integrate other information into the control decision-making process. For example, it can incorporate certain user inputs, or inputs from other subsystems, such as engine speed, path planning, etc.

The first task of the switching and tuning logic supervisor is to generate a switching signal which determines, at each instant of time, the candidate controller to be selected [1]. The switching logic is implemented using fuzzy-logic rules where the premises of the rules use the output of the behaviour recogniser as input parameters, and the consequents of rules form the controller selection decision (output parameter).

Each fuzzy rule in the switching logic takes the following form:

$$\text{IF } \tilde{y}_1(t) \text{ or } \tilde{y}_2(t),\ldots,\tilde{y}_i(t) \text{ IS } \textit{High} \text{ OR } \tilde{u}_1(t) \text{ or } \tilde{u}_2(t),\ldots,\tilde{u}_i(t) \text{ IS } \textit{High} \text{ THEN } C_1 \text{ or } C_2, \ldots, C_i \text{ IS } \textit{Controller n}$$

where *Controller n* can be the PID controller or a pole-zero placement controller, $\tilde{y}_i(t)$, $\tilde{u}_i(t)$ are the respectively overshoot of the output and the variance of the input signal of the i^{th} output and input signal of the MIMO plant, and C_i is the corresponding controller for the i^{th} output and input signal of the MIMO plant. After de-fuzzification procedure, the switching logic subsystem will switch either to Mode 1 controller, or Mode 2 controller. The middle-of-max approach is used for de-fuzzification to identify the selected controller. The second task of the switching and tuning logic supervisor is to tune the parameters of the multiple controllers online, including poles and zeros of the (simultaneous) pole-zero placement controller in addition to the PID gains. More details can be found in [1] and the references therein.

In Fig.2, a rule view and action surface are provided for the purpose of illustrating how the controller switching is made by using a set of sample fuzzy rules.

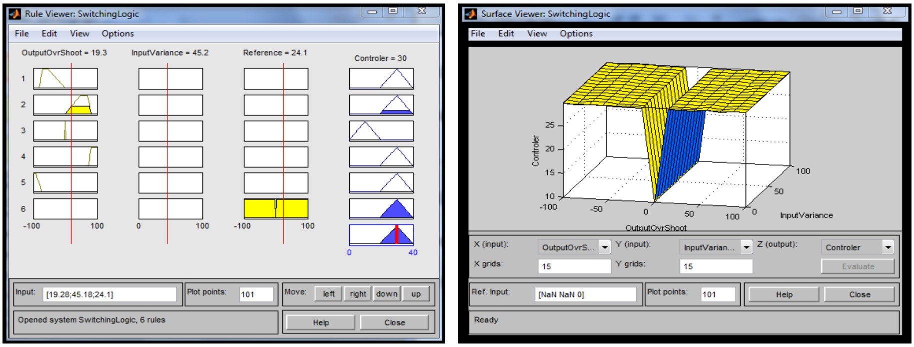

(a) Fuzzy rule's view for switching (b) Action surface for switching fuzzy rules

Fig. 2. Fuzzy rules view and action surface for multiple controllers switching

3 Autonomous Vehicle Model for Modular Control

An important component of AVC aims to simultaneously control the throttle, wheel brake and steering subsystems so that the vehicle can follow a desired path and target speed (possibly governed by a 'lead vehicle') and at the same time keep a safe inter-vehicle spacing under constraints of comfortable driving. In the developed AVC modular framework, it is the task of the driver-following module to generate the desired control elements (reference signals) which are the steering wheel angle δ_{sw}, throttle angle θ and brake torque T_b. Therefore, in this study the throttle, brake and steering subsystems are considered as one MIMO plant with the throttle angle θ, braking torque T_b, and steering angle δ_{sw} as outputs, as shown in Fig.3.

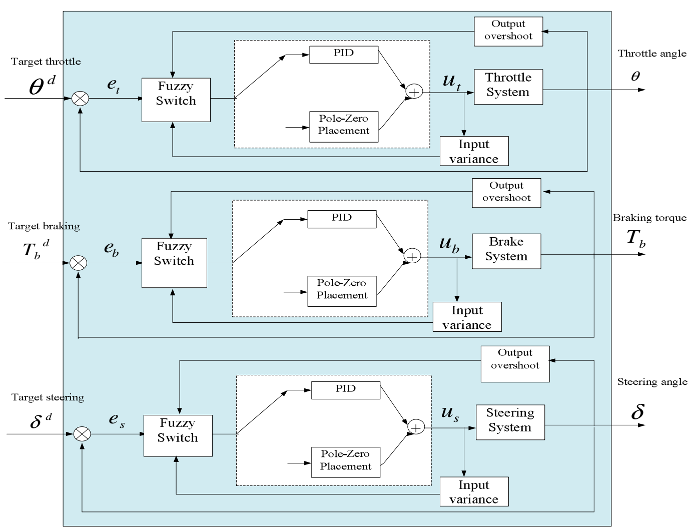

Fig. 3. Throttle, brake, and steering subsystems in AVC

3.1 Electronic Throttle System (ETC)

The ETC system uses a torque motor (DC servo-motor) to regulate the throttle plate angle θ between $0 < \theta < \pi / 2$ (i.e., closed to wide-open-throttle) in order to adjust the inlet airflow. The servo-motor is controlled by the applied armature voltage e_a in volts. The nonlinear model of the ETC can be presented by [3]:

$$y + a_1 \frac{dy}{dt} + a_2 \frac{d^2 y}{dt^2} = b_1 u - c_1 \Delta P \cos^2 y - \theta_0 ,$$

where the input and output for the ETC system are $u = e_a$ and $y = \theta$ respectively. θ_0 is the pre-tension angle of spring, the process parameters $a_1, a_2, b_1,$ and c_1 can be identified by using the input-output data from the vehicle system. ΔP is the manifold pressure across the throttle plate. Note that the nonlinear function $\Delta P \cos^2 y$ can be approximated by the RBF neural network in the GLM. The main objective of the control problem is to adjust the throttle plate angular position θ so as to maintain the desired speed v of the vehicle.

3.2 Wheel Brake System

The brake system model used in this work is given in [9], i.e.:

$$y(z) = \frac{ku(z) + dz^3}{(z - p_1)(z - p_2)(z - p_3)} .$$

The fuzzy-logic based supervisor attempts to tune the parameters k, p_1, p_2 and p_3 which represent the zeros and poles of the transfer function of the brake subsystem. The zero of the braking process model was experimentally found to be restricted as $0 \le k < 0.5$. The first two poles of the braking process were restricted to $0.9 \le p_1, p_2 < 1.1$ and the third pole (the pole of the torque sensor) was restricted to $0.6 \le p_3 < 10^{-5}$ [9]. Based on the amount of wheel slip and other factors, the controller requests a desired braking torque $y = T_b$ at the wheels. To reach the requested torque, the controller controls the brake line pressure by means of a voltage control $u = e_b$ at an actuator that consists of a DC motor and a ball-screw/piston device [9].

3.3 Steering System

The transfer function from the front wheel steering angle δ_{sw} to the desired vehicle lateral position $f_{path}(t)$ can be computed as [6]:

$$\frac{\delta_{sw}(s)}{e_{sw}(s)} = \frac{b_0(v) + b_1(v)s}{a_0(v) + a_1(v)s + a_2(v)s^2} + M_d(s) ,$$

where e_{sw} is an input voltage applied to the DC servomotor installed in the steering wheel column, b_0, b_1, a_0, a_1 and a_2 are approximated using the RLS based linear submodel. The yaw-disturbance M_d is approximated using the RBF based nonlinear submodel [1].

4 Simulation Results

The proposed intelligent multiple-controller framework was applied to the complex throttle, brake, and steering subsystems in order to demonstrate the effectiveness of the framework with respect to tracking the desired throttle angle, braking force, and steering angle (as illustrated in Fig.3) and penalising the excessive control action. This simulation was performed over 200 samples to track the reference input signals.

The control model takes as the following form:

$$[\mathbf{I}+\mathbf{A}_1 z^{-1}+\mathbf{A}_2 z^{-2}][y_1(t), y_2(t), y_3(t)]^T = z^{-1}\mathbf{B}_0[u_1(t), u_2(t), u_3(t)]^T + \mathbf{f}_{0,t}(.,.)$$

Where the variables $y_1(t)$, $y_2(t)$ and $y_3(t)$ represent the output signals θ, T_b and δ_{sw} respectively, $u_1(t)$, $u_2(t)$ and $u_3(t)$ are respectively the control inputs. $\mathbf{f}_{0,t}(.,.)$ is the approximated nonlinear dynamics. Fig. 4 shows the results obtained by controlling the throttle, brake and steering wheel subsystems with the developed intelligent AVC control framework in which fuzzy logic is used as a switch. The simulation results demonstrate that the developed framework can be used to follow control commands by tracking the desired signals (references). To track the desired system outputs in Fig. 4 (a)-(c), the required controller switching sequences for the throttle, brake, and steering subsystems are shown respectively in Fig.4(d).

5 Conclusions

In this paper, an intelligent multiple-controller framework incorporating a fuzzy logic based switching-and-tuning supervisor has been further introduced and demonstrated. The framework combined the benefits of both the PID and pole-zero placement controllers along with GLM based modelling and control. The switching decision between the different nonlinear fixed-structure controllers, and online tuning of the controller parameters were both achieved using a fuzzy logic based supervisor operating at the highest level of the system. Simulation results using a realistic autonomous vehicle model demonstrated the performance of the proposed framework for tracking the desired output variables for the throttle, brake, and steering subsystems in AVC.

Current work is focussing on further validating the multiple-controller framework in other more challenging (including multi-vehicle) driving scenarios (such as stop-and-go, overtaking, and collision avoidance). In addition, whilst the multiple controller reported here was not developed from a biologically inspired perspective, it has been recently shown to exhibit several parallels with biological action selection [16][17]. First, the presence of multiple discrete controllers is analogous to the discrete actions channels in cortico-basal ganglia loops. Second, this multiplicity of controllers immediately yields an action selection problem (which controller to use) which is resolved through a special purpose selection device (the fuzzy-logic switch) which might, therefore, be likened to the basal ganglia. A third point of contact is possible in the light of ongoing collaborative work between Stirling and Sheffield [17], which describes how the basal ganglia also play a critical role in developing and shaping actions that have useful and *predictable* effects (outcomes) on the environment. This is analogous to the learning of specific component controllers in the AVC domain. Finally, the use of error monitoring in the fuzzy switch is reminiscent of a similar role played by the anterior cingulated cortex in the brain. Future work, is thus also exploiting similarities between system architectures in control engineering and the animal brain, which is expected to lead to discovery of computational and mechanistic principles common to both, which will be validated for AVC applications in regular road driving and planetary exploration rovers. Initial findings of this exciting interdisciplinary research are being reported separately [18].

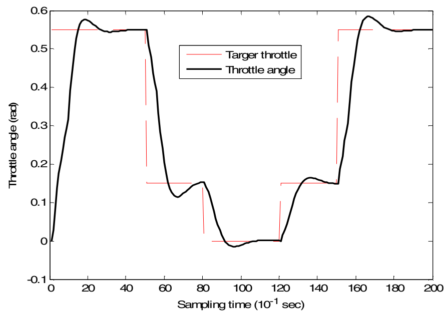

(a) Throttle control subsystem

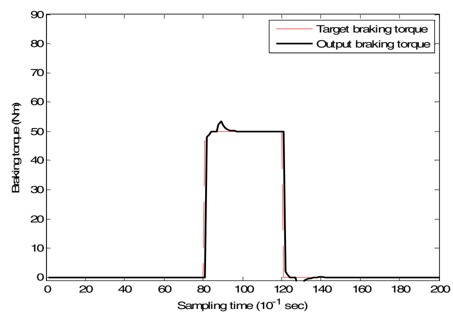

(b) Brake control subsystem

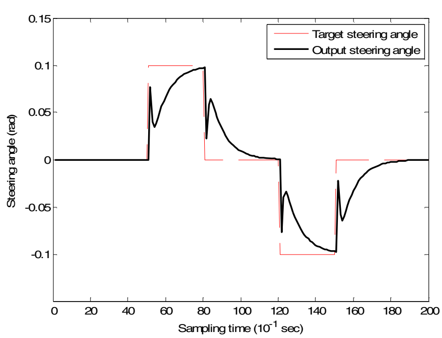

(c) Steering control subsystem

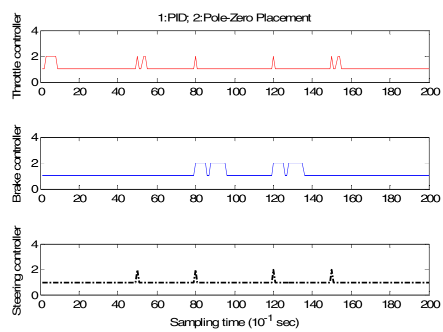

(d) Controller switching sequences

Fig. 4. Control outputs and controller switching sequences for the throttle, brake, and steering subsystems in AVC

Acknowledgments. This work is supported in part by the UK Engineering and Physical Sciences Research Council (EPSRC) [grant number EP/I009310/1]. Both Amir Hussain and Erfu Yang are also supported by The Royal Society of Edinburgh (RSE) and The National Natural Science Foundation of China (NNSFC) under the RSE-NNSFC joint projects (2012-2014) with Prof Jun Wang, Beihang University, and Prof Bin Luo, Anhui University, China. The support from our industrial partners SciSys UK Ltd., and Industrial Systems Control (ISC) Ltd. is also greatly appreciated.

References

1. Abdullah, R., Hussain, A., Polycarpou, M.: Fuzzy Logic based Switching and Tuning Supervisor for a Multi-variable Multiple Controller. In: Int. Conference on Fuzzy Systems, pp. 1644–1649. IEEE Press, London (2007)
2. Abdullah, R., Hussain, A., Warwick, K., Zayed, A.: Autonomous Intelligent Cruise Control Using a Novel Multiple-Controller Framework Incorporating Fuzzy-Logic Based Switching and Tuning. Neurocomputing 71, 2727–2741 (2008)
3. Conatser, R., Wagner, J., Ganta, S., Walker, I.: Diagnosis of Automotive Electronic Throttle Control Systems. Control Engineering Practice 12, 23–30 (2004)
4. Farrel, J., Polycarpou, M.: Adaptive Approximation Based Control: Unifying Neural, Fuzzy & Traditional Adaptive Approximation Approaches. John Wiley (2006)
5. Guo, K., Ding, H., Zhang, J., et al.: Development of a Longitudinal and Lateral Driver Model for Autonomous Vehicle Control. Int. J. Vehicle Design 36, 50–65 (2004)
6. Güvenç, B., Bünte, T., Odenthal, D., Güvenç, L.: Robust Two Degree-of-Freedom Vehicle Steering Controller Design. IEEE Trans. Control Systems Tech. 12, 627–636 (2004)
7. Hespanha, J., Liberzon, D., Morse, A., et al.: Multiple Model Adaptive Control. Part 2: Switching. Inter. Journal of Robust and Nonlinear Control 11, 479–496 (2001)
8. Lee, J., Lee, K., Kim, W.: Model-Based Iterative Learning Control with a Quadratic Criterion for Time-Varying Linear Systems. Automatica 36, 641–657 (2000)
9. Lennon, W., Passino, K.: Intelligent Control of Brake Systems. IEEE Trans. on Control System Tech. 7, 188–202 (1999)
10. Naranjo, J., Gonzalez, C., Reviejo, J., Garcia, R., Pedro, T.: Adaptive Fuzzy Control for Inter-Vehicle Gap Keeping. IEEE Trans. on Intell. Trans. Systems 4, 132–142 (2003)
11. Papoutsidakis, M., Chamilothoris, G., Dailami, F., et al.: Accurate Control of a Pneumatic System using an Innovative Fuzzy Gain-Scheduling Pattern. Trans. On Eng. Computing and Technology 8, 189–192 (2005)
12. Passino, K., Yukovich, S.: Fuzzy Control. Addison Wesley Longman, Inc. (1998)
13. Zayed, A., Hussain, A., Abdullah, R.: A Novel Multiple-Controller Incorporating a Radial Basis Function Neural Network based Generalized Learning Model. Neurocomputing 69, 1868–1881 (2006)
14. Zhao, Z., Tomizuka, M., Isaka, S.: Fuzzy Gain Scheduling of PID Controllers. IEEE Trans. on Systems, Man. and Cybernetics 23, 1392–1398 (1993)
15. Zhu, Q., Ma, Z., Warwick, K.: Neural Network Enhanced Generalised Minimum Variance Self-tuning Controller for Nonlinear Discrete-Time Systems. IEE Proc. Control Theory Appl. 146, 319–326 (1999)
16. Hussain, A., Gurney, K.N., Abdullah, R., Chambers, J.: Emergent Common Functional Principles in Control Theory and the Vertebrate Brain: A Case Study with Autonomous Vehicle Control. In: Kůrková, V., Neruda, R., Koutník, J. (eds.) ICANN 2008, Part II. LNCS, vol. 5164, pp. 949–958. Springer, Heidelberg (2008)
17. Gurney, K., Hussain, A., Chambers, J., Abdullah, R.: Controlled and Automatic Processing in Animals and Machines with Application to Autonomous Vehicle Control. In: Alippi, C., Polycarpou, M., Panayiotou, C., Ellinas, G. (eds.) ICANN 2009, Part I. LNCS, vol. 5768, pp. 198–207. Springer, Heidelberg (2009)
18. Yang, E., Hussain, A., Gurney, K.: Neurobiologically-Inspired Soft Switching Control of Autonomous Vehicles. In: BICS 2012, Shenyang, China (2012)

Evolution of Small-World Properties in Embodied Networks

Derek Harter

Department of Computer Science
Texas A&M University - Commerce
Commerce, TX 75429
Derek_Harter@tamu-commerce.edu

Abstract. The ontogenetic process that forms the structure of biological brains is believed to be ruled primarily by optimizing principles of resource allocation and constraint satisfaction for resources such as metabolic energy, wiring length, cranial volume, etc. These processes lead to networks that have interesting macroscopic structures, such as small-world and scale-free organization. However, open questions remain about the importance of these structures in cognitive performance, and how information processing constraints might provide requirements that dictate the types of macro structures observed. Constraints on the physical and metabolic needs of biological brains must be balanced with information processing constraints. It is therefore plausible that observed structures of biological brains are the result of both physical and information processing needs. In this paper we show that small-world structure can evolve under combined physical and functional constraints for a simulated evolution of a neuronal controller for an embodied agent in a navigational task.

Keywords: small-world networks, embodied cognition, evolutionary development.

1 Introduction

The human brain contains a huge number of neurons ($\sim 10^{11}$ neurons) and a huge number of interconnections ($\sim 10^{14}$ synapses). The ontogenetic process that forms this structure is believed to be ruled primarily by optimizing principles of resource allocation and constraint minimization [1,2]. These evolutionary and developmental processes lead to brain structures that are known to have certain interesting macroscopic properties, such as small-world behavior [3,4,5]. However, the nature of these constraints to building neural structure, and the relationship of such structure to cognitive performance remain important questions. Connectivity structure might be the result of wiring optimization; at least this appears to be a plausible assumption as wiring is expensive, thus evolution would prefer structures that minimize wiring and the cost of building it [6].

H. Zhang et al. (Eds.): BICS 2012, LNAI 7366, pp. 102–111, 2012.

However, this must be balanced with factors for optimizing information processing performance, as a minimally wired network may not be adequate to integrate information and support sufficient dynamics for controlling the organism. It is therefore plausible that real brain network development has both physical constraints and functional information processing constraints that guide the development of structural elements and functional dynamics [7,8].

Many complex networks have small-world properties, including at least some biological brain networks [3,5,9]. The brain likely evolved to maximize action selection performance while also minimizing physical and energy requirements needed to develop and use the brain network. Small-world networks are economical, allowing for efficient communication because average path lengths (L) remain small, and only increase at a rate proportional to the log of the size of the network (number of nodes, N). It is theorized that minimizing the number of hops needed between any structural network clusters promotes efficient information processing, and thus is important to the functional performance of the network in selecting behavior in the environment.

Previous work shows that various properties of small-world networks do have effects on performance. For example, many studies have explored the effects of various properties on performance in Hopfield network recall [10,11]. These studies have looked at the effects of varying path length and clustering on recall performance. For example, in [10], the authors looked at Hopfield performance over various small-world network structures with different clustering coefficients, as well as comparing to the actual biological network of the C.elegans organism. C.elegans is one of the worst performers at low clustering coefficients, though it does show the flattest performance, e.g. least affected by clustering. In this work, the authors did not take into account physical constraints imposed by energy needs of long-range connections. Thus the explanation for the clustering structure of the real C.elegans network may be that it evolved with the need to balance real physical costs of long-range synaptic couplings to information processing performance. It may be that the best solution evolution can find when balancing such competing needs to minimize energy costs with the requirement for good information processing performance is minimally small-world structures. Some work has also been done on Hopfield networks where wiring cost is taken into account in evolving the networks [12,13]. In most of this work, though, the functional performance is measured through associative memory formation and recall in fairly artificial tasks.

In the simulations reported here we attempt to extend this work to look at the balance between physical costs and functional information performance in artificial neural network models evolved to control an embodied robotic agent. The agent is situated in a simulated environment and must interact with the environment through a sensory-motor perceptual loop, thus the task it performs is much more life like that some of the more abstract information processing tasks used previously. The questions being explored in these simulations include: will small-world properties evolve when both structural and functional constraints are present in a relatively large scale network; and if such macroscopic structures do develop, how does this aid or assist the information processing tasks performed by the neural controller?

2 Simulations

2.1 Task, Agent and Environment

We evolve a large scale network that will control the behavior of an embodied agent. The task the agent must learn is a simple T-maze spatial learning and conditioning task [14]. The T-maze, shown in Fig. 1 consists of an indicator (I) on the left or right side of a corridor that can be sensed by the agent, and a goal location (G) towards which the robot must navigate. The T-maze and simulated Khepera robot were implemented using the Player/Stage robot simulator system [15].

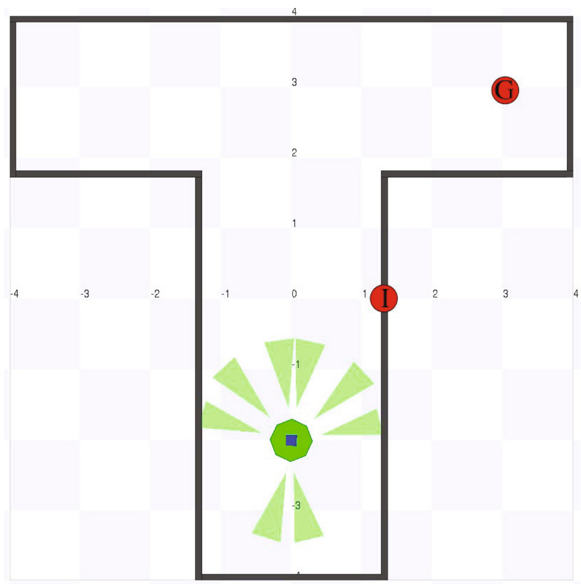

Fig. 1. T-maze environment with simulated Khepera robotic agent. Same side condition shown with goal indicator (I) and goal (G) present on right side of environment.

The simulated agent we used is a model of a Khepera robot represented in the bottom part of the T-maze in Fig. 1. The Khepera robot is equipped with 8 range sensors around the circumference of its body that can detect obstacles or walls when the robot is approximately within 1.5 body length of the obstruction. The Khepera robot in our task also has a special sensor (not represented, but located at the front of the agent, see Figs. 1 and 2) that indicates when the robot is in proximity to the reward indicator (I in Fig. 1). The robot has two motors driving two wheels, which can be rotated forwards or backwards independently, allowing the robot to move forward, backward or turn in place depending on the two separate driving speeds of the wheels.

The agent is controlled by a relatively large scale network with recurrent connections, divided into roughly 3 layers: a sensor layer S, a layer of reservoir units R, and two recurrently connected output units that drive the motor behavior M. The physical structure of the network controller is shown in Fig. 2. As depicted in the diagram, the size of all of the networks used in the simulations reported here are the same and fixed at $N = 132$. Also, all units have an exact spatial location, which is fixed and again the same for all individual networks evolved in these results.

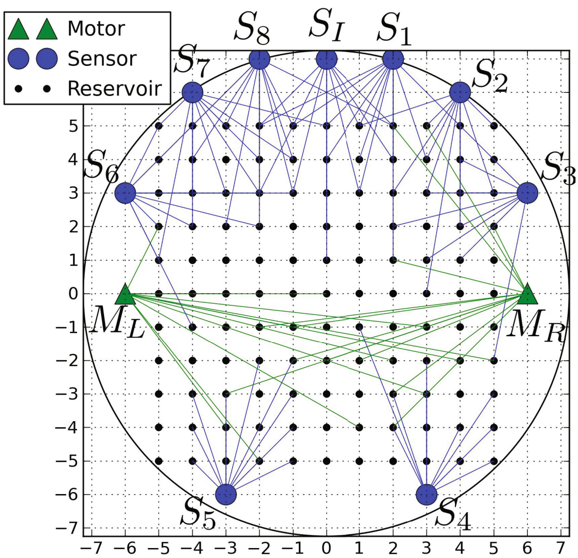

Fig. 2. Structure of the large scale network used in evolutionary simulations

The Fig. 2 also shows some example connections that resulted from evolving a network using only minimal wiring cost as the fitness criteria. Here only connections from the S to R and R to M layer units are shown, but the network also has recurrent connectivity from R to R and from M back into the reservoir R (not shown in this figure, but described below). All units have a standard location on the Cartesian grid, and distance between units will be used to calculate the cost of wiring connections between any pair of units.

The 8 range sensor units ($S_1 - S_8$) are driven by the range sensors of the Khepera robot, and will range in activation from 0.0 (no object detected) to 1.0 (sensor touching object). The goal side sensor (S_I) will become active when the robot is within range of the goal side indicator (I), with a value of −1.0 when seen on the left or 1.0 on the right, and 0.0 when otherwise not detected.

All of the artificial neurons are standard perceptron units using a weighted sum of their inputs that is transformed with the *tanh*() activation function so that activation normally ranges from $a \in [-1.0, 1.0]$. The simulation uses discrete time steps, and all activations are updated simultaneously in the next time step. The two output units drive the motors (M_L and M_R) of the agent by moving the wheel as fast as possible backwards at activations of -1.0, and as fast as possible forwards for values of 1.0 and stopped for activation values of 0.0.

The middle layer, or reservoir, of the controller is a large scale network consisting of 121 neural units arranged in a 11×11 two dimensional spatial grid. We simply use city block distance to measure the wiring length or cost of wiring up any two units in the network:

$$wirecost(u_1, u_2) = \sum^{d} |u_1^d - u_2^d| \tag{1}$$

Connectivity between layers, and within the reservoir layer, is initially randomly selected and projected. We assume that units are sparsely connected in a stochastic manner, where each unit is projected into and connected up to a predetermined percentage of target units in a target layer.

2.2 Functional and Structural Task Fitness

The functional fitness criteria used to evaluate the agent's performance is simply to reach the goal location G in the environment. The agent's controller is embodied in the simulated robot, and a trial is run that ends when either a) the trial time limit expires (we used 30 seconds of Player/Stage simulated time for simulations reported in this paper) b) the robot crashes into a wall or otherwise stalls and cannot move or c) the agent reaches the goal location. We use a simple measure of euclidean distance of the agent's closest approach to the goal G during its trial to measure the functional performance in achieving the goal fit_G:

$$fit_G = min(d_t) \tag{2}$$

Here the distance d_t is measured at each discrete time step $1..t$ of the simulation, and $d_t \in [0, D]$ where D is the maximum distance from the goal G that the robot can ever achieve in the T-maze (which is approximately 7.5 for this environment, representing the worst functional performance possible).

The physical structure of the number and location of the units in the network controller is fixed and shown in Fig. 2. However network connectivity and connection weights for projections are initially randomly generated for each controller. We use the total cost of all of the wiring of projected connections to evaluate the structural fitness of individuals. Thus the wiring cost structural fitness fit_W can be described for an individual as:

$$fit_W = \sum_{s=1}^{N} \sum_{t=1}^{T} wirecost(s, t) \tag{3}$$

where s are all units that have projections to other units in the network and t are all target units the source unit projects to for the individual network.

When combining functional and structural fitness to determine the total fitness of an individual, we scale each performance by a scaling factor in order to modify the range and combine the individual fitness measures:

$$fit_{tot} = \alpha_G \cdot fit_G + \alpha_W \cdot (fit_W - min_W) \tag{4}$$

For example, the fit_G can range from $fit_G \in [0, D]$ where D is the maximum distance from the goal in the environment and therefor represents the worst fitness. Thus we use:

$$\alpha_G = \frac{I_G}{D} \tag{5}$$

to scale fit_G to the range 0.0 to 1.0. For wiring cost fitness, the total wiring cost can range $fit_W \in [min_W, max_W]$. In our simulations with the network structure and parameters described, the minimal wiring cost $min_W = 1016$ and maximum was $max_W \approx 14000$. The average wiring cost of randomly generated networks was 6880. Thus again to range the fit_W from 0.0 to 1.0 we used:

$$\alpha_W = \frac{I_W}{max_W - min_W} \tag{6}$$

The I_G and I_W are weights that indicated the relative importance of the goal or weight component to the total fitness. If either of these is set to 0, then that component is not considered when evaluating overall fitness. If these values are equal, then equal weight will be given to fit_G and fit_W when calculating total fitness. These parameters were used to test various conditions of the relative importance of structural and functional constraints on individual fitness in the experiments reported next.

3 Results

For the results reported here, we evolved simulated populations of individuals with the described large scale network controllers, minimizing fit_{tot} for various combinations of the relative importance of the functional and structural fitness of the individual. We used standard genetic optimization with a population size of 30 individuals, stochastic universal sampling with a pool of the top 50 percent of individuals in the population, and single individual elitism. We used both mutation and crossover to generate individuals, with a mutation rate of 0.5. In individuals selected for mutation, mutations can occur by either causing a target projection to be detached and randomly attached to a new target. By changing target locations, the number of projections from a source unit will remain constant, however the length of the connection can be shortened or lengthened depending on where the new target location ends up being projected. Likewise, mutation can also involve changing the weight of a projected connection, either in a positive or negative direction. When an individual is mutated, all connections are subject to mutation, and with a 0.05 probability, either the projection is rewired, the weight is changed, or possibly both mutations occur for the projection. Simulations were run until the first individual successfully reached the goal location G in the T-maze. Results reported here are averages over 20 runs for each different experimental setup.

In Table 1 we give an overview of the major results reported here. We evolved networks with various relative importance on the fit_G and fit_W components of total fitness. We report the number of generations it took on average to evolve an individual who reached the goal, the average wiring cost of the winning individual, and the clustering coefficient C and average path length L of the winning individuals (see [16,17] for an overview of the C and L parameters, and other measures of biological network structures). The first condition, random, shows the properties of randomly generated networks with the structure and parameters we described previously, and is useful for comparison to other networks evolved in the experiments reported. Likewise, the minimum wc condition reports results for the other end of the scale, where we create networks with minimal wiring given the described network architecture.

Between random and minimal networks, other results were obtained by varying the relative importance of the physical and information processing constraints. In the Table 1, $cond_{fun}$ is evolution using only fit_G for fitness, $cond_{equal}$ are networks where equal importance is given to fit_G and fit_W,$cond_{wcemp}$ is a condition where the wiring cost fitness is given much more weight in total fitness than goal performance, and finally $cond_{struct}$ are conditions where structural constraints have most or all of the effect on the fitness of the networks.

Table 1. Performance of networks under varying conditions

Condition	I_G	I_W	Gen	wire cost	C	L
random	NA	NA	NA	6880	0.062	2.725
$cond_{fun}$	1	0	48.60	6661	0.068	2.725
$cond_{equal}$	1	1	48.40	6526	0.070	2.732
$cond_{wcemp}$	1	10	68.67	5835	0.0853	2.752
$cond_{wcemp2}$	1	20	68.67	4762	0.2120	2.823
$cond_{struct}$	1	40	103.5	2869	0.2738	2.915
$cond_{struct2}$	0	1	10000	1957	0.3431	3.128
min wc	NA	NA	NA	1210	0.386	5.663

In Table 1 the importance of the physical constraint of wiring cost has been varied using the I_G and I_W parameters. As emphasis in the fitness function is varied from being completely functional to being completely structural, the wiring cost of the evolved individuals varies. Here wiring cost of the evolved individual networks provides a measure of how close to being randomly or minimally wired the network is. For comparison, random and minimally wired networks with our given architecture are shown at both ends of the table.

To illustrate the small-world nature of the evolved networks, we plot the clustering coefficient and average path length of the evolved solutions as they vary from minimally to randomly wired networks. This plot is shown in Fig. 3. In this figure, clustering coefficient of the networks is scaled on the left vertical axis, while the average path length of the networks is scaled on the right vertical axis. The figure demonstrates typical small-world behavior displayed as the evolved networks are varied between the two extremes of completely functional to completely structural constraints. The important part of a small-world network is the large area in between the two extremes where clustering is high but average path length is low. As shown in Fig. 3, most of the range of evolved networks exhibit high clustering coefficients, similar to a minimally wired network, but low average path lengths as are seen in random networks. This range of values where both high clustering but low path lengths prevail are the definition of small-world network architectures. Interestingly, the small-world range in these results mostly occurs with wiring cost values from about 1000 to 5000. This range of values corresponds to simulations where structural constraints heavily influenced the fitness evaluation of the networks. So for these simulations, where functional information processing constraints could still be achieved, a heavy emphasis on minimizing wiring cost leads to networks able to perform the task but still also able to minimize structural wiring cost needs.

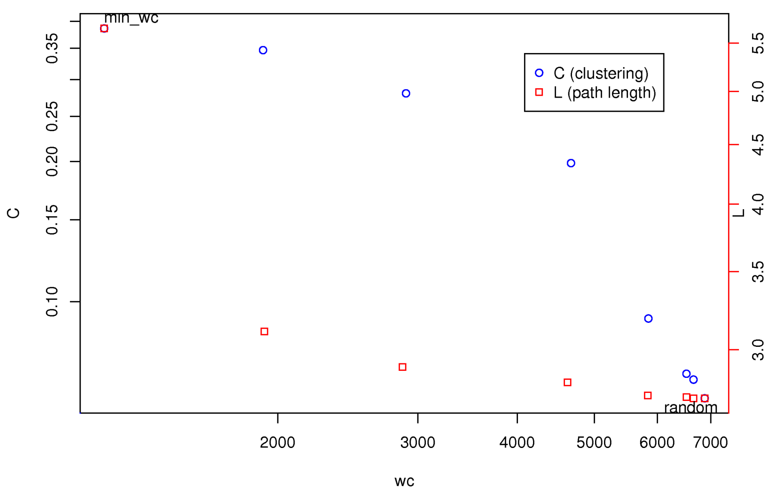

Fig. 3. Comparison of typical path length vs. clustering coefficient as physical and functional constraints are varied

4 Conclusions

The structural and functional properties of brain networks must coexist and coevolve with one another. It is an open question as to what pressures and constraints are most important in guiding the development of the physical structures and properties that we observe in mammalian nervous systems. It is further still unknown whether small-world and scale-free structures observed in such biological networks are simply the result of minimization of resource pressures, that work against optimizing functional performance, or if in fact such small-world structures may aid in cognitive performance. It has been theorized that, in fact, small-world structure does and can aid in cognitive performance, for example by striking a good balance between isolation of dynamical activity for processing vs. the need to communicate results. The balance struck by small-world structures may have similarity to ideas about the edge-of-chaos and its importance to aspects of dynamical functional performance.

In this paper we describe results of evolving complex networks in an embodied agent. The agent performs a more realistic and embodied navigation task compared with other such simulations of the relation of structural and functional constraints on the development of complex network structure. In this paper, we have shown that, given a balance between the importance of the functional evaluation to the cost of wiring the network, small-world structure will be generated in such evolved networks controlling a more naturally embodied agent performing a task. In the experiments reported here, functional information processing constraints could be satisfied within an evolved small-world architecture. However, heavy emphasis on the structural constraints was needed to obtain this result.

It may be useful in future work on this task to explore larger networks and more complex, open-ended tasks. The relative difficulty in taking into account structural constraints of wiring may disappear when the task is not as straight forward and easy in comparison to the structural constraints. Though larger networks would of course increase the difficulty of the structural performance constraint. Another interesting direction this work suggests is in looking at the developmental aspects of small-world biological networks. In particular, methods are known for creating small-world networks using preferential attachment, etc. Would simulating a developmental process using large networks with spatial properties as shown in this work also be capable of generating small-world networks.

Acknowledgments. The ideas and work described in this paper were supported by DOE grant #DE-SC0001132 and NSF grant #0916749, as well as by a Texas A&M University faculty development grant. Numerical work performed on the Lion compute cluster at Texas A&M University - Commerce. Thanks to Swathi Tummala, Manoj Indupuru and Anunay Pandey for work on developing the Khepera Player/Stage environment simulations for use on HPC cluster platform.

References

1. Boccaletti, S., Latora, V., Moreno, Y., Chavez, M., Hwang, D.-U.: Complex networks: structure and dynamics. Physics Reports 424, 175–308 (2006)
2. Koch, C., Laurent, G.: Complexity and the nervous system. Science 284, 96–98 (1999)

3. Stephan, K.E., Hilgetag, C.-C., Burns, G.A.P.C., O'Neill, M.A., Young, M.P., Kötter, R.: Computational analysis of functional connectivity between areas of primate cerebral cortex. Philosophical Transactions of the Royal Society of London B 355, 111–126 (2000)
4. Sporns, O., Tononi, G., Edelman, G.M.: Theoretical neuroanatomy: Relating anatomical and functional connectivity in graphs and cortical connection matrices. Cerebral Cortex 10, 127–141 (2000)
5. Bassett, D.S., Bullmore, E.: Small-World brain networks. The Neuroscientist 12(6), 512–523 (2006)
6. Chklovskii, D.B., Schikorski, T., Stevens, C.F.: Wiring optimization in cortical circuits. Neuron 34, 341–347 (2002)
7. Sporns, O., Tononi, G., Edelman, G.M.: Connectivity and complexity: The relationship between neuroanatomy and brain dynamics. Neural Networks 13, 909–922 (2000)
8. Kaiser, M., Hilgetag, C.C.: Modelling the development of cortical systems networks. Neurocomputing 58-60, 297–302 (2004)
9. Simard, D., Nadeau, L., Kröger, H.: Fastest learning in small-world neural networks. Phys. Letters A 336, 8–22 (2005)
10. Kim, B.J.: Performance of networks of artificial neurons: The role of clustering. Physical Review E 69(4), 45101 (2004)
11. McGraw, P.N., Menzinger, M.: Topology and computational performance of attractor neural networks. Physical Review E 68(4), 047102 (2003)
12. Ahn, Y.-Y., Jeong, H., Kim, B.J.: Wiring cost in the organization of a biological neuronal network. Physica A: Statistical Mechanics and its Applications 367, 531–537 (2006)
13. Davey, N., Christianson, B., Adams, R.: High capacity associative memories and small world networks. Neural Networks 4, 177–182 (2004)
14. Lavond, D.G., Steinmetz, J.E.: Handbook of Classical Conditioning. Kluwer Academic Publishers, Norwell (2003)
15. Gerkey, B., Vaughan, R.T., Howard, A.: The player/stage project: Tools for multi-robot and distributed sensor systems. In: Proceedings of the 11th International Conference on Advanced Robotics (ICAR 2003), Coimbra, Portugal, pp. 317–323 (June 2003)
16. Sporns, O., Chialvo, D.R., Kaiser, M., Hilgetag, C.C.: Organization, development and function of complex brain networks. Trends in Cognitive Sciences 8(9), 418–425 (2004)
17. Watts, D.J., Strogatz, S.H.: Collective dynamics of 'small-world' networks. Nature 393, 440–442 (1998)

Brain Memory Inspired Template Updating Modeling for Robust Moving Object Tracking Using Particle Filter

Yujuan Qi, Yanjiang Wang, and Tingting Xue

College of Information and Control Engineering, China University of Petroleum,
No.66, Yangtze River Western Road, Economic and Technological Development Zone,
Qingdao, China, 266555
{qiyj,yjwang}@upc.edu.cn

Abstract. In this paper, we propose a novel template updating modeling algorithm inspired by human brain memory model. Three memory spaces are defined according to the human brain three-stage memory theory. The three memory spaces are used to store the current estimated template and the historical templates. To simulate the memorization process of human brain, such as information updating or exchanging, some behaviors and rules are also defined. The proposed memory-based template updating mechanism can remember or forget what the target appearance has ever been, which helps the tracker adapt to the variation of an object's appearance more quickly. Experimental results show that the proposed algorithm can handle sudden appearance changes and occlusions robustly when tracking moving objects under complex background by particle filter.

Keywords: moving object tracking, brain inspired cognitive modeling (BICM), three-stage memory model, particle filter (PF), template updating, occlusion handling.

1 Introduction

Object tracking is a key task of computer vision and has been found wide applications in smart surveillance, image indexing, human-computer interaction, and robot navigation. Object tracking can be defined as the problem of estimating the trajectory of an object in the image plane as the object moves around a scene [1]. In the past decades, researchers have made a lot of effort in this issue and put forward many effective methods. Among these methods, particle filter[2-3] can adapt to state estimation for nonlinear and/or non-Gaussian systems, thus it has become the most popular method in object tracking recently. However, the tracked object may be lost by a basic PF tracker when the object is occluded by other objects or the appearance of the object changes suddenly.

Recently, a lot of modifications have been made for improving the performance of particle filter by researchers. For example, Zhou et al [4] presented an approach that incorporated appearance-adaptive models to stabilize the tracker. They made the following three modifications: an observation model arising from an adaptive appearance model, an adaptive velocity motion model with adaptive noise variance,

H. Zhang et al. (Eds.): BICS 2012, LNAI 7366, pp. 112–119, 2012.

and an adaptive number of particles. Li et al[5] proposed a robust observation model to handle appearance changes. Wang et al [6-7] developed an SMOG appearance model and a SMOG –based similarity measure to deal with the appearance variation in particle filter. Zhang et al[8]embedded an adaptive appearance model into particle filter to address the appearance change, and invoked an occlusion handling scheme to deal with occlusion events. However, most of these methods applied a total model updating mechanism for template updating, i.e. the initial template model is updated gradually based on the estimated information by the particle filter. If the occlusion is serious or the target appearance changes suddenly, the total model updating based PF(TMUPF) will deviate from the target gradually.

As we all know that human can recognize object with no difficulty no matter how the appearance changes and no matter whether the object is occluded. The reason why human can do this so easily is related to the human's memory system according to cognitive psychology. What a person saw and experienced are processed by his memory system. When he perceives new things, the related information which is stored in his memory is recalled. Memory is the foundation of any natural intelligence [9] and as a faculty of information retention organs in the brain it has been intensively studied in neural science, biopsychology, cognitive science, and cognitive informatics [10].

According to contemporary cognitive psychology, the popular model of a basic memory includes three stages: ultra short-term memory (*USTM*), short-term memory (*STM*), and long-term memory (*LTM*), as shown in Fig.1 [11].

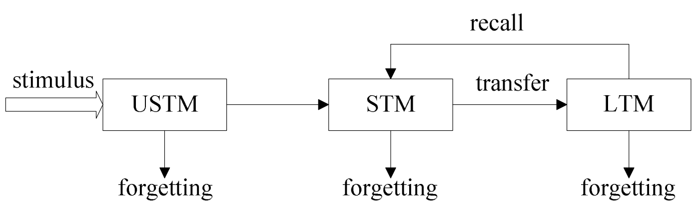

Fig. 1. The three-stage memory model

Each stage includes three processes: encoding, storage and retrieval. The information which is not always recalled or not commonly used would tend to lost from memory [12].

The human brain memory-based approach has been the subject of a lot of research over many years. However, it has rarely been applied to visual tracking. In our previous work, we have proposed a memory-based Gaussian mixture background modeling method to handle the scene with sudden partial changes [13]. The main purpose of this paper is trying to apply the memory model for solving some hot issues in object tracking.

The remainder of the paper is organized as follows. In section 2, the proposed method is described in detail, including the algorithm flow and updating, remembering and recalling of an object template. Implementation of particle filter with brain memory inspired template updating modeling algorithm is given in section 3. Section 4 demonstrates the performance of the proposed method compared with the traditional PF and TMUPF. Section 5 draws the conclusions.

2 Human Brain Memory Inspired Template Updating Model

2.1 The Three-Stage Memory Model for Template Updating

According to the cognitive psychology, the three-stage memory model for template updating can be described as shown in Fig. 2.

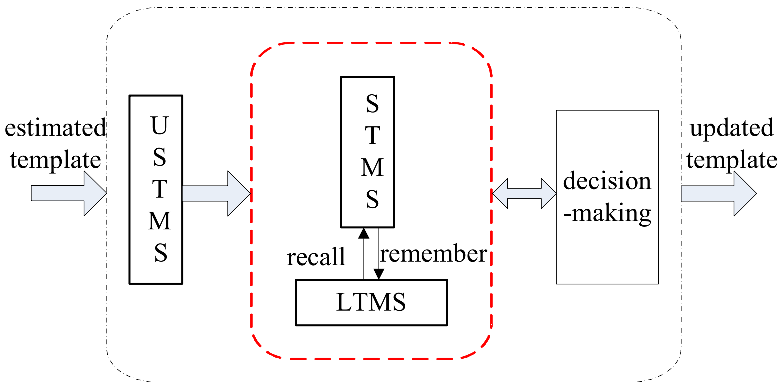

Fig. 2. Three-stage memory model for template updating

Where the input of the model is the estimated template by PF in the current video frame while the output is the updated template for prediction in the next frame. *USTMS*, *STMS*, and *LTMS* represent the three-stage memories respectively. They are defined as follows:

Definition 1. *USTMS*: an one-element set for storing the estimated template p in the current video frame, which simulates the stage of ultra short-time memory of human brain.

Definition 2. *STMS*: a set of K_s temporal templates, which imitates the stage of short-time memory of human brain. Let q_i denotes the *ith* template in *STMS*, then

$$STMS = \{ q_i, i = 1, 2, \cdots, K_s \}$$

Definition 3. *LTMS*: a set of K_l remembered templates, which simulates the dynamic stage of the long-time memory of human brain. Let q_{Mj} stand for the *jth* remembered template in *LTMS*.

$$LTMS = \{ q_{Mj}, j = 1, 2, \cdots, K_l \}$$

The templates stored in *STMS* include the estimated template transferred from *USTMS*, the updated templates in *STMS* or the templates recalled from *LTMS*.

According to the theory of cognitive psychology, only the information which is stimulated repeatedly can be stored into *LTM*. Therefore we define a parameter β

for each template in *STMS* to determine whether the templates in *STMS* can be stored into *LTMS* or not. Where β is a counter indicating the number of successful matches. The bigger of β is, the more probably the template can be stored into *LTMS*.

More specifically, for $\forall q_i \in STMS, i = 1,2,\cdots K_s$, if $q_i.\beta > T_M$ (a predefined threshold), the template will be remembered and stored into *LTMS*.

The process of template updating can be briefly described as follows:

First, the estimated template of the current frame is stored into *USTMS* and checked against the current template in *STMS* (the first one). If they are matched, update the template, otherwise check against the remaining templates in *STMS* and then *LTMS* in turn for a match. If a match exists, it will be selected for the new template. Meanwhile the *STMS* and *LTMS* are updated by some behaviors, such as *remembering, recalling, and forgetting,* etc. These behaviors are defined as follows:

Definition 4. *Remembering*: an action that a template is stored into *LTMS*.
If there is no match in *STMS* and *LTMS*, and the *STMS* reaches its maximum capacity and the last template in *STMS* (denoted by q_{Ks}) satisfies with $q_{Ks}.\beta > T_M$, then q_{Ks} will be remembered into *LTMS* and replaced by $q_{Ks\text{-}1}$. In such a circumstance, the estimated template will be reserved for the next estimation.

Definition 5. *Recalling:* an action that a matched template is loaded from *LTMS*.
If a match is found in *LTMS*, the matched template will be extracted and used as the current object template.

Definition 6. *Forgetting*: an action that a template is removed from either of *STMS* or *LTMS*.

If the *LTMS* reaches its maximum capacity and $q_{Ks}.\beta > T_M$, the oldest template in *LTMS* will be forgotten in order to remember q_{Ks}.

2.2 Detailed Description of the Human Brain Memory Inspired Template Updating Algorithm

According to the above model, the human brain memory inspired template updating algorithm can be described as follows:

Step 1: Initialization. Store the estimated template p into the *USTMS* and the current template q into the *STMS*, set $q.\beta = 1$ and the *LTMS* to be empty, where p and q are determined by the initial target region. It is worth mentioning that the *STMS* and *LTMS* will be filled up gradually after several time-steps during tracking.

Step 2: Calculate the similarity coefficient $\rho = \rho[p,q]$, if $\rho > T_{dc}$, update the current object template by

$$\begin{cases} q = (1-\alpha)q + \alpha \cdot p \\ q.\beta = q.\beta + 1 \end{cases}$$

Where T_{dc} is a predefined threshold for current template matching, α is the updating rate;

Step 3: If $\rho \le T_{dc}$, check against the remaining templates in *STMS* for a match, if

$$\rho[p, q_i] > T_{ds} \qquad i = 1, \cdots, K_s - 1$$

Update the matched template by ,

$$\begin{cases} q_i = (1-\alpha)\cdot q_i + \alpha \cdot p \\ q_i.\beta = q_i.\beta + 1 \end{cases}$$

Where T_{ds} is the threshold for template-matching in *STMS*. Then, exchange the current template and the matched one.

Step 4: If $\rho[p, q_i] \le T_{ds}$, check in *LTMS* for a match, if

$$\rho[p, q_{Mj}] > T_{dl} \qquad j = 1, \cdots, K_l$$

Where T_{dl} is the threshold for template-matching in *LTMS*. Then update the matched template by

$$\begin{cases} q_{Mj} = (1-\alpha) q_{Mj} + \alpha \cdot p \\ q_{Mj}.\beta = q_{Mj}.\beta + 1 \end{cases}$$

And then recall the matched one to use as the new object template and remember the current template q.

Step 5: If $\rho[p, q_{Mj}] \le T_{dl}$, it means that there is no any match in *STMS* and *LTMS*. The estimated template p is stored into STMS and used as the new object template (set $p.\beta = 1$). Meanwhile, if the *STMS* reaches its maximum capacity, remember or forget the oldest template in *STMS* (i.e. q_{K_s-1}) by the following sub-steps:

(1) If $q_{K_s-1}.\beta > T_M$ and the *LTMS* also reaches its maximum capacity, forget the oldest template in *LTMS* (i.e. $q_{M K_l}$) and remember q_{K_s-1}.

(2) If $q_{K_s-1}.\beta \le T_M$, forget q_{K_s-1}.

3 Object Tracking by Particle Filter

The particle filter based object tracking with brain memory inspired template modeling is described as follows:

Step 1: Initialization. Establish particle filter for each object and initialize the state model, the transition model and the memory space.

Step 2: For each new reached frame, update the transition model of each particle and gain the position of each particle;

Step 3: Compute weight;
Step 4: Re-sample and select the new particles;
Step 5: Estimate the state of the object and designate the tracked object;
Step 6: Obtain the estimated object template p according to Step 5, and update or reselect the object template using brain memory inspired template updating modeling algorithm; and then go to Step 2.

4 Experimental Results and Discussion

In order to inspect and verify the validity of the proposed algorithm, standard sequences are tested on a computer with a P4 3.0G Processor and a 512M RAM and the performances of the proposed method, traditional PF, and the total model updating PF(TMUPF) in handling different cases are shown. The size of the tested video frame is 160×128, and the frame frequency is 25 fps. Some parameters used are chosen as follows:

$$\alpha = 0.1, T_{dc} = 0.9,\ T_{ds} = T_{dl} = 0.8, K_l = K_s = 5, T_M = 1$$

The first experiment aims to track a man whose appearance changes constantly and sometimes suddenly. The experimental video is clipped from the standard sequence "seq_dk"[14]. The tracking results of the man by the proposed method, traditional PF and TMUPF at frame 19, 83, 86, 92, 95 and 106 are shown in Fig.3 (a),(b) and (c) respectively (The object is first selected manually). It is worth noting that there is a sudden appearance change from frame 86 to frame 92. The results show that when the appearance is far from the initialized template, PF loses the target and TMUPF deviates from the target gradually, while the proposed method never loses the target.

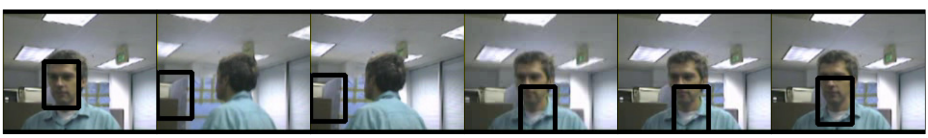

(a)Tracking results by PF

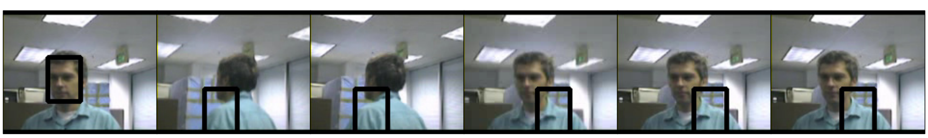

(b) Tracking results by TMUPF

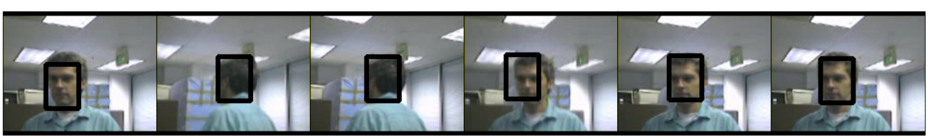

(c)Tracking results by the proposed method

Fig. 3. Tracking a man with appearance changing

The second experiment aims at tracking a person who is occluded by another object. The sequence used in this experiment is also a standard sequence "seq_jd"[14]. In this sequence, the man is occluded two times by another person. The tracking results by the proposed method at frame 15, 46, 50, 52, 55, 58, 248, 251, 253, 256, 258 and 260 are shown in Fig. 4 (The object is selected first manually). It is worth noting that the man is totally occluded at frame 52 and frame 253. The results show that the proposed method can still track the man correctly after recovered from the occlusion at frame 55 and frame 256.

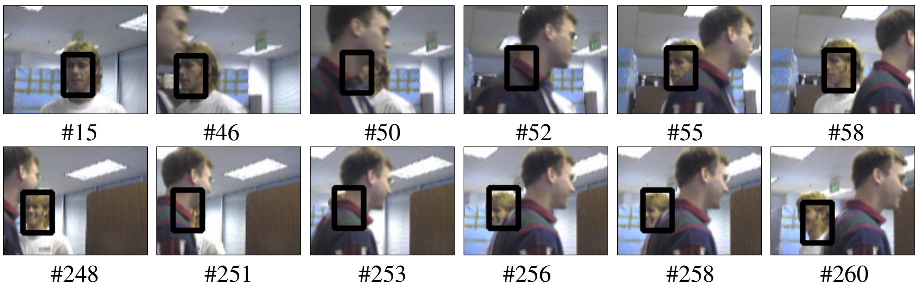

Fig. 4. Tracking a man occluded by another person by the proposed method

5 Conclusions

In this paper, we propose a novel template updating modeling algorithm inspired by human brain memory model. The proposed memory-based template updating mechanism can remember or forget what the target appearance has ever been, which helps the tracker adapt to the variation of an object's appearance more quickly. Experimental results show that the proposed algorithm can handle sudden appearance changes and serious occlusions robustly when tracking moving objects under complex background by particle filter.

Acknowledgments. The paper is funded by the National Natural Science Foundation of P.R. China (No.60873163), the Natural Science Foundation of Shandong Province, China (No.ZR2011FQ016), and the Fundamental Research Funds for the Central Universities.

References

1. Yilmaz, A., Javed, O.: Object Tracking: A Survey. ACM Computing Surveys 38, 1–45 (2006)
2. Gordonn, N.J., Salmond, D.J., Smith, A.F.M.: Novel Approach to Nonlinear / Non-Gaussian Bayesian State Estimation. IEE Proceedings F: Radar and Signal Processing 140, 107–113 (1993)

3. Arulampalam, M.S., Maskell, S., Gordon, N., Clapp, T.: A Tutorial on Particle Filters for Online Nonlinear / Non-Gaussian Bayesian Tracking. IEEE Transactions on Signal Processing 50, 174–188 (2002)
4. Zhou, S.K., Chellappa, R., Moghaddam, B.: Visual Tracking and Recognition Using Appearance-Adaptive Models in Particle Filters. IEEE Transaction on Image Processing 11, 1434–1456 (2004)
5. Li, A.P., Jing, Z.L., Hu, S.Q.: Robust Observation Model for Visual Tracking in Particle Filter. International Journal of Electronics and Communication 61, 186–194 (2007)
6. Wang, H., Suter, D., Schindler, K.: Effective Appearance Model and Similarity Measure for Particle Filtering and Visual Tracking. In: Leonardis, A., Bischof, H., Pinz, A. (eds.) ECCV 2006, Part III. LNCS, vol. 3953, pp. 606–618. Springer, Heidelberg (2006)
7. Wang, H., Suter, D., Schindler, K., Shen, C.: Adaptive Object Tracking Based on an Effective Appearance Filter. IEEE Transaction on Pattern Analysis and Machine Intelligence 27, 1661–1667 (2007)
8. Zhang, B., Tian, W.F., Jin, Z.H.: Robust Appearance-guided Particle Filter for Object Tracking with Occlusion Analysis. International Journal of Electronics and Communication 62, 24–32 (2008)
9. Wang, Y.X., Liu, D., Wang, Y.: Discovering the Capacity of Human Memory. Brain and Mind 4, 189–198 (2003)
10. Wang, Y.: Formal Description of the Cognitive Process of Memorization. In: Gavrilova, M.L., Tan, C.J.K., Wang, Y., Chan, K.C.C. (eds.) Transactions on Computational Science V. LNCS, vol. 5540, pp. 81–98. Springer, Heidelberg (2009)
11. Human Memory, `http://www.cc.gatech.edu/classes/cs6751_97_winter/Topics/human-cap/memory.html`
12. Harry, M.: Real learning: A bridge to cognitive neuroscience. Scarecrow Education, Lanham (2003)
13. Qi, Y.J., Wang, Y.J.: Memory-based Gaussian Mixture Modeling for Moving Object Detection in Indoor Scene with Sudden Partial Changes. In: 10th IEEE International Conference on Signal Processing, vol. 2, pp. 752–755. IEEE Press, New York (2010)
14. BMP Image Sequences for Elliptical head tracking, `http://www.ces.clemson.edu/~stb/research/headtracker/seq`

VLSI Implementation of Barn Owl Superior Colliculus Network for Visual and Auditory Integration

Juan Huo and Alan Murray

Shanghai Jiao Tong University, Zhengzhou University
and The University of Edinburgh
J.Huo@sjtu.edu.cn, Alan.Murray@ed.ac.uk

Abstract. A bio-inspired silicon Mixed Signal integrated circuit is designed in this paper to emulate the brain development in Superior Colliculus of barn owl. For the juvenile barn owl, it can adapt localization mismatch to prism wearing. Visual and auditory maps alignment in Superior Colliculus is adjusted. Visual and auditory input information can recover their registration after several weeks' training. A mathematical model has been built previously to emulate this process. Based on the model, we designed a VLSI circuit in $0.35\mu m$ CMOS process which has been fabricated. In this paper we present the chip test results of a silicon superior colliculus and show a novel method for adaptive spiking neural information integration when disparity is caused by the environment.

1 Introduction

Brain development is an important issue for the formation of intelligence. Axon growth and synaptic plasticity plays important role in brain adaptation to new information. A good example of adaptation is in the barn owl Superior Colliculus (SC). The barn owl can localize its prey accurately because of its advanced auditory and visual system. Usually visual and auditory localization information are registered with each other, but this registration is interrupted when the barn owl is wearing a prism or becomes blind [1]. However, young barn owl wearing prism can recover its localization accuracy after several weeks' training because of brain development [2,3].

In biological experiments, SC neurons access visual stimuli from the retina and auditory stimuli from the Inferior Colliculus (IC) [4]. Inferior colliculus is composed of central Inferior Colliculus (ICc) and external Inferior Colliculus (ICx). The area of ICc is much larger than ICx [5]. The auditory information in ICc is in two dimensions (azimuth and frequency). But the projection between ICc and ICx filter out frequency factor. Therefore the following model discussed in section 2 simplified ICc map to one dimension, we only consider azimuth factor. The point to point axon projection between ICc and ICx is changed when mismatch appeared between visual and auditory map. Large amount of evidence has shown this mismatch induces the release of neurotrophin (one kind

H. Zhang et al. (Eds.): BICS 2012, LNAI 7366, pp. 120–128, 2012.

of nerve growth factor), which promotes axon growth together with electrical activity of the cell body of axon source [6,7]. The release of neurotrophin is triggered by guiding signal from SC [8]. In this paper we call the guiding signal, Map Adaptation Cue(MAC). The instructed guiding signal MAC is generated from an inhibitory network in SC [9]. The SC neurons which accesses both visual signal and auditory signal are called bimodal neuron. Bimodal neuron can be potentiated by both visual input (from retina) and auditory input (from ICx) through synapses [10]. As we have described in [11], these synapses' Spike Timing Dependent Plasticity(STDP) property plays an important role in map adaptation.

In light of the newest biological discoveries, a model has been built to explore the adaptation in map alignment [12]. Based on this model, we described a circuit that implements the adaptive neural network in SC along with the simulation results.

2 Neural Network Model

In this model, a certain direction is represented by a pathway in space, which corresponds to 18° in azimuth [11]. A single pathway is composed of two sections shown in Fig. 1. To test the adaptive axon connection, we show two pathways. In Fig. 1(a), block I comprises the ICc, ICx and the axon connections that map between them. Block II is both the detector of any shift between visual and auditory maps and the controller of the ICx/ICc mapping in block I. The connection between ICc and ICx in block I is instructed by Map Adaptation Cue (MAC), which is generated by the inter neuron in block II. In block II, both bimodal and intern neurons in this model are Leaky Integrate-and-Fire(LIF) neurons. The synapses connected to the bimodal SC neuron are excitatory STDP synapses while the synapse between the bimodal SC neuron and the inter neuron is an inhibitory synapse. More details of discussion can be seen in our previous paper [13].

In Fig. 1(b), the connection between ICc and ICx are axons. The axon growth cone from the source layer of ICc is not active until its neural activity is strong enough, in the other words, the firing rate of the input spike train is high. On the other hand, neurotrophin release triggered by MAC is accumulated on ICx layer. When both neural activity and neurotrophin release get to their threshold separately, the active growth cone is attracted by neurotrophin and the axon connection is updated as shown in Fig. 1(b).

2.1 Input Spike Train Generation

We generate repeated stimuli from the same position in space to shorten the training time. The motivation for us to use spike is that differences in spike timing carry information about the location of objects in the environment [14]. We use two different methods to generate spike trains. In biology, sensory stimuli induce spikes in clusters, therefore in this simulation, spikes are clustered.

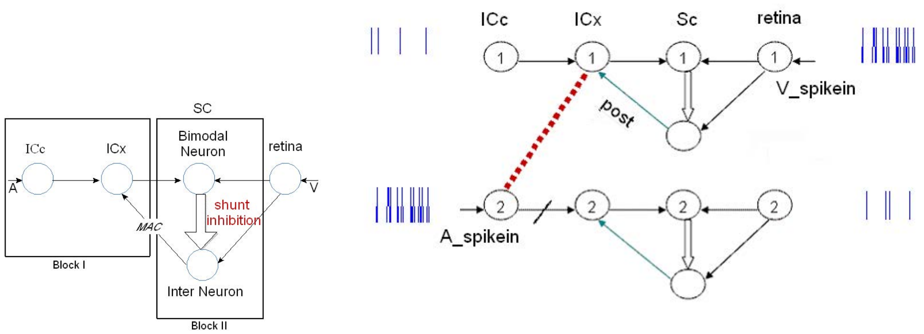

(a) (b)

Fig. 1. Schematics of this model. (a) Single pathway for auditory and visual signal processing. (b) Network after visual and auditory re-alignment caused by wearing a prism. Visual stimuli arrive at retina-1, ICx-1 receives the strongest MAC. However the auditory stimuli arriving at ICc-2 causes the axon growth cone from ICc-2 to be attracted by the neurotrophin released by ICc-1, and the new connection is built. This is depicted as a dashed line between ICc-2 and ICx-1. The old pathway is blocked.

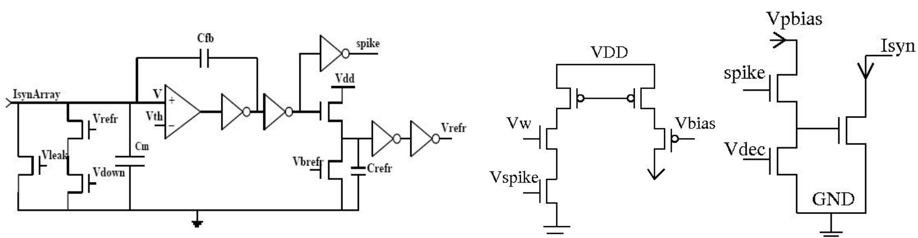

(a) (b) (c)

Fig. 2. Analog circuit for single pathway block II. (a) Leak Integrated and Fire Neuron. (b) Excitatory synapse. (c)Inhibitory synapse.

In the first method, we use spike pattern. The time intervals between spikes are set manually. The time interval between clusters is a fixed value. There are two kinds of spike pattern, high firing rate and low firing rate. The high firing rate spike pattern represents the stimuli direction in the visual or auditory map center. The low firing rate pattern corresponds to neighboring neurons of the stimuli center. The high firing rate spike pattern and the low firing rate spike pattern are independent of each other.

In the second method, we generated spike trains by Inhomogeneous Poisson Process. The instant firing rate of the center stimuli induced spike train, A_spikein and V_spikein in Fig. 1(b), is $r(t) = Rmax * cos(\frac{2\pi t}{T})$, the period T is 20ms, $Rmax = 400$. The density of this spike train varies with time and is analogous to spike clusters. Firing rate of neighboring neurons is a random sequence with average low density.

3 Learning Circuit Description

The axon circuit is shown in Fig. 3(a), where the axon network is represented by crossbar switch, each switch is a transmission gate. Transmission gate is a parallel combination of a NMOS and a PMOS transistor, it can effectively isolate the output from the input and conduct the current in either direction. Output spikes from the transmission gates are integrated by an OR gate before they arrives at the Integrate and Fire neuron.

The gate voltage of each switch, the state, is stored in a register. The fundamental storage element of the register is a simple latch. Transmission gate 1 is used as switch to update the register. As shown in Fig. 4(b), V_act is high indicates the growth cone is active. V_update represents the neurotrophin update signal. The register updates state and reads V_act when the reading-control signal V_update is high. The conflict between V_act and feedback of the latch is avoided by adding transmission gate 2. The register can keep the storage as long as the circuit power is on.

To identify whether the firing rate of the input spike train is high enough above its activity threshold, we use a digital counter to calculate its input spikes. Both V_act and V_up are asserted by their own spike calculator. The spike calculator

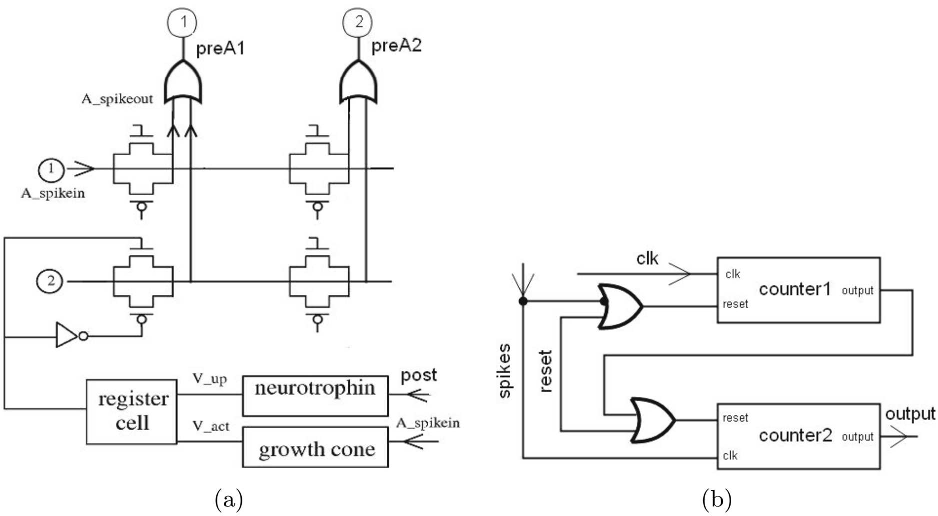

Fig. 3. Digital circuit for single pathway block I. (a) is the axon connection circuit. Or gates are used between the transmission gates and the IF neurons to integrate the axon inputs. (b) is spike calculator for neurotrophin and axon growth cone. Each counter is an 8 bit Toggle fip-flop counter. Counter2 will not start counting until the time interval between two spikes are small enough. Because the spike time interval is calculated by counter1. If counter1 counted 7 pulses of clock "clk", it resets counter2 to 0 V. This also means only more then 8 spikes come in one cluster, the output can be turned up high. The high output represents the growthcone is activated.

counts the number of spikes and the time interval between them. For V_act, the spike calculator counts the auditory input spikes in the ICc layer. We use the spike calculator to identify the spike cluster in the spike train. For V_up, the spike calculator count the MAC spikes. As shown in Fig. 4, the D flip-flop turns on when a spike arrives at the counter. This enables the (3-bit) counter1 to count clock pulses. When counter 1 reaches its maximum value, it resets both the Toggle flip-flop and counter 2. Counter 2 sums the input spike train and generates the update signal when it reaches its maximum value. When the system finishes updating, all counters are returned to their initial state. In this simulation, the period of each clock is 2ms, which means that if the time interval between two spikes is more than 14ms, counter2 will be reset.

3.1 Axon Network

The axon circuit is shown in Fig. 3(a), where the axon network is represented by crossbar switch. The gate voltage of each switch, the state, is stored in a register. The register reads the state of V_act when reading-control signal V_up is high. That V_act is high indicates that the growth cone is active. V_up is the neurotrophin update signal.

To identify whether the firing rate of the input spike train is high enough above its activity threshold, we use a digital counter to calculate its input spikes.

Both V_act and V_up are asserted by their own spike calculator. The spike calculator counts the number of spikes and the time interval between them. For V_act, the spike calculator counts the auditory input spikes in the ICc layer. We use the spike calculator to identify the spike cluster in the spike train. For V_up, the spike calculator count the MAC spikes. As shown in Fig. 4, the D flip-flop turns on when a spike arrives at the counter. This enables the (3-bit) counter 1 to count clock pulses. Counter 2 sums the input spike train and generates the update signal when it reaches its maximum value. When the system finishes updating, all counters are returned to their initial state.

In this simulation, the period of each clock is 2ms, which means that if the time interval between two spikes is more than 14ms, counter 2 will be reset.

3.2 Inhibitory Neural Network

The inhibitory neural network is an analog circuit. The circuit of LIF neuron and circuit of synapses Fig. 2 are described in [15,13]. STDP circuit can be found in [16]. These circuits are modified as required for new configuration.

4 Results

The circuitry was designed using the AMS 0.35μm C35 process. It has a digital block and an analog block as shown in Fig. 4. In the analog block, there are 2 bimodal neurons and 2 inter neurons. The digital block has 2×2 switch bar

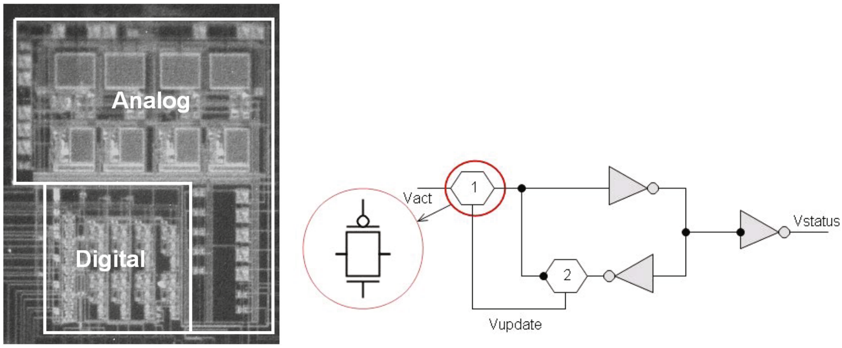

(a) (b)

Fig. 4. (a) Micrograph of mixed signal chip. The size of the chip is $0.6mm \times 0.5mm$.(b) Different from the basic latch, transmission gate 2 is added on the route of feedback. This is to avoid the conflict between the input and the feedback. Transmission gate 1 works as a switch to allow the current flows between V_act and the register. The register reads new value from V_act when V_update is high.

connections. In the layout, digital part and analog part are put in different blocks and their power inputs are also separated.

The switch bar network is initiated before spike train is generated. 1-1 and 2-2 are switched on while 1-2 and 2-1 are switched off. Vstatus represents the gate voltage that is stored in the register, $Vstatus11 = Vstatus22 = 3.3v$, $Vstatus12 = Vstatus21 = 0v$.

After the initiation finished, regular streams of spikes were sent to neurons and start to train the network. There are two kinds of input spike pattern, train-1 is shown in Fig. 5(a) D2 with high sike density and train-2 is shown in Fig.

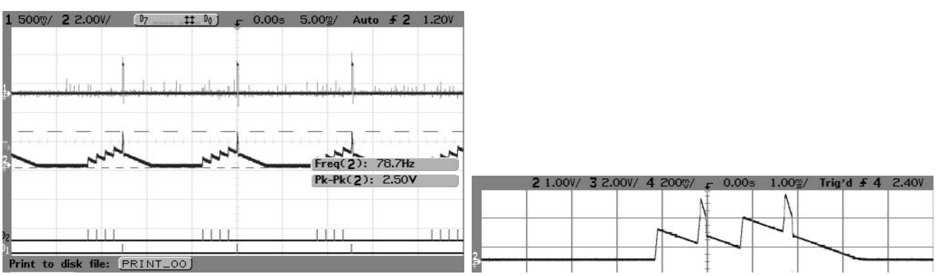

(a) (b)

Fig. 5. Chip test results of Integrate & Fire neuron. (a) "1" is the postsynaptic spike pulse. "2" is the membrane voltage on Cm. D1, D2 are the digital input spike trains. Each spike cluster triggers a postsynaptic spike. (b) The changed membrane voltage on with higher injected current.

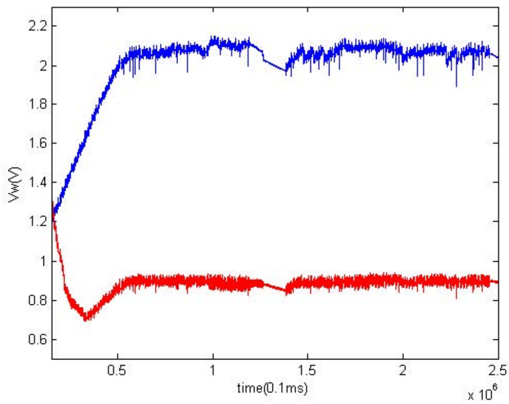

(a)

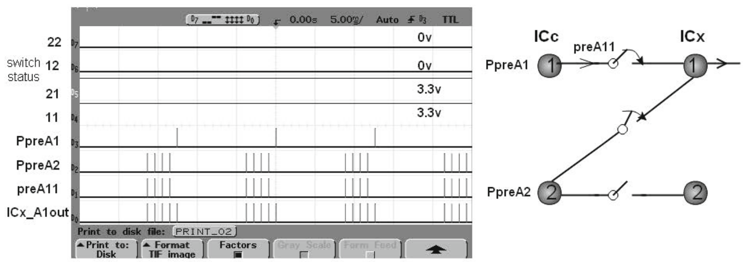

(b)

Fig. 6. On chip experimental results. (a)The synaptic weight change in normal training without change of switch status. (b) Snapshot of axon switch bar test taken from Agilent Oscilliscope. The switch from ICc-1 to ICx-1, ICc-2 to ICx-1 are on, while the switch in layer 2 is off. Eventually, the synaptic output from ICx is the summation of input 1 and input 2.

5(a) D1 with low spike density. The time interval between neighboring spikes is 1.5ms in cluster and 31ms out cluster. The spike input integrated on the neuron membrane capacitor, the effect of presynaptic spikes on the neuron is wave "2" in Fig. 5(a). Although the IF neuron membrane voltage threshold is 1.5V, the peak-to-peak amplitude of wave "2" is 2.5V. This is assumed due to the spike feedback of Cfb, the decaying speed of the membrane voltage and refractory time can be ajusted by bias voltages in IF circuit or changing the injected synaptic current. The changed Vm wave can be shown in Fig. 5(b), if we increase the value of Vw in Fig. 2(a). D2 indicates the visual input preV1, D1 is the auditory input preA1. Fig. 5 represents the bimodal neuron in pathway 1 of SC network in Fig. 1. The bimodal neuron in pathway 2 is also an IF neuorn, but its visual input is train-2 and auditory input is train-1. The inter neurons have nearly the same parameters as the bimodal neuron except its input synapses. The circuit of the excitatory synapse is the same as the bimodal neuron's. But the parameter settings of the inter neuron synapses are separated from the other synapses. In this stage, inter neurons in both pathway 1 and pathway 2 were not fired.

The axon growth cone is not actived at first. When the growth cone detects the A_spikein which has high spike density, the counter counted to 8, an update signal is generated, which represents the growth cone is actived. The gate voltage of the switch Vstatus21 is thus becomes high,more details of this process can be seen from previous simulation in [17]. The influence of gate status change towards the synaptic weight change can be seen from Fig. 6, when new connection is turned on, spikes of PpreAw go to new pathway and synaptic weight increases. When the switch is then turned off, synaptic weight decreases and returned to nearly its old state. In comparison, when the initial connection is set to normal condition, Vstuatus22=Vstatus11=1, Vstatus21=Vstatus12=0. The synaptic weight change in Fig. 6(a) is consistent with bifurcated synaptic weight change. Competition between synapses will appear and results in stable bifurcation at last.

5 Conclusion

The circuit presented can be used to study adaptive neural network in Neuroscience and possibly improve the performance of autonomous system. The updated axon connection in this paper shows bio-inspired brain development can be applied in electronic circuit level. The axon connection is represented by a crossbar switch and it is extendable and reconfigurable. The input spikes are trained through the sensory pathway and integrated by an inhibitory network with STDP. This is a new implementation of STDP in hardware level and is the first VLSI circuit for adaptive visual and auditory integration in midbrain. The chip works in low power with digital axon network and 4 neurons and 6 synapses in just $0.6mm \times 0.5mm$.

6 Discussion and Future Work

We previously applied the Superior Colliculus model to a robotic system emulating the behavior of barn owl and proved this model can correct the robotic localization error [18]. However, in the real-time experiment, the robot had to communicate with the PC by serial port to process data. This slowed down the computation speed. The analog VLSI circuit designed in this paper is considered to be embedded into the robot and process data directly. As expected, this circuit can train neurons in real time without the limitation of computer memory, which is a bottle neck for the similar network simulation as in [11]. At moment the test and configuration work is still continuing. Although as the first design of silicon Superior Colliculus with adaptive sensory information integration improvements are needed, this chip provides a new view for emulating the mechanism of adaptive spike train information integration.

Acknowledgments. We would like to thank Martin Reekie and Katherine Cameron's suggestions, Professor Feng Zhang's support in lab equipments.

References

1. Knudsen, E.I., Knudsen, P.F.: Visuomotor adaptation to displacing prisms by adult and baby barn owls. Journal of Neuroscience 9, 3297–3305 (1989)
2. Knudsen, E.I.: Auditory and visual maps of space in the optic tectum of the owl. The Journal of Neuroscience 2, 1177–1194 (1982)
3. Brainard, M.S., Knudsen, E.I.: Sensitive periods for visual calibration of the auditory space map in the barn owl optic tectum. J. Neurosci. 18, 3929–3942 (1998)
4. Meredith, M.A., Stein, B.E.: Spatial factors determine the activity of multisensory neurons in cat superior colliculus. Brain Research 365, 857–873 (1986)
5. Hyde, P.S., Knudsen, E.I.: Topographic projection from the optic tectum to the auditory space map in the inferior colliculus of the barn owl. J. Comp. Neurol. 421, 146–160 (2000)
6. Goldberg, J.L., Espinosa, J.S., Xu, Y., Davidson, N., Kovacs, G.T.A., Barres, B.A.: Retinal ganglion cells do not extend axons by default: Promotion by neurotrophic signaling and electrical activity. Neuron 33, 689–702 (2002)
7. Gillespie, L.N.: Regulation of axonal growth and guidance by the neurotrophic family of neurotrophic factors. Clinical and Experimental Pharmacology and Physiology 30, 724–733 (2003)
8. Taba, B., Boahen, K.: Silicon growth cones map silicon retina. In: Advances in Neural Information Processing System, vol. 18 (2006)
9. EI, K.: Instructed learning in the auditory localization pathway of the barn owl. Nature 417(6886), 322–328 (2002)
10. Meredith, M.A., Nemitz, J.W., Stein, B.E.: Determinants of multisensory integration in superior colliculus neurons. i. temporal factors. J. Neurosci. 10, 3215–3229 (1987)
11. Huo, J., Murray, A.: The adaptation of visual and auditory integration in the barn owl superior colliculus with spike timing dependent plasticity. Neural Networks (in pressing)
12. Huo, J., Murray, A., Smith, L., Yang, Z.: Adaptation of barn owl localization system with spike timing dependent plasticity. In: Proc. International Joint Conference on Neural Networks. IEEE World Congress on Computational Intelligence (June 2008)
13. Huo, J., Murray, A.: The Role of Membrane Threshold and Rate in STDP Silicon Neuron Circuit Simulation. In: Duch, W., Kacprzyk, J., Oja, E., Zadrożny, S. (eds.) ICANN 2005, Part II. LNCS, vol. 3697, pp. 1009–1014. Springer, Heidelberg (2005)
14. Roberts, P.D., Bell, C.C.: Spike timing dependent synaptic plasticity in biological systems. Biol. Cybern. 87, 392–403 (2002)
15. Bofill-I-Petit, A., Murray, A.F.: Synchrony detection and amplification by silicon neurons with stdp synapses. IEEE Transactions on Neural Networks 15, 1296–1304 (2004)
16. Indiveri, G.: Neuromorphic bistable vlsi synapses with spike-timing-dependent plasticity. In: Advances in Neural Information Processing Systems, pp. 1091–1098. MIT Press (2002)
17. Murray, A., Huo, J., Reekie, M.: Silicon superior colliculus for the integration of visual and auditory information with adaptive axon connection. In: ISCAS (IEEE International Symposium on Circuits and Systems) (2009)
18. Murray, A., Huo, J., Yang, Z.: Bio-inspired real time sensory map realignment in a robotic barn owl. In: NIPS, pp. 713–720 (December 2008)

Membrane Computing Optimization Method Based on Catalytic Factor

Fuluo Wang, Yourui Huang, Ming Shi, and Shanshan Wu

Anhui University of Science and Technology,
College of Electrical and Information Engineering,
Anhui 232001

Abstract. In order to further improve the convergence rate of membrane computing, the membrane computing optimization method based on the catalytic factor (BCMC) is proposed from the inspiration of biological catalyzing enzymes. This algorithm is based on the standard membrane computing, and the catalytic factor is used to control the number of communication objects between membranes, so that the number of communication objects between membrane changes with the change of membrane environment. That is to say, if the average fitness value is relatively larger than the individual fitness value of the membrane, then reduce the number of communication objects of the membrane, conversely, increase the number. In order to test the feasibility and correctness of the algorithm, the simulation test functions are used to simulate, through comparing with the calculated results by using the SGA method, we can see the convergence rate of the membrane computing optimization method based on the catalytic factor is faster and the results are more accurate.

Keywords: BCMC, membrane computing, catalytic factor, catalyzing enzymes.

1 Introduction

In recent years, the optimization methods based on biological calculation develop rapidly. The researchers put forward some intelligent optimization methods which have efficient optimization abilities and extensive adaptability from the thought of bionics. For example, artificial neural network (ANN) simulates the organizational structure and function of the human brain in a certain degree; Genetic algorithm (GA) benefits from the nature biological evolution mechanism "survival competition, survival of the fittest "; Ant colony optimization (Aco) is inspired from the optimal path that ants groups use to look for food. Tabu search theory simulates the intelligence process of human memory. These optimization methods based on biological calculation show their advantages for solving complex optimization problems. In 1998, when the European academy of sciences, Romania scientists Gheorghe Paun proposed the concept of membrane computing (P system)[1][2][3], membrane computing quickly became the hottest research areas. Membrane computing provides a new way for the study of optimization methods.

H. Zhang et al. (Eds.): BICS 2012, LNAI 7366, pp. 129–137, 2012.

Membrane computing model reflects the calculation essence, which is summarized from living cells and the function and structure of tissue or organ made up of cells. It has some characteristics such as distributed, the uncertain, maximum parallel etc. So far, the new calculation model mainly has three types: cell type, tissue type and the neural type. A lot of research results indicate that whether the cell type, tissue type or the neural calculation model are torn completely. In addition, when the P system that has "active" membrane structure is used to calculate, membrane structure changes with the execution of the membrane operating rules, and usually the exponential growth space can be produced within the linear growth operating step, so the NP-complete problem can be solved in polynomial time. However in $P \neq NP$ hypotheses, the tissue and neural type P system have not be proven that can solve the NP-complete problem in polynomial time. Along with the development and improvement of the membrane computing theory, it is parallel and distributed computing structure has been widely applied to different fields.

In solving optimization problems, in 2004, based on membrane computing NiShida proposed a kind of membrane computing optimization method based on the rules of cells contraction and relaxation, that is membrane algorithm[4][9][10]. Because the algorithm has distributed and dynamic evolutionary membrane structure during the calculation process, it can be regarded as a super evolutionary algorithm. The algorithm is used to solve a TSP, the computation result shows the superior performance of the membrane algorithm. Liang Huang, Ning Wang, and Junwei Chen put forward a kind of optimization method based on a P system, and it has been used in the controller single and multi-objective optimization design and optimization of chemical process[5][6]. Jie Fu and Ning Wang put forward the membrane optimization calculation method which has the star topological structure[7]. In this paper, a kind of membrane calculation optimization method (BCMC) based on the catalytic factor has been put forward, the membrane system is divided into simple structures of four layers, and in the membrane internal genetic algorithm is used to optimize the objects, and the number of communication objects between membranes will be controlled and adjusted. The experimental results show that the algorithm has faster convergence speed and higher precision, it will not be in local optima for the multimodal value problem, thus it can get a high precision global optimal solution.

2 The Principle of Membrane Computing and the Structure of Membrane

The concept of membrane calculating is abstracted from cell processing chemical mechanism. From the micro perspective, some material can be abstracted as the cell membrane, such as the nucleus, the capsule. From the generalized perspective, the creature can be seen as a cell membrane, and a biometric system can even be seen as a membrane. Its corresponding biological membrane is abstracted as the layered nested topology structure, as shown in figure 1. Many membranes are nested each other, the membrane include membrane. Each part that the membrane contains is called as membrane region. Each area has corresponding strings (object sets) and rules. The strings evolve according to the rules. Membrane and membrane can communicate each other.

A membrane system can be expressed as the following group which has three elements,

$$\Pi = (V, C, i) \tag{1}$$

Among them, the V is a character sheet, it is a nonempty abstract character set, and its objects are composed of the characters in the character set. V = R is a real number set, it shows that the objects in the system are adopted by the real number coding. C is the pattern, it includes three basic structures that are the system structure, the objects and rules. i means output area, it can be a membrane of the system structure, but also the external environment.

In the paper, a simple membrane computing structure of four layers as shown in figure 1 is adopted. Its initial pattern C_0 is

$$C_0 = (\mu, M_1, M_2, M_3, M_4, R_1, R_2, R_3, R_4) \tag{2}$$

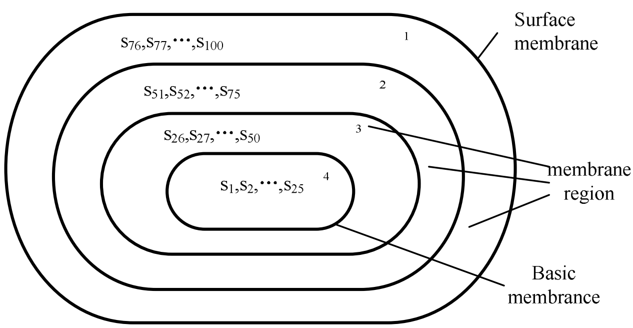

Fig. 1. Structure of membrane

Among them, μ is the system structure, $\mu = [_1[_2[_3[_4]_4]_3]_2]_1$; M_1, M_2, M_3, M_4 means the string object sets which are contained in the corresponding membrane. 25 objects have been produced randomly in 1~4 area, and they will be at the initial state, thus the BCMC algorithm has a total of 100 evolutionary objects. R_1, R_2, R_3, R_4 are the rule sets of the objects.

3 Design of Optimization Algorithm Based on the Catalytic Factor

Structure, objects and rules are three basic elements of the pattern. In the rules, the exchange rule is very important and it plays a key role in the diversity of the population and the convergence speed plays an important role. There is not an obvious function if the objects too little in the exchange. On the contrary, too much exchange object will make the population into the local minimum points. The structure and objects of BCMC algorithm are those such as mentioned above, and its rules include the choice rules, cross rails, variation rules and the exchange rules based on catalytic conditions.

3.1 The Catalytic Factor

Cell is the basic unit of the structure and function of all life activities of a human body and other organisms. All animal cells are surrounded by a layer of film, it is called as the cell membrane. The cell membrane can make cell independently exist in the environment, also it can make cell maintain life activities through selective material exchanges between the biological membrane and the surrounding environment. The factors that affect the material transport rate is the concentration of O_2, material concentration and temperature, etc. Among them, the temperature can affect the liquidity of biological membrane and the activity of relevant enzyme, so it can affect material transport rate. In active transport, macromolecule material transmembrane transportation needs the help of carrier protein. At the same time it also needs to consume the energy cells released by a chemical reaction inside the cell, the formula of generated energy is as follows:

$$ADP + P_i + \text{energy} \xrightarrow{\text{enzyme}} ATP \qquad (3)$$

Thus it can be seen, enzyme having the effect that cannot be ignored in the material transportation.

The enzyme is a kind of biological catalyst produced by living cells of the biological, Most of the enzyme is composed of protein (a few is composed of RNA). Under the very gentle body conditions, it can effectively catalyze various biological and chemical reaction, promote the metabolism of organisms. The digestion, absorption, breathing, sports and reproductive in life activities is all the reaction process promoted by enzymes. The activity of the enzyme can be adjusted and controlled by many factors, such as temperature, chemical environment (such as PH value), substrate concentration and electromagnetic wave, etc. So that the organism can fit the changes of external conditions, and maintain life activities. Drawing inspiration from the enzyme inside the cell, in the paper, a kind of catalytic factor has been proposed, It is relevant to the adaptive value of the evolutionary object, Its size changes following the changes of the adaptive value of the objects inside the membrane, thus it can control the number of communication objects between membranes. Its formula is as follows:

$$P_g = \frac{\sum_{i=1}^{n} \frac{f_i - f_{avg}}{\left| f_i - f_{avg} \right|} + n}{2n} \qquad \left(f_i \neq f_{avg} \right) \qquad (4)$$

Among them, is the number of objiects in membrane. f_i is the fitness value of an object in the membrane. f_{avg} is average fitness value $f_{avg} = \frac{1}{n}\sum_{i=1}^{n} f_i$. P_g is exchange probability. In general $0.3 < P_g < 0.5$.

So, after the population has completed the evolution each time, each membrane calculates its own average fitness value, and the number of communication objects is adjusted according to the adaptive ability of each population to the environment. If the average fitness value of the population is smaller, then properly increase the number of communication objects; if the average fitness value of the population is larger, then properly reduce the number of communication objects or remain the same.

3.2 The Rules

Like the genetic algorithm (GA), the basic rules of BCMC optimization method also contain the selection rules, the crossover rules and the mutation rules, etc. In addition, it contains the exchange rules with constraint conditions which is put forward in this paper. The rule sets can be described as follows:

$$R_i = \{ r_{iSelect} > r_{iCommunication} > r_{iCrossover} > r_{iMutation} \} \quad i = \{1,2,3,4\} \tag{5}$$

Here, the choice rule is that the objects will be copied to the next generation according to the size of the string or other conditions. The size of the string is not the particle size of biological cells, but the values of the objective function, or it is equal to the fitness value in genetic algorithms. The exchange rule is that each membrane sends the string that has good fitness value to its upper membrane, and it can be described as follows:

$$r_{iCommunication} : [s_{\max 1}, s_{\max 2}, \cdots, s_{\max q}]_i \rightarrow []_i \, s_{\max 1}, s_{\max 2}, \cdots, s_{\max q} \tag{6}$$

Among them, q is the number of exchange objects. $s_{\max 1}, s_{\max 2}, \cdots, s_{\max q}$ are the N objects which have good fitness values in the membrane i . The exchange rule based on the catalytic condition is that using the formula 4 determines the number of communication objects between the membranes.

3.3 The Process of the Algorithm

Step1: Initialize the parameters of BCMC algorithm and the search range of the optimization problem. When the initial population is not specified, the initial population is given randomly.

Step2: In each area at the same time (parallel) use its own child algorithm to update its solution.

Step3: After the specified operation generation number is completed, calculate the number of exchange objects. According to exchange rules, the membranes exchange their part of objects each other.

Step4: Repeat step 2 and 3, the algorithm stop until the termination conditions are met.

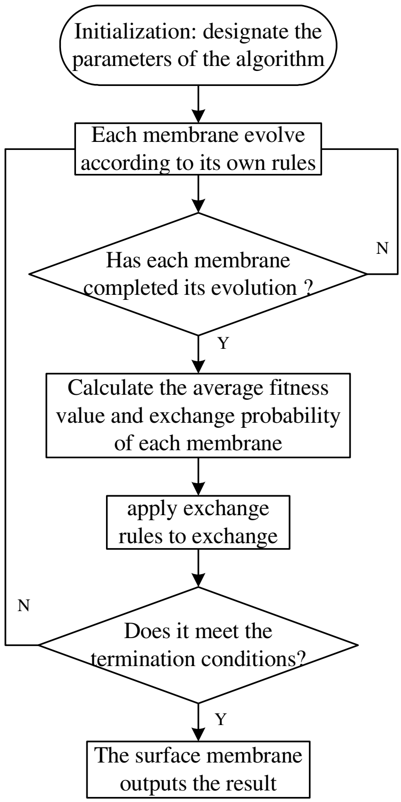

Fig. 2. Flow chart

4 Using Functions to Test

In order to evaluate the performance of the proposed membrane calculation optimization algorithm, the simulation experiment has been done to compare with other optimization algorithm, such as the standard genetic algorithm (GA) and membrane method (MC). Four typical test functions which are Ackley function, Easom function, Rastrigin function and Griewank function are adopted to test the performance of BCMC. (Fig. 3 shows the convergence process of the test functions.)

(1) Ackley function:

$$f\left(\bar{x}\right) = -c_1 \times \exp\left(-c_2\sqrt{\frac{1}{l}\sum_{i=1}^{l} x_i^2}\right) - \exp\left(\frac{1}{l}\sum_{i=1}^{l}\cos\left(c_3 x_i\right)\right) + c_1 + e$$

$$x_i \in [-32.768, 32.768], c_1 = 20, c_2 = 0.2, c_3 = 2\pi$$

Ackley function is a multi-modal function, and its global optimal point is $f(\bar{0})=0$. Make the fitness function of Ackley function as $f_1(x)=1-\frac{1}{f(x)+1}$, then the global optimal point of $f_1(x)$ is $f_1(\bar{0})=0$.

(2)Easom function:

$$f_2\left(\bar{x}\right)=-\cos x_1\times\cos x_2\times\exp\left(-\left(x_1-\pi\right)^2-\left(x_2-\pi\right)^2\right)$$
$$x_i\in[-100,100]$$

Easom function is a single-peak function, its global optimal solution is in a relatively narrow area, and its global maximum is $f_2(\pi)=0$. Its fitness function has been adjusted as $f_2(x)=f(x)$, then the global optimal point of $f_2(x)$ is $f_2(\pi)=0$.

(3)Rastrigin function:

$$f_3\left(\bar{x}\right)=\sum_{i=1}^{l}\left(x_i^2-10\cos\left(2\pi x_i\right)+10\right)$$
$$x_i\in[-5.12,5.12]$$

Rastrigin function is a multi-modal function, it has many local minimum points, and its optimal value is $f(\bar{0})=0$. Its fitness function has been adjusted as $f_3(x)=1-\frac{1}{f(x)+1}$, then the global optimal point of $f_3(x)$ is $f_3(\bar{0})=0$.

(4) Griewank function:

$$f_4\left(\bar{x}\right)=\frac{1}{4000}\sum_{i=1}^{50}x_i^2-\prod_{i=1}^{50}\left(\cos\left(\frac{x_i}{\sqrt{i}}\right)\right)+1$$
$$x_i\in[-600,600]$$

Griewank function is a function which has numerous widely distributed local minimum points, and its optimal value is $f(\bar{0})=0$. Make its fitness function as $f_4(x)=1-\frac{1}{f(x)+1}$, then the global optimal point of $f_4(x)$ is $f_4(\bar{0})=0$.

From figure 3, we can see that the performance of membrane calculation is better than the other calculation optimization algorithm. Membrane calculation can get the better solutions, and its evolution speed is faster.

At the same time, the superiority of the membrane calculation has been also fully reflected in table 1. Except that the value of f_2 is a little bad, all the optimal values of test functions which are gotten by BCMC method are better than those gotten by other algorithms. And the advantage is obvious.

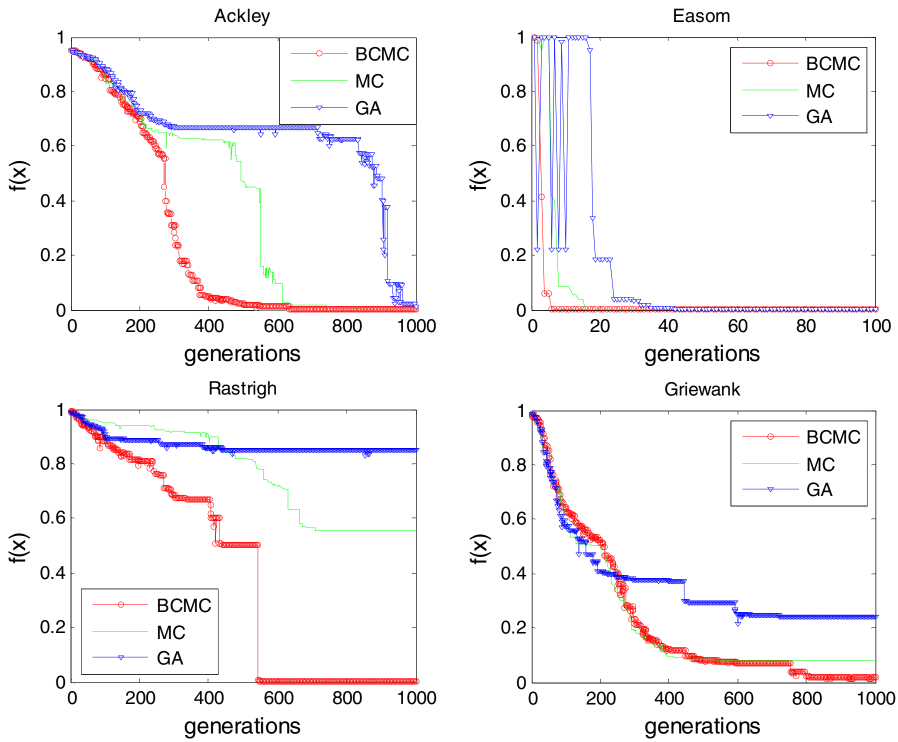

Fig. 3. Convergence curve of functions

Table 1. The comparison of simulation data

functions	Ackley	Easom	Rastrigin	Griewank
the number of variables	100	100	100	100
the specified number of generation	1000	1000	1000	1000
GA	1.33E-2	3.26E-5	0.24	0.85
MC	2.13E-3	2.92E-5	7.891E-2	0.55
BCMC	1.22E-4	6.76E-8	1.59E-2	4.35E-8
the real optimal value	0	0	0	0

5 Conclusion

Inspired by the membrane calculation, the membrane calculation optimization algorithm based on the catalytic factor has been proposed. The algorithm adopts four simple membrane structure, and the genetic algorithm is used for local search in the membrane. The exchange rules based on the catalytic factors are adopted when the objects exchange between membrane and membrane. Finally, simulation experiment the simulation experiments have been done through the four classical test functions. From the comparison, we can see that the proposed algorithm in the paper has the obvious advantages, not be in local optimum, and has high precision, good stability.

References

1. Paun, G.: Computing with membrane. Journal of Computer and System Sciences 61(1), 108–143 (2000)
2. Paun, G., Rozenberg, G.: A guide to membrane computing. Theoretical Computer Science 287(1), 73–100 (2002)
3. Paun, G.: Membrane computing. Fundamentals of Computation Theory, Proceedings 296(2), 295–326 (2003)
4. Nishida, T.Y.: An application of P system: a new algorithm for NP-complete optimization problems. In: Proceedings of 8th World Multi-Conference on Systems, Cybernetics and Information, pp. 109–112 (2004)
5. Huang, L.: Research on membrane computing optimization algorithm. Zhejiang University, Hangzhou (2007)
6. Chen, J.: Research on control system design based on the membrane computing optimization algorithm. Zhejiang University, Hangzhou (2008)
7. Fu, J.: Research on optimization algorithm inspired by the membrane computing. Zhejiang University, Hangzhou (2010)
8. Zhang, G., Linqiang, P.: A survey of membrane computing as a new branch of natural computing. Chinese Journal of Computers 33(2), 208–214 (2010)
9. Nishida, T.Y.: An approximate algorithm for NP-complete optimization problems exploiting P systems. In: Proceedings of Brainstorming Workshop on Uncertainty in Membrane Computing, Palma de Majorca, pp. 185–192 (2004)
10. Nishida, T.Y.: Membrane algorithms: Approximate algorithms for NP-complete optimization, pp. 301–312. Springer, Berlin (2005)
11. Jiang, Z.-Y., Cai, Z.-X., Wang, Y.: Hybrid self-adaptive orthogonal genetic algorithm for solving golbal optimization problems. Institute of Software 21(6), 1296–1307 (2010)

Effect of Body Position on NIRS Based Hemodynamic Measures from Prefrontal Cortex

Murat Ozgoren[1], Merve Tetik[1], Kurtulus Izzetoglu[2], Adile Oniz[1], and Banu Onaral[2]

[1] Dokuz Eylul University, Faculty of Medicine, Department of Biophysics
Izmir, Turkey
[2] Drexel University, School of Biomedical Engineering, Science & Health Systems,
Philadelphia, US
{murat.ozgoren,merve.tetik,adile.oniz}@deu.edu.tr,
(ki25,banu.onaral)@drexel.edu

Abstract. This study focuses on the positional effects on hemodynamic changes monitored by the functional near infrared (fNIR) spectroscopy. The motivation behind this exploratory study is to provide a standard approach for a number of bedside, and postural applications where the body-head position can influence the fNIR signal readings. By administering two consecutive experimental protocols, we investigated effects of the potential body-head positions that may be the cases during sleep and anesthesia recordings. Furthermore dynamic tilting was used to address positional effects from lying to standing up. Positions of supine and tilted are significantly different for HbO_2 and Hb ($p < .05$). The natural positions, i.e., sitting, prone, supine, and sideways showed differentiations in the fNIR measures. The deoxygenated hemoglobin values seem to be the least effected component of fNIR recordings across all different positions.

Keywords: fNIR, supine, body positions, tilt, prefrontal oxygenation.

1 Introduction

Monitoring of the brain activity has been an important focus of cognitive sciences. As the brain does not directly reveal its properties dynamically we have to incorporate indirect assessment methods, such as measurement of electrical activity, consumption of oxygen and glucose, etc. In recent years, near infrared spectroscopy (NIRS) based optical brain imaging technique has been widely used as a non-invasive measurement method to monitor human brain activity. Further, neuromonitoring methods such as electroencephalography (EEG), positron emission tomography (PET), single-positron emission computed tomography (SPECT), magnetoencephalography (MEG), and functional magnetic resonance imaging (fMRI) are divided into two groups which can provide direct and indirect information about brain function [9].

The functional near infrared (fNIR) spectroscopy has recently been implemented in various applications. It provides similar hemodynamic information comparable to the BOLD signals (fMRI) but has an advantage of enabling measures of both deoxyhemoglobin (Hb) and oxyhemoglobin (HbO_2) simultaneously. This method is limited to monitoring in the supine position, and may have limited availability. On the

H. Zhang et al. (Eds.): BICS 2012, LNAI 7366, pp. 138–146, 2012.

other hand, few studies reported protocols and results that may help standardize the fNIR signal acquisition as well as interpretation of potential side effects, such as body-head position changes. Unlike fNIR, for instance cardio ballistic effects, and various other artifacts have been studied in detail and now readily removed by MRI software applications.

Hence, fNIR system use may need a revisit to basic systematic and well controlled testing to set the proper and standardized adjustments in data acquisition and interpretation. For instance it has been formerly realized that the position may affect the signals from the fNIR measurements [2]. However a systematic approach to the positional effects is required to provide reliable measurement profiles. In this study, we aim to address this question by means of conducting two experiments.

2 Method

EXPERIMENT 1

2.1 Subjects

Eleven healthy subjects [five females (mean: 25.67, SD: 6.83) and six males (mean: 22.2, SD: 1.78)] were investigated.

2.2 Measurements

The continuous wave fNIR system used in this study was connected to a flexible sensor pad that contained 4 light sources with built in peak wavelengths at 730 nm and 850 nm and 10 detectors designed to scan cortical areas underlying the forehead. With a fixed source-detector separation of 2.5 cm, this configuration generates a total of 16 measurement locations (voxels) per wavelength. Data acquisition and visualization were conducted using COBI Studio software [7]. This system records two wavelengths and dark current for each of the 16 voxels, totaling 48 measurements for each sampling period [3]. The fNIR device calculates relative changes to baseline values of oxyhemoglobin (HbO_2) and deoxyhemoglobin (Hb) molecules by means of a continuous wave (CW) spectroscopy system which applies light to tissue at constant amplitude. The mathematical basis of CW-type measurements uses the modified Beer Lambert Law [8].

The sensors were attached to the forehead region after cleansing the skin with alcohol swap and scrubbing cream (NuPrep). The sensor was covered by an elastic bandage specifically designed to hold it tightly across the head. Furthermore a black colored cap was placed on top to eliminate the possible ambient light effects.

2.3 Protocol

Each volunteer underwent five positional changes during this experiment as shown in Figure 1: i. The volunteer first lay in supine position; then ii. moved to the right (R) sided position, iii. moved to the left (L) sided position, iv. moved to the prone position, and finally v. moved to sitting. Duration for each move was 8 minutes. All the protocols were applied in the Dokuz Eylul University Biophysics Department, Sleep Dynamics Laboratory.

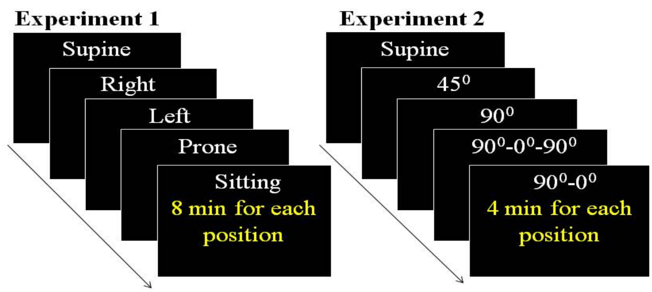

Fig. 1. The experimental protocol during fNIR recordings

2.4 Preprocessing for Artifact Removal

Raw intensity measurements at 730, and 850 nm were Butterworth low-pass filtered with MATLAB program [12]. Butterworth showed that a low pass filter could be designed whose cutoff frequency was normalized to 1 radian per second to eliminate possible respiration and heart rate signals and unwanted high frequency noise [1].

2.5 Statistical Analysis

All data are presented as mean ± standard deviation. The mean change in oxygenated hemoglobin (HbO_2), deoxygenated hemoglobin (Hb) and total hemoglobin (tHb) for all seventeen subjects were calculated for a 2-min interval near the end of each position. Statistical analyses were performed in SPSS 16.0.1 [11] using a paired t-test with significance accepted as $p < .05$.

EXPERIMENT 2

2.6 Subjects

Seventeen healthy subjects [eleven females (mean: 28.81, SD: 8.28) and six males (mean: 32.17, SD: 11.27)] were investigated.

2.7 Measurements

The same fNIR system was used as in the Experiment 1. Additionally, blood pressure, pulse oximeter, (Mindray PM9000 monitor) and ECG (Burdick Medic) were recorded simultaneously.

2.8 Protocol

Each volunteer underwent first three positional changes with 4-minute duration at each following positions (Figure 1): i. The volunteer first lay in supine position, then,

ii. moved to the tilted (45^0) position, iii. moved to the vertical position. Afterwards there was a dynamic session where the subject was moved during recording from vertical to supine position and back to vertical position (90^0-0^0-90^0). These two dynamic position change recordings continued for 5 minutes (Figure 2).

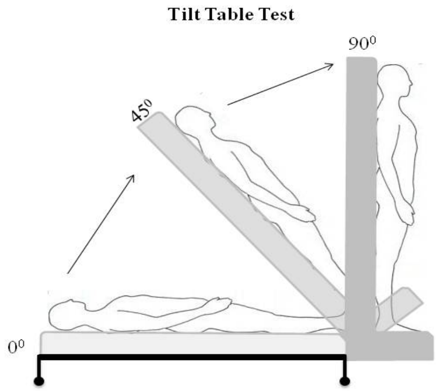

Fig. 2. The tilt table positions. The horizontal (0^0), tilted (45^0), and full vertical (90^0) positions are indicated.

3 Results

3.1 Results of Experiment 1

All subjects completed the protocol and the data was effectively processed. In Table 1 and 2 only the statistically significant results have been reported for the sake of simplicity.

Table 1. A summary of the group statistics of the mean values for ΔHb, ΔHbO_2, and ΔtHb in Experiment 1. The group means ± SD are shown (N = 11).

Channel 8					
	Positions				
Hemodynamic Parameter	**Supine**	**Right**	**Left**	**Prone**	**Sitting**
ΔHb (µmol/l)	0.05 ± 0.45	1.54 ± 2.59	1.97 ± 2.53	2.84 ± 3.72	1.43 ± 3.61
ΔHbO_2 (µmol/l)	0.03 ± 0.86	0.86 ± 0.94	1.85 ± 2.28	0.67 ± 2.92	-0.79 ± 4.72
ΔtHb (µmol/l)	0.07 ± 0.29	2.40 ± 0.52	3.82 ± 0.67	3.50 ± 0.31	0.64 ± 0.38

There were significant differences at positional changes: between supine, and other positions (prone, right, left) at channel 1, 8 ($p < .05$). The prone position showed significant differences regardless of channels (1, 8, and 16).

Table 2. Positional changes of hemoglobin concentrations with Paired *t-test* in 1, 8, and 16 channels of fNIR devices (p < .05)

	Concentrations	p
Channel 1		
Supine - Prone	Δ Hb	.033
Right - Prone	Δ Hb	.010
Left - Prone	Δ Hb	.008
Prone - Sitting	Δ Hb	.041
Channel 8		
Supine - Right	Δ HbO_2	.021
Supine - Left	Δ Hb	.021
Supine - Left	Δ HbO_2	.013
Supine - Prone	Δ Hb	.016
Left - Sitting	Δ Hb	.008
Prone - Sitting	Δ HbO_2	.004
Channel 16		
Right - Left	Δ Hb	.006
Right - Prone	Δ HbO_2	.003
Left - Prone	Δ Hb	.010

3.2 Results of Experiment 2

Figure 2 shows the positional changes in frontal cortical Hb, HbO_2, and tHb across all subjects. As tabulated in Table 3 and Table 4, paired *t-tests* showed a significant increase in the HbO_2. This significant difference was between supine and tilted positions ($p < .05$). Significant differences were also seen in the HbO_2 concentration between 90^0-0^0-90^0 and 90^0-0^0 ($p < .05$). There is no significant difference observed for the changes in Hb concentrations.

Table 3. A summary of the group statistics of the mean values for ΔHb, ΔHbO_2, and ΔtHb in Experiment 2. The group means ± SD are shown (N = 17).

	Positions				
Hemodynamic Parameter	**Supine 0^0**	**Tilted 45^0**	**Vertical 90^0**	**90^0-0^0-90^0**	**90^0-0^0**
ΔHb (µmol/l)	0.08 ± 0,39	0.87 ± 2.76	0.71 ± 3.41	0.12 ± 3.33	0.44 ± 3.32
ΔHbO2 (µmol/l)	0.42 ± 0.83	-1.57 ± 2.56	-2.30 ± 3.98	-1.00 ± 2.71	0.55 ± 2.85
ΔtHb (µmol/l)	0.49 ± 0.20	-0.60 ± 0.39	-1,64 ± 0.41	-1.00 ± 1.02	3,73 ± 2.44

Table 4. Positional changes of hemoglobin concentrations with Paired *t-test* (*p < .05)

	Concentrations	$\bar{X}$	SD	p
Supine 0^0 - Tilted 45^0	Δ Hb	-0.78	2.52	.215
Tilted 45^0 - Vertical 90^0	Δ Hb	0.15	4.63	.894
Supine 0^0 - Tilted 45^0	Δ HbO2	2.00	2.18	**.002***
Tilted 45^0 - Vertical 90^0	Δ HbO2	0.73	5.07	.560
90^0 0^0 90^0 - 90^0 0^0	Δ Hb	-0.32	1.81	.480
90^0 0^0 90^0 - 90^0 0^0	Δ HbO2	-1.55	2.78	**.035***

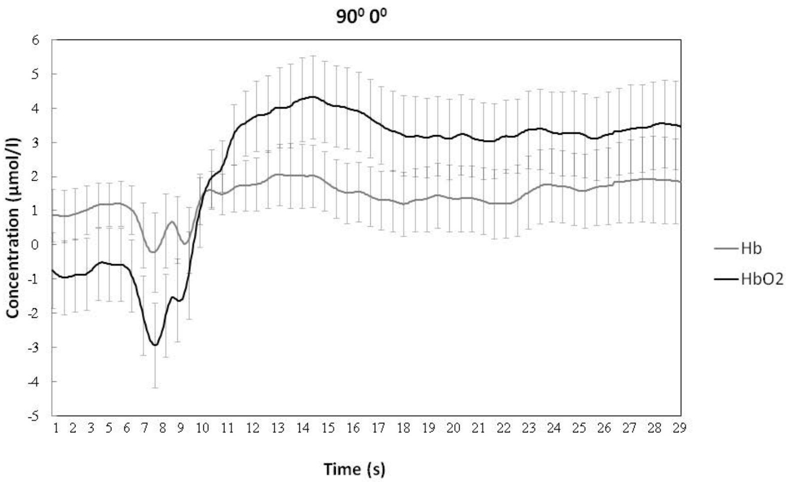

Fig. 3. Changes in Hb and HbO_2 in all subjects. These parameters for all the subjects who were tilted with tilt table test.

Between Hb and HbO_2 concentrations significant differences were found for positional changes of supine, tilted, and vertical ($p < .05$) (Table 5). Hemoglobin concentrations were significantly different in response to the supine, tilted, and vertical position changes.

Table 5. Positional changes of hemoglobin concentrations with Paired *t-test*

Positional Changes				
	Concentrations	$\bar{X}$	SD	p
Supine 0^0	Δ Hb- Δ HbO_2	-0.34	0.64	**.044***
Tilted 45^0	Δ Hb- Δ HbO_2	2.44	0.43	**.000***
Vertical 90^0	Δ Hb- Δ HbO_2	3.02	0.57	**.000***
90^0 0^0 90^0	Δ Hb- Δ HbO_2	1.12	3.70	.229
90^0 0^0	Δ Hb- Δ HbO_2	-0.11	3.51	.897

***p < .05**

3.3 Blood Pressure, sPO_2, Pulse

The accompanying parameters are presented in Figure 3. The blood pressure, sPO_2, and Pulse rates showed expected changes in regard to tilting.

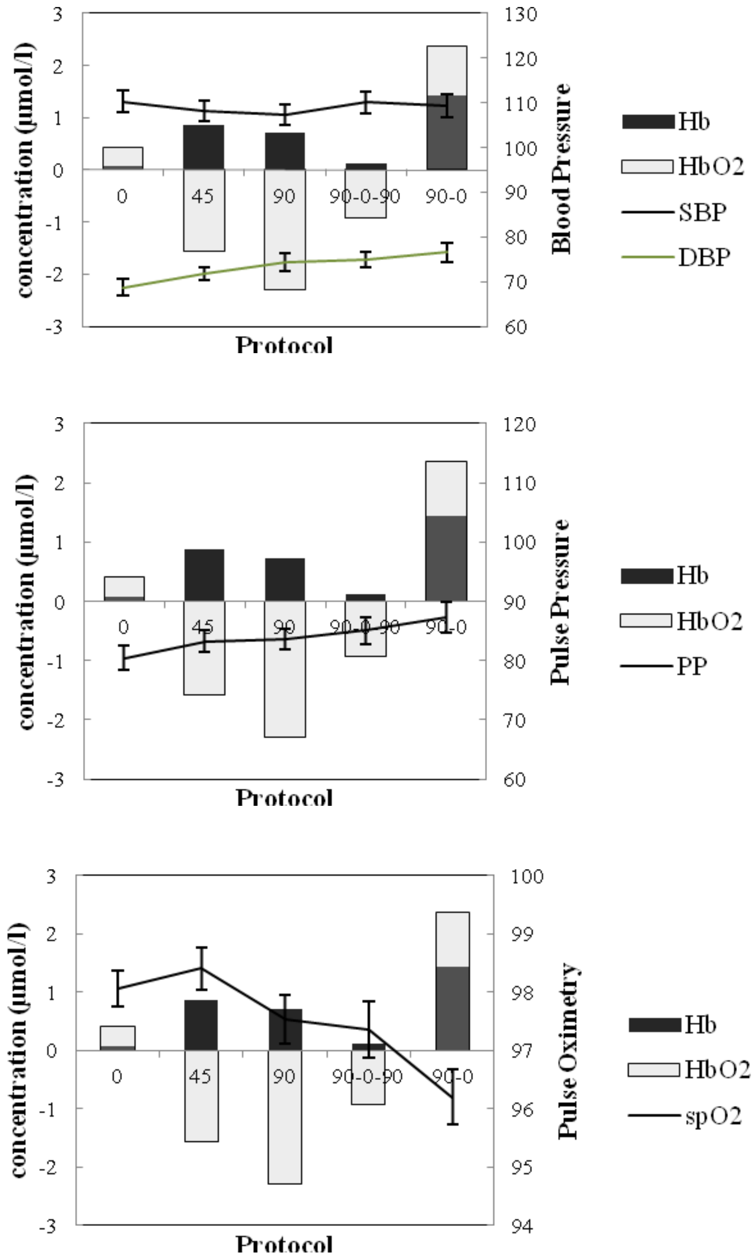

Fig. 4. Blood pressure (upper panel), pulse oximeter (central panel), and pulse (lower panel) measures in response to the positional changes

4 Discussion

This study has focused on the positional effects on the measurement of fNIR recordings. In Experiment 1, the Hb values seem to be the least effected component of fNIR recordings across all different positions. Comparing two experimental protocols, the main variations are in the HbO_2 concentration changes during supine to tilting posture change at Experiment 2. The higher the tilt-up was applied, the more the HbO_2 decreased. The study also demonstrated that changes in body-head positions have significant effect on the changes in the Hb and HbO_2 concentrations. The dynamic challenges of 90^0-0^0-90^0 test revealed an expected hemodynamic response decrease during that position in Hb and HbO_2. The recovery of the signals from a positional change takes around four minutes. This could be used for enabling a satisfactory duration in between recording sessions incorporating positional changes. Other studies have also reported similar results [4] [5]. However the findings of the current study exceed formers by introducing additional number of positions, as well as the concurrent analysis with 16 channels fNIR data. Edlow et al [10] demonstrated that supine to standing posture detect to significant decreases in rCBF, THC, and HbO_2, as well as a significant increase in Hb. Kurihara et al [13] have found difference of oxygenation concentrations during head-up tilt (90^0) and head-down tilt (6^0). HbO_2 was observed to decrease during head-up tilt testing and also to increase during head-down tilt testing. Colier et al [6] studied cerebral and circulatory hemodynamics under orthostatic stress. Their use of the NIRS device implies similar findings in the sense that close-to-vertical (80^0) position resulted in lower HbO_2. However their main comparison was with hypovolemia condition.

The plausible use of the current findings can be achieved as a safe guideline of fNIR use in bedside monitoring that may involve body-head positional changes in particular, monitoring during sleep or under anesthesia.

Acknowledgments. The authors appreciate the support of Prof. Dr. Ozhan Goldeli, and Zeynep Yildiz, MD for Tilt Table experiments, Prof. Dr. Cem Bediz for comments, MSc Eng. Ugras Erdogan for his technical supports, and O. Tugce Bezircioglu for data monitoring.

References

1. Huppert, T.J., Diamond, S.G., Franceschini, M.A., Boas, D.A.: Homer: a review of time series analysis methods for near infrared spectroscopy of the brain. Appl. Opt. 48, D280–D298 (2009)
2. Sweeney, K.T., Ayaz, H., Ward, T.E., Izzetoglu, M., McLoone, S.F., Onaral, B.: A Methodology for Validating Artifact Removal Techniques for Fnırs. In: 33rd Annual International Conference of the IEEE EMBS Boston, Massachusetts, USA (2011)
3. Ayaz, H., Shewokis, P.A., Bunce, S., Onaral, B.: An Optical Computer Interface for Environmental Control. In: 33rd Annual International Conference of the IEEE EMBS Boston, Massachusetts, USA (2011)

4. Schipper, J.M., Vloet, L.C.M., Colier, N.J.M., Hoefnagels, W.H.L., Jansen, R.: Cerebral Oxygenation Declines in Healthy Elderly Subjects in Response to Assuming the Upright Position. Stroke, 1615–1620 (2000)
5. Houtman, S., Colier, W.N.J.M., Hopman, M.T.E., Oosesburg, B.: Reproducibility of the alterations in circulation and cerebral oxygenation from supine rest to head up tilt. Clinical Physiology 19, 169–177 (1999)
6. Colier, W.N.J.M., Binkhorst, R.A., Hopman, M.T., Oeseburg, B.: Cerebral and circulatory haemodynamics before vasovagal syncope induced by orthostatic stress. Clin. Physiol. 17(1), 83–94 (1997)
7. Ayaz, H., Onaral, B.: Analytical software and stimulus-presentation platform to utilize, visualize and analyze near-infrared spectroscopy measures Masters Degree thesis (dissertation) Drexel University (2005)
8. Cope, M., Delpy, D.T.: System for long-term measurement of cerebral blood flow and tissue oxygenation on newborn infants by infrared transillumination. Med. Biol. Eng. Comput. 26(3), 289–294 (1988)
9. Strangman, G., Boas, D.A., Sutton, J.P.: Non-Invasive Neuroimaging Using Near Infrared Light. Society of Biological Psychiatry 52, 679–693 (2002)
10. Edlow, B.L., Kim, M.N., Durduran, T., Zhou, C., Putt, M.E., Yodh, A.G., Greenberg, J.H., Detre, J.A.: The effects of healthy aging on cerebral hemodynamic responses to posture change. Physiological Measurement 31, 477–495 (2010)
11. SPSS for windows, version 16.0.1. Lead Technologies, Chicago (2009)
12. MATLAB & Simulink Release 2007a. The MathWorks, Inc. (1996-2007)
13. Kurihara, K., Kikukawa, A., Kobayashi, A.: Cerebral Oxygenation monitor during head-up and –down tilt using near-infrared spatially resolved spectroscopy. Clinical Physiology and Functional Imaging 23(4), 177–181 (2003)

Using Brain Activity to Predict Task Performance and Operator Efficiency

Hasan Ayaz[1,2], Scott Bunce[2,3], Patricia Shewokis[1,2,4], Kurtulus Izzetoglu[1,2], Ben Willems[5], and Banu Onaral[1,2]

[1] School of Biomedical Engineering, Science & Health Systems,
[2] Cognitive Neuroengineering and Quantitative Experimental Research (CONQUER) Collaborative,
Drexel University, Philadelphia, PA, 19104, USA
[3] Penn State Hershey Medical Center and Penn State College of Medicine, Hershey, PA 17003 USA,
[4] College of Nursing and Health Professions, Drexel University, Philadelphia PA 19102, USA
[5] Federal Aviation Administration William J. Hughes Technical Center, Atlantic City International Airport, NJ, USA
(ayaz,pas38,ki25,banu.onaral)@drexel.edu, sbunce@hmc.psu.edu, ben.willems@faa.gov

Abstract. The efficiency and safety of many complex human-machine systems are closely related to the cognitive workload and situational awareness of their human operators. In this study, we utilized functional near infrared (fNIR) spectroscopy to monitor anterior prefrontal cortex activation of experienced operators during a standard working memory and attention task, the n-back. Results indicated that task efficiency can be estimated using operator's fNIR and behavioral measures together. Moreover, fNIR measures had more predictive power than behavioral measures for estimating operator's future task performance in higher difficulty conditions.

Keywords: fNIR, optical brain imaging, working memory, task efficiency, cognitive workload.

1 Introduction

To maximize efficiency and minimize error, an ideal human-machine system should be designed to maintain operator mental workload at an optimum level, which requires an accurate sensing and continuous update of operator workload. Such an informed mechanism is even more crucial when safety, efficiency and time-critical missions depend on the operation of the human-machine system. Importantly, behavioral measures (or task performance) alone may not be sufficiently sensitive to index overload, as operators can extend their work effort to maintain system performance, but this could come at a cost that may be reflected only in neural measures.

H. Zhang et al. (Eds.): BICS 2012, LNAI 7366, pp. 147–155, 2012.

The advent of new and improved technologies that allow the monitoring of brain activity in natural environments is expected to enable better identification of neurophysiological markers of human performance [1]. Functional magnetic resonance imaging (fMRI), positron emission tomography (PET) and Magneto-encephalography (MEG) have contributed a great deal to our current understanding of the neural basis of mental workload. Unfortunately, these techniques are not amenable to ecologically valid operational settings, as they variously are highly sensitive to motion artifact, require participants in confined positions, expose individuals to potentially harmful materials or loud noise, and are quite expensive. Other technologies with affordable and portable use potential that have been investigated for the purpose of workload assessment, such as electroencephalography (EEG) / event-related brain potentials (ERPs), can directly measure the summation of neural function with temporal resolution on the order of milliseconds. However, these technologies also have limited spatial resolution [2], and are susceptible to electromagnetic field artifacts and spatially related muscle movements.

Functional Near-Infrared Spectroscopy (fNIR) is an emerging optical brain imaging technology that relies on optical techniques to detect changes of hemodynamic responses within the cortex in response to sensory, motor, or cognitive activation [2-9]. In its most common form factor, fNIR uses near infrared light absorption changes within the observed brain area to monitor cortical concentration changes of oxygenated hemoglobin (oxy-Hb) and deoxygenated hemoglobin (deoxy-Hb). For a review of fNIR please see [9-13]. fNIR technology allows the design of battery-operated, safe and ambulatory monitoring systems, qualities that position fNIR as an ideal candidate for monitoring cognition-related hemodynamic changes under working conditions as well as the laboratory.

Recent studies at the Federal Aviation Administration (FAA) William J. Hughes Technical Center's Research, Development, and Human Factors Laboratory have utilized fNIR to monitor certified air traffic controllers as they manage realistic scenarios under typical and emergent conditions. As part of these studies, certified controllers performed an n-back task, a standard attention and working memory (WM) task with 4 levels of difficulty. Earlier reports based on this dataset indicated that average oxygenation changes at Optode 2, located within left inferior frontal gyrus in the dorsalateral prefrontal cortex, correlated with the task difficulty and increased monotonically with increasing task difficulty [14]. At incremental levels of task difficulty (cognitive task or air traffic control scenarios), there were differences in the neural activation of cortical areas known to be associated with cognitive workload when a trained controller is operating.

The purpose of this study was to assess the mental efficiency of operators utilizing both behavioral measures and a neurocognitive measure, i.e, an fNIR measure of hemodynamic response. We also evaluated the capacity to use the level of neural activation at a given level of task difficulty to predict performance at more difficult levels of task workload. In part, WM refers to the cognitive process of actively maintaining task related information in mind for brief periods of time. With consistent levels of increasing task difficulty, the n-back provided an opportunity to test the relationship and predictive power of activation in specified brain regions related to attention and working memory relative to operator performance. An efficiency graph can be a useful visual tool to assess the impact of learning on performance as defined by Clark et al. in [15]. The efficiency can be visualized by having the effort on the x-axis as input and task performance on the y-axis as output. Here, we used the construct of efficiency to determine if greater efficiency, measured at one level, would predict better operator performance at the next level of difficulty.

2 Method

2.1 Participants

Twenty-four certified professional controllers (CPC) between the ages of 24 and 55 volunteered. All participants were non-supervisory CPC with a current medical certificate and had actively controlled traffic in an Air Route Traffic Control Center between 3 to 30 years. Prior to the study, all participants signed informed consent forms.

2.2 Experiment Protocol

The n-back task used in this study included four incremental levels of difficulty [16-18]. During the task, participants were asked to visually monitor single letters presented serially on a screen and to press a button with their dominant hand when a target stimulus was identified. Targets were variously defined across the four conditions so as to incrementally increase WM load from zero to three items. In the 0-back condition, the target was defined as a single, pre-specified letter (e.g., “X”). In the 1-back condition, the target was defined as any letter identical to the one immediately preceding it (i.e., one trial back). In the 2-back and 3-back conditions, targets were defined as any letter that was identical to the one presented two or three trials back, respectively. The total test included four sessions of each of the four conditions (a total of 16 blocks) presented in a pseudo-random order. The task was implemented in E-prime (Psychology Software Tools).

2.3 Optical Brain Monitoring

During the experiment, the prefrontal cortex of each participant was monitored using a continuous wave fNIR system first described by Chance et al. [5], further developed at Drexel University (Philadelphia, PA), manufactured and supplied by fNIR Devices LLC (Potomac, MD; www.fnirdevices.com). The system was composed of three modules: a flexible sensor pad, which holds light sources and detectors to enable the rapid placement of 16 optodes (channels); a control box for hardware management; and a computer running data acquisition software (COBI Studio) [10] (Figure1).

The system operated with a sampling frequency of 2Hz. The light emitting diodes (LED) were activated one light source at a time and the four surrounding photodetectors around the active source were sampled. One scan was completed once all four LEDs were activated and respective detectors were sampled sequentially. The positioning of the light sources and detectors on the sensor pad yielded a total of 16 active optodes (channels) and was designed to monitor dorsal and inferior frontal cortical areas underlying the forehead.

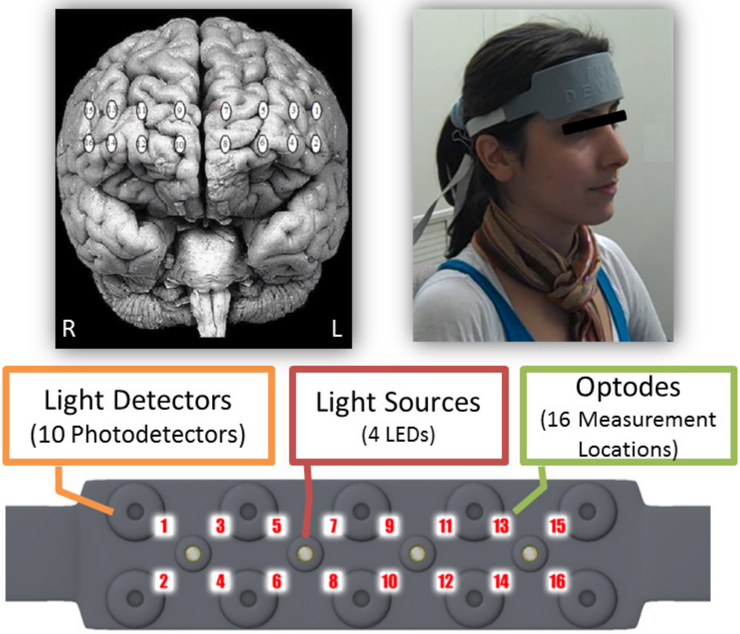

Fig. 1. fNIR sensor pad that measures from 16 locations over the forehead (right, top), measurement locations (optodes) on brain surface image [19] (left, top), and fNIR sensor pad contains 4 light sources and 10 light detectors forming 16 optodes (bottom) [10]

3 Data Analysis

To attenuate high frequency noise, respiration and cardiac cycle effects, raw fNIR data (16 optodes x 2 wavelengths) were filtered with a low-pass finite impulse response, linear phase filter with order 20 and cut-off frequency of 0.1 Hz [20]. Saturated channels (if any), in which light intensity at the detector was higher than the analog-to-digital converter limit, were excluded. fNIR data epochs for task and rest periods were extracted from the continuous data using time synchronization markers. Blood oxygenation and volume changes within each of the 16 optodes were calculated using the modified Beer-Lambert Law for task periods with respect to rest periods at beginning of each task using fnirSoft software [21].

For efficiency analysis, oxygenation data and behavioral measures for each subject were normalized by calculating the respective z-scores. The main effect for task difficulty was tested using one-way repeated measures analysis of variance (ANOVA), with Subject and Task Difficulty designated as fixed effects. Geisser–Greenhouse (G–G) correction was used when violations of sphericity occurred in the omnibus tests. Tukey's post hoc tests were used to determine the locus of the main effects with a 0.05 significance criterion.

4 Results

The behavioral data, as reported before, indicated a significant main effects of task difficulty (0-, 1-, 2- and 3-back conditions) for accuracy (correct click for targets) ($F_{3,69}$=40.68, p< 0.001 , η_p^2 = 0.639) and reaction time ($F_{3,69}$=42.76, p< 0.001, η_p^2 = 0.65). Moreover, task average fNIR data revealed that reliable changes in oxygenation as a function of n-back condition occurred only at optode #2 ($F_{3,69}$= 4.37, p < 0.05 , η_p^2 = 0.16). This site, close to AF7 in the International 10-20 System, is located within the left PFC (inferior frontal gyrus). In correspondence with previous results and our previous report, increasing task difficulty was accompanied by an increase in activation level during task performance [14].

An efficiency graph can be a useful visual tool to assess the impact of learning on performance as defined by Clark et al. in [15]. The efficiency can be visualized by having the effort on the x-axis as input and task performance on the y-axis as output. The efficiency graph in Figure 2 visualizes our overall results by plotting normalized oxygenation changes (that represent mental effort) against the normalized 'hit' ratio (that model behavioral performance). In this efficiency graph, the fourth quadrant (lower right) represents low efficiency, where minimum performance is achieved with maximum effort. The second quadrant (upper left) represents high efficiency where maximum performance is achieved with minimal effort. The diagonal y=x is the neutral axis, where efficiency is zero and effort and performance are equal.

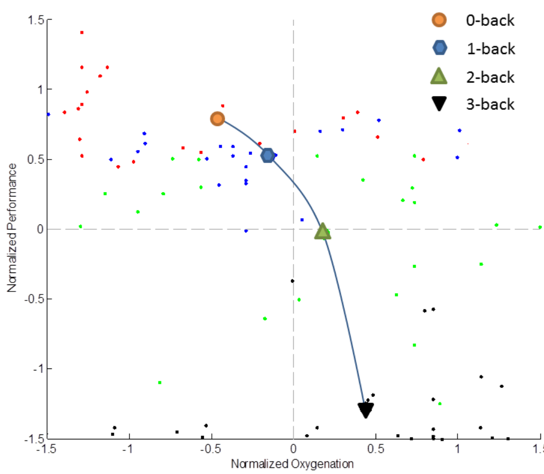

Fig. 2. Efficiency graph of performance (behavioral) vs. effort (neural measures) indicates that as task difficulty increased, efficiency monotonically decreased

The linear regression analysis of performance and oxygenation changes for each condition also indicates a negative correlation for the last two conditions (see Figure 3). For 0-back and 1-back, there was a ceiling effect with the highest performance level which, most participants easily achieved. However, for 2-back and 3-back, a similar overall trend of negative correlation is observed with r=0.23 (rmse=0.25; slope=-23.4) for 2-back and and r = 0.44 (rmse=0.19; slope=-37.1) for 3-back.

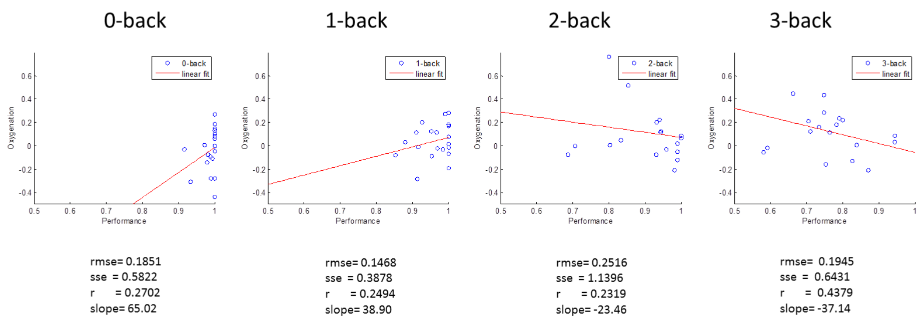

Fig. 3. First order linear regression for oxygenation vs. task performance for all n-back conditions

Next, we assessed the capacity to use the degree of neural activation required to perform at a given level of task difficulty to predict behavioral performance at a greater level of task difficulty. The 2-back condition is ideal for this purpose, as it provides a level of difficulty that most operators are able to manage behaviorally through sustained effort, whereas the next level, the 3-back, is significantly more difficult and represented a level of difficulty in which participants had the highest probability of disengaging. 0-back and 1-back had ceiling effects in task performance. Neural activation (oxygenation) in the 2-back condition was shown to be a better predictor of 3-back task performance (r = 0.57) than the performance score in the 2-back condition (r=0.33; See Figure 4).

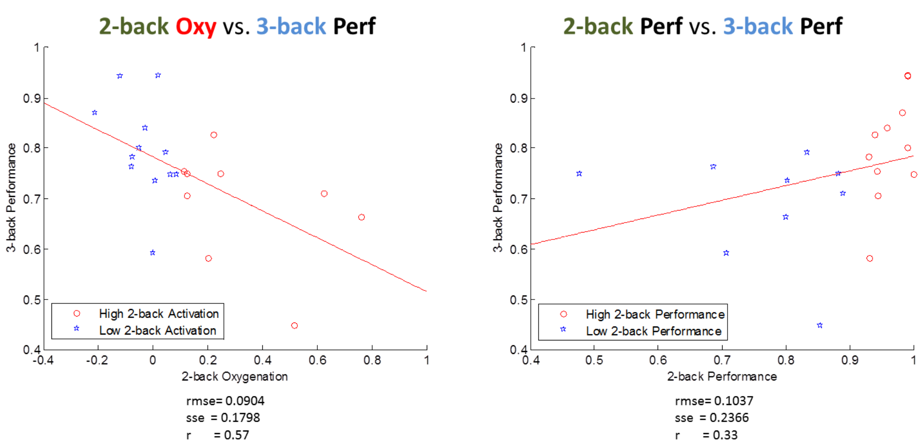

Fig. 4. Relationship of 2-back neural measures (oxy) with 3-back task performance (left) and 2-back and 3-back performance (right)

5 Discussion and Conclusion

In this study, a standard visual WM task was used to assess, the capacity to utilize objective measures of brain activation to predict performance at greater levels of task difficulty. Operator efficiency was evaluated at four levels of task difficulty using an objective measure of effort (fNIR measures of oxygenation) versus behavioral measures of task performance. As expected, efficiency dropped as task difficulty increased, indicating that participants needed to exert more effort to achieve similar levels of performance at more difficult task levels, One important aspect of this finding is that the cognitive effort was assessed using a noninvasive, objective measure that did not require operator resources to monitor (as required by self-report measures). [14, 22, 23]. More important, however, was the finding that the degree of neural activation at one level of task difficulty predicted performance at the next level of task difficulty.

fMRI has previously been used to demonstrate that neural activation during a visuospatial WM task can be used to predict performance in another cognitive domain, i.e., arithmetic [24]. In the current study, brain activation in the 2-back condition was a better predictor of performance in the 3-back condition than the 2-back performance score, indicating that the neural measure was more sensitive than the behavioral measure. This finding suggests the utility of fNIR as an objective measure of cerebral hemodynamics and its potential role in human-machine interfaces.

The current results suggest important, albeit preliminary, information about the relationship between fNIR measures of anterior prefrontal cortical hemodynamics and the performance of an attentional WM task. Although previous results suggest that it is possible to use brain activity in WM to predict another cognitive task performance [24], it remains to be determined if the relationship between task performance and brain activation is sensitive enough to be of practical use in a more complex, real-world task such as air traffic control.

In summary, fNIR is a portable, safe and minimally intrusive optical brain monitoring technology that can be used to measure hemodynamic changes in the brain's outer cortex. Changes in blood oxygenation in dorsolateral prefrontal cortex, as measured by fNIR, were shown to be associated with increasing cognitive workload [14, 23] and can be used to assess skill acquisition/learning [22, 25]. The current analysis suggested that fNIR can be used to predict future task performance for the optimization of learning/training regimens. Further work is needed to assess if these results can be generalized to other types of cognitive tasks, especially complex and realistic daily life scenarios.

Acknowledgments. The authors would like to thank Dr. Sehchang Hah and Atul Deshmukh for data collection. This work was supported by the U.S. Federal Aviation Administration through BAE Systems Technology Solutions Services Inc. under Primary Contract, DTFA01-00-C-00068 and Subcontract Number, 31-5029862.

References

1. Parasuraman, R., Wilson, G.: Putting the brain to work: Neuroergonomics past, present, and future. Human Factors 50, 468 (2008)
2. Strangman, G., Boas, D.A., Sutton, J.P.: Non-invasive neuroimaging using near-infrared light. Biological Psychiatry 52, 679–693 (2002)
3. Chance, B., Anday, E., Nioka, S., Zhou, S., Hong, L., Worden, K., Li, C., Murray, T., Ovetsky, Y., Pidikiti, D., Thomas, R.: A novel method for fast imaging of brain function, non-invasively, with light. Optics Express 2, 411–423 (1998)
4. Villringer, A., Planck, J., Hock, C., Schleinkofer, L., Dirnagl, U.: Near infrared spectroscopy (NIRS): a new tool to study hemodynamic changes during activation of brain function in human adults. Neuroscience Letters 154, 101–104 (1993)
5. Chance, B., Zhuang, Z., UnAh, C., Alter, C., Lipton, L.: Cognition-activated low-frequency modulation of light absorption in human brain. Proceedings of the National Academy of Sciences of the United States of America 90, 3770–3774 (1993)
6. Coyle, S., Ward, T.E., Markham, C.M.: Brain-computer interface using a simplified functional near-infrared spectroscopy system. Journal of Neural Engineering 4, 219–226 (2007)
7. Obrig, H., Wenzel, R., Kohl, M., Horst, S., Wobst, P., Steinbrink, J., Thomas, F., Villringer, A.: Near-infrared spectroscopy: does it function in functional activation studies of the adult brain? International Journal of Psychophysiology 35, 125–142 (2000)
8. Irani, F., Platek, S.M., Bunce, S., Ruocco, A.C., Chute, D.: Functional near infrared spectroscopy (fNIRS): an emerging neuroimaging technology with important applications for the study of brain disorders. Clin. Neuropsychol. 21, 9–37 (2007)
9. Hoshi, Y.: Functional near-infrared spectroscopy: current status and future prospects. Journal of Biomedical Optics 12, 062106 (2007)
10. Ayaz, H., Shewokis, P.A., Curtin, A., Izzetoglu, M., Izzetoglu, K., Onaral, B.: Using MazeSuite and Functional Near Infrared Spectroscopy to Study Learning in Spatial Navigation. J. Vis. Exp. e3443 (2011)
11. Izzetoglu, M., Izzetoglu, K., Bunce, S., Ayaz, H., Devaraj, A., Onaral, B., Pourrezaei, K.: Functional near-infrared neuroimaging. IEEE Trans. Neural Syst. Rehabil. Eng. 13, 153–159 (2005)
12. Orihuela-Espina, F., Leff, D., James, D., Darzi, A., Yang, G.: Quality control and assurance in functional near infrared spectroscopy (fNIRS) experimentation. Physics in Medicine and Biology 55, 3701 (2010)
13. Izzetoglu, K., Ayaz, H., Merzagora, A., Izzetoglu, M., Shewokis, P.A., Bunce, S.C., Pourrezaei, K., Rosen, A., Onaral, B.: The evolution of field deployable fNIR spectroscopy from bench to clinical settings. Journal of Innovative Optical Health Sciences 4, 1–12 (2011)
14. Ayaz, H., Shewokis, P.A., Bunce, S., Izzetoglu, K., Willems, B., Onaral, B.: Optical brain monitoring for operator training and mental workload assessment. Neuroimage 59, 36–47 (2012)
15. Clark, R., Nguyen, F., Sweller, J.: Efficiency in learning: Evidence-based guidelines to manage cognitive load. Pfeiffer, An Imprint of Wiley, San Fransico (2006)
16. Owen, A.M., McMillan, K.M., Laird, A.R., Bullmore, E.: N-back working memory paradigm: a meta-analysis of normative functional neuroimaging studies. Human Brain Mapping 25, 46–59 (2005)

17. D'Esposito, M., Aguirre, G., Zarahn, E., Ballard, D., Shin, R., Lease, J.: Functional MRI studies of spatial and nonspatial working memory. Cognitive Brain Research 7, 1–13 (1998)
18. Smith, E.E., Jonides, J.: Working Memory: A View from Neuroimaging. Cognitive Psychology 33, 5–42 (1997)
19. Ayaz, H., Izzetoglu, M., Platek, S.M., Bunce, S., Izzetoglu, K., Pourrezaei, K., Onaral, B.: Registering fNIR data to brain surface image using MRI templates. In: Conf. Proc. IEEE Eng. Med. Biol. Soc., pp. 2671–2674 (2006)
20. Ayaz, H., Izzetoglu, M., Shewokis, P.A., Onaral, B.: Sliding-window Motion Artifact Rejection for Functional Near-Infrared Spectroscopy. In: Conf. Proc. IEEE Eng. Med. Biol. Soc., pp. 6567–6570 (2010)
21. Ayaz, H.: Functional Near Infrared Spectroscopy based Brain Computer Interface. School of Biomedical Engineering Science & Health Systems, p. 214. Drexel University, Philadelphia (2010)
22. Ayaz, H., Cakir, M.P., Izzetoglu, K., Curtin, A., Shewokis, P.A., Bunce, S., Onaral, B.: Monitoring Expertise Development during Simulated UAV Piloting Tasks using Optical Brain Imaging. In: IEEE Aerospace Conference, BigSky, MN, USA, pp. 1–11 (2012)
23. Izzetoglu, K., Bunce, S., Onaral, B., Pourrezaei, K., Chance, B.: Functional Optical Brain Imaging Using Near-Infrared During Cognitive Tasks. International Journal of Human-Computer Interaction 17, 211–227 (2004)
24. Dumontheil, I., Klingberg, T.: Brain Activity during a Visuospatial Working Memory Task Predicts Arithmetical Performance 2 Years Later. Cerebral Cortex (2011)
25. Shewokis, P.A., Ayaz, H., Izzetoglu, M., Bunce, S., Gentili, R.J., Sela, I., Izzetoglu, K., Onaral, B.: Brain in the Loop: Assessing Learning Using fNIR in Cognitive and Motor Tasks. In: Schmorrow, D.D., Fidopiastis, C.M. (eds.) FAC 2011, HCII 2011. LNCS, vol. 6780, pp. 240–249. Springer, Heidelberg (2011)

"Arousal" or "Activation" Dysfunction in the Frontal Region of Children with Attention-Deficit/Hyperactivity Disorder: Evidence from an Electroencephalogram Study

Ligang Wang[1,2], Jie Kong[3], Jing Luo[1], Wenbin Gao[1,*], and Xianju Guo[4]

[1] Key Laboratory of Mental Health, Institute of Psychology, Chinese Academy of Sciences, Beijing, China
[2] Graduate University of Chinese Academy of Sciences, Beijing, China
[3] North College of Beijing University of Chemical Technology, Langfang, China
[4] Heping Hospital of Changzhi Medical College, Changzhi, China
gaowb@psych.ac.cn

Abstract. The goal of the present study is to test whether there is "Arousal" or "Activation" Dysfunction in the frontal region of children with Attention-Deficit/Hyperactivity Disorder (AD/HD). The sample consists of 62 children (31 with AD/HD and 31 non-AD/HD children as controls) who were drawn from an elementary school. Patterns of cortical activity were measured using EEG under three conditions: Eyes-Closed (EC), Eyes-Opened (EO) resting and Mental Arithmetic Task (MAT) conditions, and compared according to AD/HD diagnostic status. Significant main effects for all frequency bands across conditions were found. The AD/HD group showed less elevation of beta relative power than controls suggesting deficiency of cortical activation in the AD/HD group. AD/HD group showed significantly elevated alpha power in eyes-opened resting state. Theta/beta ratio was less reduced for AD/HD than for controls when going from EC to EO to MAT state. The implications of the results were discussed.

Keywords: Arousal, Activation, Attention-Deficit/Hyperactivity Disorder, EEG, Hypo-arousal model.

1 Introduction

Attention-deficit/hyperactivity disorder (AD/HD) refers to a variable cluster of hyperactivity, impulsivity, and inattention symptoms, the occurrence of which substantially affects normal cognitive and behavioral functioning of the individual [1]. Additionally, based on DSM- IV, the prevalence of AD/HD among school-age children was estimated to be approximately 3–5%, and studies based on these criteria have found that its prevalence rangeed from 3 to 6% [2]. In clinic, AD/HD is one of the most common disorders treated by child and adolescent psychiatrists in America,

* Corresponding author. Datun Road 4, Chaoyang District, Beijing, 100101, China.

H. Zhang et al. (Eds.): BICS 2012, LNAI 7366, pp. 156–163, 2012.

taking up as much as 50% of child psychiatry clinic populations [3], which indicated that studies in AD/HD have not only academic values but also clinical values.

Theories regarding the etiology of AD/HD have long incorporated the concepts of arousal, activation, and alertness as basic mechanisms in AD/HD. Neurophysiological measures have been a major focus of research in AD/HD. Electroencephalographic studies of the "resting state" (i.e., during eyes open or closed conditions) have observed a consistent elevation in low-frequency activity, particularly theta (4-7 Hz), in AD/HD subjects compared with control subjects [4-11]. The hypo-arousal model was a dominant theory to explain these findings of EEG studies, which saw the central nervous system (CNS) as underaroused, causing inattention and hyperactivity [12]. Recently, Barry examined whether the ratio of theta to beta in children with AD/HD was relative to skin conductance levels (SCLs) [13], which had long been used as an index of CNS arousal [14]. In an eyes-closed resting condition, EEGs were recorded and compareed between 30 children boys diagnosed with AD/HD and 30 boys in control. However, no significant correlation between the theta/beta ratio and SCL was noted, which suggested that the labeling of EEG patterns differentiating clusters of children with AD/HD in arousal terms needed to be reconsidered. Loo et al. studied 80 adults (38 with AD/HD and 42 non-AD/HD controls), using quantitative EEG in resting eyes-opened, eyes-closed and continuous performance test (CPT) conditions. They found that in frontal and parietal regions, patterns of activation in the alpha (8–10 Hz) range differed according to AD/HD status, indicating increased cortical arousal among AD/HD subjects, and beta power (13–14 and 17–18 Hz) also differed between AD/HD and controls, indicating that increased cortical activation was associated with AD/HD [15]. The apparent discrepancies between previous studies of EEG on children or adult with AD/HD might be mainly due to EEG recording states (e.g. eyes-opened or eyes-closed).

Brain electrical activity can be recorded during rest or performing a cognitive task. A limitation of previous research was that the distinction between 'arousal' and 'activation', showed in the experimental definition of rest-state (eye-opened rest vs. eye-closed rest), had not been made explicit. Comparing eyes-closed/opened conditions among adults, Barry et al. found that opening eyes could increase skin conductance levels (SCLs) and globally decrease alpha, which suggested that the eyes-closed resting condition may be better identified as a convenient 'arousal' baseline, with the eyes-open resting condition serving as a convenient 'activation' baseline, particularly for tasks that involve visual processing [16]. Barry et al' studies indicated that there was no significant correlation between SCLs and θ/β. They proposed that θ/β reflected "activation" rather than "arousal" [13]. The question that whether there was brain 'arousal' or 'activation' dysfunction in children with AD/HD need to be discussed.

With this new data on cortical activity associated with arousal and activation, the stage is set for further examination of whether children with AD/HD have different brain activity patterns in frontal regions across arousal, activation and vigilance states. The use of several different recording conditions allows to examine the differences of brain activity patterns between different diagnostic groups by condition (e.g., eyes closed [EC], eyes open [EO], Mental Arithmetic Task [MAT]) as well as across conditions (going from EC to EO = arousal, EO to MAT = activation). Given its strong relationship with arousal, power in alpha frequency range (8–13 Hz) is of particular interest, given its strong relationship with arousal. Previous studies on EEG patterns of AD/HD have identified theta and beta activity as significant markers which also seem to be important indicators of activation. Therefore, the hypotheses of the present study are that: 1.Children with AD/HD have elevated alpha power in resting state, which indicates their hypo-arousal brain activity. 2. AD/HD individuals are suffering from deficiency of cortical activation, being proved by abnormal beta activity during MAT state. 3. The ratio of theta to beta in children with AD/HD is higher comparing to control subjects' during MAT state, which means that theta/beta represents the substrate of activation.

2 Materials and Methods

2.1 Participants

The participants consisted of thirty-one children (24 boys and 7 girls) with AD/HD (11 AD/HDcom, 11 AD/HDin, 9AD/HDhyp) and 32 children as controls (19 boys and 13 girls). Their ages ranged from 5 years to 10 years. Children with AD/HD were drawn from a elementary school, on the basis of parent version of the AD/HD Rating Scale (AD/HDRS-P) [17] and assessment of a psychiatrist. Children were included only if they met the criteria for the diagnosis of AD/HD combined subtype (i.e., 6 out of 9 DSM-IV criteria of inattention or 6 out of 9 DSM-IV criteria of hyperactivity/impulsivity). Children were excluded if they had any problematic prenatal, perinatal, or neonatal period; disorder of consciousness; if they met DSM criteria for conduct or oppositional defiant disorder. The participants for controls were recruited from the same school.

2.2 Procedure

A written informed consent with the scale was obtained from a parent, with assent from each child. Diagnostic measures were administered over three visits. During the first visit, participants' parents were asked to fill out the rating scales. For the second visit, children who met the criteria for the diagnosis of AD/HD combined subtype in rating scale and children for controls were assessed and observed by a psychiatrist. The third visit was for EEG collection, which performed within 3–15 days of the second visit.

When participants arrived in the EEG laboratory they were informed their tasks in the study. Then, they were fitted with the physiological measurement equipment, and seated in an air-conditioned sound attenuated recording booth. Their EEGs were collected in three different conditions (EO, Eyes-Opened resting state; EC, Eyes-Closed resting state; and MAT, Mental Arithmetic Task state), arrayed EO (1 minute) – EC (2 minutes) – MAT (1 minute). The whole process for each participant lasted a total of 4 minutes. In the EO and MAT conditions, participants were instructed to visually fixate on a small cross presented on a computer screen in front of them. With two electrode sites (10 –20 system) with A1 and A2 references, Fp1 and Fp2, and impedances < 1k Ohm, EEG was recorded by Minerva (Cerebrum Digital Spectrum systematic software, Taiwan), with 500-Hz sampling rate, 20,604 gain, and band-pass filtered (1.5 Hz–130 Hz).

2.3 Datum Extraction and Analysis

The EEG was visually appraised to exclude artifact, and all suitable 1-sec epochs were Fourier transformed with a Hamming window. Power in each EEG band (delta [1.5–3.5 Hz], theta [4–7.5 Hz], alpha [8–13 Hz], and beta [13.5–25 Hz] bands) was converted to relative power at each site (Fp1, Fp2) divided by the sum of the four band Powers. The θ/β was calculated as the ratio of θ to β relative power at each site.

Separate repeated-measures analyses of variance (ANOVAs) were conducted for relative data, including delta, theta, alpha, and beta power and theta/beta ratios with conditions (EO, EC, and MAT) as within-subjects factor, and groups (AD/HD vs. control participants) as between-subjects factor. We were only interested in (interaction with) group effects. If the omnibus ANOVAs revealed significant interaction effects with group, Separate one-way ANOVAs were conducted to examine the group effect in each condition.

3 Results

Presented in Fig. 1 were the relative power spectra of the AD/HD and control groups across the EO, EC and MAT conditions. The repeated-measures ANOVAs indicated significant main effects of condition for all frequency bands (delta [1.5–3.5 Hz], theta [4–7.5 Hz], alpha [8–13 Hz], and beta [13.5–25 Hz] bands) across conditions ($F(2,60) = 2.79–56.05$), p-values ranged from <.05 to <.0001), which suggested that there were widespread cortical changes when going from EC to EO to MAT. Significant interaction effect of condition and AD/HD diagnostic status emerged in the beta band at each site (Fp1, $F(2, 60) = 4.41$, $p = 0.016$; Fp2, $F(2, 60) = (4.46, p = 0.037)$, and significant main effect of group for beta band existed at each site(Fp1, $F(1, 61) = 5.57$, $p = 0.021$; Fp2, $F(1, 61) = 7.44$, $p = 0.008$). Separate one-way ANOVAS revealed the group difference was due primarily to significant differences in beta power during the MAT condition (Fp1, $F(1, 61) = 8.84$, $p = 0.04$; Fp2, $F(1, 61) = 9.21$, $p = 0.04$). Results of the analyses indicated that the AD/HD group showed less elevation of beta-related power than the control group did, which suggested deficiency of cortical activation in the AD/HD group.

In the alpha band, significant main effect of group emerged at each site (FP1, $F(1, 61) = 4.398$, $p = 0.040$; FP2, $F(1, 61) = 7.437$, $p = 0.008$). This group difference may be primarily due to the significant differences during the EO state (FP1, $F(1,61) = 11.019$, $p = 0.002$; FP2, $F(1,61) = 10.738$, $p = 0.002$) where the AD/HD group displayed significantly elevated alpha power. Because alpha activity was inversely related to cortical arousal, these results suggested that the AD/HD group exhibited lower cortical arousal level during the eyes opened condition.

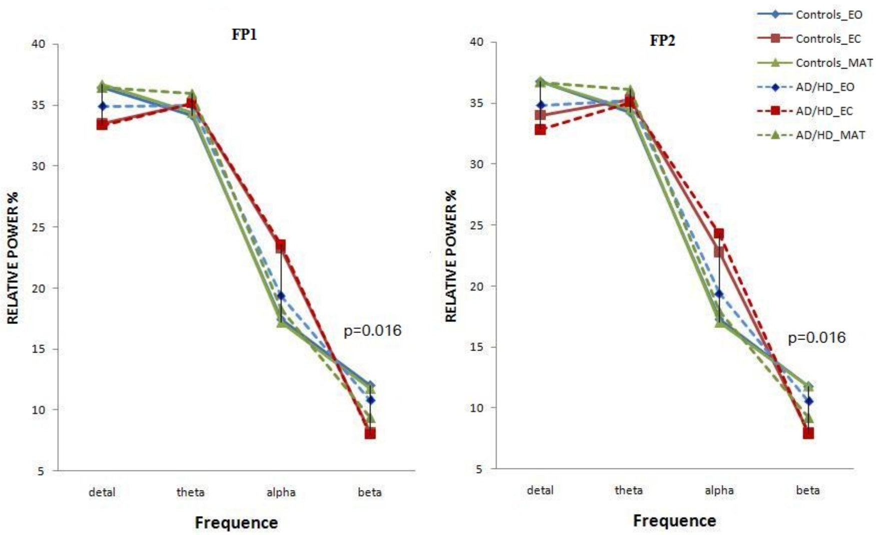

Fig. 1. Spectral power showing brain activity across conditions and by diagnosis. Lines indicate significant condition by diagnosis interaction effect; p-value is noted between the lines. Alpha power is inversely correlated with cortical arousal, therefore the AD/HD group exhibits lower cortical arousal level. Beta power is positively correlated with cortical activation, thus the AD/HD group demonstrates deficient cortical activation in the MAT conditions. EC: eyes closed, EO: eyes open, and MAT: mental arithmetic task.

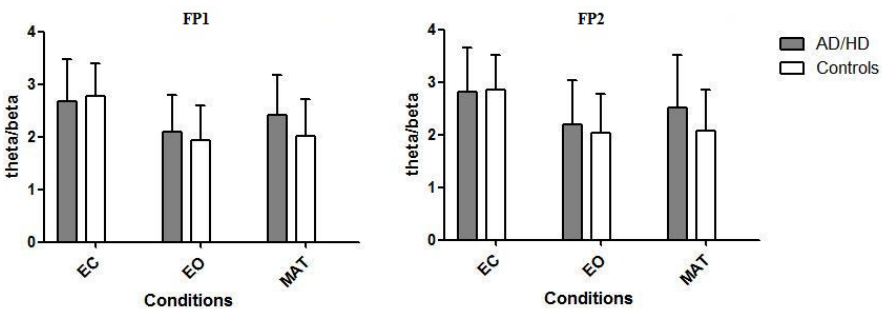

Fig. 2. Mean theta/beta ratios in EC, EO and MAT state for children with AD/HD and matched controls. Error bars represent the standard error of the mean. The left panel shows datum recorded at Fp1 site, while the panel on the right shows results from Fp2. Theta/beta ratios significantly differ between groups in MAT condition at all two sites, but not in EC and EO conditions, which indicate that θ/β reflects cortical "activation" rather than "arousal".

As shown in Fig. 2, a trend for a group × condition effect was found for theta/beta ratio (Fp1, $F(2, 60) = 3.616$, $p = 0.033$; Fp2, $F(2, 60) = 2.758$, $P = 0.047$), indicating that theta/beta ratio was less reduced for AD/HD than for controls when going from EC to EO to MAT state. Theta/beta ratios differed significantly between groups in

MAT condition at all two sites (Fp1, $F(1, 61) = 7.654$, $p = 0.007$; Fp2, $F(1, 61) = 5.974$, $P = 0.017$), but not in EC and EO conditions, which indicated that θ/β might reflect cortical "activation" rather than "arousal".

4 Discussion

The present study examined patterns of cortical arousal and activation across EO, EC and MAT states according to AD/HD diagnostic status, which was on the basis of the view that arousal and activation reflected separate processes of the attention system [19]. Although it hasn't been largely accepted in psychophysiological research, Barry et al. recently reported support for their distinction [20]. The results presented here were consistent with previous brain imaging studies suggesting different patterns of cortical activation in AD/HD and making further examination on brain activity during arousal, activation and mental arithmetic task. As revealed in the hypo-arousal model, children with AD/HD had lower levels of cortical arousal than the controls did in resting states. Meanwhile, deficiency of cortical activation in AD/HD individuals was also revealed in current study.

It was only in EO condition that significant group effects for alpha band was found, which indicated the AD/HD group displayed significantly elevated alpha power. Barry found that SCLs were negatively correlated with mean alpha levels in the resting condition, and SCLs increased significantly from eyes-closed to eyes-open, which confirmed the use of mean alpha level as a measure of resting-state arousal under eyes-closed and eyes-open conditions [16]. Since Alpha power was inversely correlated with cortical arousal, the results showed that the AD/HD group held lower cortical arousal level. However, the reason that why the group difference didn't exist in EC state was still not clear, so further research is needed to determine the reason.

The present result revealed that group difference for beta band was primarily due to the significant difference during the MAT condition. Inconsistent with previous study, the current study didn't find reduced fast wave activity in children with AD/HD in EC or EO state. It might be due to methodologic differences, while previous studies recorded brain activity only during baseline (EO or EC) conditions rather than under the cognitive activation conditions. Loo's study found that compared with the control group, AD/HD adults showed slightly increased beta activity from EO to CPT, which indicated that the AD/HD group had more cortical activation under the CPT condition than the control group did [15]. However, in current study, a significant interaction effect of condition and AD/HD diagnostic status emerged in beta band at each site, which indicated that AD/HD individuals showed an evident attenuation in frontal beta activity from EO to MAT condition while control subjects showed nothing. Since Beta power is positively correlated with cortical activation, the AD/HD group demonstrates deficient cortical activation. The inconsistence of the results above may be due to the two different cognitive tasks--- MAT and CPT.

In addition, theta/beta ratios differed significantly between groups in MAT condition at all two sites, but not in EC and EO conditions, which indicated that θ/β

could reflect cortical “activation” rather than “arousal”. The result was consistent to Barry’s view that θ/β represented the substrate of activation, particularly in cognitive/attention tasks [13]. Theta/beta ratio was less reduced for AD/HD than for controls when going from EC to EO to MAT state, which suggested that elevated theta/beta in previous study represented impaired capacity for attentional tasks, a fundamental deficit of AD/HD. This hypothesis agreed with early AD/HD EEG/event-related potential work [20] and recent data linking elevated with reduced auditory- oddball P3 in AD/HD [21].

In conclusion, compared with the control group, children with AD/HD held reduced levels of cortical arousal and activation. Examining cortical activity on baseline and during cognitive task performance is an effective measurement in the study of arousal and activation patterns associated with psychiatric diagnoses. Clinically, biofeedback training and stimulant medication (e.g. Methylphenidate) were used to treat AD/HD disorder on the basis of hypo-arousal model [12, 22]. The present study proposed that attention training may be more helpful in treating AD/HD individuals through elevating cortical activation.

Acknowledgments. This research was funded by Psychology Popularizing Committee for Chinese Psychological Society. Taiwan Hua-Yu international Education Organization provided the electroencephalograph (Minerva) and technical consulting services.

References

1. Castellanos, F.X., Sonuga-Barke, E.J.S., Milham, M.P., Tannock, R.: Characterizing cognition in ADHD: beyond executive dysfunction. Trends in Cognitive Sciences 10, 117–123 (2006)
2. Pelham, J.W.E., Gnagy, E.M., Greenslade, K.E., Milich, R.: Teacher Ratings of DSM-III-R Symptoms for the Disruptive Behavior Disorders. Journal of the American Academy of Child & Adolescent Psychiatry 31, 210–218 (1992)
3. Cantwell, D.P.: Attention Deficit Disorder: A Review of the Past 10 Years. Journal of the American Academy of Child & Adolescent Psychiatry 35, 978–987 (1996)
4. Mann, C.A., Lubar, J.F., Zimmerman, A.W., Miller, C.A., Muenchen, R.A.: Quantitative analysis of EEG in boys with attention-deficit-hyperactivity disorder: Controlled study with clinical implications. Pediatric Neurology 8, 30–36 (1992)
5. Chabot, R.J., Serfontein, G.: Quantitative electroencephalographic profiles of children with attention deficit disorder. Biological Psychiatry 40, 951–963 (1996)
6. Defrance, J.F., Smith, S., Schweitzer, F.C., Ginsberg, L., Sands, S.: Topographical Analyses of Attention Disorders of Childhood. International Journal of Neuroscience 87, 41–61 (1996)
7. Clarke, A.R., Barry, R.J., McCarthy, R., Selikowitz, M.: EEG analysis in Attention-Deficit/Hyperactivity Disorder: a comparative study of two subtypes. Psychiatry Research 81, 19–29 (1998)
8. Lazzaro, I., Gordon, E., Whitmont, S., Plahn, M., Li, W., Clarke, S., et al.: Quantified EEG activity in adolescent attention deficit hyperactivity disorder. Clin. Electroencephalogr. 29, 37–42 (1998)

9. Bresnahan, S.M., Anderson, J.W., Barry, R.J.: Age-related changes in quantitative EEG in attention- deficit/hyperactivity disorder. Biological Psychiatry 46, 1690–1697 (1999)
10. Lazzaro, I., Gordon, E., Li, W., Lim, C.L., Plahn, M., Whitmont, S., et al.: Simultaneous EEG and EDA measures in adolescent attention deficit hyperactivity disorder. International Journal of Psychophysiology 34, 123–134 (1999)
11. Clarke, A.R., Barry, R.J., McCarthy, R., Selikowitz, M.: Age and sex effects in the EEG: differences in two subtypes of attention-deficit/hyperactivity disorder. Clinical Neurophysiology 112, 815–826 (2001)
12. Satterfield, J.H., Cantwell, D.P.: Proceedings: CNS function and response to methylphenidate in hyperactive children. Psychopharmacol. Bull. 10, 36–37 (1974)
13. Barry, R.J., Clarke, A.R., Johnstone, S.J., McCarthy, R., Selikowitz, M.: Electroencephalogram [theta]/[beta] Ratio and Arousal in Attention-Deficit/Hyperactivity Disorder: Evidence of Independent Processes. Biological Psychiatry 66, 398–401 (2009)
14. Barry, R.J., Sokolov, E.N.: Habituation of phasic and tonic components of the orienting reflex. International Journal of Psychophysiology 15, 39–42 (1993)
15. Loo, S.K., Hale, T.S., Macion, J., Hanada, G., McGough, J.J., McCracken, J.T., et al.: Cortical activity patterns in ADHD during arousal, activation and sustained attention. Neuropsychologia. 47, 2114–2119 (2009)
16. Barry, R.J., Clarke, A.R., Johnstone, S.J., Magee, C.A., Rushby, J.A.: EEG differences between eyes-closed and eyes-open resting conditions. Clinical Neurophysiology 118, 2765–2773 (2007)
17. DuPaul, G.J., Power, T.J., Anastopoulos, A.D., Rcid, R.: ADHD RATING Scale IV: Checklists, norms, and clinical interpretation. Guilford, New York (1998)
18. Pribram, K.H., McGuinness, D.: Arousal, activation, and effort in the control of attention. Psychological Review 82, 116–149 (1975)
19. Barry, R.J., Clarke, A.R., McCarthy, R., Selikowitz, M., Rushby, J.A.: Arousal and Activation in a Continuous Performance Task: An Exploration of State Effects in Normal Children. Journal of Psychophysiology 19, 91–99 (2005)
20. Callaway, E., Halliday, R., Naylor, H.: Hyperactive Children's Event-Related Potentials Fail to Support Underarousal and Maturational-Lag Theories. Arch Gen. Psychiatry 40, 1243–1248 (1983)
21. Lazzaro, I., Gordon, E., Whitmont, S., Meares, R., Clarke, S.: The Modulation of Late Component Event Related Potentials by Pre-Stimulus EEG Theta Activity in ADHD. International Journal of Neuroscience 107, 247–264 (2001)
22. Lubar, J.F.: Discourse on the development of EEG diagnostics and biofeedback for attention-deficit/hyperactivity disorders. Biofeedback & Self Regulation 16, 201–225 (1991)

A New Italian Sign Language Database

Marco Fagiani, Emanuele Principi, Stefano Squartini, and Francesco Piazza

Dipartimento di Ingegneria dell'Informazione,
Università Politecnica delle Marche, Ancona, Italy
{m.fagiani,e.principi,s.squartini,f.piazza}@univpm.it

Abstract. In this work a new video database of Italian Sign Language (Lingua Italiana dei Segni - LIS) is proposed. Several other attempts have been made in the literature, but they are typically oriented to international languages (like the American Sign Language - ASL). As in speech, also this kind of language presents different peculiarities strictly depending on the geographical location where it is used. The authors have firstly observed that a specific database for LIS is missing and this shoved them to develop the one here presented. It has been conceived to be used in Automatic Sign Recognition and Synthesis (often referred as Automatic Translation into Sign Languages) applications, which represent an important technological opportunity to augment the social inclusion of people with severe hearing impairments. The Database, namely **A3LIS-147**, is free and available for download.

Keywords: Video Database, Italian Sign Language, Automatic Sign Recognition and Synthesis/Translation.

1 Introduction

Sign languages [1] are widely used among hearing impaired people communities and allow them communicate in a comfortable way. As oral languages also the sign ones are very geographical specific, with a lot of differences even in places few kilometres far away: therefore understanding among 'signers' with different background, even if belonging to the same region where a unique oral language can be recognized, often represents an issue.

Another important aspect to consider is the relationship between sign and oral languages. It is widely accepted that sign languages are independent on oral ones. It follows that anytime people using these different languages meet together, the communication between them becomes an issue. Taking into account that the hearing impaired community is, on average over all world, less than 0.1% of the total population, such a communication difficulty becomes a real barrier for 'signers' and a social inclusion problem comes out. The invaluable work of interpreters only partially alleviates it, since they cannot be always present in any situation. That is why the scientific communities have been wondering if some Information and Communication Technology (ICT) tools can be developed in support of this. Some interesting works on automatic recognition [2,3,4] and synthesis/translation [5,6,7] have recently appeared in the literature, even if

H. Zhang et al. (Eds.): BICS 2012, LNAI 7366, pp. 164–173, 2012.

pretty far to be a consolidated reality in real applications. Moreover, they strictly depend on the sign languages they are targeted to.

A central role in the development of such tools is represented by the availability of a suitable database, whose realization is made difficult by the aforementioned barriers. There are actually several databases available for other languages, like ASL, but a very limited choice for the Italian case study, specially if the objective is developing a suitable support tool to develop advanced human-machine interaction systems for severely hearing impaired people (featuring automatic recognition and/or synthesis/translation of signs). That is why the authors have realized the present database, with the precious help of the 'Ente Nazionale dei Sordi - ENS' (National Institute of Deaf People)[1] and in particular of ENS people located in Ancona, Italy. The ENS have provided an adequate number of subjects and also participated in choosing the signs composing the database, as it will be explained later on. The proposed Database has been named **A3LIS-147**, since 147 are the distinct signs contained therein. It is completely free and available online. Last but not least, the work here described wants to be a useful reference also for scientists interested in developing a Sign Language database related to other geographical places: indeed all details about video recordings methodology and technology are provided.

This is the outline of the paper. In Section 2, an overview of main international and national databases for Sign Languages is provided. Then Section 3 deals with the description of the recording issues and the material one can find within the corpus. Finally, Section 4 concludes the paper.

2 Overview of Sign Languages Databases

2.1 International Databases

There are many international projects targeted to study the Sign Language in different countries, and, as result of their work, various databases have been created both to deepen the related linguistics studies and also to develop suitable tool to support the interaction of hearing paired and impaired people. In the following some relevant examples are reported and briefly described.

RWTH-BOSTON-50 and RWTH-BOSTON-104 Databases

The RWTH-BOSTON-50 and the RWTH-BOSTON-104 are free ASL databases available online [8,9]. They have been created as a subset of the general ASL database recorded at the Boston University[2]. The video sequences have been recorded at 30 frames per second (fps) with a resolution of 312x242 pixels. Sentences have been executed by three different people, two men and one woman.

[1] The authors want to express their gratitude to the ENS Institute for the fundamental role played in the recording phase, and in particular to the involved subjects Diego, Elisa, Silvano, Remo, Aidelis, Romolo, David, Marco, Ivano, Serena, and Maria for interpreting and to Serena for logistics support.

[2] http://www.bu.edu/asllrp/ncslgr.html

All of the signers are dressed differently and the brightness of their clothes is different.

The RWTH-BOSTON-50 is made of 483 utterances of 50 signs. Each of these utterances has been stored in a different video file to create a video collection of isolated signs. Two cameras have been used on purpose: one for the frontal and the other for the lateral view. Moreover the hand positions are annotated in correspondence of the first frame of each utterance.

The RWTH-BOSTON-104 is made of 201 sentences (161 for training and 40 for testing) and the dictionary contains 104 different signs. Unlike the first one, this database is composed by sign sequence for each video.

RWTH German Fingerspelling Database

The RWTH German Fingerspelling contains finger movements of the German Sign Language (DGS in German); it is free and available online [10]. The database contains 35 signs in video sequences showing the signs related to the letters from 'A' to 'Z', the 'SCH' character, the dieresis characters 'Ä', 'Ö', 'Ü', and numbers from 1 to 5. The database is composed by isolated sequences separated in 700 training files and 700 testing ones. Twenty executors have been involved on purpose, each one repeating each sign twice in two different days. The recording has been performed in non uniform lighting conditions, with two different cameras (a webcam with resolution 320x240 and another commercial camera with resolution 352x288, both at 25 fps) located in different positions, and without any restrictions to the clothes used by signing people.

SIGNUM Database

The SIGNUM database [11] is composed by isolated signs and by sign sequences executed by different people. To facilitate the video feature extraction phase, recordings have been performed under controlled conditions, like diffuse lighting and uniform blu background. The sign executors wear dark long-sleeved shirts and stay standing. Videos have been recorded with a resolution of 780x580 pixels at 30 fps. The dictionary is made of 450 DGS signs composing a total of 780 sentences with consecutive signs; 25 people have been involved. The database is available at a price of 1000 €. Further information are available online [11].

ECHO

The ECHO corpus [12] is made of annotated data from three different sign languages: Dutch (NGT), English (BSL) and Swedish (SSL). For each of these languages, recordings about the narration of 5 distinct stories, plus some interviews to the signers, have been performed. Moreover the corpus include two annotated segments of the corpus Gehörlos So! of DGS. Each session is composed by one or more video files with the related ELAN transcriptions and IMDI based metadata descriptions.

2.2 Italian Databases

There are few national projects about Italian Sign Language. In the following are reported and briefly described just 3 of them which have directly or indirectly created LIS video databases.

Large-Scale Italian-LIS Parallel Corpus

This is one of the few LIS corpora and has been developed within ATLAS[3] project [13]. The corpus presents a tri-lingual structure, with the Italian text, the AEWLIS sequences, the signed LIS video. A LIS expert interprets the content of the cleaned text, about weather forecast, and a movie of his/her signing is recorded using a standard framing.

The corpus is under development and it will be made publicly available to the community. Actually, no informations about the number of signers, recording condition, video properties and signs dictionary are provided. As stated in [13], it includes many recordings with thousands of signs, but they are executed by single signers and this represents a limitation in the development of automatic sign recognition tools.

e-LIS and DIZLIS

For what concerns LIS, up to the authors knowledge, the sole video material available is represented by the online dictionary e-LIS[4] and the Italian Dictionary[5] (DIZLIS), at the price of 18.15 €. DIZLIS contains 2300 Italian lexemes corresponding to the translation of corresponding videos in the Sign Language. Such a material is not very useful for research purposes oriented to Automatic Sign Recognition and Synthesis/Translation applications: indeed each sign is executed by one single subject and the video quality is not well-suited to be processed by advanced signal processing algorithms.

3 Corpus Description

The proposed video database is composed by 147 distinct isolated signs executed by 10 different signers: 7 males and 3 females. The signers age is on average about 29 years, in a range between 43 and 18 years; their averaged height is about 172 cm, in a range between 190 and 156 cm.
All signs have been organized in six categories, related to different situations of the common life. These likely represent the domains where automatic tools for social inclusion of deaf people could be effectively applied. They are the following (with related English translation - the number of signs belonging to a certain category is given in brackets):

[3] http://www.atlas.polito.it/index.php/en/home
[4] http://elisdiz.eurac.edu/diz/
[5] http://www.dizlis.it/

- Ente Pubblico - *Public Institute* (39)
- Stazione - *Railway Station* (35)
- Ospedale - *Hospital* (19)
- Autostrada - *Highway* (8)
- Vita Comune - *Common Life* (16)
- Istruzione - *Education* (30)

Each video presents a single sign which is preceded and succeeded by the occurrence of the 'silence' sign. On purpose, during the recording phase, a sequence of 10 seconds during which the signer keeps the silence position has been acquired for each subject. Such a sequence has been archived within the database as the 'silence' sign indeed and named as *sil.* In Table 1 is shown an example of how signs are grouped according to the aforementioned categories. The whole list with related English translation and complete corpus are available online[6].

Table 1. Excerpt of the overall list of signs. The corresponding English translation for each word is given in italic.

Ente Pubblico ***Public Institute***	**Stazione** ***Railway Station***	**Ospedale** ***Hospital***	**Autostrade** ***Highway***	**Vita Comune** ***Common Life***	**Istruzione** ***Education***
Impiegato *Employee*	Arrivo *Arrival*	Ospedale *Hospital*	Tratta *Section*	Abitare *To Live*	Studente *Student*
Provincia *Province*	Treno *Train*	Pronto Soccorso *First Aid*	Strada *Street*	Telefono *Telephone*	Scuola *School*
Regione *Region*	Biglietto *Ticket*	Emergenza *Emergency*	Traffico *Traffic*	Acqua *Water*	Preside *Dean*
...	...	...	...	...	...

3.1 Sign Choice and Video Acquisition

Each subject has executed separately all signs of the dictionary, following a certain temporization in order to allow the correct sign recording. Such a temporization has been accomplished by means of an adequate sequence of slides projected on a screen placed in front of the subject. Each slide proposes the sign to execute, as the one depicted in Fig. 1, and it is made of two distinct phases: STOP and OK. At the starting of the slide the STOP alert appears onto the screen for 4 seconds, allowing the subject to read the word to sign and prepare himself/herself to keep the silence position. During the OK phase, which lasts 6 seconds, the signer executes the sign, looking at the camera in front of him and then he/she comes back to the silence position. In this way, the camera operator is able to start and stop the video recording ensuring to have the sequence silence-sign-silence with the subject always oriented to the camera. This procedure allowed the authors of this work to significantly reduce the inevitable errors that likely occur in the recording phase, specially due to the language barrier: an average recording time of 40 minutes per subject has been registered.

Moreover for words with a conceptual meaning, like 'Biglietto' (*Ticket*) or 'Scuola' (*School*) and differently from city names for instance, an image has

[6] http://a3lab.dibet.univpm.it/projects/a3lis

been projected onto the slide beside the word indicating the sign, as a support of the word meaning itself. Another option could be proposing the picture of the movements associated to the sign to execute, according to some specific Dictionary. This way has been followed at the beginning, by using a regional Dictionary[7]: however, after some preliminary tests, it has been abandoned since it was subject to misunderstanding among the signers.

It has to be highlighted that the background relative to each signer, often due to the geographical zone where he/she lived (note that the people involved are from different cities in the Marche region in Italy), typically results in even remarkable differences in sign execution, specially if the word to sign can be used in diverse conceptual domains. That is why, the ENS Institute supported the authors of this work in suitably pre-training the subjects in order to find a common agreement on all signs to make.

Last but not least, a few consideration about some selected signs for the present database. The names of days and months present a certain variability in signing among the subjects. That is why is has been preferred to keep just the former ones and skip the others. In contrast, the city names are not subject to sign variations among the signers (note that this occurs also at a national level).

Fig. 1. Slides proposed to the subject to sign the word ‘Telefono’ (*Telephone* in English). The STOP and OK phases are shown on the left and right side respectively.

3.2 Silence Position and Labial

A natural ‘silence’ position has been chosen, according to the usual one used by subjects in common life. As shown in Fig. 2, this position is different from the one used in the SIGNUM Database [11]. It must be observed that the position proposed in SIGNUM has been preliminarily experimented but some difficulties have been encountered during the recording phase: this has shoved the authors to opt for the other one, in agreement with the subjects and the ENS Institute.

[7] Regione Marche, Servizi Sociali e ENS, Comitato Regionale Marche (1996). Dizionario Regionale del Linguaggio Mimico Gestuale Marchigiano. Ancona: Edizione Regione Marche.

Fig. 2. Silence position used in the SIGNUM Database (left) and in **A3LIS-147** database (right)

Regarding the labial, it must be said that not all signs contain this element in their execution and it is often added at subject discretion in common life. A typical situation occurring for the word 'subscription' is given in Fig. 3. In A3LIS-147, the subjects followed the policy to add the labial only in correspondence of certain signs, a-priori decided.

3.3 Video File Properties

Video sequences have been acquired by using a commercial camera located in front of the subject. Behind the signer a green chroma-key background is placed and two diffuse lights (400 W each) are used to ensure an uniform lighting. The recording setup, with all distances among devices and subject, is shown in Fig. 4.

The video streaming has been acquired at 25 fps and at a resolution of 720x576 pixel. The video sequences have been memorized in the original camera format, Digital Video (DV), in order to keep the maximum image quality.

3.4 Database Structure

The database has been structured so that each signer, identified by a certain SIGNER-ID, corresponds to a specific folder where all video sequences performed by himself/herself are contained. Then, each video sequence is identified by a name indicating the executed sign. The SIGNER-ID is composed by 3 characters, the first denoting if the gender and the other corresponding to the initials of the signer. Since it has to be unique, a fourth letter is admitted in case of ambiguity. Details are given as follows:

FILENAME ::= <SIGNER-ID>_<SIGN>.avi
SIGNER-ID ::= <GENDER><NS> | <GENDER><NS><ABC>
GENDER ::= m | f
NS ::= aa | ab | ... | zz
ABC ::= a | b | ... | z
SIGN ::= executed sign

Fig. 3. Labial of sign 'Abbonamento' (*Subscription* in English)

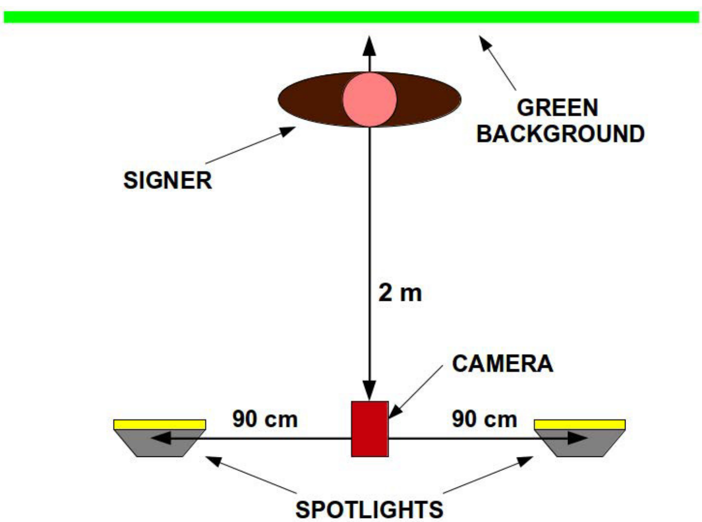

Fig. 4. Devices and Signer placement for video recording

4 Conclusions

In this paper a new LIS database has been proposed, also showing the technology and methodology employed for its development. The corpus presents some relevant characteristics, at the moment absent in the other few databases relative to the Italian Language of Sign: it is completely free and available online, and it contains a set of signs executed by multiple subjects in repeatable conditions. In particular the latter aspect is fundamental to suitably parametrize expert systems able to automatically recognize and/or synthesize/translate the sign execution. This is confirmed if we look at other international databases which have been largely used to develop automatic tool useful for social inclusion of severely hearing impaired people. The authors are actually working along this direction and an effective Automatic LIS Recognizer (trained on this database) is about to be announced.

As future work, the authors are also intended to enlarge this database with new signs and subjects. Moreover the case of sentences made of consecutive signs will be addressed, thus resulting in a more complete database for even more challenging applications.

References

1. Sandler, W., Lillo-Martin, D.: Sign Language and Linguistic Universals. Cambridge University Press (2006)
2. Yang, J., Gao, J., Zhang, Y., Chen, X., Waibel, A.: An automatic sign recognition and translation system. In: Proc. of The Workshop on Perceptive User Interfaces, pp. 1–8 (2001)
3. Efthimiou, E., Fotinea, S.-E., Vogler, C., Hanke, T., Glauert, J., Bowden, R., Braffort, A., Collet, C., Maragos, P., Segouat, J.: Sign Language Recognition, Generation, and Modelling: A Research Effort with Applications in Deaf Communication. In: Stephanidis, C. (ed.) UAHCI 2009, Part I. LNCS, vol. 5614, pp. 21–30. Springer, Heidelberg (2009)
4. Ten Holt, G.A., Van Doorn, A.J., Reinders, M.J.T., Hendriks, E.A., De Ridder, H.: Human-inspired search for redundancy in automatic sign language recognition. ACM Trans. Appl. Percept. 8, 15:1–15:15 (2011)
5. Maxime, D.: Sign language synthesis: skeleton modelling for more realistic gestures. SIGACCESS Access. Comput., 19–23 (January 2010)
6. Kipp, M., Heloir, A., Nguyen, Q.: Sign Language Avatars: Animation and Comprehensibility. In: Vilhjálmsson, H.H., Kopp, S., Marsella, S., Thórisson, K.R. (eds.) IVA 2011. LNCS, vol. 6895, pp. 113–126. Springer, Heidelberg (2011)
7. Dreuw, P., Forster, J., Gweth, Y., Stein, D., Ney, H., Martinez, G., Llahi, J.V., Crasborn, O., Ormel, E., Du, W., et al.: Signspeak–understanding, recognition, and translation of sign languages. In: Proc. of 4th Workshop on the Representation and Processing of Sign Languages: Corpora and Sign Language Technologies, pp. 22–23 (2010)
8. Zahedi, M., Keysers, D., Deselaers, T., Ney, H.: Combination of Tangent Distance and an Image Distortion Model for Appearance-Based Sign Language Recognition. In: Kropatsch, W.G., Sablatnig, R., Hanbury, A. (eds.) DAGM 2005. LNCS, vol. 3663, pp. 401–408. Springer, Heidelberg (2005)

9. Dreuw, P., Rybach, D., Deselaers, T., Zahedi, M., Ney, H.: Speech recognition techniques for a sign language recognition system. In: Proc. of Interspeech, pp. 2513–2516 (August 2007), http://www-i6.informatik.rwth-aachen.de/aslr/database-rwth-boston-104.php
10. Dreuw, P., Deselaers, T., Keysers, D., Ney, H.: Modeling image variability in appearance-based gesture recognition. In: ECCV Workshop on Statistical Methods in Multi-Image and Video Processing (ECCV-SMVP), pp. 7–18 (May 2006), http://www-i6.informatik.rwth-aachen.de/aslr/fingerspelling.php
11. von Agris, U., Kraiss, K.F.: Towards a video corpus for signer-independent continuous sign language recognition. In: International Gesture Workshop on Gesture in Human-Computer Interaction and Simulation (May 2007), http://www.phonetik.uni-muenchen.de/forschung/Bas/SIGNUM/
12. Crasborn, O., Mesch, J., Waters, D., Nonhebel, A., van der Kooij, E., Woll, B., Bergman, B.: Sharing sign langauge data online. experiences from the echo project. International Journal of Corpus Linguistics 12(4), 535–562 (2007), http://www.let.ru.nl/sign-lang/echo
13. Bertoldi, N., Tiotto, G., Prinetto, P., Piccolo, E., Nunnari, F., Lombardo, V., Mazzei, A., Damiano, R., Lesmo, L., Del Principe, A.: On the creation and the annotation of a large-scale italian-lis parallel corpus. In: International Conference on Language Resources and Evaluation, pp. 19–22 (May 2010)

Study of Phase Relationships in ECoG Signals Using Hilbert-Huang Transforms

Gahangir Hossain, Mark H. Myers, and Robert Kozma

Center for Large-Scale Integrated Optimization and Networks (CLION)
The University of Memphis, Memphis, TN 38152, USA
{ghossain,rkozma,mhmyers}@memphis.edu

Abstract. This study investigates phase relationships between electrocorticogram (ECoG) signals through Hilbert-Huang Transform (HHT), combined with Empirical Mode Decomposition (EMD). We perform spatial and temporal filtering of the raw signals, followed by tuning the EMD parameters. It can be seen that carefully tuning of EMD filter, it is possible to capture distinct features of non-stationary data. This makes EMD, combined with HHT a valuable tool of complex brain signal analysis and modeling.

Keywords: Electrocorticogram (ECoG), Hilbert Huang Transform (HHT), Empirical Mode Decomposition (EMD), Phase cone.

1 Introduction

Hilbert-Huang transform (HHT) is a recent method which generates amplitude and frequency vs. time spectra using a powerful data analysis tool called empirical mode decomposition (EMD) [1, 2]. HHT is suitable to analyze non-stationary and non-linear data. Global basis states must be replaced with adaptive, locally determined ones, a process the first stage of the HHT does perform. The resulting basis states are, in general, not strictly orthogonal. The goal of this study is to analysis different phase relationships in phase cone discovery from different types of EMD filtered datasets.

The main idea behind EMD approach is to first compute the local median of a signal via a sifting procedure and then subtract the local median of a signal before applying the amplitude spectrum method to define instantaneous frequency. Therefore, in performance comparison of EMD filtering the very recent discovery of Hou and Shi, EMD performance depends on the sensitivity on the number of sifting and the stopping criteria [3, 4], is adopted. The variance of EMD filtering is performed by carefully tuning some dependent parameters in intrinsic mode function (IMF) that decomposes the signal into modes that are intrinsic to the function using an iterative or "sifting" process considering only local extrema.

In ECoG analysis, the spatially ordered phase relationship between cortical signals is named as phase cone [5]. Instantaneous identification of phase cones therefore serves as markers by which to locate emergent AM patterns at varying latencies over sequential trials. To identify better phase cones, ECoG, data must be preprocessed

H. Zhang et al. (Eds.): BICS 2012, LNAI 7366, pp. 174–182, 2012.

without changing its inherent properties. The present work aims at studying phase relationships in ECoG data to improve the identification of salient properties of spatio-temporal brain dynamics.

This work starts with a brief introduction to the applied methodology. This is followed by describing the analyzed data obtained from intracranial experiments with chronically implanted rabbits. We study the performance of HHT processing algorithms and optimize parameters of EMD algorithm. Finally, we summarize the obtained results and conclude direction for future studies.

2 Background Study

ECoG represents complex irregular brain signals by recording of tiny electrical potentials that underlie neural activities related to perception and action. This section provides some background materials, mostly fast Fourier transform and Hilbert-Huang transformation that are used to uncover phase cones from ECoG signals. The implemented signal processing approach is explained on the block diagram as shown in Figure 1. After a very brief review of the HHT, and Phase cone identification, the comparative behavior of these two transforms on various filtered data set is explored. Along this direction the IMF parameter ‘number-of-sifting’ in iteration is varied.

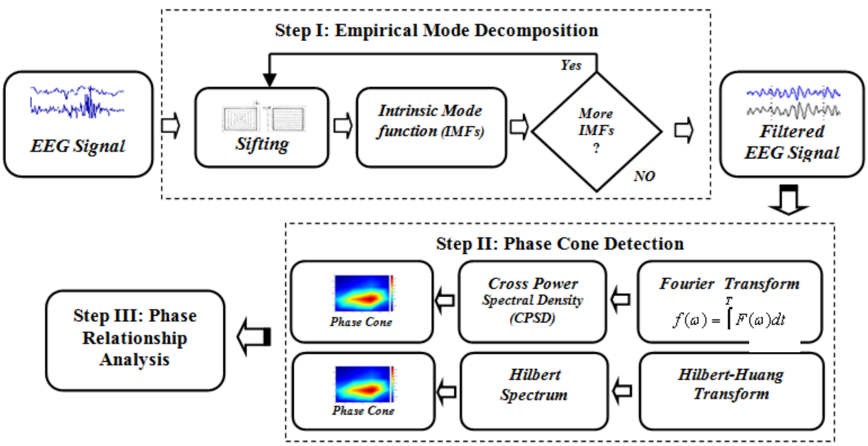

Fig. 1. Block Diagram of Experimental Steps

2.1 Hilbert Transformations

For an arbitrary signal v, the analytic signal V(t) is a complex function of time defined as:

$$v'(t) = \frac{1}{\pi} PV \int_{-\infty}^{+\infty} \frac{v(t')}{(t - t')} dt' \tag{1}$$

where PV corresponds to the Cauchy Principal Value. At each digitizing step, the time series yielded a point in the complex plane [vj'(t)]. Each signal denoted by v(t) was transformed to a vector, V(t) having a real part, v(t), and an imaginary part, v'(t). As seen from Eq. (1), the Hilbert transform *v'(t)* of v(*t*) can be considered as the convolution of the function v(*t*) with $1/\pi t$. Each ECoG signal denoted v(t) was transformed to a vector, V(t), having a real part, v(t), and an imaginary part, v'(t) (Freeman, Rogers, 2002):

$$V(t) = v(t) + i\, v'(t) = AA(t) \exp [iAP(t)] \tag{2}$$

where the length of the vector gave the analytic amplitude,

$$AA(t) = [\, v^2(t) + v'^2(t)\,]^{.5} \tag{3}$$

and arc tangent of the vector gave the analytic phase,

$$AP(t) = \operatorname{atan} [\, v'(t) / v(t)\,]. \tag{4}$$

The instantaneous amplitude AA(t) and the instantaneous phase AP(t) of the signal v(t) are thus uniquely defined by Eqs. (3,4). The real data corresponds to the raw incoming data, while the Hilbert transform (HT) provides the imaginary frequency that is changing in time. The imaginary part is a version of the original real sequence with a 90° phase shift. Sin functions are therefore transformed to cosines and vice versa [5]. The Hilbert transformed series has the same amplitude and frequency content as the original real data and includes phase information that depends on the phase of the original data. The Hilbert transform is useful in calculating instantaneous attributes of a time series, especially the amplitude and frequency. The instantaneous amplitude is the amplitude of the complex Hilbert transform; the instantaneous frequency is the time rate of change of the instantaneous phase angle [5]. For a pure sinusoid, the instantaneous amplitude and frequency are constant.

2.2 The Hilbert-Huang Transform

The Hilbert-Huang transform is the combination of empirical mode decomposition (EMD) and Hilbert transform (HT). EMD process deconstructs the signal into a set of intrinsic mode functions (IMF) and HT extracts frequency vs. time information from each of the IMF's.

The EMD is a method of signal decomposition introduced for analysis of nonlinear and non-stationary signals. It is to identify proper time scales that reveal physical characteristics of the signals, and then decomposed the signal into modes that are intrinsic to the function, referred as Intrinsic Mode Functions (IMFs). IMFs interpret signals as the zero mean oscillations at each scale and the local mean of the signal respectively. IMFs are signals satisfying two conditions: (a) in the whole dataset, the number of extrema and the number of zero-crossings must either be equal or differ at most by one, and (b) at any point, the mean value of the envelope defined by local maxima and the envelope defined by the local minima is zero.

Condition one is similar to the traditional narrow band requirements for a stationary Gaussian process. Whereas, the second condition is necessary in order to avoid unwanted fluctuations induced by asymmetric waveforms in the instantaneous frequencies will not have. An IMF is not limited as a sinusoid in the classical sense (such as in Fourier Transforms), it can be an amplitude and frequency modulated signal and, can even be a non-stationary signal. This method enables us to eliminate the drawback of a traditional time-domain to frequency-domain transformation (like Fourier transform) where frequency contents are observed by sacrificing time resolution. Instead, IMFs provide amplitude and frequency information of a signal at any given time.

Practically, EMD is implemented as an iterative or "sifting" process considering only local extrema. The EMD algorithm for amplitude and frequency extraction from a given discrete IMF is shown in Table 1.

Table 1. EMD Algorithm (sifting algorithm)

Given a discretely sampled signal y(t),
Step-1: Find the locations of all the extrema of *y(t)* – first IMF signal.
Step-2: Interpolate between all the minima (respectively maxima) to obtain the lower signal envelope, *ymin(t)* (respectively *ymax(t)*).
Step-3: Compute the local mean *m(t) = [ymin(t) + ymax(t)]/2*.
Step-4: Subtract the mean from the signal to obtain the 'oscillatory mode'
d(t)= y(t) − m(t) // removing the trend
Step-5: If *d(t)* meets stopping criteria, then
define $c_i(t)=d(t)$ and
i = i +1 // increment i
r(t)= y(t) − d(t) // extract the residual
If *d(t)* does not meets stopping criteria farther sifting is required.
set *y(t)=d(t)* and repeat from step 1.
Step-**6**: Repeat steps 1 through 5 until the residual no longer contains any useful frequency information.

Amplitudes and frequencies are extracted from these IMF's in the second stage of the HHT process. The instantaneous amplitude and angular frequency associated with each IMF depend on the amplitude and phase of a complex number that the IMF and its Hilbert transform (HT) define. The real part of the complex number is the IMF; the imaginary part of the number is the IMF's HT. The instantaneous amplitude is the amplitude of this complex number. The instantaneous angular frequency associated with that IMF is the derivative of the unwrapped phase.

The entire process is repeated for each IMF to extract the complete frequency versus time information from the original ECoG data set.

The computation of the HT is essentially a convolution of an IMF, x(t), with 1=t and effective to emphasize the local properties of x(t). This locality preserves the time structure of the signal's amplitude and frequency.

Generally, ECoG signals are represented equal to the sum of its parts. We have *N* IMFs and a final residual *rN (t)*,

$$y(t) = \sum_{i=i}^{N} c_i(t) + rN(t) \tag{5}$$

The second stage of the HHT process extracts the amplitude and frequency information from each IMF (HT algorithm in Table 2).

Table 2. Algorithm: HT

Given a discretely sampled signal y(t),
Step-1: Compute the IMF's discrete Fourier transform (DFT) using the series expression (1) for the transform.
Step-2: Compute the HT. Use the real and imaginary parts of step 1's DFT as coefficients (M = N/2): $y_j = \frac{1}{N}\sum_{t_1=0}^{M} Real\left(X_{t_1}\sin\left(2\pi t_1 \frac{j}{N}\right)\right) + Imaginary\left(X_{t_1}\cos\left(2\pi t_1 \frac{j}{N}\right)\right) + \left(\frac{-1}{N}\right)\sum_{t_2=M+1}^{N-1} Real\left(X_{t_2}\sin\left(2\pi t_2 \frac{j}{N}\right)\right) + Imaginary\left(X_{t_2}\cos\left(2\pi t_2 \frac{j}{N}\right)\right)$ **(5)**
Step-3: Form the complex number $z_j = x_j + iy_j$, extract the phase $\varphi_i = \tan^{-1}(y_i/x_i)$.
Step-4: Unwrap the phase so that it becomes a monotonically increasing function.
Step-5: Determine the frequency. Take the derivative of the phase $f_j = \frac{1}{2\pi}\frac{d\varphi_j}{dt}$
Step-6: Determine the amplitude. $a_j = \sqrt{x_j^2 + y_j^2}$

2.3 Phase Cone Detection

Phase cones describe the spatially ordered phase relationship between cortical signals. Phase cones reveals the property: a state transition is not everywhere instantaneous but begins at a site of nucleation and spreads concentrically, like the formation of a snowflake around a grain of dust.

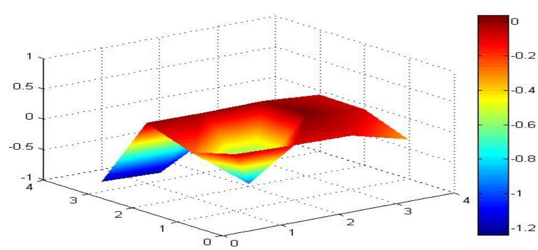

Fig. 2. A 3D plot of a special distribution of analytic phase across 8 x 8 ECoG electrode array at the time frame t = 0.256 s. The phase lags confirm as like phase cone.

The apex that marks the site in the cortex is a random variable both in sign (lead or lag) and location. The cones can appear with positive and negative phase lags, corresponding to explosive and implosive transitions in the cortical spatiotemporal dynamics and there can be several phase cones simultaneously present in a measurement window [6,7]. Phase Cones depicting an "implosion" due to a phase lag of the ECoG time series. The power spectral analysis usually reveals a dominant peak at a central frequency in short segments and near 1/f power spectra in time segment > 1sec. This dominant component of each burst is constituted by the power at the point where the central frequency rises and it drops towards the end in temporal amplitude modulation (AM) on all channels [8,9]. These AM pattern have been found to be accompanied by pattern of phase modulation and forms like a cone, that is named as phase cone.

More details on identification of propagating phase gradients in ECoG signals using Dynamic Logic (DL) approach is experimented [10]. Figure 2 shows 3D view of sample phase cones at timestamp t128. The figure explains special distribution of analytical phase across the 8 x 8 ECoG electrode array at that time frame.

3 Data and Methods

3.1 Data

To demonstrate the comparative study 64-channel ECoG recordings of rabbit data is used. The data is captured in Walter Freeman's UC Berkeley lab [11,12]. ECoG was recorded monopolarly with respect to that cranial reference electrode nearest the array and amplified by fixed-gain (10K) WPI ISO 4/8 differential amplifiers. Each channel was filtered with single pole, first order analog filters set at 100 Hz and 0.1 Hz. Records of sixty-four 12-bit samples multiplexed at 10 μs were recorded at a 2 ms digitizing interval (500 Hz) for 6 seconds and stored as signed-16-bit integers. More specifically, a sample data is a 64 x 3000 matrix, which means 64 ECoG channels measured for 6s, at 2 ms sampling time, so in total 3000 points. The incremental time delay caused by multiplexing of the ECoG was corrected off-line. Bad channels associated with movement artifact or EMG were identified by visual editing and replaced off-line by averaging the signals of two adjacent channels. Using the EMD technique described in previous section and changing the value of number-of-sifting in IMF iteration, fix different types of filtered data sets are created.

3.2 Methods

The comparative experimental procedure works as the block diagram shown in Figure 1. The filtering based system works for three steps. In first step, input ECoG signals are decomposed using EMD with couple of iterations for all signals band to be stabilized in terms of IMFs. After successful IMF iterations EMD phase ended. In step two, HT is applied on the filtered signal. That works as HHT on the applied signal. Tuning the EMD parameter finally tuned the HHT for different dataset. In farther step the reflection of amplitude and phase change is analyzed for meaningful pattern discovery. As ECoG time series are large in size, a significant sample selection is a crucial part of the comparative study. To select a good and representative sample window average phase around 60 Hz for all 64 channels (8 X 8) are analyzed for different filtered dataset. An average phase spectrum of all 64 channels for different filtered dataset is plotted. By visual inspection on the figure matrix any filtered data is compared with the top row.

4 Results

In this section three important properties of Hilbert transform namely analytic amplitude, analytic phase and unwrapped phase are plotted from all EMD filtered ECoG signal.

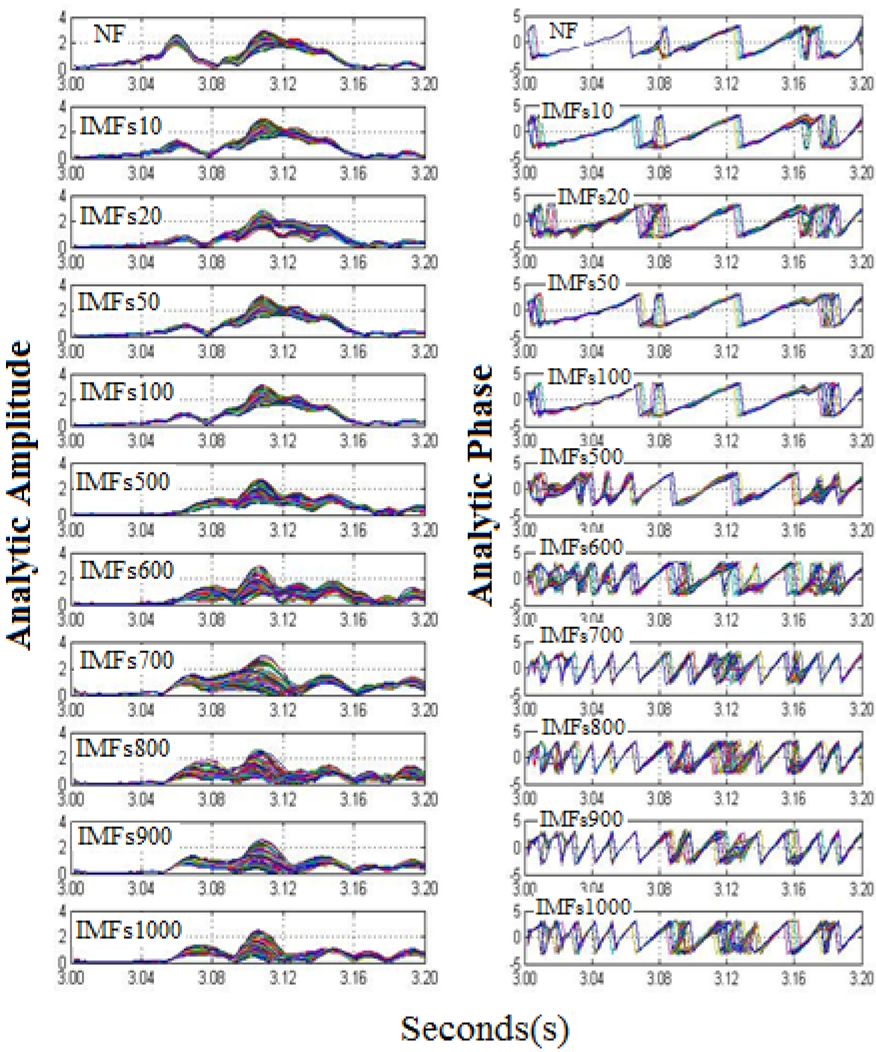

Fig. 3. Hilbert analytic amplitude and phase comparison between original data set and EMD filtered datasets

The original rabbit data is marked as not filtered (NF) whereas EMD filtered data sets are varied based on number of IMF sifting. These versions are marked as IMFs10, IMFs20, IMFs50, IMFs100, IMFs500, IMFs600, IMFs700, IMFs800, IMFs900 and IMFs1000.Hilbert analytic phase and amplitude comparison are shown in Figure 3.

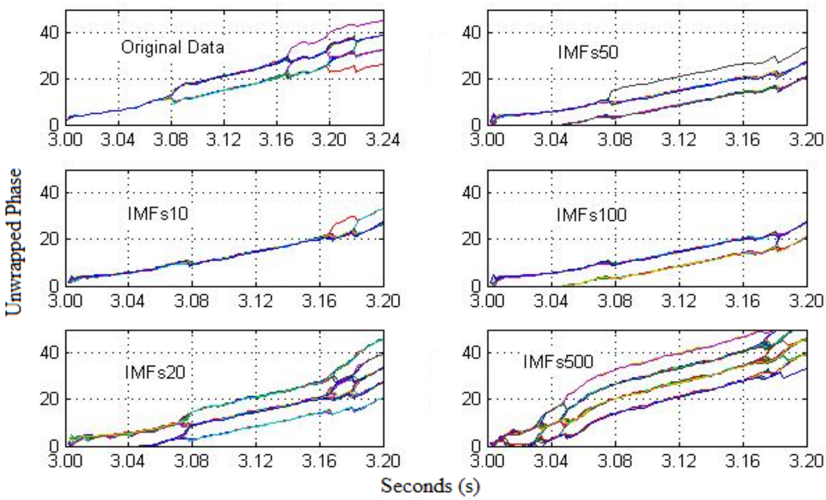

Fig. 4. Hilbert unwrap phase comparison between original data set and EMD filtered datasets

Smoothing of the time series occurs in the analytic amplitude due to an increased EMD order. A change in the phase/frequency range from higher order EMD filtering seems to increase the number of phases over time.

In Figure 4, the unwrapped phase changes dramatically between higher order EMD filtering. The challenge of filter selection may cause bifurcations of the unwrapped phase to occur due to noise and opposed to too much filtering which may cause important attributes of the signal to become smoothed over. An EMD order of less than 100 seems to enable the ECoG signal to retain its lower frequency attributes while discarding noisy artifacts.

5 Conclusion

This study revealed that combination of EMD and HT is better in lower-order filtering in ECoG analysis mostly tuning the filtering parameters related to ‘sifting’ in IMF iteration less than hundred times. Hence, EMD may be a useful and effective tool for filtering ECoG data before phase cone detection. Analysis of other EMD parameters (e.g. fidelity or noise related issues) for filter tuning can be experimented in the next phase.

Standard EMD is limited to the analysis of single data channels, whereas modern applications require its multichannel extensions. The complex ECoG signal needs to be processed using multivariate algorithms to get complex valued IMFs. In that case, a bi-variate or tri-variate EMD algorithm may be useful. On the other hand, results from the EMD with HT (HHT) method showed relatively deprived phase behavior that need more inspection in further study.

Additionally, EMD parameters that capture temporal information changes need a continuous, automatic assessment in phase gradient identification process. Therefore, a dynamic process of optimal approximation and robust identification of phase cones from filtered or noisy data can be experimented. Future work includes better phase cone detection mechanism, automation of the detection process, and performance improvement and analysis of the impact of filtering on phase relationship.

Acknowledgments. This work has been supported in part by the University of Memphis Foundation, through a grant of the FedEx Institute of Technology.

References

1. Bendat, J.S.: The Hilbert Transform and Applications to Correlation Measurements. Bruel & Kjiaer, Denmark (1985)
2. Huang, N.E., Shen, Z., Long, S.R., Wu, M.C., Shih, H.H., Zheng, Q., Yen, N.C., Tung, C.C., Liu, H.H.: The empirical mode decomposition and the Hilbert spectrum for nonlinear and nonstationary time series analysis. Proc. Roy. Soc. Lond. A, 903–1005 (1998)
3. Huang, N.E., et al.: The empirical mode decomposition and the Hilbert spectrum for nonlinear and non-stationary time series analysis. Proc. R. Soc. Lond. A. 454, 903–995 (1998)
4. Battista, B., Knapp, C., McGee, T., Goebel, V.: Application of the Empirical Mode Decomposition and Hilbert-Huang Transform to Seismic Reflection Data. Geophysics 72(2), H29–H37 (2007)
5. Freeman, W.J., Rogers, L.J.: Fine temporal resolution of analytic phase reveals episodic synchronization by state transitions in gamma EEGs. J. Neurophysiol. 87(2), 937–945 (2002)
6. Barrie, J.M., Freeman, W.J., Lenhart, M.D.: Spatiotemporal Analysis of Prepyriform, Visual, Auditory, and Somesthetic Surface EEGs in Trained Rabbits. J. Neurophysiology 76(1), 520–539 (1996)
7. Freeman, W.J., Barrie, J.M.: Analysis of Spatial Patterns of Phase in Neocortical Gamma EEGs in Rabbit. Journal of Neurophysiology 84, 1266–1278 (2000)
8. Freeman, W.J.: Origin, structure, and role of background EEG activity, Part II, Analytic Phase. Clinical Neurophysiology, 9–47 (2004)
9. Freeman, W.J.: Origin, structure, and role of background EEG activity, Part I, Analytic Amplitude. Clinical Neurophysiology 116(5), 1118–1129 (2005)
10. Kozma, R., Freeman, W.J.: Analysis of Visual Theta Rhythm – Experimental and Theoretical Evidence of Visual Sniffing. In: IEEE/INNS Int. Joint Conf. Neural Networks, Washington D.C, July 14-19, pp. 1118–1123 (2001)
11. Freeman, W.J.: Mass Action in the Nervous System. Academic Press, New York (1975)
12. Kozma, R., Perlovsky, L., Ankishetty, J.S.: Detection of propagating phase gradients in EEG signals using Model Field Theory of non-Gaussian mixtures. In: IEEE International Joint Conference on Neural Networks, IJCNN 2008. IEEE World Congress on Computational Intelligence, pp. 3524–3529 (2008)

Treatment Status Predicts Differential Prefrontal Cortical Responses to Alcohol and Natural Reinforcer Cues among Alcohol Dependent Individuals

Scott C. Bunce[1,2,3], Kurtulus Izzetoglu[2,3], Meltem Izzetoglu[2,3], Hasan Ayaz[2,3], Kambiz Pourrezaei[2,3], and Banu Onaral[2,3]

[1] Penn State Hershey Medical Center and Penn State College of Medicine Hershey, PA 17003 USA
[2] Drexel University School of Biomedical Engineering, Sciences, and Health Systems
[3] Cognitive Neuroengineering and Quantitative Experimental Research (CONQUER) Collaborative, Drexel University, Philadelphia, PA, 19104, USA
sbunce@hmc.psu.edu,
{ayaz,meltem,ki25,kambiz,banu.onaral)@drexel.edu

Abstract. This study used functional near-infrared spectroscopy (fNIRs) to test the hypothesis that non-treatment seeking alcohol-dependent participants (NTSA) would show greater response in dorsolateral prefrontal cortex (DLPFC) to alcohol cues than recovering alcoholics (RA; sober 90-180 days) or social drinkers. Opposite predictions were made for responses to natural reward cues. NTSA (n=4), RA (n=6), and social drinkers (n=4) were exposed to alcohol and natural reward cues while being monitored with fNIRs. Results confirmed enhanced responses to alcohol cues among NTSA vs. RA in right middle frontal gyrus. The opposite effect (RA>NTSA) was found in response to natural reward cues. Neural responses to alcohol and natural reward cues were negatively correlated in right DLPFC. Real-time craving ratings were positively correlated with greater neural response to alcohol cues. Differential responses to drug and natural reward cues suggest that a psychological mechanism related to treatment status may modulate drug cue responses in DLPFC.

1 Introduction

Drug addiction is widely recognized as a disorder of chronic relapse characterized by a compulsion to seek and take the drug, the inability to limit drug intake, and the emergence of a negative hedonic state associated with withdrawal when the drug is unavailable [1-2]. The addiction cycle involves a behavioral pattern of drug use to intoxication, followed by withdrawal, craving, and a renewed effort to obtain more drug even in the face of numerous harmful consequences. Until recently, most theories of addiction focused primarily on reward processes mediated by mesolimbic dopaminergic circuits [3].

Neuroimaging research investigating the central nervous system responses of human populations have identified a distributed neural network that is activated by tobacco, cocaine, and alcohol-related stimuli among addicted individuals [4-7]. A

H. Zhang et al. (Eds.): BICS 2012, LNAI 7366, pp. 183–191, 2012.

commonly used method for investigation of drug craving has been the cued response paradigm [8-9], which has produced a reasonable consensus regarding the subcortical brain areas involved in addiction and craving. However, there has been notable inconsistency with regard to DLPFC and orbitofrontal cortex (OFC; [7, 10]) which has not been systematically addressed [7] in current models of craving and addiction [10-11]. In their review of the cue reactivity literature, Wilson et al. [7] suggested that the pattern of results is not random, but is predictable if the treatment-seeking status of the participants is taken into account. Among neuroimaging studies of non-treatment seeking individuals, 8 of 10 found activation in DLPFC and 5 of 10 found activation in OFC. Among studies of treatment-seeking individuals, only 1 of 9 found activation in either DLPFC or OFC. In sum, upon exposure to drug-related cues, non-treatment seeking individuals generally exhibited increased activity in DLPFC and OFC relative to individuals in treatment. This observation is important in that it suggests there may be cortical correlates of treatment status, but more importantly, of behavioral control and commitment to treatment.

Goldstein & Volkow's [10-11] iRISA model suggests that OFC, DLPFC, ACC, and limbic areas may comprise a mesocortical dopamine circuit thought to be involved in behavioral control mechanisms and conscious experience of drug intoxication. First, prefrontal cortex (PFC) is known to be involved in mediating the primary rewarding effects of reinforcing stimuli [12]. Second, exposure to drug cues typically results in increased metabolic activity in DLPFC among current addicts [7, 10-11, 13-15] even though overall hypoactivations have been found in PFC among opioid [16] and psychostimulant abusers [11]. Third, addicted individuals often demonstrate reduced motivation to obtain natural rewards [10-11]. Together, these findings suggest increased responsivity to drug-conditioned cues, coupled with a reduced response to natural rewards among drug-addicted individuals, mediated in part by prefrontal circuits. There are currently, however, no functional neuroimaging studies of cue-reactivity that have examined both treatment-seeking and nontreatment-seeking addicted individuals in the same study. The contrast between these two groups is important because it could begin to elucidate differences associated with the treatment status and the motivation to maintain sobriety.

The current study tested the hypothesis that alcohol-related visual cues would elicit greater activation in DLPFC among non-treatment-seeking alcohol-dependent individuals relative to in-treatment, abstinent individuals. Though the suppression of prefrontal metabolism in some addicted groups [16] may be considered a confound between current users and patients in treatment, because opposite hypotheses can be made for prefrontal response to drug cues and natural rewards, the predicted outcome would suggest a psychological mechanism rather than physiologically-based explanation. We predicted that NTSA would show increased activation to drug cues, and decreased activation to natural rewards in DLPFC, whereas RA would show the opposite pattern. Social drinkers' responses were expected to resemble those of RA; therefore social drinker means were expected to differ from those of NTSA, but not from RA.

The current study utilized an emerging neuroimaging technology, functional near-infrared spectroscopy (fNIR; [17]) to examine neural responses in DLPFC while participants viewed alcohol-related and natural reward cues. The use of near infrared light as a noninvasive tool to monitor changes in the concentration of oxygenated hemoglobin (HbO2) and deoxygenated hemoglobin (deoxy-Hb) during functional brain studies has been increasing over the last several years [18-22]. Analogous to fMRI, fNIR provides information on local changes in blood oxygenation concentrations, and can be safely used for repeated measures on the same individual. In contrast to fMRI, however, fNIR is relatively inexpensive, portable, boasts a rapid application time (5-10 minutes), and has near-zero run-time costs.

2 Method

2.1 Participants

Fourteen right-handed non-smokers were recruited into three groups using newspaper advertisements; 4 nontreatment-seeking adult alcoholics (1 female), 6 alcoholic patients currently in recovery (2 females), and 4 healthy social drinkers (2 females). All participants signed written informed consents approved by the University Institutional Review Board. Diagnoses were assigned using the Structured Clinical Interview for *DSM–IV* for Axis I (Ver. 2.0). Daily alcohol use for the 180 days prior to intake were gathered using the Form-90 A interview [23]. NTSA (Mean age = 39.0$\pm$13.7 years) were selected to meet DSM-IV criteria for Alcohol Dependence, expressed no interest in treatment, nor had they sought treatment in the past year. RA (Mean age = 36.2$\pm$5.4 years) met DSM-IV criteria for Alcohol Dependence in early full remission, lived in a non-restricted environment, and reported no alcohol use for 90-180 days (Mean = 158.3$\pm$38.1 days). This pattern of sobriety was the behavioral operationalization of early commitment to sobriety, as they reported having remained sober past the critical early (90 day) phase of relapse [2, 24-25], while having had the opportunity to drink. Social drinkers reported consuming fewer than 7 drinks per week, and fewer than 5 drinks on any single occasion for males, 4 for females. Exclusion criteria for all groups included the presence of any other DSM-IV Axis I psychiatric disorder or substance dependence disorder. Participants were requested to refrain from alcohol use for 24 hours prior to the experiment. Prior to the imaging session, all participants completed a breathalyzer test and an assessment for alcohol withdrawal symptoms. All participants registered a Blood Alcohol Content (BAC) of .000 (Alco-Sensor IV), and scored 1 or less on the Clinical Institute Withdrawal Assessment for Alcohol-revised (CIWA-Ar; [26]).

2.2 Experimental Procedures

Cued Response Task. Stimulus Cue Presentations and Task: The stimulus presentation series consisted of a sequence of six 125-second epochs. Each epoch contained four 25-second blocks, one block each of a) alcohol, b) nonalcoholic beverages, c) visual control pictures, and d) a crosshair, and e) one block of natural rewards. Each 25-s block was comprised of five individual pictures, each displayed for 5 seconds. The alcohol blocks were specific to a beverage type (wine, beer, or liquor), with two blocks per type. After each block, participants rated their craving and resistance to craving in real time on a 100-point visual analog scale. Following Myrick et al. [5], participants were asked to rate their 'urge to consume alcohol' on a visual analog scale anchored at one end by 'not at all' and on the other by the 'maximum possible'. Participants also rated their 'resolution not to consume alcohol' on a 100-point scale anchored by "extremely resolute not to consume alcohol" to "plan to consume alcohol."

fNIR sensors were located by aligning the bottom row of optodes with the International 10-20 site F7, FP1, FP2, F8 line [27]. This placement situated the sensor over bilateral dorsolateral and inferior frontal gyri [28]. A priori regions of interest were optodes 11, 12, 13, 14, as these sites were consistent with previous reports of cued responses in DLPFC [29].

Stimuli. A total of 126 picture cues, 30 from each of 4 categories (alcoholic beverages, nonalcoholic beverages, color and intensity matched control pictures, and a crosshair) were presented to participants, along with 6 natural rewards stimuli. Alcohol and nonalcoholic beverages were selected primarily from the Normative Appetitive Picture System (NAPS; [30]). These stimuli were supplemented with similar pictures drawn from such magazines as Gourmet and Cigar Aficionado to avoid repeating the same stimuli during the study. Visual control pictures consisted of distorted images of the same stimuli, matching the alcohol cues for color and intensity, but lacking any object recognition.

fNIR Data Acquisition and Artifact Removal. fNIR data recorded by COBI Studio [31] were processed using a software suite developed at Drexel University and implemented in Matlab (The Mathworks, Inc., Sherborn, MA). Raw data were low-pass filtered at a frequency of 0.14 Hz to remove respiration and cardiac variation. Individual optodes were visually scanned for artifacts due to motion or poor coupling between the sensors and the scalp, and segments with significant artifact were discarded. Continuous data were then segmented into epochs consistent with the 5 stimulus types and averaged, yielding average oxygenation changes associated with the five stimulus types (alcohol, nonalcoholic beverages, non-identifiable controls, natural rewards, and crosshair). Optode locations for graphs were imaged in fnirSoft [32], by projecting the International 10-20 site measurements from the participants onto a standardized brain (used by permission, [33]) using cortical coordinates provided in [28]).

Statistical Analyses. Statistical analyses were conducted using SPSS 19.0.0 (IBM SPSS Statistics). fNIR oxygenation changes were compared separately for drug cues and hedonic stimuli using 3 (GROUP; NTSA vs. RA vs. SOCIAL DRINKERS) x 2 (CONDITION; ALCOHOL vs. NON-ALCOHOLIC BEVERAGE, or NATURAL REWARDS vs. NON-ALCOHOLIC BEVERAGE) repeated-measures ANOVAs. Region of interest (ROI) optodes for the alcohol contrast were chosen on the basis of Goldstein and Volkow's [10] meta-analysis of neuroimaging studies investigating drug cue response in addicts vs. controls.

3 Results

3.1 Alcohol Stimuli

Results for the ALCOHOL vs. BEVERAGE contrast revealed a GROUP x CONDITION interaction (F (2,11) = 7.62, p = .008; partial eta2 = .58). This finding was qualified by a GROUP x CONDITION X LOCATION interaction (F (6,20) = 2.88, p = .035; partial eta^2 = .46. Analysis of individual optode locations revealed that OPTODE 11 (F (2, 11) = 4.79, p = .03; Partial eta^2 = .465), OPTODE 13 (F (2, 11) = 10.12, p = .003; Partial eta^2 = .65), and OPTODE 14 (F (2, 11) = 8.96, p = .005; Partial eta 2 = .62) showed differential activation to alcohol vs. beverages among the groups. Although the results were in the same direction, optode 12 did not obtain a conventional level of significance (F (2, 11) = 1.73, ns). Consistent with our hypothesis, and with previous research, post hoc analyses and inspection of the means revealed that NTSA had greater activations to alcohol cues vs. nonalcoholic beverages across the three optodes relative to both RA and SOCIAL DRINKERS (see Fig 1a,b).

3.2 Natural Rewards Stimuli

For the NATURAL REWARDS – BEVERAGE contrast, main effects for CONDITION (F (1, 11) = 4.97, p = .05; Partial eta^2 = .31) and LOCATION (F (3, 9) = 5.95, p = .02; Partial eta^2 = .67) were qualified by CONDITION x GROUP (F (2, 11) = 6.05, p = .02; Partial eta^2 = .52) and CONDITION x LOCATION (F (3, 9) = 4.88, p = .03; Partial eta^2 = .62) interactions. The CONDITION x GROUP X LOCATION interaction was not significant (F (6, 20) = 1.77, ns), suggesting consistency across the four optodes. Because our primary interest was in the CONDITION x GROUP interaction, we examined this effect within each of the optodes. Optode 14 (F (2, 11) = 7.22, p = .01; Partial eta^2 = .57), Optode 15 (F (2, 11) = 4.86, p = .03; Partial eta^2 = 47) and Optode 16 (F (2, 11) = 7.56, p = .009; Partial eta^2 = .58) were all significant for the CONDITION x GROUP interaction. In each case, post-hoc analyses revealed that NTSA had significantly less neural activation in response to the NATURAL REWARDS cues than did RA, whereas RA and SOCIAL DRINKERS' responses did not differ (see Fig 1a,b). The NTSA neural responses to the NATURAL REWARDS cues were also less than the SOCIAL DRINKERS at Optode 14, although this post-hoc effect was marginal at Optodes 15 (p = .06), and 16 ($p < .10$). Further analyses revealed that no other fNIR optode sites obtained conventional levels of significance (all F's $\leq$ 3.42, p $\leq$ .07). A Pearson's correlation revealed a negative association between response to alcohol and response to natural rewards at Optode 14 (r (13) = -.51, p = .06), where significant responses to both stimulus classes were found to overlap.

Pearson's correlations also revealed a positive association between ratings of real-time craving to the alcohol cues and brain oxygenation in response to alcohol cues at Optodes 11 (Pearson's r = 0.63, p=.02) and 14 (Pearson's r = 0.61, p=.03). Real-time ratings of alcohol craving were negatively associated with brain activation in response to natural reward cues at Optode 14 (Pearson's r = 0.71, p=.006), Optode 15 (Pearson's r = 0.72, p=.006), and Optode 14 (Pearson's r = 0.70, p=.008).

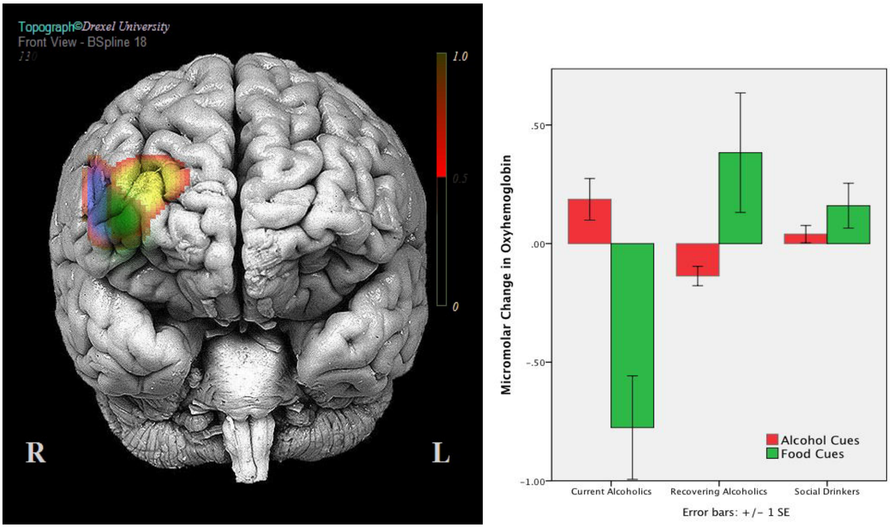

Fig. 1. a) Location of Neural Response to Alcohol Cues and Natural Rewards. Yellow = activation to alcohol – beverage cues; Blue = activation to natural rewards – beverage cues; Green = overlap in activation to both alcohol and natural reward cues (Optode 14). b) Mean oxygenation changes in response to Alcohol Cues (Red) and Natural Rewards (Green) at Optode 14.

4 Conclusions

The current study compared functional neural activation in the prefrontal cortices of social drinkers, NTSA, and RA as they viewed pictures of alcohol cues and natural rewards. Consistent with the hypotheses, NTSA showed greater oxygenation in right DLPFC (middle frontal gyrus) while viewing alcohol cues than did RA. Social drinkers' responses fell between those of the other two groups; they were marginally lower than those of the NTSA, but did not differ from RA. In contrast, the neural responses to natural reward cues showed the opposite pattern of activation relative to alcohol cues, i.e., neural responses to the natural reward cues were larger among RA and social drinkers than among NTSA. Neural responses to the natural reward cues were negatively correlated with neural responses to the alcohol cues. Across all groups, real-time ratings of craving in response to the alcohol cues were positively correlated to the magnitude of the brain activation to those cues. However, when examined within group, both NTSA and social drinkers had positive correlations with neural response (i.e., greater craving was associated with greater activation), whereas RA showed a negative correlation (reports of less craving were associated with greater activation).

The finding of increased right prefrontal activation among NTSA in response to the alcohol cues is consistent with previous findings utilizing fMRI [29, 34-35], although it does represent the first report utilizing fNIR. The finding that RA showed reduced responses to alcohol cues relative to the NTSA, however, is important for two reasons. First, as per Wilson et al. [7] this finding may help explain why many studies utilizing the cued-response method have not found differences in PFC when looking at patients in recovery. Second, it suggests that time in treatment (time away from drug use) may have an effect on the susceptibility of the individual to the drug cues (and the return of response to natural rewards).

Given that PFC responses to both alcohol and natural reward cues differed as a function of treatment status, the functional significance of these cue-induced activations is important. Although there are several theories, the functional significance of these cue-induced activations are not yet known [10]. However, it is likely they represent some aspect of salience or heightened attention. An important finding from the current study, i.e., the differential activation to natural reward cues, argues against the treatment-related reduction in cued-response being due to withdrawal-related hypoactivation. If the decreased response to alcohol cues were due to physiological hyporesponsivity, it would most likely lead to a decrease in response to all mental cues, including natural rewards, rather than to a selective decrease in response to alcohol cues. Instead, neural responses to the natural reward cues were larger among RA and social drinkers than among NTSA, suggesting at least some return of the response to natural rewards among alcoholic patients in longer-term recovery. This finding is important, as it suggests that time away from the drug will help facilitate better treatment outcomes through increased hedonic rewards over time.

There are a couple of limitations to this study. The finding of a marginal difference between NTSA and social drinkers is likely due to the small sample size, although several fMRI studies have failed to find differences between social drinkers and alcoholics in cued-response studies (e.g., [5]). It is possible that the stimuli were more appetitive to some social drinkers, less so to others. The differences between the NTSA and the RA, however, were quite robust, and the direction and location of both findings are consistent with previous cued-response studies that report activations in prefrontal cortices. Nevertheless, these results should be replicated in a larger sample. A second limitation is that unlike fMRI, fNIR cannot image the whole brain, and does not have the same spatial resolution as fMRI. However, this study does provide evidence that fNIR has the potential to provide important information about PFC activations. Given that neuroimaging studies have been shown to predict treatment outcomes for tobacco, alcohol and methamphetamines [29, 35-37], despite its limitations, fNIR may provide the potential for evidence-based medicine in the form of affordable, translational neuroimaging for routine clinical use.

References

1. Koob, G.F., Volkow, N.D.: Neurocircuitry of addiction. Neuropsychopharmacology 35, 217–238 (2009)
2. Miller, W.R., Hester, R.K.: Inpatient alcoholism treatment: Who benefits? American Psychologist 41, 794 (1986)
3. Blum, K., Braverman, E.R., Holder, J.M., Lubar, J.F., Monastra, V.J., Miller, D., Lubar, J.O., Chen, T.J.H., Comings, D.E.: Reward deficicency syndrome: A biogenetic model for the diagnosis and treatment of impulsive, addictive, and compulsive behaviors. Journal of Psychoactive Drugs 32(suppl.), i–iv, 1–112 (2000)

4. Franken, I.H.A.: Drug craving and addiction: integrating psychological and neuropsychopharmacological approaches. Progress in Neuro-Psychopharmacology and Biological Psychiatry 27, 563–579 (2003)
5. Myrick, H., Anton, R.F., Li, X., Henderson, S., Drobes, D., Voronin, K., George, M.S.: Differential brain activity in alcoholics and social drinkers to alcohol cues: relationship to craving. Neuropsychopharmacology 29, 393–402 (2004)
6. See, R.E.: Neural substrates of conditioned-cued relapse to drug-seeking behavior. Pharmacology Biochemistry and Behavior 71, 517–529 (2002)
7. Wilson, S.J., Sayette, M.A., Fiez, J.A.: Prefrontal responses to drug cues: a neurocognitive analysis. Nature Neuroscience 7, 211–214 (2004)
8. Carter, B.L., Tiffany, S.T.: Meta-analysis of cue-reactivity in addiction research. Addiction 94, 327–340 (1999)
9. Drummond, D.C.: What does cue-reactivity have to offer clinical research? Addiction 95, 129–144 (2000)
10. Goldstein, R.Z., Volkow, N.D.: Dysfunction of the prefrontal cortex in addiction: neuroimaging findings and clinical implications. Nature Reviews Neuroscience 12, 652–669 (2011)
11. Goldstein, R.Z., Volkow, N.D.: Drug addiction and its underlying neurobiological basis: neuroimaging evidence for the involvement of the frontal cortex. The American Journal of Psychiatry 159, 1642–1652 (2002)
12. Tzschentke, T.: The medial prefrontal cortex as a part of the brain reward system. Amino Acids 19, 211–219 (2000)
13. Yang, Z., Xie, J., Shao, Y.C., Xie, C.M., Fu, L.P., Li, D.J., Fan, M., Ma, L., Li, S.J.: Dynamic neural responses to cue-reactivity paradigms in heroin-dependent users: an fMRI study. Human Brain Mapping 30, 766–775 (2009)
14. Grant, S., London, E.D., Newlin, D.B., Villemagne, V.L., Liu, X., Contoreggi, C., Phillips, R.L., Kimes, A.S., Margolin, A.: Activation of memory circuits during cue-elicited cocaine craving. Proceedings of the National Academy of Sciences 93, 12040–12045 (1996)
15. Langleben, D., Ruparel, K., Elman, I., Busch-Winokur, S., Pratiwadi, R., Loughead, J., O'Brien, C., Childress, A.: Acute effect of methadone maintenance dose on brain fMRI response to heroin-related cues. American Journal of Psychiatry 165, 390–394 (2008)
16. Botelho, M.F., Relvas, J.S., Abrantes, M., Cunha, M.J., Marques, T.R., Rovira, E., Fontes Ribeiro, C.A., Macedo, T.: Brain blood flow SPET imaging in heroin abusers. Annals of the New York Academy of Sciences 1074, 466–477 (2006)
17. Bunce, S.C., Izzetoglu, M., Izzetoglu, K., Onaral, B., Pourrezaei, K.: Functional near-infrared spectroscopy. IEEE Engineering in Medicine and Biology Magazine 25, 54–62 (2006)
18. Boas, D.A., Gaudette, T., Strangman, G., Cheng, X., Marota, J.J.A., Mandeville, J.B.: The accuracy of near infrared spectroscopy and imaging during focal changes in cerebral hemodynamics. Neuroimage 13, 76–90 (2001)
19. Chance, B., Zhuang, Z., UnAh, C., Alter, C., Lipton, L.: Cognition-activated low-frequency modulation of light absorption in human brain. Proceedings of the National Academy of Sciences 90, 3770–3774 (1993)
20. Chance, B., Anday, E., Nioka, S., Zhou, S., Hong, L., Worden, K., Li, C., Murray, T., Ovetsky, Y., Pidikiti, D.: A novel method for fast imaging of brain function, non-invasively, with light. Optics Express 2, 411–423 (1998)

21. Obrig, H., Villringer, A.: Near-infrared spectroscopy in functional activation studies. Can NIRS demonstrate cortical activation? Advances in Experimental Medicine Biology 413, 113–127 (1997)
22. Villringer, A., Chance, B.: Non-invasive optical spectroscopy and imaging of human brain function. Trends in Neurosciences 20, 435–442 (1997)
23. Miller, W.R.: Form 90: A Structured Assessment Interview for Drinking and Related Behaviors (Test Manual). NIAAA Project MATCH Monograph Series, vol. 5, NIH Publication No. 96-4004. National Institute on Alcohol Abuse and Alcoholism, Bethesda (1996)
24. Emrick, C.D.: A review of psychologically oriented treatment of alcoholism: I. The use and interrelationships of outcome criteria and drinking behavior following treatment. Quarterly Journal of Studies on Alcohol 35, 523–549 (1974)
25. Hunt, W.A., Barnett, L.W., Branch, L.G.: Relapse rates in addiction programs. Journal of Clinical Psychology 27, 455–456 (1971)
26. Sullivan, J.T., Sykora, K., Schneiderman, J., Naranjo, C.A., Sellers, E.M.: Assessment of Alcohol Withdrawal: the revised clinical institute withdrawal assessment for alcohol scale (CIWA-Ar). British Journal of Addiction 84, 1353–1357 (1989)
27. Jasper, H.: Report of the committee on methods of clinical examination in electroencephalography. Electroencephalogr. Clin. Neurophysiol. 10, 370–375 (1958)
28. Okamoto, M., Dan, H., Sakamoto, K., Takeo, K., Shimizu, K., Kohno, S., Oda, I., Isobe, S., Suzuki, T., Kohyama, K.: Three-dimensional probabilistic anatomical cranio-cerebral correlation via the international 10-20 system oriented for transcranial functional brain mapping. Neuroimage 21, 99–111 (2004)
29. Heinz, A., Wrase, J., Kahnt, T., Beck, A., Bromand, Z., Grüsser, S.M., Kienast, T., Smolka, M.N., Flor, H., Mann, K.: Brain activation elicited by affectively positive stimuli is associated with a lower risk of relapse in detoxified alcoholic subjects. Alcoholism: Clinical and Experimental Research 31, 1138–1147 (2007)
30. Breiner, M., Stritzke, W., Lang, A., Patrick, C.: The Normative Appetitive Picture System (Photographic Slides). Florida State University, Tallahassee (1995)
31. Ayaz, H., Shewokis, P.A., Curtin, A., Izzetoglu, M., Izzetoglu, K., Onaral, B.: Using MazeSuite and functional near infrared spectroscopy to study learning in spatial navigation. J. Vis. Exp. 56, e3443 (2011), doi:10.3791/3443
32. Ayaz, H., Shewokis, P.A., Bunce, S., Onaral, B.: An optical brain computer interface for environmental control. In: Conf. Proc. IEEE Eng. Med. Biol. Soc., pp. 6327–6330 (2011)
33. Sundsten, J.W., Mulligan, K.: Neuroanatomy interactive syllabus. University of Washington (1998), `http://www9.biostr.washington.edu/da.html`
34. George, M.S., Anton, R.F., Bloomer, C., Teneback, C., Drobes, D.J., Lorberbaum, J.P., Nahas, Z., Vincent, D.J.: Activation of prefrontal cortex and anterior thalamus in alcoholic subjects on exposure to alcohol-specific cues. Archives of General Psychiatry 58, 345–352 (2001)
35. Grüsser, S.M., Wrase, J., Klein, S., Hermann, D., Smolka, M.N., Ruf, M., Weber-Fahr, W., Flor, H., Mann, K., Braus, D.F.: Cue-induced activation of the striatum and medial prefrontal cortex is associated with subsequent relapse in abstinent alcoholics. Psychopharmacology 175, 296–302 (2004)
36. Janes, A.C., Pizzagalli, D.A., Richardt, S.: Brain reactivity to smoking cues prior to smoking cessation predicts ability to maintain tobacco abstinence. Biological Psychiatry 67, 722–729 (2010)
37. Paulus, M.P., Tapert, S.F., Schuckit, M.A.: Neural activation patterns of methamphetamine-dependent subjects during decision making predict relapse. Archives of General Psychiatry 62, 761–768 (2005)

A Filtering Method for Pressure Time Series of Oil Pipelines*

Jinhai Liu and Zhibo Yu

School of Information Science and Engineering, Northeastern University, Shenyang, 110004, P. R. China
jh_lau@126.com, 812014656@qq.com

Abstract. This paper proposes a two-stage filtering method for pressure time series in oil pipelines. First, adopt moving mean filter to smooth the signal contaminated by noise. Second, utilize the result as the input of the discrete or stationary wavelet filter to process the signal without losing its singularities including useful information. By testing this method on real data from oil pipelines, the results demonstrate an excellent performance on filtering the pressure time series and retaining data characteristics.

Keywords: Time series, Moving mean filter, DWT, De-noising, Singularities, SWT, CWT.

1 Introduction

Pipeline transportation which acts as one of the five major transport modes undertakes the onerous task of transporting crude oil and natural gas in china. It plays a significant role in the economic development, improvement of people's livelihood, social security and the foundation of national defense. After the completion of international crude oil pipeline, the length of domestic pipeline will increase to result in a wider, cross-border and even cross-region transportation network. Meanwhile, the security problem such as pipe aging, oil theft can result in a serious loss without prompt attention.

For monitoring the pipeline leak, experts design real-time leak detection system [1] based on pressure wave, optical fiber and sound wave. The method by pressure wave is to utilize pressure sensors installed in both ends to collect data to analyze the running condition for deciding whether leakage occurs and its location. For this purpose, obtaining the time series and processing it for further analysis is important. As real data, the collected data must be mixed with noise [2] so we need to filter it to remove noise and keep the useful information as much as possible.

For real data, a single method can not achieve the ideal performance [2]-[3]. This paper proposes a two-stage filtering method in which first utilize adaptive mean filter

* This work was supported by the National Natural Science Foundation of China (61104021, 61034005), the National High Technology Research and Development Program of China (2012AA040104), the Fundamental Research Funds for the Central Universities (N100304007, N100104102).

H. Zhang et al. (Eds.): BICS 2012, LNAI 7366, pp. 192–197, 2012.

to process the signal, then use wavelet to further filter it to remove noise and restore characteristics within it.

2 Adaptive Mean Filter for Time Series

The noise mixed in the time series can intervene and even cover its original useful characteristics, because of the ignorance of the noise type, we consider it as Gaussian white noise with the mean value of zero[4]-[5]. Because the pressure time series belong to low-frequency signals, this paper adopts moving mean filter to remove the signal mutation as follows:

$$Y^N(i) = \frac{1}{N}\sum_{k=1}^{N} P(i-k+1) \qquad i = 1, 2, \cdots \tag{1}$$

Where P indicates original signal, N is the length of window, Y is the signal after filtering. Theoretically, N is set at an integer multiple of the original signal to undermine noise, but at the same time, the mean filter also has the ability of smoothing the signal [6]. So in practical, the value of N is set as small as possible while ensuring the filtering effects.

This paper adopts N =5 to process the normal pressure signal and the fault signal. The results are showed in Fig.1 and Fig.2. Fig.1-(a) indicates the normal signal, the filtering result in Fig.1-(b) demonstrates the effectiveness of mean filtering and the signal turns smooth.Fig.2-(a)is a faction of fault signal with singularities, the result in Fig.2-(b)shows that this method has the capacity for restoring singularities without removing useful information.

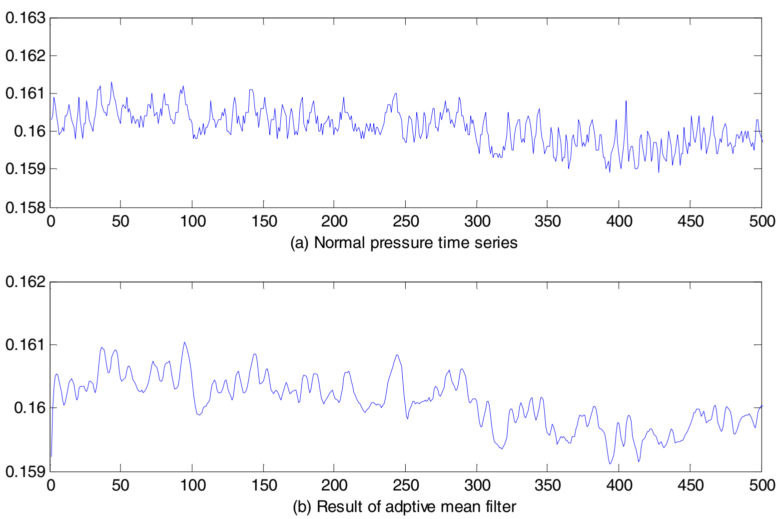

Fig. 1. Moving mean filter for normal pipeline pressure data

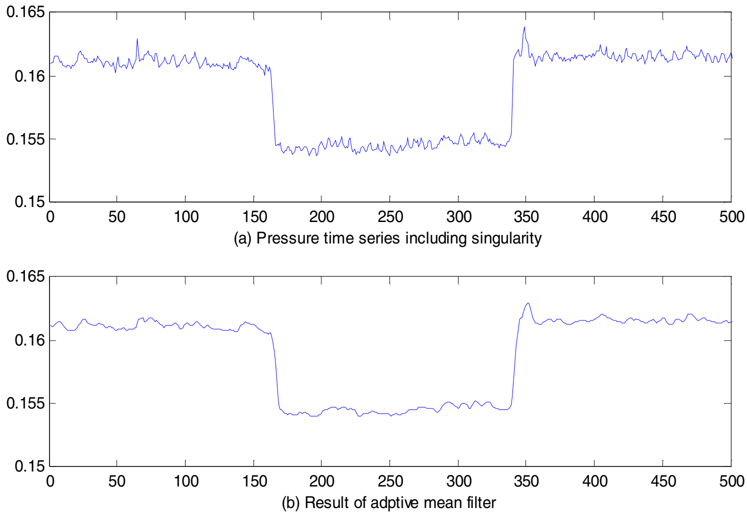

Fig. 2. Adaptive mean filter for the fault signal including singularities

3 De-noising by Discrete and Stationary Wavelet Transform for Pressure Time Series

3.1 De-noising by DWT

For unstable signals, the time-frequency domain windows need to be adjustable which require high time resolution in the high frequency region and high frequency resolution in the low frequency region. For this purpose, we introduce window function $\psi_{a,b}(t)=\frac{1}{\sqrt{|a|}}\psi(\frac{t-b}{a})$, and transformation is defined as:

$$W_{\psi}f(a,b)=\frac{1}{\sqrt{|a|}}\int_{-\infty}^{+\infty}f(t)\psi^*(\frac{t-b}{a})\mathrm{d}t \tag{2}$$

Where $a\in\mathbf{R}$ and $a\neq 0$, a is scale factor which indicates the extention about frequency. b is shift factor. Formula 2 defines the continuous wavelet transform(CWT).

Because computer can only process discrete data, scale factor and shift factor are discretized and discrete wavelet transform(DWT) is created. The rule is as follow:

$$a=a_0^{\,j}, b=ka_0^{\,j}b_0 \tag{3}$$

where $j\in Z$,step size a_0 is constant and $a_0\neq 1$ .Set $a_0=2$, $b_0=1$ to obtain dyadic wavelet. Then we get a cluster of wavelet functions $\psi_{j,k}(t)$,they are defined as

$$\psi_{j,k}(t)=a_0^{-j/2}\psi\left(\frac{t-ka_0^{\,j}b_0}{a_0^{\,j}}\right)=a_0^{-j/2}\psi\left(a_0^{-j}t-kb_0\right) \tag{4}$$

Through further analysis, we can know the coefficients of DWT are:

$$C_{j,k} = \left\langle f(t), \psi_{j,k}(t) \right\rangle = \int_{-\infty}^{+\infty} f(t)\overline{\psi_{j,k}(t)}dt \tag{5}$$

And the reconstruction function is

$$f(t) = c\sum_{-\infty}^{+\infty}\sum_{-\infty}^{+\infty} C_{j,k}\psi_{j,k}(t) \tag{6}$$

Where c is a constant which is not depend on original signals.

Stationary wavelet transform(SWT) is a wavelet transform algorithm designed to overcome the lack of translation-invariance of the discrete wavelet transform (DWT). Translation-invariance is achieved by removing the down-sampling and up-sampling in the DWT and up-sampling the filter coefficients by a factor of $2^{(j-1)}$in the *j*th level of the algorithm. The SWT is an inherently redundant scheme as the output of each level of SWT contains the same number of samples as the input. This algorithm is more famously known as refers to inserting zeros in the filters.

In essence, de-noising by wavelet is an approximation problem in which searching for an optimal approximation in the function space spanned by wavelet basis through a certain measure level. The purpose is to remove the noise from the original signal by finding the best mapping in function space from original signals to wavelets.

In terms of signal processing, de-noising by wavelet is a signal-filtering task where wavelet filter is somewhat a low-pass filter and wavelet filtering can be regarded as a combination of feature extraction and low-pass filtering. This procedure is showed in Fig.3

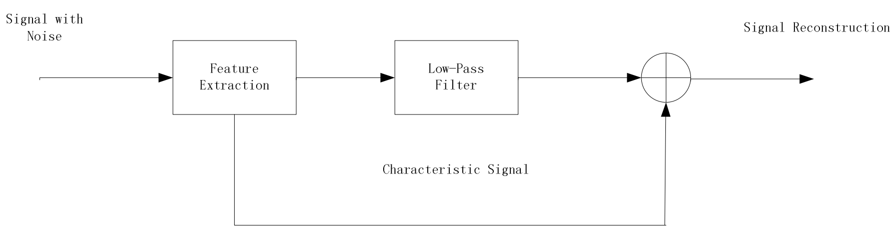

Fig. 3. The principle of wavelet de-noising

In practical, a one-dimension signal with noise can be described as

$$f(t) = s(t) + \sigma e(t), t = 0,1,\ldots, n-1 \tag{7}$$

Where $s(t)$ is the pure signal, $e(t)$ is noise, $f(t)$ indicates the signal, σ is noise-level coefficient.

In conclusion, useful information in real word usually presents as low-frequency and stable signals while noise is usually in high-frequency domain. The procedure de-noising by SWT is:

1) Decompose the original signal by wavelet transformation.
2) Threshold processing of wavelet high-frequency coefficients.
3) Signal reconstruction by wavelet.

3.2 De-noising by SWT for Pressure Time Series

De-noise the pressure time series by SWT and the results are showed in Fig.4 and Fig.5.the parameters are set as:

1) Mother wavelet: bior 3.1
2) Decomposition level:5
3) Threshold rule: Minimax
4) Rescaling method: single

Fig.4 is the result from the signal in fig.1(b) is processed which demonstrates a ideal filtering effect.Fig.5 is to test the SWT whether can keep the singularities in original signals where using the signal in fig.2(b).From this simulation, we can conclude the process has a positive effect on the subsequent analysis on the signal.

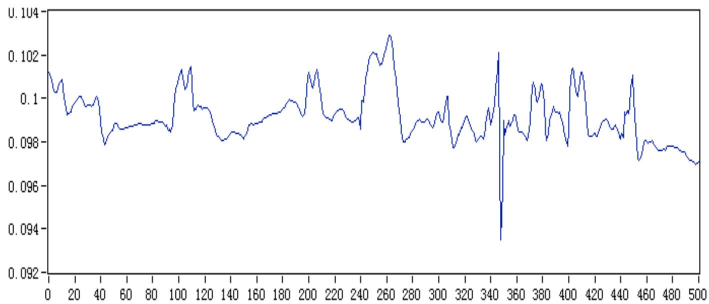

Fig. 4. SWT filtering of normal pipeline pressure data

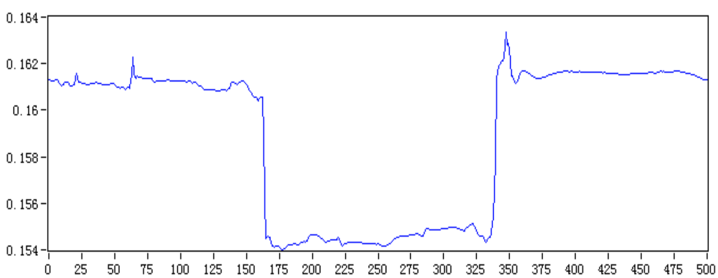

Fig. 5. SWT filtering of abnormal pipeline pressure time series

4 Conclusion

This paper designs a method to process the pressure time series. First, utilize the moving mean filter to smooth the original signal and then take the result as the input of discrete wavelet filter to complete the second filtering. If the result is not satisfactory enough, use SWT to supersede DWT to de-noise the data due to its time-invariance for retaining the original position of singularities at the cost of more compute capacity. Through this two-stage filtering, original signal can be processed without losing its inherent characteristics and build a foundation for further analysis, such as using CWT for locating singularities in fault detection. The result demonstrates the capabilities of the combination of moving mean filter , DWT and SWT to solve real-world problems.

References

1. Shen, G., Li, G., Weike, Zuo, Y.: Leakage Detection Technology for Underground Gas pipeline. Undamaged Detection 112(5), 267–271 (2006)
2. Er, M.J., Sia, A.M.: Adaptive Noise Cancellation using Dynamic Fuzzy Neural Networks Algorithm. In: Proceedings15th of IFAC World Congress, Barcelona, Spain (2002)
3. Kwon, D., Vannucci, M., Song, J.J., Jeong, J., Pfeiffer, R.M.: A Novel wavelet-based Thresholding Method for the Pre-processing of Mass Spectrometry Data that accounts for Heterogeneous Noise. Proteomics 8, 3019–3029 (2008)
4. Coombes, K.R., Tsavachidis, S., et al.: Improved Peak Detection and Quantification of Mass Spectrometry Data Acquired from Surface-enhanced Laser Desorption and Ionization by Denoising Spectra with the Undecimated Discrete Wavelet Transform. Proteomics 5, 4107–4117 (2005)
5. Cichocki, A., Vorobyov, S.A., Rutkowski, T.: Nonlinear Interference Cancellation using Neural Networks. In: Symposium on Nonlinear Theory and its Applications, pp. 875–878. IEEE Press, Hawaii (1999)
6. Gao, C.H., Qian, J.X.: Evidence of Chaotic Behavior in Noise from Industrial Process. IEEE Trans., Signal Processing 55(6), 2844–2877 (2007)

The Role of Event Boundaries in Language: Perceiving and Describing the Sequence of Simultaneous Events

Shulan Lu and Lonnie Wakefield

Department of Psychology,
Texas A & M University–Commerce, TX, 75429-3011
lu.shulan@gmail.com

Abstract. Studies in event perception have shown that people impose boundaries onto the constant flux of perceptual information and perceive the world to be composed of a series of discrete events. A significant question arises to whether humans impose boundaries onto events that unfold along multiple tracks and perceive them to be one psychological entity (i.e., temporal chunking). The traditional method of event segmentation has difficulties with investigating simultaneous events. The current study investigated whether and how talking about events reveals the psychological event boundaries imposed by perceivers. The current study manipulated the temporal parameters of stimulus events, controlled the causality of events, and thus translated the linguistic differences into measurable properties of events. Participants viewed films of simultaneous events, and performed linguistic acceptability judgments. The results showed there is a correspondence between how people talk about the event sequence and the order in which events occur following event segmentations.

1 Introduction

How do people perceive events that unfold along multiple tracks? Imagine the following scenario. John begins to read a newspaper while continuing to drink coffee. For perceivers, there appears to be two spans occurring one after another: (a) John drinking coffee alone first (initial span); and (b) John drinking coffee and reading a newspaper (coterminous span). For language users, it seems natural to say *John drinks coffee before he reads a newspaper*, where reading a newspaper is a sub-event of the coterminous span. Does talking about the sequence of simultaneous events map onto the event structure being perceived? Cognitive linguists have shown there is a close correspondence between language and event structure. For example, the semantic components of motion events are indicated to be part of the conceptual structures ([1] [2]). The current study aims to demonstrate how talking about events is important for understanding the perceptual representations of events.

1.1 Event Perception

The world is presented to humans as a continuous flux of perceptual information, however, humans impose boundaries upon this continuous stream and perceive the

H. Zhang et al. (Eds.): BICS 2012, LNAI 7366, pp. 198–207, 2012.

world to be composed of a series of discrete meaningful events. This temporal chunking of perceptual experience is crucial to the understanding of consciousness, where our phenomenological experiences are segmented and distinctions are made in terms of what is now versus what was before [3] [4]. A number of studies have demonstrated how event boundaries serve as psychological anchors for general cognitive and linguistic functioning [5] [6]. For example, event boundaries are a reliable predictor for the memory and comprehension of events.

To investigate the relationship between perceiving and communicating event structures, participants described events while watching video clips of everyday events [7]. Using a Newtson task [8], participants indicated when an event ends and another begins by pressing the spacebar on a computer keyboard. The results showed that perceivers segment sequential everyday events at multiple time scales simultaneously. That is, the perception of an event and its sub-events are orchestrated and form a temporally aligned hierarchical relationship. Moreover, describing events during segmentation reinforced participants to build such a structure.

Compared with perceiving events that unfold along a single track (i.e., one agent in service of one goal at a time), there has not been much work investigating how people perceive simultaneous events. The Newtson task is difficult if not possible to use for investigating simultaneous events. To get around the methodological difficulties, Lu, Harter, and Graesser [9] presented participants animations of fish swimming activities that systematically varied temporal parameters and obtained the benchmark for comparing the external and internal representations. Participants made judgments on temporal relations by performing a 7-alternative forced choice task. The 7-alternative choices refer to Allen's 7 temporal relations [10] [11], which will be described in details later.

Analogous to the results from Zacks et al. [5] that coarse and fine grained segmentation boundaries are temporally aligned, Lu et al. provided evidence that perceivers impose boundaries onto the simultaneous perceptual stream and thus perceive one event at a time.

1.2 Event Boundaries and Perceived Event Sequence as Encoded in Before versus After

Given the profound importance of event boundaries in our cognitive functioning, it is reasonable to think event boundaries will play a significant role in how people talk about the sequence of simultaneous events. Before formulating specific accounts of how event boundaries guiding the language of event sequence, it is necessary to describe Allen's interval based representation, which includes all of the logical possibilities of temporal relations between two separate activities.

Figure 1 illustrates Allen's seven temporal relations as well as the stimuli used in the current study. Each double headed arrow represents an activity that occurs over some time interval. For example, BEFORE means two activities occur in succession but with some time in between, whereas EQUAL means two activities begin and end at the same time. AFTER refers to the same temporal relation as BEFORE. For the sake of convenience, only BEFORE was used as the notation in Figure 1. To accurately specify

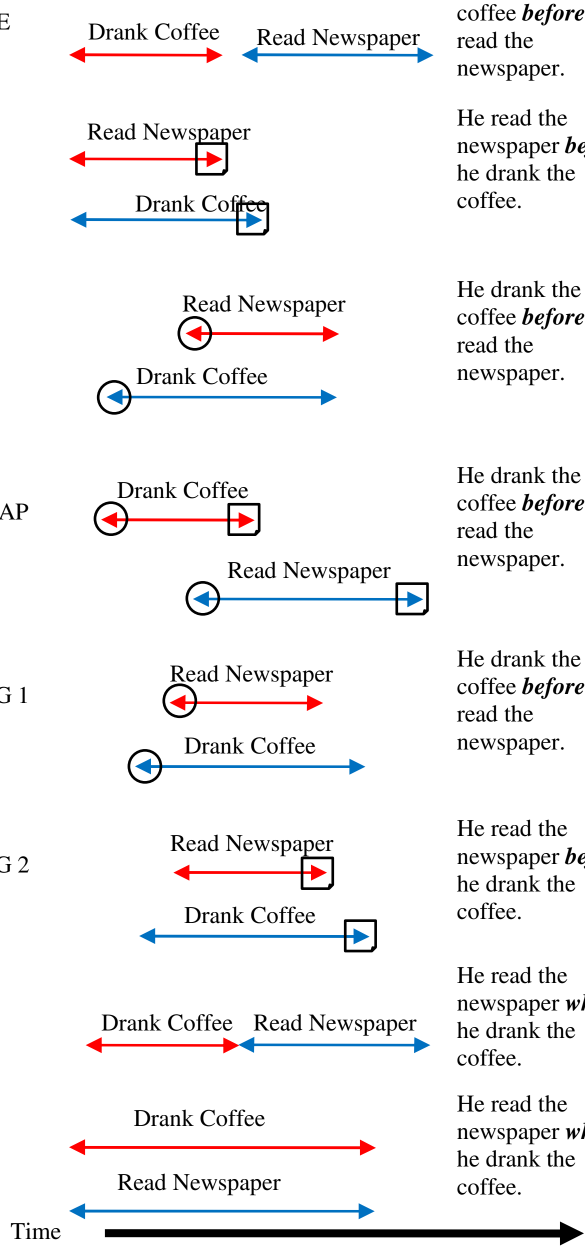

Relation	Diagram	Before	After
BEFORE		He drank the coffee ***before*** he read the newspaper.	He read the newspaper ***after*** he drank the coffee.
START		He read the newspaper ***before*** he drank the coffee.	He drank the coffee ***after*** he read the newspaper.
FINISH		He drank the coffee ***before*** he read the newspaper.	He read the newspaper ***after*** he drank the coffee.
OVERLAP		He drank the coffee ***before*** he read the newspaper.	He read the newspaper ***after*** he drank the coffee.
DURING 1		He drank the coffee ***before*** he read the newspaper.	He read the newspaper ***after*** he drank the coffee.
DURING 2		He read the newspaper ***before*** he drank the coffee.	He drank the coffee ***after*** he read the newspaper.
MEET		He read the newspaper ***while*** he drank the coffee.	He read the newspaper ***while*** he drank the coffee.
EQUAL		He read the newspaper ***while*** he drank the coffee.	He read the newspaper ***while*** he drank the coffee.

Fig. 1. Allen's temporal relations and example sentences in Experiment 1. Circles indicate the beginning, whereas square indicate the end boundaries being compared.

the physical temporal frames of simultaneous events, perceivers need to account for different type of event boundaries: the beginnings, the ends, and the boundaries where events either overlap or diverge from each other temporally (i.e., *overlap* versus no *overlap*). However, due to various constraints (e.g., attention) in processing such complex events, the perceived event boundaries may not be aligned with the physical event boundaries. Lu et al. [9], for example, showed that FINISH activities are frequently perceived to be OVERLAP events.

Allen noted that these notations such as BEFORE do not correspond to the word *before* in natural language. Thus which activity begins first and which second is of course important for the linguistic meaning of *before*, but in terms of temporal relations, both cases represent the situation where one activity precedes the other with some time in between. Note that the activities in each temporal relation are interchangeable. Therefore, Allen's representations consist of 7 relations instead of 13 relations.

In the current study, we started with a simple beginning state hypothesis that calibrates the use of before or after by comparing the beginnings of two perceived events. To avoid confusions, when we discuss events with varying temporal relations (e.g., START versus FINISH) and these events are treated as physical occurrences in the world, we will refer to them as activities. The beginning state hypothesis stipulates that *before* (or *after*) encodes the beginning of one event preceding (or following) the beginning of another perceived event. Based on this beginning state hypothesis, *before* and *after* both can encode FINISH, OVERLAP, and DURING1 activities. Use FINISH as an example. Figure 1 shows the following two perceived events: (a) drinking coffee (initial span); and (b) drinking coffee and reading a newspaper (coterminous span). According to the beginning state hypothesis, the following sentences would be acceptable: (a) he drank the coffee before he read the newspaper (i.e., the beginning of *drinking coffee* precedes the beginning of the sub-event *reading the newspaper*); and (b) he read the newspaper after he drank the coffee (i.e., the beginning of *reading the newspaper* occurred later than the beginning of *drinking coffee*).

See Table 1 for this set of predictions and Figure 1 for example events and sentences. In the case of OVERLAP activities, if people do not perceive the coterminous span as one event psychologically, then people could simply pick out any sub-event and compare the beginning state with the end state of another sub-event. To rule out this possibility, we tested the acceptability of the corresponding language descriptions as indicated in OVERLAP 2.

Alternatively, an end state hypothesis proposes that people calibrate the use of *before* (or *after*) by comparing the endings of two perceived events. The end state hypothesis would state that *before* (or *after*) encodes the ending of one event preceding (following) the ending of another perceived event. Based on the end state hypothesis, *before* and *after* can both encode START, and OVERLAP, and DURING 2 (e.g., comparing the ending of the coterminous span sub-event *reading newspaper* with that of *drinking coffee* activities).

The beginning versus end state hypothesis has overlap, which is not surprising given the event structure of simultaneous events. However, they make opposite predictions regarding the acceptability of START versus FINISH. These two hypotheses both were extreme versions. They either take into account of the earliest points of events or the end point of events. Whether the predictions on START versus FINISH could pan out provides important evidence as to whether people impose event boundaries onto the coterminous span. To our knowledge, there is hardly any experimental work investigating this question. In the section that follows, we will review relevant work in linguistics and see if theoretical analysis in linguistics yields convergent predictions.

Table 1. Predictions by Theory

	Activity type					
	BEFORE	START	FINISH	OVERLAP	DURING1	DURING2
Beginning	+	-	+	+	+	-
End	+	+	-	+	-	+

Notes: The plus (+) refers to being acceptable, whereas the minus (-) refers to being unacceptable. When a theory generates the same predictions regarding before and after, there is no parenthesis indicating whether the predictions are regarding before or after. For examples of event activity type see Figure 1.

1.3 Before versus After

In linguistics and philosophy, there has been a long tradition in studying event language. It is beyond the scope of current work to provide a comprehensive review of the literature in this area. Instead only the most relevant work will be discussed below. Vendler [12] proposed there are four types of verbs: activities (e.g., run around), accomplishments (e.g., run a mile), achievements (e.g., start / stop/ resume), and states (e.g., want). Following Vendler's tradition, Moens and Steedman [13] proposed to distinguish atomic (e.g., recognize) versus extended events (e.g., build a house). Within extended events, there are two subcategories: culminated process (e.g., build a house) versus process without consequence (e.g., swim). The function of various linguistic devices is to coerce the events and states being depicted into an elementary event-complex called a 'nucleus". The events and states in the nucleus predicates something more than temporal sequence, that is, some contingent relation such as a causal link or an enablement relation between the two events.

Anscombe [14] proposed that A *before* B versus A *after* B are not converses. More specifically, A *before* B is applicable as long as any point of time in an event A precedes all points of time in event B, whereas A *after* B is applicable if some point of time in an event A proceeds some point in event B. Anscombe's proposal clearly indicated how important the beginnings of events are when it comes to the use of before. By Anscombe's analysis, it is unacceptable to describe the temporal sequence of simultaneous events using before, whereas it is acceptable to describe the temporal sequence using after.

As a further development, Beaver and Condoravdi [15] used the operator *earliest* to define the reference point. *Before* is applicable when some point of an event A occurs prior to the earliest point of an event B, whereas *after* is applicable when some point of an event A follows the earliest point of an event B. This proposal applied a uniform analysis on *before* and *after,* and thus made the contrast of the beginning states explicit.

Following Beaver and Condoravdi's analysis, it is acceptable to describe the sequence of events in FINISH, OVERLAP, and DURING1 activities using before, whereas it is unacceptable to describe the sequence of events in START activities using before. It is acceptable to describe the sequence of events in FINISH, OVERLAP, and DURING1 using after, whereas it is unacceptable to describe the sequence of events in START. See Table 1 for this set of predictions.

Despite the fact that the above linguistic accounts generated slightly different predictions regarding the use of before versus after, they all implied the importance of using the beginning states of events in calibrating the use of before and after. Furthermore, the Beaver and Condoravdi proposal could make very similar predictions as the beginning state hypothesis formulated before. The Beaver and Condoravdi proposal include predictions regarding the temporal sequence of events and states, whereas the beginning state hypothesis only makes predictions of events.

2 Experiments: Before versus After as Conjunction

The current study aims to test the beginning versus end state hypothesis. All stimuli were constructed based on Allen's 7 temporal relations. BEFORE activities were used as the baseline comparison, whereas START, FINISH, OVERLAP, and DURING activities were used as the critical categories containing simultaneous events. MEET and EQUAL activities were used as the filler stimuli, where event temporal relations were described using while.

Two categories of stimuli were developed: humans performing routine tasks or animations of two fish swimming at various angels. These two categories of stimuli corresponded to two categories of verbs (e.g., drink coffee versus swim) according to Moens and Steedman. After viewing each stimulus, a sentence describing the temporal relationship between the two events was displayed. Participants rated the linguistic acceptability of the sentence. Experiment 1 tested the use of before as a conjunction between two clauses, whereas Experiment 2 tested the use of after. Separate groups of participants were recruited for each experiment. Thirty-six college students at Texas A&M University-Commerce participated in exchange for course credit.

2.1 Experiment 1: Before as a Conjunction between Two Clauses

Stimulus Materials and Design. There were two types of stimulus films: (a) two fish swimming; and (b) a person enacting two actions. Each fish swimming animation was rendered in 3d Studio Max, lasting 25 seconds or less, whereas each human enacting action video was recorded using a Sony HandyCam camera, lasting between 35 and 40 seconds.

Fish swimming animations. For each animation, there were two fish of different color that swim above a net with a grid shape in a 3D fish tank environment, with varied timing between the beginning and end points of their journeys. For example, one fish may start first but finish last. The animation also varied the corners from which fish swam (i.e., spatial orientation variation) along the grid. There were six variations of respective spatial orientation, including two versions where the fish swam intersecting paths and four versions where they swam in parallel. This created a total of 42 fish swimming animations (6 spatial orientations x 7 temporal relations).

Given that previous experiments did not find significant item effects [9], a subset of 18 animations of varying spatial orientations was selected to represent the critical items (START, FINISH, OVERLAPs 1-2, and DURINGs 1-2) as indicated in Figure 1. In addition, three BEFORE animations were used as baseline comparison trials, and another six animations (MEETs and EQUAL activities) were designated as filler trials, for a total of 27 fish animations.

Human enacting actions films. Each human enacting action film depicted a person enacting two distinct actions, each of which lasted over an interval of time. Like the fish swimming animations, the beginning and end points of each action was varied to correspond to Allen's seven temporal relations.

The activities performed were varied by using 12 different themes. For example, one theme depicted a man reading a newspaper and drinking coffee, while another theme showed a woman talking on the phone while sorting mail. This created a total of 84 possibilities of films (12 themes x 7 temporal relations). Consider a BEFORE stimulus film. The actor could drink coffee first. Shortly after the coffee was done, the actor began to read the newspaper. Alternatively, consider an OVERLAP film. After drinking coffee for awhile, the actor started reading newspaper. Other than the two actions, there were entrance events that led to the action of drinking coffee and exit events. For the 7 variations of the activity of drinking coffee and reading a newspaper, the actor walked into frame with the newspaper, put down the newspaper, and sat down for coffee. After reading the newspaper, the actor sat back and stared into space.

A previous study showed that people had over 90% accuracy determining whether events begin or end at the same time after seeing a stimulus film [16]. Again a subset of 18 films was selected to represent the critical test cases. In addition, six more films (BEFOREs) were used as baseline comparison trials, and another six films (MEETs and EQUALs) were designated as filler trials, for a total of 27 human enacting action films.

Block Trials. In total, 54 stimulus animations and films were used in the experiment, so that each session was not longer than one hour and repetitiveness for the same everyday activities within each block was low. These 54 stimulus films were presented in three blocks. Within each block, 9 fish swimming animations and 9 human enacting action videos were used. All the sound in the stimulus films was muted during experiments. See sample stimuli http://faculty.tamu-commerce.edu/slu/SampleStimulusFilms.html. Example sentences can be found in Figure 1.

The same two events were never repeated within a block, that is, if participants saw the DURING events composed of *drinking coffee* and *reading a newspaper* in one block, they would not see the same two events having a different temporal relation, e.g., START, in the same block.

Procedure. Before the experiment, participants were told they would be viewing some events in videos and then they would judge whether a sentence describing two events in each film was linguistically acceptable. The rating scale ranged from 1 to 6, with 1 and 6 labeled as "not at all acceptable" and "perfectly acceptable," respectively.

The experiment was conducted on PCs with 17 inch monitors using MediaLab [17]. Participants received the following events in each trial: (1) a film played and then disappeared at the end of the film, (2) a sentence describing two target events in the film was presented together with the rating scale. The presentation order within blocks was randomized, and the presentation order of the three blocks was counterbalanced.

Results and Discussion. FINISH (5.08), DURING 1 (4.83), and OVERLAP (4.92) had acceptability ratings significantly higher than START (2.93), DURING 2 (1.82). The ratings of FINISH, DURING 1, and OVERLAP were comparable to BEFORE (5.87). In addition, we randomly compared the beginning of one sub-event with the ending of another sub-event using OVERLAP activities. Consistent with our proposal that perceptual segmentation underlies the linguistic description, the acceptability rating of such sequence was significantly lower than chance (OVERLAP 2, $M = 1.77$).

We ran a 2 x 2 analysis of variance (ANOVA), comparing the beginning state (the mean acceptability ratings of FINISH and DURING 1) with the end state (the mean acceptability ratings of START and DURING 2) and taking into account of stimulus type (human enacting action versus fish swimming). The acceptability ratings for the beginning state were significantly higher than those for the end state, $F(1, 17) = 58.83$, $MSE = 2.04$, $p < .0001$, $\eta_p^2 = .78$. There were neither significant interactions nor significant main effects of stimulus type. These results showed support for the beginning state hypothesis, in that people use the order in which the beginning states of perceived events take place to calibrate the use of *before.*

2.2 Experiment 2: After as a Conjunction between Two Clauses

Materials, design, and procedure were the same as Experiment 1 except that the sentences were reworded. Unlike the ratings on the *before* sentences in Experiment 1, most of the ratings were around 3.5 except OVERLAP (4.53), the midpoint of a 1-6 point scale. We ran the same 2 x 2 ANOVA on the acceptability ratings as in Experiment 1. There were significant interactions, $F(1, 17) = 8.20$, $MSE = .67$, $p < .05$, $\eta_p^2 = .33$. For fish swimming events, the mean acceptability ratings of FINISH and DURING were 4.15. No other means were significantly above the midpoint. There were no other significant main effects.

Given the limited use of *after* in describing simultaneous events, an additional analysis was run to compare OVERLAP with the AFTER control trials. There were significantly higher ratings of AFTER as opposed to OVERLAP, $t(17) = 6.26$, $p < .001$, $d = 2.27$. In addition, participants gave higher acceptability ratings to fish swimming OVERLAP activities than human enacting action stimuli, $t(17) = 4.65$, $p < .0001$. Same as Experiment 1, the acceptability ratings of OVERLAP 2 in terms of using after was significantly lower than chance, $M = 1.97$.

3 General Discussion

Understanding how people talk about events is important for understanding nonlinguistic representations of events. To what extent does the temporal chunking of perceptual inputs guide the linguistic marking of the now and then conscious experiences? The current study systematically manipulated the temporal parameters of events and controlled the causality of events, and thus translated the linguistic differences into the measurable properties of the real world. The current study provided some evidence that people performing simultaneous segmentation. People talk about the order of simultaneous events primarily using *before* instead of *after,* and people calibrate their uses of *before* depending on the differences between beginning states. If there is no sign of simultaneous segmentation, for example, then there is a significantly greater chance of people finding the before descriptions regarding the START activities to be acceptable. If that had been the case, then people would have perceived one of the sub-events in the coterminous span to have begun earlier.

In current study, the events in the *before* sentences were described following the iconicity principle [18], whereas the events in the *after* sentences were opposite to the order in which events unfolded. To what extent might the results be affected by the sentence order? For example, *before* may not apply to most of the simultaneous events once it is moved to the beginning of a sentence because the event order in the sentence violates the iconicity principle. However, if indeed there is a correspondence between perceptual representations of events and the linguistic representations, then the predictions of the beginning state should hold. We performed an additional experiment addressing these possibilities. The results showed support for the beginning state hypothesis.

A question arises as to the role of end boundaries in describing the sequence of simultaneous events. As discussed previously, the coterminous span is perceived as one event, even though perceivers can always further segment it into sub-events. In the case of the example START activity, the coterminous span is the first event perceived, and the event of drinking coffee is the final span. However, the event of drinking coffee is perceived as an extension of the previous event. Even though the ending of drinking coffee occurred later than the sub-event of reading a newspaper, our world knowledge does not support making the statement: he drank the coffee after he read the newspaper. This idea is consistent with Moens and Steedman's [13] proposal of linguistic devices coercing events and states into contingency relations. If our knowledge of the world does not support such contingency relation, then the sentence is unacceptable.

Simultaneous events require more processing resources than sequential events. Mapping the differences in beginning states onto the linguistic representations could potentially lower the processing demands compared with mapping the differences in end states. In the former case, speakers do not have to rely on all the relative intervals between different types of event boundaries in memory representations. For example, speakers do not need to compute and map the relative intervals between the beginning of event A and end of event B.

The current study demonstrated the role of event boundaries in talking about the sequence of simultaneous events. This adds a piece of solid evidence to the position taken by a number of cognitive linguists that there is a close correspondence between language and event structure. Nevertheless, language has its own quirks. The order in which events are presented in the sentence does not affect the use of *before,* however, it affects the use of *after.* The current study used stimulus activities that did not have a strong causal contingency, particularly in the case of fish swimming events. Future studies need to investigate events that have a higher degree of causal relations. It is an exciting direction to push forward: how do our less conscious higher order knowledge structures meddle with the temporal chunking of conscious experiences and the explicit linguistic marking of such experiences?

Acknowledgments. This work is supported by a grant from Texas Advanced Research Program, a grant from US National Science Foundation (#0916749), and a grant from Texas A & M University – Commerce Faculty Research Enhancement. We thank Jeff Zacks for comments on a draft of this article, and Gang Wu for formatting this article.

References

1. Talmy, L.: Semantics and syntax of motion. In: Kimball, J.P. (ed.) Syntax and Semantics, vol. 4, pp. 181–238. Academic Press, New York (1975)
2. Talmy, L.: Toward a cognitive semantics. MIT Press, Cambridge (2000)
3. James, W.: The principles of psychology, vol. 1. Henry Holt, New York (1890)
4. Zacks, J.M.: How we organize our experience into events. Psychological Science Agenda 24 (2010)
5. Zacks, J.M., Tversky, B., Iyer, G.: Perceiving, remembering, and communicating structure in events. Journal of Experimental Psychology: General 130, 29–58 (2001)
6. Zacks, J., Speer, N., Reynolds, J.R.: Segmentation in reading and film comprehension. Journal of Experimental Psychology: General 138, 307–327 (2009)
7. Zacks, J.M., Tversky, B.: Event structure in perception and conception. Psychological Bulletin 127, 3–21 (2001)
8. Newtson, D.: Attribution and the unit of perception of ongoing behavior. Journal of Personality and Social Psychology 28, 28–38 (1973)
9. Lu, S., Harter, D., Graesser, A.C.: An empirical and computational investigation of event temporal relations. Cognitive Science 33, 344–373 (2009)
10. Allen, J.F.: Towards a general theory of action and time. Artificial Intelligence 23, 123–154 (1984)
11. Allen, J.F.: Time and time again: The many ways to represent time. International Journal of Intelligent Systems 6, 341–355 (1991)
12. Vendler, Z.: Verbs and times. Philosophical Review 66, 143–160 (1957)
13. Moens, M., Steedman, M.: Temporal ontology and temporal reference. Computational Linguistics 14, 15–28 (1988)
14. Anscombe, G.E.M.: Before and after. Philosophical Review 73, 3–24 (1964)
15. Beaver, D., Condoravdi, C.: A uniform analysis of before and after. In: Young, R., Zhou, Y. (eds.) Proceedings of SALT 13, Cornell University, Ithaca (2004)
16. Lu, S., Wakefield, L., Faulkenberry, T.: The role of beginnings, ends, and overlap in event representations. Paper Presented at the 47th Annual Meeting of the Psychonomic Society, Houston, TX (2006)
17. Jarvis, B.G.: MediaLab research software (Version 2000) (Computer Software). Empirisoft, New York (2000)
18. Zwaan, R.A., Radvansky, G.A.: Situation model in language comprehension and memory. Psychological Bulletin 123, 162–185 (1998)

Hyperchaotification Control for a Class of 3D Four-Wing Chaotic Systems via State Feedback

Shuang Wu* and Guohua Fu

School of Economics and Management, Hainan University, Haikou, China
wshteaqer@163.com
http://www.springer.com/lncs

Abstract. A novel hyperchaotification control method for a class of 3D four-wing chaotic systems is presented in this paper. A simple state feedback is introduced into this kind of chaotic systems as a new variable's evolving law. By choosing appropriate feedback gain and feedback variable, the generated system can be guaranteed to be dissipative and have two positive Lyapunov exponents. Therefore, the hyperchaos is generated. Simulation study is carried out to verify the effectiveness of the proposed hyperchaotification approach.

Keywords: hyperchaotification, 3D four-wing chaotic system, Lyapunov exponents, state feedback.

Recently, many control methods are applied to the control of chaos or hyperchaos, such as linear state feedback control, active control, passive control, neural network control, adaptive control, impulsive feedback control, delayed feedback control, inverse optimal control, guaranteed cost control, etc. For hyperchaos, some basic properties are described as follows. (i) Hyperchaos exists only in higher-dimensional systems, i.e., not less than four-dimensional (4D) autonomous system for the continuous time cases. (ii) It was suggested that the number of terms in the coupled equations that give rise to instability should be at least two, in which one should be a nonlinear function.

Based on the above analysis, the hyperchaotification control problem of a class of 3D four-wing chaotic systems is studied in this paper. To realize this object, a simple state feedback is introduced into this kind of chaotic systems as a new variable's evolving law. By choosing appropriate feedback gain and feedback variable, the generated system can be guaranteed to be dissipative and have two positive Lyapunov exponents. Therefore, the hyperchaos is generated. Simulation study is carried out to verify the effectiveness of the proposed hyperchaotification approach.

1 Preliminaries

Consider the following 3D four-wing chaotic system:

$$\begin{cases} \dot{x}_1(t) = ax_1(t) - bx_2(t)x_3(t), \\ \dot{x}_2(t) = -cx_2(t) + x_1(t)x_3(t), \\ \dot{x}_3(t) = kx_1(t) - dx_3(t) + x_1(t)x_2(t), \end{cases} \tag{1}$$

* Corresponding author.

H. Zhang et al. (Eds.): BICS 2012, LNAI 7366, pp. 208–212, 2012.

where $x_1(t)$, $x_2(t)$ and $x_3(t)$ are state variables, a, b, c, d and k are system's parameters. As is described in Ref. [**?**], the above system are hyperchaotic when the parameters are chosen appropriately. For example, when the parameters are chosen as $a = 4$, $b = 6$, $c = 10$, $d = 5$ and $k = 2$, the considered system is chaotic. The corresponding chaotic attractor is given in Fig. 1-4.

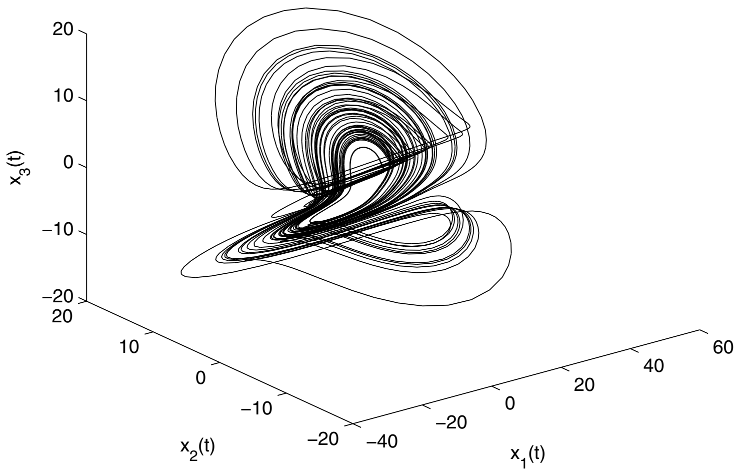

Fig. 1. The chaotic attractor (i)

The main goal is to introduce a new variable into the chaotic system (1) and choose appropriate evolving law of the new variable to make the constructed 4D system generate hyperchaotic attractor.

2 Hyperchaotification Control for 3D Four-Wing Chaotic System

First of all, a new variable $x_4(t)$ is introduced and we construct the following four-dimensional system:

$$\begin{cases} \dot{x}_1(t) = ax_1(t) - bx_2(t)x_3(t), \\ \dot{x}_2(t) = -cx_2(t) + x_1(t)x_3(t), \\ \dot{x}_3(t) = kx_1(t) - dx_3(t) + x_1(t)x_2(t), \\ \dot{x}_4(t) = hx_1(t), \end{cases} \tag{2}$$

where $x_1(t)$, $x_2(t)$, $x_3(t)$ and $x_4(t)$ are state variables, a, b, c, d, k and h are system's parameters.

For the above system, it holds that

$$\begin{aligned} \Delta V =& \frac{\partial \dot{x}_1(t)}{\partial x_1(t)} + \frac{\partial \dot{x}_2(t)}{\partial x_2(t)} + \frac{\partial \dot{x}_3(t)}{\partial x_3(t)} + \frac{\partial \dot{x}_4(t)}{\partial x_4(t)} \\ =& a - c - d \end{aligned} \tag{3}$$

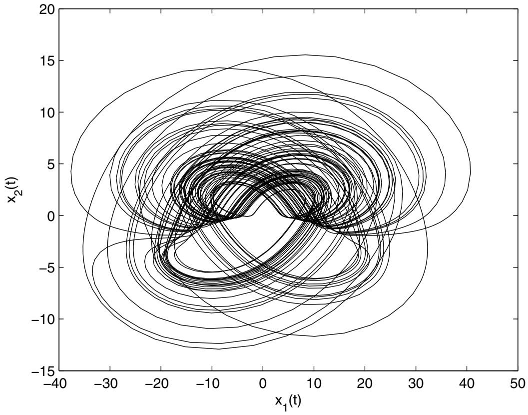

Fig. 2. The chaotic attractor (ii)

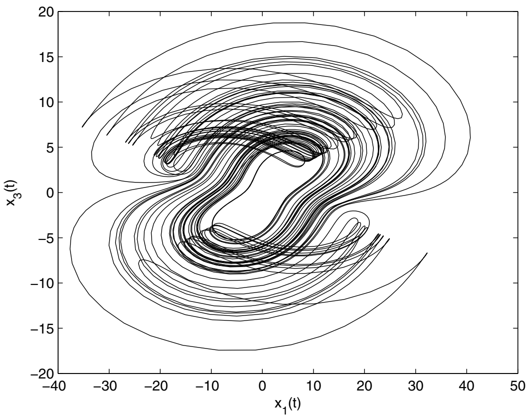

Fig. 3. The chaotic attractor (iii)

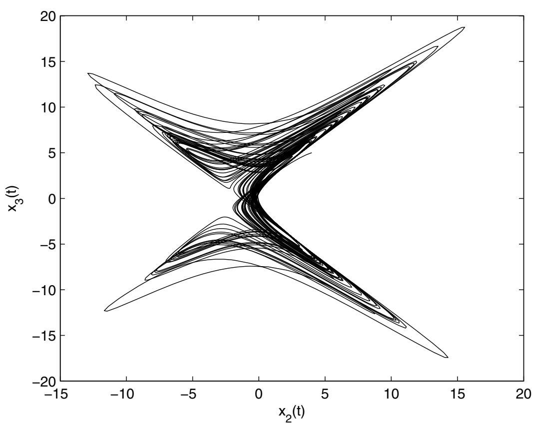

Fig. 4. The chaotic attractor (iv)

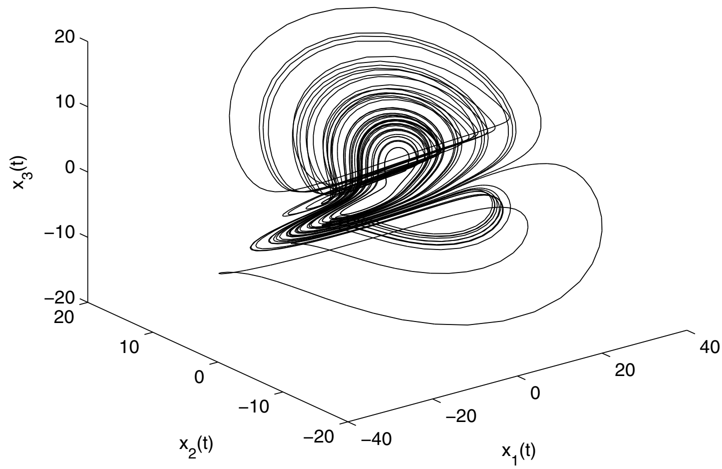

Fig. 5. The hyperchaotic attractor (i)

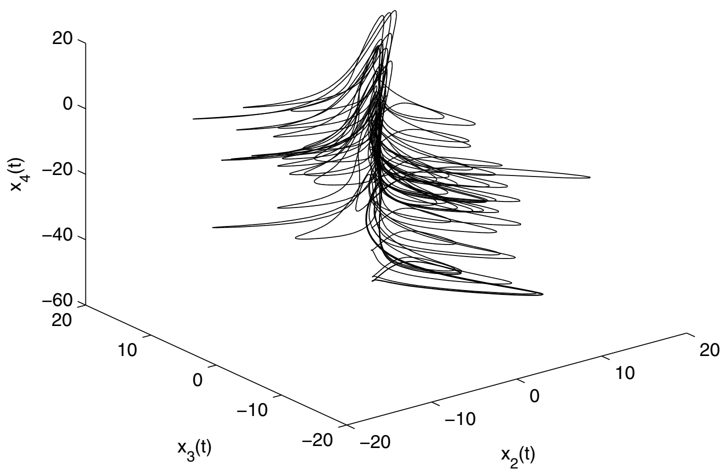

Fig. 6. The hyperchaotic attractor (ii)

In fact, the constructed system is dissipative when the system's parameters are chosen as $a = 4$, $c = 10$ and $d = 5$. There are two positive Lyapunov exponents in the above 4D system. It is obvious that hyperchaotification control is implemented in this condition. The corresponding hyperchaotic attractor is given in Fig. 5 and Fig. 6. The state response curves of the hyperchaotic system are presented in Fig. 7.

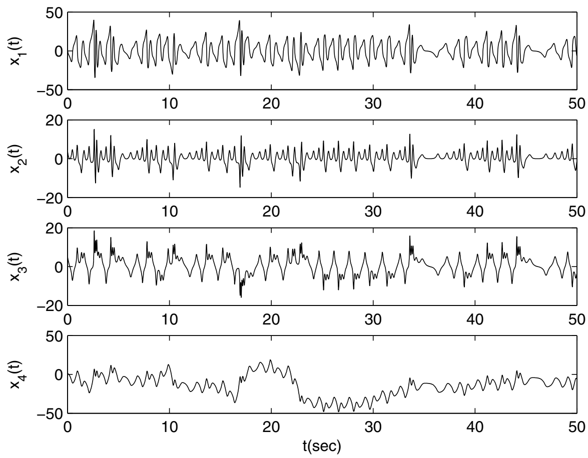

Fig. 7. The state response curve

3 Conclusions

A novel hyperchaotification control idea for a class of 3D four-wing chaotic systems is proposed. We introduce a new state variable into the considered 3D four-wing chaotic system and therefore the corresponding four-dimensional systems are set up. When the state feedback for the evolving of the new variable is designed properly, there are two positive Lyapunov exponents in the four-dimensional systems and therefore the hyperchaotification control is realized. An illustrative example is presented as well. Finally, some conclusions are drawn.

Acknowledgment. The authors gratefully acknowledge the contribution of co-workers and reviewers' comments.

References

1. Wang, X.Y., Jia, B., Wang, M.J.: Active Tracking Control of the Hyperchaotic LC Oscillator System. Int. J. Modern Phys. B 21, 3643–3655 (2007)
2. Wang, F.Q., Liu, C.X.: Passive Control of a 4-scroll Chaotic System. Chin. Phys. 16, 946–950 (2007)
3. Yang, C.D., Tao, C.H., Wang, P.: Comparison of Feedback Control Methods for a Hyperchaotic Lorenz System. Phys. Lett. A 374, 729–732 (2010)
4. Zheng, S., Deng, G.G., Bi, Q.S.: A new hyperchaotic system and its synchronization. Appl. Math. Comput. 215, 3192–3200 (2010)

Semantic-Based Affect and Metaphor Interpretation in Virtual Drama

Li Zhang

School of Computing, Egineering and Information Sciences, Northumbria University, Newscate, UK
l.zhang@cs.bham.ac.uk

Abstract. We have developed an intelligent agent to engage with users in virtual drama improvisation previously. The intelligent agent was able to perform sentence-level affect detection from user inputs with strong emotional indicators. However, we noticed that many inputs with weak or no affect indicators also contain emotional implication but were regarded as neutral expressions by the previous interpretation. In this paper, we employ latent semantic analysis to perform topic theme detection and identify target audiences for such inputs. We also discuss how such semantic interpretation of the dialog context is used to interpret affect and recognize metaphorical phenomena. Our work contributes to the conference themes on emotion and affect and semantic-based dialogue processing.

Keywords: metaphor, affect detection and semantic interpretation.

1 Introduction

Human behaviour in social interaction has been intensively studied. Intelligent agents are used as an effective channel to validate such studies. For example, mimicry agents are built to employ mimicry social behaviour to improve human agent communication [1]. Intelligent conversational agents are also equipped to conduct personalised tutoring and generate small talk behaviours to enhance users' experience. However, the Tutoring test introduced in 1950 still poses big challenges to our intelligent agent development. Especially, the proposed question, "can machines think?", makes many of our developments shallow.

We believe it will make intelligent agents possess human-like behaviour and narrow the communicative gap between machines and human-beings if they are equipped to interpret human emotions during the interaction. Thus in our research, we equip our AI agent with emotion and social intelligence as the potential attempts to answer the above Turing question. According to Kappas [2], human emotions are psychological constructs with notoriously noisy, murky, and fuzzy boundaries that are compounded with contextual influences in experience and expression and individual differences. These natural features of emotion also make it difficult for a single modal recognition, such as via acoustic-prosodic features of speech or facial expressions. Since human being's reasoning process has taken related context into consideration, in our research, we intend to make our agent take multi-channels of

H. Zhang et al. (Eds.): BICS 2012, LNAI 7366, pp. 213–222, 2012.

subtle emotional expressions embedded in social interaction contexts into consideration to draw reliable affect interpretation. The research presented here focuses on the production of intelligent agents with the abilities of interpreting dialogue contexts semantically to support affect detection as the first step of building a 'thinking' machine.

Our research is conducted within a previously developed online multi-user role-play virtual drama framework, which allows school children aged 14 – 16 to talk about emotionally difficult issues and perform drama performance training. In this platform young people could interact online in a 3D virtual drama stage with others under the guidance of a human director. In one session, up to five virtual characters are controlled on a virtual stage by human users ("actors"), with characters' (textual) "speeches" typed by the actors operating the characters. The actors are given a loose scenario around which to improvise, but are at liberty to be creative. An intelligent agent is also involved in improvisation. It included an affect detection component, which detected affect from human characters' each individual turn-taking input (an input contributed by an individual character at one time). This previous affect detection component was able to detect 15 emotions including basic and complex emotions and value judgments, but the detection processing has not taken any context into consideration. The intelligent agent made attempts to produce appropriate responses to help stimulate the improvisation based on the detected affect. The detected emotions are also used to drive the animations of the avatars so that they react bodily in ways that is consistent with the affect that they are expressing [3].

Moreover, the previous affect detection processing was mainly based on pattern-matching rules that looked for simple grammatical patterns or templates partially involving specific words or sets of specific alternative words. A rule-based Java framework called Jess was used to implement the pattern/template-matching rules in the AI agent allowing the system to cope with more general wording and ungrammatical fragmented sentences. From the analysis of the previously collected transcripts, the original affect interpretation based on the analysis of individual turn-taking input itself without any contextual inference is proved to be effective enough for those inputs containing strong clear emotional indictors such as 'yes/no', 'haha', 'thanks' etc. There are also situations that users' inputs do not have any obvious emotional indicators or contain very weak affect signals, thus contextual inference is needed to further derive the affect conveyed in such user inputs.

The inspection of the collected transcripts also indicates that the improvisational dialogues are often multi-threaded. This refers to the situation that social conversational responses of different discussion themes to previous several speakers are mixed up due to the nature of the online chat setting. Therefore the detection of the most related discussion theme context using semantic analysis is very crucial for the accurate interpretation of the emotions implied in those inputs with ambiguous target audiences and weak affect indicators.

2 Related Work

Tremendous progress in emotion recognition has been witnessed by the last decade. Endrass, Rehm and André [4] carried out study on the culture-related differences in the domain of small talk behaviour. Their agents were equipped with the capabilities of generating culture specific dialogues. There is much other work in a similar vein. Recently textual affect sensing has also drawn researchers' attention. Ptaszynski et al. [5] employed context-sensitive affect detection with the integration of a web-mining technique to detect affect from users' input and verify the contextual appropriateness of the detected emotions. However, their system targeted interaction only between an AI agent and one human user in non-role-playing situations, which greatly reduced the complexity of the modelling of the interaction context.

Scherer [6] explored a boarder category of affect concepts including emotion, mood, attitudes, personality traits and interpersonal stances (affective stance showed in a specific interaction). Mower et al. [7] argued that it was very unlikely that each spoken utterance during natural human robot/computer interaction contained clear emotional content. Thus, dialog modeling techniques, such as emotional interpolation, emotional profiling, and utterance-level hard labelling, have been developed in their work to interpret these emotionally ambiguous or non-prototypical utterances. Such development would benefit classification of emotions expressed within the context of a dialog. Moreover, as discussed earlier, naturalistic emotion expressions usually consist of a complex and continuously changed symphony of multimodal expressions, rather than rarely unimodal expressions. However, most existing systems consider these expressions in isolation. This limitation may cause inaccuracy or even lead to a contradictory result in practice. For instance, currently many systems can accurately recognize smile from facial expressions, but it is inappropriate to conclude a smiling user is really happy. In fact, the same expression can be interpreted completely different depending on the context that is given [2]. It also motivates us to use semantic interpretation of social contexts to inform affect detection in our application.

3 Semantic Interpretation of Interaction Contexts and Metaphorical Phenomena

We noticed that the language used in our previously collected transcripts is often complex, idiosyncratic and invariably ungrammatical. We implemented pre-processing components previously to deal with mis-spellings, abbreviations, etc. Most importantly, the language also contains a large number of weak cues to the affect that is being expressed. These cues may be contradictory or they may work together to enable a stronger interpretation of the affective state. In order to build a reliable and robust analyser of affect it is necessary to undertake several diverse forms of analysis and to enable these to work together to build stronger interpretations. It thus guides not only our previous research but also our current developments. For example, in our previous work, we undertook several analyses of any given utterance. These would each build representations which may be used by other components (e.g. syntactic structure) and would construct (possibly weak) hypotheses about the affective state conveyed in the input. Previously we adopted rule-based reasoning, robust parsing, pattern matching, semantic and sentimental profiles for affect detection analysis. In our current study, we also integrate contextual information to further derive the affect embedded in the interaction context and to provide metaphor identification.

Since our previous affect detection was performed solely based on the analysis of individual input, the context information was ignored. In order to detect affect accurately from inputs without strong affect indicators and clear target audiences, we employ semantic interpretation of social interaction contexts to inform affect analysis. In this section, we discuss our approaches of using latent semantic analysis (LSA) [8] for terms and documents comparison to recover the most related discussion themes and potential target audiences for those without strong affect signals.

In our previous rule-based driven affect detection implementation, we mainly relied on keywords and partial phrases matching with simple semantic analysis using WordNet etc. However, we notice many terms, concepts and emotional expressions can be described in various ways. Especially if the inputs contain no strong affect indicators, other approaches focusing on underlying semantic structures in the data should be considered. Thus latent semantic analysis is employed to calculate semantic similarities between sentences to derive discussion themes for such inputs.

Latent semantic analysis generally identifies relationships between a set of documents and the terms they contain by producing a set of concepts related to the documents and terms. In order to compare the meanings or concepts behind the words, LSA maps both words and documents into a 'concept' space and performs comparison in this space. In detail, LSA assumed that there is some underlying latent semantic structure in the data which is partially obscured by the randomness of the word choice. This random choice of words also introduces noise into the word-concept relationship. LSA aims to find the smallest set of concepts that spans all the documents. It uses a statistical technique, called singular value decomposition, to estimate the hidden concept space and to remove the noise. This concept space associates syntactically different but semantically similar terms and documents. We use these transformed terms and documents in the concept space for retrieval rather than the original terms and documents.

In our work, we employ the semantic vectors package [9] to perform LSA, analyze underlying relationships between documents and calculate their similarities. This package provides APIs for concept space creation. It applies concept mapping algorithms to term-document matrices using Apache Lucene, a high-performance, full-featured text search engine library implemented in Java [9]. We integrate this package with our AI agent's affect detection component to calculate the semantic similarities between improvisational inputs without strong affect signals and training documents with clear discussion themes. In this paper, we target the transcripts of the Crohn's disease[1] scenario used in previous testing for context-based affect analysis.

In order to compare the improvisational inputs with documents belonging to different topic categories, we have to collect some sample training documents with strong topic themes. Personal articles from the Experience project (www.experienceproject.com) are borrowed to construct training documents. These articles belong to 12 discussion categories including Education, Family & Friends, Health & Wellness, Lifestyle & Style, Pets & Animals etc. Since we intend to perform discussion theme detection for the transcripts of the Crohn's disease scenario, we have extracted sample articles close enough to the scenario including articles of Crohn's disease (five articles), school

[1] Peter has Crohn's disease and has the option to undergo a life-changing but dangerous surgery. He needs to discuss the pros and cons with friends and family. Janet (Mum) wants Peter to have the operation. Matthew (younger brother) is against it. Arnold (Dad) is not able to face the situation. Dave (the best friend) mediates the discussion.

bullying (five articles), family care for children (five articles), food choice (three articles), school life including school uniform (10 short articles) and school lunch (10 short articles). Phrase and sentence level expressions implying ‘disagreement’ and ‘suggestion’ have also been gathered from several other articles published on the Experience website. Thus we have training documents with eight discussion themes including ‘Crohn’s disease’, ‘bullying’, ‘family care’, ‘food choice’, ‘school lunch’, ‘school uniform’, ‘suggestions’ and ‘disagreement’. The first six themes are sensitive and crucial discussion topics to the above scenario, while the last two themes are intended to capture arguments expressed in multiple ways. Affect detection from metaphorical expressions often poses great challenges to automatic linguistic processing systems. In order to detect a few frequently used basic metaphorical phenomena, we include four types of metaphorical examples published on the following website: http://knowgramming.com, in our training corpus. These include cooking, family, weather, and farm metaphors. We have also borrowed a group of ‘Ideas as External Entities’ metaphor examples from the ATT-Meta project databank (http://www.cs.bham.ac.uk/~jab/ATT-Meta/Databank/) to enrich the metaphor categories. Individual files are used to store each type of the metaphorical expressions, such as cooking_metaphor.txt, family_metaphor.txt and ideas_metaphor.txt etc). All the sample documents of the above 13 categories are regarded as training files and have been put under one directory for further analysis.

We have used one example interaction of the Crohn’s disease scenario produced by testing subjects during our previous user testing in the following to demonstrate how we detect the discussion themes for those inputs with weak or no affect indicators and ambiguous target audiences.

1. Peter: im going to *have an ileostomy* [sad]
2. Peter: *im scared* [scared]
3. Dave*: i’m ur friend* peter and *i’ll stand by* you [caring]
4. Peter: yeah i know, but *the disease stuff sucks* [sad]
5. Dave: if it’s what u want, you should *go for it* though [caring]
6. Janet: peter you must go throu with this operation. *Its for the best* [caring]
7. Peter: but *no one else can do* nethin [disapproval]
8. Arnold: *take it easy*, consider all your options peter [caring]
9. Matthew: u have had operations b4 I’m sure *u’ll be ok* [caring]
10. Dave: what are your other options peter [neutral: a question sentence]
11. Peter: im trying very hard but there is too much stuff blocking my head up [Topics: family care, ideas metaphor, bullied; Target audience: Dave; Emotion: neg.]
12. Peter: my plate is already too full.... there aint otha options dave [Topics: food, cooking metaphor, bullied; Target audience: Dave; Emotion: stressful]

Affect implied by the inputs with strong affect indicators in the above interaction is detected by the previous affect detection processing. The emotion indicators are also illustrated in italics in the above examples. The inputs without an affect label followed straightaway are those with weak or no strong affect indicators (10^{th}, 11^{th} & 12^{th} inputs). Therefore further processing is needed to recover their most related discussion themes and identify their most likely target audiences in order to identify implied emotions more accurately. Our general regime for the detection of discussion themes is to create the ‘concept’ space by generating term and document vectors for all the training corpus and a test input. Then we use these transformed terms and documents in the concept space for retrieval and comparison. For example, we use the generated concept space to calculate semantic similarities between user inputs without strong affect indicators and training files with clear topic themes and search for documents including the user input closest to the vector for a specific topic theme. We start with the 11th input from Peter to demonstrate the topic theme detection. First of all, this input is stored as a separate individual test file (test_corpus1.txt) under the same folder containing all the training sample documents of the 13 categories.

In the topic theme detection processing, first of all, the corresponding semantic vector APIs are used to create a Lucene index for all the training samples and the test file, i.e. the 11th input. This generated index is also used to create term and document vectors, i.e. the concept space. Various search options could be used to test the generated concept model. In order to find out the most effective approach to extract the topic theme of the test inputs, we, first of all, provide rankings for all the training documents and the test sentence based on their semantic distances to a topic theme. We achieve this by searching for document vectors closest to the vector for a specific topic term (e.g. 'bullying', 'disease' or 'family care'). We have tested the 11th input using the vectors of all 13 topic terms mentioned above. The input from Peter obtains the highest ranking for the topic theme, 'ideas metaphor' (top 2nd), 'cooking metaphor' (top 3rd), and 'bullied' (top 5th), among all the rankings for the 13 topics. Partial output is listed in Figure 1 for the rankings of all the training documents and the 11th input based on their semantic distances to the topic theme, 'ideas metaphor'.

Semantic similarities between documents are also produced in order to further inform topic theme detection. All the training sample documents are taken either from articles under clear discussion themes within the 12 categories of the Experience project or the metaphor websites with clear metaphor classifications. The file titles used indicate the corresponding discussion or metaphor themes. If the semantic distances between files, esp. between training files and the test file, are calculated, then it provides another source of information for the topic theme detection. Therefore we use the CompareTerms semantic vector API to find out semantic similarities between all the training corpus and the test document. We provide the top five rankings for semantic similarities between the training documents and the 11th input in Figure 2.

The semantic similarity test in Figure 2 indicates that the 11th input is more closely related to topics of 'family care (family_care3.txt)' and 'ideas metaphor (ideas_metaphor.txt)' although it is also closely related to negative topic themes such as 'disease' and 'being bullied'. In order to identify the 11th input's potential target audiences, we have to conduct topic theme detection starting from the 10th input and retrieving backwards until we find the input with a similar topic theme or with a posed question for Peter. The pre-processing of the previous rule-based affect detection includes a syntactical parsing using a Rasp parser and it identifies the 10th input from Dave is a question sentence with the mentioning of Peter's name. Thus the syntactical processing regards the 10th input from Dave posed a question toward the target audience, Peter. We also derive its most likely topic themes for the 10th input to provide further confirmation. Using the processing discussed earlier, the topic theme detection identifies the following semantically most similar training documents to the 10th input: disagree1.txt, family_care5.txt and suggestion1.txt. They respectively recommend the discussion themes: 'disagreement', 'family care' and 'suggestion'.

```
Found vector for 'ideas metaphor'
Search output follows ...
0.9687636802981049:F:\ideas_metaphor.txt
0.6109025620852475:F:\test_corpus1.txt
0.468855438977363:F:\family_care5.txt
0.4384741083934003:F:\family_care2.txt
0.43717258989527735:F:\suggestion1.txt
0.43481884276082305:F:\bullied1.txt
0.42516120464904383:F:\bullied2.txt
0.42055621398181026:F:\crohn2.txt
```

Fig. 1. Partial output for searching for document vectors closest to the vector of 'ideas metaphor'(test_corpus1.txt containing the 11th input, ranking the top 2nd)

```
Similarity of "family_care3.txt" with "test_corpus1.txt":
0.7437130626759305
Similarity of "ideas_metaphor.txt" with "test_corpus1.txt":
0.7344774236952176
Similarity of "crohn3.txt" with "test_corpus1.txt":
0.7149712240914611
Similarity of "bullied1.txt" with "test_corpus1.txt":
0.689368455185548
Similarity of "family_care2.txt" with "test_corpus1.txt":
0.6773127042549564
```

Fig. 2. Part of the output for semantic similarities between training documents and the test file, i.e. the 11th input

```
Similarity of "rhetorical1.txt" with "test_corpus2.txt" ...
0.41996908397317273
Similarity of "question1.txt" with "test_corpus2.txt" ...
0.4886129715563037
```

Fig. 3. Output for semantic similarities between rhetorical and normal question training documents and the test file, test_corpus2.txt, i.e. the10th input

We also noticed that in English, the expression of question sentences is so diverse. Most of them will require confirmation or replies from other characters, while there is a small group of question sentences that do not really require any replies, i.e. rhetorical questions. Such questions (e.g. "What the hell are you thinking?", "Who do you think you are?", "How many times do I need to tell you?", "Are you crazy?") encourage the listener to think about what the (often obvious) answer to the question must be. They tend to be used to express dissatisfaction. In our application domain, we especially detect such rhetorical questions using latent semantic analysis after Rasp's initial analysis of the sentence type information. We construct two training documents for questions sentences: one with normal questions and the other with rhetorical questions. We use the semantic vector API to perform semantic similarity comparison between the two training document vectors and the 10th input from Dave.

The result shown in Figure 3 indicates that the input from Dave is more likely to be a normal question sentence rather than a rhetorical expression. Thus it is more inclined to imply a normal discussion theme such as ‘family care’ than to express ‘disagreement’ or ‘suggestion’. Thus the 10th input from Dave has the same discussion theme to one of the themes implied by the 11th input from Peter. Thus the target audience of the 11th input is Dave, who has asked Peter a question in the first place. Since the 11th input is also regarded as an ‘ideas metaphor’ with a high confidence score, the following processing using Rasp and WordNet is applied to the partial input “there is too much stuff blocking my head up” to recognize the metaphor phenomenon.

1. Rasp: ‘EX (there) + VBZ (is) + RG (too) + DA1 (much) + NN1 (stuff) + VVG (blocking) + APP$ (my) + NN1 (head) + RP(up)’

2. WordNet: ‘stuff’ -> hypernym: information abstract entity, since ‘stuff’ has been described by a singular after-determiner (‘much’). ‘Head’ -> hypernym: a body part physical entity. ‘Block’ -> hypernyms: PREVENT, KEEP.

3. The input implies -> ‘an abstract subject entity (stuff) + an action (block) + a physical object entity’ (head) -> showing semantic preference violation (an abstract entity performs an action towards a physical object) -> recognised as a metaphor.

In this example, ideas are viewed in terms of external entities. They are often cast as concrete physical objects. They can move around, or be active in other ways. The above processing recognises that this ‘ideas as external entities’ metaphorical example shows semantic preference violation, i.e. an information abstract subject performs physical actions. Since the 11th input is also semantically close to disease and bullied topics derived from the above topic theme detection processing, this metaphorical input implies a ‘negative’ emotion.

In a similar way, the 12th input from Peter also does not contain strong affect indicators. Thus the conversation theme detection has identified its input vector is semantically most closely related to the vector of the topic term, ‘food’ (top 5th ranking) and ‘cooking metaphor’ (top 6th ranking). The topic theme detection also identifies the 12th input shows high semantic similarities with training corpus under the themes of ‘cooking metaphor (cooking_metaphor.txt: 0.563)’ and ‘being bullied (bullied3.txt: 0.513)’. Since Dave’s name is mentioned in this input, our processing automatically classifies Dave as the target audience. Thus the 12th input is regarded as a potential cooking metaphor related to a negative bullying theme. The above syntactic and semantic processing using Rasp and Wordnet is also applied to this input. The first part of the 12th input closely related to cooking and food themes is interpreted as ‘a physical tableware-object subject followed by a copular form and a quantity adjective’. However it does not show any semantic preference violation as the 11th input did and the only cooking related term is ‘plate’. Context information is also retrieved for the recognition of this cooking metaphorical phenomenon.

We start from the 11th input to find out the topic themes of those inputs most similar to the topics of the 12th input. As discussed earlier, the 11th input is contributed by Peter as well with embedded ‘family care’ and ‘bullied’ themes, but not related to ‘food’. The 10th input is a question sentence from Dave with a ‘family care’ theme. The 8th and 9th inputs contain strong affect indicators (see italics) implying ‘family care’ themes as well. The backward retrieval stops at the 7th input, the last round input contributed by Peter. Thus the 11th input shares the same ‘bullied’ topic with the 12th input and the 12th input contributed by the same speaker is regarded as a further answer to the previous question raised by Dave. Moreover the 11th input is recognised as an 'ideas as external entities' metaphor with a negative indication. Thus the 12th input is not really 'food' related but an extension of the ideas metaphor and more likely to indicate a physical tableware object entity, plate, is a flat, limited space for solid ideas. Therefore it is recognised as a cooking metaphor. The most recent interaction context (8th – 11th) also shares a consistent positive theme of 'family care', but not a bullying context. Incorporation of Peter's profile, a sick character, Peter is thus more likely to indicate a 'stressful' emotion because of 'being bullied by disease' in the 12th input. Rule sets are generated for such metaphorical and affect reasoning using emotions embedded in interaction contexts, character profiles and relationships.

The conversation theme detection using semantic vectors is able to help the AI agent to detect the most related discussion themes and therefore to identify the target audiences. We believe these are important aspects for the accurate interpretation of the emotion context. We envisage it would also be useful to distinguish task unrelated small talk and task-driven behaviours during human agent interaction.

4 Evaluation and Conclusion

We have taken previously collected transcripts recorded during our user testing with 200 school children to evaluate the efficiency of the updated affect detection component with contextual inference. In order to evaluate the performances of the topic theme detection and the rule based affect detection in the social context, three transcripts of the Crohn's disease scenario are used. Two human judges are employed to annotate the topic themes of the extracted 300 user inputs from the test three transcripts using the previously mentioned 13 topic categories. Cohen's Kappa is a statistical measurement of inter-annotator agreement. It provides robust measurement by taking the agreement occurring by chance into consideration. We used it to measure the inter-agreement between human judges for the topic theme annotation and obtained 0.83. Then the 265 example inputs with agreed topic theme annotations are used as the gold standard to test the performance of the topic theme detection. A keyword pattern matching baseline system has been used to compare the performance with that of the LSA. We have obtained an averaged precision, 0.736, and an averaged recall, 0.733, using the LSA while the baseline system achieved an averaged precision of 0.603 and an averaged recall of 0.583 for the 13 topic theme detection. The detailed results indicated that discussion themes of 'bullying', 'disease' and 'food choices' have been very well detected by our semantic-based analysis. The discussions on 'family care' and 'suggestion' topics posed most of the challenges. For example, the following input is from Peter classified as a 'suggestion' topic by the human annotators, "This is so hard and I need your support". The semantic analysis has given the highest similarity score (0.905) to one of the 'bullying' theme training documents and the 2nd highest score (0.901) to the training document with the 'suggestion' theme. Although the topic detection using LSA made errors like the above sometimes, the similarity scores for the ideal classifications became very close to the top score for another topic category. We also notice that sometimes without many contexts, the test inputs showed ambiguity for topic detection even for judges. Generally the semantic-based interpretation achieves promising results.

The two human judges have also annotated these 265 example inputs with the 15 frequently used emotions. Cohen's Kappa is used again to as an effective channel to measure our system's performance. In our application, since 15 emotions were used for annotation and the annotators may not experience the exact emotions as the test subjects did, it led to the low inter-agreement between human judges. The inter-agreement between human judge A/B is 0.63. While the previous version of the affect detection without any contextual inference achieves 0.46 in good cases, the new version achieves inter-agreements with human judge A/B respectively 0.56 and 0.58. Although the inter-agreement improvements are comparatively small due to using a large category of emotions, many expressions regarded as 'neutral' by the previous version have been annotated appropriately as emotional expressions.

Moreover, in future work, we will use articles published on the Experience website to evaluate our AI agent on metaphor recognition using context. We are also interested in using topic extraction to inform affect detection directly, e.g. the suggestion of a topic change indicating potential indifferent to or uninterested in the current discussion theme. It will also ease the interaction if our agent is equipped with culturally related small talk behavior. In the long term, we also aim to incorporate each weak affect indicator embedded in semantic analysis, speech, facial expression and gestures to benefit affect interpretation in social context. We believe these are crucial aspects for the development of personalized intelligent agents with social and emotion intelligence.

References

1. Sun, X., Lichtenauer, J., Valstar, M., Nijholt, A., Pantic, M.: A Multimodal Database for Mimicry Analysis. In: D'Mello, S., Graesser, A., Schuller, B., Martin, J.-C. (eds.) ACII 2011, Part I. LNCS, vol. 6974, pp. 367–376. Springer, Heidelberg (2011)
2. Kappas, A.: Smile when you read this, whether you like it or not: Conceptual challenges to affect detection. IEEE Transactions on Affective Computing 1(1), 38–41 (2010)
3. Zhang, L., Barnden, J.A.: Affect and Metaphor Sensing in Virtual Drama. International Journal of Computer Games Technology 2010, Article ID 512563 (2010)
4. Endrass, B., Rehm, M., André, E.: Planning Small Talk Behavior with Cultural Influences for Multiagent Systems. Computer Speech and Language 25(2), 158–174 (2011)
5. Ptaszynski, M., Dybala, P., Shi, W., Rzepka, R., Araki, K.: Towards Context Aware Emotional Intelligence in Machines: Computing Contextual Appropriateness of Affective States. In: Proceeding of IJCAI (2009)
6. Scherer, K.R.: Vocal Communication of Emotion: A Review of Research Paradigms. Speech Communication 40, 227–256 (2003)
7. Mower, E., Metallinou, A., Lee, C., Kazemzadeh, A., Busso, C., Lee, S., Narayanan, S.S.: Interpreting ambiguous emotional expressions. In: International Conference on Affective Computing and Intelligent Interaction, Amsterdam, The Netherlands (2009)
8. Landauer, T.K., Dumais, S.: Latent semantic analysis. Scholarpedia 3(11), 4356 (2008)
9. Widdows, D., Cohen, T.: The Semantic Vectors Package: New Algorithms and Public Tools for Distributional Semantics. In: IEEE Int. Conference on Semantic Computing (2010)

A Framework for Experience Representation

Jan Kaczmarek and Dominik Ryżko

Warsaw University of Technology, Intitute of Computer Science,
Ul. Nowowiejska 15/19, 00-665 Warsaw, Poland

Abstract. This paper proposes a framework for representing the subjective dimension of experience within artificial systems, in particular information systems that emulate behaviour of natural agents. As opposed to the mainstream approach in knowledge engineering it is proposed that knowledge is not equal to experience, in the sense that experience is a broader term which encapsulates both knowledge and subjective, affective component of experience and as such can be represented in formal systems, which has not been so far properly addressed by knowledge representation theories. We show also how our work could enhance the mainstream approach to modelling rational agency with BDI framework.

1 Introduction

Under the paradigm of mind intentionality [2], which assumes that minds have this special intrinsic feature that they can relate to external word and thus are *about* external world, it can be asserted that experience is one in all intentional mind state composed of knowledge that is the intentional contents of this state, the world-to-mind relation, meanwhile its inseparable subjective component is composed of subjective feelings of the mindful individual corresponding to this intentional mind states.

Importantly, it does not particularly matters if we define experience as a set of mind states or a mind state process for assessing if the overall relation between knowledge and subjective experience that we have outlined above is valid. Whether there is *knowing* rather then *knowledge* or *experiencing* rather than *experience*, which appears the dominant contemporary view remains irrelevant to the present discussion as for either way our propositions hold.

Furthermore we propose that the subjective component of experience is also intrinsically intentionalistic, but meanwhile the intentionality in case of knowing is directed outward, to the external world, in case of feeling it is directed inwards to the within of the experiencing mindbody. We tap into the contemporary thinking in the philosophy of mind that the primordial, intrinsic intentionalistic capacity of mind is non-linguistic, as there must be other more primordial, non-linguistic form of intentionality that allows human children, as well as other language-capable animals, to learn language in first place. Contemporary cognitive neuroscience suggest that this capacity is tightly related to *affect* [6].

We also embrace the theories of *consciousness* and *self* coming from brain scientists such as Damasio [4] and Panksepp [12] who believe that there is a primordial component of self, a so called protoself composed of raw feelings coming

H. Zhang et al. (Eds.): BICS 2012, LNAI 7366, pp. 223–231, 2012.

from within the body, which are representations of bodily states in the mind. Therefore we can look at this compound of primordial feelings as a mirror in which external world reflects via the interface of the senses. This results in experience that has this conceptually dual, yet united within the conscious mindbody, composition of intentional contents that is knowledge and subjective component that is build up by feelings coming from within the experiencing mindbody. For it is problematic to state sharply either that this composition is dual or united we can refer thereof to these two separately considered aspects of experience either as components or dimensions.

Therefore experience can be modelled in information systems when defined as remembered states of mind which are composed of the aforementioned two components: objective contents of intentional state that are characterised by mind-to-world relationship and the subjective component that reflects the private, primordial feelings that constitute the mirror accompaniment to intentional contents. These two dimensions of mindful experience are inseparable within the united field of consciousness [18].

As we have shown in our previous work [16] the modelling of experience is essential for building any system modeling human behaviour e.g. Customer Experience Mamagement. Here we present a more general framework, which provides necessary components for modelling of experience in an artificial system.

2 Experience Model

The Kaczmarek-Ryżko Experience Representation Framework (KRERF) starts with a general purpose definition of experience understood as remembered intentional states of mind. Formally, experience can be defined as a pair of sets K and A, where K represents knowledge, that contents of remembered intentional states of mind, or intentional contents of experience, whereas A represents affect, i.e. the subjective qualitative component of experience, therefore:

$$E_J =< K, A >, \text{ where, } E \text{ - experience of agent J.}$$

Further we define a funcion mapping intentional content into affective state

$$f : K \to A$$

The element representing affective component of experience – A can be further defined as a set of tripples:

$A = \{< v, i, m >: v \in V, i \in I, m \in M\}$, where V – valence, I – intensity, M – mode, and M is a k-combination of C where C – n-element set of core affects and $k < n$ – the number of core affects involved in a compound affect.

In line with the contemporary neurocognitive theories of emotion and affect [12], affective component of an experiential state is characterized by *valence*, as a mindful organism can always discriminate between wanted, unwanted or neutral subjective states, *intensity* as there can be degrees to which these states are wanted or not and finally they are characterised by a *mode* as there are neurologically recognised emotions each corresponding to the activation of a particular neural circuit in the brain, or a few circuits at a time. For this reason we can distinguish between low-level, primordial affective states, i.e. *core affects*, like fear, lust, etc, and compound or high-level affects that can involve a combination of core affects, which is why we have defined M - mode, as k-combination of the set C, where k is any integer such that $k \in < 1; n >$. Noteworthy, we do not take into account to what degree each particular system corresponding to an element of C is activated. We judge valence and intensity for the elements of M only, which is in line with the account of the affective component of experience as unified and subjective, and subjectively such nuances cannot be consciously appreciated. We consider it a fair and accurate approximation.

Furthermore KRERF emphasises that the experience is gained over time in course of agent's interactions with the environment. Each such an interaction for us is an *event*. For this reason we take experience gaining as a learning process to which machine learning approach can be applied. Any learning process involves training data, which goes through the learning algorithm and results in a set of outputs that are learned concepts, in our case these concepts are experiential intentional states, elements of E_J. Consequently, in experience gaining process we will consider *events* as training data. For the purpose of memory modelling, incl. memory decay and consolidation, we will need to control the time line of events for which reason more formally define it in the following way

$$T(t) = \{(e_1..e_n) : \forall k \in (1, n)\ time(e_k) > time(e_{k-1})\ and\ time(n) <= t\}, \text{ where } time(e) \text{ is the time of occurrence of } e$$

Each event is a tuple:

$e =< B_e, t, a >$, where B_e - believes resulting from the event e (a set of intentional states to be remembered), t - time, $a \in A$ - affective value of the event as defined earlier.

It is important to note that we assume that affective value is assigned to an event and inherited by B_e, however this value may result both from the affective response to external stimuli prompting the event, as well as mind processes caused by the stimuli, i.e. reconstruction of affected past experiences. This is to embrace a situation when an agent involved in cognitive response to a stimulus recalls strongly affected facts and this sets the affective value for the event and consequently the new output believes resulting from the event. It is important because so derived affective value of an event a can reach a certain threshold level such that it may trigger an autonomous behavioural response instead of a deliberative response, i.e. a fully fledged emotional response, which intervenes a regular deliberation process and may result in behaviours that are irrespective of cognitive appraisal of the event. This calls for defining a mechanism for updating a both at the level of event as well at the level of believes B.

So far we have focused on E and A, let us consider K briefly now. As we mentioned in previous subsection in principle K could be represented with any

KR approach. As K is composed of intentional states of propositional nature the elements of K can be represented with simple logical propositions, or predicates, so as truth/false-valued formulas of a formal language, with or without variables, where logical value is determined by mind-to-world relationship. In KRERF we favour predicate calculus for representing agent knowledge and reasoning. However as we argued before K is not enough to represent comprehensively the state of mind of agents, as it lacks the subjective, affective component of experience. Consequently, while considering intelligent agents, incl. BDI agents, their knowledge base, B – believes set in case of BDI, should not be limited to K but should be assumed E.

Consequently, under KRERF using predicate calculus we can represent experiential intentional states, remembered by an agent from the event, as a set

$E = \{p_1(a_{11}, x_{12}, ..., x_{1m}, c_1, a_1), ..., p_k(x_{k1}, x_{k2}, ..., x_{kl}, c_k, a_k)\}$, where $p_1...p_k$ are predicate symbols and $x_{11}...x_{kl}$ its attributes, while c_k and a_k are *consolidation coefficient* and *affective value* of a predicate p_k.

Variable a_k is derived and updated dynamically during each event from the affective value of the current event e as well as affective value of remembered past experiential states in which $p_k(x_{kl})$ appears. Moreover, the variable a_k should be also dependant on affective value of *related* affected predicates, which relation could be determined by co-occurrence of certain events or based on associations between contents of the predicates. For the purpose of a_k estimation an *affect update function* should be defined. As there are only general premises on how such a funcion should be build, we define it on purpose in a general way so that a more specific implementation can be used for a particular application.

Variable c_k is derived taken into account the time of the current event and the time of the past events in which the same predicate was remembered. For the purpose of c_k estimation a *decay function* must be defined. This function should reflect the fact that experience consolidation depends both on time, repetitive recall of the given predicate from the memory, as well as the role of affect in the memory processes [8]. For defining the decay function one could build on available memory models and algorithms such as Woźniaks algorithms based on spaced repetition [19]. We insist that the temporal dimension is one of the most important aspects of the experience. As an agent is confronted with new events, the experience gained from the old ones will be steadily forgotten. As forgetting is intrinsic to learning the model of experience must take this into account. So the decay function governing the vividness of past experiences, represented by consolidation coefficient (c_k) must be provided for to enable modelling of the memory volatility linked to experiential outputs of events.

The K component of experience represented in KRERF as set of predicates with additional variables is also subject to update. This process is governed by the learning function as well as reasoning within the already acquired set of believes. The architecture presented in the paper is general in the sense that it does not assume any particular formalism for representing user knowledge, or theoretical/practical reasoning. However, we argue that some form of defeasible reasoning seems a suitable approach to reflect the commonsense way of human reasoning. We will show how this can be done in the case of default logic as defined by Reiter [15].

This reasoning process has two features important in this case. Firstly, it is non-monotonic, so that adding new facts does not always result in adding new conclusions but can lead to invalidation of some of them. This reflects aptly the way humans reason. With limited information at hand, we first take assumptions to make preliminary conclusions and then revise them in case of new evidence.

Second important feature of default reasoning is that the order of applying the rules is important and can lead to deriving different conclusions. In practice this means a single theory can have multiple extensions. Such phenomenon is also common in human thinking when taking decisions. People construct different concurrent alternatives and weight arguments for each of them, before finally committing to one of them. This is confirmed by neurological studies of human brain referred to earlier. In this model it is natural to use intensity as a driver for rule priorities.

$$Priority(D) = \sum_{p=1..k} |f(p)|$$

where $f(p)$ is a function returning intensity of p which takes into account the forgetting process.

Example: Let us assume the following default theory modelling the user experience learning function:

$$D = \{\frac{expensive(X):durable(X)}{durable(X)}, \frac{plastic(X):-durable(X)}{-durable(X)}\}$$

If both $expensive(X)$ and $plastic(X)$ are known two extenstions exist, one containing $durable(X)$ and another with $-durable(X)$. To choose one of them, we wieght the emotional value related to the input events and give priority to the one with higher value.

The model for experience representation we propose challenges the mainstream affective computing accounts of emotion representation is so far as intelligent, rational artificial agents are concerned. As we speculate that our take on representing affect and affective experience in artificial agents, for being more in line with contemporary account of consciousness, affective neuroscience and rational agency, is likely to outperform currently available approaches in emulating natural agent behaviour in information systems, we will briefly discuss in the next section how our account could enhance the mainstream approach to modelling rational agency with BDI framework. We will also undertake to explain why we believe our approach to experience modelling is superior, especially in the context of rational, deliberative agency.

3 Rational Experiencing Agent

In KRERF we pay particular attention to the role of affective component of experience to organism behaviour, and we use the concept of rational agency to discuss the relations between agent experience and behaviour. This role is primarily about motivation and experience vividness. The affective dimension of experience facilitates drivers for agent action and influences the remembering and forgetting (memory) processes that experience is prone to. We reflect on how the above presented framework could enhance the mainstream rational agency model which is the Belives, Desires, Intentions model (BDI) underpinned by Bratmann's theory of rationality and later applied by Rao and Georgeff [14] that is the mainstream rational agency model which dominates information science and artificial intelligence literature. Again contemporary brain science provides evidence to that separation of reason from emotion in rational decision making by natural agents is wrong [3]. Affect plays important role in behaviour and reasoning, which mainstream computational models of rational agency fail to recognize, lacking relevant formal expressions. Our framework paves the way for filling up this gap as it provides ways for representation of affective dimension of experience in artificial systems.

Typically, deliberative BDI agents are enhanced with emotions by enlarging their knowledge set, beliefs set to be more specific, with propositions about their emotional states. However we do not accept such a solution as a satisfactory one because it confuses the state of being aware of an emotion with the affective state associated with any intentional state.

Inspired by Davidson who, in contrary to Humean account that the passions (desires) drive action, while reason (belief) merely directs its force, concluded that

> "(...) belief and desire seem equally to be causal conditions of action. But (...) desire is more basic in that if we know enough about a person's desires, we can work out what he believes, while the reverse does not hold." [5],

we conclude that in so far as BDI model provides, desires are equal to beliefs. Indeed a desire in the above sense is a *verbalised desire*, i.e. in order for a proposition to be included in the deliberation an agent must have internally verbalize it and accept it by which he converts it into a belief. As a result an agent acquires a belief about his desire. However, apart from desires made so explicit and becoming beliefs there are implicit experiential states that directly influence behaviour, these are not embraced by the Desires set under the current formulation of BDI framework or other instrumentalist rationality models as adequate forms of their representation are missing. If this is so, the BDI models looses the D component which results in a gap which we try to fill up with the subjective dimension of experience. Under such an account each belief, either the proper one or about a desire, represented formally with a proposition should have an extra component added which would stand for the subjective affective state to this belief. Some preliminary suggestions how this could be implemented has been proposed and discussed.

Furthermore the typical approach to modelling emotional BDI agents is by defining emotional state as cognitively appreciated mind state, i.e. an emotion is a belief about an agent being under emotion a_1. Such an account is largely influenced by outdated appraisal theories of emotion like the one worked out by Ortony et al. [11] or Lazarus [9]. These theories of emotion underpin the most cited computational models of emotional agency [10,7,13,17,1], where different emotions are treated as heuristics, are introduced into the beliefs set, and determine agent behaviour in a predefined way, which is dealt with so that additional axioms are added to the given BDI framework specifying agent's behavioural tendencies corresponding to a given emotional state. Such approaches inherit the flaws of the underlying emotion theories, present limited expressiveness, they confuse emotions understood as hard-wired programmes and emotional feelings, affective states that bias decision making and reasoning, can capture only those affective states that can be consciously and cognitively appreciated by an agent, ignore the memory volatility which govern decay of experience in time, are inconsistent with contemporary theories of human mind, cannot express non-linguistic intentional states of mind.

Now, let us consider how the experience representation framework could enhance the BDI emotional agency frameworks. First of all it must be noted that our approach to experience representation could be applied primarily to enhanced representation of the B (beliefs) set. We shall recognize that the BDI theory of practical reason as proposed by Bratman is one of the most advanced AI friendly accounts of agency. Bratman's contribution to understanding how human take action is highly valuable. However it pretty much neglects the role of affect in practical reason. This constitutes a constraint for any BDI agency formalization right from the start. Our account of experience understood as affected knowledge could patch this evident gap. This would be achieved in two ways: (1) by providing a framework for affect control in the framework, in particular as far as modulating memory volatility processes as far as both knowledge and affective dimension of experience is concerned, (2) for orchestrating affect influence on behaviour.

We could risk formulating a simplification that there are two basic ways in which affect influences agent's action: (1) via immediate impact on behaviour when one of the known emotional systems is activated, i.e. when emotion program sets off, altering immediately behaviour of an agent, interfering its normal deliberation and means-ends reasoning processes, (2) indirectly influencing deliberation process via impacting believes set. These two main types of influence overlap in situations when recalled affective states associated with processed beliefs invoke affective arousal intensive enough to trigger fully-fledged emotion. This is we believe one of the biggest advantages that our account could bring to BDI framework. In wider terms this is about providing for a proper temporal dimension of experience and modelling experience as learning associative process, including memory processes.

Moreover, as detailed control of affective state of an artificial agent would be provided the BDI framework could be enriched with more sophisticated rules definition for mapping these states onto behavioural consequences. Affect could influence deliberation in variety of ways, by highlighting dynamically importance of certain desires and believes on the expense of another. Intention formulation could also be modulated by the affective state of the agent at any point in time. Reconstruction of past mental states and their amalgamation with current new perceptions, as unified field of consciousness account dictates, could be emulated. With enhanced affective dimension BDI framework could better address motivational aspects of intention formulation. Finally, the gap of the free will could be bridged, even if only with provisional approximations, based on the affective value estimation of alternative states.

4 Conclusions

The evidence from both contemporary philosophy of mind and neuroscience appears to us sufficient, to assert that affect plays a central role in human and animal decision making [3,12]. Based on this evidence we postulate that any intentional state, which is a representation of external world in the mind, has an affective value, which is characterised by valence (positive or negative), intensity (arousal level) and mode (affective state kind), which has implications on agent's behavioural response and is an integrated component of agent's rationality. A framework for representing thus defined experience has been proposed and related to the mainstream approaches to modelling emotions of rational agents.

References

1. Adam, C.: Emotions: from psychological theories to logical formalization and implementation in a BDI agent. PhD thesis, Université Paul Sabatier. Institut de Recherche en Informatique de Toulouse (July 2007)
2. Anscombe, G.: Intention. Harvard University Press (1957)
3. Damasio, A.: Descartes' error: emotion, reason, and the human brain (1994)
4. Damasio, A.: Self Comes to Mind: Constructing the Conscious Brain. Pantheon Books, New York (2010)
5. Davidson, D.: Problems of rationality. Oxford University Press (2004)
6. Greenspan, S., Shanker, S.: The first idea: How symbols, language, and intelligence evolved from our early primate ancestors to modern humans. Da Capo Press (2004)
7. Jiang, H., Vidal, J., Huhns, M.: Ebdi: an architecture for emotional agents. In: Proceedings of the 6th International Joint Conference on Autonomous Agents and Multiagent Systems, p. 11. ACM (2007)
8. Kandel, E.: In search of memory: The emergence of a new science of mind. WW Norton & Co. (2006)
9. Lazarus, R.: Emotion and adaptation. Oxford University Press, USA (1991)
10. Meyer, J.: Reasoning about emotional agents. In: Proceedings of European Conference on Artificial Intelligence - ECAI 2004, pp. 129–133. IOS Press (2004)
11. Ortony, A., Clore, G., Collins, A.: The cognitive structure of emotions. Cambridge University Press (1988)
12. Panksepp, J.: Affective consciousness: Core emotional feelings in animals and humans. Consciousness and cognition 14(1), 30–80 (2005)
13. Pereira, D., Oliveira, E., Moreira, N.: Modelling emotional bdi agents. In: Workshop on Formal Approaches to Multi-Agent Systems, FAMAS 2006 (2006)

14. Rao, A., Georgeff, M.: Modeling Rational Agents within a BDI-Architecture. In: Allen, J., Fikes, R., Sandewall, E. (eds.) Proceedings of the Second International Conference on Principles of Knowledge Representation and Reasoning (KR 1991), pp. 473–484. Morgan Kaufmann (1991)
15. Reiter, R.: A logic for default reasoning. Artificial Intelligence 13, 81–132 (1980)
16. Ryżko, D., Kaczmarek, J.: Customer Experience Management Architecture for Enhancing Corporate Customer Centric Capabilities. Springer (2011)
17. Steunebrink, B., Dastani, M., Meyer, J.: A logic of emotions for intelligent agents. In: Proceedings of the 22nd National Conference on Artificial Intelligence, vol. 1, pp. 142–147. AAAI Press (2007)
18. Tye, M.: Consciousness and persons: Unity and identity. MIT Press (2003)
19. Woźniak, P., Gorzelańczyk, E.: Optimization of repetition spacing in the practice of learning. Acta Neurobiologiae Experimentalis 54(1), 59–62 (1994)

Emotional Balance as a Predictor of Impulse Control in Prisoners and Non-prisoners

Yunfeng Duan[1,2] and Feng Jin[1,*]

[1] Key Laboratory of Mental Health, Institute of Psychology, Chinese Academy of Sciences, Beijing, China
[2] Graduate University of Chinese Academy of Sciences, Beijing, China
jinfeng@psych.ac.cn

Abstract. Self-control is considered one of the strongest predictor of crime. Low self-control has emerged as a consistent and strong predictor of criminal behaviors. Theory and emerging evidence suggest that failing to regulate emotion may result in one's emotional state being in disorder. Emotional balance may, therefore, be related to self-control or even delinquency. The present study examined emotional balance as a predictor of self-control within prisoners and non-prisoners samples, by using the modified Affect Balance Scale (ABS) and the Self-Control Scale (SCS). Five forms of self-control were assessed: Impulse control (IC), Healthy habit (HH), Resist temptation (RT), Focus on work (FW) and Restrained amusement (RA). However, emotional balance emerged as a significant predictor of only impulse control, after controlling for age, marital status, income and education. Notably, the high emotional balance level was most predictive of increased impulse control capability. Finally, these results would be helpful to preventive interventions of delinquency, criminal or social deviance behaviors.

Keywords: Self-control, Emotional balance, Impulse control, Self-control theory, General theory of crime.

1 Introduction

Self-control is a kind of self-regulation and defined as the capacity to overcome impulses and automatic or habitual responses. Thoughts, emotions, desires, and behaviors are what one wants to control[1]. Low self-control would lead to substance abuse, eating disorder and criminal behavior. Higgins reported that low self-control had a link with delinquency for all races studied[2,3]. Besides, low self-control was positively related to juvenile delinquency[4]. DeWall, Finkel et al. argued that self-control failure played an integral role in many acts of aggression, violence and other criminal behaviors[5]. Reisig and Pratt's results suggested that low self-control not only explained traditional offending-oriented outcomes, but also insufficiently

---

* Corresponding author.

H. Zhang et al. (Eds.): BICS 2012, LNAI 7366, pp. 232–239, 2012.

studied forms of social deviance[6]. Peter, LaGranger et al. demonstrated that both self-control and strain were important contributors to delinquency [7]. Both parenting factors and low self-control are predictive of late adolescent delinquency[8]. A result from China suggested that it was the combination of self-control and social factors in the prediction of delinquency [9].

Low self-control theory was regarded as the most popular criminological theory and had been empirically studied across diverse populations and behaviors[10].

A self-report scale result indicated that self-control has differing relationships with antisocial behavior and personality factors[12]. However, some found that low self-control was a correct and certain, yet weak, predictor of certain deviant behaviors [13]. Cochran, Wood et al. used academic dishonesty as a unique type of fraudulent behavior upon which to test the theory of crime and provide qualified support for the theory[14].

Emotions are meaningful responses to internal or external events that convey information to us as well as to others, about who we are and what we are dealing with. One may experience a range of emotional states, some positive and some that are negative or distressing. Bradburn and Noll claimed that the psychological well-being was based on the balance of positive and negative affect[15]. The emotional state was particularly important because it affected how we behave and the results we obtain. The regulation of emotion was closely associated with violence and impulse control. Irritability, bad temper, or other negative emotional responsiveness were often present in violent or impulsive individuals[16]. Impulsivity and strong emotional states often accompany aggressive or violent acts[16]. From empirical experiences, crime behaviors were often related to negative affect or the offenders felt hopeless. We assumed that lack of emotional balance may often lead to self-control failure or even criminal behaviors.

To test our hypothesis, we conducted a questionnaire survey in male prisoners and non-prisoners. We found that emotional balance state was not significantly correlated with the total SCS scores directly, but significantly and positively correlated with the impulse control subscale of the SCS. Emotional balance was also a predictor of impulse control, with higher positive affect state indicating higher impulse control capability.

The present study has demonstrated a relationship between emotional balance and impulse control. It is possible that lacking of balanced emotions exerts an impact on self-control, which in turn contributes to the likelihood of criminal behaviors. It seems likely that people should pay more attention to their individual feelings of hope or happiness, and that these would be more predictive of impulse control capability or criminal behaviors. These results are presumed to be helpful to preventive interventions of delinquency, criminal or social deviance behaviors.

2 Method

2.1 Participants

The sample in this study was composed of 117 adult male prisoners and 123 adult male non-prisoners. The valid sample thus comprised 228 adult male subjects (113 prisoners and 115 non-prisoners).

The adult male prisoners were from northern of China (Mage=24.18 years, *SD*=0.995). Fifty-five percent were sentenced for an offense against a person including murder, violence, and sexual assault, 45% for others.

The comparison sample of 115 non-prisoners were also recruited from northern of China (Mage=20.95 years, *SD*=0.931).

2.2 Materials

2.2.1 The Affect Balance Scale (ABS) (Chinese version)

We used a two dimensional scale which contains 20 items each to evaluate the emotional balance level[15]. Jianxin, Zhang has revised Bradburn's scale according to Chinese culture[17]. The Chinese version consists of 16 items, and each item is followed by a yes or no option. All the items were arranged according to the positive and negative affect interval order. The total score was the positive affect score minus the negative affect score and plus a constant 5. The higher the score, the more positive emotional experience, the stronger the sense of psychological well-being.

2.2.2 The Self-Control Scale (SCS) (Chinese version)

We incorporated a new measure of individual differences in self-control. It was a revised Self-Control Scale (SCS) including 19 items and five factors[18]. Tangney, Baumeister et al. reported the original SCS[19]. Five subscales presence, involving Impulse Control (IC); Healthy Habit (HH); Resist Temptation (RT); Focus on Work (FW) and Restrained Amusement (RA)[18]. The summation or mean of all items was calculated as overall SCS scores, with higher scores positively correlating with higher self-control tendency.

3 Procedure

Non-prisoners individuals were recruited through the participants' pool or random street-seeking. Each subject was paid ￥20 for taking part in the study. The questionnaires were bound in a volume and put in a sealed envelope, together with an introductory letter. Before starting, all need to sign an informed consent. All the subjects filled out the questionnaire individually.

Prisoners were gathered and asked to participate in the study by the correctional officers. All procedure was the same as the non-prisoners.

At all times, no special instruction about the questionnaire was given to the prisoners and non-prisoners during their participation.

Statistical Analysis. For data analysis, Pearson’s correlation analysis, independent samples *t*-test, and multiple regression analysis were employed. All statistical tests were performed with SPSS version 17.0 for Windows.

4 Results

4.1 Correlations between Scale Measures

There were significant differences between the prisoners (M=6.10; *SD*=1.84) and non-prisoners (M=6.72; *SD*=1.86) on the ABS scores ($P<0.05$). The result revealed that the prisoners were not affect balanced. By testing the internal consistency, the result was proved to be reliable (Cronbach's Alpha= 0.778, n=220). Subscales were also proved reliable (Positive affect : Cronbach's Alpha= 0.664, n=224; Negative affect: Cronbach's Alpha=0 .714, n=221). Higher scores indicate an increased tendency toward the emotional balance level or well-being.

Table 1. Independent sample *t*-test results

	Prisoner (n=112)	Control (n=115)	*t*
Affective balance	6.10 (1.84)	6.72 (1.86)	-2.31*
Self-control	3.14 (0.69)	3.17 (0.54)	-0.41
Impulse Control (IC)	2.87 (0.87)	3.24 (0.68)	-3.59***
Healthy Habit (HH)	3.60 (1.11)	3.17 (0.89)	3.16**
Resist temptation (RT)	3.07 (0.75)	3.04 (0.65)	0.26
Focus on work (FW)	3.27 (0.93)	3.25 (0.79)	0.14
Restrained amusement (RA)	3.18 (1.00)	3.13 (0.87)	0.41

Note: The values are Mean (*SD*), *$P<0.05$; **$P<0.01$; ***$P<0.001$

No significant differences were found among the prisoners (M=3.14; *SD*=0.69) and non-prisoners (M=3.17; *SD*=0.54) on the total SCS scores ($P>0.05$) (see table 1). There were five domains of SCS, only IC ($P<0.001$) and HH ($P<0.01$) had significant differences between the prisoners (IC:M=2.87, *SD*=0.87; HH: M=3.6, *SD*=1.11) and non-prisoners (IC:M=3.24, *SD*=0.68; HH: M=3.17, *SD*=0.89). The other three domains were not significant (see table 1). By testing the internal consistency, the result was proved to be reliable (Cronbach's Alpha= 0.823, n=218). Two subscales were also proved reliable: IC: Cronbach's Alpha= 0.678, n=225; HH: Cronbach's Alpha= 0.691, n=224). However, the other three were proved less reliable: RT: Cronbach's Alpha= 0.391, n=226; FW: Cronbach's Alpha=0.507, n=226; RA: Cronbach's Alpha=0.458, n=222). Higher scores indicate an increased tendency toward self-control level. Accordingly, we chose emotional balance, impulse control and healthy habit as independent variables in the next step.

As expected, we identified significant correlations among these variables from Pearson's correlation analysis(Data not show). Age was significantly correlated with income and marital status. Education was significantly correlated with income, healthy habit and impulse control. Income was significantly related to marital status, age and education. Emotional balance was only positively and significantly related to impulse control (n =194; Pearson's r = 0.18; P < 0.05). This result indicated that increased emotional balance state was related to increased impulse control capability. Healthy habit and impulse control had a significant low correlation (n =227; r = 0.36; P < 0.01).

4.2 Effect Balance Can Be a Predictor of Impulse Control

A sets of multiple regression analyses were conducted to examine the predicted interactions. Age, marital status, education and income were performed as control variables. The dependent variable represented the IC score. Analyses were completed across the overall sample using the enter method. ABS was selected as independent variable.

As shown in table 2, IC was predicted by ABS (B=0.09, Standardize Beta=0.22, t =2.96, P<0.01) with controlling age, marital status, education and income. As a result, ABS had a significant positive main effect on the IC score, with an increased IC score predicted by increased ABS score.

Table 2. Multiple regression analyses results of predictors of impulse control

	B	β	t
Constant	3.05		5.98
Age	0.12	0.15	1.70
Marital status	-0.07	-0.05	-0.51
Education	0.15	0.29	3.91***
Income	-0.04	-0.10	-1.26
ABS	0.09	0.22	2.96**

Note: R=0.41; R^2=0.14; F=6.29. R^2 = adjusted multiple correlation coefficient; The Affect Balance Scale(ABS). β=Standardize β. * P<0.05; ** P<0.01; *** P<0.001

5 Discussion

The present investigation from the prisoners and non-prisoners explored emotional balance as a predictor of self-control. Only impulse-control was found to contribute to the affective balance based prediction. Although no other self-control domains could be predicted by the emotional balance, the impulse control only had a strong relationship with impulsiveness and aggression. It has been fully demonstrated that self-control failure played an integral role in aggression, violence and other criminal behaviors[5,20].

It seems that impulse control, but not the other self-control domains, was linked to criminal behaviors directly. It has been long noticed that self-control is a "now" versus "later" issue[21]. Gottfredson and Hirschi claimed that criminal behaviors provided 'immediate, easy, and certain short-term pleasure[11]. People with low self-control are unable to delay gratification, for they are focused on the present. As a result, low self-control people act impulsively—without much thought and based on what they are feeling at the moment[22]. Therefore, criminal behaviors could be impulsive, happening immediately, at present or on the spur of the moment without any planning. Previous studies also supported this conclusion. Low self-control has been linked to behavioral and impulse-control problems[11,19,23].

Demographic variables may have an impact on our dependent variables. Age was directly related to self-control, children with low levels of self-control was more prone to crime[8]. Others found that some criminal opportunities may be more common among older individuals[24]. Perkins argued that violent crime victimization varied across the age spectrum and aged 14-25 were the peak ages for criminal activity[25]. Our results showed that the mean age of the prisoners was around 23 years old. There was no significant difference between the prisoners and non-prisoners' age. Marriage reduced the odds of a crime and was a central consideration in contemporary theories of crime and resistance[26,27]. Forrest and Hay reported that marriage might promote resistance, in part, by enabling offenders to develop and exercise increased self-control[28]. King, Massoglia et al. demonstrated that marriage could suppress offending for males, even when accounting for their likelihood to marry[27]. Age and education had small positive effects on white collar crime[29]. High school reduced the probability of incarceration[30]. School attendance reduced contemporaneous property crime but increased contemporaneous violent crime among juveniles[31]. Poverty and income were also powerful predictors of homicide and violent crime[31,32]. Besides, homicide and assault may be more closely associated with poverty or income inequality[33]. Accordingly, we excluded the impact by introducing the four demographic variables as control variables.

In our study, we took all the demographic variables mentioned above as control variables to evaluate the emotional balance prediction power of self-control. It is remarkable that the emotional balance remained a predictor of self-control, especially impulse control. It should be noted, however, that low self-control, was probably linked to low intelligence, will detract from the scale's predictive power[34]. However, our study was somewhat limited by its use of only male sample and reliance on self report measures. Future research investigating the causes and mechanism of criminal behaviors , should focus more specifically on the relationship between emotion and self related personality.

Acknowledgments. This work was supported by the Key Laboratory of Mental Health Institute of Psychology, Chinese Academy of Sciences. The authors would like to thank Ye Zhang and Hui Tang for their excellent support and Prof. Walter Hannak for critically reviewing the manuscript and his valuable recommendations.

References

1. Gailliot, M.T., Baumeister, R.F.: The physiology of willpower: linking blood glucose to self-control. Personality and Social Psychology Review 11(4), 303–327 (2007)
2. Higgins, G.E.: Parental criminality and low self-control: an examination of delinquency. Criminal Justice Studies 22(2), 141–152 (2009)

3. Higgins, G.E., Ricketts, M.L.: Self-control theory, race, and delinquency. Journal of Ethnicity in Criminal Justice 3(3), 5–22 (2005)
4. Li, S.D.: The impacts of self-control and social bonds on juvenile delinquency in a national sample of midadolescents. Deviant Behavior 25(4), 351–373 (2004)
5. DeWall, C.N., Finkel, E.J., Denson, T.F.: Self-control inhibits aggression. Social and Personality Psychology Compass 5(7), 458–472 (2011)
6. Reisig, M.D., Pratt, T.C.: Low self-control and imprudent behavior revisited. Deviant Behavior 32(7), 589–625 (2011)
7. Peter, T., LaGrange, T., Silverman, R.: Investigating the interdependence of strain and self-control. Canadian Journal of Criminology and Criminal Justice 45(4), 431–464 (2003)
8. McCartan, L.M., Gunnison, E.: Examing the origins and influence of low self control. Journal of Crime and Justice 30(1), 35–62 (2007)
9. Cheung, N., Cheung, Y.: Self-control, social factors, and delinquency: a test of the General Theory of crime among adolescents in Hong Kong. Journal of Youth and Adolescence 37(4), 412–430 (2008)
10. Hirschi, T., Gottfredson, M.: Age and the explanation of crime. American Journal of Sociology 89(3), 552–584 (1983)
11. Gottfredson, M., Hirschi, T.: A general theory of crime. Stanford University Press, Stanford (1990)
12. Romero, E., Gómez-Fraguela, A., Luengo, A.N., Sobral, J.: The self-control construct in the general theory of crime: an investigation in terms of personality psychology. Psychology, Crime & Law 9(1), 61–86 (2003)
13. Stylianou, S.: The relationship between elements and manifestations of low self-control in a general theory of crime: two comments and a test. Deviant Behavior 23(6), 531–557 (2002)
14. Cochran, J.K., Wood, P.B., Sellers, C.S., Wilkerson, W., Chamlin, M.B.: Academic dishonesty and low self-control: An empirical test of a general theory of crime. Deviant Behavior 19(3), 227–255 (1998)
15. Bradburn, N.M.: The structure of psychological well-being. Aldine Pub. Co., Oxford (1969)
16. Krakowski, M.: Violence and serotonin: influence of impulse control, affect regulation, and social functioning. The Journal of Neuropsychiatry and Clinical Neurosciences 15(3), 294–305 (2003)
17. Chen, W., Zhang, J.: Factorial and construct validity of the Chinese positive and negative affect scale for student. Chinese Mental Health Journal 18(11), 763–765 (2004) (in Chinese)
18. ShuHua, T., Yong-yu, G.: Revision of self-control scale for chinese college students. Chinese Journal of Clinical Psychology 16(5), 468–470 (2008) (in Chinese)
19. Tangney, J.P., Baumeister, R.F., Boone, A.L.: High self-control predicts good adjustment, less pathology, better grades, and interpersonal success. Journal of Personality 72(2), 271–324 (2004)
20. Conner, B., Stein, J., Longshore, D.: Examining self-control as a multidimensional predictor of crime and drug use in adolescents with criminal histories. The Journal of Behavioral Health Services and Research 36(2), 137–149 (2009)
21. Rachlin, H., Green, L.: Commitment, choice and self-control. Journal of the Experimental Analysis of Behavior 17(1), 15–22 (1972)
22. Krueger, R.F., Caspi, A., Moffitt, T.E., White, J., Stouthamer-Loeber, M.: Delay of gratification, psychopathology, and personality: is low self-control specific to externaiizing problems? Journal of Personality 64(1), 107–129 (1996)
23. Baumeister, R.F., Vohs, K.D., Tice, D.M.: The strength model of self-control. Current Directions in Psychological Science 16(6), 351–355 (2007)

24. Steffensmeier, D.J.: The invention of the “New” senior citizen criminal. Research on Aging 9(2), 281–311 (1987)
25. Perkins, C.A.: Age patterns of victims of serious violent crime. U.S. Department of Justce, USA (1997)
26. Sampson, R.J., Laub, J.H., Wimer, C.: Does Marriage Reduce Crime? A Counterfactual Approach to Within-Individual Causal Effects. Criminology 44, 465–508 (2006)
27. King, R.D., Massoglia, M., Macmillan, R.: The context of marriage and crime: gender, the propensity to marry, and offending in early adulthood. Criminology 45(1), 33–65 (2007)
28. Forrest, W., Hay, C.: Life-course transitions, self-control and desistance from crime. Criminology and Criminal Justice 11(5), 487–513 (2011)
29. Steurer, S.J., Smith, L.G.: Education reduces crime: three-state recidivism study. executive summary. Correctional Education Association, Online (2003)
30. Lochner, L.: Education and crime. Elsevier Ltd., Online (2008)
31. Kennedy, B.P., Kawachi, I., Prothrow-Stith, D., Lochner, K., Gupta, V.: Social capital, income inequality, and firearm violent crime. Social Science & Medicine 47(1), 7–17 (1998)
32. Virtanen, M., Kivimäki, M., Kouvonen, A., Elovainio, M., Linna, A., Oksanen, T., Vahtera, J.: Average household income, crime, and smoking behaviour in a local area: The Finnish 10-Town study. Social Science & amp; Medicine 64(9), 1904–1913 (2007)
33. Hsieh, C.-C., Pugh, M.D.: Poverty, income inequality, and violent crime: A meta-analysis of recent aggregate data studies. Criminal Justice Review 18(2), 182–202 (1993)
34. Arneklev, B.J., Grasmick, H.G., Tittle, C.R., Bursik, R.J.: Low self-control and imprudent behavior. Journal of Quantitative Criminology 9(3), 225–247 (1993)

Time Scales of Sensorimotor Contingencies

Alexander Maye and Andreas K. Engel

University Medical Center Hamburg-Eppendorf
Dept. of Neurophysiology and Pathophysiology
Martinistr. 52, D-20246 Hamburg, Germany
{a.maye,ak.engel}@uke.de

Abstract. In Sensorimotor Contingency Theory (SMCT) differences between the perceptual qualities of sensory modalities are explained by the different structure of dependencies between a human's actions and the ensuing changes in sensory stimulation. It distinguishes modality-related Sensory-Motor Contingencies (SMCs), that describe the structure of changes for individual sensory modalities, and object-related SMCs, that capture the multisensory patterns caused by actions directed towards objects. These properties suggest a division of time scales in that modality-related SMCs describe the immediate effect of actions on characteristics of the sensory signal, and object-related SMCs account for sequences of actions and sensory observations. We present a computational model of SMCs that implements this distinction and allows to analyze the properties of the different SMC types. The emergence of perceptual capabilities is demonstrated in a locomotive robot controlled by this model that develops an action-based understanding for the size of its confinement without using any distance sensors.

1 Introduction

One of the main propositions of SMCT [1,2] is that the brain neither builds nor uses internal representations of the world to generate sensory awareness. Instead the theory suggests, that the interrelations between actions and changing stimulation patterns impinging on the sensory organs while exploring the environment constitute its perceptual contents and conscious experience. The idea that action plays a constitutive role in perception has been developed by a school of philosophers taking a pragmatic stance on cognition (see [3] for an overview). In robotics, the construction of reliable, internal world models and their sensible employment for the generation of behavior are major challenges, that to date have not been satisfied. Therefore SMCT should be highly relevant for the development of control architectures for artificial agents with cognitive capabilities. However, surprisingly few approaches implement the core concept of SMCT [4,5,6,7]. Many more approaches are *inspired* by SMCT, but in our view fail to realize the constitutive role of action for perception.

SMCT postulates two types of SMCs, namely modality- and object-related SMCs. Inspired by studying a computational model of SMCs that was proposed by the authors previously [8], we argue here that these two SMC types "live" on

H. Zhang et al. (Eds.): BICS 2012, LNAI 7366, pp. 240–249, 2012.

different time scales. This idea will be further motivated in the next section. In section 3 we present the results of a study in which a robot learned the SMCs defined by the specific properties of its embodiment and the environment, and used them to optimize its behavior. The study demonstrates how the longer temporal context of object-related SMCs can be used as the basis for knowledge about the size of the robot's confinement. To make the case more interesting, the robot does not use sensors that measure distance directly (e.g. infra-red distance sensors) or indirectly (e.g. camera images). In the last section we discuss implications and hypothesize about possible extensions of this approach.

2 Time Scales of SMCs

2.1 Two Types of SMCs

The different sensory organs of the human body measure different physical quantities: luminance at the retina, sound pressure at the ear-drum, force at the tactile skin receptors and in the muscle spindles, accelerations in the vestibular system etc. It comes as no surprise, therefore, that the structure of changes in the sensory signal caused by actions is different for each sensory modality. O'Regan and Noë ([1] p. 941) mention the differences between vision and audition: while eye movements generate changes in the sensory stimulation on the retina, they do not affect the sensory signal coming from the ear. On the other hand, movements of the head change the temporal asynchrony of sounds hitting the ear-drums, which is the basis for sound localization. Of course head movements change the luminance distribution on the retina as well, but the pattern is different from both, the changes caused by eye movements and the changes in temporal asynchrony of sound waves. They conclude that

> ... what does differentiate vision from, say, audition or touch, is the *structure of the rules* governing the sensory changes produced by various motor actions, that is, what we call the *sensorimotor contingencies* governing visual exploration. Because the sensorimotor contingencies within different sensory domains (vision, audition, smell, etc.) are subject to different (in)variance properties, the structure of the rules that govern perception in these different modalities will be different in each modality. (p. 941, emphasis theirs)

This structure of rules is what we call modality-related SMCs. Since they are a direct consequence of the "(in)variance properties" of the physical quantities as such, contingent on the agent's actions, we conjecture that they capture the instantaneous effects of these actions on the patterns of sensory stimulation.

The second type of SMCs that O'Regan and Noë identify are determined by (visual) attributes of objects. When inspecting an object, the signals in the visual domain change in a lawful way that is characteristic for the object at hand. An example is the change of light reflection and color when the object is manipulated, and the fact that we have to turn it around to be able to perceive its backside. They suggest

> ... that the visual quality of shape *is precisely* the set of all potential distortions that the shape undergoes when it is moved relative to us, or when we move relative to it. Although this is an infinite set, the brain can abstract from this set a series of laws, and it is this set of laws which codes shape. (p. 942, emphasis theirs)

The fact that these object-related SMCs require some kind of exploration suggests that they are activated on a longer time scale, and that they establish a form of context. To perceive an object requires to explore its attributes, be they visual or tactile, in a process that extends over longer times than the rather direct modulation of the signals in the different sensory modalities by the actions in this process. This is why we think that the different types of SMCs are associated with different time scales.

2.2 Accounting for Different Time Scales in a Computational Model of SMCs

The idea to consider the relations between types of SMCs and time scales has been inspired by studying a computational model of SMCs that was previously proposed by the authors. The details are given in [8], but the general idea is pictured here again. While the agent executes an action a, sensory observations o are recorded. The model works in discrete time, so after each time step a new action-observation pair $ao(t)$ – an SMC – is available. These action-observation couplets are pushed on a first-in-first-out queue that keeps a memory of recently executed actions and resulting sensory observations (see Fig. 1). An array of Markov models is employed to learn the probability distributions of patterns in this queue, corresponding to the different action-observation contexts the agent experiences. Each Markov model takes a finite history of actions and observations into account[1]. These probability distributions are a model of the SMCs of the respective agent. Since the Markov models with short history lengths disregard the longer context of specific situations that the agent goes through, they capture general regularities of the sensorimotor patterns. In this respect they seem to have similar properties like modality-related SMCs. In contrast, the models that take a longer history of actions and observations into account, represent sensorimotor patterns that depend on the specific context. Exploration of the visual attributes of an object is an example of such a context, and hence Markov models with longer histories are deemed to realize object-related SMCs.

We would like to point out that in these considerations we do not make any assumptions about the number of sensory modalities involved. In particular we do not interpret the term modality-related in a way that suggests this SMC type would capture structural regularities of each sensory modality in isolation. Rather than employing different subsystems for different modalities, our approach is based on the joint probability distributions of all sensory modalities. Therefore differences in the sensorimotor laws between individual modalities

[1] Note that the probability distribution for history length h can be determined from the one for $h+1$ by computing the marginal distribution over all $ao\,(t-(h+1))$.

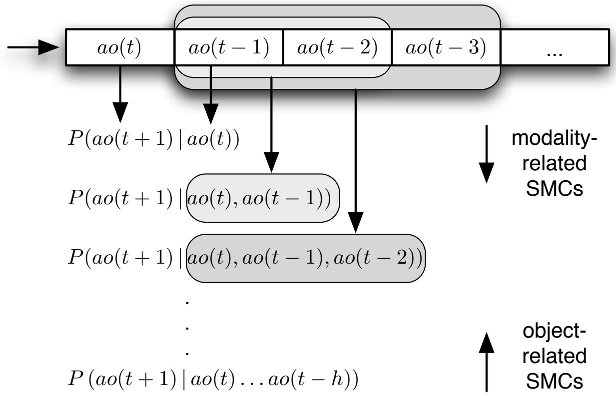

Fig. 1. Schema of the proposed computational model of SMCs. The sequence of actions and sensory observation (*ao*) is used to train Markov models of different history lengths *h*. We suggest that object-related SMCs are captured by models with longer context sizes, and modality-related SMCs by models with a short context.

are reflected in the qualitative differences of projections of the joint probabilities to (the dimensions of) individual modalities, and not in physically distinct, modality-specific subsystems. We believe that this agrees well with the very idea of SMCT. Technically, though, it is still possible for an external observer to visualize strictly unimodal SMCs by computing marginal probability distributions.

3 Robot Study

In this section we present a particular implementation of the model described in the previous section. It demonstrates the simultaneous acquisition of modality- and object-related SMCs, how the former control efficient instantaneous behavior, and how the latter lead to meaningful long-term behavior.

3.1 Hardware

The Robotino® robot (Festo Didactic, Esslingen, Germany) is equipped with an omnidirectional (Swedish) wheel drive, a webcam, 9 distance sensors, and a collision detector. For this study locomotion was restricted to forward and backward movements at constant speed. Camera and distance sensors were not used, because in the experimental setting (described below) the robot should rely only on the proximal senses that are described in the following. The collision detector is implemented in the Robotino® by a compressed air tube, that is attached around the circular periphery and registeres pressure changes. It does not yield directional information about the side of the collision. Readings of the instantaneous current consumption of the motors were used to detect whether the robot pushes against an obstacle that had not triggered the bumper. A custom-made accelerometer was attached to the chassis of the robot giving three-dimensional acceleration information.

The model for controlling the robot's behavior uses discrete time steps, and we set the update rate to 1 Hz. Every action (move forward or backward) was executed for 1 second. During this time sensor values were sampled at 10 Hz. At the end of each epoch the raw sensor values were averaged and quantized. This preprocessing step did not serve to recognize or classify the sensory input, as is the case in conventional robot control architectures, but to reduce the complexity of the sensory signals to a level that allows fast learning of SMCs.

3.2 Experimental Setting

The robot was placed on a flat ground between two walls at about 4 times the diameter of the robot apart. Traveling from one wall to the opposite took about 5 seconds. While the wall in the back of the robot triggered the bumper on collisions, the wall in the front had a protrusion that prevented further forward movement, but did not trigger the bumper (Fig. 2). The robot should learn to move in an smooth and energy-efficient way, and to respond appropriately to collisions. Collision avoidance is typically implemented in the lowest levels of conventional control architectures, relying on bumpers or distance sensors. However, in the future we would like to employ our approach in scenarios in which the robot is allowed to push objects around. A reflex-like obstacle-avoidance mechanism could not be used in this case. Instead the robot must have the opportunity to observe the sensory feedback from the bumper, the motors, and the distance sensors to feel if it is pushing an object or bumping into a wall.

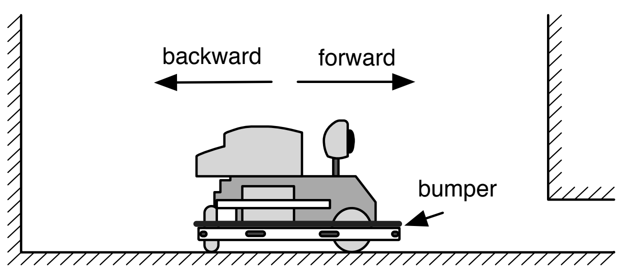

Fig. 2. Profile view of the experimental setup. The robot could freely move forward and backward between the two walls. The shape of the front wall (right) stopped the movement, but did not trigger the bumper.

An analogous setting for humans would be a confinement in the darkness, where the prisoner can only walk forward and backward. After exploring the prison cell for a while, he would know that it takes 5 steps from wall to wall, and while the one in the back feels hard, the one in the front is soft.

3.3 Model

We employed a slightly modified version of the computational model of SMCs described in [8]. Apart from the sensory preprocessing, the value system and the action selection schema had to be adapted to the Robotino's® embodiment.

Value System. Defining a value system is a method "to make an agent do something in the first place" [9]. Here we used only internal values as the experimental setting did not feature any rewards coming from the environment. The features from the bumper ($\in 0,1$), motors ($\in 0,1,2$), and accelerometer ($\in [-2,+2]$) contributed to the internal value in the following way:

$$v_{int} = -bumper - 0.5motor - 0.2 \max_{x,y,z}(|accel|)$$

The internal value was always less than zero, and the robot should try to find a behavior that makes it least "negative".

Action Selection. In addition to the probabilities of action-observation pairs ao conditional on a history of length h of previous action-observation pairs, $P^h\left(ao(t+1)|ao(t)\dots ao(t-h)\right)$, the model keeps track of the average value associated with each context of size h:

$$\bar{v}^h_{int}\left(ao(t+1)|ao(t)\dots ao(t-h)\right) = \frac{\sum v_{int}\left(ao(t+1)|ao(t)\dots ao(t-h)\right)}{N\left(ao(t)\dots ao(t-h)\right)}$$

with $N()$ being the number of times having experienced this context. Using this value probability, a simple schema to select the next action is used: Working down from large context sizes h to smaller ones, for each possible action the average value is found. This requires that the current context, given by the sequence $ao(t)\dots ao(t-h)$ has been experienced before, i.e. $N\left(ao(t)\dots ao(t-h)\right) > 0$. Now the action with the best predicted value gets executed with probability $p = \bar{v}^h_{int} + 1$. Actions that reliably have led to a perfect internal value ($\bar{v}^h_{int} = 0$), for example, would be readily executed again. Actions with an average internal value at or below -1 would never get executed. All intermediate values leave the opportunity to explore alternatives, with a probability depending on the previous experience with this action.

3.4 Results

We can evaluate the behavior of the robot by comparing the components of the value function when it is controlled by the just described SMC-based action selection schema, and when actions are selected randomly. The plots in Fig. 3 show the time course of the internal value components for about 35 minutes run time of the robot. During the first 5 minutes the robot has learned that fewer switches between forward and backward drive lead to fewer acceleration peaks and a reduced energy consumption, and hence improve the internal value. Stability of motor current, acceleration and turning probability between 5 and about 10 minutes runtime characterizes the conclusion of the learning phase

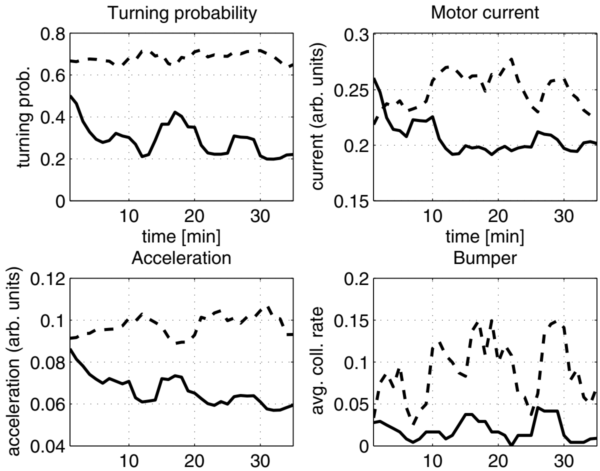

Fig. 3. Time course of the sensory signals in the three modalities that affect the internal value associated with each SMC: acceleration, current consumption, and bumper. The solid line is from a run with the described action selection schema, the dashed line resulted from randomly switching forward and backward drive. Turning probability is not considered for the internal value, but gives an idea how straight the robot moved (low values). All curves are smoothed with a moving average window of 4 minutes.

of modality-related SMC. The robot now knows how to move in an efficient manner, but still tries to improve its internal value and explores different action sequences. This is achieved at around 12 minutes when it discovers the full extent of its confinement, allowing to move with a minimum number of turns. The robot continues to switch occasionally to exploration (e.g. at around 25 minutes) for two reasons. First it might have experienced a hitherto unknown SMC and starts searching for appropriate responses. And second, the turn it makes in front of a wall to avoid the collision still incurs an "unpleasant" sensation of acceleration. Therefore it checks out the only alternative action, resulting in a collision.

One might be interested in the question why the probability of triggering the bumper shows no significant change over time. This has to be analyzed in conjunction with the motor current. The combination of high collision frequency and high currents in the beginning indicates that the robot frequently pushed against the wall for several epochs. It had not yet learned the appropriate behavior upon a collision, which is to immediately drive in the opposite direction. It shows this behavior after learning has progressed, e.g. around 15 and 25 minutes, when it encounters again phases of frequent collision, but without a corresponding increase in current consumption. The other reason for a sustained rate of collisions is the slip between the wheels and the ground. Even though the robot knows after some time the distance between the walls in terms of the number of consecutive steps in one direction, it has no means to determine its absolute position. The only way to do this is to check the wall once in a while to bring its internal model in register with the world.

An impression of the modality-related SMCs that the robot acquired during the experiment can be gained from Table 1. It shows SMCs in human readable form for a history of length 0, i.e. $P(ao(t+1))$. Most movements required only little current, were not associated with acceleration peaks, nor triggered the bumper. This kind of behavior was of good internal value, and hence was exercised frequently. When the movement in the previous epoch was in the opposite direction, the robot incured an acceleration peak, leading to somewhat lower internal values. Collisions with the walls made for a bad experience and were tried to be avoided.

In Table 2 three examples of SMCs of history length 5 are given. The first block shows the most frequently observed SMC of history length 5 ($p = 0.06$), reflecting a peak in acceleration when the movement direction is changed from forward to backward after 3 time steps. The second block shows an SMC of

Table 1. Listing of the 6 most frequently observed SMCs of history length 0. Most of the time going forward or backward caused a low current consumption, no acceleration peaks, and didn't trigger the bumper (first two rows). The robot "felt" the acceleration when it was changing the direction of movement (third and fourth row). Pushing forward against the protrusion increased the current consumption (fifth row), and pushing backward compounded a signal from the bumper (last row).

Probability	Value	Action	Current	AccelX	AccelY	AccelZ	Bumper
0.41	0.00	→	+	0	0	0	
0.36	0.00	←	+	0	0	0	
0.10	-0.20	←	+	-	0	0	
0.06	-0.20	→	+	+	0	0	
0.03	-0.50	→	++	0	0	0	
0.01	-1.50	←	++	0	0	0	*

Table 2. Selection of SMCs of history length 5. The arrangement of features has been transposed in comparison to Table 1. Action-observation pairs are now shown in rows, and columns represent different time steps (progressing from right to left).

Feature	$ao(t+1)$	$ao(t)$	$ao(t-1)$	$ao(t-2)$	$ao(t-3)$	$ao(t-4)$	$ao(t-5)$
Action	←	←	←	←	→	→	→
Current	+	+	+	+	+	+	+
AccelX	0	0	0	-	0	0	0
Bumper							
Action	→	←	←	←	←	←	→
Current	+	+	+	+	+	+	+
AccelX	+	0	0	0	0	-	0
Bumper							
Action	←	←	←	←	←	←	→
Current	++	+	+	+	+	+	+
AccelX	0	0	0	0	0	-	0
Bumper	*						

successful turning behavior between the walls ($p = 0.02$). The last block is an example for the robot's experience when it collides with the rear wall ($p = 0.001$). After switching to backward movement in time before an imminent collision with the front wall at $t - 4$, it continues to move backwards until it eventually bumps into the rear wall at $t + 1$, triggering the bumper and increasing the current consumption. Since these SMCs result from exploring the properties of the confinement, it is suggested that they correspond to object-related SMCs.

4 Conclusions

The properties of modality- and object-related SMCs suggest that they differ with respect to the temporal context they take into account. Modality-related SMCs reflect the momentary changes in the properties of sensory signals, and give rise to the different qualities of sensory experiences like seeing, hearing, touching etc. Object-related SMCs, in contrast, reflect changes in the sensory information during exploratory processes, and hence, account for sequences of actions and sensory observations that extend over time. They are more specific than modality-related SMCs in the sense that their acquisition and exercise requires a specific configuration of the environment, e.g. the presence of a particular object. Beyond that, we suggest that this type of SMCs actually constitutes what potential objects are for the agent, which then would be defined as repertoires of family-resemblant SMCs.

Our proposed model of SMCs makes the different temporal context sizes explicit. Markov models for the probability distribution of a new action-observation pair conditional on only recent histories of previous actions and observations represent the direct effects that the actions of an artificial agent have on the associated changes of the sensory signal properties. Models in which this probability distribution depends on a longer history of events are more specific for a particular environmental situation, corresponding to object-related SMCs. The robot study shows how both SMC types determine the overt behavior of the agent: While modality-related SMCs let it move in a coordinated and energy-efficient manner, object-related SMCs support its optimal behavior in the specific environmental situation.

It might be interesting to ponder about the implications of extrapolating the idea of a relation between types of SMCs and time scales to contexts beyond object-related SMCs. Behavior is nothing an agent happens to have, but is something that is exercised to bring about specific consequences. These consequences are fed back to the behaving system on a longer time scale. Time-extended actions, like driving to work or preparing a cake for example, are highly structured and involve a similar regularity of sensorimotor correlations like SMCs in the sense of SMCT. It is the precise sequence of turns taken with the car that determines the final destination of the ride, and the specific selection of ingredients and instructions followed from the recipe that define the type of cake made. We suggest, therefore, that the concept of SMCs can be extended to what might be called "intention-related" SMCs that capture these long term regularities in action sequences, and that constitute our conscious experience beyond the time scale of object perception, like "driving to work" or "preparing a cake" in this example. We will develop models of intention-related SMCs and examine the implications of this idea in the future.

Acknowledgement. This work was supported by the Sino-German research training group CINACS, DFG GRK 1247, www.cinacs.org, and by the EU project 'Extending sensorimotor contingencies to cognition - eSMCs', IST-270212, esmcs.eu.

References

1. O'Regan, J., Noë, A.: A sensorimotor account of vision and visual consciousness. Behavioral and Brain Sciences 24, 939–1031 (2001)
2. Noë, A.: Action in perception. MIT Press (2004)
3. Engel, A.: Directive minds: how dynamics shapes cognition. In: Stewart, J., Gapenne, O., Di Paolo, E.A. (eds.) Enaction: Towards a New Paradigm for Cognitive Science, pp. 219–243. MIT Press, Cambridge (2011)
4. Choe, Y., Yang, H.F., Eng, D.Y.: Autonomous learning of the semantics of internal sensory states based on motor exploration. International Journal of Humanoid Robotics 4, 211–243 (2007)
5. Fine, P., Di Paolo, E.A., Izquierdo, E.: Adapting to Your Body. In: Almeida e Costa, F., Rocha, L.M., Costa, E., Harvey, I., Coutinho, A. (eds.) ECAL 2007. LNCS (LNAI), vol. 4648, pp. 203–212. Springer, Heidelberg (2007)
6. Bovet, S., Pfeifer, R.: Emergence of delayed reward learning from sensorimotor coordination. In: Proceedings of the IEEE/RSJ International Conference on Intelligent Robots and Systems (IROS), pp. 2272–2277 (August 2005)
7. Möller, R., Schenck, W.: Bootstrapping cognition from behavior – a computerized thought experiment. Cognitive Science 32(3), 504–542 (2008)
8. Maye, A., Engel, A.: A discrete computational model of sensorimotor contingencies for object perception and control of behavior. In: 2011 IEEE International Conference on Robotics and Automation (ICRA), pp. 3810–3815. IEEE (May 2011)
9. Pfeifer, R., Scheier, C.: Understanding Intelligence. MIT Press (September 2001)

Analysis of Birefringent Characteristics of Photonic Crystal Fibers Filled Magnetic Fluid

Yuyan Zhang[1] and Donghua Li[2]

[1] Automation Department of ShenYang college of Engineer, 110036, Shenyang, China
[2] China Petroleum & Gas Pipeline Engineering Co. Northeast Branch, 110031, Shenyang, China
{zhgyylby,Lidonghua}@163.com

Abstract. The birefringent properties of a new type of Total Internal Reflection Photonic Crystal Fiber(TIR-PCF) filled symmetrically with magnetic fluid in the holes are studies by using the full-vector finite element method. To improve numerical precision, the perfectly matched layer is used as an absorbing boundary condition in computing. Theoretical calculations show that it may exhibit high birefringence in a properly designed PCF (whose birefringence can be as high as 0.05), and the birefringence can be tuned by magnetic fields or the structure parameter of the PCF. The birefringence effect is ten times higher than the general fiber and there is a fairly good linearity. This scheme provides theoretical foundation to use magnetic field to control light in PCF and also offers a potential method for making high-birefringent polarization fiber.

Keywords: photonic crystal fiber, magnetic fluid, birefringence.

1 Introduction

Photonic crystal fiber (PCF) proposed by P.St.J.Russell for the first time in 1992, and it is a kind of special structure fiber based on photonic crystal [1]. The PCF is optical fibers with a periodic arrangement of low-index material in a background with higher refractive index. The background material in PCF is usually undoped silica and the low-index region is typically provided by air-holes running along their entire length. Its waveguide properties are decided by the size and the arrangement of air holes. There are two kinds PCF (high-index guiding fibers and photonic bandgap ones) according to the different light guiding mechanisms. PCFs belonging to the first category are more similar to conventional optical fibers, because light is confined in a solid core by exploiting the modified total internal reflection mechanism. [2-3]. When the PCF core region has a lower refractive index than the surrounding photonic crystal cladding, light is guided by a mechanism different from total internal reflection that is, by exploiting the presence of the photonic bandgap (PBG). In fact, the air-hole microstructure which constitutes the PCF cladding is a two-dimensional photonic crystal, which is a material with periodic dielectric properties characterized by a photonic bandgap, where light in certain wavelength ranges cannot propagate [4-6].

H. Zhang et al. (Eds.): BICS 2012, LNAI 7366, pp. 250–258, 2012.

Due to the huge variety of air-holes arrangements, PCFs offer a wide possibility to control the refractive index contrast between the core and the photonic crystal cladding and, as a consequence, novel and unique optical properties. For example, nonlinear effects, novel dispersion characteristics high birefringence and single-mode transmission characteristics [7-9]. Since PCFs provide new or improved features, beyond what conventional optical fibers offer, they are finding an increasing number of applications in ever-widening areas of science and technology.

Birefringent fibers, where the two orthogonally polarized modes carried in a single-mode fiber propagate at different rates, are used to maintain polarization states in optical devices and subsystems [10-12]. The guided modes become birefringent if the core microstructure is deliberately made two fold symmetric, for example, by introducing capillaries with different wall thicknesses above and below the core. By slightly changing the air-hole geometry, it is possible to produce levels of birefringence that exceed the performance of conventional birefringent fiber by an order of magnitude. It is important to underline that, unlike traditional polarization maintaining fibers [13-14], such as bow tie, elliptical-core or Panda, which contain at least two different glasses, each one with a different thermal expansion coefficient, the birefringence obtainable with PCFs is highly insensitive to temperature, which is an important feature in many applications. The tunable high-birefringence PCFs can be obtained by filling symmetrically the sensitive materials (the refractive index can be controlled by external parameters) into air holes.

As a new type of functional material, the magnetic fluid (MF) seem to be particularly interesting substances to infiltrate PCF, since its refractive index is sensitive to external magnetic field [15-16]. The birefringence of PCF filling symmetrically MF can be tuned by opposed external magnetic field.

In this paper, we designed the construction of a tunable birefringence MF-filled index-guiding photonic crystal fiber (TIR-PCF). We have simulated and analyzed the magnetically induced tuning of the MF-filled PCF birefringence properties by the full-vector finite element method under external magnetic field. In addition, we have investigated the relationships between the effective refractive index, normalized birefringence parameter B and polarization beat length L_B of the MF-filled PCF on magnetic field in detail.

2 Theoretical Model

All of microscopic electromagnetic, including the propagation of light in a PCF, is governed by the Maxwell equations. The eigenvalue equations of a PCF can be obtained from the Maxwell equation, and they are

$$\frac{1}{\varepsilon(r)}\nabla\times\left[\nabla\times E(r)\right]=\frac{\omega^2}{c^2}E(r) \tag{1}$$

$$\nabla\times\left[\frac{1}{\varepsilon(r)}\nabla\times H(r)\right]=\frac{\omega^2}{c^2}H(r) \tag{2}$$

Where $H = H(x,y)e^{-j\beta z}$ is magnetic field, $E = E(x,y)e^{-j\beta z}$ is electric field, ε_r, μ_r respectively are the dielectric constant and the magnetic permeability of medium, c is the vacuum speed of light, ω is the angular frequency of light, and β is the mode propagation constant. When we analyze the propagation of light in a PCF by the full-vector finite element method, the quadrature hybrid wave model is adopted. After setting the material parameters, the incident wavelength and perfectly matched layer, we can calculate the mode field distribution and the effective index of fundamental mode.

Birefringence can be characterized by two important parameters, normalized birefringence parameter B and polarization beat length L_B. These two parameters were defined as

$$B = n_y - n_x = \frac{\lambda}{2\pi}(\beta_y - \beta_x) \tag{3}$$

$$L_B = \frac{\lambda}{n_x - n_y} \tag{4}$$

Where β_x and β_y are the two orthogonal polarization mode propagation constant, and n_x and n_y are the effective refractive index of orthogonal polarization mode.

3 Simulations and Analysis

We design a PCF showed in Fig. 1. This structure contains a solid core surrounded with four hexagons of air holes characterized by a diameter d and the hole to hole spacing Λ of 1.8μm and 2μm respectively. The middle row air holes were filled with MF.

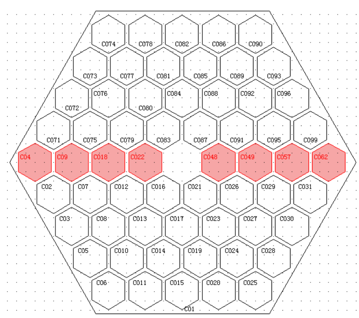

Fig. 1. The cross section of the PCF filling MF

In order to make that the average index of the solid-core is higher than that of the cladding with periodic air-holes. Therefore, the guiding mechanism is governed by the modified TIR. The water-based Fe_3O_4 with concentration of 1.21% was selected as filling material, and the filling length was 2cm. When H increased from 25Oe to 175Oe, the corresponding n_{MF} increased from 1.4355 to 1.5895. The refractive index of core n_{co} doped metal oxides can be 1.5 ~ 1.8 by adjusting the ratio of metal oxides. Here n_{co} =1. 65. When Λ=2μm, and the duty ratio d/Λ is 0.6, 0.8, 0.9 respectively, we analyze the effects the geometric parameters and the magnetic field on the birefringence of the PCF.

3.1 Mode Field Distributions

When incident wavelength λ =1550nm and duty ratio d/Λ=0.9, the mode field distributions of the MF-filled PCF under different magnetic field H (H=25Oe, 75Oe, 125Oe and 175Oe respectively) are shown in Fig. 2. It can be seen that the mode field distributions can be tuned with the applied magnetic field, i.e. the birefringence of the MF-filled PCF are sensitive to external magnetic field. With the magnetic field enhancing, the n_{MF} is increasing, then the effective refractive index of cladding mode is increasing. As a result, the birefringence of the PCF is higher.

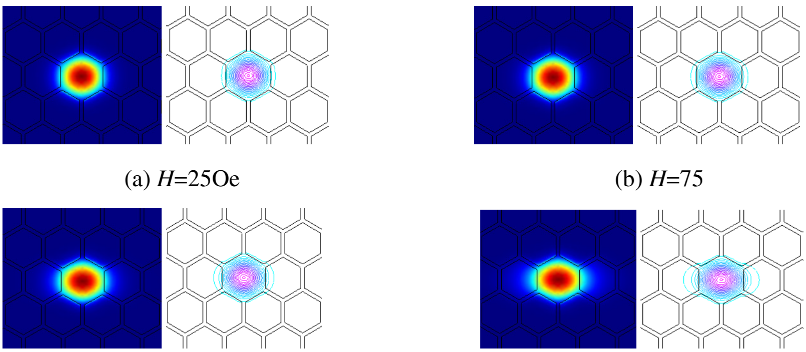

(a) H=25Oe (b) H=75

(c) H=125Oe (d) H=175Oe

Fig. 2. the mode field distributions of the PCF filled MF under different magnetic field H under λ=1550nm, d/Λ = 0.9 (a) H=25Oe, (b) H=75Oe, (c) H=125Oe, (c) H=175Oe

3.2 The Effective Refractive Index vs. Magnetic Field

When Λ is fixed to 2μm and the duty ratio d/Λ is 0.6, 0.8, 0.9 respectively, the relationships between the effective refractive index n_x and n_y of the MF-filled PCF with different duty ratios were analyzed under λ =1550nm. Tab.1 shows the effective refractive index n_x and n_y of the MF-filled PCF for the magnetic field between 25Oe and175Oe.

Tab.1 (a) shows the effective refractive index n_x and n_y of the MF-filled PCF with d/Λ=0.9. It was found that n_x change from 1.586896 to 1.591754 and n_y change from 1.589922 to 1.596851. Tab.1 (b) shows the effective refractive index n_x and n_y of the MF-filled PCF with d/Λ=0.8. It was found that n_x change from 1.597578 to 1.601994 and n_y change from 1.599684 to 1.605543. Tab.1 (c) shows the effective refractive index n_x and n_y of the MF-filled PCF with d/Λ=0.6. It was found that n_x change from 1.613511 to 1.617318 and n_y change from 1.614505 to 1.618987. It can be concluded, firstly, the n_x and n_y of these kinds PCF increases with the magnetic field increasing. The reason is that the refractive index of MF n_{MF} is increases with magnetic field increasing, which lead to the n_{eff} increases significantly with magnetic field.

Secondly, the n_x and n_y of these kinds PCF reduces with the duty ratio d/Λ increasing, and the larger the duty ratio is, the faster is the changing of n_x and n_y with magnetic field. It is possible to notice the PCF filled MF with larger d/Λ is more sensitive to magnetic field.

Table 1. Effective refractive indexes n_x and n_y of different magnetic field under λ=1550nm. (a) d/Λ=0.9, (b) d/Λ=0.8, (c) d/Λ=0.6

(a)

H(Oe)	n_x	n_y	H(Oe)	n_x	n_y
25	1.586896	1.589922	105	1.588622	1.592597
35	1.587065	1.590198	115	1.588927	1.593041
45	1.587242	1.590484	125	1.589264	1.593522
55	1.587433	1.590778	135	1.589636	1.594044
65	1.587637	1.591109	145	1.590058	1.594624
75	1.587854	1.591445	155	1.59054	1.595273
85	1.58809	1.591805	165	1.591093	1.596001
95	1.588346	1.59219	175	1.591754	1.596851

(b)

H(Oe)	n_x	n_y	H(Oe)	n_x	n_y
25	1.597578	1.599684	105	1.599115	1.601884
35	1.597726	1.599907	115	1.599351	1.602256
45	1.597883	1.60014	125	1.599696	1.602662
55	1.598052	1.600388	135	1.600035	1.603105
65	1.598234	1.600651	145	1.600422	1.603602
75	1.598427	1.600927	155	1.600865	1.604162
85	1.598638	1.601225	165	1.601378	1.604796
95	1.598867	1.601544	175	1.601994	1.605543

(c)

H(Oe)	n_x	n_y	H(Oe)	n_x	n_y
25	1.613511	1.614505	105	1.614784	1.616093
35	1.613632	1.614661	115	1.615018	1.616373
45	1.613759	1.614824	125	1.615281	1.616684
55	1.613897	1.615	135	1.615575	1.617026
65	1.614046	1.615118	145	1.615914	1.617417
75	1.614206	1.615388	155	1.616307	1.617863
85	1.614382	1.615604	165	1.616764	1.618375
95	1.614574	1.615839	175	1.617318	1.618987

3.3 The Effects of Normalized Birefringence Parameter *B* and Polarization Beat Length L_B on Magnetic Field

We calculate the β_x and β_y by finite element method, and then we can obtain the normalized birefringence parameter *B* and polarization beat length L_B by formula (3) and (4). Fig. 3 describes the relationship between normalized birefringence parameter *B* of the PCF filled MF and the external magnetic field at different duty ratio d/Λ. It was found that the normalized birefringence parameter *B* under d/Λ=0.9 increase from 0.003026 to 0.005097, the *B* under d/Λ=0.8 increase from 0.002106 to 0.003549 and the *B* under d/Λ=0.6 increase from 0.000994 to 0.001669 when the magnetic field *H* change between 25Oe and 175Oe. Notice that the normalized birefringence parameter *B* increases with the increasing magnetic field *H* at the same duty ratio and *B* increases with the increasing duty ratio d/Λ at the same magnetic field *H*. Although the refractive index n_x and n_y decreases with the increase of magnetic field *H*, but the difference of n_x and n_y has increased. The normalized birefringence parameter *B* with different d/Λ increase linearly with magnetic field *H* from 25Oe to175Oe. The reason is that the refractive index of the radial hole increases with magnetic field, the ability to controlling the light in the direction decreases, which result in birefringence increase.

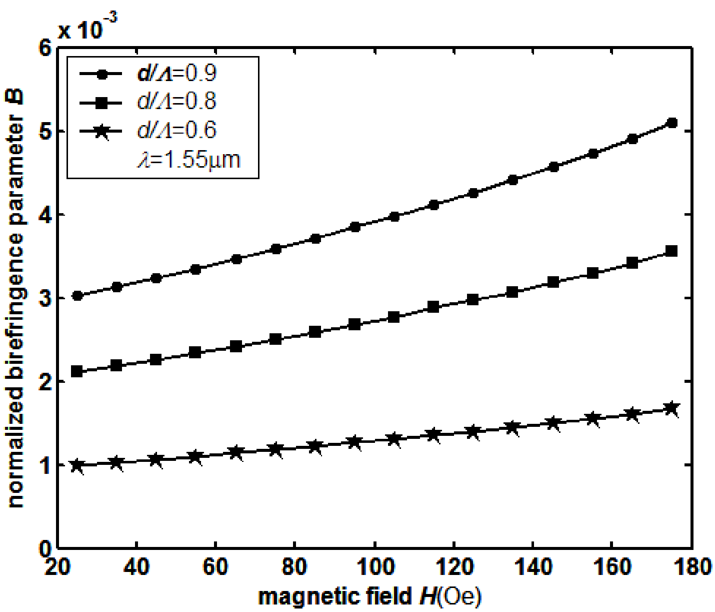

Fig. 3. The normalized birefringence parameter *B* of the PCFs with different duty ratio vs. magnetic field

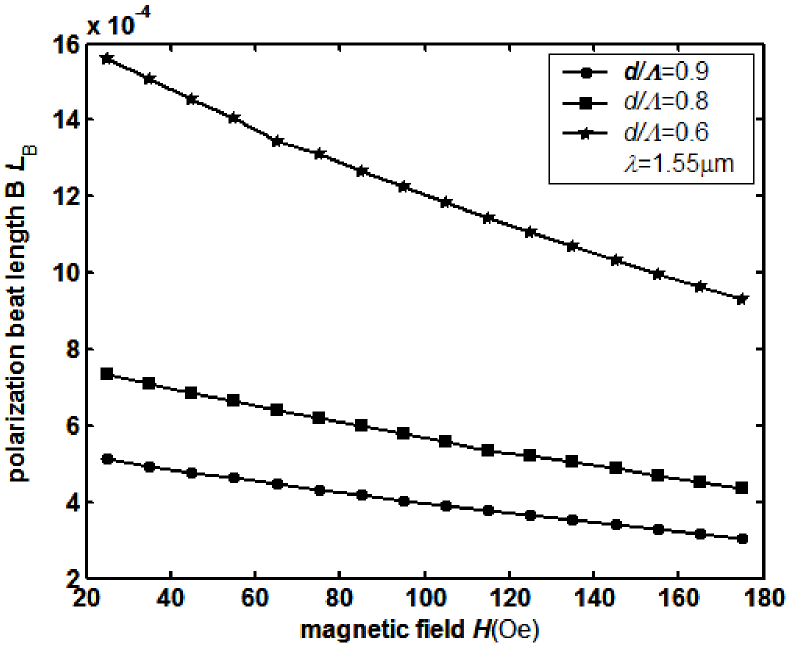

Fig. 4. The polarization beat length L_B of the PCFs with different duty ratio vs. magnetic field

Fig. 4 describes the relationship between polarization beat length L_B of the PCF filled MF and the external magnetic field at different duty ratio d/Λ. Notice that the polarization beat length L_B decreases with the increasing magnetic field H at the same duty ratio and L_B decreases with the increasing duty ratio d/Λ at the same magnetic field H. the results are consistent with the theoretical analysis.

According to the above analysis, we can concluded that the birefringence of MF-filled PCF can be tuned by adjusting the magnetic field and d/Λ. the birefringence effect is significantly enhanced, and birefringence effect is ten times higher than the general fiber.

4 Conclusion

The magnetically induced tuning birefringence properties of the TIR-PCF filled MF, which contains a solid core surrounded with four hexagons of air holes, were simulated and analyzed by the full-vector finite element method under external magnetic field. The relationships between the effective refractive index n_x and n_y, normalized birefringence parameter B and polarization beat length L_B of the MF-filled PCF on magnetic field for different duty ratio were investigated. The results show that the birefringence of MF-filled PCF can be tuned by adjusting the magnetic field and d/Λ. the normalized birefringence parameter B increases with the increasing magnetic field H at the same duty ratio and B increases with the increasing duty ratio d/Λ at the same magnetic field *H.* When the wavelength λ=1550nm, the duty ratio d/Λ=0.9, normalized birefringence parameter *B* increases from 0.003026 to 0.005097 as the magnetic field changes from 25Oe to 175Oe. The birefringence effect is ten times higher than the general fiber and there is a fairly good linearity. This scheme provides theoretical foundation to use magnetic field to control light in PCF and also offers a potential method for making high- birefringent polarization fiber.

Acknowledgments. This work was supported in part by the Scientific Research Fund of Liaoning Provincial Education Department under Grant No.L2011235, the Key Technologies R & D Program of Liaoning Province (Grant No. 2011224006, 2011217003), the Program for Liaoning Innovative Research Team in University (Grant No. LT2011019) and the Technology Program of Shenyang (Grant No. F11-044-2-00).

References

1. Russell, P.S.J.: Photonic-crystal fibers. Science 299, 358–362 (2003)
2. Knight, J.C.: Photonic crystal fibers. Nature 424, 847–851 (2003)
3. Russell, P.S.J.: Photonic-crystal fibers. J. Lightwave Technol. 24, 4729–4749 (2006)
4. Haakestad, M.W., Alkeskjold, T.T., Nielsen, M.D., Scolari, L., Riishede, J., Engan, H.E., Bjarklev, A.: Electrically tunable photonic bandgap guidance in a liquid crystal filled photonic crystal fiber. IEEE Photon. Technol. Lett. 17(4), 819–821 (2005)
5. Zografopoulos, D.C., Kriezis, E.E., Tsiboukis, T.D.: Tunable Highly Birefringent Bandgap-Guiding Liquid-Crystal Microstructured Fibers. J. Lightwave Technol. 24(9), 3427–3432 (2006)
6. Alkeskjold, T.T., Laegsgaard, J., Bjarklev, A., Hermann, D.S., Broeng, J., Li, J., Gauza, S., Wu, S.T.: Highly tunable large-core single-mode liquid-crystal photonic bandgap fiber. Appl. Opt. 45(10), 2261–2264 (2006)
7. Monro, T., Richardson, D., Holey, J.: optical fibres:Fundamental properties and device applications. Comptes Rendus Physique 4(4), 175–186 (2003)
8. Nielsen, M.D., Folkenberg, J.R., Mortensen, N.A., Bjarklev, A.: Bandwidth comparison of photonic crystal fibers and conventional single-mode fibers. Opt. Exp. 12(3), 430–435 (2004)
9. Gates, J.C., Hillman, C.W., Baggett, J.C.: Structure and propagation of modes of large mode area holey fibers. Opt. Exp. 12(5), 847–852 (2004)
10. Ortigosa-Blanch, A., Knight, J.C., Wadsworth, W.J., Arriaga, J., Mangan, B.J., Birks, A., Russell, P.S.J.: Highly birefringent photonic crystal fibers. Opt. Lett. 25, 1325–1327 (2000)
11. Hansen, T.P., Broeng, J., Libori, S.E.B., Knudsen, E., Bjarklev, A., Jensen, J.R., Simonsen, H.: Highly birefringentindex-guiding photonic crystal fibers. IEEE Photon.Technol. Lett. 13, 588–590 (2001)
12. Sapulak, M., Statkiewicz, G., Olszewski, J., Martynkien Urbanczyk, T.W., Wojcik, J., Makara, M., Klimek, J., Nasilowski, T., Berghmans, F., Thienpont, H.: Experimentaland theoretical investigations of birefringent holey fiberswith a triple defect. Appl. Opt. 44, 2652–2658 (2005)

13. Frazão, O., Baptista, J.M., Santos, J.L., Roy, P.: Curvature sensor using a highly birefringent photonic crystal fiber with two asymmetric hole regions in a Sagnac interferometer. Appl. Opt. 47, 2520–2523 (2008)
14. Kerbage, C., Eggleton, B.J.: Numerical analysis and experimental design of tunable birefringence in microstructured optical fiber. Opt. Express 10(5), 246–255 (2002)
15. Zhao, Y., Zhang, Y.Y., Lv, R.Q., Wang, Q.: Novel optical devices based on the tunable refractive index of magnetic fluid and their characteristics. Journal of Magnetism and Magnetic Materials 323(23), 2987–2996 (2011)
16. Yang, S.Y., Horng, H.E.: Structures, Optical Properties and Potentially Electro-Optical Applications of Magnetic Fluid Films. Tamkang Journal of Science and Engineering 5(2), 85–93 (2002)

A Lateral Inhibitory Spiking Neural Network for Sparse Representation in Visual Cortex

Jiqian Liu and Yunde Jia

Beijing Key Lab of Intelligent Information Technology
School of Computer Science and Technology
Beijing Institute of Technology, Beijing 100081, P.R. China
{liujiqian,jiayunde}@bit.edu.cn

Abstract. Sparse representation has been validated to be a common phenomenon in many sensory neural systems, but its underlying neural mechanism still remains unclear. This paper proposes a neurally plausible model towards solving this problem. We find that lateral inhibition is the fundamental neural mechanism for sparse representation in the visual cortex, by which cortical neurons not only compete with each other so that the input signal can be represented sparsely but also cooperate with each other to make the representation more accurate. We integrate this result into the matching pursuit framework, a quite suitable solution for neural implementation, to illustrate how an input signal is sparsely represented in V1. Our simulation results show that lateral inhibition can evidently decrease the average squared error in the representation and then the input signal can be sparsely represented very well by the proposed algorithm.

1 Introduction

The information processing mechanism of the primary visual cortex (V1) has been intensively investigated for several decades. Most early studies were much inspired by the seminal works of Shannon [1], [2] which are very important measurable quantities to the understanding of sensory coding. Barlow [3] considered that the signals from the natural environment were highly structured, meaning that the information in these signals was redundant. He suggested the goal of visual information processing could be to reduce statistical redundancy in the visual signals, and proposed a theory of redundancy reduction for neuronal populations to represent the stimuli efficiently. Now it is believed that cortical neurons are adapted, through the process of evolution, to the signals to which they are exposed. Along this line, much effort has been made to investigate the coding strategy employed by V1. Olshausen and Field [4] demonstrated that an algorithm maximizing the sparseness of the code for a given image can produce basis functions which are similar to the receptive field shapes of simple cells. Rehn and Sommer [7] then pointed out it is the number of activated neurons rather than the neuronal activity that should be optimized to produce the diverse distribution of receptive field structures as those obtained from physiological experiments [6]. And this gives a clearer direction to the way in which V1 neurons

H. Zhang et al. (Eds.): BICS 2012, LNAI 7366, pp. 259–267, 2012.

form the sparse representation of a stimulus. There has been much experimental evidence supporting the sparse representation in the sensory cortex [8], [9], [10], [11], [12]. But the plausible neural mechanism for this phenomenon has seldom been considered so far.

Perrinet [13], [14] suggested that the implementation of a matching pursuit (MP) algorithm [16] using a network of spiking neurons with a parallel architecture and lateral interactions provided an efficient representation of natural images. Rozell et al. [17] proposed a locally competitive algorithm which could be implemented in a dynamical system composed of neuron-like elements operating in parallel and was particularly appropriate for time-varying stimuli important to biological systems. These two studies together with many other studies [5], [7], [15] have noticed the important role of lateral inhibition in sparse representation. A model that performs predictive coding [18], [19], in which intracortical inhibition is fundamental, has been shown to account for a large range of V1 response properties. But lateral inhibition was usually thought to be competitive in all these previous studies, which however is proved not to be the whole truth by our research.

As pointed out by Olshausen and Field [4], there were only two global objectives, that the representation is sparse and that the representation error is small, need to be optimized for sparse coding. In this paper, we start our investigation with the objective of representing an input signal in the best way with a given basis set. It turns out that lateral inhibition is the neural mechanism responsible for the modification of neuronal activity corresponding to the best approximation of the input signal. That is, the spike rates of active neurons are decreased to levels corresponding to best representation of the input signal by lateral inhibitory interactions. This result indicates that lateral inhibition is not only a competitive interaction but also a cooperative interaction between output neurons. This is a whole new understanding of lateral inhibition ever since Hartline and Ratliff [20], [21] gave the quantitative analysis of lateral inhibitory interactions in the Limulus retina 50 years ago. We integrate this result into the matching pursuit framework and propose a lateral inhibitory spiking neural network to show how the spike rates of output neurons are updated through lateral inhibition to produce a sparse representation of the input signal.

2 Theory of Lateral Inhibition

2.1 Geometrical Description of Sparse Representation

Rehn and Sommer [7] employed the hard-sparseness constraint: the number of active neurons instead of the neural activity is very limited when stimuli are fed to the inputs, and they proposed the optimization problem of sparse coding:

$$min\{(I - \sum_j a_j \boldsymbol{w}_j)^2 + \lambda \|\boldsymbol{a}\|_0\}, \quad (1)$$

where I is the input image, $\boldsymbol{w}_j$ is a basis vector, a_j is its coefficient, $\boldsymbol{a}$ is the vector of coefficients and λ is the trade-off. From Eq. (1) we can see that the two global objectives, the one of finding the best representation of the input image $(I-\sum_j a_j \boldsymbol{w}_j)^2$ and the one of guaranteeing the representation being sparse $\|\boldsymbol{a}\|_0$ are put together with the trade off parameter λ. Because the l_0 norm is non-differentiable, the optimization problem of Eq. (1) is difficult to solve. To make the problem tractable, we consider an alternative model:

$$min\{\|a_j\|_0\} \;\; s.t. \;\; (I-\sum_j a_j \boldsymbol{w}_j)^2 < \varepsilon. \tag{2}$$

where ε is the trade off parameter. Compared with Eq. (1), the major difference of the new model is that the two global objectives are treated separately. In this way, the objectives may be easily achieved through different neural mechanisms. The goal of Eq. (2) is quite clear which can be described as representing the input pattern well enough by as few basis vectors as possible.

A natural way to solve this problem is to carefully select several basis vectors to see whether the best representation of the input signal by these basis vectors satisfies the constraint. Considering this process being implemented in the visual cortex where the LGN input is encoded by the activity of V1 neurons, the fact that the number of V1 neurons is much larger than the number of LGN cells implies that the basis set is overcomplete. Therefore each basis vector cannot be orthogonal to all the others. Meanwhile since the number of active neurons or the selected basis vectors is usually very small, the space spanned by these selected basis vectors is usually a low dimensional subspace. These mean the solution procedure of the proposed model is actually a process of finding the orthogonal projection $\hat{\boldsymbol{x}}$ of $\boldsymbol{x}$ onto a low dimensional subspace where $\hat{\boldsymbol{x}}$ is decomposed into several non-orthogonal components (see Fig. 1). In this way, $\boldsymbol{x}$ is best represented by

$$\hat{\boldsymbol{x}} = \sum_j a_j \boldsymbol{w}_j. \tag{3}$$

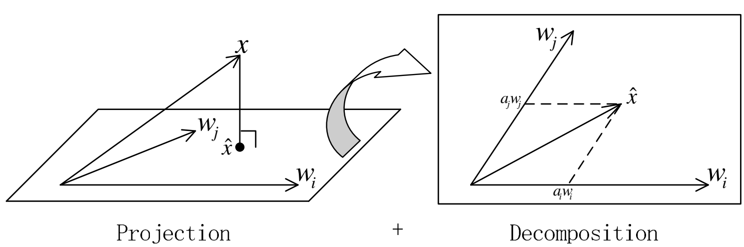

Fig. 1. Geometrical description sketch of sparse representation. Sparse representation can be regarded as the orthogonal projection of $\boldsymbol{x}$ onto a low-dimensional subspace spanned by the basis vectors $\{\boldsymbol{w}_j\}$ and the non-orthogonal decomposition of the projection vector $\hat{\boldsymbol{x}}$ into the sum of these basis vectors.

2.2 Relational Equations for Lateral Inhibition

For a neural network performing the above procedure, an input signal $\boldsymbol{x}$ will first activate only a few output neurons. Suppose the jth output neuron is activated and the output value of this neuron is y_j. Then we put forward the assumption: y_j is proportional to the coefficient a_j in Eq. (3). In other words, the assumption is the output values of active neurons are modified to represent the input signal in the best way. We call it the best representation assumption (BRA). Denote $a_j = \lambda y_j$ where λ is the proportional factor. In order to determine λ, we consider the situation in which only the jth output neuron is activated. The receptive field of this neuron corresponding to the weight vector of the neural network is $\boldsymbol{w}_j$. For this situation, the output y_j is equal to $\boldsymbol{x} \cdot \boldsymbol{w}_j$, and a_j can be easily obtained by computing $\hat{\boldsymbol{x}}$ using the scalar projection of $\boldsymbol{x}$ on $\boldsymbol{w}_j$ which is:

$$\hat{\boldsymbol{x}} = (\boldsymbol{x} \cdot \frac{\boldsymbol{w}_j}{\|\boldsymbol{w}_j\|})\frac{\boldsymbol{w}_j}{\|\boldsymbol{w}_j\|} = \frac{y_j}{\|\boldsymbol{w}_j\|^2}\boldsymbol{w}_j. \tag{4}$$

Thus we obtain at once that $a_j = \frac{y_j}{\|\boldsymbol{w}_j\|^2}$ and $\lambda = \frac{1}{\|\boldsymbol{w}_j\|^2}$. Substituting the result into Eq. (3) yields

$$\hat{\boldsymbol{x}} = \sum_j \frac{y_j}{\|\boldsymbol{w}_j\|^2}\boldsymbol{w}_j. \tag{5}$$

Eq. (5) shows how the neural network represents the input $\boldsymbol{x}$ in the best way. The ith coordinate of $\hat{\boldsymbol{x}}$ then can be expressed as

$$\hat{x}_i = \sum_j \frac{y_j}{\|\boldsymbol{w}_j\|^2} w_{ij} \tag{6}$$

where w_{ij} is the ith coordinate of $\boldsymbol{w}_j$.

Given the set of activated neurons for the input signal, we now consider how the output values are calculated by the neural network. Let $\boldsymbol{e}$ denote the residual error vector, that is, $\boldsymbol{e} = \boldsymbol{x} - \hat{\boldsymbol{x}}$. Then the equation $\boldsymbol{e} \cdot \boldsymbol{w}_j = 0$ must hold for every j. Thus

$$\boldsymbol{x} \cdot \boldsymbol{w}_j = (\hat{\boldsymbol{x}} + \boldsymbol{e}) \cdot \boldsymbol{w}_j = \hat{\boldsymbol{x}} \cdot \boldsymbol{w}_j. \tag{7}$$

$\boldsymbol{x} \cdot \boldsymbol{w}_j$ is the output value of the jth output neuron , denoted as Y_j, when no other output neurons are activated. This value corresponds to the best representation of $\boldsymbol{x}$ in the direction of $\boldsymbol{w}_j$. And $\hat{\boldsymbol{x}}$ is the best representation of $\boldsymbol{x}$ at the case that several output neurons are activated and their output values are $\{y_j\}$. Expand Eq. (7) and substitute $\hat{x}_i$ with Eq. (6), we have

$$\begin{aligned} Y_j = \hat{\boldsymbol{x}} \cdot \boldsymbol{w}_j &= \sum_i \hat{x}_i \cdot w_{ij} \\ &= \sum_i (\sum_k \frac{y_k}{\|\boldsymbol{w}_k\|^2} w_{ik}) w_{ij} \\ &= \sum_k \frac{y_k}{\|\boldsymbol{w}_k\|^2} \boldsymbol{w}_k \cdot \boldsymbol{w}_j \\ &= y_j + \sum_{k \neq j} \frac{\boldsymbol{w}_k \cdot \boldsymbol{w}_j}{\|\boldsymbol{w}_k\|^2} y_k. \end{aligned}$$

That is,

$$\Delta Y_j = Y_j - y_j = \sum_{k \neq j} \frac{\boldsymbol{w}_k \cdot \boldsymbol{w}_j}{\|\boldsymbol{w}_k\|^2} y_k. \tag{8}$$

Eq. (8) has the same form as the Hartline-Ratliff equation for lateral inhibition [21] indicating that the activities of output neurons are suppressed to low levels, which correspond to the new best representation of the input signal, by lateral inhibition. This provides a whole new perspective on lateral inhibitory interactions through which the output neurons not only compete with each other to make the representation more efficient but also cooperate with each other to represent the input signal more accurate. Because of this we can say that lateral inhibition is the fundamental mechanism of sparse representation in visual cortex. Furthermore Eq. (8) gives the concrete calculation of the inhibitory coefficient of the kth output neuron on the jth output neuron $C_{k,j}$:

$$C_{k,j} = \frac{\boldsymbol{w}_k \cdot \boldsymbol{w}_j}{\|\boldsymbol{w}_k\|^2}. \tag{9}$$

It should be noted that $C_{k,j} \neq C_{j,k}$ unless $\|\boldsymbol{w}_k\|^2 = \|\boldsymbol{w}_j\|^2$. The result is consistent with the direct measurement reported by Hartline and Ratliff [20]. From Eq. (9) we can see that the more correlated the neurons are, the stronger the inhibitory connection between them is. This reconciles with the observation that synaptic inhibition is primarily tuned to similar orientations [22], [23].

3 Lateral Inhibition-Based Matching Pursuit

Eq. (8) can be rewritten and transformed into the iterative formula for calculating y_j:

$$y_j^{\tau} = Y_j - \sum_{k \neq j} \frac{\boldsymbol{w}_k \cdot \boldsymbol{w}_j}{\|\boldsymbol{w}_k\|^2} y_k^{\tau}. \tag{10}$$

where y_k^{τ} is the output value of the kth output neuron at the moment τ. Eq. (10) is a Jacobi iterative process which converges when $\sum_{k \neq j} \frac{\boldsymbol{w}_k \cdot \boldsymbol{w}_j}{\|\boldsymbol{w}_k\|^2} < 1$. In practice, the criterion is very easy to be satisfied for the reason that both the dot product $\boldsymbol{w}_k \cdot \boldsymbol{w}_j$ and the number of selected basis vectors are usually very small, which also makes the convergence of the calculation very fast. Eq. (10) shows that the low level steady state of an active output neuron y_j is achieved through an iterative process driven by the input signal while updated by lateral inhibition. This explains why the decrease in excitation from Y_j to y_j leads to a decrease in inhibition [23], [24].

On the basis of the above analysis, we next give an algorithm for the sparse representation model described by Eq. (1). The selection of basis vectors in the presented algorithm is similar to that of the original matching pursuit [16]. But in the original MP, the basis vectors are required to be orthogonal to each other which makes it quite easy to guarantee the residual error vector to be orthogonal to all the selected basis vectors. We have proved that this also can be achieved

Table 1. Lateral Inhibition-based Matching Pursuit

Input	a stimulus $\boldsymbol{x}$, the basis set $\boldsymbol{W}$
Output	the best representation $\hat{\boldsymbol{x}}$ of $\boldsymbol{x}$
Initialization	$\boldsymbol{W} = \Phi$
step 1.	Chose the basis vector that matches $\boldsymbol{x}$ best and put it into $\boldsymbol{W}$.
step 2.	For all $\boldsymbol{w}_j$ in $\boldsymbol{W}$, compute $\{y_j^{(n)}\}$ iteratively using Eq. (10).
step 3.	Compute $\boldsymbol{e}^{(n)} = \boldsymbol{x} - \hat{\boldsymbol{x}}^{(n)}$ with equation (5) and, if($\lVert\boldsymbol{e}^{(n)} - \boldsymbol{e}^{(n-1)}\rVert > \varepsilon$), $\boldsymbol{x} = \boldsymbol{e}^{(n)}$ and Goto 2; else, print $\hat{\boldsymbol{x}}$ and stop.

by lateral inhibitory interactions between output neurons in the case of basis vectors being not orthogonal. By combining these results, we propose the lateral inhibition-based matching pursuit (LIMP) algorithm for sparse representation as shown in Table 1.

The LIMP algorithm is quite suitable to be implemented in sensory cortex. Each step of this algorithm can be realized by neural circuits. For a stimulus presented to a sensory neural system, the sparse representation procedure could be: first, the neuron that matches the stimulus best will be activated; then, it fires a spike to neighboring highly correlated neurons and delays their activation; next, the neuron that matches the residual error vector best will be activated. Finally, this procedure goes on until no more neurons are activated. In this way, most of the neighboring neurons would receive too much lateral inhibition to be activated and then show no response to the stimulus. As a consequence, the stimulus is represented well enough by a small number of neurons chosen from a large number of neuronal populations. We call such a neural network, as shown in Fig. 2, a lateral inhibitory spiking neural network (LISNN).

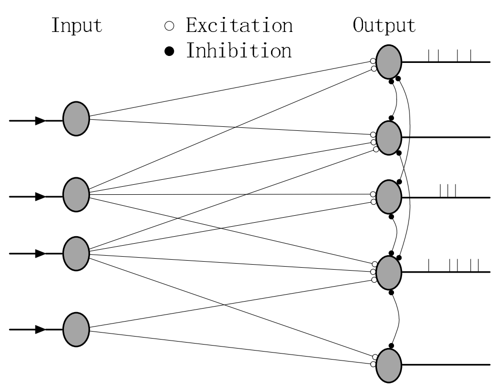

Fig. 2. Sketch of lateral inhibitory spiking neural network (LISNN). Output neurons integrate excitatory afferents (open circles) from input neurons and interact with each other through lateral inhibitory connections (filled circles). The activated neurons fire spikes to suppress the activity of neighboring highly correlated neurons.

4 Results

We test the LIMP algorithm with a 250×250 sized "Lena" image (see Fig. 3(b)). To make the test simpler, we use a group of two dimensional trigonometric functions and several Gaussian functions illustrated in Fig. 3(a) as the basis set. According to the receptive field properties of neurons in the early stages of visual pathway, we first perform a convolution of the "Lena" image with the Difference of Gaussian (DoG) filter. Then we cut the DoG filtered "Lena" image (see Fig. 3(c)) into 25×25 patches with a size of 10×10 pixels as the inputs of the LIMP algorithm. And then each of the image patches, corresponding to $\boldsymbol{x}$, is reconstructed by the LIMP algorithm with no more than 6 basis vectors. At last, we stitch the reconstructed image patches, corresponding to $\hat{\boldsymbol{x}}$, back together into the new image as shown in Fig. 3(d). Comparing Fig. 3(c) with Fig. 3(d), we

(a) (b) (c) (d)

Fig. 3. Illustration of the DoG filtered "Lena" image being reconstructed by the LIMP algorithm. (a) The filters used in this paper. (b) The "Lena" image. (c) The DoG filtered "Lena" image which is cut into 625 (10×10) patches as the inputs of the LIMP algorithm. (d) The stitched image from the reconstructed patches by the LIMP algorithm.

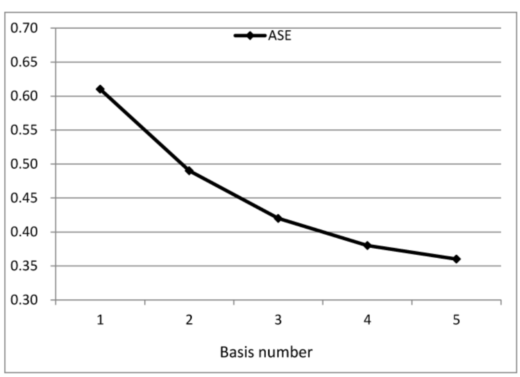

Fig. 4. The impact of lateral inhibition on the average squared error (ASE). ASE is significantly reduced by lateral inhibition and decreases with the increasing of the number of selected basis functions.

see that the DoG filtered image is reconstructed very well. We use the average squared error (ASE) over all image patches to assess the reconstruction quality of the LIMP algorithm. ASE is significantly reduced with the increasing of the number of selected basis functions (see Fig. 4) indicating that lateral inhibition is the neural mechanism by which input stimuli could be represented better.

5 Conclusion

In this paper we focused on modeling the process of sparse representation in visual cortex. The key finding of our research is that the lateral inhibition between output neurons helps to represent the inputs as well as possible. Based on this finding, the LIMP algorithm was presented to illustrate how sensory neural systems encode the inputs efficiently and correctly. The experimental results demonstrate the good performance of our presented LIMP algorithm.

Acknowledgments. This work was supported in part by the NSFC-Guangdong Joint Fund under Grant No. U1035004 and Natural Science Foundation of China (NSFC) under Grant No. 90920009.

References

1. Shannon, C.E., Weaver, W.: The mathematical theory of communication. University of Illinois Press, Urbana (1949)
2. Shannon, C.E.: Prediction and Entropy of Printed English. Bell Systems Technical Journal 30, 50–64 (1951)
3. Barlow, H.: Possible principles underlying the transformation of sensory messages. Sensory Communication, 217–234 (1961)
4. Olshausen, B.A., Field, D.J.: Emergence of simple-cell receptive field properties by learning a sparse code for natural images. Nature 381, 607–609 (1996)
5. Olshausen, B.A.: Principles of Image Representation in Visual Cortex. In: Chalupa, L.M., Werner, J.S. (eds.) The Visual Neurosciences, pp. 1603–1615. MIT Press (2003)
6. Ringach, D.L.: Spatial structure and symmetry of simple-cell receptive fields in macaque primary visual cortex. J. Neurophysiol. 88, 455–463 (2002)
7. Rehn, M., Sommer, F.T.: A network that uses few active neurones to code visual input predicts the diverse shapes of cortical receptive fields. Journal of Computational Neuroscience 22, 135–146 (2007)
8. Vinje, W.E., Gallant, J.L.: Sparse Coding and Decorrelation in Primary Visual Cortex During Natural Vision. Science 287, 1273–1276 (2000)
9. Perez-Orive, J., Mazor, O., Turner, G.C., Cassenaer, S., Wilson, R.I., Laurent, G.: Oscillations and Sparsening of Odor Representations in the Mushroom Body. Science 297, 359–365 (2002)
10. Laurent, G.: Olfactory network dynamics and the coding of multidimensional signals. Nature Reviews Neuroscience 3, 884–895 (2002)
11. Lewicki, M.S.: Efficient coding of natural sounds. Nature Neuroscience 5, 356–363 (2002)

12. Smith, E.C., Lewicki, M.S.: Efficient auditory coding. Nature 439, 978–982 (2006)
13. Perrinet, L.: Feature detection using spikes: the greedy approach. Journal of Physiology-Paris 98, 530–539 (2004)
14. Perrinet, L.: Efficient Source Detection Using Integrate-and-Fire Neurons. In: Duch, W., Kacprzyk, J., Oja, E., Zadrożny, S. (eds.) ICANN 2005, Part I. LNCS, vol. 3696, pp. 167–172. Springer, Heidelberg (2005)
15. Perrinet, L.U.: Role of homeostasis in learning sparse representations. Neural Computation 22, 1812–1836 (2010)
16. Mattlat, S.G., Zhang, Z.: Matching Pursuits with Time-Frequency Dictionaries. IEEE Transactions on Signal Processing 41, 3397–3415 (1993)
17. Rozell, C.J., Johnson, D.H., Baraniuk, R.G., Olshausen, B.A.: Sparse Coding via Thresholding and Local Competition in Neural Circuits. Neural Computation 20, 2526–2563 (2008)
18. Spratling, M.W.: Predictive Coding as a Model of Response Properties in Cortical Area V1. The Journal of Neuroscience 30, 3531–3543 (2010)
19. Spratling, M.W.: A single functional model accounts for the distinct properties of suppression in cortical area V1. Vision Research 51, 563–576 (2011)
20. Hartline, H.K., Ratliff, F.: Inhibitory interaction of receptor units in the eye of Limulus. Journal of General Physiology 40, 357–376 (1957)
21. Hartline, H.K., Ratliff, F.: Spatial summation of inhibitory influences in the eye of Limulus, and the mutual interaction of receptor units. Journal of General Physiology 41, 1049–1066 (1958)
22. Anderson, J.S., Carandini, M., Ferster, D.: Orientation Tuning of Input Conductance, Excitation, and Inhibition in Cat Primary Visual Cortex. J. Neurophysiol. 84, 909–926 (2000)
23. Priebe, N.J., Ferster, D.: Mechanisms underlying cross-orientation suppression in cat visual cortex. Nat. Neurosci. 9, 552–561 (2006)
24. Ozeki, H., Finn, I.M., Schaffer, E.S., Miller, K.D., Ferster, D.: Inhibitory Stabilization of the Cortical Network Underlies Visual Surround Suppression. Neuron 62, 578–592 (2009)

Global Stability of a Class of High-Order Recurrent Neural Networks with Multiple Delays

Zhanshan Wang[1], Yongbin Zhao[1], and Shuxian Lun[2]

[1] School of Information Science and Engineering, Northeastern University
Shenyang, Liaoning, 110004, People's Republic of China
wangzhanshan@ise.neu.edu.cn
[2] College of Engineering, Bohai University, Jinzhou 121000, People's Republic of China

Abstract. Global asymptotic stability problem for a general class of higher order recurrent neural networks (HRNN) with multiple delays has been studied based on delay-matrix decomposition method and linear matrix inequality (LMI) technique. The proposed stability criterion is suitable for a general class of multiple delayed higher order recurrent Neural Networks. Especially, for this system, we have also established corresponding LMI-based stability criteria which are simple in expression form and easy to check to deal with the different multiple delays. Compared with the existing results, our results are new and can be regarded as an alternative of M-matrix based stability results in the literature.

Keywords: High-order recurrent neural networks, asymptotic stability, multiple delays, linear matrix inequality (LMI).

1 Introduction

It is well known that recurrently connected networks have been extensively studied both in theory and applications. They have been successfully applied in signal processing, pattern recognition and associative memories, especially in static image treatment. (see [1-4] and references therein). However, these applications heavily depend on its strong approximation property. In this point, high-order neural networks do better than ordinary neural networks, that is to say, high-order neural networks have stronger approximation property, faster convergence rate, great stronger capacity, and higher fault tolerance. Due to this, recently HRNNs have attracted considerable attention. In [5], the author studied the JADE algorithm of high-order neural networks. In [6], some criteria are derived to ascertain global asymptotic stability of high-order neural networks, and in [7] some sufficient conditions are presented for the exponential stability of high-order Hopfield type neural networks. These previous literature only consider the stability of a special high-order neural networks without delays.

However, In hardware implementation, time delays inevitably occur due to the finite switching speed of the amplifiers and communication time. High-order

H. Zhang et al. (Eds.): BICS 2012, LNAI 7366, pp. 268–277, 2012.

neural networks with time delays have much more complicated dynamics due to the incorporation of delays. Therefore, stability analysis for high-order neural networks with different delays have been received many attentions. In the existing references, different kinds of delays have been considered, for example, with constant time delays, the existence and global asymptotic stability conditions were obtained in [8-9], which were based on LMI approach and with the assumption that the activation functions are monotonic non-decreasing. In [10], the author derived some sufficient conditions for the exponential stability of high-order BAM neural networks. It is easy to see that these results are only for the case of single constants delay. For the cases of multiple delays, in [11,12], based on M-matrix method, the authors acquired several stability criteria for some special systems. However, to the best of our knowledge, due to the difficulty of combining the set of differential dynamical systems into a compact vector-matrix form, there are no LMI stability results reported for high-order neural networks with multiple delays up to now.

Motivated by the aforementioned discussions, in this paper, we will establish several new sufficient conditions for the global asymptotic stability of the equilibrium point for high-order neural networks with multiple time delays. Compared to some previously published results, results of this paper are less conservative and more general. The main contributions of the paper include the following. 1) First, we present some linear matrix inequality (LMI)-based stability results for a class of neural networks with different multi-delays and with different activation functions. The concerned model regards the models in [13-15], and [16] as special cases. Our present results can directly be applied to the models studied in these papers. In these works, stability results are obtained mainly in the form of M-matrix or algebraic inequality. No LMI-based results have been reported in the existing literature. On the other hand, because the LMI-based results consider the sign difference of the elements in connection matrices, neurons excitatory and inhibitory effects on the neural network have been considered, which overcome the shortcomings of the results based on M-matrix and algebraic inequality. Correspondingly, results obtained using LMI techniques will be less conservative. 2) Many existing stability results in the form of LMI are special cases of the present results. Therefore, comparing to existing results, the present results are less conservative and have wider fields of applications.

2 Problem Description and Preliminaries

The following multiple delayed Higher Order Recurrent Neural Networks will be discussed in this paper:

$$\begin{aligned}\dot{u}_i(t) &= -a_i u_i(t) + \sum_{j=1}^{n}\sum_{k=1}^{n} w_{ij}\bar{w}_{ijk}\bar{h}_j(u_j(t))\bar{h}_k(u_k(t)) \\ &+ \sum_{j=1}^{n}\sum_{k=1}^{n} w_{ij}^1\bar{w}_{ijk}^1\bar{r}_j(u_j(t-\tau_{ij}))\bar{r}_k(u_k(t-\tau_{ik})) + U_i \qquad (1)\end{aligned}$$

where $x_i(t)$ is the neural state and n denotes the number of neurons; τ_{ij} represents the transmission delay which satisfies $0 \leq \tau_{ij} \leq \tau_M$, $(i, j = 1, 2, \ldots, n)$. $\bar{h}_i(x_i(t)), \bar{r}_i(x_i(t))$ are the neuron activation functions. $a_i > 0$ denotes the rate with which the i-th cell resets its potential to the resting state when isolated from the other cells and inputs; while w_{ij}, w_{ijk} and w^1_{ij}, w^1_{ijk} are the second-order synaptic weights of the neural network. U_i denotes the i-th component of an external input source introduced from outside the network to the i-th cell. The activation functions in (1) are assumed to be bounded and satisfy the following assumption.

Assumption 21. The activation functions $\bar{h}_i(x_i)$ and $\bar{r}_i(x_i)$ are bounded and continuous, which satisfy $|\bar{h}_i(x_i)| \leq H^b_i$ and $|\bar{r}_i(x_i)| \leq R^b_i$, $H^b_i > 0$ and $R^b_i > 0$,

$$0 \leq \frac{\bar{h}_i(\eta) - \bar{h}_i(v)}{\eta - v} \leq \delta^h_i, \tag{2}$$

$$0 \leq \frac{\bar{r}_i(\eta) - \bar{r}_i(v)}{\eta - v} \leq \delta^r_i, \tag{3}$$

for any $\eta \neq v, \eta, v \in \Re$, and $\delta^h_i > 0, \delta^r_i > 0$, $i = 1, \cdots, n$.

Let $\Delta_h = \mathrm{diag}(\delta^h_1, \cdots, \delta^h_n)$, $\Delta_r = \mathrm{diag}(\delta^r_1, \cdots, \delta^r_n)$.

Lemma 1. (see [17]) Let X, Y and P be real matrices with appropriate dimensions, P is a positive definite symmetric matrix. Then for any positive scalar $\epsilon > 0$, the following inequality holds,

$$X^TY + Y^TX \leq \epsilon^{-1}X^TP^{-1}X + \epsilon Y^TPY. \tag{4}$$

3 Main Results

In this section, we will establish two global asymptotic stability criteria for neural networks (1) with same activation functions and different activation functions, respectively.

Under assumption 2.1, system (1) can be transformed into the following form:

$$\begin{aligned}
\dot{u}_i(t) =& - a_iu_i(t) + \sum_{j=1}^{n}\sum_{k=1}^{n} w_{ij}\bar{w}_{ijk}\bar{h}_j(u_j(t))\bar{h}_k(u_k(t)) \\
&+ \sum_{j=1}^{n}\sum_{k=1}^{n} w^1_{ij}\bar{w}^1_{ijk}\bar{r}_j(u_j(t-\tau_{ij}))\bar{r}_k(u_k(t-\tau_{ik})) + U_i \\
=& - a_iu_i(t) + \sum_{j=1}^{n}\Big(c_{ij1}\bar{h}_1(u_1(t)) + c_{ij2}\bar{h}_2(u_2(t)) \\
&+ \cdots + c_{ijn}\bar{h}_n(u_n(t))\Big)\bar{h}_j(u_j(t)) + U_i
\end{aligned} \tag{5}$$

$$
\begin{aligned}
&+\sum_{j=1}^{n}\Big(d_{ij1}\bar{r}_1(u_1(t-\tau_{i1}))+d_{ij2}\bar{r}_2(u_2(t-\tau_{i2}))\\
&+\cdots+d_{ijn}\bar{r}_n(u_n(t-\tau_{in}))\Big)\bar{r}_j(u_j(t-\tau_{ij}))\\
=&-a_iu_i(t)+U_i\\
&+\Big(\bar{h}_1(u_1(t))\ \bar{h}_1(u_1(t))\ \cdots\ \bar{h}_n(u_n(t))\Big)\\
&\times\begin{pmatrix} c_{i11} & c_{i21} & \cdots & c_{in1}\\ c_{i12} & c_{i22} & \cdots & c_{in2}\\ \vdots & \vdots & \ddots & \vdots\\ c_{i1n} & c_{i2n} & \cdots & c_{inn}\end{pmatrix}\begin{pmatrix}\bar{h}_1(u_1(t))\\ \bar{h}_2(u_2(t))\\ \vdots\\ \bar{h}_n(u_n(t))\end{pmatrix}\\
&+\Big(\bar{r}_1(u_1(t-\tau_{i1}))\ \bar{r}_2(u_2(t-\tau_{i2}))\ \cdots\ \bar{r}_n(u_n(t-\tau_{in}))\Big)\\
&\times\begin{pmatrix} d_{i11} & d_{i21} & \cdots & d_{in1}\\ d_{i12} & d_{i22} & \cdots & d_{in2}\\ \vdots & \vdots & \ddots & \vdots\\ d_{i1n} & d_{i2n} & \cdots & d_{inn}\end{pmatrix}\begin{pmatrix}\bar{r}_1(u_1(t-\tau_{i1}))\\ \bar{r}_2(u_2(t-\tau_{i2}))\\ \vdots\\ \bar{r}_n(u_n(t-\tau_{in}))\end{pmatrix}\\
=&-a_iu_i(t)+\bar{h}^T(u(t))C_i^T\bar{h}(u(t))\\
&+\bar{r}^T(u(t-\bar{\tau}_i))D_i^T\bar{r}(u(t-\bar{\tau}_i))+U_i,
\end{aligned}
\tag{6}
$$

where

$$
c_{ijk}=w_{ij}\bar{w}_{ijk},d_{ijk}=w_{ij}^1\bar{w}_{ijk}^1,\bar{\tau}_i=\Big(\tau_{i1}\ \tau_{i2}\ \cdots\ \tau_{in}\Big)^T,
$$

$$
\bar{h}(u(t))=\Big(\bar{h}_1(u_1(t))\ \bar{h}_1(u_1(t))\ \cdots\ \bar{h}_n(u_n(t))\Big)^T,
$$

$$
\bar{r}(u(t-\bar{\tau}_i))=\Big(\bar{r}_1(u_1(t-\tau_{i1})),\cdots,\bar{r}_n(u_n(t-\tau_{in}))\Big)^T,
$$

$$
C_i=\begin{pmatrix} c_{i11} & c_{i12} & \cdots & c_{i1n}\\ c_{i21} & c_{i22} & \cdots & c_{i2n}\\ \vdots & \vdots & \ddots & \vdots\\ c_{in1} & c_{in2} & \cdots & c_{inn}\end{pmatrix},\ D_i=\begin{pmatrix} d_{i11} & d_{i12} & \cdots & d_{i1n}\\ d_{i21} & d_{i22} & \cdots & d_{i2n}\\ \vdots & \vdots & \ddots & \vdots\\ d_{in1} & d_{in2} & \cdots & d_{inn}\end{pmatrix}.
$$

We can rewrite the model (5) in a compact matrix-vector form as follows,

$$
\dot{u}(t)=-Au(t)+\bar{H}(u(t))\bar{C}\bar{h}(u(t))+\sum_{i=1}^{n}\bar{R}(u(t-\bar{\tau}_i))\bar{D}_i\bar{r}(u(t-\bar{\tau}_i))+U, \tag{7}
$$

where $\bar{H}(u(t))=\mathrm{diag}(\bar{h}^T(u(t))\ \bar{h}^T(u(t))\ \cdots\ \bar{h}^T(u(t)))_{n\times n^2}$, $\bar{R}(u(t-\bar{\tau}_i))=\mathrm{diag}(\bar{r}^T(u(t-\bar{\tau}_i))\ \bar{r}^T(u(t-\bar{\tau}_i))\ \cdots\ \bar{r}^T(u(t-\bar{\tau}_i)))_{n\times n^2}$, $U=(U_1\ U_2\ \cdots\ U_n)^T$,

$$
\bar{C}=\begin{pmatrix}C_1^T\\ C_2^T\\ \vdots\\ C_n^T\end{pmatrix},\bar{D}_1=\begin{pmatrix}D_1^T\\ 0\\ \vdots\\ 0\end{pmatrix},\ldots,\bar{D}_n=\begin{pmatrix}0\\ 0\\ \vdots\\ D_n^T\end{pmatrix},
$$

that is, i-th block in $\bar{D}_i$ is composed of D_i^T, and the other blocks are all zeros.

Suppose that u^* is an equilibrium point of (7), and let $x(t) = u(t) - u^*$, then we have

$$
\begin{aligned}
\dot{x}(t) =& - Ax(t) + \bar{H}(u(t))\bar{C}\bar{h}(u(t)) + \sum_{i=1}^{n} \bar{R}(u(t-\bar{\tau}_i))\bar{D}_i\bar{r}(u(t-\bar{\tau}_i)) \\
& - \bar{H}(u^*)\bar{C}\bar{h}(u^*) - \sum_{i=1}^{n} \bar{R}(u^*)\bar{D}_i\bar{r}(u^*) \\
=& - Ax(t) + \bar{H}(u(t))\bar{C}[\bar{h}(u(t)) - \bar{h}(u^*)] + [\bar{H}(u(t)) - \bar{H}(u^*)]\bar{C}\bar{h}(u^*) \\
& + \sum_{i=1}^{n} \bar{R}(u(t-\bar{\tau}_i))\bar{D}_i[\bar{r}(u(t-\bar{\tau}_i)) - r(u^*)] \\
& + \sum_{i=1}^{n} [\bar{R}(u(t-\bar{\tau}_i)) - \bar{R}(u^*)]\bar{D}_i\bar{r}(u^*).
\end{aligned} \tag{8}
$$

Since

$$
\begin{aligned}
& [\bar{H}(u(t)) - \bar{H}(u^*)]\bar{C}\bar{h}(u^*) \\
=& \text{diag}(\bar{h}^T(u(t)) - \bar{h}^T(u^*), \ldots, \bar{h}^T(u(t)) - \bar{h}^T(u^*))_{n\times n} \begin{pmatrix} C_1^T \\ C_2^T \\ \vdots \\ C_n^T \end{pmatrix} \bar{h}(u^*) \\
=& \begin{pmatrix} (\bar{h}^T(u(t)) - \bar{h}^T(u^*))C_1^T\bar{h}(u^*) \\ (\bar{h}^T(u(t)) - \bar{h}^T(u^*))C_2^T\bar{h}(u^*) \\ \vdots \\ (\bar{h}^T(u(t)) - \bar{h}^T(u^*))C_n^T\bar{h}(u^*) \end{pmatrix} \\
=& \begin{pmatrix} \bar{h}^T(u^*)C_1(\bar{h}(u(t)) - \bar{h}(u^*)) \\ \bar{h}^T(u^*)C_2(\bar{h}(u(t)) - \bar{h}(u^*)) \\ \vdots \\ \bar{h}^T(u^*)C_n(\bar{h}(u(t)) - \bar{h}(u^*)) \end{pmatrix} \\
=& \text{diag}(\bar{h}^T(u^*), \ldots, h^T(u^*))_{(n\times n)} \begin{pmatrix} C_1 \\ C_2 \\ \vdots \\ C_n \end{pmatrix} (\bar{h}(u(t)) - \bar{h}(u^*)) \\
=& \bar{H}(u^*)\hat{C}(\bar{h}(u(t)) - \bar{h}(u^*)),
\end{aligned} \tag{9}
$$

where $\hat{C} = (C_1^T, C_2^T, \ldots, C_n^T)^T_{n\times n^2}$. Similarly, let $\bar{r}(u(t-\bar{\tau}_i)) = \bar{r}_{u_{\bar{\tau}_i}}$, then we can obtain:

$$
[\bar{R}(u(t-\bar{\tau}_i)) - \bar{R}(u^*)]\bar{D}_i\bar{r}(u^*) \tag{10}
$$

$$
\begin{aligned}
&= \begin{pmatrix} \bar{r}^T_{u_{\bar{\tau}_i}} - \bar{r}^T(u^*) & 0 & \cdots & 0 \\ 0 & \bar{r}^T_{u_{\bar{\tau}_i}} - \bar{r}^T(u^*) & \cdots & 0 \\ \cdots & \vdots & \ddots & \vdots \\ 0 & 0 & \cdots & \bar{r}^T_{u_{\bar{\tau}_i}} - \bar{r}^T(u^*) \end{pmatrix} \begin{pmatrix} 0 \\ D_i^T \\ \vdots \\ 0 \end{pmatrix} \bar{r}(u^*) \\
&= \begin{pmatrix} 0 \\ (\bar{r}^T_{u_{\bar{\tau}_i}} - \bar{r}^T(u^*)) D_i^T \bar{r}(u^*) \\ \vdots \\ 0 \end{pmatrix} \\
&= \begin{pmatrix} 0 \\ \bar{r}^T(u^*) D_i (\bar{r}^T_{u_{\bar{\tau}_i}} - \bar{r}(u^*)) \\ \vdots \\ 0 \end{pmatrix} \\
&= \begin{pmatrix} \bar{r}^T(u^*) & 0 & \cdots & 0 \\ 0 & \bar{r}^T(u^*) & \cdots & 0 \\ \cdots & \vdots & \ddots & \vdots \\ 0 & 0 & \cdots & \bar{r}^T(u^*) \end{pmatrix} \begin{pmatrix} 0 \\ D_i \\ \vdots \\ 0 \end{pmatrix} (\bar{r}^T_{u_{\bar{\tau}_i}} - \bar{r}(u^*)) \\
&= \bar{R}(u^*) \hat{D}_i (\bar{r}^T_{u_{\bar{\tau}_i}} - \bar{r}(u^*)), \qquad (11)
\end{aligned}
$$

where $\hat{D}_1 = (D_1^T, 0, \cdots, 0)^T$, $\hat{D}_n = (0, 0, \cdots, D_n^T,)^T$, that is to say, i-th block in $\hat{D}_i$ is composed of D_i, and the other blocks are all zeros.

Define $g(x(t)) = (\bar{h}(u(t)) - \bar{h}(u^*))$ and $f(x(t - \bar{\tau}_i)) = (\bar{r}(u(t - \bar{\tau}_i)) - \bar{r}(u^*))$, then system (8) is equivalent to the following form,

$$
\begin{aligned}
\dot{x}(t) &= -Ax(t) + \bar{H}(u(t))\bar{C}g(x(t)) + \bar{H}(u^*)\hat{C}g(x(t)) \\
&+ \sum_{i=1}^{n} \bar{R}(u(t - \bar{\tau}_i))\bar{D}_i f(x(t - \bar{\tau}_i)) + \sum_{i=1}^{n} \bar{R}(u^*)\hat{D}_i f(x(t - \bar{\tau}_i)). \qquad (12)
\end{aligned}
$$

Now we will present a stability result for system (12).

Theorem 1. Suppose that Assumption 21 holds. If there exist positive definite diagonal matrices P, P_2, P_3, Y_i, positive constants $\epsilon_a, \epsilon_b, \epsilon_i$ and η_i, $i = 1, \cdots, n$, such that the following LMI holds,

$$
\Phi_d = \begin{bmatrix} \Phi_{11} & P_2\Delta_g & P_3\Delta_f & 0 & \Phi_{bb} \\ * & \Phi_{22} & 0 & 0 & 0 \\ * & * & \Phi_{33} & 0 & 0 \\ * & * & * & \Phi_{aa} & 0 \\ * & * & * & * & \Phi_{cc} \end{bmatrix} \qquad (13)
$$

then the equilibrium point of (12) is globally asymptotically stable, where
$\Phi_{11} = -2PA + \epsilon_a^{-1}G_bPP + \epsilon_b^{-1}G_bPP + \sum_{i=1}^{n} \epsilon_i^{-1}F_bPP + \sum_{i=1}^{n} \eta_i^{-1}F_bPP$,
$\Phi_{22} = -2P_2 + \epsilon_a\bar{C}^T\bar{C} + \epsilon_b\hat{C}^T\hat{C}$,

$\Phi_{33} = -2P_3 + \sum_{i=1}^{n} Y_i$,
$\Phi_{aa} = \text{ diag } (-Y_1 + \epsilon_1 \bar{D}_1^T \bar{D}_1 + \eta_1 \hat{D}_1^T \hat{D}_1, \cdots, -Y_n + \epsilon_n \bar{D}_n^T \bar{D}_n + \eta_n \hat{D}_n^T \hat{D}_n)$,
$\Phi_{bb} = (\sqrt{G_b}P, \sqrt{G_b}P, \sqrt{F_b}P, \cdots, \sqrt{F_b}P, \sqrt{F_b}P, \cdots, \sqrt{F_b}P)$,
$\Phi_{cc} = \text{diag}(-\epsilon_a, -\epsilon_b, -\epsilon_1, \cdots, -\epsilon_n, -\eta_1, \cdots, -\eta_n)$.

Proof. Consider the following Lyapunov function

$$V(t) = \sum_{i=1}^{n} 2p_i \int_0^{x_i(t)} sds + \sum_{i=1}^{n}\sum_{j=1}^{n} Y_{ij} \int_{t-\tau_{ij}}^{t} f_j^2(x_j(s))ds, \tag{14}$$

where $P = \text{diag}(p_1,\ p_2,\ \cdots, p_n)$ is a positive definite diagonal matrix, $Y_{ij} > 0$ are some positive scalars. The derivative of $V(t)$ along the trajectories of system system (12) is as follows,

$$\begin{aligned}\dot{V}(t) &= 2x^T(t)P\dot{x}(t) + \sum_{i=1}^{n}\sum_{j=1}^{n} Y_{ij}[f_j^2(x_j(t)) - f_j^2(x_j(t-\tau_{ij}))] \\ &= 2x^T(t)P\Big[-Ax(t) + \bar{H}(u(t))\bar{C}g(x(t)) + \bar{H}(u^*)\hat{C}g(x(t)) \\ &+ \sum_{i=1}^{n} \bar{R}(u(t-\bar{\tau}_i))\bar{D}_i f(x(t-\bar{\tau}_i)) + \sum_{i=1}^{n} \bar{R}(u^*)\hat{D}_i f(x(t-\bar{\tau}_i))\Big] \\ &+ \sum_{i=1}^{n}\Big[f^T(x(t))Y_i f(x(t)) - f^T(x(t-\bar{\tau}_i))Y_i f(x(t-\bar{\tau}_i))\Big],\end{aligned} \tag{15}$$

where $Y_i = \text{diag}(Y_{i1},\ Y_{i2},\ \cdots\ Y_{in})$, $i = 1, \cdots, n$.
By Lemma 2.1, we have

$$\begin{aligned}&2x^T(t)P\bar{H}(u(t))\bar{C}g(x(t)) \\ &\leq \epsilon_a^{-1} x^T(t)P\bar{H}(u(t))\bar{H}^T(u(t))Px(t) \\ &+ \epsilon_a g^T(x(t))\bar{C}^T\bar{C}g(x(t)) \\ &\leq \epsilon_a^{-1} G_b x^T(t)PPx(t) + \epsilon_a g^T(x(t))\bar{C}^T\bar{C}g(x(t)),\end{aligned} \tag{16}$$

$$\begin{aligned}&2x^T(t)P\bar{H}(u^*)\hat{C}g(x(t)) \\ &\leq \epsilon_b^{-1} x^T(t)P\bar{H}(u^*)\bar{H}^T(u^*)Px(t) + \epsilon_b g^T(x(t))\hat{C}^T\hat{C}g(x(t)) \\ &\leq \epsilon_b^{-1} G_b x^T(t)PPx(t) + \epsilon_b g^T(x(t))\hat{C}^T\hat{C}g(x(t)),\end{aligned} \tag{17}$$

$$\begin{aligned}&2x^T(t)P\bar{R}(u(t-\bar{\tau}_i))\bar{D}_i f(x(t-\bar{\tau}_i)) \\ &\leq \epsilon_i^{-1} x^T(t)P\bar{R}(u(t-\bar{\tau}_i))\bar{R}^T(u(t-\bar{\tau}_i))Px(t) \\ &+ \epsilon_i f^T(x(t-\bar{\tau}_i))\bar{D}_i^T\bar{D}_i f(x(t-\bar{\tau}_i)) \\ &\leq \epsilon_i^{-1} F_b x^T(t)PPx(t) + \epsilon_i f^T(x(t-\bar{\tau}_i))\bar{D}_i^T\bar{D}_i f(x(t-\bar{\tau}_i)),\end{aligned} \tag{18}$$

$$
\begin{aligned}
&2x^T(t)P\bar{R}(u^*)\hat{D}_i f(x(t-\bar{\tau}_i)) \\
&\leq \eta_i^{-1} x^T(t)P\bar{R}(u^*)\bar{R}^T(u^*)Px(t) \\
&+ \eta_i f^T(x(t-\bar{\tau}_i))\hat{D}_i^T\hat{D}_i f(x(t-\bar{\tau}_i)) \\
&\leq \eta_i^{-1} F_b x^T(t)PPx(t) + \eta_i f^T(x(t-\bar{\tau}_i))\hat{D}_i^T\hat{D}_i f(x(t-\bar{\tau}_i)),
\end{aligned} \tag{19}
$$

where $\epsilon_a, \epsilon_b, \epsilon_i$ and η_i are all positive constants, and we have used the following conditions,

$$
\begin{aligned}
&\bar{H}(u(t))\bar{H}^T(u(t)) \\
=&\mathrm{diag}(\bar{h}^T(u(t))\bar{h}(u(t)), \bar{h}^T(u(t))\bar{h}(u(t)), \cdots, \bar{h}^T(u(t))\bar{h}(u(t))) \\
=&\mathrm{diag}(\sum_{i=1}^n \bar{h}_i^2(u(t)), \sum_{i=1}^n \bar{h}_i^2(u(t)), \ \cdots, \sum_{i=1}^n \bar{h}_i^2(u(t))) \\
\leq&\sum_{i=1}^n (G_i^b)^2 I = G_b I,
\end{aligned} \tag{20}
$$

$$
\begin{aligned}
&\bar{R}(u(t-\bar{\tau}_i))\bar{R}^T(u(t-\bar{\tau}_i)) \\
=&\mathrm{diag}(\bar{f}^T(u(t-\bar{\tau}_i))\bar{f}(u(t-\bar{\tau}_i)), \cdots, \bar{f}^T(u(t-\bar{\tau}_i))\bar{f}(u(t-\bar{\tau}_i))) \\
=&\mathrm{diag}(\sum_{i=1}^n \bar{f}_i^2(u(t-\bar{\tau}_i)), \ \cdots, \sum_{i=1}^n \bar{f}_i^2(u(t-\bar{\tau}_i))) \\
\leq&\sum_{i=1}^n (F_i^b)^2 I = F_b I,
\end{aligned} \tag{21}
$$

$$
\bar{H}(u^*)\bar{H}^T(u^*)) \leq \sum_{i=1}^n (G_i^b)^2 I = G_b I, \tag{22}
$$

$$
\bar{R}(u^*)\bar{R}^T(u^*) \leq \sum_{i=1}^n (F_i^b)^2 I = F_b I, \tag{23}
$$

where $G_b = \sum_{i=1}^n (G_i^b)^2$ and $F_b = \sum_{i=1}^n (F_i^b)^2$, I is an identity matrix with appropriate dimension.

By Assumption 21, the following conditions hold

$$
2g^T(x(t))P_2\Delta_g x(t) - 2g^T(x(t))P_2 g(x(t)) \geq 0, \tag{24}
$$

$$
2f^T(x(t))P_3\Delta_f x(t) - 2f^T(x(t))P_3 f(x(t)) \geq 0, \tag{25}
$$

where P_2 and P_3 are all positive diagonal matrices.

Combining (16), (17), (18), (20), (24) and (25), we have

$$
\dot{V}(t) \leq -2x^T(t)PAx(t) + \epsilon_a^{-1} G_b x^T(t)PPx(t)
$$

$$
\begin{aligned}
&+ \epsilon_a g^T(x(t))\bar{C}^T\bar{C}g(x(t)) + \epsilon_b^{-1}G_b x^T(t)PPx(t) \\
&+ \epsilon_b g^T(x(t))\hat{C}^T\hat{C}g(x(t)) + \sum_{i=1}^{n}\Big[\epsilon_i^{-1}F_b x^T(t)PPx(t) \\
&+ \epsilon_i f^T(x(t-\bar{\tau}_i))\bar{D}_i^T\bar{D}_i f(x(t-\bar{\tau}_i))\Big] \\
&+ \sum_{i=1}^{n}\Big[\eta_i^{-1}F_b x^T(t)PPx(t) + \eta_i f^T(x(t-\bar{\tau}_i))\hat{D}_i^T\hat{D}_i f(x(t-\bar{\tau}_i))\Big] \\
&+ \sum_{i=1}^{n}\Big[f^T(x(t))Y_i f(x(t)) - f^T(x(t-\bar{\tau}_i))Y_i f(x(t-\bar{\tau}_i))\Big] \\
&+ 2g^T(x(t))P_2\varDelta_g x(t) - 2g^T(x(t))P_2 g(x(t)) \\
&+ 2f^T(x(t))P_3\varDelta_f x(t) - 2f^T(x(t))P_3 f(x(t)) \\
&\le \xi_d^T\varPhi_e\xi_d < 0,
\end{aligned} \tag{26}
$$

for any $\xi_d = \Big(x^T(t)\ g^T(x(t))\ f^T(x(t))\ f^T(x(t-\bar{\tau}_1))\ \cdots\ f^T(x(t-\bar{\tau}_n))\Big)^T \neq 0$,

$$
\varPhi_e = \begin{bmatrix}
\varPhi_{11} & P_2\varDelta_g & P_3\varDelta_f & 0 & 0 & 0 \\
* & \varPhi_{22} & 0 & 0 & 0 & 0 \\
* & * & \varPhi_{33} & 0 & 0 & 0 \\
* & * & * & \varPhi_{44} & 0 & 0 \\
* & * & * & * & \ddots & 0 \\
* & * & * & * & \cdots & \varPhi_{nn}
\end{bmatrix} \tag{27}
$$

$\varPhi_{11} = -2PA + \epsilon_a^{-1}G_bPP + \epsilon_b^{-1}G_bPP + \sum_{i=1}^{n}\epsilon_i^{-1}F_bPP + \sum_{i=1}^{n}\eta_i^{-1}F_bPP$,
$\varPhi_{22} = -2P_2 + \epsilon_a\bar{C}^T\bar{C} + \epsilon_b\hat{C}^T\hat{C}$, $\varPhi_{33} = -2P_3 + \sum_{i=1}^{n}Y_i$,
$\varPhi_{44} = -Y_1 + \epsilon_1\bar{D}_1^T\bar{D}_1 + \eta_1\hat{D}_1^T\hat{D}_1, \cdots, \varPhi_{nn} = -Y_n + \epsilon_n\bar{D}_n^T\bar{D}_n + \eta_n\hat{D}_n^T\hat{D}_n$.

By Schur Complement lemma, we can see that matrix inequality (27) is equivalent to LMI (13). This completes the proof.

4 Conclusions

An LMI-based sufficient conditions has been derived to ensure the global stability of a class of HRNN with multiple delays. Based on delay-matrix decomposition method, we proposed a less conservative criterion, which is easy to verify and better than existing results.

Acknowledgements. This work was supported by National Natural Science Foundation under Grants 61074073, 61034005 and 60974071, Program for New Century Excellent Talents in University of China under Grant NCET-10-0306, and the Fundamental Research Funds for the Central Universities under Grants N110504001 and N100104102.

References

1. Zeng, Z., Wang, J., Liao, X.: Global exponential stability of a general class of recurrent neural networks with time-varying delays. IEEE Trans. Circuits and Systems-I: Fundamental Theory and Applications 50, 1353–1358 (2003)
2. Zhang, H., Wang, Z.: Global asymptotic stability of delayed cellular neural networks. IEEE Trans. Neural Networks 18, 947–950 (2007)
3. Zhang, H., Wang, Z., Liu, D.: Global asymptotic stability of recurrent neural networks with multiple time varying delays. IEEE Trans. Neural Networks 19, 855–873 (2008)
4. Zhang, H., Wang, Z., Liu, D.: Robust stability analysis for interval cohen-grossberg neural network with unknown time-varying delays. IEEE Trans. Neural Networks 19, 1942–1955 (2008)
5. Ziegaus, C., Lang, E.: A neural implementation ofthe JADE algorithm (nJADE) using higher-order neurons. Neurocomputing 56, 79–100 (2004)
6. Xu, B., Liu, X., Liao, X.: Stability analysis of high-order Hopfield type neural networks with uncertainty. Neurocomputing 71, 508–512 (2008)
7. Xu, B., Wang, Q., Liao, X.: Global exponential stability of high order Hopfield type neural networks. Appl. Math. Comput. 174, 98–116 (2006)
8. Qiu, J.: Dynamics of high-order Hopfield neural networks with time delays. Neurocomputing 73, 820–826 (2010)
9. Cao, J., Liang, J., Lam, J.: Exponential stability of high-order bidirectional associative memory neural networks with time delays. Physica D 199, 425–436 (2004)
10. Huo, H., Li, W., Tang, S.: Dynamics of high-order BAM neural networks with and without impulses. Applied Mathematics and Computation 215, 2120–2133 (2009)
11. Hu, H., Jiang, H., Teng, Z.: The boundedness of high-order Hopfield neural networks with variable delays. Neurocomputing 73, 2589–2596 (2010)
12. Ou, C.: Anti-periodic solutions for high-order Hopfield neural networks. Computers and Mathematics with Applications 56, 1838–1844 (2008)
13. Chen, T., Lu, W.: Stability analysis of dynamical neural networks. In: IEEE Int. Conf. Neural Networks and Signal Processing, Nanjing, China, December 14-17 (2003)
14. Chen, T.: Universal Approach to Study Delayed Dynamical Systems. In: Wang, L., Chen, K., S. Ong, Y. (eds.) ICNC 2005, Part I. LNCS, vol. 3610, pp. 245–253. Springer, Heidelberg (2005)
15. Liu, P., Yi, F., Guo, Q., Yang, J., Wu, W.: Analysison global exponential robust stability of reactioncdiffusion neural networks with s-type distributed delays. Physica D 237, 475–485 (2008)
16. Wang, L., Xu, D.: Global asymptotic stability of bidirectional associative memory neural networks with s-type distributed delays. Internat. J. Syst. Sci. 33, 869–877 (2002)
17. Wang, Z., Zhang, H., Liu, D., Feng, J.: LMI Based Global Asymptotic Stability Criterion for Recurrent Neural Networks with Infinite Distributed Delays. In: Yu, W., He, H., Zhang, N. (eds.) ISNN 2009, Part I. LNCS, vol. 5551, pp. 463–471. Springer, Heidelberg (2009)
18. Chen, T.: Universal Approach to Study Delayed Dynamical Systems. In: Wang, L., Chen, K., S. Ong, Y. (eds.) ICNC 2005, Part I. LNCS, vol. 3610, pp. 245–253. Springer, Heidelberg (2005)
19. Chen, T.: Universal approach to study delayed dynamical systems. SCI, vol. 35, pp. 85–110 (2007)

Hybrid Neural Network Based on ART2—BP Information Fusion Control in Circulating Fluidized Bed Boiler (CFBB)

Peifeng Niu[1,2,*], Yunfei Ma[1,2], Pengfei Li[1,2], Yang Zhang[1,2], Guoqiang Li[1,2], and Xiangye Zhang[1,2]

[1] Key Lab of Industrial Computer Control Engineering of Hebei Province, Yanshan University, Qinhuangdao 066004, China
[2] National Engineering Research Center for Equipment and Technology of Cold Strip Rolling, Qinhuangdao 066004, China
niupeifeng2011@163.com

Abstract. Circulating Fluidized Bed Boiler (CFBB) involves a kind of combustion boiler that can clean and desulfurize the coal efficiently in the combustion process. It is highly adapted to all kinds of high quality coals and low grade coals. CFB boiler has more superior performance, features and a wide range of applications than other boilers, accordingly, problems on automatic control underlined in the combustion process blocked its wide application. This is a typical thermal object, hard to control, and due to the special combustion type of CFBB that makes it a great inertia, multivariable, strong coupling, nonlinear, time-varying object. This paper designs an ART2-BP-BP Hybrid Neural Network of fusion cluster control system and completes data fusion from the data level, the feature level to the decision level. Results of simulation show that the control system in this paper is feasible and effective, in particular, the control system still has more satisfactory control effects in the case of a variety of sensor failures.

Keywords: Hybrid neural network, Circulating Fluidized Bed Boiler, Clustering fusion control, Data Preprocessing, Situation threat estimate.

1 Introduction

Since the nineties of last century, China has started to research about combustion process control technology of CFBB. Henderson et al. studies and develops an expert control system based on knowledge according to the characteristics of CFBB combustion process[1]. Lim et al. presents new control ideas combining fuzzy control and generalized predictive control for dynamic mathematical model of CFBB combustion process[2]. Hu and Yang et al. presents a kind of feed-forward compensation fuzzy controller with the settings, in which controller parameters is online self-tuning and function of steam load is adaptive[3, 4]. In order to overcome

[*] Corresponding author.

H. Zhang et al. (Eds.): BICS 2012, LNAI 7366, pp. 278–287, 2012.

the disadvantages of the standard genetic algorithm whose convergence rate is low due to huge search space when it obtains the control rule base of MIMO system, Ma et al. defines the fine mode of the chromosome and proposes a new bed temperature control strategy combining operating characteristics of CFBB combustion process[5]. Zhao et al. has established mathematical model which describes the dynamic characteristics of CFBB combustion process and main steam pressure, and has designed fuzzy neural network self-learning control and fuzzy mononeural compound control system separately[6].

Modern industrial production (such as CFBB combustion process) has integrated, complex, large-scale, continuous characteristics, and it uses a large variety of sensors to monitor and control the production process[7]. In this multi-sensor system, the sensor information in space, time, expression are different. Its credibility degrees of uncertainty are different, and its focus and purpose are also different. So it puts forward new demands for information processing and management. In the traditional approach, processing and handling the information collected by each sensor individually will not lead to increase workload, but will also cut off all contact information between sensors and lose information characteristics contained in the information through organic combination ,which results in a waste of information resources. The integration of MSIF and industrial monitoring control will bring new mechanism for traditional industries, and it is expected to form a new type of industrial monitoring and control system --- cluster fusion control system. To our knowledge, there are no references about clustering fusion control methods applied in combustion process of CFBB.

For automatic control problems in CFBB, this paper applies the multi-sensor information fusion in the process of CFBB combustion control. Based on ART-2 and BP neural network, it uses feature level fusion and decision-making fusion to achieve the fusion and classification for collected sensor information, and at last forms an effective control strategy. Simulate the control system by MATLAB, and the simulation results prove that this control system is feasible and effective.

2 The Mathematical Model and Burning Control System of the Burning Process of CFBB

2.1 The Mathematical Model of the Burning Process of CFBB

When disturbance occurs in the combustion rate and turbine uses hydraulic control system, according to identification situations in site, we can get the mathematical model of steam pressure:

$$W_P(s) = \frac{(1-\alpha s)}{(1+T_P S)^2} K_P e^{-\tau_p s} \tag{1}$$

Through the identification in site, we find that static gain K_p ,inertia time constant T_p and pure delay time τ_p are parameters changing with different situations,the variation range of a is smaller. When boiler duty is changing between 40%~90%, the variation ranges of all parameters above are as follow: K_p : 6~10s; T_p :190~300s ; τ_p : 160~230s; a : 20~30s. The steam pressure is essentially the same under a wind disturbance.

Under the disturbance of coal input, the mathematical model of bed temperature is as follows:

$$W_\theta(s) = \frac{(1-bs)}{(1+T_\theta s)^2} K_\theta e^{-\tau_\theta s} \tag{2}$$

Through the identification in site ,we find that K_θ 、 T_θ 、 τ_θ 、 b are parameters changing with different situations. When boiler duty is changing between 40%~90%, the variation ranges of all parameters above are as follows: K_θ : 10~20s; T_θ : 150~300s; τ_θ :40~80s; b :10~18s.

3 The Clustering Fusion Control System of Circulating Fluidized Bed Boiler in the Burning Process

The burning process of circulating fluidized bed boiler (CFBB) has essential controlled variables such as coal feeding, air feeding, induced draft, and cinder discharging.

The idea and the structure of coal feeding, air feeding, induced draft and cinder discharging control systems are the same. They all use a group of sensors detecting relevant variations which can describe the boiler combustion process condition. Relevant variations of circulating fluidized bed boiler process condition P_X , $X \in \{Q,V,M,F\}$, is respectively concerned about coal feeding, air feeding coal, cinder discharging, induced draft. According to clustering fusion control concept, after the sensor data S_X , $X \in \{Q,V,M,F\}$ is clustered, we obtain the corresponding operation categories (furnace condition) B_X , $X \in \{Q,V,M,F\}$ For example, for coal capacity control system, in order to get B_Q which control the capacity of coal, process variables P_Q can be taken for bed temperature, steam pressure, load, etc. At this time, the sensor group of coal capacity control system can gain sensor data vectors S_Q . In the coal capacity control system, form control output of coal on the basis of furnace condition associated with coal. The coal feeding points in large CFBB are at least two, therefore, the control output of coal is a vector:

$$U_Q = [u_{Q1,} u_{Q2,} \cdots, u_{Qn}] \tag{3}$$

Similarly, the control output of air flow (including the control of primary air flow and secondary), U_V is also a vector:

$$U_V = [u_{V1,} u_{V2}] \tag{4}$$

Cinder discharging control output and induced draft output control are also vectors:

$$U_M = [u_{M1}, u_{M2}, \cdots, u_{Mn}] \tag{5}$$

$$U_F = [u_{F1}, u_{F2}] \tag{6}$$

This paper mainly studies design and application of clustering fusion control system, and researches its performance through the actual data. Therefore, it only takes one of the four control systems as an example to undertake the key research. This control system is the coal feeding one, the design methods of the other three control systems are similar.

3.1 Overall Structure of Circulating Fluidized Bed Boiler Coal Feeding Clustering Fusion Control System

The change of coal feeding will affect both the boiler steam pressure and bed temperature meanwhile. Using three groups of sensors separately to detect the boiler

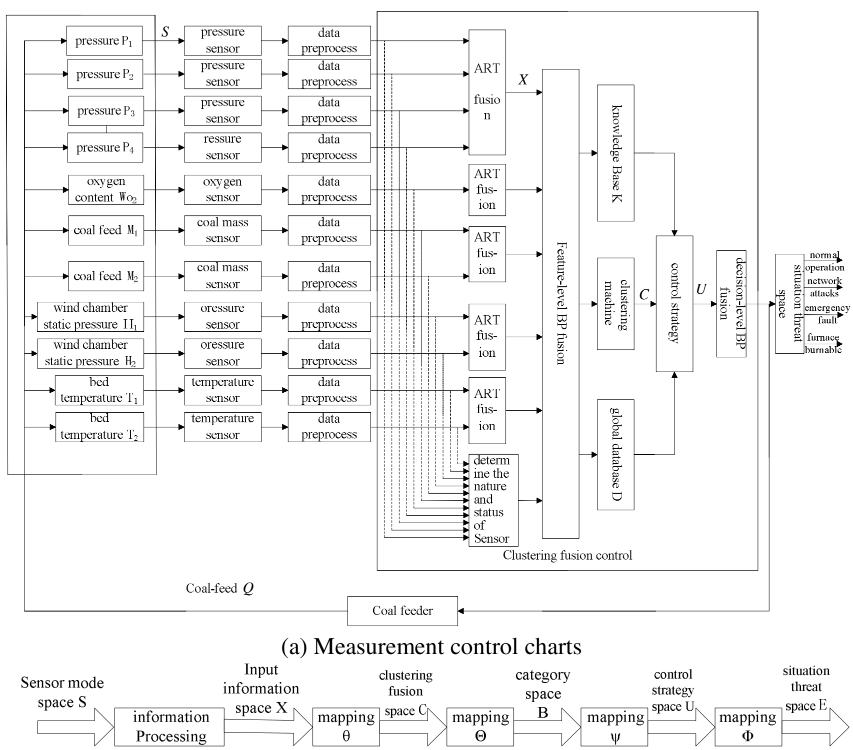

(a) Measurement control charts

(b) Information mapping

Fig. 1. CFCS structure of quantity of coal

steam pressure (four points), coal feeding (two points) and oxygen content (one point), the pressure error in material layer (two points) and bed temperature (two points), and the control values is coal feeding. These five tested physical quantities describe respectively the operating condition of the boiled from a side, but each cannot fully describe the operating condition of the furnace. Clustering fusion control system's task is to make these five physical values fuse so that they can comprehensively describe the furnace condition. According to the hearth furnace conditions, it can adjust the coal feeding to maintain the normal operation of the boiler. The diagram of system structure is shown in Fig. 1.

The system showed in Fig. 1 adopts a distributed and three levels clustering fusion control system. Among them, the first level uses eleven ART-2 neural network to fuse the sensor signal with time series respectively; the second level uses a BP neural network to fuse of the first level's fusion results again. Considering the sensor failure, the last level adopts a BP network to achieve decision-level fusion for control strategies again.

3.2 Coal Feeding Clustering Fusion Control System Design of Circulating Fluidized Bed Boiler

The Input Information Space

(1) Sensor Data

Steam pressure $S_1 = [P_1, P_2, P_3, P_4]$; Oxygen content $S_2 = w_{o2}$; coalfeeder $S_3 = [M_1, M_2]$;wind chamber static pressure $S_4 = [H_1, H_2]$; the Main Steam pressure $S_5 = [T_1, T_2]$; the speed of coal feeder n.

(2) Data Preprocessing

The combustion process of CFBB belongs to a slow changing process .In the design, each window length takes mode for 90s, and each 5s we sample one time. So for each information source in a pattern window there will be 18 data. After data pretreatment, 5 groups of sensor data participate in 1st level of ART-2 fusion, and their pattern vectors are written separately:

Steam Pressure

$$X_1 = \begin{bmatrix} x_{11}^{(1)} & x_{11}^{(2)} \cdots & x_{11}^{(18)} \\ x_{12}^{(1)} & x_{12}^{(2)} \cdots & x_{12}^{(18)} \\ x_{13}^{(1)} & x_{13}^{(2)} \cdots & x_{13}^{(18)} \\ x_{14}^{(1)} & x_{14}^{(2)} \cdots & x_{14}^{(18)} \end{bmatrix}^T = \begin{bmatrix} P_1^{(1)} & P_1^{(2)} \cdots & P_1^{(18)} \\ P_2^{(1)} & P_2^{(2)} \cdots & P_2^{(18)} \\ P_3^{(1)} & T_3^{(2)} \cdots & P_3^{(18)} \\ P_4^{(1)} & P_4^{(2)} \cdots & P_4^{(18)} \end{bmatrix}^T \tag{7}$$

Oxygen Content

$$X_2 = [x_2^{(1)} \quad x_2^{(2)} \cdots \quad x_2^{(18)}]^T = \begin{bmatrix} w_{o_2}^{(1)} & w_{o_2}^{(2)} \cdots & w_{o_2}^{(18)} \end{bmatrix}^T \tag{8}$$

Coal Feeding

$$X_3 = \begin{bmatrix} x_{31}^{(1)} & x_{31}^{(2)} \cdots & x_{31}^{(18)} \\ x_{32}^{(1)} & x_{32}^{(2)} \cdots & x_{32}^{(18)} \end{bmatrix}^T = \begin{bmatrix} M_1^{(1)} & M_1^{(2)} \cdots & M_1^{(18)} \\ M_2^{(1)} & M_2^{(2)} \cdots & M_2^{(18)} \end{bmatrix}^T \tag{9}$$

The Pressure Error in Material Layer

$$X_4 = \begin{bmatrix} x_{41}^{(1)} & x_{41}^{(2)} \cdots & x_{41}^{(18)} \\ x_{42}^{(1)} & x_{42}^{(2)} \cdots & x_{42}^{(18)} \end{bmatrix}^T = \begin{bmatrix} H_1^{(1)} & H_1^{(2)} \cdots & H_1^{(18)} \\ H_2^{(1)} & H_2^{(2)} \cdots & H_2^{(18)} \end{bmatrix}^T \tag{10}$$

Bed Temperature

$$X_5 = \begin{bmatrix} x_{51}^{(1)} & x_{51}^{(2)} \cdots & x_{51}^{(18)} \\ x_{52}^{(1)} & x_{52}^{(2)} \cdots & x_{52}^{(18)} \end{bmatrix}^T = \begin{bmatrix} T_1^{(1)} & T_1^{(2)} \cdots & T_1^{(18)} \\ T_2^{(1)} & T_2^{(2)} \cdots & T_2^{(18)} \end{bmatrix}^T \tag{11}$$

Sensor Characteristic Information

Feature information only participates in level 2 of the BP network integration, and it can be expressed as

$$X_6 = [Z_1, Z_2, Z_3, Z_4, Z_5] \tag{12}$$

dT and the Speed of the Coal Feeder n

dT and n do not participate in information fusion, and are written together as follows:

$$X_7 = [dT, n] \tag{13}$$

The Whole System of Input Information Space

$$X = [X_1, X_2, X_3, X_4, X_5, X_6, X_7] \tag{14}$$

Clustering Fusion Space

Clustering fusion space C is constituted by the mapped Θ input information space X,

$$\Theta : X \to C \tag{15}$$

$$C = [C_1 \quad C_2 \cdots \quad C_n] \tag{16}$$

$$\Theta = [\theta_1 \quad \theta_2 \cdots \quad \theta_N] \tag{17}$$

n :Spatial dimension, N :Spatial dimension

According to the specific circumstances of this system, in other word, inputting information space is 5 groups of sensor time series vector X1,X2,X3,X4,X5, which constitute the subspace by 11 ART - 2 network completed mapping Θ . Now analyze a ART-2 network work, and the rest 10 are similar.

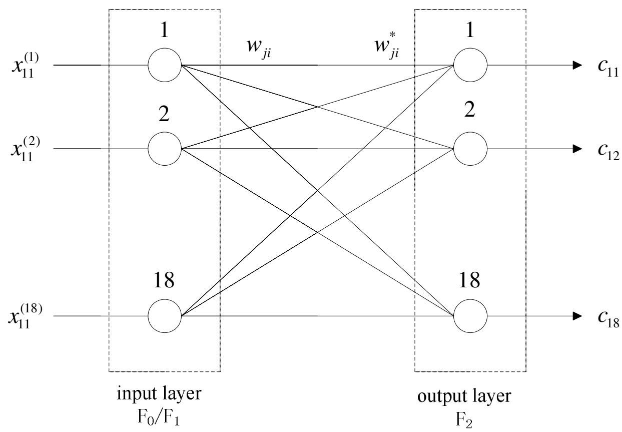

Fig. 2. ART-2 strucure in CFBB CFCS

Fig. 2 shows the steam pressure sensor data fusion time sequence of ART-2 network diagram. Vector X11 (a column of X1) in the number of dimensions is 18*1, namely dimension K=18, as a result ART-2 network design has 18 input terminals of the network. The remaining related parameters are elected: contrast constants a = b = 10, Adjusting subsystem constant c = 0.1, F2 place gain d = 0.9, Similarity ρ = 0.9, Filtering threshold theta θ= 1 / k = 1/18, Filtering transformation function

$$f(x)=\begin{cases}0, 0\le x\le\theta\\ x, x>\theta\end{cases} \tag{18}$$

Operation Space

Operating space (category space) B is constituted by clustering fusion space C after Φ alludes.

$$\Phi : C \to B \tag{19}$$

$$B=[b_1,\quad b_2,\cdots,\quad b_P] \tag{20}$$

$$\Phi=[\varphi_1,\quad \varphi_2,\cdots,\quad \varphi_P] \tag{21}$$

In the study of boiler system, the mapping Φ is realized by BP neural network. It also includes the failure information X_6 besides the input vector C.

In this system, in order to guarantee the study speed, take the BP network three layers, 20 units in hidden layer. The whole BP network structure is 15 x 20 x 6 structure. As shown in Fig. 3.

Control Strategy Space

Control strategy space U is constituted by category space B through the mapping ψ. In the process, we need to use input information X , global database D and the related knowledge of comprehensive knowledge base K:

$$\psi:(X,D,K,B)\rightarrow U \tag{22}$$

$$\psi=[\varphi_1,\quad \varphi_2,\cdots,\quad \varphi_m] \tag{23}$$

$$U=\left[u_1,\quad u_2,\cdots,\quad u_m\right] \tag{24}$$

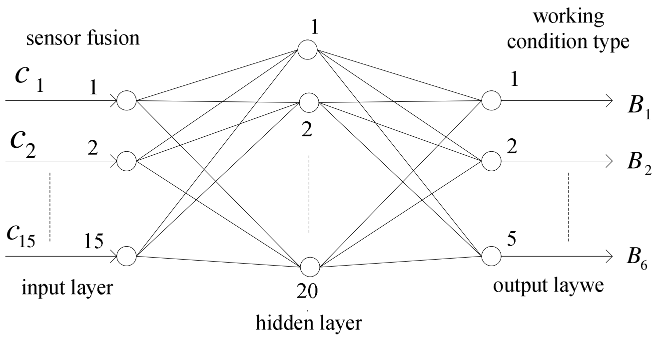

Fig. 3. BP network of realizing run-space mapping

In type (24) expression, $u_i(i=1,2,...m)$ represents the various control strategy, therefore, U is a multi-mode control vector. In the boiler system studied in this paper, input information which participated in output control is:

$$X=\left[P\quad P_0\quad n\right]^T \tag{25}$$

In the type, P is steam temperature ; P_0 steam temperature set value; n is the speed of coal feeder. According to the theory of clustering fusion control, the location (furnace condition) of the running space B and steam pressure control the output size. clustering fusion control output is the plow speed control values:

$$n(k)=n(k-1)+\Delta n(k) \tag{26}$$

4 Simulation Research on Clustering Fusion Control System in Combustion Process

As main steam pressure p is an important parameter in boiler combustion process. Therefore, this paper only mentions MATLAB simulation curve of the main steam pressure and the other simulation curves are omitted. In the process of simulation, we adopt conventional PID controller, self-adaptive PID controller, fuzzy controller, fuzzy self-adaptive controller and clustering fusion controller to control the vapor pressure respectively.

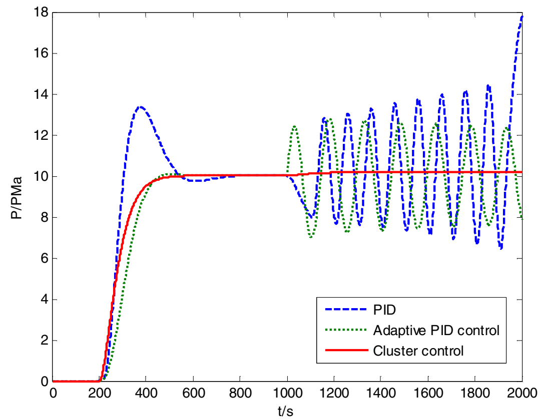

(a)

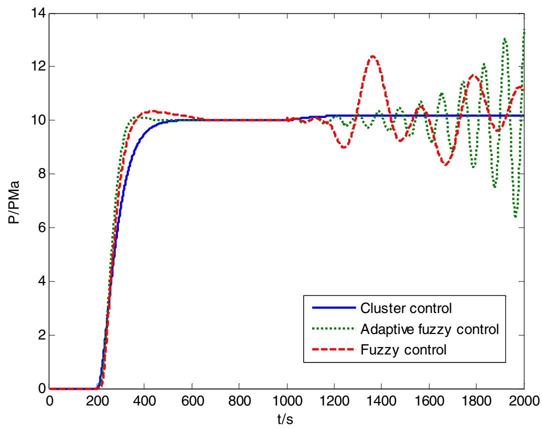

(b)

Fig. 4. Bed temperature changes under temperature sensor failure

Fig. 4(a)describes the simulation results which adopt conventional PID controller, self - adaptive PID controller and clustering fusion controller for steam temperature. It can be seen from the step response that the conventional PID controller displays divergence oscillation, and the self - adaptive PID controller displays undamped oscillation when the bed temperature sensor fails at 1000s. Nevertheless, the clustering fusion controller is not affected by the interruption. The system operates stably and the control effect is good. Fig. 4(b)describes the simulation results which adopt fuzzy controller, fuzzy self - adaptive controller and clustering fusion controller for the steam pressure control. It could be seen from the step response that fuzzy controller, fuzzy self - adaptive controller and clustering fusion controller have relatively small fluctuation. When the bed temperature sensor loses efficacy at 1000s, fuzzy controller generates irregular oscillation, fuzzy self - adaptive controller generates divergence oscillation, and whereas, clustering fusion controller is not subject to interruption. Tab. 1 shows the five control methods, and it can be seen that clustering fusion control has no overshoot and short transition time.

Table 1. Comparison of five methods of bed temperature control

Function	delay τ	t_r	t_p	σ_p	t_s $(\Delta = 3\%)$	Pressure sensor failure (1000s)
PID	200s	300s	380s	38%	660s	divergence oscillation
Adaptive PID	200s	410s	420s	1%	490s	undamped oscillation
Fuzzy control	200s	310s	360s	3%	540s	irregular oscillation
Adaptive fuzzy control	200s	290s	340s	1.5%	460s	divergence oscillation
Cluster control	200s	430s	--	--	430s	undisturbed

5 Conclusion

Automatic control in Circulating Fluidized bed boiler combustion has been one of the major problems in the engineering field. With neural network algorithm for cluster control method as a implementation tool, this article proposes a cluster control method which is based on Information Fusion technology after the analysis of dynamic characteristics of circulating fluidized bed boiler burning control. It employs/operates fusion classification of the sensor data acquisition, achieves appropriate control after judging from different data corresponding policy space, finally the system simulation achieves satisfactory results.

References

1. Henderson, A.K., Mann, M.D.: Developing an expert control system for fluidized bed combustors. Energy and Environmental Research Center, University of NorthDakota, USA (1990)
2. Lim, X., Xu, D.: CFB boiler control system. Journal of Tsinghua University 42(5), 23–28 (2002)
3. Zhang, H., Lu, J.F., Yang, H.R., et al.: Heat transfer measurements inside the furnace of a 135Mwe CFB boiler. In: Cen, K. (ed.) Circulating Fluidized Bed Technology VIII, pp. 254–260. International Academic Publishers, WorldPublishing Corporation (2005) ISBN 7-5062-7442-6
4. Yang, L., Xun, S.: Fuzzy control for bed temperature control system of circulation fluidized-bed boilers. Journal of Beijing Jiaotong University 26(2), 94–96 (2002)
5. Yang, H.R., Lu, J.F., Zhang, H., et al.: Update progress of supercritical circulating fluidized bed boiler. Boiler Technology 36(5), 1–6 (2005)
6. Zhao, J.: Study on the intelligent control of combustion system of CFB boiler. North China Electric Power University, Baoding (2002)
7. Cheng, L.M., Wang, Q.H., Shi, Z.L., et al.: Heat transfer in a large circulating fluidized bed boler. Journal of Power Engineering 26(3), 305–310 (2006)

An Improved Single Neuron Adaptive PID Controller Based on Levenberg-Marquardt Algorithm

Ting-Ting Hu, Yu-Feng Zhuang, and Jin Yu

School of Automation, Beijing University of Posts and Telecommunications
Beijing, China, 100876
{ivyhutt,zhuangyf}@bupt.edu.cn, yujin_bupt@sina.com

Abstract. A new single neuron adaptive Proportional-Integral-Derivative (PID) controller based on Levenberg-Marquardt (LM) algorithm is presented in this paper. This new controller overcomes some drawbacks of the conventional single neuron adaptive PID controllers. There are two kinds of problems in traditional algorithms. Firstly, gradient descent algorithm is a one-order optimization method. Secondly, Newton iterative method costs much computing resource. For the improved controller, LM algorithm is applied, which combines steepest gradient descent and Gauss-Newton method. As a consequence, the convergence speed is increased and the control performance is greatly improved. The simulation results show that the control effect of this novel controller has strong robustness and good self-adaptation.

Keywords: single neuron, adaptive, PID control, LM algorithm.

1 Introduction

The conventional PID control is one of the most classical and mature control strategies. For its simple structure and high reliability, the conventional PID control is widely used in the field of process control. However, it is difficult for the fixed PID controllers to adapt to the time-variation and non-linearity of the industry processes [1].

Computational intelligence has been utilized to control problems for many years. Among it neural networks [2], fuzzy systems [3] and genetic algorithms [4] are the most popular approaches. The neural networks have been widely applied for state feedback controller design, nonlinear system control, nonlinear dynamical system identification, and optimal control synthesis. Thus, simple neural network structure is needed, especially for real-time control system [5].

In order to improve performances of complex system, single neuron adaptive PID control which is the combination of neuron and the conventional PID control, has been proposed to realize better control performance. The structure of single neuron adaptive PID controller is very simple. During its working process, it can learn and adjust on line by itself, so it can adapt to the complex environmental variations. It means the single neuron adaptive PID controller has self-adaptation and strong robustness. In recent years, various single neuron adaptive PID controllers appeared using algorithm based on Hebb learning rule [6], quadratic object function [7-8], and auto gain regulation [9]. However, the single neuron PID controllers deal with the problem that the learning

H. Zhang et al. (Eds.): BICS 2012, LNAI 7366, pp. 288–295, 2012.

speed is slow and its response time is long. For this reason, an improved single neuron adaptive PID controller is presented in this paper, which is derived of LM algorithm to achieve optimal control effect. LM algorithm that combines steepest gradient descent and Gauss-Newton method, using three processes to adjust the parameters, enormously improves the convergence speed and improve the control performance.

This paper is organized as follows. Section II presents the brief introduction of conventional single neuron adaptive PID controller, and section III comprehensively discusses the method of an improved single neuron adaptive PID control. In section IV, both the simulation of conventional and the improved single neuron adaptive PID control algorithm are presented, followed by some concluding remarks in section V.

2 Single Neuron Adaptive PID Controller

The structure of single neuron adaptive PID controller is shown in Fig. 1. The inputs of the state convertor are the reference input $r(k)$ and the actual output $y(k)$ of the controlled system.

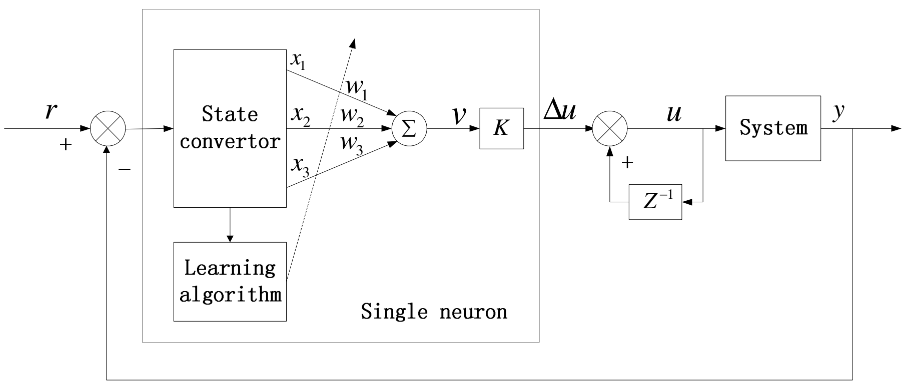

Fig. 1. Structure of single neuron adaptive PID controller

The outputs of state convertor are as follows:

$$\begin{aligned} x_1(k) &= e(k) - e(k-1) \\ x_2(k) &= e(k) \\ x_3(k) &= e(k) - 2e(k-1) + e(k-2)\ . \end{aligned} \tag{1}$$

The error at time k is $e(k) = r(k) - y(k)$, and the error at time $k-1$ and $k-2$ is $e(k-1)$ and $e(k-2)$. The outputs of the state convertor are the inputs of the single neuron. The weights matrix of the neuron is defined as $W = (w_1, w_2, w_3)^T$. Then, the output of the neuron with the gain K is

$$\Delta u(k) = K\sum_{i=1}^{3} w_i(k)x_i(k)\ . \tag{2}$$

Larger K value leads to better property of speediness and bigger overshoot.

The single neuron adaptive PID controller has the same structure with the conventional incremental PID control method. The advantage of the single neuron adaptive PID controller is that the weights can be adaptively adjusted online according to the defined performance function. The quadratic performance function to be minimized is defined as

$$P(k) = \frac{1}{2}\left[r(k+1) - y(k+1)\right]^2 = \frac{1}{2}e^2(k) . \tag{3}$$

Using the gradient descent algorithm and the chain rule, the weights are update by

$$\begin{aligned} \Delta w_i(k) &= w_i(k+1) - w_i(k) = -l_i \frac{\partial P(k)}{\partial w_i(k)} \\ &= l_i K e(k) \frac{\partial y(k+1)}{\partial u(k)} x_i(k), \ i = 1,2,3 , \end{aligned} \tag{4}$$

where l_i is the learning rate for each weight updating. For unknown systems, the term $\partial y(k+1)/\partial u(k)$ is unknown, thus symbol function $\mathrm{sgn}\left[\partial y(k+1)/\partial u(k)\right]$ can be used instead. After standardizing the algorithm, we compute the control input according to

$$u(k) = u(k-1) + \Delta u(k) = u(k-1) + K\sum_{i=1}^{3} \overline{w}_i(k) x_i(k) , \tag{5}$$

$$\overline{w}_i(k) = w_i(k) / \sum_{i=1}^{3} \left|w_i(k)\right|, \ i = 1,2,3 . \tag{6}$$

In order to keep the closed loop controlled system stable, it is very important to select the learning rates and the gain K .

For the conventional single neuron adaptive PID controllers, there are some problems. Firstly, the algorithm of the controllers is derived based on the gradient method. But the gradient method is a typical one-order optimization method which has the disadvantages of slow learning speed and easily getting into local minimum value. This can influence the abilities of fast tracking and anti-interference of the algorithm. Secondly, the values of learning rate in the conventional controllers have great influence on the performance of the algorithm in the process of neural network weight training. There are three learning rate coefficients to be adjusted. That is to say that the algorithm has three parameters to be tuned artificially which may increase the difficulties of the parameter tuning.

3 An Improved Single Neuron Adaptive PID Controller Based on LM Algorithm

The gradient descent method is a one-order optimization method which has the disadvantages of slow learning speed and easily getting into local minimum value. The

Newton iterative algorithm needs to calculate the second-order Hession matrix which costs much computing resource. The LM algorithm which combines steepest gradient descent and Gauss-Newton method can increase the convergence speed and improve the control performance, and it costs less computing resource. Thus, we choose LM algorithm to adjust the weights.

The optimal weights W^* are denoted by

$$W^* = \arg\min\{P_W(k) = \frac{1}{2}e^2(k)\} . \tag{7}$$

To make the weights W of the neuron converge to the optimal values W^*, the step h is calculated by

$$h = -\left(J_W^T J_W + \mu I\right)^{-1} J_W^T e , \tag{8}$$

where $J_W(k)$ is the Jacobian matrix, $\mu > 0$ is the damping parameter, I is an identity matrix, and e is the error function standing for $e(k)$. For $\mu > 0$, the matrix $\left(J_W^T J_W + \mu I\right)$ is positive definite, which makes its inverse exist and h be a negative direction. For large values of μ, we have

$$h \simeq -J_w^T e . \tag{9}$$

It is a steepest descent direction, which will be used when the weights W are far from the optimal values W^*. For little values of μ, we have

$$h \simeq -\left(J_W^T J_W\right)^{-1} J_W^T e . \tag{10}$$

It is Gauss-Newton step with quadratic convergence, which will be used when the weights W are close to the optimal values W^*.

The LM algorithm mainly includes three processes: calculation of the Jacobi matrix J_W and the step h, evaluating whether W is getting closer to W^* or not, updating the damping parameter μ and the parameters of the single neuron.

3.1 Calculation of the Jacobian Matrix J_W

Since the weight modification of $\delta w_i(k)$ is calculated by

$$\begin{aligned}\delta w_i(k) &= \frac{\partial e(k)}{\partial w_i(k)} = \frac{\partial e(k)}{\partial u(k)}\frac{\partial u(k)}{\partial w_i(k)} \\ &= -K\frac{\partial y(k+1)}{\partial u(k)} x_i(k),\ i = 1,2,3 ,\end{aligned} \tag{11}$$

the Jacobian matrix $J_w(k)$ is

$$J_W = [\delta w_1(k)\ \delta w_2(k)\ \delta w_3(k)]\ . \tag{12}$$

Then, the step h can be calculated by (8).

3.2 Evaluating the Current Parameter W

We use the gain ratio λ in [10] to evaluate whether W is getting closer to the optimal solution W^* or not. The gain ratio λ is defined as follows:

$$\lambda = \frac{P_w - P_{w+h}}{E_0 - E_h}\ , \tag{13}$$

where λ is the ration between the actual and predicted decrease in performance function. E_h is defined as

$$E_h = \frac{1}{2}\left(e + J_w h\right)^T \times \left(e + J_w h\right)\ , \tag{14}$$

and E_0 is defined as

$$E_0 = \frac{1}{2} e^T e\ . \tag{15}$$

So, we have

$$\begin{aligned} E_0 - E_h &= -h^T J_w^T e - \frac{1}{2} h^T J_w^T J_w h \\ &= -\frac{1}{2} h^T \left[2J_w^T e + \left(J_w^T J_w + \mu I - \mu I \right) h \right] \\ &= \frac{1}{2} h^T \left[\mu h - J_w^T e \right]\ . \end{aligned} \tag{16}$$

which is positive.

A small or negative value of λ indicates that we should increase the damping parameter so that the next step is closer to the steepest direction. A large value of λ indicates that we should decrease the damping parameter so that the next step is closer to Gauss-Newton step.

3.3 Updating the Damping Parameter μ and Weights W

The updating strategy of the damping parameter μ in [10] is adopted, which converts the traditional updating strategy from a piecewise function with discontinuities to a smooth function. The initial value of damping parameter μ is chosen by

$$\mu = \tau \max\left\{\mathrm{diag}\left(J_w^T J_w\right)\right\} . \tag{17}$$

This algorithm is not sensitive to τ, and we can choose τ in $[10^{-6},1]$. The damping parameter μ is updated according to the following rule:

$$\begin{aligned} &\text{if } \lambda > 0 \\ &\quad \mu \leftarrow \mu \times \max\left\{\frac{1}{3}, 1-(2\lambda-1)^3\right\}, \ \eta \leftarrow 2 \\ &\quad w \leftarrow w + h \\ &\text{else} \\ &\quad \mu \leftarrow \mu \times \eta \text{ , } \eta \leftarrow 2\eta \text{ ,} \end{aligned} \tag{18}$$

where η is used to increase the damping parameter μ. The relationship between gain ratio λ and updating of damping parameter μ is illustrated in Fig. 2.

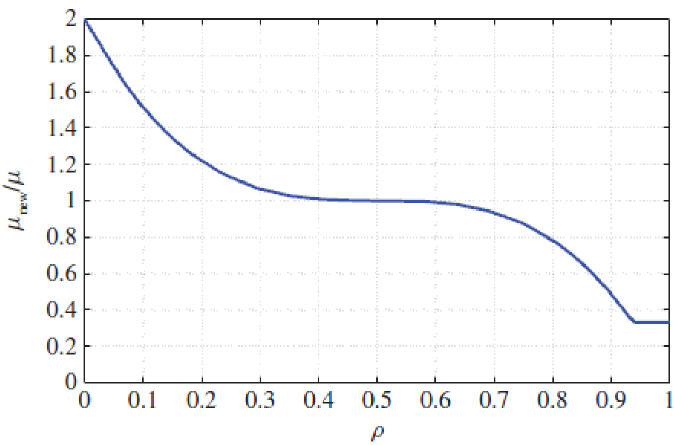

Fig. 2. Relationship between gain ratio λ and updating of damping parameter μ

The algorithm is iterated according to the process given in 3.1, 3.2, and 3.3. The stopping criteria is that the performance function is within prespecified threshold, or the training step reaches the max value.

4 Simulation Results

In order to verify the performance of the improved single neuron adaptive PID control method, a simulation example is given in this part. We use a discrete-time nonlinear system as our example which is given by

$$y_{k+1} = 0.368 y_k^2 + 0.264 y_{k-1} + 0.632 u_k \text{ .} \tag{19}$$

The reference input is a step-function signal $r(k)=1$. The gain is set $K=0.15$, $\tau=0.01$, and the initial weights are set $w_1=2, w_2=0.5, w_3=0.3$. The number of simulation is 500. Comparison between the performance of the conventional single neuron adaptive PID controller and that of the improved one based on LM algorithm is given in Fig. 3.

Simulation results in Fig. 3 show that the performance of the improved single neuron adaptive PID controller is better than that of the classical single neuron adaptive PID control algorithm. Firstly, the dynamic response speed of the system is faster than the regular ones. Secondly, the overshooting value is smaller in the improved single neuron adaptive PID controller. In addition, the controller can reduce the output error greatly. Thus, the results show that the new controller has a strong ability of online self-learning and robustness, which proves the effectiveness of the improved algorithm presented.

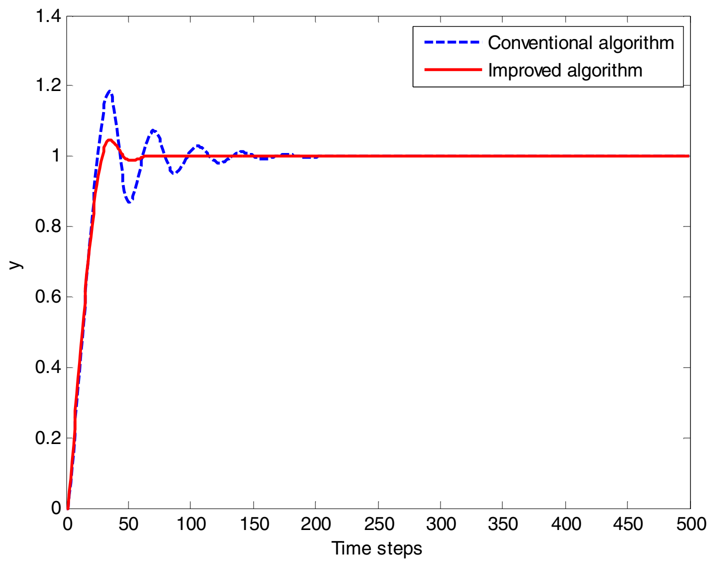

Fig. 3. Comparison between the convention algorithm and the improved algorithm

5 Conclusions

The single neuron adaptive PID controller is a new kind of controller which combines the advantage of neural network and the conventional PID controller, which has the advantages of good robustness and easy implementation. In this paper, an improved single neuron adaptive PID controller based on LM algorithm, which combines steepest gradient descent and Gauss-Newton method, is presented and discussed to solve some shortcomings of the conventional single neuron adaptive PID controllers. LM algorithm deals with the problem that the gradient descent method is a one-order optimization method and Newton iterative algorithm costs much computing resource.

From the simulation results, we find that convergence speed is increased and the control performance is greatly improved by using LM algorithm. In conclusion, the novel controller has strong robustness and good self-adaptation. So it is a valuable method for single neuron adaptive PID controller using LM algorithm.

References

1. Xu, B.-C., Wu, J.-Z., Chen, Y.-K.: An Improved Single Neuron Adaptive PID Control Algorithm. In: Fifth International Conference on Natural Computation, pp. 558–562. IEEE Press (2009)
2. David, W.T., John, J.H.: Simple ‘neural’ optimization networks: An A/D converter, signal decision circuit, and a linear programming circuit. J. IEEE Transaction on Circuits System CAS-33, 53–541 (1986)
3. Mamdani, E.H.: Application of fuzzy algorithms for control of simple dynamic plant. J. Proceedings of the Institution of Electrical Engineers, Control & Science 121(12), 1585–1588 (1974)
4. Wang, X.-W., Tan, D.-J., Guo, Y.-N., Hao, R.: Expert-PID Control Based on Genetic Algorithm. J. Control and Instruments in Chemical Industry 29(4), 35–37 (2002)
5. Liu, T.-K., Juang, J.-G.: A Single Neuron PID Control for Twin Rotor MIMO System. In: IEEE/ASME International Conference on Advanced Intelligent Mechatronics, pp. 186–191. IEEE Press, Singapore (2009)
6. Fang, H., Yu, X.-H.: Design and Simulation of Neuron PID Controller. In: International Conference of Information Technology, Computer Engineering and Management Sciences, pp. 80–82. IEEE Press (2011)
7. Zuo, J.-M., Pan, C., Shen, C.-J.: The Single Neuron PID Control of PMLSM Based on Quadratic Index. J. Manufacture Information Engineering of China 36(19), 20–23 (2007) (in Chinese)
8. Tang, X.-J., Huang, T.-L., Liu, X.-Y., Wang, J.: Application of PID with Single-Neuron Adaptive Control in Liquid Level Control. In: Third International Conference on Genetic and Evolutionary Computing, pp. 533–536. IEEE Press (2009)
9. Wang, X., Shi, H.-R.: Study on the single neuron adaptive PID control with self-adaptive gain. J. Automation and Instruments 5, 51–52 (2005) (in Chinese)
10. Fu, J., He, H.-B., Zhou, X.-M.: Adaptive Learning and Control for MIMO System Based on Adaptive Dynamic Programming. J. IEEE Transactions on Neural Networks 22(7), 1133–1148 (2011) (in Chinese)

Variable Step Length Best Combination AEC Algorithm in IPC*

Long Wu[1], Li-kun Xing[2], Meng-ran Zhou[2], and Shuai Chen[1]

[1] Huainan Normal University, Huainan 232001
[2] Anhui University Of Science & Technology, Huainan 232001

Abstract. Based on the echo interference in audio transmission of Network Camera (IPC), this paper presents Variable Step Length Best Combination acoustic echo cancellation (AEC) algorithm .It adjusts the convergence speed of variance by changing the step of the adaptive filter , in accordance with the best ratio combination of NLMS algorithm and RLS algorithm, to achieve faster convergence speed and good steady state characteristics of a short delay. Simulation and measurement under the network environment show that, the residual echo signal is more than 30dB lower than the far-end signal, delays 25ms below the steady-state characteristics.

Keywords: IPC, AEC, NLMS, RLS, Variable Step Length Best Combination.

1 Introduction

With the rapid development of communications, microelectronics and network technology, video surveillance system is developing in the direction of embedded, digital, networked and intelligent. Network Camera (IPC) is a new generation product that combine a traditional camera with network video technology, it integrates video, audio, network transmission and other features of embedded electronic devices and has a separate IP address and embedded operating system. Through the acquisition, compression of video signal, the network transfer monitoring video images directly to a remote video monitoring platform by the Internet [1].

In recent years, the IPC using MPEG4 or H-264 dynamic compression appearing on the market , it supports synchronization compression package transmission of audio. Because it is not as exclusive bandwidth as traditional telephony communications, when the audio in real-time transmission on the Internet, the common problem encountered is the poor sound quality [2]. during development process of the coal mine network camera project, We found echo is the main factor affecting the audio quality in the both direction audio transmission (two-way real-time intercom),. Therefore, the paper focuses on acoustic echo cancellation (AEC) algorithm in the audio transmission, to improve the audio transmission quality when IPC products on the Internet effectively. In the study proposed a variable step length best combination AEC

* National Natural Science Foundation (51104003); Natural Science Foundation of Anhui Province (KJ2010B200).

H. Zhang et al. (Eds.): BICS 2012, LNAI 7366, pp. 296–303, 2012.

algorithm ,e algorithm can be applied to VOIP Internet phone, video intercom systems, remote environment.

2 AEC Basic Principles and Related Algorithms

2.1 AEC Basic Principles

Bell Labs proposed an adaptive echo cancellation AEC filtering method [3], based on the AEC principle of the discrete time shown in Figure 1.

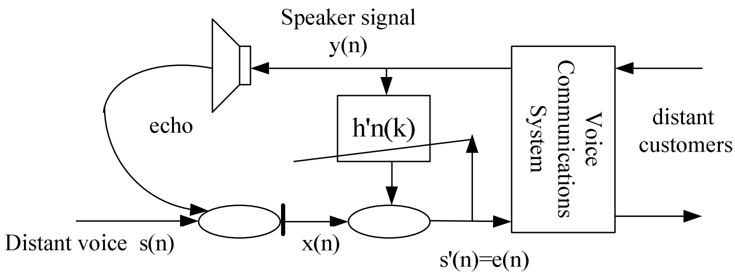

Fig. 1. AEC Principle block diagram

If the current time is n, the echo response of the system is hn(k) (k = 0,1, ..., M), the input signal x (n) contains the proximal user voices and echo: x(n)=s(n)+∑hn(k)y(n-k), in which y (n) for the speaker output signal, Σ is the k summation. Because hn (k) is unknown and time-varying, AEC's purpose is to forecast echo system model h'n (k) based on the correlation between x (n) and y (n), to estimate echo size∑h'n(k) y(n-k)), and to modify the filter coefficients continually, making the estimated value close to a real echo. Then, the echo estimate is subtracted from the input signal, to be Local user voice s' (n) that offset by the echo: s'(n)=x(n)-∑h'n(k) y(n-k). If the local user-quiet s (n) = 0,

s '(n) is the prediction filter prediction error e(n) = x(n)-∑hn'(k) y(n-k), so the core of the AEC is an adaptive filter.

2.2 Related Algorithms

The adaptive filtering algorithms commonly used in Echo cancellation are: LMS algorithm, NLMS algorithm, RLS algorithm, FLMS algorithm; LMS algorithm is simple to calculate,it has the minimum amount,but its convergence is slow, filter order is too high, and is likely to cause error accumulation , leading to algorithm divergence; NLMS algorithm is the normalized LMS algorithm, is one of the most widely used algorithms in adaptive signal processing.It is easy to achieve. Its computation amount is moderate and performance is better than LMS algorithm, but the convergence is slow , Ability to adapt to non-stationary signals is poor; RLS algorithm convergence is better, but the operation amount proportional to the square of the order of the filter, IP phone, the echo signal delay of tens of milliseconds, or even longer, which requires filter order higher ,computation is also large, steady-state performance is not good; FLMS is a method in the frequency domain calculated algorithm . Due to the general noise suppression in frequency domain , if the echo cancellation using FLMS algorithm, then the noise will have some filtering effect, but computation is large, and convergence is slow. Based on the above analysis, presents a adaptive filtering algorithm of variable step size combination proportion, combinatorial algorithms selected in terms of convergence and steady-state must have some complementary features.

1.2.1 RLS Algorithm

Recursive least square algorithm aims to make the squares sum of difference between the expected signal and output of model filter is minimum. When receiving the new samples value of the input signal in each iteration, can use recursive form solve least squares problem, get a recursive least squares (RLS). The purpose of this algorithm lies in selecting the adaptive filter coefficients, the output of the observation period signal y (n) and desired signal in least square on the significance of the matching [4]. First, the algorithm initialization, $\omega(0)=0; P(0)=\delta^{-1}I$ where I is the identity matrix: δ={High SNR take small normal and Low SNR take small normal}Then, each time, n = l, 2, ... to calculate the gain vector k(n)=P(n-1)u(n), g(n)=k(n)/[λ +(n)k(n)],

$$e(n)=d(n)-w^T(n-1)u(n),\ g(n)=P(n-1)u(n)/\left\{\lambda+u^T(n)P(n-1)u(n)\right\}$$

filter: $y(n)=w^T(n-1)u(n)$; Error estimation: e(n)=d(n)-y(n); Update right vector: W(n)=W(n-1)+g(n)e(n); Define tap the input vector u (I) the time average of correlation matrix said: $H(n)=\sum_{i=1}^{n=1}\lambda^{n-1}u(i)u^T(i)+\delta\lambda^{n-1}I$, Available for updating the tap input correlation matrix of the recursive formula H(n)= λ H(n-1)+u(n)uT(n) and P(n)=H-1(n)and get updates inverse matrix: P(n)= λ -1[P(n-1)-g(n)uT(n)P(n-1)].

Which P (n) is the inverse matrix of the autocorrelation matrix H (n), constant λ is forgetting factor, and 0 < λ <1.simillar to classical least squares algorithm, recursive least squares (RLS) algorithm determines the weight coefficient vector W (n) of adaptive filter so that the weighted estimation error is minimum. However, RLS algorithm updates the inverse of the input signal autocorrelation matrix H (n) by recursive estimation, to reduce the computational and storage capacity, improve the operation speed.

1.2.2 LMS Algorithm and NLMS Algorithm

Standard LMS algorithm is linear adaptive filtering algorithms. Algorithm consists of two basic processes: filtering process and adaptive process. These two processes work together to form a feedback loop, shown in Figure 2, first of all, constructed LMS algorithm around the transversal filter, is to complete the filtering process; Secondly, the "adaptive control algorithm" part controls adaptive process of transversal filter tap weights. adaptive filter Control principle is to use error sequence e (n) to adjust its coefficient w (n) according to the mean square error minimization criterion and algorithm .the final goal is the adaptive filter (cost) function to minimize, and filter status to optimal. The basic idea of LMS algorithm is used the squared error to replace mean square error.

The standard computing of LMS algorithm are as follows:

1) Initial Setup tap input vector u (n) (n = l, 2, ..., N-1) arbitrary value (usually zero mean), and then make cycle operation for each sample as the following steps;
2) calculate weight vector wH (n) Output through the filter tap: y(n)= wH(n) u(n)
3) calculate the estimation error: e (n) = d (n)-y (n), of which, d (n) is the desired response;
4) Update four filters weighting coefficient: w(n)=w(n-1)+μu(n) e(n) (n=l, 2,…, N-1)

Where μ is the step factor and is parameter to control the stability and convergence rate;

5) loop back to 2)

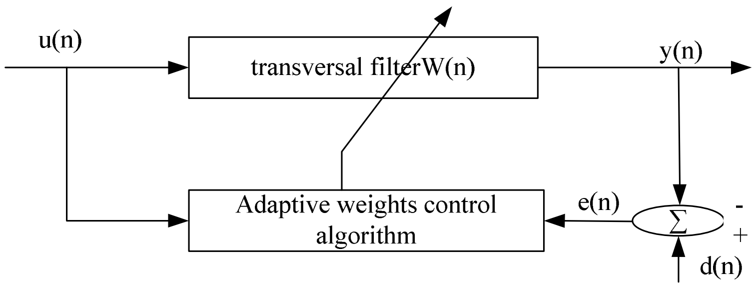

Fig. 2. Adaptive filter diagram

NLMS algorithm is the normalized LMS algorithm (NLMS algorithm) ,it is used to correcte the coefficients of FIR filter in the LMS adaptive filter equation [5]. NLMS algorithm and the LMS algorithm is almost the same, only difference is using variable step size controlling factor in the NLMS algorithm instead of the constant factor in the LMS algorithm. Its purpose is to accelerate the convergence rate, AEC convergence speed depends largely on the step parameters and remote signal power. Large step size parameter, you can speed up the convergence rate of the filter, but will increase the echo elimination of errors. On the contrary,it will increase the amount of computation, effect the impact of eliminating the echo in real-time.So, the subject of the step factor μ using the estimated value to normalization, normalization equation as follows : $2B = 2B(n) = B1 / P_y(n)$ Of which, B is a step size constant factor in LMS algorithm; B1 is the step size constant average; $P_y(n)$ is the sampling time n corresponding to the remote audio signal average power estimates, calculated as follows: $p_y(n) = (1-\rho)\, p_y(n-1) + \rho * y^2(n)$ where is a ρ constant, y (n) is the input signal.

3 Variable Step Length Best Combination Algorithm

Optimum combination algorithm of variable step size is a certain percentage of the portfolio that combine the advantages of NLMS algorithm and the RLS algorithm, we can solve the conflicts about convergence speed and steady-state offset, on the other hand questions that an algorithm can be solved, which is difficult to performance in a number of performance indicators. The algorithm approach is to choose the combination of two algorithms, at the same time , different algorithms arte to adjust different parameters to achieve the optimal combination. With the minimal error energy method to adjust the combination scale factor in order to acquire a good performance algorithm. The algorithm's calculation is large. However, the current chip technology has greatly increased the speed of the chip's operation, which provides the basis for running the algorithm, so the computation is not a problem. Therefore, the two algorithms NLMS and RLS are combined with in a certain proportion to form the Variable Step Length Best Combination algorithm (VSL-BC-RNLMS, Variable Step Length Best Combination RLS And NLMS). block diagram the Variable Step Length Best Combination algorithm shown in Figure 2 . The first step,improve convergence by adjusting the speed, and then calculate the error of NLMS and RLS algorithms, and calculate the each frame error energy , analysis the energy error of NLMS and RLS algorithm, adjust the ratio of multiplying parameters λ(n) and 1-λ(n)of the NLMS and RLS to get an algorithm, making the VSL-BC-RNLMS algorithm error smaller than NLMS and RLS algorithms. Finally, the error of smallest frame error energy is outputed.

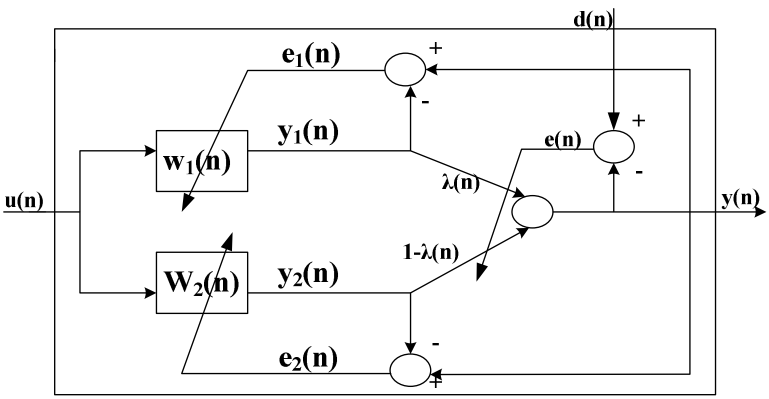

Fig. 3. VSL-BC-RNLMS adaptive filter diagram

Optimum combination algorithm of variable step size is described as

$y(n)=\lambda(n)y_1(n)+\left[1-\lambda(n)\right]y_2(n)$ where $y_1(n)$ and Are outputs of two filters in n time $y_1(n)=w^T(n)u(n)$, i=1、2, $w^T(n)$ and $u(n)$ weight vector Filter components By $\lambda(n)$ defining a function $a(n)$ to limit the range of [0,1], the corresponding functional relation of the function $a(n)$ and $\lambda(n)$ is: $\lambda(n)=sgm\left[a(n)\right]=\dfrac{1}{1+e^{-u(n)}}$. Best filter can be got according to the parameters $\lambda(n)$ combination from Independent filter $w_1(n)$,

$w_2(n)$. $e(n)=d(n)-y(n)$, $w(n)=\lambda(n)w_1(n)+[1-\lambda(n)]w_2(n)$ According to the definition of the steepest descent algorithm known $a(n+1)=a(n)-u_n\nabla_n$ Which can get the update $a(n)$ as following deformation

$$a(n+1)=a(n)-\frac{u_a}{2}\frac{\partial e^2(n)}{\partial a(n)}=a(n)-\frac{u_a}{2}\frac{\partial e^2(n)}{\partial\lambda(n)}\frac{\partial\lambda(n)}{\partial a(n)}$$

$$=a(n)+u_a e(n)[y_1(n)-y_2(n)]\lambda(n)[1-\lambda(n)]$$

Where the parameters to adjust the step size, its dimension is the inverse of the signal power.

4 Simulation and Experimental Analysis

4.1 Simulation Analysis

In the laboratory, using MATLAB algorithm to do effect simulation for the optimal combination in IP echo processing, the results in Figure 4

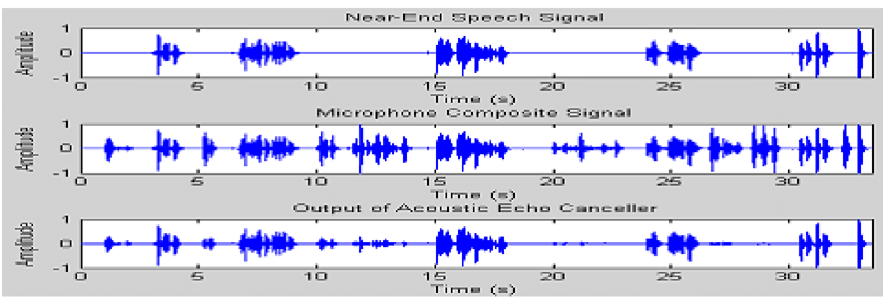

Fig. 4 -1. NLMS echo processing figure

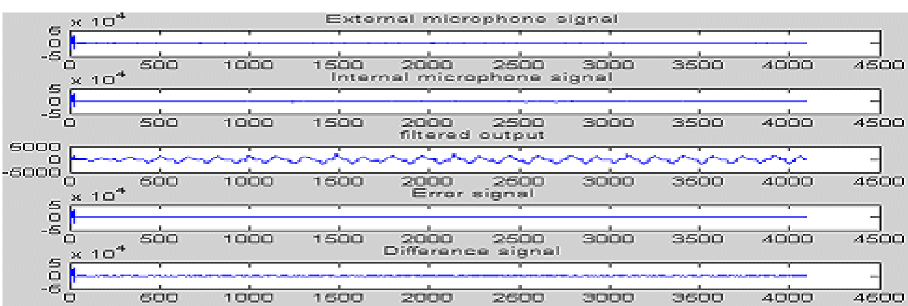

Fig. 4 -2. VSL-BC-RNLMS echo processing figure

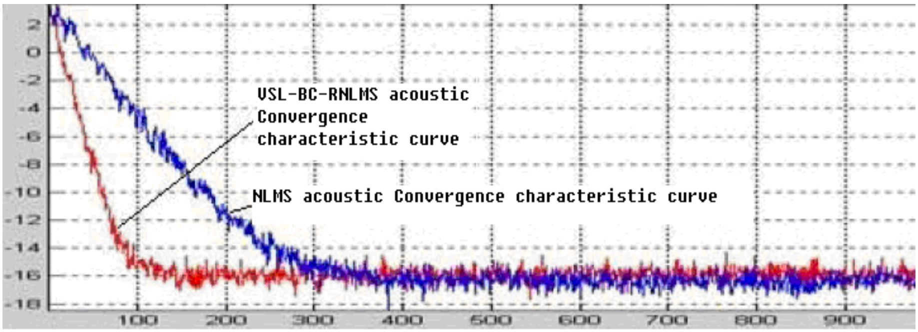

Fig. 4 -3. VSL-BC-RNLMS and NLMS Convergence property comparison chart

Figure 4-1 from top to bottom are outputs of near the speech signal, a microphone composite signal and echo cancellation, Figure 4-2 from top to bottom are the external microphone signal, the internal microphone sub-signal, filtered output, error signal and the residual signal curve, Figure 4-3 from left to right are performance curve of the VSL-BC-RNLMS and NLMS, Figure 4 shows the improved VSL-BC-RNLMS algorithm has significantly improved than the NLMS algorithm , its convergence and convergence speed have been greatly improved.

4.2 Measured Analysis of the Network Environment

VSL-BC-RNLMS algorithm use replaced step size is to improve the convergence speed. In the implementation, the authors used different parameters values 10ms to 30ms to adjust the remote signal power of the short window calculation .Because the step adjustment, the software calculated time changes, resulting in the delay time of the sound change, it can only get a compromise, which requires test in the actual environment, to achieve the desired effects.

In achieving AEC, there are still a key technical problem that we should calculate the signal power of a variety of situations, because the audio active detection and NLMS algorithm factor correction require the power estimates. Short-time average power calculated formula is the same as the previous one:

$p_y(n) = (1-\rho)\, p_y(n-1) + \rho * y^2(n)$ Among them, the constant ρ value of ρ =l/32(Short delay of 4ms window power estimation); = 1 / 128 (16ms delay for the shorter window power estimation); = l/16384 (delay of 2048ms long window power estimation).

5 Summary

This paper focuses on the Variable Step Length Best Combination AEC algorithm, AEC eliminator with the application of the algorithm are used in coal mine practice in the IPC, has 16-bit fixed-point DSP (TI's TMs320 series) programming, using such ARM implementation of the echo canceller can meet the accuracy requirements of G.168/G.165 . And the echo residual signal is more than 30dB lower than the far-end signal, delay 25ms below the steady-state characteristics, to achieve good results.

References

[1] Zhu, C.: RAM-based design and implementation of network cameras. Chengdu University of Technology Master's thesis (2010)
[2] Zhang, S., Qi, X.: Video standard based on digital video recorders MPEG_4 Design and implementation. Modern Electronic Technology 20, 51–55 (2008)
[3] Wang, S.: Adaptive echo cancellation algorithm. China University of Science and Technology School of Information Science and Technology, Hefei (2007)
[4] Liu, J., Zhang, Y.-F., et al.: NLMS and the RLS algorithm and its application in the simulation compared FECG Extraction. Computer Simulation 23(04), 78–80 (2006)
[5] To the race-hui. Conference call in the multi-channel echo cancellation system theory and application of. Kunming University of Science, Kunming (2008)

Stochastic Resonance in Excitable Neuronal System with Phase-Noise

Xiaoming Liang and Liang Zhao

Institute of Mathematics and Computer Science,
University of São Paulo, São Carlos, 13560-970, Brazil

Abstract. Stochastic resonance has been revealed as an important cue for understanding the performance of biological systems in detecting external weak signal. Here we show that the noise originated from signal phase may also induce stochastic resonance in an excitable neuronal system. We find that the neuronal system is better at detecting a subthreshold signal when the signal phase is not constant but time-varying like noise. Further, we find that an intermediate intensity of phase noise may help the neuronal system to obtain a optimal detection, forming an resonance-like phenomenon. Finally, a brief theory is formulated to explain the mechanism behind the resonance behavior.

Keywords: Stochastic resonance, excitable system, phase noise, subthreshold signal.

1 Introduction

Three decades ago, stochastic resonance (SR) was firstly discovered and proposed for explaining why the earth ice ages occurred periodically [1]. It refers to a phenomenon that a suitable value of noise added to the dynamics causes an increasing of the system's sensitivity to discriminate external weak signals, rather than a decreasing. This counterintuitive effect points out that noise can also play a positive role in enhancing the detection of weak signal. Due to its generic nature, SR is widely employed in explaining the performance of signal detection in nervous systems since noise is ubiquitous in these systems [1,2,3].

The classical SR specifies that an external signal input to a system must be periodic and regular. This is not realistic, because many actual signals are often aperiodic and noisy. Considering this, Collins *et al.* generalized the theory of SR to aperiodic SR and found that an suitable noise can serve to enhance the response of a nonlinear system to the aperiodic signals [4,5,6,7]. Except external noise, it is also found that the "inner noise" from the diversity of neurons themselves can induce SR [8]. Recently, Liang *et al.* found that the "noise" from the phases of input signals may enable the coupled excitable neurons to catch the input signals [9]. This finding clearly demonstrated that the positive role of disordered signal phases played in a sensory nervous system. However, in that work, the disordered phases of each neuron are constant. In addition, the influence of disordered signal phase is unclear yet for a single neuronal system

H. Zhang et al. (Eds.): BICS 2012, LNAI 7366, pp. 304–310, 2012.

which constitutes the coupled ensemble. Thus, an interesting question would be what will happen if a single neuron receive a signal with time-varying phase.

Actually, this kind of noisy signal is indeed existing in many real situations. For instance, the variation of the distance to the signal source makes the neuron sensors receive external signal with continuous phase shift. To pinpoint prey in a dark environment, the barn owl adjusts the direction of its head toward the sound source for obtaining optimal interaural time difference between both ears. During the adjustment, the arriving times and intensities of sound between the ears change accordingly [10]. Besides, periodic wave traveling through a fluctuating medium or interface also may generate phase variation [11]. In addition, some sensory organs are very sensitive to phase difference of the received stimulus [12,13,14,15]. For instance, the weakly electric fish Eigenmannia has a sensory capability of discriminating subtle time disparities on the order of 10^{-8}s to 10^{-5}s [13,14], by which Eigenmannia can keep changing its signal phase in order to avoid jamming between signals coming from other nearby fishes. Summing up all these facts, it is necessary for us to know how the signal with time-varying phase influences the neuronal performance in signal detection.

In this paper, we examine the effect of phase noise on the dynamics of a single excitable neuronal system, where the signal phase is time-varying by noise. We find that even a small phase noise can assist the neuron to efficiently detect subthreshold external signals. Moreover, we show the existence of an optimal value on the phase noise, where the detection can be significantly improved, resulting in a resonance-like behavior. Finally, we apply a simple theory for analyzing the underlying mechanism.

2 Model

To investigate whether the phase noise enables a excitable neuronal system respond to subthreshold signal, we choose the Hindmarsh-Rose (HR) model neuron [16], which can reproduce a lot of realistic neuronal response properties, such as periodic, chaotic, and irregular bursting behaviors depending on the model parameter. In particular, we consider the following system:

$$\begin{aligned}\dot{x} &= y - ax^3 + bx^2 - z + I_{ext} + A\sin\Big[\varOmega t + \varphi(t)\Big],\\ \dot{y} &= c - dx^2 - y,\\ \dot{z} &= r[s(x - x_0) - z],\end{aligned} \tag{1}$$

where x is the membrane potential, y is associated with the fast current, Na^+ or Ka^+, and z with the slow current, for example, Ca^{2+}. The parameters are taken as $a = 1.0$, $b = 3.0$, $c = 1.0$, $d = 5.0$, $s = 4.0$, $r = 0.006$, $x_0 = -1.60$. The external inputs are given by a constant signal I_{ext} and a sinusoidal signal $A\sin(\varOmega t + \varphi(t))$. When $A = 0$, the single HR neuron displays excitability for $I_{ext} < 1.32$ and generates multi-time scaled burst-spike behaviors for $1.32 < I_{ext}$, see Fig. 1(a). Here we set $I_{ext} = 1.2$, so that the HR model is excitable. Besides, the sinusoidal signal is set to be subthreshold, i.e., it is unable to trigger the

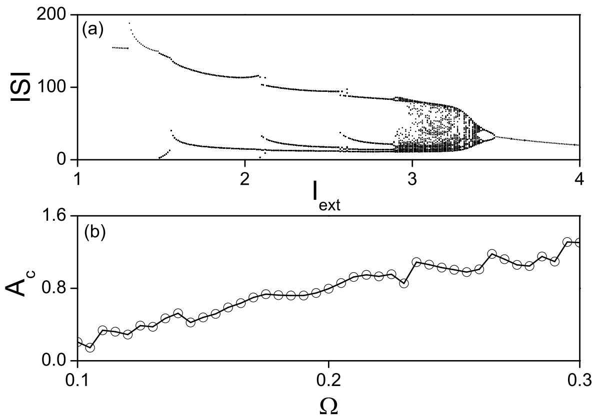

Fig. 1. (a) The bifurcation diagram of interspike interval (ISI) versus external current I_{ext} with $A = 0$. (b) The thresholds of A_c to trigger spikes as a function of signal frequency Ω with $D = 0$ and $I_{ext} = 1.2$.

HR neuron to generate spikes at $I_{ext} = 1.2$ and $\varphi(t) = 0$. Figure 1(b) shows the thresholds of A_c to trigger spikes of a single HR neuron as a function of signal frequency Ω. To ensure that the sinusoidal signal is subthreshold, $\Omega = 0.2$ and $A = 0.7 < A_c$ ($A_c \approx 0.8$ for $\Omega = 0.2$) are used in which Eq. (1) generates subthreshold oscillations around its resting state and does not fire. As real signals are often aperiodic and noisy, the sinusoidal signal with time-varying phase $\varphi(t)$ is considered. For simplicity, the signal phase $\varphi(t)$ is set to be varied as a Wiener process. Accordingly, the mean value and autocorrelation of $d\varphi(t)$ are 0 and $\langle d\varphi(t)d\varphi(t')\rangle = 2D\delta(t - t')$, respectively. Thus, the parameter D governs the intensity of phase noise. Easy to see, $D > 0$ just disturbs the perfect periodicity of the sinusoidal signal (at $D = 0$) but does not change the range of signal amplitude. Our goal is to study such noisy signal generated by time-varying phase $\varphi(t)$ affects on the response of HR neuron to the subthreshold sinusoidal signal.

2.1 Numerical Results

In biological systems with spiking behavior, only the spikes are important for the information transmission while the local dynamics is not important [17]. For this reason, in the following we transform the original time series $x(t)$ of Eq. (1) into a series pulses. To this aim, we set a threshold x_{th} of $x(t)$ to distinguish the spikes and subthreshold oscillations. If $x(t)$ is smaller than x_{th}, we replace the value of $x(t)$ by 0. For $x(t) \geq x_{th}$, $x(t)$ is set as 1. In this work, $x_{th} = 1$ is chosen as the threshold. Such replacement also helps to give a better observation of the firing and resting behaviors of $x(t)$.

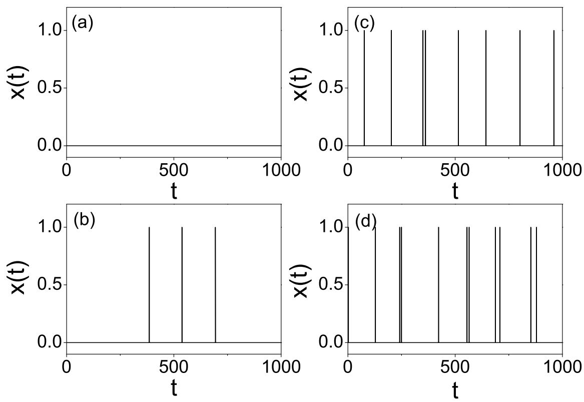

Fig. 2. Time series of the HR system for $\Omega = 0.2$, $A = 0.7$, and $I_{ext} = 1.2$. (a) $D = 0$, (b) $D = 10^{-3.6}$, (c) $D = 10^{-2}$, and (d) $D = 10^{-0.6}$.

Firstly, we show the case of constant phase, i.e., $D = 0$. Our numerical simulations show that the time series of $x(t)$ have no spikes, which supports the fact that subthreshold driving signal is incapable of inducing firing. Figure 2(a) shows the result. Interestingly, we find that it is possible for HR neuron to generate spikes when D increases to $10^{-3.6}$, see Fig. 2(b). This means that a small intensity of phase noise may sharply improve the neuronal response to subthreshold signal. As D is increased to 10^{-2}, we find that the firing rate is enhanced and the intervals between two successive spikes are more regular, see Fig. 2(c). Further increasing of D to $10^{-0.6}$ results in the decreasing of the firing regularity, see Fig. 2(d). Therefore, we have observed a novel phenomenon that the regular firing pattern is purely induced by time-varying signal phase in a single neuronal system and it is enhanced when the intensity of phase noise is at the intermediate level.

As mentioned above, the HR neuron exhibits different responses to the sinusoidal signal with phase noise. To measure these responses, we then define signal amplification Q at the signal frequency Ω as follows [18,19]:

$$Q = \left| \frac{\Omega}{n\pi} \int_0^{\frac{2n\pi}{\Omega}} x(t) e^{i\Omega t} dt \right|, \tag{2}$$

where n is a parameter determining the length of integration. Let $n = 50$, we plot the measurements of Q on D in Fig. 3(a). From this figure, we see a bell-shaped Q as a function of D, which is the signature of SR. Moreover, we see the threshold value of D corresponding to $Q > 0$ is $D \approx 10^{-3.6}$ and the optimal value of D corresponding to the maximums Q is $D \approx 10^{-2}$, respectively. These quantities are supported by the firing activities as shown by Figs. 1(b) and (c).

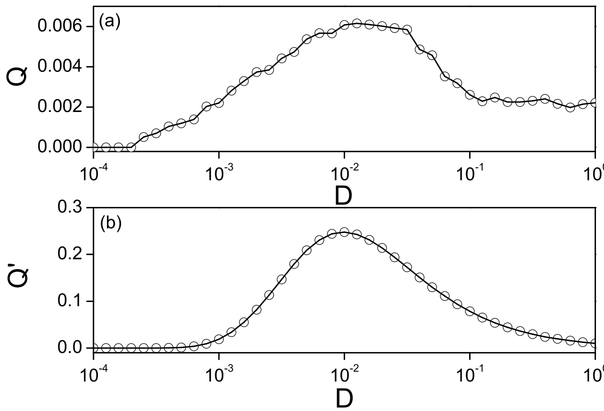

Fig. 3. Signal amplification as a function of phase noise. (a) The numerical result Q of Eq. (1) with $\Omega = 0.2$, $A = 0.7$, and $I_{ext} = 1.2$. (b) The analytical result Q' of Eq. (7) with $U = 4 \times 10^{-3}$ and $\eta = 1$.

3 Analysis

To understand the mechanism of the above phenomena, we rewrite the membrane potential of Eq. (1) as

$$\dot{x} = y - ax^3 + bx^2 - z + I_{ext} + A\sin(\Omega t)\cos(\varphi(t)) + A\cos(\Omega t)\sin(\varphi(t)). \quad (3)$$

Considering that the onset of amplifications ($Q > 0$) are occurred at small noise ($D \approx 10^{-3.6}$), then we suppose that the noise is so weak that Eq. (3) can be simplified to

$$\dot{x} \approx y - ax^3 + bx^2 - z + I_{ext} + A\sin(\Omega t) + \Psi(t), \quad (4)$$

where the approximations $\cos(\varphi(t)) \approx 1$ and $\sin(\varphi(t)) \approx \varphi(t)$ are used. $\Psi(t) = A\cos(\Omega t)\varphi(t)$ is the periodically modulated noise with autocorrelation:

$$\langle \Psi(t)\Psi(s) \rangle = 2DA^2\cos^2(\Omega t)\delta(t - s). \quad (5)$$

It should be noted that for Winner process of $\varphi(t)$, the Eq. (4) is not always hold even for very small D because there still exists a probability for $\varphi(t)$ to have large values. As the probability is very small, we can get the approximation of Eq. (4) at small D. Then, applying Kramer-type formula [1], the time-dependent firing rate $r(t)$ of Eq. (1) can be approximately obtained as

$$r(t) \propto \exp\left[-\frac{U(1 - \eta A\cos(\Omega t))}{DA^2\cos^2(\Omega t)}\right], \quad (6)$$

where $U(1 - \eta A\cos(\Omega t)$ is the effective barrier height modulated by the forcing $A\sin(\Omega t)$, $DA^2\cos^2(\Omega t)$ is the total effective noise, and η is a scale factor satisfying $\eta A < 1$ since signal is subthreshold.

According to Eq. (6), $r(t) \approx 0$ for a tiny intensity of phase noise. In this condition, the HR neuron cannot generate spikes because the influence of phase noise is not sufficient to disturb the subthreshold oscillations of Eq. (1). For slightly stronger but still small intensity of phase noise, the value of $r(t)$ is increased. This corresponds to the case that the phase noise may perturb the subthreshold oscillations to cross the firing threshold. However, the intensity is insufficient to maintain continuously the regular firing pattern. On the other hand, for large intensity, $r(t)$ increases to a large value, but the firing regularity will be polluted by the large intensity of phase noise. Considering the above observations, the intensity D is at its optimal value, $r(t)$ has a intermediate value, guaranteeing the HR neuron fire spikes regularly. As a result, the HR neuron has the largest response in this regime. Therefore, we arrive at a conclusion that phase noise can significantly change the system behavior even though it does not change the range of signal amplitude.

Using Eq. (6), we further obtain the theoretical Q' as

$$Q' = \left| \frac{\Omega}{n} \int_0^{\frac{2n\pi}{\Omega}} r(t) e^{i\Omega t} dt \right| . \tag{7}$$

Let $U = 4 \times 10^{-3}$ and $\eta = 1$, we calculate Q' as a function of D in Fig. 3(b). Here U and η are not specific and can be set as other values. Obviously, Q' displays a similar bell-shape on D as shown in Fig. 3(a), indicating the reasonable of Eq. (4). Note that the above analysis are based on an assumption that phase noise intensity D is very tiny. For large D, Eq. (3) cannot simplify to Eq. (4) so that Eq. (7) cannot be obtained. Therefore, the result shown in Fig. 3(b) is approximately valid for small D.

4 Conclusions

In conclusion, we have investigated the effects of phase noise in relation to firing pattern of a single excitable neuron with subthreshold signal, where the phase noise mimics the time-varying phase of input signal. The signal amplification factor Q shows bell-shaped behavior by varying the phase noise, indicating that we have uncovered an resonance phenomenon. This resonance implies that biological systems may exploit the power of randomness to enhance signal detection. Applying a brief theory, we explain the mechanism of phase noise in amplifying signal. Since irregular signals are common in natural environment, our findings are useful in learning about the capability for signal detection of neuron sensories, which deserves further experimental and theoretical investigation.

Acknowledgments. X. Liang is supported by the FAPESP of Brazil. L. Zhao is partially supported by CNPq and FAPESP of Brazil.

References

1. Gammaitoni, L., Hänggi, P., Jung, P., Marchesoni, F.: Stochastic Resoance. Rev. Mod. Phys. 70, 223–287 (1998)
2. Lindner, B., Garcia-Ojalvo, J., Neiman, A., Schimansky-Geier, L.: Effects of Noise in Excitable Systems. Phys. Rep. 392, 321–424 (2004)
3. Douglass, J.K., Wilkens, L., Pantazelou, E., Moss, F.: Noise Enhancement of Information Transfer in Crayfish Mechanoreceptors by Stochastic Resonance. Nature (London) 365, 337–340 (1993)
4. Collins, J.J., Chow, C.C., Imhoff, T.T.: Aperiodic Stochastic Resonance in Excitable Systems. Phys. Rev. E 52, R3321–R3324 (1995)
5. Park, K., Lai, Y., Liu, Z., Nachman, A.: Aperiodic Stochastic Resonance and Phase Synchronization. Phys. Lett. A 326, 391–396 (2004)
6. Liu, Z., Lai, Y., Nachman, A.: Enhancemnet of Detectability of Noisy Signals by Stochastic Resonance in Arrays. Int. J. Bifurcation and Chaos 14, 1655–1670 (2004)
7. Lai, Y., Liu, Z., Nachman, A., Zhu, L.: Suppression of Jamming in Excitable Systems by Aperiodic Stochastic Resonance. Int. J. Bifurcation and Chaos 14, 3519–3539 (2004)
8. Tessone, C.J., Mirasso, C.R., Toral, R., Gunton, J.D.: Diversity-Induced Resonance. Phys. Rev. Lett. 97, 194101 (2006)
9. Liang, X., Dhamala, M., Zhao, L., Liu, Z.: Phase-Disorder-Induced Double Resonance of Neuronal Activity. Phys. Rev. E 82, 010902(R) (2010)
10. Konishi, M.: Listening with Two Ears. Sci. Am. 16, 28–35 (2006)
11. Chapeau-Blondeau, F.: Stochastic Resonance at Phase Noise in Signal Transmission. Phys. Rev. E 61, 940 (2000)
12. Mason, A.C., Oshinsky, M.L., Hoy, R.R.: Hyperacute Directional Hearing in a Microscale Auditory System. Nature (London) 410, 686–690 (2001)
13. Lytton, W.W.: Simulations of a Phase Comparing Neuron of the Electric Fish Eigenmannia. J. Comp. Physiol. A 169, 117–125 (1991)
14. Matsushita, A., Kawasaki, M.: Neuronal Sensitivity to Microsecond Time Disparities in the Electrosensory System of Gymnarchus niloticus. J. Neurosci. 25, 11424–11432 (2005)
15. Pitcher, T.J., Parrish, J.K.: In: Pitcher, T.J. (ed.) Behaviour of Telost Fishes, ch. 7, pp. 201–246. Chapman and Hall, London (1993)
16. Liang, X., Tang, M., Dhamala, M., Liu, Z.: Phase Synchronization of Inhibitory Bursting Neurons Induced by Distributed Time Delays in Chemical Coupling. Phys. Rev. E 80, 066202 (2009)
17. Kumar, A., Rotter, S., Aertsen, A.: Spiking Activity Propagation in Neuronal Networks: Reconciling Different Perspectives on Neural Coding. Nat. Rev. Neurosci. 11, 615–627 (2010)
18. Zaikin, A.A., García-Ojalvo, J., Schimansky-Geier, L., Kurths, J.: Noise Induced Propagation in Monostable Media. Phys. Rev. Lett. 88, 010601 (2001)
19. Zhang, Y., Hu, G., Gammaitoni, L.: Signal Transmission in One-Way Coupled Bistable Systems: Noise Effect. Phys. Rev. E 58, 2952–2956 (1998)
20. Pikovsky, A.S., Kurths, J.: Coherence Resonance in a Noise-Driven Excitable System. Phys. Rev. Lett. 78, 775–778 (1997)

Emotion Recognition Based on Physiological Signals*

Naiyu Wu[1,2,**], Huiping Jiang[1], and Guosheng Yang[1]

[1] Information Engineering College, Minzu University of China, Beijing, 100081, China
[2] College of Science, Minzu University of China, Beijing, 100081, China

Abstract. Emotion recognition has aroused great concern recently. Physiological signals show its objective in the field of emotion recognition. This paper introduces emotion recognition system and physiological signals processing. The recognition system can be divided into four sections: signal preprocessing, biological feature extraction, feature matching to and feature classification. For each part, we studied existed methods and discussed their performance and characteristics. Lastly, the trend of emotion recognition for physiological signals was given.

Keywords: Physiological signals, Emotion recognition, Signal processing.

1 Introduction

Professor Lee Min Chomsky [1], in monograph (The Society of Mind) pointed out: the problem is not that intelligent computer can have emotion, but rather machines without emotion can achieve intelligence. Since then, with the development of computer technology and bioinformatics computing technology, emotional recognition and expression increasingly highlights its importance as a supplementary means of brain computer interaction(BCI), giving computer the ability of observation, understanding similar to humans', as well as generating a variety of emotions. The ability was highly concerned by academic community and business community [2-5].

Emotion is internal, subjective experience, and it is always accompanied by some kinds of facial expressions or physiological characteristics. Expression contains facial expressions, gestures, and expressions of tone, which are known as body language. Physiological characteristics include: skin temperature (SKT), electroencephalogram (EEG), electrocardiogram(ECG), electromyogram (EMG), skin response (GSR), the photoelectric pulse diagram (PPG), eye movements (EOG) respiratory signal (RSP) and pupil diameter. Therefore, the main methods for emotion recognition of human are mainly based on body languages and physiological signals.

* This work was supported in part by 985 Funding Project (3rd Phase) of Minzu University of China (Grant 9850100300107), Independent Research Funding Project of Minzu University of China (Multisource information based Research on Ethnic Relationship) and Youth Funding Project of Minzu University of China (Anthropology based multimode Ethnic Facial Information Coding Research), Beijing Municipal Public Information Resources Monitoring Project (Grant 104-00102211)

** Corresponding author.

H. Zhang et al. (Eds.): BICS 2012, LNAI 7366, pp. 311–320, 2012.

Emotion recognition based on body language, extracts body language signal features, matches features, and then makes a classification on sentiment of the subjects. However, the results cannot rule out subjective factors of the subjects; physiological signal-based emotion recognition can be dominated by the autonomic nervous system, which can hardly be controlled by the subjective. Thus, the results based on physiological signals emotional identity can be more objective [4].The research has aroused great interests for many emotion recognition researchers at home and abroad. According to existed literatures, we analyzed emotion recognition system and its algorithm deeply. This paper was divided into four parts mainly: basic framework of the system, physiological signal preprocessing, feature extracted and classification.

2 The Emotion Recognition System Based on Physiological Signals

The emotional recognition system of the physiological signals can be divided into four parts. Through all kinds of effective sensors, directly or indirectly, we obtain various physiological signals, using mathematical tools to extract of its feature for a special emotional state, choosing the minimize physiological feature in order to reduce the complexity of the signal processing system, and the emotion classification will be done. More detail information will be introduced in the following.

2.1 Physiological Signal Perception

The perception of physiological signals relies on a variety of sensors, thus the perception study of physiological signals mainly depends on the development of transducers. The MIT Media Lab [5] has developed a variety of sensors. As the main objects of medical analysis, such as ECG, the earliest physiological signals perception is divided into two parts: (1) the stimulation of the physiological signals that induces the signals of emotional states; (2) use of various types of sensor, and changing non-electric physiological signals into electrical signals, zooming, and removing interference, filtering, shaping, sampling and being digital, etc.

2.2 Feature Extraction of Physiological Signals

Using relevant mathematical tools, we can be able to describe the emotional state of physiological features extracted from the physiological signals based on the mapping between physiological signal and emotional state. This includes amplitude in the time domain and various frequency components in frequency domain, phase and the correlation between the electrodes in space [6]. However, the determination of the correspondence between emotional state and physical or behavioral characteristics is a basic premise of the theory for affective computing, but these corresponding relations are not very clear, and need further exploration or research. Commonly used feature extraction methods can be divided into time domain and frequency domain methods [17-19], space method [20-21], spatial and temporal combination methods [6]. Among them, the time domain and frequency domain methods have discrete Fourier transform, wavelet transform, and regression model and so on; the space methods have the principal component analysis, space complexity model and the independent component analysis; time and space methods include space-time filter, multiple regression model, time and space complexity model spatial and spatial and temporal synchronization model. Literature [6] used the more commonly used method in EEG data processing, and the total space patterns in the previous EEG signal processing. This approach has been proved very good as well as a strong adaptation.

2.3 Physiological Signal Feature Selection

As a result of the complexity of emotion, physiological characteristics of a certain emotional state are of wide variety. In order to ensure accuracy, we minimize physiological characteristics to reduce complexity. But to make the system accord with fact, we must find the combination mode of the most representative emotional characteristics. The feature selection problem is essentially a multidimensional variable combinatorial optimization problem. During the emotion recognition process based on physiological signals [22], the more features extracted, the better the ability to distinguish emotions is. However, due to algorithm limitations, more characteristics do not mean a stronger ability to identity in practical problems. This shows that the feature set must has some redundant features. The literature [23] has mentioned different feature selection algorithms will focus on different benefits. The benefits of feature selection is beneficial to data visualization and data understanding; reducing the requirements of data measurement and data storage; reducing the time of training or application; challenging "dimension disaster" and improving the prediction performance of the system.

The task of feature selection [24] selected a number d $(D>d)$ optimal features from a set of D features. It is a combinatorial optimization problem, so you can use the method of solving the optimization problem to solve feature selection problem. The commonly used methods are branch and bound method, SFS, SBS, increased l reduction r method, SFFS, SFBS, etc. we can also use intelligent heuristic algorithm, such as simulated annealing, genetic algorithms and Particle Swarm Optimization, etc.

In the process of emotion recognition, feature selection is usually only the intermediate stage of the learn system, the sample set corresponded to the finally chosen feature subset will be processed by classification or regression analysis, so the final result of feature selection is to judge by the learning algorithm. The frequently used classification learning algorithms [24] in conjunction with feature selection are K-nearest neighbor algorithm, BP algorithm, Multilayer Perceptron (MLPN), Fisher projection criteria, support vector machine (SVM), linear discriminant function (LDF), the probability neural network (PNN), the Bayesian classifier, etc.

2.4 Classification Based on Physiological Signals

The last step of the emotion recognition based on physiological signals is emotion classification. Since physiological signals are controlled by the sympathetic and parasympathetic, it mainly reflects the extent of the body waken-up [4].For this reason, researchers generally classified physiological signals along the wake dimension distribution of the types of emotions; emotional categories are divided by different scholars from two to eight kinds in variety. The classification methods often used are SVM [13], neural network [26], fuzzy C-mean [15], hidden Markov model [27] methods, etc.

3 Algorithms for Emotion Recognition

3.1 Induction and Perception of the Physiological Signals

In the study of physiological signals perception, we generally use sound, pictures, text, videos and other stimulus information to induce the emotional reactions. Sound stimulation can be music, voice, noise and so on. Image text stimulation use pictures from the IAPS (International Affective Picture System). Video stimulation can be a collection of voice and visual to stimulate. Generally believed that, the effective stimulus of sound, pictures, text, videos, and other stimuli can cause human body's physiological responses. Human emotions are triggered by sympathetic and parasympathetic. Nyklicek.Ivan [28] used music-induced materials to stimulate pleased, calm, sad and excited emotional state and neutral state. He tested 26 subjects (18 to 26 years) at a variety of heart respiratory variables. To study cardiac autonomic response to unpleasant film stimuli, Dabiela Palomba [29], used movies in the theme of surgery and threat of violence as well as generally neutral materials, tested heart rate, respiratory rate, respiratory sinusoidal rhythm, T wave amplitude and skin conductance level of 46 subjects. Jianping Li [30] used five kinds of emotion (sadness, anger, fear, happiness and disgust) from six emotional movie clips from 92 female college students. And then he tested blood pressure, respiratory rate, finger temperature, heart rate (RR interval Mean) and heart rate variability (RR interval of the maximum , RR interval of the minimum, HRV LF power, HRV high frequency power, HRV total power). Pierre Rainillel [9] asked 43 healthy volunteers to recall one or two emotional experiences of the fragment and a neutral fragment in order to inspire fear, anger, sadness, and pleased emotional states, and recorded their ECG and respiratory activity. An actor can perform eight kinds of emotions [31], and his or her physiological signals are collected.

3.2 Physiological Signals Feature Extraction

Feature extraction is the process of extracting useful information from the original signals, providing original feature set for subsequent feature selection, classification and identification. Original features [32] can be calculated or measured by the instrument or sensors. Some of the original features can be used directly, but some need to go through a specific process in order to become a useful set of features. Extract signal features can be considered from time domain and frequency domain. Characteristics of signals extracted in time domain include: mean, variance, median, maximum, minimum [33-34], maximum ratio, minimum ratio, the first difference, second difference [35-36] and so on. However, time-domain characteristics show strong dependence on signal amplitude, signal amplitude is vulnerable to impact of noise and baseline drift. Relatively, characteristics of the frequency are less affected by the amplitude of the signals. Statistical characteristics of the frequency can be extracted by Fourier transform method as well as wavelet transform method.

Physiological changes are only dominated by autonomic nervous and endocrine systems without subjective control; therefore, data obtained from physiological signals is more realistic and objective. And the main physiological signals include galvanic skin response (GSR), electromyography (EMG), electroencephalogram (EEG), blood volume pulsation (BVP), electrocardiogram (ECG), photoelectric pulse (PPG), eye movements (EOG), skin temperature (SKT), and skin signal (SC), blood pressure (BP) and respiration (RSP) and other physiological signals. These signals can express different emotions.

In reference [25] discrete binary particle swarm optimization in intelligent algorithm was first applied to characteristics selection of emotional physiology signals, and tests showed that this was a good feature selection method. Ref [8] and ref [9] investigated electromyography, skin conductance response, respiration and blood volume pulse, they used SFFS, and Fisher projection combined with feature selection method, Fisher linear discriminant function respectively achieved a higher recognition rate.

In the international arena, MIT laboratory analyzed the various factors affecting acquisition of physiological signals, and then introduced several feature extraction and classification methods [10]. As the main target of medical analysis, ECG signal, was entirely analyzed by a doctor with electronic amplifier for the earliest time. Oscilloscope and thermal pen recorder ARE used to record shows. In the late 1950s, with the appearance of computer-aided ECG analysis and diagnosis system, ECG analysis technology had a rapid development [11]. Ref[12] using products of German brain, 256 guided ERP apparatus for recording and analysis, also recorded the behavioral response data, with baseline correction to remove the blink of an eye, eye movements, electromyography artifact, adopted 200~800ms ERPS analysis duration. They made statistical analysis of the data with spass2.0 to get a better result.

Professor Guangyuan Liu and his team members used MP150 to collect 300 freshmen skin conductance, heart rate, ECG, respiration, pulse, electromyography, and frontal lobe two roads EEG. Then signals were extracted by using wavelet, neural networks. The average recognition rate was more than 60% [37]. Xuekui Wu and Jihua Chen used the production of AD Instruments, Power Lab Multi-channel physiological signal acquisition system. The former collected ECG, RSP, SKT signals and extract the respiratory sinus arrhythmia signal (RSA) from RSP and ECG signals as auxiliary discriminant, and the correct rate was 72% [38]. The latter extracted physiological characteristics from RSP, ECG, SKT, and SC. He used SPSS on dealing with various physiological parameters of emotional single-factor ANOVA analysis, and then made gradually multi-class discriminant feature extraction parameters to identify emotion. The correct rate was 88%, happy was 92%, fear was 80%, and the overall discriminant correct rate was 86.7%, which were easily gotten [39].

3.3 Physiological Signals Feature Selection

Original feature set includes redundant features. Feature selection is a combinatorial optimization problem. It is essential to make feature selection in emotion recognition. Feature selection algorithms need to determine search starting point, search strategy, feature evaluation function, and termination conditions. The common used feature selection algorithms are: FP, ANOVA, PCA, SFS, SBS, SFFS, etc. However, in the case of small samples, the within-class scatter matrix is often singular. Picard and his collaborators systematic analyzed the various factors affecting the physiological signal acquisition, and 40 kinds of characteristics of EMG, RSP, BVP, SC signals were extracted to classify four kinds of emotions. Fischer projection is adopted to identify four emotional states in character selection method where recognition rate could be more than 70 percent [9].

Analysis of variance (ANOVA) [4] is one of the important methods in classical statistics. In character selection, it is used to test a character whether there is a big difference. A linear growth of computation following a growing number of characteristics is its advantage. So it is faster in computing even if there are too many characteristics. It is not easy to find optimal characteristic which is its drawback. Wagner used music as an inducement tool to arouse four kinds of emotions: anger, happy, sadness and pleasure, collected EMG, ECG, SC and RSP from a single trial. Four emotion recognition rates achieved more than 90 percent [1].

Sequential forward selection (SFS) [4] is the most simple bottom-up search method. Each time it chooses one character from unselected features. Its criterion value is maximum when making it together with selected ones until reach the number of d . The main drawback is once certain character is selected, it cannot be emitted though one what seems being of useless. This is the so-called effect of “Nesting”. Johannes Eagner from Germany Augsburg University has an analysis on characteristics of ECG, EMG, SC, and RSP. In this way, it has achieved better results [40].

Sequential backward selection (SBS) is a tip-down approach. Each time one is removed from the beginning of the overall features. In compare with SFS, SBS has two features: first, it can estimate the reduction of divisibility caused by removing a feature in calculation process; secondly, owing that calculation is in high dimensional space, therefore, there are more computational complexity than SFS. Kim and J had identified emotions into anger, happy, sad and so on. Each type contains 90 samples. They adopted SBF on physiological signals for EMG, ECG, GSR and RSP, and gained satisfying classification results [41].

3.4 Classification Algorithms

The last step of emotion recognition is classification. Classification methods are K-the Nearest Neighbor (KNN), support vector machine (SVM), neural network, c-means and so on.

The classification algorithm of KNN (K-the Nearest Neighbor) is a relatively mature method in theory, which is one of the most simple machine learning algorithms at the same time. The train of thought of the method is: there is a sample in feature space, if most of the nearest k samples in feature space belong to a same category, the sample also belongs to this category.

Before we use KNN, the chosen neighbors are already classified correctly. In one word, KNN is only based on the category of the nearest one or some samples to decide which category the given sample belongs to. Although KNN method also depends on the limit theorem from the principle, but in category decision, it is only relevant to a small bit of adjacent samples. Because KNN method does not use discrimination class domain to determine category, but mainly base on limited adjacent samples around, so for samples waiting for classification whose class domains are more cross or overlap, KNN method is more suitable than other methods. When data features of each category are quite different, the size of a sample is very big, and another is very small, that can lead to serious errors. When the amount of data is big; calculating efficiency is a problem. Johannes Eagner found the effect of KNN classification algorithm is better [42].

The support vector machine (SVM) can solve small sample learning problems. It is a classifier based on structural risk minimization; it applies in the solution of quadratic programming problem. The basic idea of it is that for nonlinear separable problem in input space, it selects appropriate kernel function, makes the space of the sample points map to a higher dimension characteristics space, so that the corresponding sample space can be divided linearly. Either for the theoretical basis or the application prospect, SVM is superior to other learning approaches in many ways. Kim Bang and Kim of South Korea developed a multiple-access short-time monitoring emotional recognition system which is based on the signals of the physiological and achieved the recognition rate for 78.4% [43].

4 Problems and Research Trends

With the development of computer technology and pervasive computing technology, emotional recognition and expression as supplementary means for human-computer interaction is becoming more and more important, giving computer observation, understanding abilities which are similar to humans'. It has become a hotspot of human-computer emotional interaction. It has become one of the next-generation computer development goals. If computer can simulate human emotions, the first and foremost problem is that the computer must recognize emotional state. Emotion recognition based on physiological signals with its unique potential advantage has been attached to great importance. But research in this area is still in its infancy, there are many issues that need further research. In the author's opinion, the following is urgent research bottlenecks:

(1) How many categories are basic emotions in human feelings?
(2) Categories of features or feature combination that are more effective to identify specific emotion have not been given;
(3) There isn't an emotional model that complies with the laws of human emotion, and at the same time it is suitable for the machine to achieve;
(4) How to carry out credibility and objectivity from emotional information, associating with recognition and understanding from a multi-modal perspective;

(5) Human emotion is a complex process that triggered by a variety of factors, and it cannot be directly measured. This is one of the difficulties in this field;
(6) Emotion is triggered by a variety of factors, and it cannot be directly measured. But among those emotions factors, for emotion inference, some gain great contributions, others provide less. The research of the relationships between these factors and emotional state is significant to simplify model and reduce dimension, namely the so-called feature selection; Emotion is triggered by a variety of factors, and it cannot be directly measured. But among those emotions factors, for emotion inference, some gain great contributions, others provide less. The research of the relationships between these factors and emotional state is significant to simplify model and reduce dimension, namely the so-called feature selection;
(7) The resistance to interference and wireless multi-synchronous acquisition of physiological signals.

5 Conclusion

In this paper, based on previous study results, we pointed out the significance of emotion recognition , provided a more systematic introduction to the research subject and did a further analysis on research state, gave the current bottleneck in the development, and the trend of research in the future has been further predicted. For the study of physiological signal emotion recognition, more and more foreign institutions in research have achieved many research results. Although the domestic do much research in emotion recognition, but relatively few studies are based on physiological signals. Although it is not well developed, the standard of practical application in industrialization and commercialization needs a long way to pass. But it has shown its unique advantages and vitality. The application looks promising in the future as well as the commercial huge value. It can be said that the research will promote further progress of scientific research in the field of human-computer interaction, and it will have a positive impact on human activities in the future.

References

1. Minsky, M.: The Society of Mind. Simon & Schuster, New York (1985)
2. Hu, B., Tan, T., Wang, Y.: Affective computing - computer science and technology development of a new topic, 3rd edn., March 24. Science Times (2000) (in Chinese)
3. Picard, R.W.: Affective Computing. MIT Press, London (1997)
4. Mao, X., Xue, Y.: Human-computer emotional interaction. Science Press, Beijing (2011) (in Chinese)
5. Luo, S., Pan, L.: Affective Computing Theory and Technology. Systems Engineering and Electronics 25(7), 905–909 (2003) (in Chinese)
6. Palomba, D., Sarlo, M., Angrilli, A., et al.: Cardiac responses associated with affective processing of unpleasant film stimuli. International Journal of Psychophysiology 36(1), 45–57 (2000)
7. Elias, V., Picard, R.: Affective pattern classification. MIT Media Laboratory, Florida (1998)

8. Picard, R., Jennifer, H.: Digital processing of affective signals. MIT Media Laboratory, Massachusetts (1998)
9. Picard, R., Vyzas, E., Healey, J.: Toward machine emotional intelligence analysis of affective physiological state. IEEE Transactions Pattern Analysis and Machine Intelligence 23(10), 1175–1191 (2001)
10. Ahn, H., Pard, R.W.: Affective Cognitive Learning and Decision Making: The Role of Emotions. MIT Media Laboratory, Cambridge (2006)
11. Jiang, D.: Based on wavelet (packet) transform the ECG signal feature extraction method. Southwest University Journal (2009) (in Chinese)
12. Xu, J., Liang, N., Wang, Y., Wang, X.: ERP of the implicit self-esteem. Psychological Science 28(4), 792–796 (2005) (in Chinese)
13. Zhou, J.: Based on rough sets and SVM speech emotion recognition. Journal of Southwest Jiaotong University (2007) (in Chinese)
14. Zhang, W.: Semi-supervised SVM-based intrusion detection. Journal of Hebei University (2009) (in Chinese)
15. Wang, W.: Improved Fuzzy C-means clustering algorithm. Journal of Dalian Maritime University (2007) (in Chinese)
16. Jiang, J.: Based on the natural picture, face detection and recognition system. Journal of Dalian University of Technology (2008) (in Chinese)
17. Jung, T.P., Makeig, S.: Estimating Alertness from the EEG Power Spectrum. IEEE Trans. BME 44(1), 60–69 (1997)
18. Oken, B.S., Kishiyama, S.S., Salinsky, M.C.: Pharmacologically Induced Changes in Arousal: Effects on Behavioral and Electrophysiological Measures of Alertness and Attention. Electrophysiology and clinical Neurophysiology 95(5), 359–371 (1995)
19. Liang, S.F., Lin, C.T.: Monitoring Driver's Alertness Based on the Driving Performance Estimation and the EEG Power Spectrum Analysis. In: Proceedings of the 2005 IEEE Engineering in Medicine and Biology Society, pp. 5738–5741 (2005)
20. Vuckovic, A., Radivojevic, V.: Antomatic Recognition of Alertness and Drowsiness from EEG by an Artificial Neural Network. Medical Engineering and Physics 24(5), 349–360 (2002)
21. Tononi, G., McIntosh, A.R.: Functional Clustering: Identifying Strongly Interactive Brain Regions in Neuroimaging Data. Neuroimage 7, 133–149 (1998)
22. Lin, Y.: The speech signal-based emotion recognition research. South China University of Technology Doctoral Dissertation (2006) (in Chinese)
23. Isabelle, G., Andre, E.: An Introduction to variable and feature selection. Journal of Machine Learning Research 3, 1157–1182 (2003)
24. Bian, Z., Gong, Z.: Pattern Recognition, 2nd edn. Tsinghua University Press, Beijing (2000) (in Chinese)
25. Yang, R.: Emotional recognition of the physiological signal based on BPSO. Southwest University (2008) (in Chinese)
26. Micheloyannis, S., Sakkalis, V., Vourkas, M., Stam, C.J., Simos, P.G.: Neural networks involved in mathematical thinking: Linear and non-linear analysis of electroencephalographic activity. Neuroscience Letters 373, 212–217 (2005)
27. Wang, S.: A hidden Markov model-based speech emotion recognition. Science and Technology Information (28) (2010) (in Chinese)
28. Nyklicek, I., Thayer, J.F., Van Doornen, L.J.P.: Cardio respiratory differentisyion of musically-induced emotions. Journal of Psychophysiology 11(4), 304–321 (1997)

29. Li, J., Zhang, P., Wang, L., Dai, J., Yan, K.: Experimental study of the five kinds of basic emotions, autonomic nervous system response patterns specificity. Behavior of Chinese Medical Sciences 14(3), 257–259 (2005) (in Chinese)
30. Rainville, P., Bechara, A., Naqvi, N., et al.: Basic emotions are associated with distinct patterns of cardio respiratory activity. International Journal of Psychophysiology 61(1), 5–18 (2006)
31. Fu, J.: EEG-based preference analysis. Journal of Shanghai Jiaotong University (2009) (in Chinese)
32. Shi, Y., Eberhart, R.C.: Parameter selection in particle swarm optimization. In: Evolutionary Programming VII: Proceedings of the Seventh Annual Conference on Evolutionary Programming, New York, pp. 591–600 (1998)
33. Cai, L., Wang, Z.: EMG identification method based on wavelet transforms. Data acquisition and processing. Department of Biomedical Engineering of Shanghai Jiaotong University (June 2000) (in Chinese)
34. Liu, N., Lei, M.: Characteristics of surface EMG action based on wavelet and nonlinear indicators. Tissue engineering research and clinical rehabilitation. State Key Laboratory of Shanghai Jiaotong University Mechanical System and Vibration (2008) (in Chinese)
35. Shao, X., Rui, K.: Different intensity stimulation internally, the extraversion heart rate, the preliminary study of the impact of the T-wave amplitude. Yin. Psychological Science 27(2), 466–467 (2004) (in Chinese)
36. Wang, X., Li, X., Xiong, G.: Comparative analysis of short-range heart rate variability and long-term heart rate variability. Journal of Clinical Electrocardiology 11(1), 11–13 (2002) (in Chinese)
37. Wen, W., Liu, G.: Physiological signal-based emotion recognition method research, pp. I-II. Southwestern University, Chongqing (2010) (in Chinese)
38. Wu, X., Ren, L., Ding, Y., Wu, Y.: Emotional discrimination of multiple physiological information fusion for smart clothing. Computer Engineering and Applications 33, 218–221 (2009) (in Chinese)
39. Chen, J., Li, L., Qian, K.: Preliminary identification based on multiple physiological signals of sentiment. Biomedical Engineering Research (25), 141–146 (2006) (in Chinese)
40. Wagner, J., Kim, J., Andre, E.: From Physiological Signals to Emotions: Implementing and Comparing Selected Methods for Feature Extraction and Classification. In: IEEE International Conference on Multimedia & Expo (ICME 2005), pp. 940–943 (2005)
41. Litman, D., Forbes, K.: Recognizing Emotions from Student Speech in Tutoring Dialogues. In: IEEE Workshop on Automatie on Automate Speech Recognition and Understanding, pp. 25–30 (2003)
42. Wagner, J., Kim, J., Andre, E.: From Physiological Signals to Emotions: Implemeniing and Comparing Selected Methods for Feature Extraction and Classification (2005)
43. Kim, K.H., Bang, S.W., Kim, S.R.: Emotion recognition system using short-term monitoring of physiological signals. Med. Biol. Eng. Compute. 42, 419–427 (2004)

A Comparative Study of Two Reference Estimation Methods in EEG Recording*

Sanqing Hu[1,**], Yu Cao[2], Shihui Chen[1], Jianhai Zhang[1], Wanzeng Kong[1], Kun Yang[1], Xun Li[1], and Yanbin Zhang[1]

[1] College of Computer Science
Hangzhou Dianzi University, Hangzhou, Zhejiang, China
[2] College of Engineering and Computer Science
The University of Tennessee at Chattanooga
Chattanooga, TN 37403 USA
{sqhu,jhzhang,kongwanzeng,yangkun,
zhyb,xunli}@hdu.edu.cn,
yu-cao@utc.edu

Abstract. In [1] we proposed two methods to identify the reference electrode signal under the key assumption that the reference signal is independent from EEG sources. This assumption is shown to be possibly true for intracranial EEG with a scalp reference. In this paper, we theoretically prove that the obtained reference signal by using the second method in [1] or the equivalent MPDR approach [2] outperforms the widely used average reference (AR) if the real reference is independent from EEG sources. The simulation results confirm the advantages over AR.

Keywords: EEG, Reference signal, Independent component analysis, Average reference.

1 Introduction

The unsurpassed temporal resolution of electroencephalography (EEG) has led to its widespread use by clinicians and scientists investigating physiologic and pathologic brain function. The EEG signal reflects the difference between electrical potentials measured at two different electrodes, and as such it is always necessary to select a reference electrode. The vast majority of clinical and research EEG recordings, both scalp and intracranial, are obtained using a common cephalic reference. As a result, the reference signal generally has an effect on the EEG. To reduce this effect, a neutral potential is the most desirable reference. However, it is impossible to find a point of neutral or zero

* The work was partially supported by National Natural Science Foundation of China under Grants (61070127, 61102028, 61100102), International Cooperation Project of Zhejiang Province, China (No. 2009C14013), Qianjiang Project of Zhejiang Province, China, under Grant 2011R10063, U.S.National Science Foundation (NSF) under Grant 0821820, and Tennessee Higher Education Commission,the State of Tennessee, USA, and NIH R01 NS063039.

** Corresponding author.

H. Zhang et al. (Eds.): BICS 2012, LNAI 7366, pp. 321–328, 2012.

potential on the body surface [3]. Physically, the potential at infinity is the ideal reference since it is far from all the neural sources, and would have no effect on the EEG recordings. However, such a distant reference is not realistic in practice [4]. Therefore, the widely used cephalic electrode, non-cephalic electrode, earlobe, neck, and average references etc. each generally have an effect on both scalp and intracranial EEG recordings. In fact, the effect of an active reference on EEG recording is one of the oldest technical problems in the study of human EEG [4,5].

Reference signal, especially reference signal contaminated by non-cerebral artifacts like muscle, EKG etc., not only hinders visual interpretation of the EEG tracings, but also complicates quantitative analysis of EEG (see [6] and references therein). Due to important impact of reference signal, most of researchers in EEG field focus on average reference EEG which is reference-free EEG. Here the primary difficulty is that we do not know apriori how many cephalic electrodes are adequate to get an unbiased AR. There is clear evidence that the 10-20 system coverage is inadequate [7,8] and a full dense coverage of the head surface is necessary for a good average scalp EEG reference [9]. Additionally, calculating a common AR from a selection of implanted grids, strips, and depth electrodes is not well supported geometrically [5].

Recently independent component analysis (ICA) [10] has received wide attention in biomedical engineering [11]–[15]. Especially in [1] we applied ICA technology to estimate reference signal from intracranial EEG for the first time in the literature. In [1] based on the assumption of independence between scalp reference and intracranial sources we proposed two methods to obtain two reference signals called $\mathbf{R}_1$ and $\mathbf{R}_2$. $\mathbf{R}_1$ played an important role to explain why the obtained signal is close to the real reference signal. $\mathbf{R}_2$ was shown to be better than $\mathbf{R}_1$. The $\mathbf{R}_2$ method was shown to be equivalent to a constrained power minimization approach, that is, the minimum power distortionless response (MPDR) approach [2], which is the optimal solution in terms of least squared error as pointed in [2]. The above assumption of independence was verified by three patients for iEEG with scalp refernce [1]. Once this assumption is satisfied, the two methods in [1] can be applied to automatically identify the real reference and remove it from original referential EEG (scalp EEG or intracranial EEG).

In this paper, we theoretically prove that under the assumption of independence the obtained $\mathbf{R}_2$ signal is much better than the widely used AR. We showed that $\mathbf{R}_2$ is very close to the real reference $\mathbf{R}$ when the number of channels tends to be large enough, however, in general AR is not close to the real reference $\mathbf{R}$ even if the number of channels tends to infinity. Our simulation results confirm these theoretical results.

2 Methods

As described in [1], the EEG recordings can be described by the following multichannel model:

$$\mathbf{X}(t) = \mathbf{R}(t)\mathbf{E} - \mathbf{B}(t) \quad \text{or} \quad \mathbf{X}(t) = \mathbf{R}(t)\mathbf{E} - \mathbf{AS}(t) \tag{1}$$

where $\mathbf{B}(t) = [b_1(t), \cdots, b_n(t)]^T$ and each b_i is a localized region potential of the brain at the i-th surface electrode for scalp EEG or the i-th deep electrode for intracranial EEG (iEEG), $\mathbf{S}(t) = [s_1(t), \cdots, s_m(t)]^T$ and each s_i is a source potential (or source for brevity) of the brain, $\mathbf{A} = [a_{ij}]$ is an $n \times m$ unknown constant mixing matrix determined by source locations and orientations, $\mathbf{R}(t)$ is a reference potential (or reference for brevity) from the common electrode (scalp electrode used in literature or body electrode used in this paper), $\mathbf{E} = [1, \cdots, 1]^T$ with n unit 1, $\mathbf{X}(t) = [x_1(t), \cdots, x_n(t)]^T$ and each x_i is a measured potential difference between the common electrode and the i-th electrode, and $t = 1, \cdots, N$ is sample time. In this model, we assume that each localized region potential b_i is a linear mixture of m source potentials $s_1, \cdots, s_m$ where each source potential s_i actually consists of many local time-correlated dipole source potentials. This assumption is often made in the analysis of EEG signals. As such, Model (1) can be rewritten as

$$\mathbf{X} = \begin{bmatrix} 1 & \\ \vdots & -\mathbf{A} \\ 1 & \end{bmatrix} \begin{bmatrix} \mathbf{R} \\ \mathbf{S} \end{bmatrix} \triangleq \mathbf{Q} \begin{bmatrix} \mathbf{R} \\ \mathbf{S} \end{bmatrix} \tag{2}$$

where $\mathbf{Q}$ is usually called the mixing matrix of dimension $n \times (m+1)$, $\mathbf{X}$ is an $n \times N$ matrix, $\mathbf{S}$ is an $m \times N$ matrix, and $\mathbf{R}^T$ is a vector of dimension N.

In [1] we proposed two methods to obtain two reference signals called $\mathbf{R}_1$ and $\mathbf{R}_2$. $\mathbf{R}_1$ plays an important role to explain why the obtained signal is close to the real reference signal. $\mathbf{R}_2$ is shown to be better than $\mathbf{R}_1$.

The main idea in $\mathbf{R}_2$ is that the reference electrode signal is assumed to be independent from the scalp source electrode signals or intracranial source electrode signals. The independence between scalp reference electrode signal and intracranial electrode signals was verified by three patients in [1]. The method II in [1] can be described as follows: Let all independent components (ICs) of the bipolar montage EEG derived from (1) be $\bar{s}_j, j = 1, \cdots, k$ where $k \leq m$. Then, $\mathbf{R}_2$ signal can be obtained as

$$\mathbf{R}_2 = \frac{1}{n} \sum_{i=1}^{n} \left[x_i - \sum_{l=1}^{k} \frac{E[x_i \bar{s}_l]}{E[\bar{s}_l^2]} \bar{s}_l \right] \tag{3}$$

(see (7) in [1]).

3 A Comparative Study: R_2 Signal and Average Reference

It is noted that in the first method [1] ICA is applied to obtain all independent components having variance of 1 and mean value of zero [16]. In this section, without a loss of generality for equation (1) we always assume that $\mathbf{R}$ and all sources $s_1, \cdots, s_m$ are independent and each has variance of 1 and mean value of zero. Next we will theoretically prove that $\mathbf{R}_2$ signal is much better than AR by calculating correlation coefficients between $\mathbf{R}$ and $\mathbf{R}_2$, and between $\mathbf{R}$ and AR. Now we present our two main theoretical results as follows.

Theorem 1: Assume that each a_{ij} is independently uniformly distributed in the interval $[-a, a], i = 1, \cdots, n, j = 1, \cdots, m$. Then mean of correlation coefficient between $\mathbf{R}$ and AR (that is, $E[corr(\mathbf{R}, \mathrm{AR})]$) is

$$E[corr(\mathbf{R}, \mathrm{AR})] = \frac{1}{\sqrt{1 + \frac{ma^2}{3n}}}. \tag{4}$$

Proof. From (1) it follows that

$$\mathrm{AR} = \frac{1}{n}\sum_{i=1}^{n} x_i = \frac{1}{n}\sum_{i=1}^{n}(\mathbf{R} - [a_{i1}, \cdots, a_{im}]\mathbf{S}) = \mathbf{R} - \frac{1}{n}\sum_{i=1}^{n}\sum_{j=1}^{m} a_{ij}s_j$$

Since $\mathbf{R}$ is independent from all sources $s_1, \cdots, s_m$ and has variance of 1, we have

$$E[\mathbf{R} \times \mathrm{AR}] = E[\mathbf{R} \times (\mathbf{R} - \frac{1}{n}\sum_{i=1}^{n}\sum_{j=1}^{m} a_{ij}s_j)] = E[\mathbf{R}^2] = 1. \tag{5}$$

Since $\mathbf{R}$ and all sources $s_1, \cdots, s_m$ are independent and each has variance of 1 and mean value of zero, we obtain the variance of AR as

$$\begin{aligned}
\sigma_{\mathrm{AR}}^2 &= E[\mathrm{AR}^2] = E\left[\left(\mathbf{R} - \frac{1}{n}\sum_{i=1}^{n}\sum_{j=1}^{m} a_{ij}s_j\right)^2\right] \\
&= E[\mathbf{R}^2] - 2E\left[\mathbf{R} \times \frac{1}{n}\sum_{i=1}^{n}\sum_{j=1}^{m} a_{ij}s_j\right] + E\left[\left(\frac{1}{n}\sum_{i=1}^{n}\sum_{j=1}^{m} a_{ij}s_j\right)^2\right] \\
&= E[\mathbf{R}^2] + E\left[\left(\frac{1}{n}\sum_{i=1}^{n}\sum_{j=1}^{m} a_{ij}s_j\right)^2\right] \\
&= 1 + \frac{1}{n^2}E\left[\left(\sum_{i=1}^{n}\sum_{j=1}^{m} a_{ij}s_j\right)^2\right] = 1 + \frac{1}{n^2}E\left[\left(\sum_{j=1}^{m}\left(\sum_{i=1}^{n} a_{ij}\right)s_j\right)^2\right] \\
&= 1 + \frac{1}{n^2}\sum_{j=1}^{m}\left(\sum_{i=1}^{n} a_{ij}\right)^2 E[s_j^2] = 1 + \frac{1}{n^2}\sum_{j=1}^{m}\left(\sum_{i=1}^{n} a_{ij}\right)^2,
\end{aligned} \tag{6}$$

so,

$$\sigma_{\mathrm{AR}}^2 = E[\mathrm{AR}^2] = 1 + \frac{1}{n^2}\sum_{j=1}^{m}\left(\sum_{i=1}^{n} a_{ij}\right)^2. \tag{7}$$

Since each $a_{ij}, (i = 1, \cdots, n, j = 1, \cdots, m)$ is a random variable, from (7) we conclude that σ_{AR}^2 or $E[\mathrm{AR}^2]$ is also a random variable. Based on the assumption that each

a_{ij} is independently uniformly distributed in the interval $[-a, a], i = 1, \cdots, n, j = 1, \cdots, m$, from (7) we can obtain mean value of σ^2_{AR} or $E[\mathrm{AR}^2]$ as

$$E[\sigma^2_{\mathrm{AR}}] = E[E[\mathrm{AR}^2]] = 1 + \frac{1}{n^2}\sum_{j=1}^{m} E\left[\left(\sum_{i=1}^{n} a_{ij}\right)^2\right]$$

$$= 1 + \frac{1}{n^2}\sum_{j=1}^{m}\sum_{i=1}^{n} E\left[a_{ij}^2\right] \qquad \text{(based on independence among } a_{ij}\text{)}$$

$$= 1 + \frac{1}{n^2} \times n \times m \times \frac{(a+a)^2}{12} = 1 + \frac{ma^2}{3n}. \tag{8}$$

From $\sigma^2_{\mathbf{R}} = 1$, (5) and (8) it follows that

$$E[corr(\mathbf{R}, \mathrm{AR})] = E\left[\frac{E[\mathbf{R} \times \mathrm{AR}]}{\sigma_{\mathbf{R}} \times \sigma_{\mathrm{AR}}}\right] = E\left[\frac{1}{\sigma_{\mathrm{AR}}}\right] = \frac{1}{E[\sigma_{\mathrm{AR}}]}$$

$$= \frac{1}{E\left[\sqrt{\sigma^2_{\mathrm{AR}}}\right]} = \frac{1}{\sqrt{E[\sigma^2_{\mathrm{AR}}]}} = \frac{1}{\sqrt{1 + \frac{ma^2}{3n}}}.$$

Theorem 2: Assume that each a_{ij} is independently uniformly distributed in the interval $[-a, a], i = 1, \cdots, n, j = 1, \cdots, m$. Then mean of correlation coefficient between $\mathbf{R}$ and $\mathbf{R}_2$ (that is, $E[corr(\mathbf{R}, \mathbf{R}_2)]$) is

$$E[corr(\mathbf{R}, \mathbf{R}_2)] = \frac{1}{\sqrt{1 + \frac{ma^2}{3n} - \frac{ka^2}{3n}}}. \tag{9}$$

Its proof is omitted here for space reason.

From (4) and (9) we easily have the following corollary.

Corollary 1: i) Since $k \le m, \forall m, n$, from (4) and (9) we can see

$$E[corr(\mathbf{R}, \mathrm{AR})] = \frac{1}{\sqrt{1 + \frac{ma^2}{3n}}} < \frac{1}{\sqrt{1 + \frac{ma^2}{3n} - \frac{ka^2}{3n}}} = E[corr(\mathbf{R}, \mathbf{R}_2)]$$

which implies that $\mathbf{R}_2$ signal is always better than the average reference under the assumption of independence between the real reference and sources.

ii) When $m < n$, from (1) one can easily see $k = m$ in this case, then from Theorem 2 we can have

$$E[corr(\mathbf{R}, \mathbf{R}_2)] = 1$$

which means the obtained $\mathbf{R}_2$ signal is exactly the real reference $\mathbf{R}$. However, in this case, according to (4) average reference is not the real reference at all.

iii) For real EEG data, when n is large enough, in general m and k are also large enough such that $\frac{m}{n} \approx 1$ and $\frac{m-k}{n} \approx 0$, then from (4) we get

$$E[corr(\mathbf{R}, \mathrm{AR})] = \frac{1}{\sqrt{1 + \frac{ma^2}{3n}}} \approx \frac{1}{\sqrt{1 + \frac{a^2}{3}}}.$$

From (9) we get

$$E[corr(\mathbf{R}, \mathbf{R}_2)] = \frac{1}{\sqrt{1 + \frac{ma^2}{3n} - \frac{ka^2}{3n}}} \approx 1.$$

Therefore, even if n (that is, the number of channels) tends to infinity, it is impossible for the obtained average reference to be close to the real reference $\mathbf{R}$. For example, independence between the scalp reference and intracranial sources was verified by three patients [1], hence, even if a large number of Grid electrodes are used for a patient, the obtained average reference from the recorded iEEG is not close to the real scalp reference at all. However, in this case the obtained $\mathbf{R}_2$ is very close to the real reference.

iv) From (4) and (9) one can see that both of $E[corr(\mathbf{R}, \mathbf{R}_2)]$ and $E[corr(\mathbf{R}, \mathrm{AR})]$ increasingly tend to 1 as a decreasingly tends to zero, that means, the more large amplitude for the real reference, the more close to the real reference for $\mathbf{R}_2$ and average reference.

4 Simulation Results

In this section, we first present some simulation results to demonstrate the truth of our theoretical results. For real EEG data of n channels, when fastICA is applied, we can generally get n components. Accordingly we can get $n - 1$ components for the bipolar montage EEG, so $k = n - 1$. For the mixing matrix $\mathbf{A}$, three cases can be considered: overdetermined, square, and underdetermined. For simplicity, here we only consider underdetermined case for $\mathbf{A}$ (the other two cases can be similarly analyzed), e.g., $m = n + 1$. In this case, from (4) we have

$$E[corr(\mathbf{R}, \mathrm{AR})] = \frac{1}{\sqrt{1 + \frac{ma^2}{3n}}} = \frac{1}{\sqrt{1 + \frac{n+1}{n}\frac{a^2}{3}}}$$

which monotonically increases to $\frac{1}{\sqrt{1+a^2/3}}$ as n tends to infinity. From (9) we get

$$E[corr(\mathbf{R}, \mathbf{R}_2)] = \frac{1}{\sqrt{1 + \frac{ma^2}{3n} - \frac{ka^2}{3n}}} = \frac{1}{\sqrt{1 + \frac{2a^2}{3n}}}$$

which monotonically increases to 1 as n tends to infinity. Let's consider (1) where $n = 3, 4, \cdots, 30$ and $m = n + 1$, the real reference $\mathbf{R}$ is always the IC1 of Patient 3 [1], and the sources are from IC2, $\cdots$, IC32 of patient 3 [1]. For each n we do 2000 realizations of $\mathbf{A}$ of $n \times (n + 1)$ dimension whose entries are uniformly distributed in the interval $[-a, a]$. For all these 2000 realizations of $\mathbf{A}$ the sources are keep same, that is, when $\mathbf{A}$ is a 3×4 dimensional matrix, the source $\mathbf{S}$ =[IC2,IC3,IC4,IC5]^T, when $\mathbf{A}$ is a 4×5 dimensional matrix, the source $\mathbf{S}$ =[IC2,IC3,IC4,IC5,IC6]^T, etc. For each realization we obtain $\mathbf{R}_2$ and AR and calculate correlation coefficient between $\mathbf{R}$ and AR (or $\mathbf{R}_2$), and then compute average value over these 2000 realizations, that is, $E[corr(\mathbf{R}, \mathrm{AR})]$ or $E[corr(\mathbf{R}, \mathbf{R}_2)]$. The results are shown in Fig. 1 where three cases for a are considered: (A) $a = 0.5$; (B) $a = 1$; (C) $a = 2$. From Fig. 1 one can find that i) $E[corr(\mathbf{R}, \mathbf{R}_2)] > E[corr(\mathbf{R}, \mathrm{AR})]$ for any one of three cases which is consistent with the conclusion in i) of Corollary 1. ii) Increasing trend holds for each curve (all curves related to $\mathbf{R}_2$ increase to 1, $E[corr(\mathbf{R}, \mathrm{AR})]$ in (A) increases to $0.96 = \frac{1}{\sqrt{1+0.5^2/3}}$, $E[corr(\mathbf{R}, \mathrm{AR})]$ in (B) increases to $0.87 = \frac{1}{\sqrt{1+1/3}}$, $E[corr(\mathbf{R}, \mathrm{AR})]$ in (C) increases to $0.65 = \frac{1}{\sqrt{1+2^2/3}}$), which are consistent with above theoretical analysis results. iii) The more small for a (or the more large amplitude for the real reference signal $\mathbf{R}$), the more close to the real reference signal for the obtained $\mathbf{R}_2$ and AR. This conclusion was made in iv) of Corollary 1.

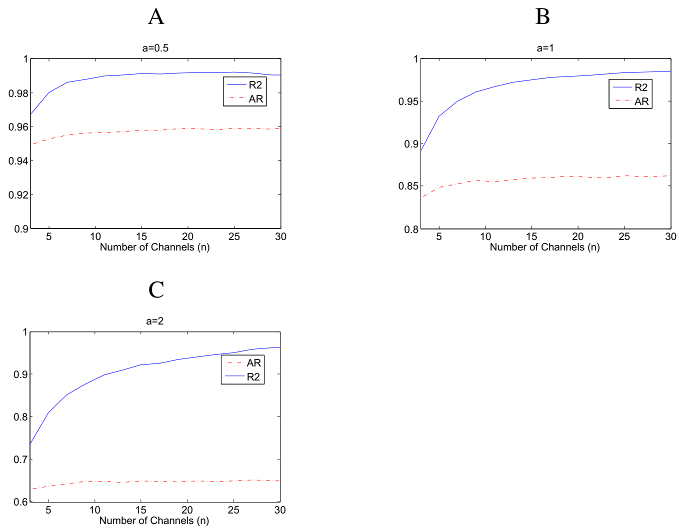

Fig. 1. Average value of correlation coefficients between $\mathbf{R}$ and AR (or $\mathbf{R}_2$) for 2000 realizations of $\mathbf{A}$ when the number of channels n is given ($n = 3, 4 \cdots, 29, 30$). (A) $a = 0.5$. (B) $a = 1$. (C) $a = 2$.

5 Discussion and Conclusions

In [1] we proposed a novel method ($\mathbf{R}_2$ method) to estimate the real reference signal in EEG recording. The key issue in this method requires that the reference electrode signal is independent from all source signals. In [1] the independence between the scalp reference and intracranial sources was verified by three patients. Hence, $\mathbf{R}_2$ signal may provide a better way to estimate the real reference only with a simple assumption of independence. It is noted that this requirement is different from the assumption [17] that the reference signal is a linear mixture of scalp sources. As such, the method in [17] cannot be used in the case that the reference signal is independent from sources, e.g., intracranial EEG.

Another widely used reference in EEG field is AR. In this paper, we theoretically proved that under the assumption of independence the obtained $\mathbf{R}_2$ signal is better than AR. We showed that $\mathbf{R}_2$ is very close to the real reference $\mathbf{R}$ when the number of channels tends to be large enough, however, in general AR never closes the real reference $\mathbf{R}$ even if the number of channels tends to infinity. Our simulation results were consistent with these theoretical results.

References

1. Hu, S., Stead, S., Worrell, G.: Automatic identification and removal of scalp reference signal for intracranial EEGs based on independent component analysis. IEEE Trans. on Biomedical Engineering. 54, 1560–1572 (2007)
2. Ranta, R., Madhu, N.: Reference Estimation in EEG: Analysis of Equivalent Approaches. IEEE Signal Processing Letters 19, 12–15 (2012)
3. Geselowitz, D.B.: The zero of potential. IEEE Eng. Med. Biol. Mag. 17, 128–132 (1998)
4. Nunez, P.L.: Electric fields of the brain: the neurophysics of EEG. Oxford University Press, New York (1981)
5. Schiff, S.J.: Dangerous Phase. Neuroinformatics 3, 315–318 (2006)
6. Hu, S., Stead, S., Dai, Q., Worrell, G.: On the recording reference contribution to EEG correlation, phase synchrony and coherence. IEEE Transactions on SMC-Part B 40, 1294–1304 (2010)
7. Guevara, R., Velazquez, J.L., Nenadovic, V., Wennberg, R., Senjanovic, G., Dominguez, L.G.: Phase synchronization measurements using electroencephalographic recordings: what can we really say about neuronal synchrony? Neuroinformatics 3, 301–314 (2005)
8. Bertrand, O., Perrin, F., Pernier, J.: A theoretical justification of the average reference in topographic evoked potential studies. Electroencephalogy Clin. Neurophysiol. 62, 462–464 (1985)
9. Junghofer, M., Elbert, T., Tucker, D.M., Braun, C.: The polar average reference effect: a bias in estimating the head surface integral in EEG recording. Clin. Neurophysiol. 110, 1149–1155 (1999)
10. Hyvarinen, A., Oja, E.: Independent component analysis: algorithms and applications. Neural Networks 13, 411–430 (2000)
11. Senhadji, L., Kachenoura, A., Albera, L., Comon, P.: On the use of independent component analysis techniques in the field of brain computer interface. IRBM 30, 211–217 (2009)
12. Kachenoura, A., Albera, L., Senhadji, L., Comon, P.: ICA: a potential tool for BCI systems. IEEE Signal Processing Magazine, Special Issue on Brain-Computer Interfaces 25, 57–68 (2008)
13. Albera, L., Comon, P., Parra, L., Karfoul, A., Kachenoura, A., Senhadji, L.: Biomedical applications. In: Comom, P., Jutten, C. (eds.) Handbook of Blind Source Separation. Academic Press (2010)
14. Onton, J.L., Westerfieldb, M., Townsendb, J., Makeiga, S.: Imaging human EEG dynamics using independent component analysis. Neuroscience & Biobehavioral Reviews 30, 808–822 (2006); J. Neurosci Methods 134, 9–21 (2004)
15. Urrestarazu, E., LeVan, P., Gotman, J.: Independent component analysis identifies ictal bitemporal activity in intracranial recordings at the time of unilateral discharges. Clin. Neurophysiol. 117, 549–561 (2006)
16. http://www.cis.hut.fi/projects/ica/fastica/
17. Yao, D.: A method to standardize a reference of scalp EEG recordings to a point at infinity. Physiol. Meas. 22, 693–711 (2001)

Single LFP Sorting for High-Resolution Brain-Chip Interfacing

Mufti Mahmud[1,2,⋆], Davide Travalin[3], Amir Hussain[4], Stefano Girardi[1], Marta Maschietto[1], Florian Felderer[5], and Stefano Vassanelli[1]

[1] NeuroChip Laboratory, University of Padova, via f. Marzolo 3, 35131−Padova, Italy
{stefano.girardi.1,marta.maschietto,stefano.vassanelli}@unipd.it
http://neurochiplab.cyberrat.eu/

[2] Institute of Information Technology,
Jahangirnagar University, Savar, 1342−Dhaka, Bangladesh
mahmud@dei.unipd.it
http://www.juniv.edu/iit/index.php

[3] St. Jude Medical Italia S.p.A, Centro Direzionale Colleoni,
Palazzo Andromeda, 16/1, 20864 Agrate Brianza (MB), Italy
dtravalin@sjm.com

[4] Centre for Cognitive & Computational Neuroscience,
University of Stirling, Stirling FK9 4LA, UK
ahu@cs.stir.ac.uk
http://cosipra.cs.stir.ac.uk/

[5] Max Planck Institute of Biochemistry, D-82152 Martinsried, Germany
ffeldere@biochem.mpg.de
http://www.biochem.mpg.de/

Abstract. Understanding cognition has fascinated many neuroscientists and made them put their efforts in deciphering the brain's information processing capabilities for cognition. Rodents perceive the environment through whisking during which tactile information is processed at the barrel columns of the somatosensory cortex (S1). The intra– and trans–columnar microcircuits in the barrel cortex segregate and integrate information during activation of this pathway. Local Field Potentials (LFPs) recorded from these barrel columns provide information about the microcircuits and the shape of the LFPs provide the fingerprint of the underlying neuronal network. Through a contour based sorting method, we could sort neuronal evoked LFPs recorded using high–resolution Electrolyte–Oxide–Semiconductor Field Effect Transistor (EOSFET) based neuronal probes. We also report that the latencies and amplitudes of the individual LFPs' shapes vary among the different clusters generated by the method. The shape specific information of the single LFPs thus can be used in commenting on the underlying neuronal network generating those signals.

Keywords: Neuronal probe, whisker stimulation, evoked brain activity, neuronal signal, neuronal signal analysis.

⋆ Corresponding author.

H. Zhang et al. (Eds.): BICS 2012, LNAI 7366, pp. 329–337, 2012.

1 Introduction

The availability of cutting–edge neuronal probes provide unprecedented information about the brain activity as a basis to understand the underlying neuronal networks at a greater detail [1]. To understand the signal propagation and processing pathways, scientists rely on evoked field potentials which are cumulative activity of population(s) of neurons. Scientists use stimulus–locked field potentials to assess and understand effect of stimuli on a brain area under study as the LFPs provide a finger–print of the activation and inactivation of underlying neuronal networks [2]. However, the individual information provided by a single LFP may disappear if one considers an average over several runs under same stimulus conditions [3]. Furthermore, for certain brain functions (e.g., signal processing pathway [7], [8]) and operations (e.g., current source density analysis) signal shape plays an important role [4]. As the shape of an LFP represents underlying neuronal network activity, it is necessary to extract different shapes present in a pool of single LFPs to decipher the activation and inactivation of neuronal networks generating them.

The LFPs recorded by whisker stimulation from rat S1 cortex can be characterized by a template of four consecutive events: event 1 (E1) – small positive/negative peak; event 2 (E2) – large and fast negative peak; event 3 (E3) – relatively slow positive peak; event 4 (E4) – slow negative peak returning to zero [5], [6], [7], [8].

The single LFP sorting based on their shape is done through four steps: preprocessing, template generation, single LFP recognition, and sorting of the recognized single LFPs. The LFPs are preprocessed using nonlinear least square estimation to reduce the spatial oscillations and determine the response part. The template is obtained by averaging the response parts from various LFPs. The contour of this template is compared to each of the single LFP's contour with a predefined boundary condition. If the single LFP falls within the boundary condition, it is considered to be recognized. Intelligent K–means clustering is applied on the recognized LFPs to sort them as per their shapes. The sorted single LFPs are locally averaged, and latency and amplitude of the events are calculated to have an insight about the underlying neuronal network's temporal activity of the brain area under the same stimulus [9], [10].

2 Sorting Method

2.1 Preprocessing and Template Generation

A Gauss–Newton based nonlinear least square estimation is performed to get rid of the spatial oscillations present in the single LFPs.

From the definition of least square [11], for a given vector function $f : \mathbb{R}^n \mapsto \mathbb{R}^m$ with $m \geq n$, we want to minimize $\|f(x)\|$ or equivalently find:

$$x^* = argmin_x \mathbb{F}(x) \;\; with \;\; \mathbb{F}(x) = \frac{1}{2}\sum_{i=1}^{m}(f_i(x))^2 = \frac{1}{2}\|f(x)\|^2 = \frac{1}{2}f(x)^T f(x) \quad (1)$$

To obtain a probable analytical solution of the above problem, a generic signal model is considered with its prediction error's covariance matrix (Σ_{ν}) as a weight function (equation 2).

$$\chi = y(\chi^*) + \nu \ \ where, \ \ \chi^* = (y^{\mathcal{T}} \Sigma_{\nu}^{-1} y)^{-1} y^{\mathcal{T}} \Sigma_{\nu}^{-1} \chi \tag{2}$$

To solve the nonlinearity, parameter vector is assigned initial value at χ_k^*, $k = 0$, expanded using first order Taylor's expansion, and the stable parameter vector is obtained iteratively (equation 3).

$$\Delta\chi = \mathcal{P}\Delta\chi^* + \nu; \ with \ \Delta\chi^* = (\mathcal{P}^{\mathcal{T}} \Sigma_{\nu}^{-1} \mathcal{P})^{-1} \mathcal{P}^{\mathcal{T}} \Sigma_{\nu}^{-1} \chi; \ and \ {\chi_{k+1}}^* = {\chi_k}^* + \Delta{\chi_k}^* \tag{3}$$

The estimated signals are scanned for occurrence of the signal events to mark the starting and end of the response part.In case of varied length of response parts, signals are zero–padded and averaged to obtain a template.

2.2 Single Sweep Recognition

Once the template is generated, the contour of the template is used to recognize the single sweeps. Boundary conditions (lower and upper bounds) are imposed to facilitate the recognition process. The variance vector (calculated using equation 4) of the template is necessary for calculating the boundary conditions.

$$\mathcal{V}_{tmp} = \frac{1}{\mathcal{N}} \sum_{i=1}^{\mathcal{N}} [\mathcal{S}w_i(k) - \mathcal{T}emp(k)]^2 \tag{4}$$

where $\mathcal{S}w$ is the zero–padded and truncated single sweeps and $\mathcal{T}emp$ is the template.

The upper and lower bounds are calculated using equation 5.

$$\mathcal{U}p(k) = \mathcal{T}emp(k) + (a \times \mathcal{V}_{tmp}(k)^{\frac{1}{2}} + b) \ \& \ \mathcal{L}ow(k) = \mathcal{T}emp(k) - (a \times \mathcal{V}_{tmp}(k)^{\frac{1}{2}} + b) \tag{5}$$

with a, b are constant; the values of a, b ($a = \sigma(\mathcal{T}emp)$, and $b = 3 \times \sigma(\mathcal{T}emp)$) are determined empirically. A signal is considered to be recognized, *iff* all of its data points lie within the range of the boundary conditions.

2.3 Clustering the Recognized Sweeps

The K–means clustering method [12], [13] involves a set of N entities, I, a set of M features, $\mathcal{V}$, and an entity–to–feature matrix $\mathcal{Y} = (yiv)$, where yiv is the value of feature $v \in \mathcal{V}$ at entity $i \in I$. The method produces a partition $\mathcal{S} = \mathcal{S}_1, \mathcal{S}_2, \cdots, \mathcal{S}_{\mathcal{K}}$ of I in K non–overlapping classes $\mathcal{S}_k$, each with a centroid $c_k = (c_{kv})$, an M–dimensional vector in the feature space ($k = 1, 2, \cdots \mathcal{K}$). Centroids form set $\mathcal{C} = c_1, c_2, \cdots, c_{\mathcal{K}}$ using a within–cluster summary distance to centroids criterion minimized by the method:

$$\mathcal{W}(\mathcal{S}, \mathcal{C}) = \sum_{k=1}^{\mathcal{K}} \sum_{i \in \mathcal{S}_k} d(i, c_k) \tag{6}$$

with d is the Euclidean distance squared.

However, to avoid inputting the K, we adapted intelligent K–Means (iK–Means) clustering method as proposed in [14]. This iK–Means method uses an anomalous pattern (AP) to find out the appropriate number of clusters.

Finally, when the single sweeps are sorted into their respective clusters, they are cluster–wise averaged for further processing.

3 Signal Acquisition

3.1 Chip Description

The CyberRat probes were fabricated from silicon–on–insulator (SOI) wafers (4 in.) with 100 μm n–type silicon (1–10 Ω cm) and 2 μm SiO_2 on a 400 μm thick silicon substrate (SiMat, Landsberg, Germany). Each chip consisted of two parts: a needle (2 mm long) with an array of four transistors (gate area 10 μm $\times$ 10 μm, pitch 80 μm, Figure 1, a) and a contact plate with the bond pads [15]. For stability reasons, the chips of the prototype series were relatively massive with a thickness of 100 μm and a width of 360 μm. A rather blunt shape of the tip was fabricated in order to place the transistors close to the tip. The contact plate was 500 μm thick, 5 mm wide and 10 mm long. Its edge was displaced with respect to the needle in order to allow a visual control of the impalement.

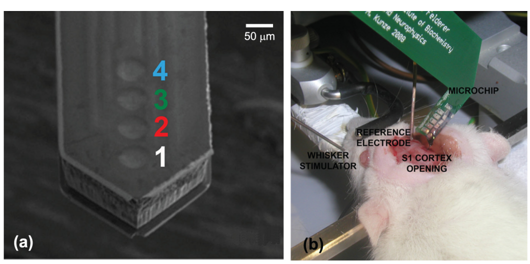

Fig. 1. Setup for recording of neuronal signals with EOSFET based multisite neuronal probe. (a) Scanning electron microscope picture of the probe with the 4 FETs shown in different colors. (b) Magnification of the rat head: the opening in the skull in correspondence of the S1 cortex and the chip inserted into the cortical area are visible. The chip was carefully inserted through a slit in the meninges. A selected whisker was inserted into a tube mounted on the piezoelectric for stimulation.

3.2 Animal Preparation

Wistar rats (P30–P40) maintained in the Animal Research Facility of Department of Human Anatomy and Physiology (University of Padova, Italy) were anesthetized with an induction mixture of Tiletamine and Xylazine (2 mg/100 g weight and 1.4 g/100 g weight, respectively). The animal's eye and hind–limbs' reflexes, respiration, and whiskers' spontaneous movements were monitored throughout the experiment and whenever necessary, additional doses of Tiletamine (0.5 mg / 100 g weight) and Xylazine (0.5 g / 100 g weight) were provided.

Rats were positioned on a stereotaxic apparatus and fixed by teeth– and ear–bars; ECG and the body temperature constantly monitored and maintained at about 37°C. Anterior–posterior opening in the skin was made in the center of the head and the skull was drilled to open a window in correspondence of S1 (AP $-1 \div -4$, LM $+4 \div +8$). In order to reduce brain edema only cut at coordinates AP -2.5, LM $+6$ was performed [16]. At the end of the surgery the controlateral whiskers were trimmed at about 10 mm from the rat snout.

Throughout all surgical operations and recordings, the brain was bathed by standard Krebs solution oxygeneted and warmed at 37°C using a perfusion system (composition in mM: NaCl 120, KCl 1.99, $NaHCO_3$ 25.56, KH_2PO_4 136.09, $CaCl_2$ 2, $MgSO_4$ 1.2, glucose 11).

3.3 Stimulation and Signal Recording

Neuronal signals were evoked by single whiskers mechanical stimulation performed with a piezoelectric bender through a connected tube. The bender was driven by a waveform generator (Agilent 33250A 80 MHz, Agilent Technologies) providing 0.5 Hz stimuli. Each whisker, starting from the posterior group, was individually inserted into the tube and the corresponding response was checked in S1 cortex IV layer (at 640 μm depth) in order to find the "principal whisker". Depth recording profiles were obtained by moving the chip up and down in order to monitor all cortical layers. The chips were left into the brain for about 5 hours, throughout all the duration of the experiment.

The chips were connected to the computer by custom–built amplifiers and the neuronal signals were recorded by custom–made software developed in LabVIEW (`http://www.ni.com/labview/`). At each recording depth LFPs were recorded by stimulating the whisker at different angles ranging from 0° to 315° at a step of 45° [17].

4 Results and Discussion

The method is implemented in MATLAB (Version: 7.9, release: 2009b, `www.mathworks.com`). Each dataset on which the method was applied comprised of recordings from about 20 different depths, and each of them contained as many as 50–100 single LFP signals. However, the usefulness of this method is elaborated with some findings revealed by the sorted clusters.

The Figure 2 (b) shows the template, smoothed single LFPs truncated to the size of template, and the upper and lower bounds of the template used for the recognition. Single LFPs falling within the boundary limits are considered to be recognized.

The Figure 2 (a) shows different clusters of sorted LFPs with their respective averages. Once the single LFPs are recognized, an event detection algorithm [8] is used to detect the various signal events as described in section 1. The feature matrix is created by taking features of each single LFP's detected events, and the start and end of the response part. In addition to these six points, 194 more points are selected arbitrarily within the response part to facilitate the appropriate representation of the shape. However, relatively more points are selected near the event peaks than that of distant locations from the peaks. Thus, the N single LFPs, each represented by 200 feature points, generate a feature matrix of size N $\times$ 200 and is sorted using the iK–means clustering.

Table 1 tabulates the recording depths, total number of recognized sweeps, single sweep distribution among different clusters. This table shows that the feature matrix is well classified into different clusters.

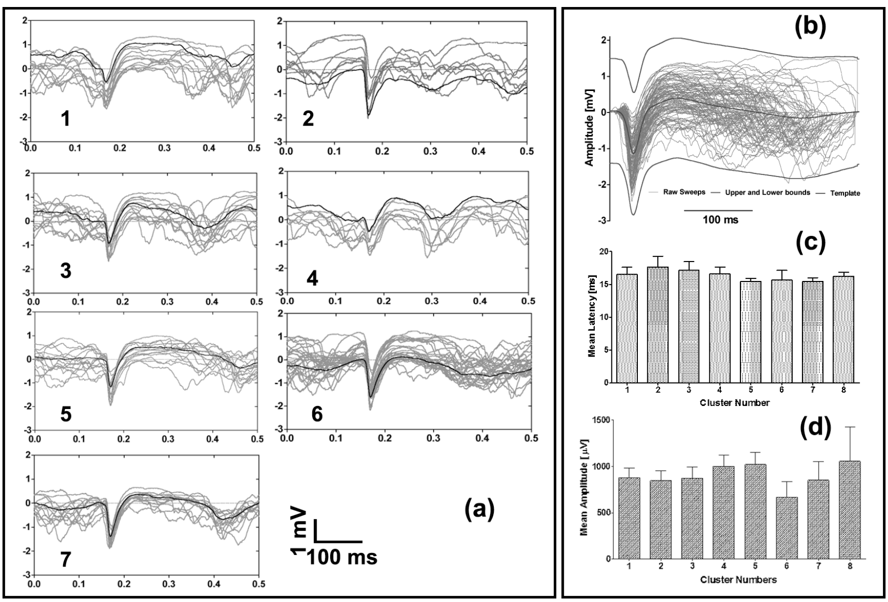

Fig. 2. (a) Sorted single LFPs into different clusters. The numbers at the left hand side denote cluster number. The local averages of each cluster is seen in black. (b) The template, its lower and upper boundary conditions, and recognized single LFPs. (c) Mean latency of E2 event obtained from different clusters using another experiment. (d) Mean amplitude of the E2 event obtained from different clusters during the same experiment as of (c). The error bars indicate the standard deviations of the mean latencies and amplitudes.

Table 1. Total Recognized LFPs, Single LFP Allocation to Clusters for signals from different depth along the cortex

Depth	Recognized LFPs	Cluster Numbers									
		1	**2**	**3**	**4**	**5**	**6**	**7**	**8**	**9**	**10**
80μm	65	5	10	6	4	11	7	3	10	6	4
160μm	94	17	15	12	15	21	10	4	–	–	–
240μm	83	7	2	8	16	15	5	3	6	7	14
320μm	78	10	7	4	11	12	8	10	16	–	–
400μm	92	16	9	10	6	12	16	10	6	7	–
480μm	83	12	12	7	14	7	18	13	–	–	–
560μm	85	16	6	15	14	17	9	8	–	–	–
640μm	96	12	10	15	16	11	14	13	5	–	–
720μm	92	10	9	13	9	13	8	14	6	10	–
800μm	97	11	15	6	8	14	10	6	9	9	9
880μm	96	19	15	15	10	5	17	15	–	–	–
960μm	97	12	13	10	9	13	10	8	10	8	4
1040μm	100	17	23	15	13	10	22	–	–	–	–
1120μm	100	11	20	16	16	7	13	7	5	5	–
1200μm	100	14	17	9	19	9	12	10	10	–	–
1280μm	98	13	10	16	10	14	12	9	5	9	–
1360μm	100	9	10	15	10	12	10	10	12	12	–
1440μm	99	10	10	11	10	11	10	10	12	9	6
1520μm	99	9	13	12	13	14	12	10	8	8	–
1600μm	100	12	20	13	10	16	16	13	–	–	–

After the single LFPs are sorted into different clusters, local averages of each cluster are calculated for further processing. Analyses of these local averages (latency and amplitudes shown in figure 2 (c), (d), respectively are calculated from the signal events) have revealed significant differences in their values. Now, this significant difference is very important as it might point towards different underlying neuronal networks for the generation the signals even if we are recording from the same recording site with the same stimulus.

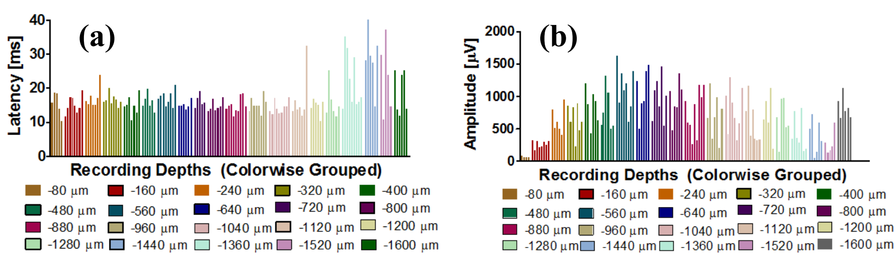

Fig. 3. Latency (a) and amplitude (b) variation of the E2 event among different clusters' local averages. Each bar corresponds to a local average of a cluster and each color corresponds to a recording depth consisting of a number of clusters.

Now, the hypothesis of underlying neuronal network activation is again backed up by the results shown in the Figure 3. This figure shows the different latencies and amplitudes of E2 event calculated from the different local averages of the sorted clusters across many different recording positions. Interestingly, in all the recording positions the generated clusters demonstrated similar behavior. The variations in these two important entities of the LFPs support the hypothesis as well. However, this hypothesis require further experimental validation by combining technologies like – histology or high resolution optical imaging.

5 Conclusion

Whisking for rats is like touch and vision for human. They perform very fine discrimination of the environment that they are in through whisking. To understand the tactile information processing pathway better scientists depend on the LFPs and the shapes of the LFPs work as a fingerprint of the activated neural network near the recording probe. To understand and assess these multiple networks' activity at one recording position, it is necessary to distinguish between the different shapes of signals recorded at a single recording site. Till date scientists have relied on conventional average, which might lead to erroneous results, thus, this method is a tool for them to extend their vision beyond the conventional network activity. This software module is a part of the SigMate software package [18], [19], [20] which will be made available to the research community shortly.

Acknowledgments. This work was carried out as a part of the European Commission funded CyberRat project under the Seventh FrameworkProgramme (ICT-2007.8.3 Bio-ICT convergence, 216528, CyberRat).

References

1. Maschietto, M., Mahmud, M., Girardi, S., Vassanelli, S.: A High Resolution Bi–Directional Communication through a Brain–Chip Interface. In: 2009 ECSIS Symposium on Advanced Technologies for Enhanced Quality of Life (AT-EQUAL 2009), pp. 32–35. IEEE Press, New York (2009)
2. Legatt, A., Arezzo, J., Vaughan, H.G.: Averaged multiple unit activity as an estimate of phasic changes in local neuronal activity: effects of volume–conducted potentials. J. Neurosci. Meth. 2(2), 203–217 (1980)
3. van Hemmen, J., Ritz, R.: Neural Coding: A Theoretical Vista of Mechanisms, Techniques, and Applications. In: Andersson, S.I. (ed.) Summer University of Southern Stockholm 1993. LNCS, vol. 888, pp. 75–119. Springer, Heidelberg (1995)
4. Okun, M., Naim, A., Lampl, I.: The subthreshold relation between cortical local field potential and neuronal firing unveiled by intracellular recordings in awake rats. J. Neurosci. 30(12), 4440–4448 (2010)
5. Ahrens, K.F., Kleinfeld, D.: Current flow in vibrissa motor cortex can phase–lock with exploratory rhythmic whisking in rat. J. Neurophysiol. 92, 1700–1707 (2004)

6. Kublik, E.: Contextual impact on sensory processing at the barrel cortex of awake rat. Acta. Neurobiol. Exp. 64, 229–238 (2004)
7. Mahmud, M., Bertoldo, A., Girardi, S., Maschietto, M., Vassanelli, S.: Automatic detection of layer activation order in information processing pathways of rat barrel cortex under mechanical whisker stimulation. In: 32nd Intl. Conf. of IEEE EMBS, pp. 6095–6098. IEEE Press, New York (2010)
8. Mahmud, M., et al.: An Automated Method for the Detection of Layer Activation Order in Information Processing Pathways of Rat Barrel Cortex under Mechanical Whisker Stimulation. J. Neurosci. Meth. 196, 141–150 (2011)
9. Mahmud, M., et al.: A Contour Based Automatic Method to Classify Local Field Potentials Recorded from Rat Barrel Cortex. In: 5th Cairo Intl. Biomed. Eng. Conf., pp. 163–166. IEEE Press, New York (2010)
10. Mahmud, M., et al.: An Automated Method for Clustering Single Sweep Local Field Potentials Recorded from Rat Barrel Cortex. In: 2011 ISSNIP Biosignals and Biorobotics Conf., pp. 1–5. IEEE Press, New York (2011)
11. Madsen, K., Nielsen, H.B., Tingleff, O.: Methods for Non–Linear Least Squares Problems, 2nd edn. Technical University of Denmark (DTU), Kgs, Lyngby (2004)
12. Macqueen, J.: Some methods for classification and analysis of multivariate observations. In: Fifth Berkeley Symp. on Math. Statist. and Prob., vol. 1, pp. 281–297. University of California Press, Berkeley California (1967)
13. Bock, H.H.: Clustering Methods: a History of K–Means Algorithms. In: Brito, P., Cucumel, G., Bertrand, P., Carvalho, F. (eds.) Selected Contributions in Data Analysis and Classification, pp. 161–172. Springer, Heidelberg (2007)
14. Chiang, M.M.T., Mirkin, B.: Intelligent choice of the number of clusters in K-Means clustering: an experimental study with different cluster spreads. J. Classif. 27(1), 3–40 (2010)
15. Felderer, F., Fromherz, P.: Transistor needle chip for recording in brain tissue. App. Phys. A. 104, 1–6 (2011)
16. Swanson, L.W.: Brain Maps: Structure of the Rat Brain. Academic, London (2003)
17. Mahmud, M., Bertoldo, A., Girardi, S., Maschietto, M., Vassanelli, S.: An Automated Method to Determine Angular Preferentiality using LFPs Recorded from Rat Barrel Cortex by Brain-Chip Interface under Mechanical Whisker Stimulation. In: 33rd Intl. Conf. of IEEE EMBS, pp. 2307–2310. IEEE Press, New York (2010)
18. Mahmud, M., Bertoldo, A., Girardi, S., Maschietto, M., Vassanelli, S.: SigMate: a Matlab–based neuronal signal processing tool. In: 32nd Intl. Conf. of IEEE EMBS, pp. 1352–1355. IEEE Press, New York (2010)
19. Mahmud, M., et al.: SigMate: A Comprehensive Software Package for Extracellular Neuronal Signal Processing and Analysis. In: 5th Intl. Conf. on Neural Eng., pp. 88–91. IEEE Press, New York (2011)
20. Mahmud, M., Bertoldo, A., Girardi, S., Maschietto, M., Vassanelli, S.: SigMate: A MATLAB-based automated tool for extracellular neuronal signal processing and analysis. J. Neurosci. Meth. 207(1), 97–112 (2012)

Variable Momentum Factor Odd Symmetry Error Function Blind Equalization Algorithm

Li-kun Xing, Xin Li, and Ying-ge Han

Department of Electrical and Information Engineering,
Anhui University of Science and Technology, Huainan 232001

Abstract. By the analysis of Odd symmetry error Function blind equalization Algorithm based Decision Feedback Equalizer (OFA-DFE), Variable Momentum Factor Momentum Odd symmetry error Function blind equalization Algorithm based Decision Feedback Equalizer（VMFMOFA-DFE）is proposed. The proposed algorithm uses error function with characteristics of odd symmetry to reduce mean square error, in order to further improve the performance of the algorithm using variable factors to control the momentum term and introducing variable momentum factor to decision feedback equalizer to adjust farword equalizer of decision feedback. Simulation tests with underwater acoustic channel indicate that the proposed algorithm has not only faster convergence rate but also less mean square error.

Keywords: blind equalization, decision feedback, Variable Momentum Factor, Momentum, underwater acoustic channel.

1 Introduction

The underwater acoustic channel blind equalization is at present a more active research subject , Especially in high-speed underwater acoustic communication having a very Important application[1]. But underwater acoustic channel frequency selective decline more serious, often with spectrum zero, At this time, the linear equalizer in Spectrum near zero to high power gain, increased the bonus received signal noise. And the decision feedback equalizer (DFE) can compensate to provide Serious intersymbol interference (inter-symbol interference, ISI) channels, And there was no linear equalizer enhance the effect of noise[2-5], So the decision feedback equalizer research in underwater acoustic equalization is of great significance.

The norms decision feedback blind equalization algorithm (CMADFE) is more frequently used in the underwater acoustic channel blind decision feedback algorithm [6] , But its convergence speed is slow, and the rest of the steady-state error big [7]. In this article, the odd symmetry error function and will change into the factor of decision feedback blind equalization algorithm, Variable Momentum Factor Odd symmetryerror Function blind equalization Algorithm Was puting forward.The algorithm has higher convergence speed and the smaller the characteristics of the steady-state error.

H. Zhang et al. (Eds.): BICS 2012, LNAI 7366, pp. 338–344, 2012.

2 Decision Feedback Blind Equalization Algorithm of Odd Symmetry Error Function

Decision Feedback Equalizer compose a prior to the filter and a feedback filter, Feedback to the ruling of the output filter as input, Used to eliminate has previously detected symbols sequence on the current symbols of interference. Basic structure as shown in figure 1, Because the input contains decision feedback filter is used the code yuan output, so, the DFE is typical of nonlinear equalizer

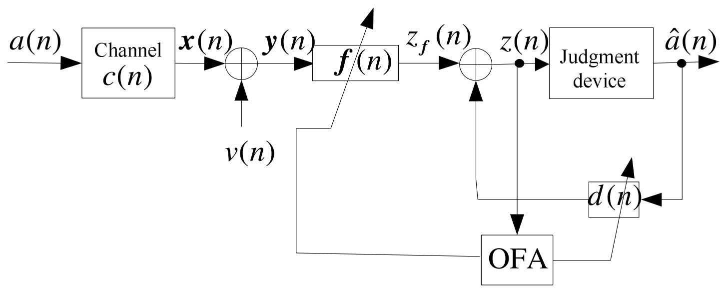

Fig. 1. Symmetry error function based on the decision feedback blind equalization algorithm diagram

a(n) is independent of the distribution of the signal with sequence, c(n) is channel impulse response, v(n)is the white Gaussian noise sequence(WGN), $\boldsymbol{y}(n)=[y(n),y(n-1),\cdots,y(n-L_f+1)]^T$ (T says deferring) is the equalizer input sequences $\boldsymbol{f}(n)=[f_0(n),f_1(n),\ \cdots,f_{L_f-1}(n)]^T$ is filter weight vector and feed-forward length is L_f (L_f for positive integer) z_f(n)is the feed forward filter output sequence, $\boldsymbol{d}(n)=[d_0(n),\ldots,d_{L_d-1}(n)]^T$ is filter weight vector and feedback length L_d, z(n) is equalizer outputs, $\hat{a}(n)$ signal for launch estimates of the a(n),OFA（Odd symmetry error Function blind equalization Algorithm）.

In this algorithm using the following error function Expression such as type (1), Error curve as figure2 shows (R=1).

$$e(n)=\begin{cases}\sqrt{|z(n)|^2-R^2} & |z_3(n)|>R\\ -\sqrt{R^2-|z(n)|^2} & |z_3(n)|<R\end{cases} \tag{1}$$

A said signal modulus, $R=E[|a(n)|^4]/E[|a(n)|^2]$ (2)

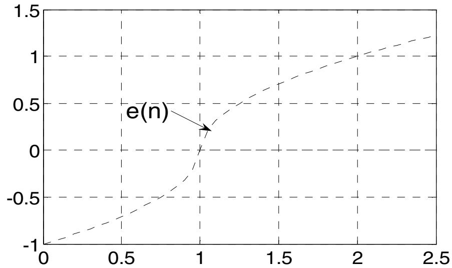

Fig. 2. Error function curve

Can see from figure 2, error on a curve into the center point (0,R)symmetrical, so e(n) is an odd symmetry error function. Below will based on the theory of the error function of decision feedback blind equalization algorithm for research.

The odd symmetry error function decision feedback equalizer weight vectors for iterative process:

$$y(n) = c^{\mathrm{T}}(n)\boldsymbol{x}(n) + v(n) \tag{3}$$

$$\boldsymbol{f}(n+1) = \boldsymbol{f}(n) + \mu_1 \mathrm{sign}(|z(n)| - R) z(n) \boldsymbol{y}^*(n) \tag{4}$$

$$\boldsymbol{d}(n+1) = \boldsymbol{d}(n) - u_2 \mathrm{sign}(|z(n)| - R) z(n) \hat{\boldsymbol{A}}^*(n) \tag{5}$$

$$z_f(n) = \sum_{l=0}^{L_f - 1} f^*(n,l) y(n-l) = \boldsymbol{f}^{\mathrm{T}}(n) \boldsymbol{y}(n) \tag{6}$$

Set $\hat{\boldsymbol{A}}(n) = [\hat{a}(n), \hat{a}(n-1), \cdots, \hat{a}(n-N_b+1)]^T$ is feedback filter input recursionvector, then the output feedback filter for

$$z_d(n) = \boldsymbol{d}^T(n) \hat{\boldsymbol{A}}(n) \tag{7}$$

Equalizer outputs

$$\begin{aligned} z(n) &= z_f(n) - z_d(n) \\ &= \boldsymbol{f}^{\mathrm{T}}(n) y(n) - \boldsymbol{d}^T(n) \hat{\boldsymbol{A}}(n) \end{aligned} \tag{8}$$

μ_1、 $\mu_2$says feed forward filter and feedback of the filter step length

Type (1 ~ 8) based on the odd symmetry error function is called the decision feedback blind equalization algorithm (OFA-DFE).

3 Odd Symmetry Error Function Momentum Decision Feedback Momentum Blind Equalization Algorithm

Momentum algorithm [9-11] can effectively to speed up the convergence rate of the blind equalization algorithm, In order to improve the OFA-DFE the convergence of the algorithm is, will be introduced to the momentum algorithm in algorithm, Its weight vectors iterative process.

$$\boldsymbol{f}(n+1)=\boldsymbol{f}(n)+\mu_w\mu_1\text{sign}(|z(n)|-R)z(n)\boldsymbol{y}^*(n)+\alpha[\boldsymbol{f}(n)-\boldsymbol{f}(n-1)] \tag{9}$$

$$\boldsymbol{d}(n+1)=\boldsymbol{d}(n)-u_d\text{sign}(|z(n)|-R)z(n)\hat{\boldsymbol{A}}^*(n) \tag{10}$$

$$z_f(n)=\sum_{l=0}^{L_f-1}\boldsymbol{f}^*(n,l)\,y(n-l)=\boldsymbol{f}^{\mathrm{T}}(n)\boldsymbol{y}(n) \tag{11}$$

$$z(n)=\boldsymbol{f}^{\mathrm{T}}(n)\boldsymbol{y}(n)-\boldsymbol{d}^{\mathrm{T}}(n)\boldsymbol{A}(n) \tag{12}$$

Type (8) to (11) called the odd symmetry error function momentum decision feedback blind equalization algorithm (MOFA-DFE). the error function, symmetrical momentum decision feedback momentum blind equalization algorithm

In a momentum blind equalization algorithm, the momentum of a role in the early stages of the balanced convergence plays an important role, but the convergence later, we expect a smaller momentum. So in the algorithm convergence to the larger before a momentum, in order to accelerate the convergence , but after the algorithm convergence, we expect the momentum of smaller, if a momentum will cause disorder, may even make spread algorithm. The mean square error (MSE) of the rule changes of quantity and transformation of thought the requirement for law of transformation of momentum almost the same, namely the mean square error is remaining steady-state error square expectations.

In order to suit the momentum of control, article use Mean square error (MSE) controlling momentum factors of change. MSE is defined as

$$MSE(n)=E\left\{e^2(n)\right\}=E\{[z(n)-\hat{a}(n)]\} \tag{13}$$

Define momentum factor function

$$\alpha(n)=\beta[1-e^{\rho-MSE(n)}] \tag{14}$$

Parameter ß is constant of Controlling function a (n) size, decision to rise the speed of the curve, parameterρis constant of Controlling function a(n)Plus or minus symbols change. When the algorithm convergence, adapt to choose ρ value, Momentum take a negative value, To reduce the role of a learning rate, To reduce the static error, Decrease Bit Error Rate, In order to achieve optimization algorithm performance.

3.1 The Algorithm Theory

Variations under factor is introduced to Odd symmetry error function momentum decision feedback blind equalization algorithm, drawing forth Odd symmetry error function change quantity factor decision feedback momentum blind equalization algorithm, Its weight vectors iterative process.

$$\boldsymbol{f}(n+1)=\boldsymbol{f}(n)+\mu_f\text{sign}(|z(n)|-R)z(n)\boldsymbol{y}^*(n)+\alpha_M(n)[\boldsymbol{f}(n)-\boldsymbol{f}(n-1)] \tag{15}$$

$$\alpha_M(n) = \beta[1 - e^{\rho - MSE(n)}] \tag{16}$$

$$\boldsymbol{d}(n+1) = \boldsymbol{d}(n) - u_d \text{sign}(|z(n)| - R) z(n) \hat{\boldsymbol{A}}^*(n) \tag{17}$$

μ_f、 μ_d said steps, $a_M(n)$ said Variations under factor.

Type (15) to (17) called Odd symmetry error function change quantity factor decision feedback momentum blind equalization algorithm, (VMFMOFA-DFE, Variable Momentum Factor MOFA-DFE).

3.2 The Simulation Experiment

In order to verify the effectiveness of the algorithm VMFMOFA-DFE, Adopt double diameter underwater acoustic channel simulation experiment. Compare with (CMADFE), OFA-DFE and MOFA-DFE.

[experiment] channelc=[-0.35 0 0 1], This channel zero pole distribution and frequency response as shown in figure 3, 4, signal is 8PSK, Equalizer right long is 16, SNR is 20dB, Wavelet decomposition layers are 2, Other parameters Settings as table 1 1500 times monte carlo simulation results, as shown in figure 5.

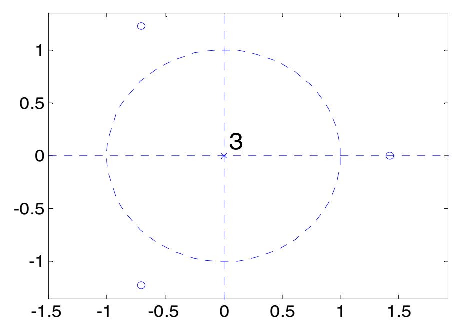

Fig. 3. Pole-zero plots of channel c

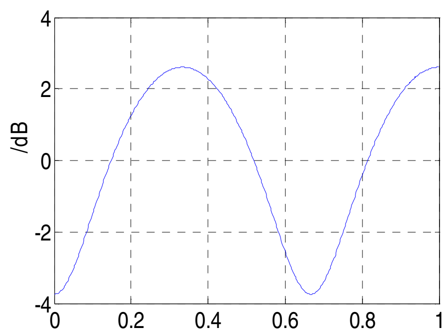

Fig. 4. Frequency response of channel c

Table 1. Simulation parameter

Error function	algorithm	simulation steps	wavelet	β	Initialized weights
$e_1(n)$	CMA WT-CMA	0.00004 0.00005	Db2	0.99	Fourth tap Initialized to 1, The rest is 0
$e_2(n)$	WT-OSE	$\alpha = 0.05$ $\lambda = 0.008$	Db2	0.99	
$e_3(n)$	WT-OSE	$\alpha = 0.06$ $\lambda = 0.008$	Db3	0.99	

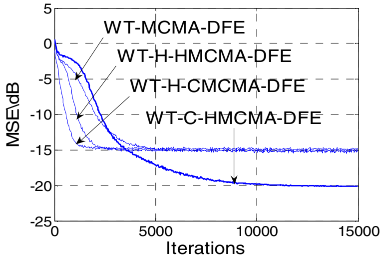

(a) Mean square error curve

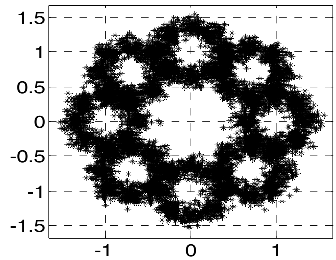

(b) Input

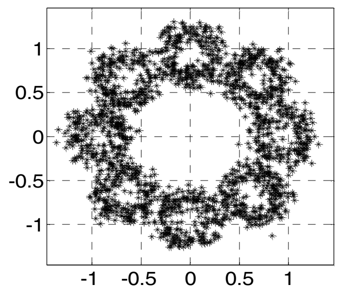

(b) CMADF output

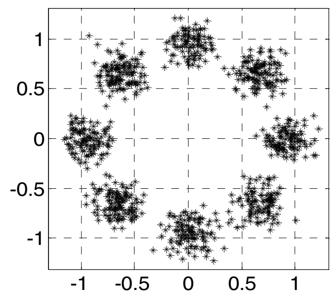

(c) OFA-DFE output

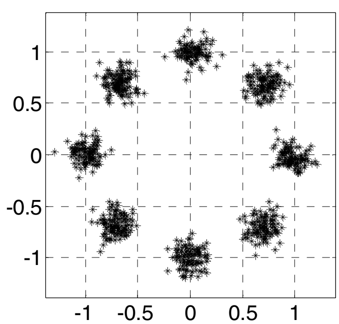

(d) MOFA-DFE output

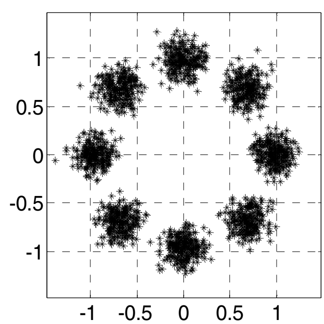

(e) VMFMOFA-DFE output

Fig. 5. Experimental simulation results

4 Conclusion

Using odd symmetry error function can effectively reduce the equalizer error function, Momentum can effectively to speed up the convergence rate of the equalizer, The odd symmetry error function and momentum are introduced to the decision feedback blind equalization algorithm, drawing forth Odd symmetry error function change quantity factor decision feedback momentum blind equalization algorithm.

Algorithm was simulated by Double diameter underwater acoustic channel, Tests show that the algorithm is fast convergence rate, and the mean square error of the small excellent properties.

References

[1] Zhang, Y.-B., et al.: BasedRENYI Entropy Underwater Acoustic Channel Equalization Algorithm. Electronics and Information Technology 81(4), 911–915 (2011)
[2] Guo, Y.-C., Lin, R.-G.: Based on fractionally spaced decision feedback blind equalization algorithm. Data Acquisition and Processing 23(3), 284–287 (2010)
[3] Feng, W.-J., Wang, Y.: The use of error feedback decision feedback equalizer performance analysis. Information and Electronic Engineering 4(2), 107–110 (2006)
[4] Guo, Y.-C., Zhang, Y.-P.: Decorrelation of a fractionally spaced decision feedback blind equalization algorithm. Ship Science and Technology 31(5), 137–140 (2009)
[5] Zhu, X.-T., Zhao, X., Liu, Y.-L.: Based DD-LMS and MCMA Blind Decision Feedback Equalization Algorithm. Microwave Journal 23(2), 67–70 (2007)
[6] Guo, Y.-C.: Odd symmetry error estimates based on different blind equalization algorithm. System Simulation 19(24), 5639–5642 (2007)

A Flexible Implementation Method of Distributed ANN

Yuzhen Pi*, Quande Yuan, and Xiangping Meng

School of Electrical Engineering and Information Technology,
Changchun Institute of Technology, 130012, Changchun, China
Research Center of Power Distribution Automation of Jilin Province,
130012, Changchun, China
{piyuzhen,yuanquande}@gmail.com, xp_meng@ccit.edu.cn

Abstract. The implementation methods of Artificial Neural Network (ANN) can be classified into two types: hardware implementation methods and software implementation methods. The former can build truly distributed, parallel, high-speed ANN, but it is complicated and expensive. The latter can build ANNs on classical computer using software technology. It's necessary in some cases, although the performance of ANNs built by this type of methods is limited because they are not parallel computing. In this paper, we propose a distributed implementation method based on multi-agent theory. Neurons in ANN are distributed, and the ANN can be easily to extend.

Keywords: Distributed ANN, MAS, SSDP.

1 Introduction

Method of implementation of Artificial Neural Network is bridge between an ANN model and its applications. There are two type methods: hardware and software implementation. The former using electronics, VLSI or optics to building ANN [1,2,3], which can build truly distributed, parallel, high-speed ANN, however, it is complex and expensive. In some of cases, it is necessary to implement ANN using software virtual method. Most of implementation of ANNs on classical computer is neither parallel nor distributed. There are researchers try to make ANN algorithms run on parallel computers [4,7]. They take advantage of supper computing power of parallel computers to improve ANNs performance.

In [6]we proposed a method of building ANN based on multi-agent system theory. We treat neuron as agent, thus an ANN can be viewed as a multi-agent system. There are two types agent (manager agent and neuron agent) in ANN. Communication between two neuron agents should be routed by manager agent. Neuron agents in the network built using this method are running parallel. However, manager agent should do too much work, which limited the speed and

* This work is supported by National Natural Foundation of China grant NO. 60974055, Department of Education of Jilin Province grant NO.2011242.

H. Zhang et al. (Eds.): BICS 2012, LNAI 7366, pp. 345–350, 2012.

scale of ANN. To solve this problem, we propose a new decentralized architecture. In this new distributed implementation method, there isnt a manager agent to route messages and maintain information of all neuron. New neuron agent can be added easily to neural network with auto-configuration.

2 Key Technology

2.1 Multi-agent System

Autonomous agents and multi-agent systems (MASs) are rapidly emerging as a powerful paradigm for designing and developing complex software systems. In fact, the architecture of a multi-agent system can be viewed as a computational organization. But there is no agreement on what an agent is: there is no universally accepted definition of the term agent. These problems had been discussed in [5] and other papers in detail. We are agree on this concept that an agent should have characters as follows:

1. Autonomy
   The agent is capable of acting independently, and exhibiting control over their internal state.
2. Reactivity
   Maintains an ongoing interaction with its environment, and responds to changes that occur in it (in time for the response to be useful)
3. Pro-activity
   That means the agent is generating and attempting to achieve goals, not driven solely by events
4. Social ability
   The ability to interact with other agents (and possibly humans) by some kinds of agent-communication language, and perhaps cooperate with others.

As intelligent agent, an agent should have another important ability, thats learning, which can help agent adapt the dynamic environment. A multi-agent system contains a number of agents which interact through communication, able to act in an environment and will be linked by other (organizational) relationships. MAS can do more things than a single agent.

From this perspective, every neuron in an artificial neuron networks can be viewed as an agent, who takes input and decide what to do next according its own state and policy. Through the interactive of the agents, the MAS will output a result. Then supervisor gives feedback to output agent, and output gives feedback to others agent.

2.2 Simple Service Discovery Protocol

Simple Service Discovery Protocol shorted for SSDP, is designed as a solution to find local network HTTP resource. SSDP uses a decentralized approach to service discovery whereby no central store maintains information about resources. Each

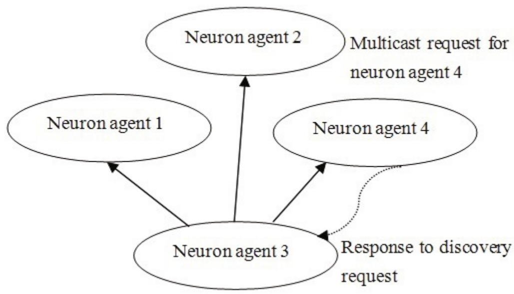

Fig. 1. Decentralized Discovery

client using SSDP queries network, and each resource on network responses to these requests, shown in Fig. 1.

The decentralized discovery mechanism makes network more robust. It does not require any central knowledge or configuration by a network administrator. The information is always up-to-date since neuron agent respond directly to queries and issue updates to other agents about their status. However, this system requires every agent to listen for and process the discovery requests. As the number of agents on the network grows, this approach becomes less attractive state information is duplicated across agents, more network bandwidth is consumed with discovery traffic, and computational power is wasted as every resource has some processing dedicated to listening for and processing discovery messages.

To solve this problem, there are two types of SSDP requests provided. The first, discovery requests, allow SSDP clients to look for SSDP resources. The second, presence announcements, allow SSDP resources to announce their presence on the network. SSDPs balance of discovery requests and presence announcements is designed to make the protocol efficient, reducing network traffic.

3 Distributed Implementation Method of ANN

To illustrate this method, we study the construction of BP neural network.

3.1 Neuron Agent

We treat neurons in ANN as neuron agents. The agents have abilities as follows:

1. Join into a WLAN automatically.
2. Advertise on neural network to announce that it have been in network.
3. Receive announce of new neuron agent. If the new neuron agent is in next layer, add information of this agent to its memory maintained as a list.
4. Broadcast quit message on the network before it quit from network.
5. Remove the information of agent who quits from network, if a neuron agent belongs to its next layer, from its agent list.

6. Search other neuron agent using SSDP discovery request message.
7. Output to neuron agents belong to next layer.
8. Get feedback from neuron agents of next layer.

3.2 Addressing

The first thing a neuron agent to do after its initialization is to join into network. Getting a valid address is foundation of everything. Only have a proper network address can it communicates with other agents. We using both DHCP and Auto-IP to ensure it work well. The addressing steps can be presented in Fig. 2:

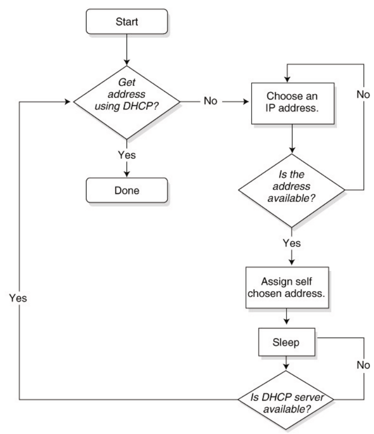

Fig. 2. Addressing Flowchart

3.3 Messages in ANN

A neuron agent needs to listen to two addresses:

1. Multi-cast address: 239.255.255.250:1900. It receives two kinds of messages. One is search request. When the neuron agent received search request and the search target is Neuron Agent, itll send its information to the address of requester. Another is announcement of joining or leaving the network. If neuron agents received announcement of joining, they will check the layer id of announcer, if announcer belongs to the next layer of neuron agent, it will add the information of this announcer into it internal agent list. If neuron agents received announcement of joining, they also will check whether announcer belongs to its next layer, if true, agent will remove its information from memory.

2. Its own IP address: In this address, the messages it receives include: output values from neuron agents of previous layer at stage of forward propagation and request of error value at stage of error back-propagation. When received the output values, agent will update its internal value corresponding to sender;

When a neuron agent joins into network, it will broadcast via SSDP. The format of announcement is shown as follow:

an advertisement on ANN example

```
NOTIFY * HTTP/1.1
Server: Windows 7/6.1
Cache-Control: max-age=1800
Location: http://192.168.0.11:4004/?my-layer-id=2
NTS: ssdp:alive
NT: uuid: neuronAgent
USN: uuid: neuronAgent
HOST: 239.255.255.250:1900
```

When a neuron agent output, it will send the output value encapsulated in an xml document to agents in its internal agents list. The format of the xml document is shown below:

DTD of output data

```
<?xml version=1.0 encoding=‘‘utf-8’’?>
<!ELEMENT output (type, sender, value)>
<!ELEMENT type (#PCDATA)>
<!ELEMENT sender (neuronID , layerID, location)>
<!ELEMENT neuronID (#PCDATA)>
<!ELEMENT layerID(#PCDATA)>
<!ELEMENT location (#PCDATA)>
<!ELEMENT value (#PCDATA)>
```

Where the value of type is either “e” shorted for errors or “o” shorted for output.

4 Experiment Result

There are three layers in this new BP neural network, an input layer to accept input data, a hidden layer and an output layer. To increase the number of neuron

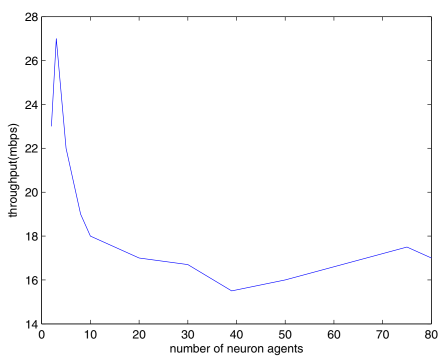

Fig. 3. number of neuron agents VS throughput of network

agents gradually to see the performance of network, shown in Fig. 3. The max number of computer in a WLAN can up to 100.

In fact, one computer can be host of more than one neuron agents. According our computer configuration, we can run more than 100 such neuron agents. That is to say, in a normal WLAN, we can build an ANN including nore than 10000 neurons using this method.

5 Conclusion

In this paper, we propose a decentralized implementation method of ANN. All neurons in system are viewed as agents. New neuron agent can be added to neural network with auto-configuration. This kind of ANN runs distributed and parallel, which can improve the performance of ANN.

References

1. Ota, Y., Wilamowki, B.M.: Analog Implementation of Pulse-Coupled Neural Networks. IEEE Transactions on Neural Networks 10(3), 539–544 (1999)
2. Lont, J.B., Guggenbhl, W.: Analog CMOS Implementation of a Multi-layer Perceptron with Nonlinear Sysnapse. IEEE Transactions on Neural Networks 3(3), 457–465 (1992)
3. Card, H.C., et al.: Analog VLSI Circuits for Competitive Learning Networks. Analog Integrated Circuits and Signal Processing 15, 291–314 (1998)
4. Nordstrom, T., Svensson, B.: Using and designing massively parallel computers for artificial neural networks. Journal of Parallel and Distributed Computing 14(3), 260–285 (1992)
5. Jennings, N.R., Sycara, K.P., Wooldridge, M.: A Roadmap of Agent Research and Development. Journal of Autonomous Agents and Multi-Agent Systems 1(1), 7–36 (1998)
6. Meng, X., Yuan, Q., Pi, Y., Wang, J.: A Novel Method of Constructing ANN. In: Liu, D., Fei, S., Hou, Z., Zhang, H., Sun, C. (eds.) ISNN 2007, Part II. LNCS, vol. 4492, pp. 493–499. Springer, Heidelberg (2007)
7. Ghosh, J., Hwang, K.: Mapping neural networks onto message-passing multicomputers. Journal of Parallel and Distributed Computing 6(2), 291–330 (1989)

Prediction of Thermal Comfort Index Using Type-2 Fuzzy Neural Network

Chengdong Li[1,⋆], Jianqiang Yi[2], Ming Wang[1], and Guiqing Zhang[1]

[1] School of Information and Electrical Engineering, Shandong Jianzhu University, Jinan 250101, P.R. China
[2] Institute of Automation, Chinese Academy of Sciences, Beijing 100190, P.R. China

Abstract. Predicted Mean Vote (PMV) is the most widely-used index for evaluating the thermal comfort in buildings. But, this index is calculated through complicated iterations so that it is not suitable for real-time applications. To avoid complicated iterative calculation, this paper presents a prediction model for this index. The proposed model utilizes type-2 fuzzy neural network to approximate the input-output characteristic of the PMV model. To tune the parameters of this type-2 fuzzy neural prediction model, a hybrid algorithm which is a combination of the least square estimate (LSE) method and the back-propagation (BP) algorithm is provided. Finally, simulations are given to verify the effectiveness of the proposed prediction model.

Keywords: Type-2 fuzzy, Neural network, Predicted mean vote, Least square estimate method, Back-propagation algorithm.

1 Introduction

The main purpose of the heating-ventilating-air conditioning (HVAC) systems in buildings is to provide comfortable living or working environments for occupants. But the word “comfort” is a very vague and not easily defined term, and it is influenced by both the physical environment (air temperature, radiant temperature, relative humidity and air velocity) and the individuals physiology or psychology [1-3]. To evaluate the thermal comfort, a number of indices have been studied, but the most widely used thermal comfort index is the Predicted Mean Vote (PMV) proposed by Fanger [4]. Based on the PMV index, ASHRAE (American Society of Heating, Refrigerating and Air-Condition Engineers) suggested to measure the thermal comfort level as: -3 (*cold*), -2 (*cool*), -1 (*slightly cool*), 0 (*neutral*), +1 (*slightly warm*), +2 (*warm*), +3 (*hot*).

Complicated iterative calculation is needed for the computation of the PMV index, so that Fanger’s PMV model is not very applicable for real-time applications. Many researchers have simplified Fanger’s PMV model under some

⋆ This work is supported by National Natural Science Foundation of China (61105077, 60975060 and 61074149), Science and Technology Development Program of Higher Education of Shandong (J11LG15, J11LG16).

H. Zhang et al. (Eds.): BICS 2012, LNAI 7366, pp. 351–360, 2012.

assumptions to predict thermal comfort values [5, 6], but the simplified PMV model can not precisely approximate the input-output characteristic of the PMV model when the assumptions used to derive the simplified model can not be met. In [7-9], the authors adopt neural network to realize the approximation of Fanger's PMV model. And, in [10], Fanger's PMV model is achieved using a Takagi-Sugeno fuzzy model, where type-1 fuzzy sets are used. But both neural network model and fuzzy model have some shortcomings. The neural network model can not make good use of existing experience and knowledge about the PMV index, and is also difficult to understand, while the fuzzy model can remedy such disadvantages. On the other hand, fuzzy model lacks of self-learning and adaptive capacity, which is the advantage of neural network model. Therefore, to take advantages of both the neural network model and the fuzzy model, a fuzzy neural model is presented in this study.

As "*Thermal sensations are different among people even in the same environment*" [1], and type-1 fuzzy sets, whose membership grades are crisp, can not deal with high levels of uncertainties contained in the vague words used to describe "comfort", so higher order fuzzy sets are needed. Type-2 fuzzy sets provide such a tool for modeling high levels of uncertainties, and can be adopted to model vague words when "*words mean different things to different people*" [11-13]. Hence, to obtain more reasonable fuzzy neural model for the PMV index, in this study, type-2 fuzzy sets (T2FSs) are utilized to model vague terms, such as "*hot*", "*warm*", "*cold*", etc. Another reason for the utilization of T2FSs is that type-2 fuzzy models can achieve better performance than type-1 fuzzy models, as type-2 fuzzy models can provide additional degrees of freedom and have more parameters than type-1 fuzzy models [14-18].

For the type-2 fuzzy neural prediction model, its parameters should be tuned in order to precisely approximate the input-output characteristic of the PMV model. In this paper, to realize the training of the proposed model, we provide a hybrid algorithm, which is a combination of the least square estimate (LSE) method and the back-propagation (BP) algorithm. Also, to show the effectiveness of the proposed model and the hybrid algorithm, simulations are given. From simulation results, we can see that, with the training algorithm, the proposed prediction model can give satisfactory performance.

2 Problem Description

The PMV index is a function of six variables, such as air temperature, radiant temperature, relative humidity, air velocity, human activity level and clothing thermal resistance. The value of PMV ranges from -3 to 3, and can be calculated by [4, 7-9]

$$\begin{aligned} PMV = &\big(0.303e^{-0.036M} + 0.028\big)\big\{M - W - 3.05 * 10^{-3}[5733 - 6.99(M - W) - \\ &P_a] - 0.42[(M - W) - 58.15] - 1.7 * 10^{-5}M(5867 - P_a) - 0.0014M * (34 \\ &- t_a) - 3.96 * 10^{-8} f_{c1}[(t_{c1} + 273)^4 - (t_r + 273)^4] - f_{c1}h_c(t_{c1} - t_a)\big\} \end{aligned} \quad (1)$$

$$t_{c1} = 35.7 - 0.0278(M - W) - I_{c1}\{3.96 * 10^{-8} f_{c1} * [(t_{c1} + 273)^4 - (t_r + 273)^4 - f_{c1} h_c (t_{c1} - t_a)]\} \quad (2)$$

In above equations, t_{c1}, h_c, f_{c1} and P_a can be computed respectively as

$$h_c = \begin{cases} 2.38(t_{c1} - t_a)^{0.25} & 2.38(t_{c1} - t_a)^{0.25} > 12.1\sqrt{v_a} \\ 12.1\sqrt{v_a} & 2.38(t_{c1} - t_a)^{0.25} < 12.1\sqrt{v_a} \end{cases} \quad (3)$$

$$f_{c1} = \begin{cases} 1.00 + 0.2 I_{c1} & I_{c1} < 0.5clo \\ 1.05 + 0.1 I_{c1} & I_{c1} > 0.5clo \end{cases} \quad (4)$$

$$P_a = \frac{P_s R_H}{100} \quad (5)$$

where PMV is the Predicted Mean Vote, M is the human metabolic rate (W/m^2), W is the external work (W/m^2), P_a is the water vapor pressure (Pa), t_a is the indoor air temperature (° C), t_r is the radiation temperature (° C), I_{c1} is the thermal resistance of clothing (clo), v_a is the relative air velocity (m/s), t_{c1} is the surface temperature of clothing, R_H is the relative humidity in percent, h_c is the convectional heat transfer coefficient (W/m^{2}K), f_{c1} is the ratio of clothed body surface area to nude body surface area, P_s is the saturated vapor pressure at specific temperature (°C).

From the above PMV calculation equations, we can observe that such equations are nonlinear and rather complicated. Also, we need computing t_{c1} iteratively to obtain the root of the nonlinear equation (2). This is a problem for real-time applications. Except this difficulty, we can encounter another problem when we use the PMV index, which has six input variables, to solve practical problems. In real-world applications, usually it is quite difficult and costly to measure all the six input variables of the PMV model. And, sometimes, some input variables are rather complicated and not easy to be measured online. Therefore, it is reasonable for us to pick the most important input variables and make sound assumptions on the other input variables.

In [3], the authors have discussed that "*the results show that thermal comfort votes were highly correlated with the two environmental conditions, namely, temperature and humidity*". So, to make the proposed prediction model easier to apply in practice, in this study, we adopt the air temperature t_a and the relative humidity R_H as input variables of the type-2 fuzzy neural prediction model. And the other variables are reasonably set as discussed in Section 4.

3 Type-2 Fuzzy Neural Prediction Model for the Thermal Comfort Index

In this section, we first discuss the architecture of the type-2 fuzzy neural prediction model for the thermal comfort PMV index, and then, clarify the structure and learning algorithm of the type-2 fuzzy neural model.

Fig. 1 shows the tuning schedule of the type-2 fuzzy neural model. To construct the type-2 fuzzy neural prediction model, the training data are obtained from Fager's PMV model to reflect the relationship between the inputs and the thermal comfort index. The inputs of the training data are the values of t_a, R_H, while the outputs of the training data are the PMV index values. In the training process, a hybrid algorithm, which is a combination of the least squares estimate (LSE) algorithm and the back-propagation algorithm, is utilized to update the parameters of the prediction model.

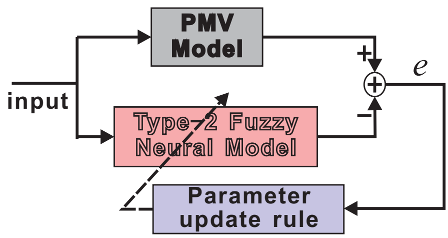

Fig. 1. Tuning schedule of type-2 fuzzy neural prediction model

3.1 Structure of the Type-2 Fuzzy Neural Model

The type-2 fuzzy neural prediction model for the PMV index is a type-2 fuzzy neural network (T2FNN), whose structure is shown in Fig. 2. This is a two-input-one-output network.

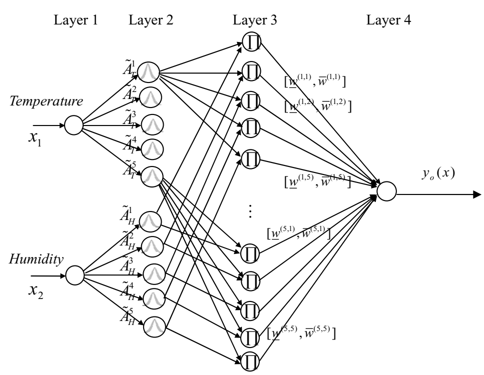

Fig. 2. Structure of type-2 fuzzy neural prediction model

A T2FNN is very similar to a conventional (type-1) fuzzy neural network (T1FNN). Both of them have four layers, but some differences exist between them: 1) In the membership function layer (Layer 2), the fuzzy sets of T1FNN are type-1, but the fuzzy sets of T2FNN are type-2; 2) The consequent weights between Layer 3 and Layer 4 are crisp values for T1FNN, while the consequent weights between Layer 3 and Layer 4 are interval values for T2FNN; 3) Layer 4 is only used to carry out the defuzzification process for a T1FNN, but, for a T2FNN, Layer 4 needs to accomplish the type-reduction and defuzzification processes. Details of T2FNN can be found from [19-22].

By assigning the air temperature and the relative humidity N_1 and N_2 type-2 fuzzy sets (T2FSs), we can obtain $N_1 * N_2$ fuzzy rules, each of which has the following form

Rule(i, j): If x_1 is $\widetilde{A}_T^i$, x_2 is $\widetilde{A}_H^j$,Then y_o is $[\underline{w}^{(i,j)}, \overline{w}^{(i,j)}]$,
where $x_1 = t_a$ represents the air temperature, and $x_2 = R_H$ represents the relative humidity, and $i = 1, 2..., N_1$, $j = 1, 2..., N_2$. $[\underline{w}^{(i,j)}, \overline{w}^{(i,j)}]$s are the intervals of the consequent part, $\widetilde{A}_T^i$s and $\widetilde{A}_H^j$s are T2FSs for the air temperature and the relative humidity.

Once a crisp input $\boldsymbol{x} = (x_1, x_2)$ is applied to the T2FNN, through the singleton fuzzifier (layer 1) and the type-2 inference process (layer 2), the interval firing strength of the rule (i, j) (node (i, j)) can be obtained as

$$F^{(i,j)}(\boldsymbol{x}) = [\underline{\mu}_{\widetilde{A}_T^i}(x_1)\underline{\mu}_{\widetilde{A}_H^j}(x_2), \overline{\mu}_{\widetilde{A}_T^i}(x_1)\overline{\mu}_{\widetilde{A}_H^j}(x_2)], \tag{6}$$

where product t-norm is adopted, $\underline{\mu}_{\widetilde{A}}$ and $\overline{\mu}_{\widetilde{A}}$ denote the grades of the lower and upper membership functions of the T2FS $\widetilde{A}$.

Once the interval firing strengths in layer 3 are computed, to generate a crisp output from the fourth layer, the outputs of the third layer should be type-reduced and then defuzzified. In this layer, different type-reducers and defuzzifiers may give different results. There exist several output processing methods. In this paper, we adopt Begian-Melek-Mendel (BMM) method proposed in [16] to realize the type-reduction and defuzzification. Using the BMM method, the output of the fourth layer can be computed as

$$y_o(\boldsymbol{x}) = (1 - \eta)y_{ol}(\boldsymbol{x}) + \eta y_{ou}(\boldsymbol{x}), \tag{7}$$

where $0 \leq \eta \leq 1$ is the weight coefficient, and

$$y_{ol}(\boldsymbol{x}) = \frac{\sum_{i=1}^{N_1}\sum_{j=1}^{N_2}\underline{\mu}_{\widetilde{A}_T^i}(x_1)\underline{\mu}_{\widetilde{A}_H^j}(x_2)\underline{w}^{(i,j)}}{\sum_{i=1}^{N_1}\sum_{j=1}^{N_2}\underline{\mu}_{\widetilde{A}_T^i}(x_1)\underline{\mu}_{\widetilde{A}_H^j}(x_2)} \tag{8}$$

$$y_{ou}(\boldsymbol{x}) = \frac{\sum_{i=1}^{N_1}\sum_{j=1}^{N_2}\overline{\mu}_{\widetilde{A}_T^i}(x_1)\overline{\mu}_{\widetilde{A}_H^j}(x_2)\overline{w}^{(i,j)}}{\sum_{i=1}^{N_1}\sum_{j=1}^{N_2}\overline{\mu}_{\widetilde{A}_T^i}(x_1)\overline{\mu}_{\widetilde{A}_H^j}(x_2)} \tag{9}$$

3.2 Training of the Type-2 Fuzzy Neural Model Using Hybrid Algorithm

To achieve better performance and obtain precise prediction result, in this subsection, we will propose a hybrid algorithm, which is a combination of the BP algorithm and the LSE method, to tune the parameters of the designed type-2 fuzzy neural model.

Given the input-output training data $(\boldsymbol{x}^t, y^t) = (x_1^t, x_2^t, y^t)$, where y^t is the PMV index value for the input $\boldsymbol{x}^t$, the BP algorithm is used to adjust all the parameters of the type-2 fuzzy neural model by minimizing the following function:

$$J(t) = \frac{1}{2}e^2(t) = \frac{1}{2}[y_o(\boldsymbol{x}^t) - y^t]^2, \tag{10}$$

Now, let us present the BP update rules for the parameters of the type-2 fuzzy neural model, in which Gaussian T2FSs are adopted.

For any parameter ϕ, its BP update rule is

$$\phi(t+1) = \phi(t) - \alpha_\phi \frac{\partial J(t)}{\partial \phi} = \phi(t) - \alpha_\phi e(t) \frac{\partial y_o(\boldsymbol{x}^t)}{\partial \phi} \tag{11}$$

where α_ϕ is the learning rate.

(1) BP update rule for the consequent parameters

$$\underline{w}^{(i,j)}(t+1) = \underline{w}^{(i,j)}(t) - \alpha_w e(t)(1-\eta(t)) \frac{\underline{\mu}_{\widetilde{A}_T^i}(x_1^t)\underline{\mu}_{\widetilde{A}_H^j}(x_2^t)}{\sum_{i=1}^{N_1}\sum_{j=1}^{N_2}\underline{\mu}_{\widetilde{A}_T^i}(x_1^t)\underline{\mu}_{\widetilde{A}_H^j}(x_2^t)}$$

$$\overline{w}^{(i,j)}(t+1) = \overline{w}^{(i,j)}(t) - \alpha_w e(t)\eta(t) \frac{\overline{\mu}_{\widetilde{A}_T^i}(x_1^t)\overline{\mu}_{\widetilde{A}_H^j}(x_2^t)}{\sum_{i=1}^{N_1}\sum_{j=1}^{N_2}\overline{\mu}_{\widetilde{A}_T^i}(x_1^t)\overline{\mu}_{\widetilde{A}_H^j}(x_2^t)}$$

(2) BP update rule for the weight coefficient η

$$\eta(t+1) = \eta(t) - \alpha_\eta e(t)[y_{ou}(x^t) - y_{ol}(\boldsymbol{x}^t)] \tag{12}$$

(3) BP update rule for parameters of antecedent Gaussian T2FSs

For any given parameter θ_T^i of $\widetilde{A}_T^i$,

$$\begin{aligned}\theta_T^i(t+1) = \theta_T^i(t) - \alpha_{\theta_T} e(t) \Bigg[(1-\eta) \frac{\sum_{j=1}^{N_2}(\underline{w}^{(i,j)} - y_{ol}(\boldsymbol{x}^t))\frac{\partial \underline{\mu}_{\widetilde{A}_T^i}(x_1^t)}{\partial \theta_T^i}\underline{\mu}_{\widetilde{A}_H^j}(x_2^t)}{\sum_{i=1}^{N_1}\sum_{j=1}^{N_2}\underline{\mu}_{\widetilde{A}_T^i}(x_1^t)\underline{\mu}_{\widetilde{A}_H^j}(x_2^t)} \\ + \eta \frac{\sum_{j=1}^{N_2}(\overline{w}^{(i,j)} - y_{ou}(\boldsymbol{x}^t))\frac{\partial \overline{\mu}_{\widetilde{A}_T^i}(x_1^t)}{\partial \theta_T^i}\overline{\mu}_{\widetilde{A}_H^j}(x_2^t)}{\sum_{i=1}^{N_1}\sum_{j=1}^{N_2}\overline{\mu}_{\widetilde{A}_T^i}(x_1^t)\overline{\mu}_{\widetilde{A}_H^j}(x_2^t)} \Bigg]\end{aligned} \tag{13}$$

Similar update rules can be derived for any given parameter θ_H^j of $\widetilde{A}_H^j$.

As well known, BP algorithm is sensitive to initial values. And, it is easy to set reasonable initial values of the antecedent parameters, but difficult to determine reasonable initial values of the consequent parameters. Therefore, in this study, we utilize the LSE method to get the initial values of the consequent parameters, as the outputs of the type-2 fuzzy neural model are linear with the consequent parameters. Detailed materials about least squares estimate method can be found in [23].

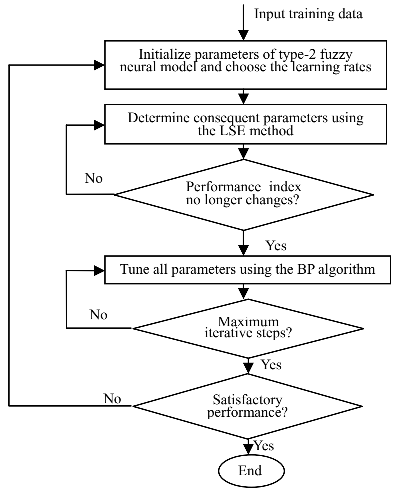

Fig. 3. Hybrid algorithm for the type-2 fuzzy neural prediction model

Based on the discussion above, we can use a hybrid algorithm which combines LSE method and BP algorithm together to tune the type-2 fuzzy neural prediction model. The hybrid algorithm is demonstrated in Fig. 3.

4 Simulation

4.1 Simulation Description

In our simulation, the air temperature and the relative humidity are the input variables of the type-2 fuzzy neural model. And, some reasonable assumptions are made to the other four variables (radiant temperature, air velocity, activity level and clothing thermal resistance) as follows:

1): Generally speaking, occupants usually engage in light work when they are indoor. In this case, the human metabolic rate is 69.78 W/m^2, so we suppose the activity level to be 69.78 W/m^2;

2): we set clothing thermal resistance to 0.7 (clo);

3): the radiant temperature is set to be equal to the air temperature;

4): As the specifications of the air conditioning design requires the air velocity to be less than 0.25m/s in summer, so the air velocity is set to 0.20m/s.

Under such assumptions, the training data pairs are generated. The sampling range of the air temperature is $[10°C, 36°C]$, and the sampling step is $1°C$. The sampling range of the relative humidity is $[0\%, 100\%]$, and the sampling step is 5%. Thus, 567 training data pairs are obtained.

In the simulation, we assign each input variable 5 Gaussian T2FSs as shown in Fig. 5 (a) and (b).The initial consequent parameters $[\underline{w}^{(i,j)}, \overline{w}^{(i,j)}]$ and the weight coefficients η are set to zero and 0.5, respectively.

4.2 Simulation Results

Fig. 4 demonstrates the RMSE (root mean squared error) curve in the training process. After being trained, the T2FSs for the antecedent parts of fuzzy rules are shown in Fig. 5 (c) and (d). The trained weight coefficients $\eta = 0.53$, and the optimized consequent parameters $[\underline{w}^{(i,j)}, \overline{w}^{(i,j)}]$ are shown in Table 1.

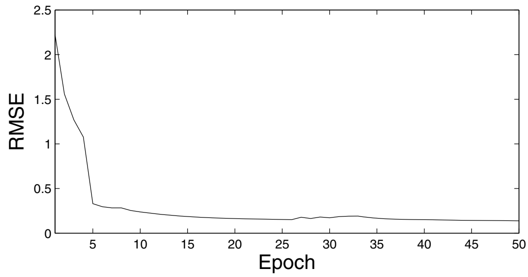

Fig. 4. RMSE curve in the training process

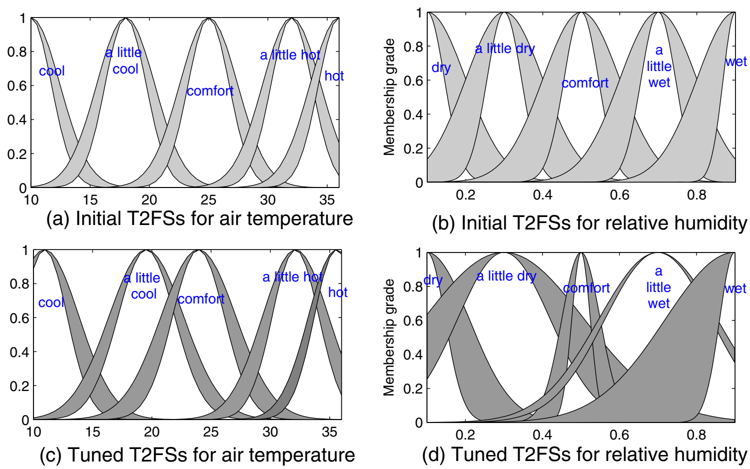

Fig. 5. Initial and tuned T2FSs in the antecedent part of fuzzy rules

Also, 100 data pairs are generated randomly for checking the effectiveness of the proposed prediction model. Comparison between the PMV value and the value obtained from the type-2 fuzzy neural prediction model is demonstrated in Fig. 6. The prediction errors are also shown in Fig. 6 (bule line). From this figure, we can see that the proposed prediction model can achieve satisfactory performance and the prediction error lie in a fine scale. Hence, the proposed type-2 fuzzy neural prediction model can be used as a good alternative in real-time applications where the PMV index should be computed online.

Table 1. Final consequent parameters

$[\underline{w}^{(i,j)}, \overline{w}^{(i,j)}]$		i = 1	2	3	4	5
j	1	$[-3.60, -3.59]$	$[-2.21, -2.11]$	$[0.09, 0.21]$	$[0.90, 1.70]$	$[3.16, 3.19]$
	2	$[-3.58, -3.40]$	$[-2.14, -1.92]$	$[0.25, 0.66]$	$[1.04, 2.16]$	$[3.54, 3.84]$
	3	$[-3.43, -3.42]$	$[-2.04, -1.75]$	$[0.35, 0.69]$	$[1.22, 2.45]$	$[3.84, 3.98]$
	4	$[-3.47, -3.36]$	$[-2.05, -1.64]$	$[0.45, 0.94]$	$[1.32, 2.59]$	$[3.84, 4.43]$
	5	$[-3.28, -3.27]$	$[-1.71, -1.50]$	$[0.83, 1.02]$	$[1.95, 2.99]$	$[4.38, 4.80]$

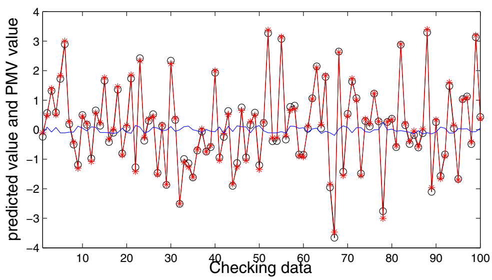

Fig. 6. Comparison between the predicted value and the PMV value

5 Conclusion

To provide comfortable living or working environments by the Heating, Ventilation, and Air-Conditioning (HVAC) systems, determination of the thermal comfort index is an essential step. But it is not practical to compute the most widely-used PMV index in real time. A promising way to solve this problem is to use prediction model to approximate the input-output characteristic of the PMV model. In this work, a type-2 fuzzy neural prediction model was proposed to approximate the PMV model. To enhance the performance of the proposed model, a hybrid algorithm, which is a combination of the least square estimate (LSE) method and the back-propagation (BP) algorithm, was adopted to tune all the parameters. Simulation results demonstrated that the the proposed model is effective and it can be used as a good alternative of the PMV model in real-time applications. Our future work is to apply the proposed model to actual HVAC control problems to verify its validity further.

References

1. Djongyang, N., Tchinda, R., Njomo, D.: Thermal Comfort: A Review Paper. Renewable and Sustainable Energy Reviews 14, 2626–2640 (2010)
2. Chen, K., Rys, M.J., Lee, E.S.: Modeling of Thermal Comfort in Air Conditioned Rooms by Fuzzy Regression Analysis. Mathematical and Computer Modelling 43, 809–819 (2006)

3. Chen, K., Jiao, Y., Lee, E.S.: Fuzzy Adaptive Networks in Thermal Comfort. Applied Mathematics Letters 19, 420–426 (2006)
4. Fanger, P.O.: Thermal Comfort: Analysis and Applications in Environmental Engineering. McGraw-Hill, New York (1970)
5. Sherman, M.: A Simplified Model of Thermal Comfort. Energy Buildings 8, 37–50 (1985)
6. Federspiel, C.C., Asada, H.: User-Adaptable Comfort Control for HVAC Systems. Trans. ASME 116, 474–486 (1994)
7. Atthajariyakul, S., Leephakpreeda, T.: Neural Computing Thermal Comfort Index for HVAC Systems. Energy Conversion and Management 46, 2553–2565 (2005)
8. Liang, J., Du, R.: Thermal Comfort Control Based on Neural Network for HVAC Application. In: Proceedings of the 2005 IEEE Conference on Control Applications, pp. 819–824. IEEE Press, New York (2005)
9. Ma, B., Shu, J., Wang, Y.: Experimental Design and the GA-BP Prediction of Human Thermal Comfort Index. In: Proceedings of the 2011 Seventh International Conference on Natural Computation, pp. 771–775 (2011)
10. Homod, R.Z., Mohamed Sahari, K.S., Almurib, H.A.F., Nagi, F.H.: RLF and TS Fuzzy Model Identification of Indoor Thermal Comfort Based on PMV/PPD. Building and Environment 49, 141–153 (2012)
11. Mendel, J.M.: Uncertain Rule-Based Fuzzy Logic Systems: Introduction and New Directions. Prentice-Hall (2001)
12. Mendel, J.M.: Computing with Words and its Relationships with Fuzzistics. Information Sciences 177, 988–1006 (2007)
13. Liu, F., Mendel, J.M.: Encoding Words into Interval Type-2 Fuzzy Sets Using an Interval Approach. IEEE Trans. Fuzzy Syst. 16, 1503–1521 (2008)
14. Liang, Q., Mendel, J.M.: Interval Type-2 Fuzzy Logic Systems: Theory and Design. IEEE Trans. Fuzzy Syst. 8, 535–550 (2000)
15. Juang, C.F., Hsu, C.H.: Reinforcement Ant Optimized Fuzzy Controller for Mobile Robot Wall Following Control. IEEE Trans. Ind. Electron. 56, 3931–3940 (2009)
16. Begian, M., Melek, W., Mendel, J.M.: Stability Analysis of Type-2 Fuzzy Systems. In: Proceedings of 2008 IEEE International Conference on Fuzzy Systems, pp. 947–953. IEEE Press, New York (2008)
17. Li, C., Yi, J., Wang, T.: Encoding Prior Knowledge into Data Driven Design of Interval Type-2 Fuzzy Logic Systems. International Journal of Innovative Computing, Information and Control 7(3), 1133–1144 (2011)
18. Li, C., Yi, J.: SIRMs Based Interval Type-2 Fuzzy Inference Systems: Properties and Application. International Journal of Innovative Computing, Information and Control 6(9), 4019–4028 (2010)
19. Li, C., Yi, J., Zhao, D.: Interval Type-2 Fuzzy Neural Network Controller (IT2FNNC) and its Application to a Coupled-Tank Liquid-Level Control System. In: Proceedings of 3rd International Conference on Innovative Computing Information and Control, Dalian, Liaoning, China, pp. 508–511. IEEE Press, New York (2008)
20. Li, C., Yi, J., Yu, Y., Zhao, D.: Inverse Control of Cable-Driven Parallel Mechanism using Type-2 Fuzzy Neural Network. Acta Automatica Sinica 36(3), 459–464 (2010)
21. Lin, F.-J., Shieh, P.-H., Hung, Y.-C.: An Intelligent Control for Linear Ultrasonic Motor Using Interval Type-2 Fuzzy Neural Network. IET Electr. Power Appl. 2(1), 32–41 (2008)
22. Abiyev, R.H., Kaynak, O.: Type 2 Fuzzy Neural Structure for Identification and Control of Time-Varying Plants. IEEE Trans. Ind. Electron. 57(12), 4147–4159 (2010)
23. Nelles, O.: Nonlinear System Identification. Springer, Berlin (2001)

The Possibility of Using Simple Neuron Models to Design Brain-Like Computers

Hong Hu and Zhongzhi Shi

Key Laboratory of Intelligent Information Processing, Institute of Computing Technology, Chinese Academy of Science Beijing 100190, China
huhong@ict.ac.cn

Abstract. IBM Research and five leading universities are partnering to create computing systems that are expected to simulate and emulate the brain's abilities. Although this project has achieved some successes, it meets great difficulties in the further research. The main difficulty is that it is almost impossible to analyze the dynamic character of neural networks in detail, when more than ten thousands neurons of complex nonlinear neural models are piled up. So it is nature to present such question: in order to simplify the design of *brain-like computers*, can we use simple neuron models to design *brain-like computers* or can we find a simplest neuron model which can simulate most neuron models with arbitrary precision? In this paper, we proved that almost all neural models found by neural scientists nowadays can be simulated by Hopfield neural networks. So it is possible to use simple neuron model to design *Brain-like computers.*

Keywords: IBM 's Blue Brain Project, Neuron Models' Equivalence, RH neuron, Brain-Like Computer.

1 Introduction

By exploiting the computing power of Blue Gene, IBM 's Blue Brain aims to build accurate models of the mammalian brain (Henry Markram et. al(2006) [1]. Just as Henry Markram et. al. mentioned(2006) [1] "the brain seems to make the next quantum leap in the quality of intelligence, beyond the physical structures to form dynamic electrical 'molecules'." For this purpose, real neuron models which can describe dynamical process of neural cells should be used in the designation of *brain-like computer*. But most neuron models are very complicate, for example the Hodgkin–Huxley neuron model used in the IBM 's Blue Brain project(see the equation (1) which is a generalized Hodgkin–Huxley function proposed by H D I Abarbanel et al. (1996)[2]) has very complicate nonlinear character. In order to make a *brain-like computer* smart enough to deal with the intricate cognition task, more than ten thousands neurons should be used, in such cases, it is very difficult to design a *brain-like computer* by using complicate neuron models such as Hodgkin–Huxley neuron model(for the sake of pages, the expleination of the parameters in Eq.(1), please refer to H D I Abarbanel et al. (1996)[2]).

H. Zhang et al. (Eds.): BICS 2012, LNAI 7366, pp. 361–372, 2012.

$$C\frac{dv}{dt} = I - \sum_{i=1}^{N} g_i a_i^{p_i}(t) b_i^{q_i}(t)[V(t) - V(i)]$$
$$\frac{da_i}{dt} = \frac{a_{\infty i}(V) - a_i}{\tau_{a_i(V)}} \quad . \tag{1}$$
$$\frac{db_i}{dt} = \frac{b_{\infty i}(V) - b_i}{\tau_{b_i(V)}}$$

It is nature to present such question: in order to simplify the design of *brain-like computers*, can we use simple neuron models to design *brain-like computers* or can we find a simplest neuron model which can simulate most neuron models with arbitrary precision?

In 1986, Hopfield and Tank proposed a very simple neuron model which takes the *logistic function* as its activation function [see Eq. (3)] (Hopfield& Tank, 1986[3]). The Hopfield neuron model described by Eq. (3) is the most simplest neuron model and has some sound characters, such as logical character which can be used to simplify the design of *brain-like computers*, layered structure that it can be used to build layered neural networks and be trained by *Back-propagation* approach, etc. The Hopfield neuron model is simplified from the equation (2) which is based on biological data of visual cortex (Barlow et al. (1967)[4]). In the Eq. (2), cells are arranged on a regular 2-dimensional array with image coordinates $i=(n_i,m_i)$ and divided into two categories: excitatory cells $x_{i\theta}$ and inhibitory cells $y_{i\theta}$. At every position $i=(n_i,m_i)$, there are M cells with subscript t_θ that are sensitive to a bar of the angle θ. Only excitatory cells receive inputs from the outputs of edge or bar detectors. The direction information of edges or bars is used for segmentation of the optical image.

$$\dot{x}_{i\theta} = -a_x x_{i\theta} - g_y(y_{i\theta}) + J_c g_x(x_{i\theta}) + I_c - \sum_{\nabla\theta\neq 0} \psi(\nabla\theta) g_y(y_{i,\theta+\nabla\theta}) + \sum_{j\neq i,\theta'} J_{i\theta,j\theta'} g_x(x_{j\theta'}) + I_{i\theta} \; .$$
$$\dot{y}_{i\theta} = -a_y y_{i\theta} - g_x(x_{i\theta}) + g_x(x_{i\theta}) + I_c + \sum_{j\neq i,\theta'} W_{i\theta,j\theta'} g_x(x_{j\theta'}) \tag{2}$$

where $g_x(x)$ and $g_y(x)$ are sigmoid-like activation functions, and ψ is the local inhibition connection in the location i, and $J_{i\theta,j\theta'}$ and $W_{i\theta,j\theta'}$ are the synaptic connections between the excitatory cells and from the excitatory cells to inhibition cells, respectively. If we represent the excitatory cells and inhibitory cells with same symbol U_i and summarize all connections (local ψ, global exciting $W_{i\theta,j\theta'}$ and global inhibiting $J_{i\theta,j\theta'}$) as w'_{ij}, the Eq. (2) can be simplified as Hopfield model Eq.(3).

$$\begin{aligned} \dot{U}_i &= -b_i \cdot U_i + \sum_j w'_{ij} V_j + \beta \sum_k w_{ik} I_k \\ V_i &= L(U_i) \end{aligned} . \qquad (3)$$

Where $L(U_i) = \dfrac{1}{1+\exp(-r(U_i - T_i))}$ is the *logistic function.*

In this paper, we prove that the simplest Hopfield neuron model described by Eq. (3) has a universal meaning, almost all neural models described by first order differential equations with continuous functions in it can be simulated by Hopfield neural networks with arbitrary small error (see Theorem 2). These neuron models include Hodgkin –Huxley model(1952) [see Eq.(1)], Fitz Hugh(1961) model, Rose-Hindmarsh (RH) model(1984) [see Eq.(15)] and so on. So it is reasonable to use the Hopfield neuron model to design *brain-like computer*s. Logical designing and back propagation learning approach can be used in the designing of Hopfield neuron networks. These approaches can simplify the designing of *brain-like computer*s. In the experiment, we give a concrete example of using the back-propagation approach to design a Hopfield neural network which simulates a Rose-Hindmarsh (RH) neuron. Hopfield neural networks are considered as the second generation neural network by Maass W. (1997)[5], and so are totally different from the third generation spiking neural networks. But we show that Hopfield neural networks do really can simulate spiking neural networks, so Hopfield neural networks is versatile enough to build *brain-like computers*.

The rest of the paper is organized as follows. Section 2 gives the two main theorems about the ability of Hopfield neural networks. Section 3 provides an example, which tries to simulate a Rose-Hindmarsh (RH) neuron. The algorithm to train the Hopfield neural network is also mentioned. Section 4 gives a summary of our paper which gives a brief discussion of the aim of designing brain-like computers and how to use simple neural model designing neural circuits for brain-like computers, at last an open problem is presented for further research.

2 The Main Theorem

H D I Abarbanel et al (1996)[2] studied the synchronization of 13 neuron models. These models include Van-der-Pol generator (1935), Hodgkin Huxley (1952), Golovasch(1990), integrate-and-fire model(1995), etc. It is easy to see that except Van-der-Pol generator models [see Eq.(4a)] and the integrate-and-fire model[see Eq.(5)], the rest 11 neuron models are all the special cases of the generalized model described by the *ordinary differential equation* Eq.(7) .

$$\begin{aligned} &\ddot{x}_i + \mu(x_{ai}^2 - p^2)\dot{x}_i + g^2 x_{ai} = f(t). \\ &x_{ai} = x_i + \sum_j \lambda_{ji} x_j \end{aligned} \qquad (4a)$$

$$\dot{x}_i = y_i,$$
$$\dot{y}_i + \mu(x_{ai}^2 - p^2)y_i + g^2 x_{ai} = f(t). \quad (4b)$$
$$x_{ai} = x_i + \sum_j \lambda_{ji} x_j$$

$$\frac{dv}{dt} = -\frac{v}{\tau_0} + I_{ext} + I_{syn}(t) \quad . \quad (5)$$

Where $0 < v < \Theta$, and $v(t_0^+)=0$ if $v(t_0^-)=\Theta$. Usually $I_{syn}(t)$ is defined by Eq.(6).

$$I_{syn}(t) = g \sum_{spikes} f(t - t_{spike})$$
$$f(t) = A[\exp(-\tfrac{t}{\tau_1}) - \exp(-\tfrac{t}{\tau_2})] \quad . \quad (6)$$

In fact, if we introduce a new variable $y_i = \dot{x}_i$, the Van-der-Pol generator model can be changed to Eq.(4b) which is just a special case of Eq.(7); for the integrate-and-fire model, if we use *logistic function* $\frac{1}{1+\exp(-\lambda(x-T))}$ to replace the step function, the integrate-and-fire model can also has the form of the Eq.(7). So the Eq.(7) can be viewed as a general representation of almost all neuron models, if we can prove the Eq.(7) can be simulated by a neural network based on the Hopfield neuron model[see Eq.(3)], then almost all neuron models can be simulated by neural networks based on the Hopfield neuron model.

$$\begin{cases} \dot{x}_1 = -a_1 x_1 + w_1 f_1(x_1, x_2, ..., x_n) + u_1 \\ \dot{x}_2 = -a_2 x_2 + w_2 f_2(x_1, x_2, ..., x_n) + u_2 \\ \vdots \\ \dot{x}_n = -a_n x_n + w_n f_n(x_1, x_2, ..., x_n) + u_n \end{cases} \quad . \quad (7)$$

Where every $f_i(x_1, x_2, ..., x_n), 1 \le i \le n$, has the continuous partial differential $\frac{\partial f_j}{\partial x_i}$ in the finite hypercubic domain $D = [a_1, b_1] \times [a_2, b_2] \times ... \times [a_n, b_n]$ of its trajectory space $TR = \{(x_1(t), x_2(t), ..., x_n(t)) : 0 \le t \le T\}$.

If a neural network of Hopfield neuron model has a layered structure, the fixed point of a neuron at the layer l is

$$U_{l,i} = \beta \sum_k w_{l,i,k} V_{l-1,i} / b_i$$
$$V_{l,i} = L(U_{l,i}) \quad . \quad (8)$$

Eq. (8) is just a perception neural network, so a perception neural network can be viewed as an abstract of static points or stable states of a real Hopfield neural network. As a continuous function can be simulated by a multi layered perception neural network with arbitrary small error, a layered Hopfield neural network can also do this, **Theorem 1** tells this fact.

Theorem 1. If $f(x_1,...,x_m)=(f_1(x_1,...,x_m),f_2(x_1,...,x_m),...,f_p(x_1,...,x_m))$ is a continuous mapping from $[0,1]^m$ to $(0,1)^p$, for anyε>0, we can build a layered neural network Ψdefined by Eq. (8), and its fixed point can be viewed as a continuous map $F(x_1,...,x_m)=(F_1(x_1,...,x_m),F_2(x_1,...,x_m),...,F_p(x_1,...,x_m))$ from $[0,1]^m$ **to** $(0,1)^p$**,** such that $|F(x_1,...,x_m)-f(x_1,...,x_m)|<\varepsilon$ **, here** $\boldsymbol{x_1,x_2,\ldots,x_m}$ are m inputs of the neural network.

Proof. According to the universal approximation theorem(Simon Haykin, 1999[6]), it is easy to prove it. □

Theorem 2 tries to prove that all kind recurrent neural networks described by the Eq.(7) can be simulated by Hopfield neural networks described by Eq.(3). The *ordinary differential equation* Eq.(7) has a strong ability to describe neural phenomena. The neural network described by Eq. (7) can have feedback. For the sake of the existence of feedback of a recurrent neural network, chaos will occur in such a neural network. As we know the important characteristics of chaotic dynamics, i.e., aperiodic dynamics in deterministic systems are the apparent irregularity of time traces and the divergence of the trajectories over time(starting from two nearby initial conditions). Any small error in the calculation of a chaotic deterministic system will cause unpredictable divergence of the trajectories over time, i.e. such kind neural networks may behave very differently under different precise calculations. So any small difference between two approximations of a trajectory of a chaotic recurrent neural network may create two totally different approximate results of this trajectory. Fortunately, all animals have only limited life and the domain of trajectories of their neural network are also finite, so for most neuron models, the Lipschitz condition is hold in a real neural system, and in this case, the simulation is possible.

Theorem 2. If $[0,T]$, +∞>T>0, is an arbitrary finite time interval, and the partial differential $\frac{\partial f_j}{\partial x_i}$ for all $f_i(x_1,x_2,...,x_n)$ and x_j in Eq.(7), $i,j=1,2...,n$ are continuous in the finite domain $\boldsymbol{D}$ of its trajectory space then every neural network $\boldsymbol{NC}$ described by Eq.(7) can be simulated by a *neural network* described by Hopfield neurons described by the Eq.(3) in the time interval $[0,T]$and the finite domain $\boldsymbol{D}$ with an arbitrary small error $\varepsilon>0$.

Proof: We can build a Hopfield neural network $\boldsymbol{HC}$ described by Eq.(3) which has n Hopfield neurons $(x_1,...,x_n)$ which simulate n neurons in Eq.(7). As Hopfield neurons use *logistic function* as their activation function, Eq.(7) should be changed to Eq.(10).

$$\begin{cases} \dot{x}_1 = -a_1 \cdot x_1 + w_1 f_1(rs(V_{x_1}), rs(V_{x_2}), \ldots, rs(V_{xn})) + u_1 \\ V_{x_1} = 1/(1+\exp(-x_1)) \\ \dot{x}_2 = -a_2 \cdot x_2 + w_2 f_2(rs(V_{x_1}), rs(V_{x_2}), \ldots, rs(V_{xn})) + u_2 \\ V_{x_2} = 1/(1+\exp(-x_2)) \\ \vdots \\ \dot{x}_n = -a_n \cdot x_n + w_n f_n(rs(V_{x_1}), rs(V_{x_2}), \ldots, rs(V_{x_n})) + u_n \\ V_{x_n} = 1/(1+\exp(-x_n)) \end{cases} \quad (10)$$

Where $rs(x) = thr - \ln((1-x)/x)$ is the reverse function of the logistic function $L(x) = 1/1+\exp(-x+thr)$.

For every $f_j(x_1,x_2,...,x_n), 1 \le i \le n$ has the continuous partial differential $\frac{\partial f_j}{\partial x_i}$, so it is a continuous and bounded function in its trajectory space $TR = \{(x_1(t), x_2(t), ..., x_n(t)) : 0 \le t \le T\}$ which is located in the finite hypercubic domain $D = [a_1,b_1]\times[a_2,b_2]\times...\times[a_n,b_n]$. Not loosing generality, we can suppose every $f_i(rs(y_1), rs(y_2), ..., rs(y_n)), 1 \le i \le n$, here $rs(y_i) = x_i$, is a continuous map from $H = [L(a_1), L(b_1)]\times[L(a_2), L(b_2)]\times...\times[L(a_n), L(b_n)]$ to [0,1]. In fact if a $f_i(rs(y_1), rs(y_2), ..., rs(y_n))$ isn't a continuous map from $\boldsymbol{H}$ to [0,1], by modifying w_i and u_i in Eq.(10), we can use a continuous map from $\boldsymbol{H}$ to [0,1] to replace it. According to the universal approximation theorem(Simon Haykin, 1999[6]), given any continuous map $f(\cdot)$ on the hypercubic $\boldsymbol{H}$ to [0,1] for any $\varepsilon > 0$, there exists a function $\boldsymbol{F}(y_1,\ldots,y_n)$ which be an approximate realization of the map $f(\cdot)$ with an arbitrary precision ε_1, $0 < \varepsilon_1 << \varepsilon$, i.e. $| F(y_1,..., y_n) - f(y_1,..., y_n) | < \varepsilon_1$, for all vectors $(y_1,\ldots,y_n)$ that lie in the input space, and $\boldsymbol{F}(y_1,\ldots,y_n)$ can be defined by an integer m and a set of real constants α_i, β_i and w_{ij}, where $i=1,\ldots, m$ and $j=1,\ldots,n$, i.e.

$$F(y_1,..., y_n) = \sum_{i=1}^{m} \alpha_i \varphi(\sum_{j=1}^{n} w_{ij} y_j + \beta_i)$$

where $\varphi(\cdot)$ is a nonconstant, bounded and monotone continuous function, for Hopfield neuron, $\varphi(\cdot)$ is the *logistic function*.

In this way, $F(y_1,..., y_n) = \sum_{i=1}^{m} \alpha_i \varphi(\sum_{j=1}^{n} w_{ij} y_j + \beta_i)$ can be computed by a m Hopfield neurons.

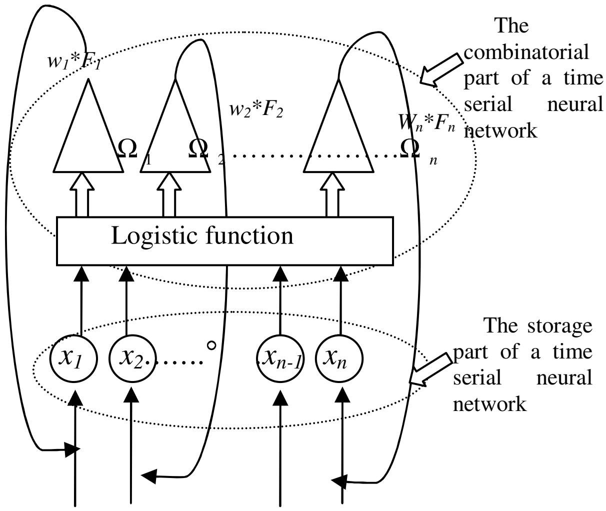

Fig. 1. Every neural network described by Eq .(7) can be simulated by a Hopfield neural network described by Eq. (3) with arbitrary small precision . Here each Ω_i is a layered neural network which has $f_i(x_1,x_2,..x_n)$ as its output at fixed point.

We denote the Hopfield neural network which computes $f_k(rs(y_1),rs(y_2),...,rs(y_n))$ as Ω_k (see Fig. 1). Every neuron φ in Ω_k takes the outputs of n neurons $(x_1,\ldots,x_n)$ as its input. The outputs of all neurons in Ω_k are summed up as $w_k \bullet F_k(y_1,...,y_n) = \sum_{i=1}^{m^K} w_k \cdot a_i^k \varphi(\sum_{j=1}^{n} w_{ij}^k y_j + b_i^k)$ (see Fig. 1) and feed back to the input of the neuron x_k, by choosing enough large **time coefficient** b_i in Eq.(3), the feedback will be fast enough, i.e. , $b_i >> \max_{1\le i\le n}(a_i)$, here a_i, $i=1..,n$ are time coefficients in Eq.(10).

Because every $f_i(x_1,x_2,...,x_n), 1\le i\le n$, is a continuous and bounded function and the partial differential $\frac{\partial f_j}{\partial x_i}$ for all $i,j=1,2\ldots,n$ are continuous in the domain ***D*** of its trajectory space ***TR*** which is finite, so the Eq.(7) accords with the Lipschitz condition, for a definite initial condition $\vec{X}(0) = (x_1(0), x_2(0),\ldots, x_n(0))$, the neural network ***NC*** described by Eq.(7) has one and only one continuous trajectory $\vec{X}_{NC}(t) = (x_1^{NC}(t), x_2^{NC}(t),..., x_n^{NC}(t)) = F_{NC}(t)$, here $F_{NC}: R \to R^n$. Similarly, when starts at same initial condition $\vec{X}(0)$, the neural network ***HC*** simulating the Eq.(10) also accords with the Lipschitz condition and has one and only one continuous trajectory $\vec{X}_{HC}(t) = (x_1^{HC}(t), x_2^{HC}(t),..., x_n^{HC}(t)) = F_{HC}(t)$, here $F_{HC}: R \to R^n$. Based on above analysis, the difference $F_{NC}(t) - F_{HC}(t)$ can be described by Eq.(11a).

$$\begin{cases} \dot{x}_1 = \eta_1(t, x_1, x_2, ..., x_n) \\ \dot{x}_2 = \eta_2(t, x_1, x_2, ..., x_n) \\ \vdots \\ \dot{x}_n = \eta_n(t, x_1, x_2, ..., x_n) \end{cases} . \tag{11a}$$

Where $|\eta_i(t, x_1, x_2, ..., x_n)| < \varepsilon_1,\ i = 1, ..., n$, and the Lipschitz condition is still hold for (11a). So the difference of the trajectories' between *NC* and *HC* described by Eq.(11b) can be smaller than ε, if we select an enough small ε_1, $0 < \varepsilon_1 << \varepsilon$. In fact, we can prove that $err_G \le nT \cdot \varepsilon_1$.

$$err_G = \int_0^T \| F_{NC}(t) - F_{HC}(t) \| dt = \int_0^T \sum_{i=1}^{n} | x_i^{NC}(t) - x_i^{HC}(t) | dt \ . \tag{11b}$$

In this way we can use a Hopfield neural network which has a standard structure to simulate an arbitrary neural network defined by Eq.(7). □

Deduction 1: For a neuron model ***N***, if the fixed point of its neuron can be viewed as a nonconstant, bounded and monotone continuous function of input, i.e. the output *y* of a neuron can be described by $y = f_{fix}(I)$ at its fixed point and $f_{fix}()$ is a nonconstant, bounded and monotone continuous function of *I*, then every neural network ***NC*** described by Eq. (7) can be simulated by a *neural network* of this neuron model ***N*** in an arbitrary finite time interval [*0,T*] with an arbitrary small error $\varepsilon > 0$.

Proof: We can prove this deduction by simply replacing the logistic function by $f_{fix}()$ in the proof of above Theorem 2. □

If we set the coefficients in The RH model [see Eq.(15)] as $a = -1,\ b = c = d = r = s = 0,$ The RH function will degenerate to the equation $\dot{x} = e^{-t} - x^3 + I_{stim}$, when time *t* trends to infinite, *x* has a fixed point $x = \sqrt[3]{I_{stim}}$ which is a nonconstant, bounded and monotone continuous function of input, so in this degenerated case, RH neural network can simulate all neural networks ***NC*** described by Eq. (7).

The Eq.(12) is the equation of the static point of a single Hopfield neuron, where I_k is the input. It is not difficult to prove that Eq.(12) can simulate binary logical operators.

$$\bar{U}_i = \sum_k w_{ik} I_k / a_i,\ \bar{V}_i = 1 / (\exp(-\bar{U}_i + T_i) + 1) \ . \tag{12}$$

3 Experiment

Simulating the Rose-Hindmarsh (RH) model neuron by a Hopfield neural network. RH model consists of a system of three coupled nonlinear first-order differential equations which can be used to describe the bursting behavior of certain neurons(Hindmash J L. and Rose R M. ,1984 [7]). The Eq. (15) is the differential equation of RH model .

$$\begin{aligned} \dot{x} &= y + ax^3 - bx^2 - z + I_{stim} \\ \dot{y} &= c - dx^2 - y \\ \dot{z} &= r\left[s\left(x - x_0 \right) - z \right] \end{aligned} \tag{15}$$

where x stands for the membrane potential, y is the fast recovery currents, z describes slow adaptive currents, and I_{stim} means the afferent input current, a, b, c, d, r, s, x_0 are constants. In Eq. (15), the membrane potential x may go to infinite under some parameters, but for a real biochemical system, a RH neuron can never have an infinite trajectory. So Eq. (15) can be simulated by a Hopfield neural network according to the Theorem 2 under the finite trajectory condition.

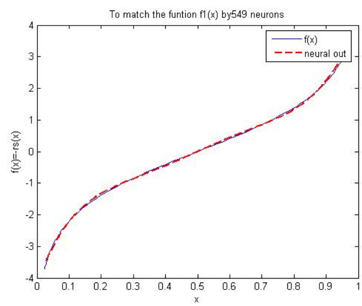

(a)

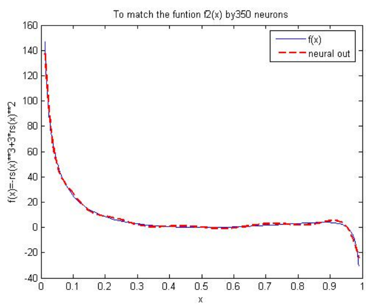

(b)

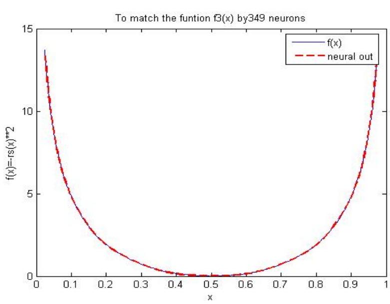

(c)

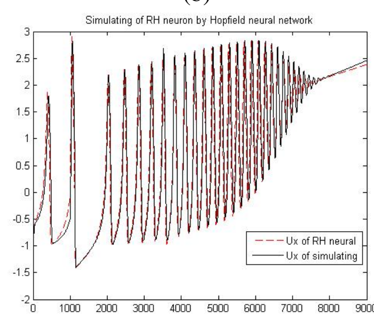

(d)

Fig. 2. The key to simulate a RH neuron by a Hopfield neural network lies in the perfect simulation of the three function f_1(x), f_2(x) and f_3(x). The simulation results are showed in (a),(b) and (c) respectively. (d) is the simulation result of a RH neuron. The dash line is the electromotive force Ux of the RH neuron and the solid line is the corresponding Ux of simulating.

In this paper, the parameter a=1, b=3, c=1, d=5, s=4 ,r=0.015, and x_0=-1.6. For the Rose-Hindmarsh neuron, the time scale is defined as 5 units of Eq. (15) equaling 1 ms. in order to simulate RH model, we change Eq. (15) to Eq. (16):

$$\begin{aligned}
&\dot{U}_x = -U_x + (a \cdot rs(V_x)^3 - b \cdot rs(V_x)^2 - rs(V_z) + rs(V_y) + rs(V_x)) + I_{stim} \\
&V_x = 1 \big/ (1+\exp(-U_x)) \\
&\dot{U}_y = -U_y + c - d \cdot rs(V_x)^2 \\
&V_y = 1 \big/ (1+\exp(-U_y)) \\
&\dot{U}_z = -r \cdot U_z + r\left[s\left(rs(V_x) - x_0\right)\right] \\
&V_z = 1 \big/ (1+\exp(-U_z))
\end{aligned} \quad . \tag{16}$$

Where $rs(x) = -\ln((1-x)/x)$ is the reverse function of the logistic function. According to the Theorem 2, it is easy to see that the key to simulate Eq. (16) by Hopfield model neurons is to simulate the three functions $f_1(x) = rs(x)$, $f_2(x) = a \cdot rs(x)^3 - b \cdot rs(x)^2$ and $f_3(x) = rs(x)^2$. The $f_1(x)$, $f_2(x)$ and $f_3(x)$ are simulated by Ω_1 with 549 neurons, Ω_2 with 350 neurons and Ω_3 with 349 neurons. The simulating result shows that a 1251 neurons Hopfield neural network can simulate a RH neuron perfectly (see Fig. 2.). The coefficients are learned by a new Back propagation approach. In order to enhance the efficiency of Back Propagation learning, we propose a novel approach denoted as Back propagation vector machine (BPVM) which combine BP approach with Support vector machine. Support vector machines (Vapnik, Esther Levin ,Yann Le Cun, 1994)[8] learn classifiers which maximize the margin of the classification: An input $z \in R^d$ is classified by sign(α ·z), and α is calculated such that for all training examples $\mathbf{z_k}$ the dot product $|\boldsymbol{\alpha} \cdot \mathbf{z_k}|$ is large. As the learning approach is not the main point of this paper, we only simply introduce our approach. In the Theorem 2, every Hopfield neural network Ω_k which computes $f_k(rs(y_1), rs(y_2), ..., rs(y_n))$ has two layers weights, in our algorithm, the output layer's weights is computed by psvm(Fung G.& Mangasarian O.,2001[5]) approach and the input layer's weight is computed by ordinary Bp approach.

BPVM algorithm:

Step 1: Randomize the input layers' weights of Ω_k ;

Step 2: If ***X*** is the input train set, computing the inner layer's output ***F***(***X***) based on ***X***;

Step 3: Using *psvm* to compute the output layer's weights according to the target set ***Y*** and ***F***(***X***);

Step 4: Back propagate the error to the inner layer by gradient-based learning and modify the input layer's weights.

Step 5: Repeat the step 2 to step 4, until the output error is small enough.

In fact, above simulation has a general meaning, if the parameter a and b of a RH neuron are changed, with a suitable weight set ($w_{i,1}$,$w_{i,2}$,$w_{i,3}$), the new function $f_i(x)$ with new parameters can be simulated by $w_{i,1} \cdot \Omega_1 + w_{i,2} \cdot \Omega_2 + w_{i,3} \cdot \Omega_3$.

4 Discussion and Conclusion

The brain science in cognitive activation studies, nowadays, pays special attention to approaches that deal with the distributed and integrated nature of neuronal processing and the questions they address and human-brain mapping plays an important role in these studies(Karl J. Friston [9]). A natural progression is then to simulate neurons embedded in micronetworks, micronetworks the local networks of brain regions, and networks within regions and the whole brain (Henry Markram 2006[101])". This is the aim of designing brain-like computers. In order to designing brain-like computers, we should firstly answer the question that which neuron model among more than 30 neuron models should be used in our designing. This is the main topic discussed in our paper. As we know it is very difficult to design or analyze a large-scale nonlinear dynamical neural network based on complex neuron models, e.g. RH neuron model. From mathematical point of view, it is impossible to replace complex neuron models by simple ones for the sake of chaos. Fortunately, all animals have only limited life and the domain of trajectories of their neural networks are also finite, for most neuron models, the Lipschitz condition is hold in a real neural system, so we can find a suitable neuron model to simulate other neuron models.

We think the neuron model we selected should have three benefits:

(1). It has a clear biological meaning, i.e. it is abstracted from a true biological background and can simulate behaves of neurons both at time dimension and space dimension.

(2). It has general meaning that it can simulate other neuron models' circuits with arbitrary precision;

(3). It is simple and easy to designing of complex neural circuits of such neuron model. It is easy to know that it is great helpful when a neuron model has a clear meaning of logic, and can be easily supervised or unsupervised trained.

In this paper, we proved that the Hopfield neural model has all above three benefits. In fact, we have designed a concrete example of Hopfield neural circuit which simulates the function of primary visual cortex (Huhong et .al. (2008)[10]) under the help of the logical character of Hopfield neural model. The paper which deals with the detailed approaches about designing brain-like computer by using Hopfield neural model in more complicate applications will be published later. In this paper, we only prove that the Hopfield neural model has universal meaning.

Acknowledgments. Supported by the National Natural Science Foundation of China (No. 61072085,60933004, 61035003, 60903141).

References

1. Markram, H.: The Blue Brain Project. Nature Reviews, Neuroscience 7, 153–160 (2006)
2. Abarbanel, H.D.I., Rabinovich, M.I., Selverston, A., Bazhenov, M.V., Huerta, R., Sushchik, M.M., Rubchinski, L.L.: Synchronisation in neural networks. Physics - Uspekhi 39(4), 337–362 (1996)

3. Hopfield, J.J., Tank, D.W.: Computing with neural networks: A model. Science 233, 625–633 (1986)
4. Barlow, H.B., Blakemore, C., Pettigrew, J.D.: The neural mechanism of binocular depth discrimination. J. Physiol. (Lond.) 193, 327–342 (1967)
5. Maass, W.: Networks of spiking neurons: the third generation of neural network models. Neural Networks 10(9), 1659–1671 (1997)
6. Haykin, S.: Neural Networks -a Comprehensive Foundation. Prentice-Hall, Inc. (1999)
7. Hindmash, J.L., Rose, R.M.: A model of neuronal bursting using three coupled first order differential equations. Proc. R. Soc. Lond., B. 221, 87–102 (1984)
8. Vapnik, V., Levin, E., Le Cun, Y.: Measuring the VC-dimension of a learning machine. Neural Computation 6(5), 851–876 (1994)
9. Friston, K.J.: Modalities, Modes, and Models in Functional Neuroimaging. Science 326(5951), 399–403 (2009)
10. Hong, Wang, Y., et al.: The universal fuzzy logical framework of neural circuits and its application in modeling primary visual cortex. Sci. China Ser. C-Life Sci. 51(9), 1–11 (2008)

A Parametric Survey for Facial Expression Database

Siyao Fu*, Guosheng Yang, Xinkai Kuai, and Rui Zheng

Department of Automation, School of Information and Engineering,
Minzu University of China, 100081, Beijing, China

Abstract. In an effort to exploring the wealth of individual and social signals conveyed by human facial cues, collecting a high quality facial database is a resource-intensive yet important task, not to mention the manual labeling the captured emotional facial expressions, which can be error prone and expensive. To date, most facial expression analysis has been based on the databases which are, however, often plagued for limited scale, lack of flexibility and static, etc. Furthermore, many existing facial expression databases are even lack of categorization and detailed organization, not to mention the functional analysis. A comprehensive survey then become necessary for current analysis and future design. This paper surveys the current representative facial expression databases, we have analyzed and categorized facial expression databases according to the functional and non-functional attributes. Our survey provides a basis for comparison of existing databases. In doing so, we assist the readers to gain insights into the technology, strategies, and practices that are currently followed in this field.

Keywords: facial expression database, survey, culture.

1 Introduction

Facial expression, in which human emotions are uniquely embodied and manifest, is one of the most powerful ways that people coordinate conversation and communicate emotions and other related cognitive cues [1]. Correspondingly, facial expression recognition plays an extremely important role in a variety of applications such as automated tools for non-verbal behavior analysis, bimodal speech processing, video conference, airport security and access control, building surveillance, human computer intelligent interaction and perceptual interfaces, etc. In an effort to exploring the wealth of individual and social signals conveyed

* This work was supported in part by 985 Funding Project (3rd Phase) of Minzu University of China (Grant 98501-00300107), Independent Research Funding Project of Minzu University of China (Multi-source information based Research on Ethnic Relationship) and Youth Funding Project of Minzu University of China (Anthropology based multi-mode Ethnic Facial Information Coding Research), Beijing Municipal Public Information Resources Monitoring Project (Grant 104-00102211)

H. Zhang et al. (Eds.): BICS 2012, LNAI 7366, pp. 373–381, 2012.

by emotional facial cues, collecting a high quality facial expression database is a resource-intensive yet important task.

Currently, there are many existing facial expression databases available, and some of them have already been proven to be quite useful, either for direct facial expression recognition, or for psychological and neurophysiological analysis. However, the problems are also evident. The majority of the current databases share the common properties like static, frontal, unsorted facial expression images captured by limited subjects without any prior background knowledge about race, culture, etc, consequently, the generalizability of different approaches to facial expression analysis remains unknown. In most data sets, only relatively universal recognized emotional facial expressions (happiness, sadness, fear, anger, disgust, and surprise) have been considered, subjects are often homogeneous with respect to age, gender and ethnic background, as well as recording conditions have been optimized. Approaches to facial expression analysis that have been developed in this way may transfer poorly to applications in which expressions, subjects, contexts, or image properties are more variable. Apart from that, facial expression should be evaluated by some other essential parameters, such as intensity and transitional representation, meaning dynamically switching from one emotion state to the others, which are physically encapsulated into the cognition process, making current static, isolated facial database an interesting yet incompetent tools to use. Let alone the discussion of some critical issue such as in-group/out-group advantage or cross-race effect phenomena. Facial expressions, as an visually explicit representation of inner emotion, are actually highly adaptive and culture dependent. With no doubt that a person's culture plays a very strong role in determining how they perceive emotions and needs to be considered when interpreting facial expression. Typical examples include the experiment conducted by Rachael et al [2] who point that culture confusions imply facial expressions are not universal and culture-specific, and in a multi-culture society, where emotion perception is interfered with cognition level, motivation behavior, culture background, educational level and regional difference, facial expression can varies as well, even faced to the same stimuli. However, to our best knowledge, there is no such literature concerning about this category.

The report we present here is the retrospective of the current facial expression databases. However, we are not going to repeat the previous review works. Rather, we focus here on 1) the efforts recently proposed in literature that have not been extensively reviewed elsewhere, and 2) address the problem of culture and ethnic background meaning. Due to limitations on space and our knowledge, we sincerely apologize to those authors whose work is not included in this paper, for an exhaustive survey of past efforts in this field, we refer the readers to the great survey work of [3], [4] and [5], all of which focus on the different topic.

2 Facial Expression Database: State of Art

We begin our discussion by briefly reviewing the current facial expression databases, many of which are taking the role of testing benchmark. These are

Table 1. Existed Facial Expression Databases

Name	Size	Elicitation Method	Environment	Expression Description
JAFEE[8]	10	Subjects watch emotion-inducing photos and videos	Indoor	6 typical emotional face and neutral emotion.
NVIE [9]	215	Subjects watch emotion-inducing videos.	Indoor	6 typical emotions.
MMI [10]	29	Subjects watch emotion-inducing videos.	Variable	79 Aus and their combinations.
UT-Dallas [11]	284	Subjects watch emotion-inducing videos.	Indoor	Happy, sad, fear, anger, boredom.
UA-UIUC [12]	28	Subjects watch emotion-inducing videos.	Indoor	Neutral, joy, surprise, disgust.
Belfast [13]	125	Subjects go interactive chats to mimic emotions.	N/A	6 typical emotional face and 6 untypical emotions.
AAI [14]	60	Subjects were interviewed to mimic emotions.	N/A	33 Aus and their combinations..
RU-FACS [15]	100	Subjects tried to mimic truth telling emotions.	Indoor	Neural, relaxed, moderately and highly aroused emotion.
AvID [16]	15	Subjects describe and mimic neural photographs.	Indoor	6 typical emotions.
GAExpression [17]	109	Unobtrusive videotaping of subjects' expression	Outdoor	Anger, humor, indifference, stress and sadness.
SALAS [18]	20	Subjects talk to artificial listener to show emotion	N/A	Wide range of emotions and related emotion states.
VAM [19]	104	Television talk show emotion scene	N/A	Negative and positive emotions and excitation emotion.
HUMANE [20]	48	Television recordings to show emotion scene.	In/Outdoor	Variant emotional states
CMU PIE [21]	68	Subjects tried to mimic truth telling emotions.	Indoor	4 basic facial expressions
		Culture Variant Facial Expression Databases.		
Name	**Size**	**Elicitation Method**	**Environment**	**Culture Background**
JAFEE[8]	10	Subjects watch emotion-inducing photos and videos	Indoor	6 All Japanese posers with typical stress and sadness.
CAFE [22]	60	Subjects tried to mimic FACS coded prototypical emotions.	Indoor	Caucasians, East Asians, and "Japanese" facial expressions.
JACFEE[23]	8	Subjects tried to mimic FACS coded prototypical emotions.	Indoor	4 Japanese, 4 Caucasian with "American" facial expressions.
KFDB [24]	1000	Subjects tried to display typical emotions.	Indoor	All Korean posers for neutral. happy, surprise, anger, and blink.
CAS-PEAL[25]	1040	Subjects tried to display typical emotions	Indoor	All Chinese posers for 5 affects.
Cohn-Kanada[26]	100	Subjects tried to mimic FACS coded prototypical emotions	Indoor	African-American, Asian, Latino.

listed in Table 1, together with details of configuration of the database such as size, elicitation method, illumination, expression descriptions. For each database, we specifically provide the following detailed information:

1, facial expression or affect elicitation method (i.e. capture description, wether the elicited facial expression displays are posed or spontaneous, note that this part is important for affect intensity evaluation procedure.)

2, size (the number of subjects and available samples),

3, affect description (category or dimension, intensity, forced choices or not)

4, labeling scheme,

5, environment constraints (illumination variation, head posture or orientation)

Examples of facial expression database include the following:

1) the famous JAFFE [8], The JAFFE dataset contains 213 images of seven facial expressions which include six basic facial expressions and one neutral expression posed by ten Japanese models. JAFFE is used as the benchmark database for several methods. Also, for its pure Japanese characteristic, sometimes it is also used for the comparison research for cross-culture exploration such as Cottrel et al [6]. JAFFE also stands out for the psychological view that woman tend to percept and display more explicit emotional facial expressions than man.

2) the CMU PIE [21]. The CMU PIE database (Fig. 2) consists 41,368 images of 68 people, under 13 different poses, 43 different illumination conditions, and with 4 different expressions. 68 captured images with under 9 total poses and 3 illumination conditions of 21 from the pose and illumination subset are selected. CMU has the merit of covering as many parameters as possible.

3, the NVIE [9]. A natural visible and infrared facial expression database, which contains both spontaneous and posed expressions of more than 100 subjects, recorded simultaneously by a visible and an infrared thermal camera, with illumination provided from three different directions. The posed database also includes expression image sequences with and without glasses.

4, The CAS-PEAL (pose, expression, accessory, lighting) database [25] is a large scale database, currently it contains 99,594 images of 1040 individuals (595 males and 445 females). It considered 5 kinds of expressions, 6 kinds accessories, and 15 lighting directions. CAS-PEAL database is now partly made available (CAS-PEAL-R1, contain 30,900 images of 1040 subjects) for research purpose. CAS-PEAL has long been viewed as the first Chinese face database, though the facial expression subset is not strong by variety standards, it still provide the possibility for comparing the facial expression between east asians and western caucasians.

5, Cohn-Kanade AU-Coded Facial Expression Database [26] contains 504 image sequences of facial expressions from men and women of varying ethnic backgrounds. Facial expressions are coded using the facial action coding system (FACS) and assigned emotion-specified labels. Emotion expressions included happy, surprise, anger, disgust, fear, and sadness.

Based on Table. 1, it is obvious that current facial expression databases focus mainly on single shot and frontal view, limited in race or ethnicity. Therefore, we propose and establish a multi-race and comprehensive facial expression database, enriching the existing databases for expression recognition and emotion inference.

3D facial expression database is not included in this talk for the sake of space, but we do think that it is a trend for the 3D recognition, in fact, there are already several database emerges such as BU-3DFE [7], which consists of 100 subjects (56 female and 44 male) of different ethnicities, each of whom elicits 6 universal facial expressions (anger, disgust, fear, happiness, sadness, and surprise) with 4 levels of intensities. for the details readers are refereed to [7].

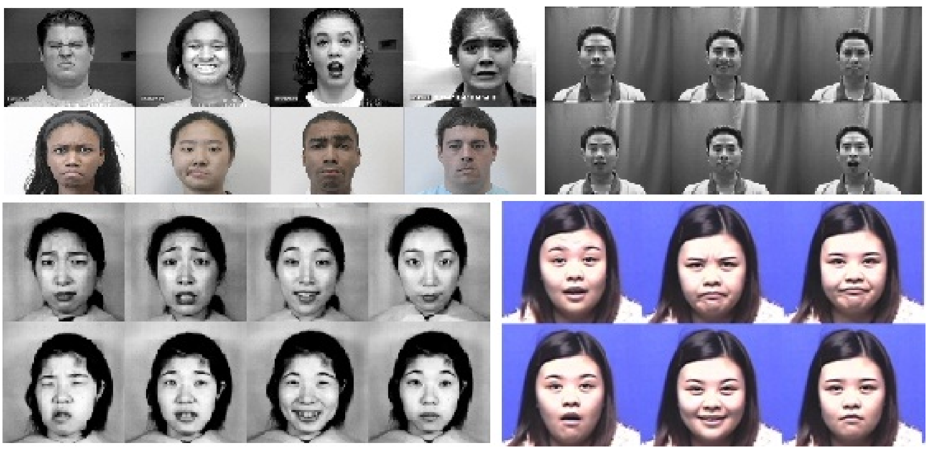

Fig. 1. Different face databases, from top left to bottom right: Cohn-Kanade AU-Coded Facial Expression Database, CAS-PEAL database, JAFFE dataset, CUN database

3 A Parametric Discussion of the Existing Databases

From the table mentioned above, we can list some essential parameters worth consideration during the design of facial expression databases:

3.1 Emotional Facial Expression Elicitor

We divide the elicitor method into three groups: 1) natural expression, in which subject are recorded with their naturally occurring emotional facial changes by watching several emotional-invocative video material, obviously, this approach takes time and effort. 2)induced emotional expression, in which specific emotional facial expression are recorded by using indirect paradigm. and 3) simulated (posed, portrayed, enacted) facial expressions, which means obtaining emotional expression following precise instruction, or portraying which means producing an expression that is typical for a given scenario, or enacting, which means producing an emotional expression based on reliving inappropriate emotional experience of ones own. Apparently, most of the existing datasets use the eliciting method based on the 'artificial' material of deliberately expressed emotions, either by asking the subjects to perform a series of emotional expression in front of cameras, or directly mimicking the typical emotional pictures. Only several datasets collected spontaneous affective photos. Therefore, most methods of automated facial expression analysis which trained on these deliberate and often exaggerated facial representation datasets may fail to generalize to the more subtlety and more implicit affect analysis applications.

3.2 Emotional Facial Expression Recording Format

Many of the existing datasets have the record of single shot of the captured picture. There are not so many datasets recorded with the high-quality video clips, which has the merit of recording emotional dynamics from the initial point to the vanishing point, offering the potentials for analyzing micro-emotional facial cues. The existing datasets are also mainly consisted of single shot, frontal viewed pictures, while being lack of multi-view variation. Correspondingly, most methods of automated facial expression analysis which trained on these datasets may be difficulties to generalize to more comprehensive, broader view.

3.3 Emotional Facial Expression Recording Condition

Other factors should also be considered into the design process. Such as lighting condition and accessaries. Illumination condition are often restricted to the single and frontal view in the most existed datasets, lack of illumination variation may degrade the facial recognition system's performance which is trained on aforementioned datasets when dealing with high lighting contrast and shade cases. Another factor needed to mention is that nearly all the datasets using the subjects recruited cross the campus, which has the advantage of easy recusation, while being plagued of lacking variation of age, which is also an essential indicator for facial expression analysis.

3.4 Ethnic Groups and Culture Background

Almost all the datasets use the subjects from the same countries or at least Anglophobe. Though we know the basic facial expressions are universal cross the cultural background, nevertheless, subjects from different cultural background may have different understanding towards the emotion and therefore they may elicits different kinds of emotional facial expressions, at least with different intensity levels. As the result, categorization of elicited facial expressions by ethnic groups or cultural background is a careful-must-taken task and intensity ranking should be evaluated with care, which are, unforgettably, hardly seen in the above mentioned datasets.

Currently a new database is attempting to change this issue. The CUN database [27] is a large-scale racially diverse face database, which covers different source of variations, especially in race, facial expression, illumination, backgrounds, pose, accessory, etc. Currently, it contains 141,500 images of 1,415 individuals (697 males and 718 females) from 56 Chinese "nationalities" or ethnic groups, as well as some other overseas subjects. The database is characterized by cross-race effect research on face and facial expression recognition. Aimed at being a multi-modular database, CUN database tries to find association between affect, eye tracking, ERP signal by building a comprehensive multi-channel database center. Fig. 2 shows the configuration of the photographic room, including lamps, camera system, etc, and some typical images of subjects. CUN database is still under construction so we exclude it from the table.

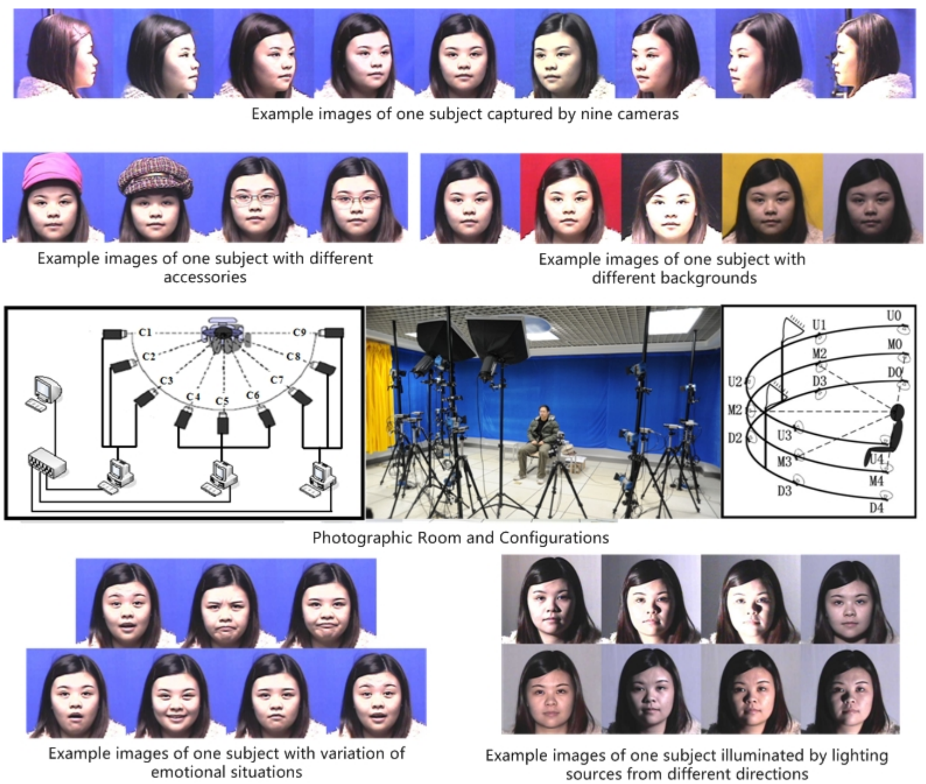

Fig. 2. Diagram showing the whole configuration of the CUN database. CUN database is a large scale database includes several subsets such as face database, audio database, EEG database, we only consider facial expression subset here. Adopted from original version in [27].

3.5 Emotional Labels

In most of the aforementioned existed databases, discrete, prototypical emotion categories (six universal facial expression categories plus one neutral) are applied as the affect labels. However, this kind of taxonomy does not apply in the databases of spontaneously elicited affects, which are usually more coarse and flexible. Some databases use dimensional descriptors based on psychological viewpoint. A typical example of emotional state based database may have descriptions such as interest, boredom, frustration, or embarrassment. These emotional states are suitable to describe the richness of our spontaneous facial cues, however, they are incompatible with the universal category-orientated datasets, consequently, the algorithms and methods developed on either base will suffer from anormalization, making the comparison of the system performance sometimes meaningless.

4 Discussions

In summary, we believe a database should meet the following criterion:

1, enough size and samples.

2, standardized and normalized elicited emotional facial expressions.

3, automatic capture system.

4, well structured storage and indexing scheme.

5, variant capture condition, including illumination, backdrop, orientation and possible accessaries, etc.

6, coverage of various kinds of ethnically variant subjects.

7, publicity.

5 Conclusion

Collecting a high quality facial expression database is a resource-intensive yet important task. This paper reviews the currently existing facial expression databases. We list some functional parameters which worth considering during the design of such databases, we hope this will be of any help for the future design of affect database and corresponding facial expression analysis approaches.

References

1. Dolan, R.J.: Emotion, Cognition, and Behavior. Science 298, 1191–1194 (2002)
2. Jack, R.E., Blais, C., Scheepers, C., Schyns, P.G., Caldara, R.: Cultural Confusions Show that Facial Expressions Are Not Universal. Current Biology 19, 1543–1548 (2009)
3. Anitha, C., Venkatesha, M.K., Adiga, B.S.: A Survey on Facial Expression Databases. International Journal of Engineering Science and Technology 2(10), 5158–5174 (2010)
4. Li, S.Z., Jain, A.K.: Handbook of Face Recognition. Springer Press (2004)

5. Zeng, Z.H., Pantic, M., Roisman, G.I., Huang, T.S.: A Survey of Affect Recognition Methods: Audio, Visual, and Spontaneous Expressions. IEEE Transactions on Pattern Analysis and Machine Intelligence 31(1), 39–58 (2009)
6. Dailey, M.N., Joyce, C., Lyons, M.J., Kamachi, M., Ishi, H., Gyoba, J., Cottrell, G.W.: Evidence and a computational explanation of cultural differences in facial expression recognition. Emotion 10(6) (2010)
7. 3DFE dataset, http://www.cs.binghamton.edu/lijun/Research/3DFE/3DFE-Analysis
8. JAFEE dataset, http://www.kasrl.org/jaffe.html
9. Wang, S., Liu, Z.L., Lv, S.L., Lv, Y.P., Wu, G.B., Peng, P., Chen, F., Wang, X.F.: A Natural Visible and Infrared Facial Expression Database for Expression Recognition and Emotion Inference. IEEE Trans. Multimedia 12(7), 682–691 (2010)
10. Pantic, M., Stewart Bartlett, M.: Machine Analysis of Facial Expressions. In: Grgic, K.D.A.M. (ed.) Face Recognition, pp. 377–416. I-Tech Education and Publishing, Vienna (2007)
11. OToole, A.J., Harms, J., Snow, S.L., Hurst, D.R., Pappas, M.R., Ayyad, J.H., Abdi, H.: A video database of moving faces and people. IEEE Trans. PAMI 27(5), 812–816 (2005)
12. Sebe, N., Lew, M.S., Cohen, I., Sun, Y., Gevers, T., Huang, T.S.: Authentic facial expression analysis. In: Int. Conf. Automatic Face and Gesture Recognition (2004)
13. Douglas-Cowie, E., Cowie, R., Schroeder, M.: The description of naturally occurring emotional speech. In: Proc. Int. Conf. Phonetic Sciences, pp. 2877–2880 (2003)
14. Roisman, G.I., Tsai, J.L., Chiang, K.S.: The emotional integration of childhood experience: Physiological, facial expressive, and self-reported emotional response during the adult attachment interview. Development. Psychol. 40(5) (2004)
15. Bartlett, M.S., Littlewort, G., Frank, M., Lainscsek, C., Fasel, I., Movellan, J.: Recognizing facial expression: Machine learning and application to spontaneous behavior. In: CVPR, pp. 568–573 (2005)
16. Gajsek, R., Struc, V., Mihelic, F., Podlesek, A., Komidar, L., Socan, G., Bajec, B.: Multi-modal emotional database: AvID. Informatica 33, 101–106 (2009)
17. Scherer, K.R., Ceschi, G.: Lost luggage emotion: A field study of emotion-antecedent appraisal. Motivation and Emotion 21, 211–235 (1997)
18. http://www.image.ntua.gr/ermis/
19. http://emotion-research.net/download/vam
20. D5i: Final Report on WP5, IST FP6 Contract no. 507422 (2008)
21. Sim, T., Baker, S., Bsat, M.: The CMU Pose, Illumination, and Expression Database. IEEE Trans. PAMI 25(12), 1615–1618 (2003)
22. CAFE dataset, http://www.cse.ucsd.edu/~gary
23. Biehl, M., Matsumoto, D., Ekman, P., Hearn, V., Heider, K., Kudoh, T., Ton, V.: Matsumoto and Ekman's Japanese and Caucasian Facial Expressions of Emotion (JACFEE): Reliability Data and Cross-National Differences. Journal of Nonverbal Behavior 21(1), 3–21 (1997)
24. Roh, R.C., Lee, S.W.: Performance Evaluation of Face Recognition Algorithms on Korean Face Database. International Journal of Pattern Recognition and Artificial Intelligence 21(6), 1017–1033 (2007)
25. CAS-PEAL dataset, http://www.jdl.ac.cn/peal/index.html
26. Cohn-Kanada AU-Coded dataset, http://vasc.ri.cmu.edu/idb/html/face/facialexpression.html
27. Fu, S.Y., Hou, Z.G., Yang, G.S.: Spiking Neural Networks based Cortex Like Mechanism: A Case Study for Facial Expression Recognition. In: IJCNN (2011)

Analysis of Pesticide Application Practices Using an Intelligent Agriculture Decision Support System (ADSS)

Ahsan Abdullah[1], Amir Hussain[2], and Ahmed Barnawi[1]

[1] Faculty of Computing and IT, King Abdulaziz University, Jeddah, Saudi Arabia
[2] Dept. of Computing Sciences & Mathematics, University of Stirling, Scotland, UK
aabdullah1@kau.edu.sa

Abstract. Pesticides are used for controlling pests, but at the same time they have impacts on the environment as well as the product itself. Although cotton covers 2.5% of the world's cultivated land yet uses 16% of the world's insecticides, more than any other single major crop [1]. Pakistan is the world's fourth largest cotton producer and a major pesticide consumer. Numerous state run organizations have been monitoring the cotton crop for decades through pest-scouting, agriculture surveys and meteorological data-gatherings. This non-digitized, dirty and non-standardized data is of little use for strategic analysis and decision support. An advanced intelligent Agriculture Decision Support System (ADSS) is employed in an attempt to harness the semantic power of that data, by closely connecting visualization and data mining to each other in order to better realize the cognitive aspects of data mining. In this paper, we discuss the critical issue of handling data anomalies of pest scouting data for the six year period: 2001-2006. Using the ADSS it was found that the pesticides were not sprayed based on the pests crossing the critical population threshold, but were instead based on centuries old traditional agricultural significance of the weekday (Monday), thus resulting in non optimized pesticide usage, that can potentially reduce yield.

Keywords: Data Mining, Decision Support, Clustering, Pesticide, Agriculture, Visualization.

1 Introduction

Cotton and cotton products are part of our everyday life, at the same time cotton is considered to be world's 'dirtiest' crop due to heavy usage of pesticides. The cotton crop is susceptible to attack by 96 worms and mite pests [2]. In view of the importance of the cotton crop, different government and private agencies monitor dynamic pest situations in the field, called as pest scouting. China is the world's biggest cotton producer and Pakistan being the fourth largest one [3]. China has one of the most extensive government pest scouting systems in the World [4]. Every year different Pakistani government departments perform pest scouting all over the Punjab province; the bread-basket of Pakistan. As a result, thousands of records are generated

H. Zhang et al. (Eds.): BICS 2012, LNAI 7366, pp. 382–391, 2012.

from pest-scouting, yield surveys, meteorological recordings and other such undertakings. The multivariate data collected from different sources has not been integrated and thus fails to provide a holistic picture and the semantic relationships. The lack of data digitization, integration and standardization also contributes to an under-utilization of the valuable and expensive historical data that is being collected for decades. This results in a limited capability to support data-driven cognitive decision making, analysis and subsequent research [5].

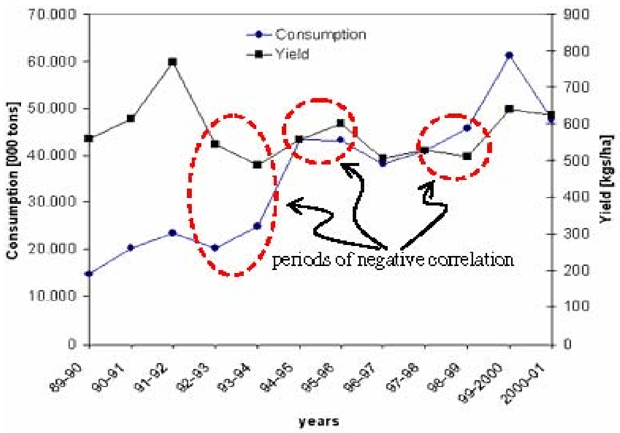

Fig. 1. Yield and Pesticide Usage in Pakistan: Source FAO (2001)

Consider Fig-1 that shows the relationship between cotton yield and pesticide usage during a 10-year period in Pakistan. The interesting observation here is the negative correlation between cotton yield and the pesticide usage i.e. when the pesticide usage increases to control pest incidence, the yield goes down, which infact should have gone up. One of the objectives of this paper is to endeavor to give a possible explanation of this apparent anomaly using the pest scouting data made available in the Agriculture Decision Support System (ADSS).

In view of the need for more informed data-driven cognitive decision making in the agriculture sector, the need for an Agriculture Data warehouse was felt resulting in the (ongoing) development of an intelligent Agriculture Decision Support System (ADSS). The ADSS project was launched at the Center for Agro-Informatics Research (C@IR) Islamabad. This initial 26-month, 35-people strong project was supported with approximately US $ 0.5 million grant by the National ICT R&D Fund. Although the initial stage the ADSS project completed in Aug. 2008 i.e. data collection, digitization, intelligent data mining tools development etc., but the invaluable semantic data mining and visualization resource is being re-used and further developed by researchers on an ongoing basis. The complete two year ADSS project report is available online [19]. The main research hypothesis of this paper is that since ADSS has already been used for tackling difficult agriculture problems, such as Bt cotton cultivation [6] and Mealybug incidence [7], therefore, ADSS can be used to address and answer other agriculture and related problems.

2 Background

In the context of this paper, a pest is an insect that damages the crop. ETL_A: Economic Threshold Level in agriculture extension is that pest population beyond which the benefit of spraying outweighs its cost. It is highly infeasible and expensive to eradicate all pests, therefore, pest control measure are employed, when pest populations cross a certain population threshold. This threshold varies from pest to pest, and from crop to crop.

Generally all hierarchical clustering heuristics begin with *n* clusters where n is the number of elements or records. Subsequently, the two most similar clusters are combined to form n-1 clusters. In the next iteration, *n-2* clusters are formed with the same logic and this process continues until we are left with only one cluster. In various hierarchical clustering heuristics only the rules used to merge clusters differ. For example, in the “Simple Linkage” approach clusters are merged by finding the minimum distance between one observation in one cluster and another observation in the second cluster. In “Furthest Neighborhood” approach, the furthest distance between two observations is taken, while in the “Average Linkage” approach the average distance between observations belonging to each cluster is considered, subsequently merging them with a minimum average distance between all pairs of observations in the respective clusters. In Ward’s method, the distance is the ANOVA sum of squares between the two clusters.

3 Related Work

Business applications of Data Warehouses is a fairly established domain, but lately lot of work has been undertaken in the area of Agriculture Data Warehouses [8], [9], [10].

A pilot intelligent ADSS based on pest scouting data was developed and demonstrated in [5]. The ADSS attempts to closely link data mining with visualization through the use of a novel graph-drawing-based biclustering technique - based on the so called crossing minimization paradigm - that has been shown to work effectively for asymmetric overlapping biclusters in the presence of noise [11]. The ADSS thus helps to provide not only a global but also a more detailed local view of the data thereby enabling the cognitive aspects of data mining to be realized. It is pertinent to note that cognitive data mining is only possible through the use of visual techniques, without which, there cannot be an effective communication between people and programs. Cotton pest-scouting data consisting of about 250 data sheets for the years 2001-02 of District Multan was processed and used in the pilot project along with some forecasted values of weather parameters. The pilot project consisted of a part-time team of 3 personnel. The work reported in this paper is based on a full-scale implementation of the ADSS using 24,000+ cotton data sheets with a full-time team of 35 professionals, thus the breadth and depth of data employed and subsequent novel analysis is very comprehensive as compared to that of the pilot system.

In [12] an agricultural spatial DSS (ADSS) frame was studied and developed to meet the increasing food demands. The ADSS was aimed at suggesting efficient strategies for problems in crop growth and food safety as well as providing timely and accurate information about crop growth and food supply. The system, based on the spatial information technologies and crop growth simulation methods, consisting of three parts i.e. i) a spatial agricultural resources data warehouse ii) a crops monitoring and simulation package and iii) a spatial decision support package for food-supply security. The ADSS was applied to the Northeast China and been proven to be a successful tool for crop growth monitoring and food security strategies. Unlike the Intelligent ADSS discussed in this paper, the ADSS [12] does not employ Data Mining or Data Visualization Techniques, no information was provided about the type of schema used for running high performance queries and resolution of ETL issues.

NASS (National Agricultural Statistics Service), USDA (U.S. Department of Agriculture) [13] has developed an easy-to-understand and easy-to-use Data Warehouse System that integrates previous survey and census data, and makes the data readily accessible to all NASS employees. Users of the integrated and generalized Data Warehouse must navigate only seven tables- a central data table containing all the survey and census data, and six corresponding dimension tables that provide all the necessary metadata to access the data readily. The ADSS developed at the C@IR is different from the NASS Data Warehouse because it uses pest-scouting and Metrological data. In addition to this, ADSS not only provides useful information to the researchers but has been basically designed for decision makers, so that they can make appropriate decisions by using OLAP (On-Line Analytical Processing) [7].

As part of the NATP (National Agriculture Technology Project), Central Data Warehouse (CDW) was developed that provided systematic and periodic information to research scientists, planners, decision makers and development agencies in the form of an Online Analytical Processing (OLAP) decision support system [14]. The ADSS is different from INARIS because it not only provides detailed analysis of pest scouting data by the decision makers and farmers using the web-based OLAP tool but also has four other applications namely, ADSS Macro, ADSS Micro, ADSS Data Mining Tool and Yield Loss Forecasting Tool developed to provide analysis at different geographical levels based on monthly and weekly grains.

4 Materials and Methods

The ADSS project aims at extraction, transformation, cleansing and subsequently using the agro-met data (being collected for decades) for analysis, decision making, research, and ultimately, to solve agriculture and related problems. In Pakistan, traditionally agricultural analysis and decision making is based on expert opinion which has the potential to suffer from subjectivity. ADSS employs in-house cutting-edge intelligent data mining and visualization tools and techniques using primary data and offers decision makers a significant advantage over traditional way of analyzing data by exploiting the semantic power of the data. To support better decision making, data inscribed on pest-scouting sheets has been collected, digitized, cleansed and loaded in the agriculture Data Warehouse. This wealth of agricultural data is then made available for cognitive analysis through the intelligent ADSS tools, which aim to closely connect data mining and visualization, to facilitate strategic analysis and support decision making by relevant stakeholders.

For the development of the ADSS the 12-step Shaku Atre [15] approach was observed as follows:

Phase-1: Planning and Design	Phase-2: Building and Testing	Phase-3: Roll-Out and Maintenance
1. Determine Users' Needs 2. Determine DBMS Server Platform 3.Determine Hardware Platform 4. Information and Data Modeling 5. Construct Metadata Repository	6. Data Acquisition and Cleansing 7. Data Transform, Transport and Populate 8. Determine Middleware Connectivity 9. Prototyping, Querying & Reporting 10. Data Mining	11. On Line Analytical Processing (OLAP) 12. Deployment and System Management

In view of the space constraints, only the key step of each phase will be briefly discussed, which are step-1: Determine user needs, Step-6: Data acquisition and cleansing and Step-10: Data Mining.

3.1 Step-1. Determine User Needs

Two Agro-Informatics Workshops were held, both were chaired by the chairman PARC (Pakistan Agriculture Research Council). The first workshop was attended by sixteen delegates from five different organizations, the second workshop by 18 delegates from eight different organizations. In the first workshop questionnaires were given to the workshop's participants, who were asked to provide their feedback, to be ultimately used as the system requirements for the Agriculture Decision Support System (ADSS). On receipt of user feedback, a team of Agriculture and IT experts brainstormed the questions and their answers, in order to incorporate the user requirements into ADSS and also to identify those questions which could be answered within the framework of ADSS. Subsequently the Working Group reviewed and approved the system requirements.

3.2 Step-6: Data Acquisition and Cleansing

This section describes the procedure followed for data collection, data organization, scanning, data-entry, cleansing and validation of data. Further details available online [19].

Data acquisition consists of a number of steps, such as i) data recorded at the field level using hand-filled sheets, a sample sheet is shown in [6] ii) transferring field data to scouting sheets by typing or hand-written, a sample sheet is shown in [7] iii) collection of data sheets by the C@IR staff and sending to project premises iv) receiving and labeling the sheets and storing in folders v) scanning of numbered sheets vi) data entry and cross checking and finally vii) data validation.

An important component of ADSS is the primary pest scouting data. Pest scouting is a systematic field sampling process that provides field specific information on pest pressure and crop injury. For over two decades the scouts of the Directorate General of Pest Warning and Quality Control of Pesticides (PW&QCP) have weekly sampled 50 points at field level in each Tehsil of the cotton-growing districts of Punjab. The current strength of PW&QCP personnel is 500+ and is headed by a Director General. Presently, 60 Tehsils are sampled on a weekly basis upto the Mouza level, resulting in the sampling of 3,000 points (farmer fields) within Punjab, with approximately 150 such points located in District Multan (with three Tehsils). Usually the sampled points are not revisited during a season, resulting in increase in geographical coverage. It is estimated that the cotton pest-scouting data accumulated to be in access of 1.5 million records, and growing. In this paper we will not go into the details of the mostly manual processes of data acquisition, but concentrate on automatic data cleansing by working on data anomalies.

3.3 Data Anomalies

The pest-scouting sheets contain non-standardized as well as erroneous data gathered by pest scouts during surveys. Moreover, errors could have been introduced during the data-entry process due to the low quality of photocopied pest-scouting sheets. The end result is a dataset which could be dirty and may not ready for scientific analysis. Data standardization and cleansing procedures are therefore performed to address these problems and anomalies. There are three main classes of data anomalies, which are categorized as follows:

Syntactically Dirty Data	Coverage Anomalies	Semantically Dirty Data
• Lexical Errors • Irregularities	• Missing Attributes • Missing Records	• Integrity Constraint Violation • Business rule contradiction • Duplication

Before proceeding with anomaly identification and resolution, we need to get an overall visual profile of the data, preferably column by column. To achieve this objective we use the “Detailed Profiling” option of our Data Profiler Tool especially for the relevant dates, for example unique value distribution. Analysis of unique value distribution helps in identification of any data hot-spots which may be cross-checked with primary data for errors, if any.

Because of space constraint, we will not discuss all the data anomalies in this paper, however, we will briefly cover only one of the semantic anomalies i.e. duplication. One way of duplicating identification is by creating a composite sort key based on the relevant attributes and then performing a sort resulting in similar or duplicate records being identified. This rather simplistic approach has a high time complexity, so the way out is the Basic Sorted Neighborhood (BSN) approach.

Figure-2 shows the screen-shot of the Data Profiling tool being used for duplicate identification using attributes of visit_date and spray_date (both not visible) along with the spray_date. The color-coded BSN results are displayed, with same color assigned to same records, which is not true for our case. This shows that there is no repetition of records using these attributes.

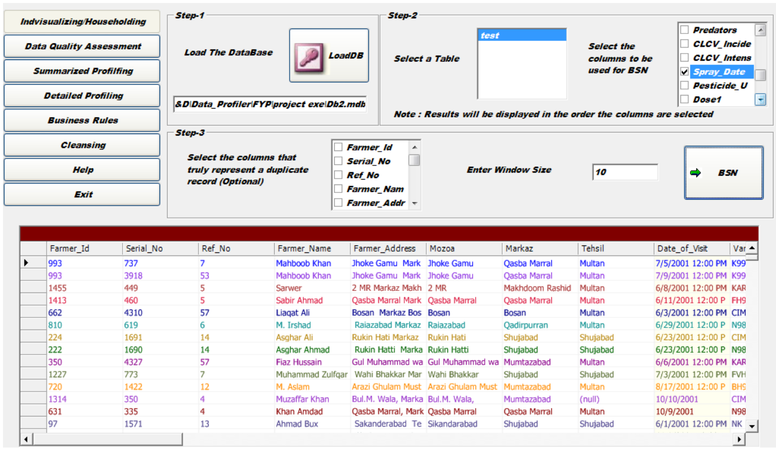

Fig. 2. Screen-shot for duplicate date identification

4 Results and Discussion

In this section the results of the cotton sowing patterns for District Multan with reference to pest incidence and time over six years period will be presented and discussed. Figure-4 shows the relationship between the numbers of sowings with reference to the day of the week for six years.

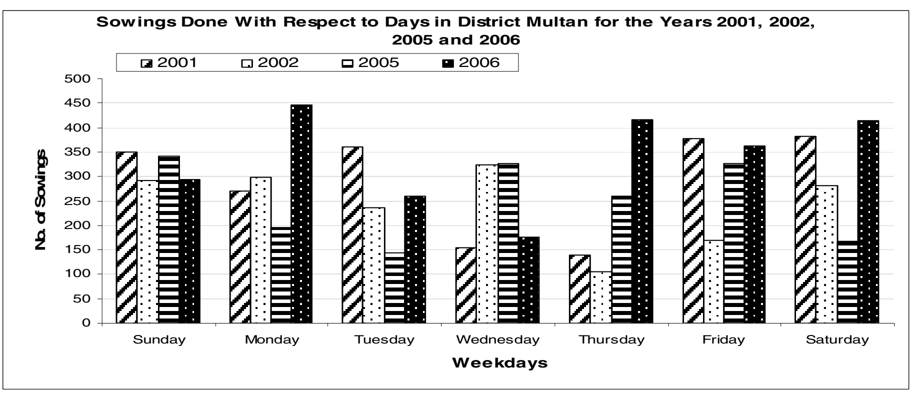

Fig. 3. Comparison of sowings done with respect to Weekdays during 6 years in District Multan

From Fig-3 no conclusive relationship is evident between the sowing date and the weekday; therefore, we perform data mining supported by visualization, such that the semantic relationships in the data are highlighted. To do this we use the data for the years 2001-2002 and 2005-2006 and categorize it into three activities i.e. i) the number of sowings as per each weekday i.e. activity_A, ii) the number of sprays as per each weekday i.e. activity_B and iii) the volume of sprays as per each weekday i.e. activity_C. The reason for considering the selected time slots is to observe the effect of farmer behavior over a five year time period. To have a consistent range of values for each of the three activities, we sort the values resulting in a ranking of each weekday for each activity with a range of values between 1 and 7. Subsequently the resulting table is clustered using Hierarchical Clustering Explorer (HCE 3.5) [20], the results are shown in Fig-4.

From Fig-4 it can be visually observed that all the three agriculture activities are clustered on the weekday of Monday (shown by dotted boundary), while the value of the weekday was not actually used in HC. Observe that for the four years considered, the activities on Monday are agriculture activities which should be synchronized with the seasonal requirements and ETL_A crossings (Fig-2) instead of any other factor. However, pest populations are not centered on weekdays, but understandably follow their own seasonal life-cycle that gets affected due to pesticide application.

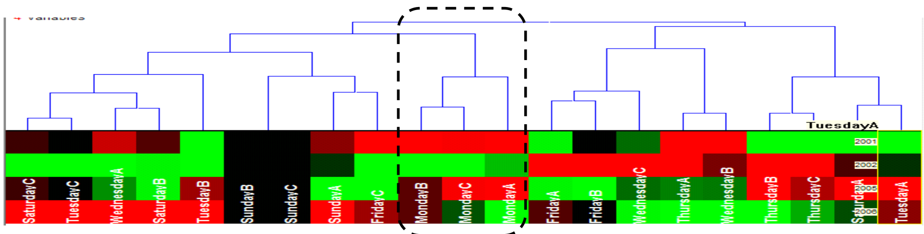

Fig. 4. Clustering of sowings and sprays with respect to weekdays during four years

A possible explanation of the Monday-centric farmer behavior is based on the caste system. Caste system has been present in the sub-continent for centuries, for a detailed study see [16], [17]. Rural Punjab is no exception, where caste, creed, religion or some other commonality brings a group of people together and forms a community. Community and intercommunity relations determine the social and economic behavior of people. Taking decisions independently is rare practice in a rural society: most of the decisions are influenced by community leaders and opinion makers, including agricultural practices. A general observation is that farmers belonging to the same community often go for the same crop, variety, pesticide and even utilization of extension services, etc. Although Pakistan is a predominantly Muslim country, but living with Hindus for thousands of years prior to advent of Islam in the subcontinent, the Muslims in the Pakistani part are also influenced by old traditions. The caste of most of the farmers whose data is used in this paper is predominantly from the post-Muslim era castes.

The seven days a week system is prevalent throughout the world, with the week-end associated with different days; such as Friday in Pakistani villages. Vedic or Hindu Muhurt (electional) astrology provides detailed guidance as to which activity will bear fruit on specific weekdays. Weekdays are given due importance in selection of election as the desired activity which bears fruit (Siddhi) when its day lord is strong, meaning the same work does not get fruitful when day lord is weak / powerless, even after extra efforts and pain, but at no meaningful gain. As per Vedic astrology, on Monday, Wednesday, Thursday and Friday all types of works are fruitful; while on Sunday, Tuesday and Saturday only prescribed activities are fruitful. Monday is said to be suited for: Agriculture, farming, gardening, fragrant trees, lotus & flowers, milk, food, food-grains etc. [18]. Thus the farmers were following centuries old traditions and spraying pesticides when it may not be required. This practice results in non optimum pesticide usage, non-lethal dose causing development of resistance in pests i.e. robust pests causing more damage to the crop and subsequent reduction in yield.

5 Conclusions and Future Work

The centuries old traditions that don't seem to be related to ground realities still seem to play a major role while making important agriculture decisions, such as when to spray and how much to spray, even though these decisions may result in loss of revenue to the farmer, pollution of the environment an reduction in yield. Centuries old habits and traditions are not likely to change even in decades, thus confirming the validity or our findings.

In the future, the visualization capabilities of ADSS will be further developed, with the introduction of animation and also a more 'natural' visual query system, in order to further improve its cognitive data mining capabilities. The application of ADSS to relevant data from other countries with a strong agricultural base, including China, is also planned.

Acknowledgements. This work was made possible by the funding of the National ICT R&D Fund, guidance of Dr. Amir Muhammed, provision of pest scouting data by Dr. Ijaz Pervaiz and the hard work of the entire ADSS team, especially Shahid Saleem (Agriculture Specialist), Salman Jeelani, Mansoor Nadeem and Syed Jawad.

References

1. EJF, The deadly chemicals in cotton. In: Environmental Justice Foundation in collaboration with Pesticide Action Network UK, London, UK (2007) ISBN No. 1-904523-10-2
2. Wilson, et al.: Crop damage and control practices with irrigated cotton in a tropical environment. Cotton Grow., Rev. 49, 272–282 (1972)
3. International Cotton Advisory Committee, `http://www.icac.org`
4. Kalaitzandonakes, N.G.: The economic and environmental impacts of Agbiotech: a global perspective. Springer (2003)
5. Abdullah, A., Hussain, A.: Data Mining a New Pilot Agriculture Extension Data Warehouse. Journal of Research and Practice in Information Technology 38(3) (2006)
6. Abdullah, A.: Analysis of mealybug Incidence on the Cotton Crop Using ADSS-OLAP (Online Analytical Processing) Tool. Elsevier Journal of Computers and Electronics in Agriculture 69, 59–72 (2009)
7. Abdullah, A.: An analysis of Bt-Cotton cultivation in Punjab, Pakistan using the Agriculture Decision Support System (ADSS). Agbioforum Journal 13(3), 274–287 (2010)
8. Malinowski, E., Zimanyi, E.: Advanced Data Warehouse Design: From Conventional to Spatial and Temporal Applications, 435 p. Springer (2008)

9. Nilakanta, S., Scheibe, K., Rai, A.: Dimensional issues in agricultural data warehouse Designs. Computers and Electronics in Agriculture 60(2), 263–278 (2008)
10. Schulze, C., Spilke, J., Lehner, W.: Data modeling for Precision Dairy Farming within the competitive field of operational and analytical tasks. Computers and Electronics in Agriculture 59(1), 39–55 (2007)
11. Abdullah, A., Hussain, A.: A new Biclustering technique based on crossing minimization. Neurocomputing 69(16), 1882–1896 (2006)
12. Wang, Z.-Q., Chen, Z.-C.: A Web-based Agricultural Decision Support System on Crop Growth Monitoring and Food Security Strategies. In: Proc. 3rd Intl. Symposium on Computer Science and Computational Technology (ISCSCT 2010), pp. 487–491 (2010)
13. Nealon, J., Yost, M.: Easy and fast data acess for everyone. National Agricultural Statistics Services, U.S. Department of Agriculture (2008)
14. Rai, A.: Data Warehouse and Its Applications in Agriculture. Agricultural Statistics Research Institute. Library Avenue, New Delhi-111, 012, India (2007)
15. Atre, S.: 12-step approach, http://www.atre.com/dw_navigator/index.html (accessed January 4, 2010)
16. Andhra Pradesh Government, Indian caste system and social stratification (Online), http://www.ap.gov.in
17. Ronald, E.: Aspect of Caste in South India, Ceylon and North-West Pakistan, p. 113. Cambridge University Press (1971)
18. What to do on specific weekdays – Guidance from Vedic Muhurt Astrology, http://www.indiadivine.org
19. ADSS project report, http://www.ahsanabdullah.com/downloads/htm
20. HCE, http://www.cs.umd.edu/hcil/multi-cluster/

Survey of the Facial Expression Recognition Research*

Ting Wu[1,2,**], Siyao Fu[1], and Guosheng Yang[1]

[1] Information Engineering College, Minzu University of China, Beijing, 100081, China
[2] College of Science, Minzu University of China, Beijing, 100081, China

Abstract. Facial expression recognition is one of the hot spots in recent years, it applies in the emotional analysis, pattern recognition and interpersonal interaction. This paper introduces the recent advances and applications in facial expression recognition from the face detection, feature extraction, classification, and the ethnic expression recognition. The methods of feature extraction are divided to several different characteristic categories. Researches of classifications are based on space or time and space. What's more, according to the facial expression recognition history and achievements, the development of ethnic facial expression recognition and the trend of facial expression recognition are given.

Keywords: Facial Expression Recognition, Facial Expression Classification, Ethnic Minority Facial Expressions.

1 Introduction

Facial expression is an important form of emotional state and mental state. Psychologist [1] Mehrabian's research shows that only 7% of the total information is passed by language, and 38% is transported by language auxiliary, such as the rhythm of speech, tone, etc. But the Ratio of information which passed by facial expression has reached 55% of the total. Therefore, a lot of valuable information can get by facial expression recognition that gives an effective way to the perceive person's consciousness and mental activity. Because of this, facial expression recognition, showing important theoretical research value, practical value and the life application value, has become an important research topic.

Facial expression recognition researches date back to the 19th century. In 1872, Darwin [2] firstly announced the consistency of expression .In his opinion the meaning of facial expressing was not judged by gender and race. In the 1970s, Ekman and Friesen [3, 4] made a pioneering work for facial expression recognition that they defined six basic expression categories of human: surprise, fear, disgust, anger,

* This work was supported in part by 985 Funding Project (3rd Phase) of Minzu University of China (Grant 9850100300107), Independent Research Funding Project of Minzu University of China (Multisource information based Research on Ethnic Relationship) and Youth Funding Project of Minzu University of China (Anthropology based multimode Ethnic Facial Information Coding Research), Beijing Municipal Public Information Resources Monitoring Project (Grant 104-00102211).

** Corresponding author.

H. Zhang et al. (Eds.): BICS 2012, LNAI 7366, pp. 392–402, 2012.

happiness and sadness which provided a way for current expression recognition research[1]. Until the 1990s, the developing of image processing and pattern recognition technology made the facial expression recognition computer automated processing possible. In 1991, Mase and Pentland proposed a new theory using optical flow method to recognize facial expression [5]. Since then, using computer technology in feature extraction and classification of facial expression has aroused widespread attention from researchers. Facial expression recognition have been widely used in human computer interaction, affective computing, intelligent control, psychological analysis, pattern recognition, security monitoring, social cognition, machine vision, social entertainment and other fields [6].

Based on research literatures at home and abroad in recent years, from the expression feature extraction, classification and face recognition, the present paper reviews the studies and research results of facial expression recognition ,then points out the trends. The rest of this article is organized as follows: Section II introduces expression recognition system framework, Section III describes the state of the art including face detection, feature extraction, training classifier , and the application and development of ethnic expression recognition , Section IV gives the development bottleneck and research trends, Section V is conclusion.

2 Facial Expression Recognition System Framework

According to people's way of thinking from face, facial expression recognition use computer for feature extraction, analysis of facial expression information, analyzing and understanding human emotions, such as happiness, surprise, anger, fear, disgust , sadness and so on. In general, facial expression recognition is divided into training and testing, shown in Figure 1.

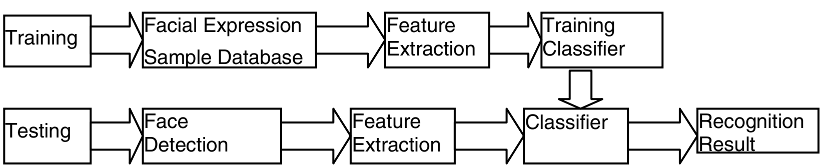

Fig. 1. Facial expression recognition system framework

In the training phase, the researchers need to extract features in the sample images, at first train the feature classification and lastly get the feature classifier. In the testing phases, first they need to detect human faces from the obtained face images then extract facial expression features, after that classifies facial expression features with the trained classifier, finally output recognition result [7].

[1] Ekman and Friesen established facial movement coding system (Facial Action Coding System, FACS) [4], with approximately 44 independent and interrelated action units(AU) to describe facial movements, and the unit's movement characteristics are analyzed for the detection of facial expression, the relationship between the expression and facial region.

3 State of the Art

3.1 Facial Expression Feature Extraction

Expression feature selection methods can be divided into three categories: deformation feature extraction method, motion feature extraction method, and statistical feature extraction method.

3.1.1 The Deformation Feature Extraction Method

Deformation feature extraction method means extracting some facial deformation informations, such as: geometric deformation or texture changes, the former one mainly refers to the changed relative distance between feature points caused by the variety of expression, the latter one mainly refers to the textures' appearance or disappearance and changes in gradient caused by the changing expressions.

Based on the geometrical feature extraction method, Gao Wen et al [8] established facial image model based on the component decomposition and combination, put forward the expression classification tree based on analyzing facial features' location and distance to express face in a set of feature vectors. Essa et al [9] constructed a parameter which can express the independent muscle motor unit on face to accurately estimate the facial deformation. Lanitis,Taylor and Cootes [10] recognized facial expression through detecting feature points' position and shape, and made a deformable model which comprised of a series of characteristic points on face. This recognition method based on the geometric feature has the following advantages: 1, It has a relatively simple and easy recognition processing; 2, It requires a small memory space due to expressing each image in a set of feature vectors, which leads to the less calculation for the feature classification;3, The feature requires less about the illumination difference. However, this method also has disadvantages: it contains incomplete facial information, no local subtle features make it easy to loss information and have not accurate judgment results.

Based on the texture feature extraction method, Liu Shanshan [11] used Gabor wavelet transform to extract facial feature from the segmented expression sub-regions, then used Fisher linear discriminate analysis for selection what can effectively eliminate the redundancy and the relativity of facial feature; Ma et al [12] proposed a method to combine the Gabor wavelet transform with the two-dimensional principal component analysis, The author did Gabor wavelet transform to extract facial feature from facial images and got the wavelet transform coefficient as the feature vector; Ye [13] used Gabor wavelet transform to extract facial feature vector from the segmented expression to structure the expression elastic graph. The texture feature extraction can contain the expression information effectively, and is insensitive to light intensity changing and individual differences, but it has a large amount of calculation that it should be cooperated with other dimensionality reduction algorithms.

3.1.2 Motion Feature Extraction Method

Motion feature extraction method is mainly used to extract some feature points or feature area's motion information from sequential expression images, such as: the movement distance and direction of feature points. The common methods include: feature point tracking, optical flow approaches, and model methods.

Feature point tracking method means tracking the movement of feature points which are chosen in face feature region, and getting parameters to do the face recognition. At present, this method has little calculation to extract only part of the feature points, but it loses some useful features. Lien et al [14] found feature point tracking useful to subtle motion such as eye blinking, but it lost tracking for large motion such as suddenly raising eye brows and mouth opening mouth. These feature points are mainly labeled by artificial which leads a big automatic tracking error.

Mase [15] used optical flow to track the movement units. Lien et al [14] analyzed the movement of entire face using the method of wavelet-based multi-resolution analysis optical flow; Otsuka et al [16] analyzed the movement of some special area such as: area around eye and mouth, etc; Jin Hui et al [17] analyzed the expression movement with feature-flow; Yang Guoliang [18] proposed a facial expression recognition algorithm based on the improved optical flow and HMM. Optical flow focuses on the facial deformation. Although it can reflect the trend of the face movement well. The method is easy to be affected by uneven illumination and non-rigid facial movement.

3.1.3 Statistical Feature Extraction Method

Statistical feature extraction method describes the characteristics of expression images by statistics, such as: histogram or moment invariant. Choudhury et al [19] processed special parts such as the eyes and eyebrows in the way of using consecutive frames subtraction, and then obtained the expression characterization. Shinoharal et al [20] used 35 kinds of high-order local autocorrelation features as face features. Other researchers calculated the moment invariant of some regions as expression features [21, 16].

Because of it’s invariance, statistical feature extraction method is more useful than other methods to the image’s rotation, translation and size variation .At the same time it requires a long time for the large amount of computing, and it is easy to ignore specific information of local subtle features.

3.2 Expression Classification

The classification algorithms are usually divided into space-based method, time and space-based method. The former mainly contains neural networks, support vector machine, AdaBoost method, K-Nearest-Neighbor (KNN), independent component analysis (ICA), Fisher linear discriminant analysis et al .The latter contains the hidden markov model method (HMM), regression neural network method, spatial and temporal motion energy templates method. In recent years, hidden markov model, artificial neural network (ANN), Bayesian classification, support vector machine (SVM) and AdaBoost have become the most mainstream method of facial expression recognition [22].

3.2.1 Methods Based on Hidden Markov Model

Hidden Markov Model (HMM) is a markov process that contains hidden unknown parameters, and can effectively describe the statistical model of the random signal information. It’s successful in speech recognition and has begun to be used in face recognition. Lien [16] used HMM to classify the extracted motion vector sequences in facial expression recognition. Yeasin et al [23] who proposed a two-step HMM analysis method trained the data set using discrete hidden markov model. Researches on HMM become more in China , Zhou Xiaoxu et al proposed an embedded hidden markov model based on AdaBoost for facial expression recognition in real time [24]. Xiaojun et al [25] proposed a face recognition method based on one-dimensional hidden markov model and singular value decomposition. HMM-based face recognition methods have the following advantages: they allow expression changes and large head rotation, do not need to retrain all the samples after adding new samples, but part of parameters are given by experience.

3.2.2 Methods Based on Artificial Neural Networks

Artificial neural network (ANN) system is an algebra arithmetic system about information processing simulated human brain neural system. Tian et al [26] proposed a facial action analyzing system based on Gabor wavelet and FACS (Facial Action Coding System), the system used neural network as a classifier and the rate of recognition classification up to 90%. Artificial neural network has the advantage of the high-speed ability due to it's parallel processing mechanism, it's distributed storage lead to the ability to recover feature extraction and have a self-learning function, while it's high parallelism and non-linear characteristic limit development to some degree.

3.2.3 Methods Based on Bayesian Network

A Bayesian network is a probabilistic graphical model which is based on Bayesian formula and presents random variables via directed acyclic graphs. Sebe et al [27] used Cauchy Bayesian classifier that characteristics were distributed by the Cauchy distribution instead of the Gaussian distribution to improve the accuracy. Based on the Bayesian model, Shan et al [28] proposed a Bayesian classification that taked into account the prior test samples' impacting while classifying a sample in the image sequences. Research [29] applied Naive Bayes classifier, tree enhanced simple Bayesian classifier and HMM as the classification of feature expression. Bayesian network can improve the classification accuracy, but it requires a bunch of parameters that part of them are given by human experiences, and the estimated result deviates from the actual result if the number of training samples is small.

3.2.4 Methods Based on Support Vector Machine

Support vector machine method is based on structural risk minimization principle for classification method. In a high- or infinite- dimensional space, it constructs a hyperplane or set of hyperplanes that training data points are marked as belonging to one of the categories which has the largest distance to other categories. Osuna et al [30] proposed a decomposition algorithm for SVM's slowly training and complexity in time and space, and the algorithm achieved good results in face detection. Because of the difficult classifier training and big computing in testing and other issues, Ma et al [31] proposed a SVM-based hierarchical structure classifier which combined a linear SVM and a nonlinear SVM, the former ruled out most of the non-face region quickly in the image while the latter confirmed face candidate region. With the advantages like structural risk minimization of support vector machine, SVM's applied researches will become more.

3.2.5 Methods Based on Adaboost Algorithm

The core idea of Adaboost is combining weak classifiers together to a stronger final classifier (strong classifier) by changing the distribution of data. Wang et al [32] proposed a classification method based on the Adaboost algorithm, the author used Haar features to construct a weak classifier space, and got a facial expression classifier using continuous Adaboost algorithm for learning. Experiment results show that this method has the same accuracy but is 300 times faster nearly than support vector machine. However research also shows that this classification is not good in small samples [33].

3.3 The Ethnic Expression Recognition's Application and Development

China is a country of 56 ethnicities, in the history of thousands each nation's facial features are not disappeared while changing, but new features emerge and some different facial features compared to other nations still exist although there is mutual fusion. Timely research and maintain each nation's facial features are conducive to find out the differences between ethnics and study the development history, migration processing of the ethnic Chinese. It is convenient for further improving the knowledge of the relationship between different ethnic groups and it also has practical application value to individual identification.

Chen et al [34] has measured 27 marks on the face of 3182 adult cases of 15 ethnic minorities and has observed the morphological characteristics. He compared the result with the Han nationality, and draw a conclution that the Northeast Manchu ethnicity and Korean approximate to Han ethnicity. Li et al [35] has described 24 observational features in 5 kinds like eye, nose, et al, in order to calculate the genetic distance among populations, and found that it was more consistent in Northwest Yunnan's Qiang groups face using the method of cluster analysis with the reported data. Duan et al [36] have established a China face database of ethnic minorities and used face recognition technology for feature extraction, collected the face of global and local features by building a deformable template of those features .Research [37] extracted the algebraic features of human face images using LDA algorithm and located feature points using Gabor wavelet and ultimately distinguished facial features of ethnic minorities after learning on the dataset by the multi-feature -classifier. The average recognition accuracy rates of Tibetan, Uygur and Mongolian are respectively 82.2% and 92% using the algebraic feature method and geometric feature method.

The characters of ethnic studies in China are: 1.Cumbersome manual operation and large time-consuming. 2. Not establish an authoritative face database of ethnic minorities 3. Less researches in ethnic identification classification.Currently, the study is still at the beginning stage [38-40], Shakhnarovich used boosting, Xiaoguang Lu and Anil K. Jain used the nearest neighbor classifier to classify Asians and non-Asians. Satoshi Hosoi et al researched the Mongoloid, Caucasian and black people's feature extraction and recognition. These studies focused on major races' facial features, but different ethnicities of the same ethnic group are studied less in interethnic and domestic. These studies in ethnic facial recognition can affect the development of ethnic facial expression recognition.

4 Challenges and Research Trend

4.1 Difficulties in Facial Expression Recognition

There are many aspects to be studied [41]: It is large time-consuming and complicated that many models' feature points or specific areas are marked by hand. The expression images contain information of both the face identity and changes in expression, so sometimes the extracted features are often a mixture of expression changes and identity characteristics. Light on the face in different directions and different intensity impact significantly on feature extraction (Figure 2),but with few studies. The obscure key areas, such as eyes, forehead, etc, will affect the feature extraction and thus interfere with facial expression recognition (Figure 3).

Fig. 2. Subject captured with variant illumination conditions

Fig. 3. The subject with different accessories

4.2 Development Trend of Facial Expression Recognition

4.2.1 Measurement of the Distance

Expression images contain the identity information and the changing information in expression. Thus, an effective, accepted and accurate definition of the expression distance of any two images needs further study.

4.2.2 Feature Extraction of Micro-expression

Micro-expression refers to the short expression lasting not more than 1/4s, it's not easy to be perceived owing to the short time and the difficulties in automatic identification, but it can express the non-subjective emotion. [42]Ekman (2002) developed a new micro-expression recognition test: Japanese and Caucasian Brief Affect Recognition Test (JACBART).

4.2.3 The Psychological Study

Facial expression reflects person's emotion, changes in face also reflect psychological changes. How to analyze human emotional changes and the emotional state of mind by using the various parameters from extracted features with knowledge of psychology is a complex, but meaningful challenge.

4.2.4

China is a multi-ethnic country, it is valuable to the expression recognition and will become a hotspot to know the relations and different between different ethnic groups' facial features.

4.2.5 The Construction of Facial Expression Database

Face images collected in commonly used facial expression databases ignore the effect of time and age. Studying the effects of age on facial expression needs to take into account wrinkles,so the facial expression sequent images should be included in different ages. The current facial expression databases collect European or Japanese faces, China researchers should pay more attention on establishing a Chinese face database of ethnic minorities. A standardized training and testing database is required that contains sequent images of people displaying spontaneous expressions under different conditions [43].

4.2.6 Three-Dimensional Face Recognition

Compared to 3D face recognition, two-dimensional image recognition is vulnerable to the adverse effects of light, the face attitude, materials covered on the face. Constructing 3D database will provide completely information in facial expression recognition. It is notable that some 3D databases have been established, such as the BU-3DFE [44], MSU [45].

4.2.7 Face Recognition Based on Multi-feature Fusion

Multi-feature recognition system is used in order to optimize feature extraction and improve the robustness. How to find a reliable and accurate algorithm for local feature extraction and integration is an important research direction.

4.2.8 The Integration of Facial Expression Recognition with other Biometric Identification Technologies

Some human biological characteristics are individualities and will not easily change, such as: facial features, eye characteristic (retina, iris), and fingerprint. It should vastly improve identify system performance to mix together face recognition and other biometric identification technologies.

5 Conclusion

Expression recognition connects with many areas and is the basis of emotional study. This paper's objective is to introduce the recent advances in facial expression recognition. In order to do this, the paper has looked at details in the various aspects of facial expression recognition and then describes the state of the art in face detection and extraction. The important parts are development of ethnic expression recognition, the challenges and development trend. There are still some difficulties, but researches of facial expression recognition have improved a lot over the past decade. Expression recognition machines will be developed and be used as an important role in real world.

References

1. Mehrabian, A.: Communication without words. Psychology Today 2(4), 53–56 (1968)
2. Darwin, C.: The Expression of the Emotions in Man and Animals, pp. 88–144. John Murray, London (1872)
3. Ekman, P., Friesen, W.V.: Constants across cultures in the face and emotion. Journal of Personality and Social Psychology 17(2), 124–129 (1971)
4. Ekman, P., Friesen, W.V.: Facial Action Coding System: A Technique for the Measurement of Facial Movement. Consulting Psychologists Press, Palo Alto (1978)
5. Mase, K., Pentland, A.: Recognition of facial expression from optical flow. IEICE Transaction E74(10), 3474–3483 (1991)
6. Jiang, B., Gu, K., Yang, G.: Research progress of Facial expression recognition. Computer Science 38(4), 25–31 (2011) (in Chinese)
7. Wang, Y.: Face Recognition Principles, methods and technology. Science Press, Beijing (2010) (in Chinese)
8. Gao, J.: Analysis and recognition of facial images. Computer Science 20(9), 782–790 (1997) (in Chinese)
9. Essa, I.A.: Coding, analysis, interpretation, and recognition of facial expressions. IEEE Transactions on Pattern Analysis and Machine Intelligence, 757–763 (1997)
10. Lanitis, A., Taylor, C., Cootes, T.F.: Automatic interpretation and coding of face images using flexible models. IEEE Transactions on Pattern Analysis and Machine Intelligence, 743–756 (2002)
11. Liu, S., Wang, L.: The local Gabor wavelet facial expression recognition algorithm based on automatic segmentation. Computer Science, 3040-3043 (in Chinese)
12. Ma, X., Yang, G., Feng, F., Ying, W., Wang, J.: Face recognition based on Gabor wavelet and two dimension principal component analysis. Computer Applications, 55–57 (2006) (in Chinese)
13. Ye, J., Chan, Y.: Facial expression feature extraction based on Gabor wavelet transform. Computer Engineering, 172–174 (in Chinese)
14. James Lien, J.-J.: Automatic recognition of facial expressions using hidden markov models and estimation of expression Intensity. Doctoral dissertation, Robotics Institute, Carnegie Mellon University (April 1998)
15. Mase, K.: Recognition of facial expressions for optical flow. IEICE Transactions on Special Issue on Computer Vision and Its Applications E74(10), 3474–3483 (1991)
16. Otsuka, T., Ohya, J.: Spotting segments displaying facial expression from image sequences using HMM. In: Proceedings of the 3rdConference on Conference on Automatic, pp. 442–447. IEEE Computer Face and Gesture Interethnic Recognition Society, USA (1998)
17. Jin, H., Gao, W.: Motion and applications of facial expressions based on the flow characteristics. Journal of Software 14, 2098–2105 (2003) (in Chinese)
18. Yang, G.: Facial expression recognition based on optical flow algorithm and HMM. Micro Computer Information, 284–286 (2008) (in Chinese)

19. Choudhury, T.A.: Pentland Motion field histograms for robust modeling of facial expressions. In: Proceeding of the 15th ICIP, USA, vol. 2, pp. 929–932 (2000)
20. Shinohara, Y., Otsu, N.: Facial expression recognition using fisher weight maps. In: Proceedings of the Sixth IEEE Conference on Automatic Face and Gesture Recognition, pp. 499–504. IEEE Computer Society, USA (2004)
21. Zhu, Y., DeSilva, L.C., et al.: Using moment invariants and HMM in facial expression recognition. Pattern Recognition Letters 23(1-3), 83–91 (2002)
22. Mao, X., Xue, Y.: Human emotional interaction. Science Press (2011) (in Chinese)
23. Yeasin, M., Bullot, B., Sharma, R.: From facial expression to level of interest: a spatio-temporal approach. In: Proceedings of Interethnic Conference on Computer Vision and Pattern Recognition, vol. 2, pp. 922–927. IEEE Computer Society, Washington, DC (2004)
24. Zhou, X., Xu, B., Wang, Y., Huang, X.: The real-time facial expression recognition based on Boost improved embedded hidden Markov model. Computer Science, 175–178, 190 (2005) (in Chinese)
25. Liu, X., Wang, D., Zhang, L.: Face Recognition based on singular value decomposition and Hidden Markov Model. Computer Science, 340–344 (2003) (in Chinese)
26. Tian, Y., Takeo, K., Cohn, J.F.: Recognizing Facial Actions by Combining Geometric Features and Regional Appearance Patterns. Carnegie Mellon University, Pittsburgh (2001)
27. Sebe, N., Cohen, I., Garg, A., et al.: Emotion recognition using a Cauchy naive Bayes classifier. In: Proceedings of the 16th Interethnic Conference on Pattern Recognition, vol. 1, pp. 17–20. IEEE Computer Society, Washington, DC (2002)
28. Shan, C., Gong, S., McOwan, P.: Dynamic facial expression recognition using a Bayesian temporal manifold manifold model. In: Proceedings of the 17th British Machine Vision Conference, pp. 84–89. The British Machine Vision Association, Edinburgh (2006)
29. Cohen, I., Sebe, N., et al.: Facial expression recognition from video sequences; temporal and static modeling. Computer Vision and Image Understanding, 160–187 (2003)
30. Osuna, E., Freund, R.: Training Support Vector Machines: an Application to Face Detection. In: Proc. of Computer Vision and Pattern Recognition, pp. 130–136. IEEE Computer Society, San Juan (1997)
31. Ma, Y., Ding, X.-Q.: Face detection based on hierarchical support vector machine. Tsinghua University (Natural Science Edition) 43(1), 35–3810 (2003) (in Chinese)
32. Wang, Y., Ai, H., Huang, C., Wu, B.: Real-time facial expression classification, Computer-Aided Design and Computer Graphics, 1296–1300 (2005) (in Chinese)
33. Guo, G.D., Dyer, C.R.: Simultaneous feature selection and classifier training via linear programming:a case study for facial expression recognition. In: Proceeding of IEEE Computer Society Conference on Computer Vision and Pattern Recognition, pp. 346–352 (2003)
34. Chen, S., Deng, G.: Differences of facial morphology-landmarks of 15 Chinese minority ethnicities. Chinese Journal of Forensic Medicine (1999) (in Chinese)
35. Li, P.F., Zhang, M.-H.: Cluster analysis of eight ethnic groups' face observed features in Northwest Yunnan. Fudan University (Natural Science) 05 (2001) (in Chinese)
36. Duan, X., Wang, R., Liu, H., Shi, S.: Research on Facial Features of Ethnic Minorities Based on Face Recognition. The Proceedings of Dalian Minzu University 11 (2009) (in Chinese)
37. Duan, X., Wang, R., Liu, X.: Minorities Features Extraction and Recognition of Human Faces. Computer Science 08 (2010) (in Chinese)

38. Shakhnarov, G., Viola, P., Moghaddam, B.: A unified learning frmnework for real tine face detection and classification. In: Proceedings of the Fifth Intemational Conference on Automatic Face and Gesture Recognition, pp. 16–23 (2002)
39. Lu, X., Jain, A.K.: Ethnicity identification from face images. Bull. Inst. Math. Acad. Sinica (33), 77–87 (2005)
40. Hosoi, S., Takikawa, E., Kawade, M.: Ethnicity estimation with facial images. In: Proceedings of the Sixth IEEE Interethnic Conference on Automatic Face and Gesture Recognition, vol. 110, pp. 10–16 (2004)
41. Zhu, M.: Study on facial expression recognition based on manifold learning. Central South University; Doctoral Thesis (2009) (in Chinese)
42. Ekman, P.: MicroExpression Training Tool (METT) (retrieved April 15, 2002)
43. http://www.wikipedia.org/
44. Yin, L.J., Wei, X.Z., Sun, Y., et al.: A 3D facial expression database for facial behavior research. In: Proceedings of 7th International Conference on Automatic Face and Gesture Recognition, Southampton, pp. 211–216 (2006)
45. Lu, X.G., Jain, A.K., Colbry, D.: Matching 2.5D face scans to 3D models. IEEE Transactions on Pattern Analysis and Machine Intelligence 28(1), 31–43 (2006)

The Intelligent Identification and Elimination of Non-precipitation Echoes in the Environment of Low-Latitude Plateaus

Jian Wang[1,4,**], Na Zhao[2,3,*,**], Peng Li[2], Yong Yu[2], Fei Dai[2], Zhongwen Xie[2], and Jianglong Qin[2]

[1] College of Information Engineering and Automation, Kunming University of Science and Technology, Kunming, China
[2] Yunnan University, Kunming, China
[3] Key Laboratory in Software Engineering of Yunnan Province, Kunming, China
[4] Computer Technology Application Key Laboratory of Yunnan Province, Kunming University of Science and Technology, Kunming, China
{obcs2002,yuy1219}@163.com, {zhaonayx,xiezw56}@126.com, {lipeng,qinjianglong}@ynu.edu.cn, flydai.cn@gmail.com

Abstract. Considering the important reference value of weather radar data in the process of weather modification and based on the analysis of historical weather modification data of Yunnan province, china, and the study of various non-precipitation removal algorithms, this paper proposed a new model of intelligent identification and elimination of non-precipitation radar echoes in the environment of low-latitude plateaus, which has been proven to be effective in practical use.

Keywords: Intelligent recognition, Neighborhood average, Field incremental, Weather radar, Radar echoes.

1 Introduction

Echoes in radar reflectivity data do not always correspond to precipitating particles. Echoes on radar may result from biological targets such as insects, birds, or wind-borne particles; from anomalous propagation or ground clutter; or from test and interference patterns that inadvertently seep into the final products. Although weather forecasters can usually identify and account for the presence of such contamination, automated weather-radar algorithms are drastically affected. According to statistical data of 2 months and 60 months WSR288D precipitation product conducted by Moszkowicz, et al. [1], Joss et al [2], the estimated error on precipitation caused by ground echo reached 15% and 13% respectively. Hence, a completely automated algorithm that can remove regions of non-precipitating echo, such as ground clutter, anomalous propagation, radar artifacts, and clear-air returns, from the radar

* Corresponding author.
** These authors contributed equally to this work.

H. Zhang et al. (Eds.): BICS 2012, LNAI 7366, pp. 403–410, 2012.

reflectivity field would be very useful in improving the performance of other automated weather-radar algorithms.

2 Relative Work

Research on the removal of non-precipitating echoes include but not limited to: using chaos theory to classify radar echoes and to generate various filtering algorithm on the WSR288D data [3-6]; using the characteristics of 3-dimentional radar reflectivity factor remove the noise that correspondent to “bad echoes” [7-8]; utilizing neural networks(NNs)to classify pixels in WSR-88D data as either anomalous propagation/ground clutter (AP/GC) or good echo[9]. Several research groups from European have endeavored to do the same research based on the data gathered from radar, satellite, ground precipitation and digital forecasting products [10-13]; Experts from China, LiPing Liu, et al., carried out the research of ground clutter identification and removing based on the characteristics of dual polarization radar data products[14]. The researches mentioned above has been performed through analyzing the characteristics of contamination in weather-radar data and a series of automated algorithms have been designed.

This paper discusses a intelligent echo-filtering algorithm based on the examining of the non-precipitation echoes from the historical Doppler radar data in the region of Yunnan, southwest P.R.C. This algorithm has been proven effective in practice.

3 The Characteristics of Weather Modification of Yunnan

Yunnan-Guizhou Plateau, the low-latitude plateau located in southwest China and southeast of Qinghai-Tibet Plateau, is geographically near to the two heat and water vapor source of South China Sea and the Bay of Bengal. The downpour-causing mesoscale convective systems occurs frequently due to the influences of the East Asian summer monsoon, the Indian southwest monsoon, the cold air mass from the north and Tibetan Plateau, coupled with the complicated factor of terrain elevation. The World's three major weather issues: low-latitude, the role of large terrain, tropical seas, are significantly manifested in this low-latitude plateau.

Affected by the factors such as the tropical and sub-tropical weather systems, the two conveyor belt of South China sea and the Bay of Bengal, and the terrain, Yunnan suffered a high frequency of weather disasters which influenced greatly on local economies, social development, people’s life and property. Hence, the weather modification of Yunnan has a long way to go.

4 The Model of Intelligent Identification and Elimination of Non-precipitation Echoes

The biggest difference between the precipitation echoes and non-precipitation echoes is the relative color discontinuous and the discrete property on distribution in product of Z, V, W. the improper smoothing processing of radar echo images will deteriorate the image quality and blur the boundary or the outline of an image. How to filter the bad echoes form the original images while keeping the details of precipitation echoes unchanged as much as possible has became the main issue in the area of radar reflectivity data processing.

In addition to taking full account of the relationship between computational efficiency and effect, there are several principles need to comply with when modeling:

In the model design, taking full account of computational efficiency and the relationship between the game calculation results based on the need to comply with the following principles as the concept of: (1)accuracy, to ensure the data integrity and accurate when filtering;(2)independence, to filter the echo noises according to each characteristic independently; (3)plurality, to utilize pluralistic data to its maximum including pluralistic data layers (Z, V, W, etc.) and spatial layers (different elevation data) and some other live data.

In our model, we did our identification and elimination tasks by resorting to the image processing technologies and exploiting the data of pluralistic data layers. This paper discusses two image recognition algorithms that are designed for the echo-filtering, which has been tested on the data from the Doppler radar in Yunnan province.

5 Using Neighborhood Average Algorithm to Identify and Eliminate Non-precipitation Echoes

The idea of neighborhood average:

Let us assume that the image prior processing is f(x,y) and image after is g(x,y), then the smoothing process of neighborhood average algorithm is given by mathematical equation below:

$$\mathrm{g(x,y)}=\frac{1}{M}\sum_{(m,n)\in s} f(x-m, y-n) \tag{1}$$

Where M is the total number of pixels in M's neighbor field, S is the neighbor field determined before where pixel (x,y) is excluded.

For example, the neighbor field with radius of 1 is given by $S_1 = \{(x, y+1), (x, y-1), (x+1, y), (x-1, y)\}$, correspondingly, M=4; the neighbor field with radius of $\sqrt{2}$ is given by $S_{\sqrt{2}} = \{(x, y+1), (x, y-1), (x+1, y),$ $(x-1, y), (x-1, y-1), (x-1, y+1)$ $(x+1, y+1), (x+1, y-1)\}$;, the corresponded M=8. Using convolution to represent equation (1), we obtain:

$$g(x,y)=h(x,y)*f(x,y) = \sum_{(m,n)\in s}\sum h(m,n)f(x-m,y-n) \quad (2)$$

It is obvious that, correspondent to the neighborhood with radius of 1, the h(x,y) is $\frac{1}{4}\begin{bmatrix}0&1&0\\1&0&1\\0&1&0\end{bmatrix}$, the h(x,y) corresponding to the neighborhood with radius of $\sqrt{2}$ is $\frac{1}{8}\begin{bmatrix}1&1&1\\1&0&1\\1&1&1\end{bmatrix}$.

The advantages of neighborhood average is its simplicity and high speed of computation, the disadvantages is it blurred the image and the bigger the neighborhood is , the more the image blurred. The figure below shows the contrast of echo images before and after smoothing:

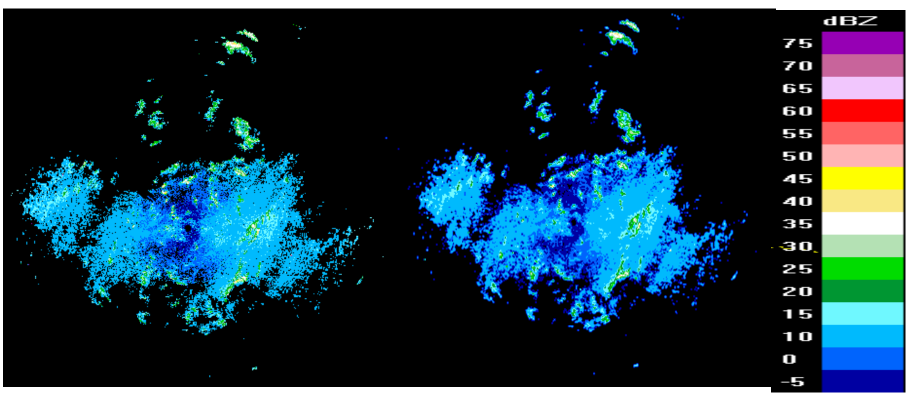

a. original radar echo b. radar echo after smoothing

Fig. 1. Radar Echo

6 Using Field Incremental Algorithm to Identify and Eliminate Non-precipitation Echoes

The idea of field incremental[15] is: gathering together the pixels with similar characteristics to form the field and choosing a "seed pixel" within this field to use it as the starting point of grow, to merge those neighboring pixels who have the characteristics that is similar to the "seed pixel" into the field where the "seed pixel" is located. Once the new pixel is merged, a new round of choosing and merging process is carried out until there is no more available pixels n the neighboring area. Thus, a field has grown.

Assuming that we use array C[500*500] to save the dbz value of C, the data of radar echo reflectivity ratio. In array C, the white grid has a null value while the black grid has value of C[x,y].

We perform filed incremental algorithm form the starting point (x4,y3).

Assuming we have an array scan[] with initial value scan[0]=(x4,y3):

0	1	2	3	4	5	6	7	8	9
1									
2			3	2	1				
3			4	x4, y3	0				
4			5	6	7				
5									
6									
7									
8									
9									

1. Starting from scan[0], check the ‘0’ direction of (x4,y3) that is saved in scan[0]. We discover the pixel on ‘0’ direction of (x4,y3) is (x5,y3), which is not equals to zero, thus we save (x5,y3) into scan[1];
2. Check the ‘1’ direction of (x4,y3) that is saved in scan[0]. The pixel (x5,y2) equals to zero, thus no operation occurs;
3. Continue checking the ‘2’ direction of (x4,y3) that is saved in scan[0]. The pixel (x4,y2) is not equals to zero, thus save (x4,y2) into scan[2];
4. Continue checking the direction of ‘3’, ‘4’, ‘5’, ‘6’, ‘7’ one by one, Save the pixels who’s value are no null into array ‘scan’;
5. After done with all the eight directions of scan[0], move present pointer to subsequent position and begin checking the eight direction of scan[1]. If the pixels checked are exist in scan generated previously, then none operation is occurred. Similarly, add those pixels which are not exist in the array of scan to scan;
6. Repeat the operations described above till the pointer of array scan reach its last position.

7. Till now, the array of scan has recorded all the grids that are neighboring the coordinate of (x4, y3) which is chosen by user as the starting pixel. These grids constitute the exact echo field that are ready to be extracted from the image.

In our field incremental algorithm, a non-precipitation echo is identified by counting the total number of grids of a certain field and comparing it to a pre-set limit value(threshold). A bad echo is identified and eliminated if the grid number is less than the threshold. See Fig.2.

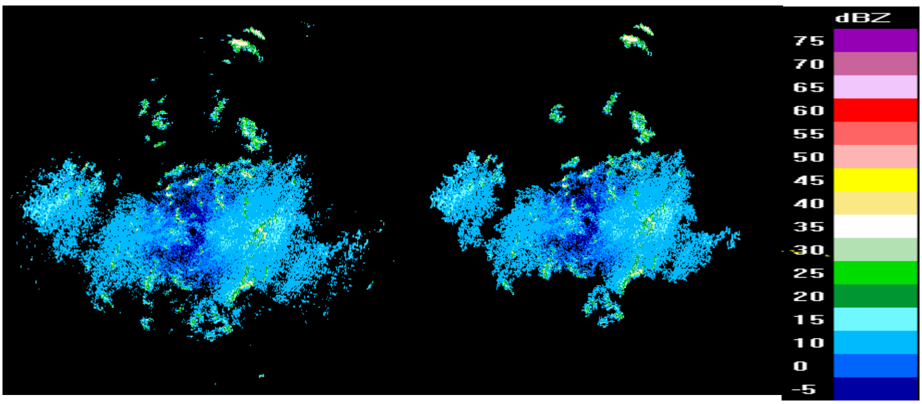

a. original radar echo b. radar echo after smoothing

Fig. 2. Radar Echo

7 Summary

To verify effect, we tested the samples of weather radar echoes of Yunnan province by using the two algorithms given above. The test results show that:

1. The two algorithms of neighborhood average and filed incremental can be used to identify and eliminate the unwanted radar echoes.
2. Compared with field incremental, The effect of neighborhood average algorithm is not obvious and it causes certain degree of echo data loss.
3. Field incremental algorithm provides a processed image with better quality and cleaner boundary. Besides, the no-data-loss attribute of this algorithm helps to improve the whole image processing effect furthermore.

We conclude that the use of field incremental algorithm to Yunnan weather radar echoes for noise elimination is a practical approach. Meanwhile, since the field incremental algorithm can effectively identify the precipitation echo from the non-precipitations, thus it laid a foundation for the further identification of the storm.

Acknowledgments. This work has been supported by the National Science Foundation of China under Grant No. 60963007, by the Key Subject Foundation of School of Software of Yunnan University and the Open Foundation of Key

Laboratory in Software Engineering of Yunnan Province under Grant No. 2010KS01, by the Science Foundation of Yunnan Province, China under Grant No. 2010CD026, 2011FB036, 2010ZC030, by the Science Foundation of Yunnan Province Education Department of China under Grant No. 2011Y388, by the Science Foundation of Key Laboratory in Software Engineering of Yunnan Province under Grant No. 2011SE05, 2011SE04, by the Postgraduates Science Foundation of Yunnan University under Grant No. ynuy201131, by the Education Innovation Foundation for Students of School of Software of Yunnan University Grant No.33.

References

1. Moszkowicz, S., Ciach, G.J., Krajewski, W.F.: Statistical detection of anomalous pattern in radar reflectivity patterns. J. Atmos. Oceanic. Technol. 11, 1026–1034 (1994)
2. Joss, J., Lee, R.: The application of radar-gauge comparisons to operational precipitation profilecorrections. J. App. Meteor. 34, 2612–2630 (1995)
3. Kessinger, C., Ellis, S., Van Andel, J.: The radar echo classifier: A fuzzy logic algorithm for the WSR-88D. In: 19th Int'Conf. on Inter. Inf. Proc. Sys. (IIPS) for Meteor Ocean, and Hydr., Amer. Meteor. Soc., Long Beach (2003)
4. Saffle, R.E., Istok, M.J., Johnson, L.D.: NEXRAD open systems-progress and plans. In: 17th International Conference on Interractive Information and Processing Systems (IIPS) for Meteorology, Oceanography, and Hydrology, January 14-18, pp. 97–100. American Meteorological Society, Albuquerque (2001)
5. Kessinger, C., Scott, E., Van Andel, J., et al.: NEXRAD data quality optimization. NCAR Annual Report FY98, p. 154 (Available from the National Center for Atmospheric Research, Research Applications Program, Atmospheric Technology Division, Boulder, CO 80307) (1998)
6. Pratte, F., Ecoff, D., Van Andel, J., et al. AP clutter mitigation in the WSR-88D. In: 28th Radar Meteor. Conf., AMS, Austin, TX, 7212 (September 1997)
7. Zhang, J., Wang, S., Clarke, B.: WSR288D reflectivity quality control using horizontal and vertical reflectivity structure, http://ams.confex.com/ams/pdfpapers/81858.pdf
8. Steiner, M., Smith, J.A.: Use of three-dimensional reflectivit y structure for atomated dtection and removal of nonprecipitating echoes in radar data. J. Atmos. Ocean Technol. 19, 673–686 (2002)
9. Grecu, M., Krajewski, W.F.: An efficient methodology for detection of anomalous propagation echoes in radar reflectivity data using neural networks. J. Atmos. Ocean Technol. 17(2), 121–129 (2000)
10. Pamment, J.A., Conway, B.J.: Objective identification of echoes due to anomalous propagation in weather radar data. J. Atmos. Ocean Technol. 15, 98–113 (1998)
11. Joss, J., Lee, R.W.: The application of radar-gauge comparisons to operational precipitation profile corrections. J. Appl. Meteor. 34, 2612–2630 (1995)
12. Magaldi, A., Bech, J., Delgado, G.: Filtering weather radar AP echoes with MSG observations and NWP data. In: Proceedings of ERAD 2006 (2006), http://www.grahi.upc.edu/ERAD2006/proceedingsMask/00053.pdf
13. Bovith, T., Gill, R.S., Overgaard, S., et al.: Detecting weather radar clutter, using satellite-based nowcasting products. In: Proceedings of ERAD 2006 (2006), http://www.grahi.upc.edu/ERAD2006/proceedingsMask/00041.pdf

14. Liu, L., Wang, Z.: The Properties of Cloud and Clutter Echoes Measured by Dual Linear Polarization Radar and Discrimination 15(3), 303–310 (1996)
15. Sun, J., Yang, C.: Computer graphics. Tsinghua University Press, Beijing (1998)
16. Zhao, N., Dai, F., Yu, Y., Li, T.: An Extended Process Model Supporting Software Evolution. In: Proceedings of 2008 International Symposium on Intelligent Information Technology Application (IITA 2008), Shanghai, China, pp. 1013–1016. IEEE Computer Society (December 2008)
17. Zhao, N., Li, T., Yang, L.L., Yu, Y., Dai, F., Zhang, W.: The Resource Optimization of Software Evolution Processes. In: Proceedings of 2009 International Conference on Advanced Computer Control (ICACC 2009), Singapore, pp. 332–336 (January 2009)
18. Zhao, N., Wang, J., Li, T., Yu, Y., Dai, F., Xie, Z.: ESDDM: A Software Evolution Process Model Based on Evolution Behavior Interface. In: Chen, R. (ed.) ICICIS 2011 Part II. CCIS, vol. 135, pp. 562–567. Springer, Heidelberg (2011)
19. Wang, J., Zhao, N., You, J., Li, L., Zhao, L.: A Software Evolution Process Model under the Circumstances of Cloud Computing. Applied Mechanics and Materials 55-57, 1370–1375 (2011)
20. Wang, J., Zhao, N., Xie, Z., Yu, Q., Liu, J.: The Performance Analysis on a Software Evolution Process Model under the Circumstances of Cloud Computing. Applied Mechanics and Materials 55-57, 1376–1381 (2011)
21. Na, Z., Yang, Z., Tong, L.: A Method of Modelling and Performance Analysis for Concurrent Development Process of Software. In: Proceedings of the 11th Joint International Computer Conference, pp. 803–809. World Scientific, New Jersey (2005)
22. Wang, J., Zhao, N., Du, W., Zhao, Y., Qian, Y., Jiang, Z.: Using Fuzzy Clustering Method to Classify the Component in the Process of Software Evolution. Information Technology Journal 11(3), 396–398 (2012)

Road Sign Detection and Recognition from Video Stream Using HSV, Contourlet Transform and Local Energy Based Shape Histogram

Usman Zakir[1], Eran A. Edirishinghe[1], and Amir Hussain[2]

[1] DIRG, Department of Computer Science, Loughborough University LE11 3TU
[2] COSPIRA laboratory, Division of Computing Science,
School of Natural Sciences University of Stirling, Stirling FK9 4LA
{u.zakir,e.a.edirisinghe}@lboro.ac.uk
a.hussain@cs.stir.ac.uk

Abstract. This paper describes an efficient approach towards road sign detection and recognition. The proposed system is divided into three sections namely; Colour Segmentation of the road traffic signs using the HSV colour space considering varying lighting conditions, Shape Classification using the Contourlet Transform considering occlusion and rotation of the candidate signs and the Recognition of the road traffic signs using features of a Local Energy based Shape Histogram (LESH). We have provided three experimental results and a detailed analysis to justify that the algorithm described in this paper is robust enough to detect and recognize road signs under varying weather, occlusion, rotation and scaling conditions using video stream.

Keywords: Road Signs, HSV, Contourlet Transform, LESH, And Autonomous Vehicles.

1 Introduction

RSDR (Road sign detection and recognition) has drawn considerable research attention in recent years, due to its challenging nature as a computer vision problem. Road signs have a direct impact on ones daily life as possible life threats can easily be formed due to lack of concentration or ignorance. In recent years, a number of Driver *Assistance Systems* have been proposed and implemented including vision-based algorithms, claiming to be efficient towards the RSDR. In addition, due to increased amount of possible threats on the roadside the impact of the road signs on the road users has considerably increased during the last decades. Many new road signs have been introduced according to the necessity and due to increase usage of the roads. Vehicle drivers specially need to learn to identify all road signs for road safety. For example drivers require the knowledge of cyclist signs, pedestrian signs, obligatory signs and advisory signs etc. and ignorance of any sign can cause possible accident hazards. In conjunction to other ADAS *(*Advanced Driver Assistance Systems) such as lane departure warning systems, in-car navigation systems, adaptive cruise control

H. Zhang et al. (Eds.): BICS 2012, LNAI 7366, pp. 411–419, 2012.

system, automatic parking etc., the RSDR systems help in detecting and translating the road signs for the attention and understanding of drivers. Specifically, drivers with visual impairments can benefit from this important computer based visual aid. In more sophisticated systems, the RSDR systems can utilise other features of ADAS such as adaptive cruise control system to automatically drive the vehicle according to varying road speeds. Highway agencies and road maintenance engineers have the responsibilities to maintain the roads and the state of signposting, which are vital for the safety of the road users. The RSDR can be used for road sign inventory and inspection purposes. Damaged, occluded, tilted, rotated, colour faded road signs can be recognised and replaced to reduce possible risks. With the RSDR, the inventory and inspection process can be made semi automatic where video footage of the road with signage information is recorded, prior to locating and investigating a particular damage. Generally, road signs consist of three properties; firstly colours such as Red, Green, Blue and Brown etc. represent them. Secondly, they consist of a particular shape such as Circular, Triangular, Octagonal, and Square etc. The inner contents of the road signs represent the third property, which may vary depending on the application of the road sign. In this paper we have considered the importance of using these properties separately by considering different problems including various lighting conditions, scaling, angular rotation and occlusion.

2 State of the Art

This section introduces existing literature in the application domain of the RSDR. The study of these approaches will conceptually compare the performance of the state-of-the-art to the performance of the proposed approaches. This allows fair comparison, particularly when no standard dataset is available for researchers to carry out performance analysis. Fig 1 illustrates the general framework used in the majority of the RSDR approaches proposed in the literature. These approaches largely differ due to the differences in the algorithms used within each of the three functional blocks of Fig 1.

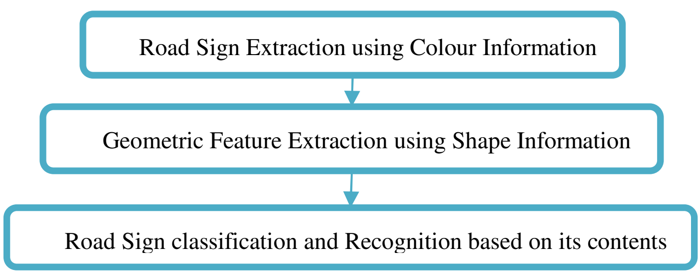

Fig. 1. General framework of Road Sign Detection and Recognition

Road sign detection from an image or image sequence is the first key step of the RSDR. An extensive investigation of existing literature [1] , [2] has been made which reflects that using the properties of colour; shape or joint information carries out the detection step. Secondly road sign recognition is performed on the contents of the candidate road signs and is mostly dependent on an extensive shape analysis and classification. In addition, road sign tracking is adopted by some researchers to enhance the accuracy of the detection and recognition stages and to reduce the computational cost of having not to repeat the above processes on each video frames. A detailed taxonomy is provided in [2] shows the varying ranges and combinations of the algorithms utilised by the RSDR systems in the literature within the three key stages (see Fig 1). Colour based segmentation is achieved by using different colour models, Shape is also considered as an important feature of the road sign representation and Contents are recognised by utilizing various feature extraction techniques and classifiers. The next section aims to overcome previous research gaps in designing a robust road sign detection and recognition system that is capable of performing on video streams under wide variations of illumination and environmental conditions.

3 System Overview

The proposed road sign detection and recognition system comprises of three stages, which are detailed in this section. Fig 2 gives an overview of the road sign detection and recognition framework.

3.1 Colour Segmentation

The Taxonomy presented in [2] highlights the fact that the colour segmentation is majorly initiated by employing a computer based colour space. Video footage/images captured by a digital camera are not always appropriate to perform the desired image processing tasks. Different video systems such as NTSC (National Television System Committee), PAL (Phase Alternating Line) and SECAM (Séquentiel Couleur à Mémoire) that are used to capture the Videos/images, significantly affect the original (i.e. raw) pixel intensity values by Gamma Encoding [3]. The Gamma is represented with the Greek letter γ, has encoding and decoding standard values according to the above-mentioned video systems. The videos/images captured for experimental purposes have adopted the NTSC video system, which encodes gamma at the rate $\gamma = 1/2.2$. Therefore, this non-linearity in the videos/images is required to be decoded in order to achieve pre processing task prior to Pixels of Interest (POI) selection by using HSV (Hue, Saturation, and Value) colour space [1], [4]. In the segmentation process pixels belonging to Red, Blue and Green colours, are represented by 1 and rest of the pixels are treated as background or 0. The corresponding bounding boxes of the segmented object(s) are analysed according to its centre and corner points as illustrated in [1].

3.2 Shape Classification

Apart from colour of the road sign, which was the focus in earlier section, shape is the second most distinctive attribute that can be used to further identify the type of a road sign. The input images to the shape classification module are the binary images resulting by applying the colour based segmentation algorithms.

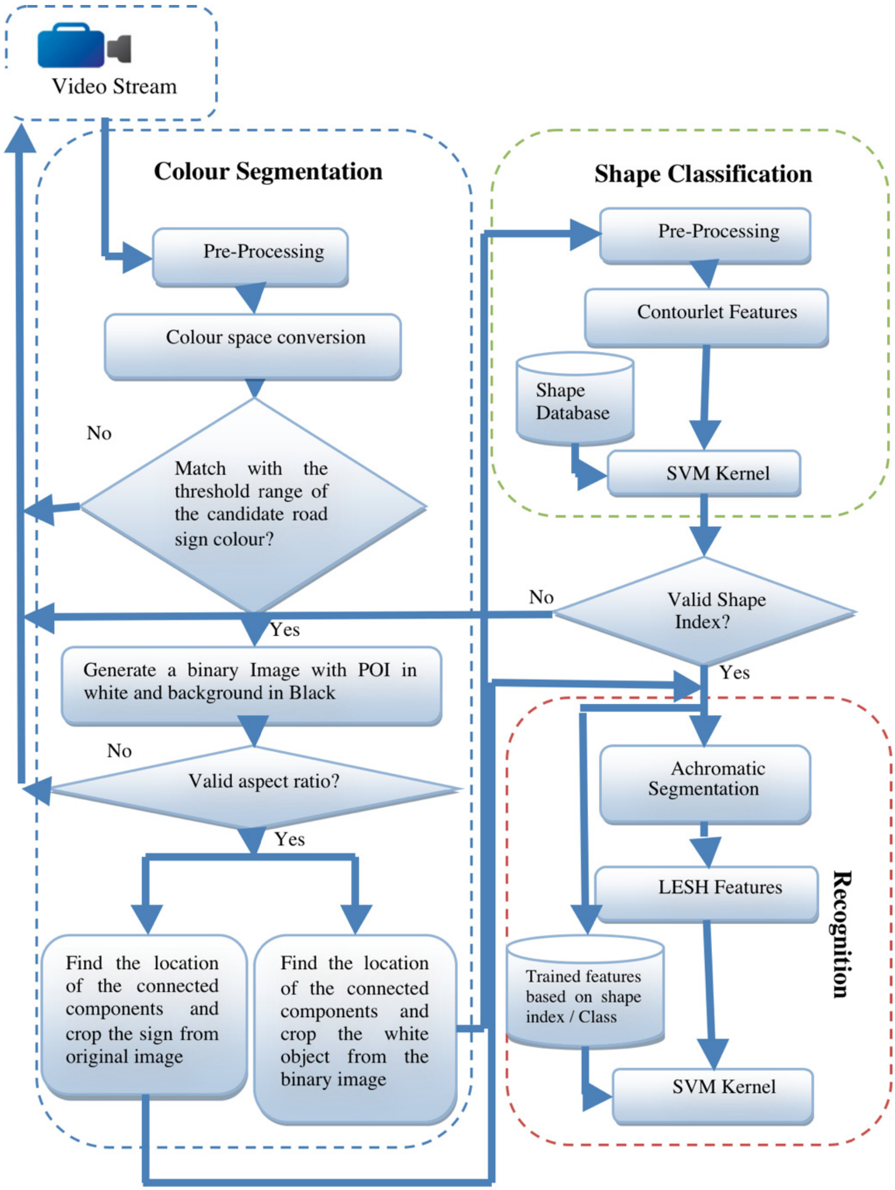

Fig. 2. Road Sign Detection and Recognition framework

The binary input images are pre processed in such a way that only outer candidate shapes are considered in later processing stages. The shape features are extracted by using Contourlet Transform [6] and SVM polynomial kernel [7] is employed to classify the extracted features. The robustness of the proposed shape identification and classification is particularly tested on road signs with abnormal appearances, i.e. ones that are partially occluded, may be of different sizes (scale) and orientations. The shape-based analysis of road signs is helpful in two ways in the RSDR. Firstly, it removes the false positives extracted as candidate road signs during colour-based segmentation. Secondly, subsequent detailed content recognition in road signs will only be performed on road signs belonging to a particular shape group i.e., circular, rectangular or triangular.

3.3 Recognition

Once the candidate shape is classified, it initiates the process of recognition and classification of the road sign contents. The recognition process comprises of the LESH [1], [5] features extraction of the road sign contents and training/testing of these features by employing SVM polynomial kernel. The candidate road signs, which are validated in first two modules i.e. Colour Segmentation and Shape Classification, are further processed to obtain the valid road sign contents for feature extraction. The internal contents of road signs are normally represented as black and white colours. The white and black areas can be extracted by simple black and white region extraction using adaptive threshold. After obtaining the binary images, the connected components from the binary image are extracted which removes the noisy objects (non sign objects) at the same time. The image(s) are normalised to a square dimensional image of size 128×128 and at the same time converted to grey level image. It should be reminded that the image normalisation to a fixed dimensional size and its grey level conversion are the valid input requirements for LESH feature extraction. The next stage is to extract the LESH features of the normalized images, which are obtained through the pre processing stage. LESH features are obtained by computing the local energy along each filter orientation of image sub-region. The overall histogram represents the concatenated histograms, which are computed along each sub-region of the image. These extracted LESH features from different classes of road signs are trained and classified with the help of multiclass SVM polynomial kernel.

4 Experimental Setup and Results

This section provides three experiments carried out on the video samples, which were recorded during varying lighting conditions. The resolution 640×480 pixels is used to capture testing video samples where as 2592×1944 pixels resolution is used to capture images for training purposes. The hardware comprises of *Canon IXUS80IS* digital camera for image and video acquisition, Pentium 4 Dual Core 3.2 Ghz, and 4 GB of RAM. The RSDR application is developed and tested by using Visual Studio .Net and signal and image processing toolboxes of MATLAB.

4.1 Experiment-1

The experiment provided in this section is carried out on speed limit (*Set-1*) signs i.e. ‘15’,’30’,’40’,’50’ and,’70’ which are given class labels as T1, T2, T3, T4 and T5 respectively as presented in Table 1. The *Set-1* road signs were already trained using 40 image samples per class. The testing is performed on video samples containing only speed limit signs; captured during various lighting conditions, were influenced by scale changes and partial occlusions. The confusion matrix of tested road signs is tabulated in Table 1. The ROC (Receiver Operating Characteristic) curve for tested *Set-1* signs is presented in Fig 3 in red colour where true positives are plotted against false positives.

Table 1. Confusion Matrix of tested speed limit road signs

Set-1	True Labels	Estimated Labels					Totals
		1	2	3	4	5	
	**T1**	28	0	0	0	0	**28**
	**T2**	0	64	0	0	1	**65**
	**T3**	0	0	40	1	1	**42**
	**T4**	0	0	0	18	4	**22**
	**T5**	0	2	1	2	24	**29**
	Totals	**28**	**66**	**41**	**21**	**30**	**186**

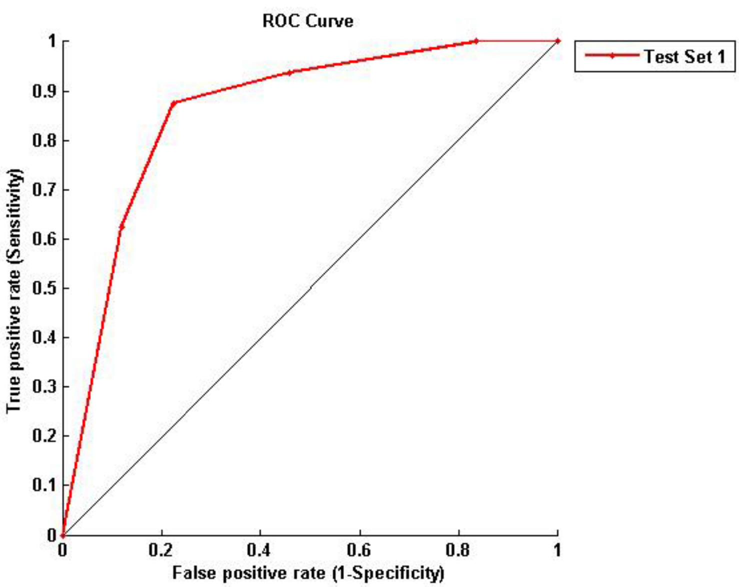

Fig. 3. ROC curve of Set-1

4.2 Experiment-2

This experiment is carried out on 5 different triangular (*Set-2*) signs, i.e., 'GIVEWAY', 'Round About', 'Bend to Left Ahead', 'T-Junction' and 'Slippery Road' which are given class labels as T6, T7, T8, T9 and T10 respectively (see Table 2). The training of *Set-2* road signs was performed on 40 image samples per class. The testing is performed on the video samples which represents only *Set-2* road signs, captured during varying lighting and environmental conditions, with changes in scale and includes partial occlusion. The confusion matrix of tested road signs for this experiment is presented in Table 2. Finally, the ROC curve for the tested *Set-2* road signs is presented in Fig. 4 in blue colour where true positives are plotted against false positives.

Table 2. Confusion Matrix of tested Set-2 road signs

Set-2	True Labels	Estimated Labels					Totals
		6	7	8	9	10	
	T6	56	0	0	0	0	**56**
	T7	0	64	0	1	0	**65**
	T8	0	0	49	0	1	**50**
	T9	0	1	1	35	7	**44**
	T10	0	0	0	9	52	**61**
	Totals	**56**	**65**	**50**	**45**	**60**	**276**

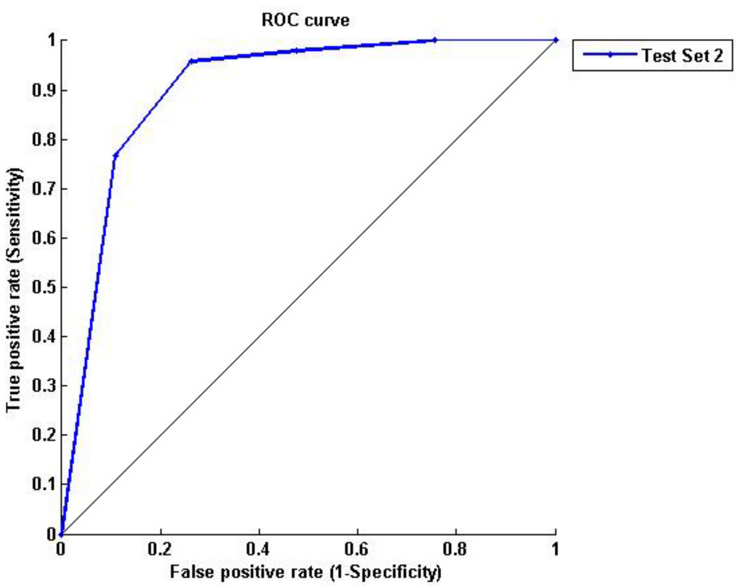

Fig. 4. ROC curve of Set-2

4.3 Experiment-3

Set-3 is a further group of miscellaneous road signs (e.g. Advisory and Obligatory etc.) i.e. '*Priority*', '*Stop*', '*Turn Left*', '*No Entry*' and '*Round About*', and they are given class labels for this experiment as *T11, T12, T13, T14 and T15* respectively presented in Table 3. The training of *Set-3* road signs is performed on 40 image samples per class. The testing is performed on the video samples of Set-3 road signs captured during poor weather conditions, partial occlusion and abnormal orientation. The confusion matrix of tested road signs belongs to *Set-3* is presented in table 3. The ROC curve for tested *Set-3* road signs is presented in Fig.5 in colour green where true positives are plotted against false positives.

Table 3. Confusion Matrix of tested Set-3 road signs

Set-3	**True Labels**	**Estimated Labels**					**Totals**
		11	**12**	**13**	**14**	**15**	
	**T11**	12	0	0	0	1	**13**
	**T12**	1	28	0	0	2	**31**
	**T13**	0	0	8	0	6	**14**
	**T14**	1	3	3	12	0	**19**
	**T15**	0	0	3	5	18	**26**
	Totals	**14**	**31**	**14**	**17**	**27**	**103**

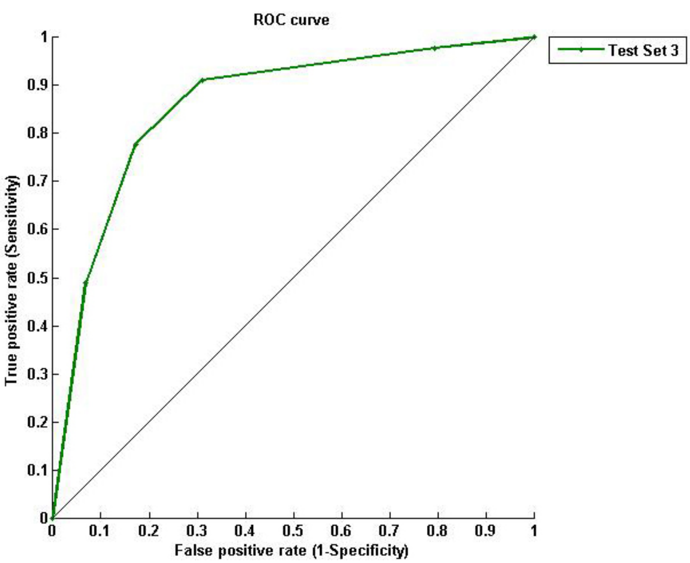

Fig. 5. ROC curve of Set-3

5 Conclusion

In this paper we have presented a novel approach towards road sign detection and recognition. The system utilizes a robust method of Colour Segmentation by employing the HSV colour space and using empirically determined threshold values suitable for various illumination conditions. A novel Shape Classification methodology is proposed in which all possible road sign shapes are classified by introducing the use of Contourlet Transform with SVM classifier. The Recognition stage introduces the SVM classifier with the Local Energy based Shape Histogram (LESH) features. Providing three experiments considering varying levels of illumination and environmental conditions proves the effectiveness of proposed approach. Overall accuracy figures of 96-98% have been reported. We are currently working on real time application of the algorithm within an in-car navigation system.

Acknowledgments. The Royal Society of Edinburgh (RSE) and the National Natural Science Foundation of China (NNSFC) supports Dr. Amir Hussain under the RSE-NNSFC joint projects (2012-2014) with Prof. Jun Wang of Beihang University China and Prof. Bin Luo of Anhui University China.

References

1. Zakir, U., Zafar, I., Edirisinghe, A.E.: Road Sign Detection and Recognition by using Local Energy Based Shape Histogram (LESH). International Journal of Image Processing 4(6), 566–582 (2011) ISSN: 1985-2304
2. Automatic Road Sign Detection and Recognition. PhD Thesis, Computer Science Loughborough University (2011), `http://lboro.academia.edu/usmanzakir/Papers/1587192/Automatic_Road_Sign_Detection_And_Recognition`
3. Gamma Correction, `http://en.wikipedia.org/wiki/Gamma_correction`
4. Zakir, U., Leonce, J.N.A., Edirisinghe, A.E.: Road sign segmentation based on colour spaces: A Comparative Study. In: Proceedings of the 11th Iasted International Conference on Computer Graphics and Imgaing, Innsbruck, Austria (2010)
5. Sarfraz, S.M., Hellwich, O.: An Efficient Front-end Facial Pose Estimation System for Face Recognition. International Journal of Pattern Recognition and Image Analysis, distributed by Springer 18(3), 434–441 (2008)
6. Do, N.M., Vetterli, M.: The Contourlet Transform: An Efficient Directional Multi resolution Image Representation. IEEE Transactions on Image Processing 14(12) (2005)
7. Duin, W.P.R., Juszczak, P., Paclik, P., Pekalska, E., de Ridder, D., Tax, J.M.D., Verzakov, S.: PRTools4.1, A Matlab Toolbox for Pattern Recognition. Delft University of Technology (2007)

Author Index